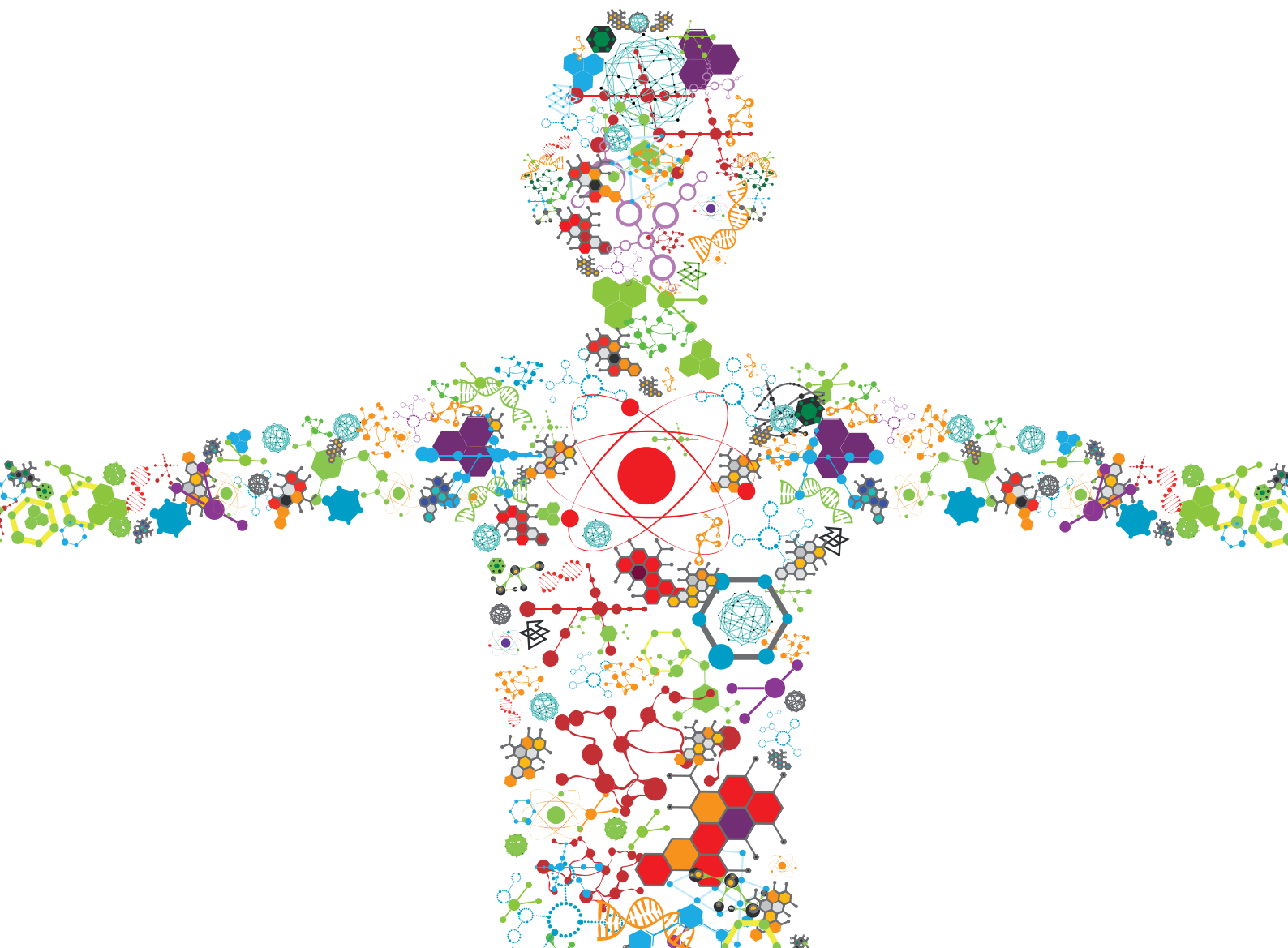


# 3D-PRINTED BIOMATERIALS IN OSTEOCHONDRAL REPAIR

EDITED BY: Lei Zhang, Xiaofeng Jia, Changchun Zhou and Lan Li  
PUBLISHED IN: Frontiers in Bioengineering and Biotechnology





# frontiers

## Frontiers eBook Copyright Statement

The copyright in the text of individual articles in this eBook is the property of their respective authors or their respective institutions or funders. The copyright in graphics and images within each article may be subject to copyright of other parties. In both cases this is subject to a license granted to Frontiers.

The compilation of articles constituting this eBook is the property of Frontiers.

Each article within this eBook, and the eBook itself, are published under the most recent version of the Creative Commons CC-BY licence.

The version current at the date of publication of this eBook is CC-BY 4.0. If the CC-BY licence is updated, the licence granted by Frontiers is automatically updated to the new version.

When exercising any right under the CC-BY licence, Frontiers must be attributed as the original publisher of the article or eBook, as applicable.

Authors have the responsibility of ensuring that any graphics or other materials which are the property of others may be included in the CC-BY licence, but this should be checked before relying on the CC-BY licence to reproduce those materials. Any copyright notices relating to those materials must be complied with.

Copyright and source acknowledgement notices may not be removed and must be displayed in any copy, derivative work or partial copy which includes the elements in question.

All copyright, and all rights therein, are protected by national and international copyright laws. The above represents a summary only. For further information please read Frontiers' Conditions for Website Use and Copyright Statement, and the applicable CC-BY licence.

ISSN 1664-8714

ISBN 978-2-83250-135-1

DOI 10.3389/978-2-83250-135-1

## About Frontiers

Frontiers is more than just an open-access publisher of scholarly articles: it is a pioneering approach to the world of academia, radically improving the way scholarly research is managed. The grand vision of Frontiers is a world where all people have an equal opportunity to seek, share and generate knowledge. Frontiers provides immediate and permanent online open access to all its publications, but this alone is not enough to realize our grand goals.

## Frontiers Journal Series

The Frontiers Journal Series is a multi-tier and interdisciplinary set of open-access, online journals, promising a paradigm shift from the current review, selection and dissemination processes in academic publishing. All Frontiers journals are driven by researchers for researchers; therefore, they constitute a service to the scholarly community. At the same time, the Frontiers Journal Series operates on a revolutionary invention, the tiered publishing system, initially addressing specific communities of scholars, and gradually climbing up to broader public understanding, thus serving the interests of the lay society, too.

## Dedication to Quality

Each Frontiers article is a landmark of the highest quality, thanks to genuinely collaborative interactions between authors and review editors, who include some of the world's best academicians. Research must be certified by peers before entering a stream of knowledge that may eventually reach the public - and shape society; therefore, Frontiers only applies the most rigorous and unbiased reviews.

Frontiers revolutionizes research publishing by freely delivering the most outstanding research, evaluated with no bias from both the academic and social point of view. By applying the most advanced information technologies, Frontiers is catapulting scholarly publishing into a new generation.

## What are Frontiers Research Topics?

Frontiers Research Topics are very popular trademarks of the Frontiers Journals Series: they are collections of at least ten articles, all centered on a particular subject. With their unique mix of varied contributions from Original Research to Review Articles, Frontiers Research Topics unify the most influential researchers, the latest key findings and historical advances in a hot research area! Find out more on how to host your own Frontiers Research Topic or contribute to one as an author by contacting the Frontiers Editorial Office: [frontiersin.org/about/contact](http://frontiersin.org/about/contact)



# 3D-PRINTED BIOMATERIALS IN OSTEOCHONDRAL REPAIR

Topic Editors:

**Lei Zhang**, Wenzhou Medical University, China

**Xiaofeng Jia**, University of Maryland, United States

**Changchun Zhou**, Sichuan University, China

**Lan Li**, Nanjing Drum Tower Hospital, China

**Citation:** Zhang, L., Jia, X., Zhou, C., Li, L., eds. (2022). 3D-printed Biomaterials in Osteochondral Repair. Lausanne: Frontiers Media SA.  
doi: 10.3389/978-2-83250-135-1

# Table of Contents

- 05 Editorial: 3D-printed Biomaterials in Osteochondral Repair**  
Changchun Zhou, Lan Li, Xiaofeng Jia and Lei Zhang
- 08 Biomimetic Methacrylated Gelatin Hydrogel Loaded With Bone Marrow Mesenchymal Stem Cells for Bone Tissue Regeneration**  
Jun Li, Wenzhao Wang, Mingxin Li, Ping Song, Haoyuan Lei, Xingyu Gui, Changchun Zhou and Lei Liu
- 19 Laser Additively Manufactured Iron-Based Biocomposite: Microstructure, Degradation, and In Vitro Cell Behavior**  
Youwen Yang, Guoqing Cai, Mingli Yang, Dongsheng Wang, Shuping Peng, Zhigang Liu and Cijun Shuai
- 31 Synthesis of Silica-Based Solid-Acid Catalyst Material as a Potential Osteochondral Repair Model In Vitro**  
Rui-Min Long, Yan Jiang, Jia-Qi Guo, Gang Ren, Xian-Xin Guo, Xue Xie, Yue Wu, Rui-Da Yan, Zi-Zhen Lin, Shi-Bin Wang and Yuan-Gang Liu
- 40 Analysis of Mechanical Properties and Permeability of Trabecular-Like Porous Scaffold by Additive Manufacturing**  
Long Chao, Chen Jiao, Huixin Liang, Deqiao Xie, Lida Shen and Zhidong Liu
- 53 Porous Bioactive Prosthesis With Chitosan/Mesoporous Silica Nanoparticles Microspheres Sequentially and Sustainedly Releasing Platelet-Derived Growth Factor-BB and Kartogenin: A New Treatment Strategy for Osteoarticular Lesions**  
Zhiguo Yuan, Zhuocheng Lyu, Wei Zhang, Jue Zhang and You Wang
- 68 3D Printing for Bone-Cartilage Interface Regeneration**  
Jialian Xu, Jindou Ji, Juyang Jiao, Liangjun Zheng, Qimin Hong, Haozheng Tang, Shutao Zhang, Xinhua Qu and Bing Yue
- 87 A Novel Adjustable EndoButton Fixation Assisted by 3D Printing Technology for Tibiofibular Syndesmosis Injury: A Biomechanical Study**  
Lei Zhang, Junjie Xu, Xiangyu Tang, Xin Zhou, Bingkun Li and Guoyou Wang
- 96 Injectable Photo-Crosslinked Bioactive BMSCs-BMP2-GelMA Scaffolds for Bone Defect Repair**  
Senlin Chai, Jianhao Huang, Abdurahman Mahmut, Bin Wang, Yao Yao, Xiaofeng Zhang, Zaikai Zhuang, Chunmei Xie, Zhihong Xu and Qing Jiang
- 107 Preparation of BMP-2/PDA-BCP Bioceramic Scaffold by DLP 3D Printing and its Ability for Inducing Continuous Bone Formation**  
Ziyang Yang, Li Xie, Boqing Zhang, Gang Zhang, Fangjun Huo, Changchun Zhou, Xi Liang, Yujiang Fan, Weidong Tian and Yinghui Tan
- 123 A Biomimetic Platelet-Rich Plasma-Based Interpenetrating Network Printable Hydrogel for Bone Regeneration**  
Shijia Tang, Lin Wang, Yunyang Zhang and Feimin Zhang
- 137 Osteogenesis of Iron Oxide Nanoparticles-Labeled Human Precartilaginous Stem Cells in Interpenetrating Network Printable Hydrogel**  
Wei Liao, Jingwei Lu, Qianjin Wang, Sen Yan, Yan Li, Yibo Zhang, Peng Wang, Qing Jiang and Ning Gu

- 149** *Three-Dimensional Cartilage Regeneration Using Engineered Cartilage Gel With a 3D-Printed Polycaprolactone Framework*  
Gaoyang Wu, Lixing Lu, Zheng Ci, Yahui Wang, Runjie Shi, Guangdong Zhou and Shengli Li
- 162** *Customized Design 3D Printed PLGA/Calcium Sulfate Scaffold Enhances Mechanical and Biological Properties for Bone Regeneration*  
Tao Liu, Zhan Li, Li Zhao, Zehua Chen, Zefeng Lin, Binglin Li, Zhibin Feng, Panshi Jin, Jinwei Zhang, Zugui Wu, Huai Wu, Xuemeng Xu, Xiangling Ye and Ying Zhang
- 177** *Surface Roughness and Biocompatibility of Polycaprolactone Bone Scaffolds: An Energy-Density-Guided Parameter Optimization for Selective Laser Sintering*  
Jian Han, Zehua Li, Yuxuan Sun, Fajun Cheng, Lei Zhu, Yaoyao Zhang, Zirui Zhang, Jinzhe Wu and Junfeng Wang



## OPEN ACCESS

EDITED AND REVIEWED BY  
Hasan Uludag,  
University of Alberta, Canada

## \*CORRESPONDENCE

Lei Zhang,  
zhanglei@wmu.edu.cn

<sup>†</sup>These authors contributed equally to this work

## SPECIALTY SECTION

This article was submitted to Biomaterials, a section of the journal Frontiers in Bioengineering and Biotechnology

RECEIVED 01 July 2022

ACCEPTED 01 July 2022

PUBLISHED 16 August 2022

## CITATION

Zhou C, Li L, Jia X and Zhang L (2022), Editorial: 3D-printed biomaterials in osteochondral repair. *Front. Bioeng. Biotechnol.* 10:983945. doi: 10.3389/fbioe.2022.983945

## COPYRIGHT

© 2022 Zhou, Li, Jia and Zhang. This is an open-access article distributed under the terms of the [Creative Commons Attribution License \(CC BY\)](#). The use, distribution or reproduction in other forums is permitted, provided the original author(s) and the copyright owner(s) are credited and that the original publication in this journal is cited, in accordance with accepted academic practice. No use, distribution or reproduction is permitted which does not comply with these terms.

# Editorial: 3D-printed biomaterials in osteochondral repair

Changchun Zhou<sup>1†</sup>, Lan Li<sup>2†</sup>, Xiaofeng Jia<sup>3†</sup> and Lei Zhang<sup>4\*</sup>

<sup>1</sup>National Engineering Research Center for Biomaterials, College of Biomedical Engineering, Sichuan University, Chengdu, China, <sup>2</sup>Nanjing Drum Tower Hospital, Nanjing, China, <sup>3</sup>Department of Neurosurgery, Orthopaedics, and Anatomy & Neurobiology, School of Medicine, University of Maryland, Baltimore, MD, United States, <sup>4</sup>Department of Orthopaedics, The First Affiliated Hospital of Wenzhou Medical University, Wenzhou, China

## KEYWORDS

3D printing, bone repair, chondral regeneration, tissue engineering, regenerative medicine

## Editorial on the Research Topic

### 3D-printed biomaterials in osteochondral repair

Osteochondral lesion appears a significant challenge for orthopaedic surgeons worldwide, and is often associated with multiple factors such as acute trauma or degenerative processes. To overcome major challenges facing massive bone or cartilage defects, three-dimensional (3D) printing technology has been developed rapidly in recent years, and shows broad prospects in osteochondral repair, leading to favorable clinical outcomes. Currently, an increasing number of novel nanocomposite biomimetic biomaterials, based on 3D printing technology, have shown promise for bone and cartilage engineering. Therefore, to highlight the latest progress, this Research Topic aims to provide an update on the novel 3D printing technologies and biomaterials.

Here, the Research Topic collected a total of 14 papers, including 13 original articles and one review, which cover a wide range of the novel 3D-printed biomaterials, from the design, preparation, evaluation to preclinical application, and summarize the significant progress and applications of 3D printing technology for bone-cartilage interface regeneration. The papers in this topic are briefly shared below.

To overcome the limitations of mismatched mechanical and unsatisfactory biological properties of PLGA in bone tissue engineering, [Liu et al.](#) added calcium sulfate and prepared a new customized-designed 3D porous PLGA/CaSO<sub>4</sub> scaffold. These 3D-printed scaffolds exhibited not only satisfactory biocompatibility, but enhanced mechanical and biological properties as well. These customized fabricated PLGA/CaSO<sub>4</sub> scaffolds show great potential for precisely repairing irregular load-bearing bone defects.

Recommendations for surgical fixation of tibiofibular syndesmosis injuries are challenging task for many clinical orthopedists due to international consensus has not been published for the optimal treatment of the injury. [Zhang et al.](#) created a 3D printed navigation template for a precise bone tunnel and a novel adjustable EndoButton fixation

(NAE) for the ideal treatment. The accuracy of the 3D-printed navigation template and the biomechanical performance of the NAE technique have been well evaluated and explored. The 3D printing technology application may become beneficial and favorable for locating and preparing the bone tunnel.

The rational structural design of the trabecular porous scaffold is a key point for the satisfactory efficacy of the implant. [Chao et al.](#) prepared porous scaffolds with biomimetic potential based probability balls and the Voronoi–Tessellation approach. These 3D-printed biomaterials appeared trabecular-like porous microstructure and tissue morphology, which can address stress shielding and bone ingrowth in existing biomimetic bone structures. In addition, the scaffolds could also promote cell adhesion, migration, and eventual new bone attachment. Based on the existing research, animal implantation experiments should be carried out to verify the biological properties of porous micro-structures.

[Chai et al.](#) created a photo-crosslinked composite bioactive scaffold based on GelMA-BMSCs-BMP2. The composite bioactive scaffolds effectively promoted the osteogenic differentiation and bone tissue regeneration of BMSCs, and the biosafety of the composite scaffold was verified *in vivo* and *in vitro* experiments. Therefore, BMP2 and BMSCs in GelMA hydrogel scaffolds showed good synergistic effects on encouraging bone defect repair, and thus offered a new option for the treatment of irregular bone deformities.

Precartilaginous stem cells (PCSCs) can be used as seed cells and incorporated with bioactive scaffolds for reconstructive tissue therapy of bone defects, and iron oxide nanoparticles (IONPs) can enhance osteogenic differentiation potential by modulating the fate of PCSCs. [Liao et al.](#) revealed osteogenesis of PCSCs induced by IONPs, as evidenced by enhanced ALP activity levels, mineralized matrix nodules, and osteogenesis-related gene expression. In addition, the IONPs-labeled PCSCs-incorporated polymeric printable network (IPN) hydrogel was of great printability, biosafety, and improvement of cell spreading and proliferation. Therefore, PCSCs-based scaffolds could enrich the stem cell-based therapeutic strategies for bone tissue regeneration.

For osteochondral damage, the pH value change of the damaged site will influence the repair efficacy of the patient. [Long et al.](#) constructed a *vitro* model which provided a simple and practical platform to evaluate the influence of the acid-base effect. The study prepared a porous silica-based solid-acid catalyst material by additive manufacturing technology and the results showed excellent catalytic performance. The catalytic strategy by constructing a *vitro* model supplies an alternative way in environment evaluation of osteochondral repair and it also shows potential for the enzymatic catalytic research during the body's metabolism process in the future studies.

Besides cartilage itself, the research of cartilage regeneration should additionally consider the subchondral bone, which also

plays a critical role in its process. Therefore, the integrated repair of bone-cartilage may be the future direction of tissue engineering scaffolds. [Xu et al.](#) summarized the latest and significant developments in bone-cartilage interface regeneration using 3D printing techniques. The recent progress of bioinks, scaffold structures, bioactive factors, and bioreactors were detailed described in this review. In addition, the potential prospects and challenges of 3D printing techniques in bone-cartilage tissue engineering were also particularly exhibited.

Based on the concept of integrated repair of bone-cartilage, [Yuan et al.](#) designed a novel polyetheretherketone (PEEK) scaffold. This porous non-degradable scaffold was modified using the chitosan, mesoporous silica nanoparticles, platelet-derived growth factor BB, kartogenin, and polydopamine. The composite scaffold gained both osteogenic and chondrogenic capacity. It could promote cell migration and enhance chondrogenic differentiation of BMSCs *in vitro*, and facilitate cartilage regeneration *in vivo*. This study reveals a new therapeutic concept of porous bioactive prosthesis for osteoarticular lesions.

Polycaprolactone (PCL) is another generally used biomaterial for fabricating rigid scaffold framework. [Wu et al.](#) explored the feasibility of replacing the decalcified bone matrix (DBM) framework with a PCL framework. They found that the inflammatory response was reduced and the mature cartilage can be constructed by this scaffold. The components of the regenerated cartilage were closer to the natural cartilage. The 3D-printed PCL framework method shows the unique advantage in clinical cartilage regeneration due to the features of customizable shape design, mechanical strength control, and standardized production.

For the purpose of mimicking the natural bone components and promoting bone regeneration using a cell-free scaffold, [Tang et al.](#) developed a photocrosslinked interpenetrating polymeric network (IPN) bioink. Through the introducing of platelet-rich plasma and biological mineralization, the osteogenic bioactivities can be effectively enhanced. The *in vivo* study has proved that this IPN hydrogel can significantly accelerate bone regeneration and can be regarded as a promising strategy in the fabrication of 3D-printed bone scaffolds.

The metal-based 3D printed scaffolds are one of the options for bone regeneration. [Yang et al.](#) employed laser additive manufacturing technique to fabricate a Fe/calcium chloride (CaCl<sub>2</sub>) based composite scaffold. Compared to traditional Fe-based scaffold, the addition of CaCl<sub>2</sub> could strongly improve the stability and corrosion resistance. The surface topography was also affected by the release of chloride ion during the manufacture and corrosion process. The osteogenic ability was enhanced due to the existence of Ca ion. This composite iron combination demonstrated admirable prospects in bone scaffold fabrication.

The organic combination of biomimetic materials and stem cells offers new strategies for bone tissue engineering, and the fate

of stem cells is closely related to their extracellular matrix (ECM) properties. Li et al. prepared a photocrosslinked biomimetic methacrylated gelatin (Bio-GelMA) hydrogel scaffold loaded with BMSCs to examine the therapeutic effects of ECM-loaded cells in a 3D environment simulated for segmental bone defects. The results showed that the BMSC-carrying GelMA hydrogel scaffold has good mechanical properties and biological compatibility. In addition, the bio-GelMA scaffold can be used as a cell carrier of BMSC to promote the regeneration of bone and blood vessels, to improve the mechanical strength of bone defects, and to effectively promote the repair of bone defects. Therefore, the BMSC-carrying GelMA hydrogel scaffold offered a new option for the treatment of segment bone defects.

The micro geometry and surface roughness of PCL scaffolds may change the biocompatibility and bioactivity of the scaffolds during the SLS process. However, it is still unknown how SLS process parameters affect the surface roughness of PCL scaffolds and the relationship between roughness and biocompatibility of scaffolds. Han et al. prepared five PCL scaffolds with different laser power and scanning speed. Furthermore, the study calculated the energy density range (Ed1-Ed3) suitable for PCL sintering by using the energy density model (EDM) combined with the thermodynamic properties of PCL powder. As the result, the dense and smooth surface of scaffolds had poor cytocompatibility, while the low energy density (Ed1) resulted in weak mechanical properties, but the rough surface caused by incomplete sintered PCL particles facilitated the cells adhesion and proliferation. Therefore, the surface roughness and related biocompatibility of PCL bone scaffolds should be considered in energy-density-guided SLS parameters optimization.

Yang et al. fabricated porous DLP-printed BCP bioceramic scaffolds coated with polydopamine/BMP-2. The scaffolds with superhydrophilicity and BMP-2 delivery and sustained-release abilities exhibited an interconnected porous structure and

acceptable compressive strength matched with load-free cancellous bone. In addition, the BMP-2/PDA-BCP scaffold presented favorable effects on the adhesion, proliferation, osteogenic differentiation, and mineralization of BMSCs. *In vivo* results of SD rats demonstrated the PDA coating induced cell aggregation nearby the coating and continuous lamellar new bone formation within the scaffold. This study provided a promising strategy to fabricate bone substitute scaffolds for enhanced bone regeneration for bone defects in demand for high precision and small size.

## Author contributions

CZ, LL and LZ drafted the manuscript. XJ revised the manuscript critically.

## Conflict of interest

The authors declare that the research was conducted in the absence of any commercial or financial relationships that could be construed as a potential conflict of interest.

## Publisher's note

All claims expressed in this article are solely those of the authors and do not necessarily represent those of their affiliated organizations, or those of the publisher, the editors and the reviewers. Any product that may be evaluated in this article, or claim that may be made by its manufacturer, is not guaranteed or endorsed by the publisher.





# Biomimetic Methacrylated Gelatin Hydrogel Loaded With Bone Marrow Mesenchymal Stem Cells for Bone Tissue Regeneration

Jun Li<sup>1†</sup>, Wenzhao Wang<sup>1†</sup>, Mingxin Li<sup>1</sup>, Ping Song<sup>2,3</sup>, Haoyuan Lei<sup>2,3</sup>, Xingyu Gui<sup>2,3</sup>, Changchun Zhou<sup>2,3\*</sup> and Lei Liu<sup>1\*</sup>

<sup>1</sup>Department of Orthopedics, Orthopedic Research Institute, National Clinical Research Center for Geriatrics, West China Hospital, Sichuan University, Chengdu, China, <sup>2</sup>National Engineering Research Center for Biomaterials, Sichuan University, Chengdu, China, <sup>3</sup>College of Biomedical Engineering, Sichuan University, Chengdu, China

## OPEN ACCESS

### Edited by:

Liqiang Wang,  
Shanghai Jiao Tong University, China

### Reviewed by:

Jianxun Ding,  
Changchun Institute of Applied  
Chemistry (CAS), China  
Jennifer Patterson,  
Instituto IMDEA Materiales, Spain

### \*Correspondence:

Changchun Zhou  
changchunzhou@scu.edu.cn  
Lei Liu  
liuinsistence@163.com

<sup>†</sup>These authors have contributed  
equally to this work

### Specialty section:

This article was submitted to  
Biomaterials,  
a section of the journal  
Frontiers in Bioengineering and  
Biotechnology

**Received:** 03 September 2021

**Accepted:** 08 November 2021

**Published:** 02 December 2021

### Citation:

Li J, Wang W, Li M, Song P, Lei H,  
Gui X, Zhou C and Liu L (2021)  
Biomimetic Methacrylated Gelatin  
Hydrogel Loaded With Bone Marrow  
Mesenchymal Stem Cells for Bone  
Tissue Regeneration.  
Front. Bioeng. Biotechnol. 9:770049.  
doi: 10.3389/fbioe.2021.770049

Large-segment bone defect caused by trauma or tumor is one of the most challenging problems in orthopedic clinics. Biomimetic materials for bone tissue engineering have developed dramatically in the past few decades. The organic combination of biomimetic materials and stem cells offers new strategies for tissue repair, and the fate of stem cells is closely related to their extracellular matrix (ECM) properties. In this study, a photocrosslinked biomimetic methacrylated gelatin (Bio-GelMA) hydrogel scaffold was prepared to simulate the physical structure and chemical composition of the natural bone extracellular matrix, providing a three-dimensional (3D) template and extracellular matrix microenvironment. Bone marrow mesenchymal stem cells (BMSCs) were encapsulated in Bio-GelMA scaffolds to examine the therapeutic effects of ECM-loaded cells in a 3D environment simulated for segmental bone defects. *In vitro* results showed that Bio-GelMA had good biocompatibility and sufficient mechanical properties (14.22kPa). A rat segmental bone defect model was constructed *in vivo*. The GelMA-BMSC suspension was added into the PDMS mold with the size of the bone defect and photocured as a scaffold. BMSC-loaded Bio-GelMA resulted in maximum and robust new bone formation compared with hydrogels alone and stem cell group. In conclusion, the bio-GelMA scaffold can be used as a cell carrier of BMSC to promote the repair of segmental bone defects and has great potential in future clinical applications.

**Keywords:** large segment bone defect, GelMA, hydrogel, BMSCs, ECM

## INTRODUCTION

Bone defects are serious health problems that cause hundreds of millions of surgical procedures worldwide each year (Fang et al., 2016). Large bone defects are often sequelae of trauma, tumor (osteosarcoma), or congenital disease (Agarwal and García, 2015). Deficiency of blood supply, infection of the bone or surrounding tissue, systemic diseases, and so on can adversely affect bone healing, leading to delayed union or nonunion of the bone (Giannoudis et al., 2016; Zakhary and Thakker, 2017; Biggemann et al., 2018). Autogenous bone transplantation is the gold standard in the treatment of bone defect (Stanovici et al., 2016). However, the lack of bone donors and the high time and cost of surgery have seriously hindered the clinical application. In addition, allografts from

genetically different species face immune rejection and high reabsorption rates, leading to associated complications (Larsen et al., 2011; Bez et al., 2017). Various artificial materials, such as polymers, inorganic nonmetallic materials, metal materials, and composites, have been used for bone repair or replacement (Cao et al., 2020). However, none of these approaches can help treat patients economically and effectively (Bose et al., 2012; Garot et al., 2020). Repairing large bone defects remains a huge challenge. Bone tissue engineering has become an interdisciplinary field with great potential for development (Kupikowska-Stobba and Kasprzak, 2021). Bone tissue engineering is using new knowledge-based and cell-friendly materials capable of simulating the structural, mechanical, and biological properties of natural bone (Haleem et al., 2020; Gonçalves et al., 2021). Scaffolds and cells are essential components of bone tissue engineering, and the right combination is expected to provide improved clinical treatment (Moreno Madrid et al., 2019). Scaffolds that mimic the structure and composition of bone tissue, also known as bionic scaffolds, have been extensively studied (Cox et al., 2015; Wade et al., 2015).

Bone tissue consists of osteocytes and extracellular matrix (ECM) (Benmassaoud et al., 2020). The ECM is a reservoir of proteins and proteoglycan, and growth factors (Ravindran and George, 2014; Murshed, 2018). ECM provides a cellular microenvironment that is the basis for mineral phase deposition, bone conduction, and bone induction (Alcorta-Sevillano et al., 2020). Some studies have used ECM as a bone conduction matrix for bone regeneration (Chen et al., 2019). Traditional synthetic, biodegradable polymers have been used to improve the performance of biomaterials (Zhang et al., 2019a; Cui et al., 2020). However, most of these polymers are hydrophobic, limiting their ability to encapsulate cells. Hydrogel is a hydrophilic polymer with inherent three-dimensional structure (Zhao et al., 2021). Gelatin is a protein substance obtained from the hydrolysis of collagen, which has good biocompatibility and biodegradation. Gelatin has fewer aromatic groups, so its immunogenicity is obviously low (Xiao et al., 2019). Gelatins contain arginine–glycine–aspartic acid peptide sequences that promote cell adhesion, proliferation, and differentiation, and are therefore suitable for ECM simulation (Sun et al., 2018). In addition, the matrix metalloproteinase of gelatin can promote cell remodeling and further enhance its biological activity (Xiao et al., 2019). The addition of methacrylic anhydride makes the advantages of gelatin easier to be exploited (Pepelanova et al., 2018). Gelatin methylacrylyl (GelMA), made of gelatin and methacrylic anhydride, is a thermally stable cross-linked hydrogel formed by photoinitiator or ultraviolet irradiation (Xiao et al., 2019). Some studies have shown that GelMA can be used to repair bone defects, deposit extracellular matrix and rich type II collagen, and has a good performance in promoting angiogenesis (Xiang and Cui, 2018). In addition, GelMA can be injected into irregularly shaped bone defects and solidified (Gu et al., 2019). However, GelMA lacks the osteogenic induction capacity required for bone mineralization (Qiao et al., 2020). In most studies, GelMA has been used to repair skull defects, but there has been a lack of

research on segmental bone defects, which is one of the most clinically difficult. Mesenchymal stem cell (MSC) is a kind of widely distributed, self-renewing, and differentiated multi-lineage cells (Fu et al., 2019). Bone marrow mesenchymal stem cells (BMSCs) are the most commonly used stem cells in cell therapy and tissue engineering, which can mobilize and migrate from bone marrow to damaged tissue to repair bone and cartilage defects (Zhang et al., 2019b).

In this study, a “soft” and injectable GelMA hydrogel matrix was designed to mimic bone ECM. By rationally controlling the degree of cross-linking density and aperture size, the elastic mechanical properties of GelMA and the mechanical microenvironment of ECM were obtained. Subsequently, BMSC cells were incubated in the hydrogel to test the biocompatibility of the hydrogel *in vitro*. Finally, the *in vivo* reparability of hydrogels was demonstrated in rat models of segmental bone defects. GelMA hydrogel matrix encapsulated with BMSC was an ideal synthetic substitute with excellent osteogenic and angiogenic capabilities.

## MATERIALS AND METHODS

### Animals

In this study, a total of 120 healthy and clean adult female SD rats, aged 4 weeks and weighing 200–250 g, were used and provided by the Experimental Animal Center of West China Clinical Medical College of Sichuan University. Ninety-six of them were only used to construct bone defect models, while the others were used for BMSC isolation and culture. All animal experiments conducted in this study were approved by the animal management and use committee of the West China Clinical Medical College of Sichuan University (approval number: SCXK20150012). The rats were put into a cage 1 week before the experiment to adapt to the environment. Three rats/cage were served with sufficient conventional animal feed, maintaining the room temperature at 21°C, 60% air humidity, and 12-h circadian rhythm.

### Preparation of methacrylated gelatin

The GelMA was synthesized following the procedure described. Briefly, 10 g of gelatin derived from porcine skin was dissolved in 100 ml of PBS in a cleaned Erlenmeyer flask with magnet fish. Then 5 ml of methacrylic anhydride was added very slowly and dropwisely with a syringe pump, and the emulsion was rotated (240 rpm) at 50°C for 2 h and covered with an aluminum foil. Dialysis membrane (Pectro/Por molecular porous membrane tubing, Fisher Scientific, USA) was prepared by cutting them in proper sizes and immersed them into distilled water to soften them. One side was closed by twisting the membrane end and making a knot. The GelMA was transferred with a funnel into the membranes. The second end of the membrane was closed the same way as the first. Membranes were placed into distilled water in a 5-L plastic beaker, and the dialysis was ran at 40°C for 7 days with a magnetic stirrer and covered. The GelMA solution was then quickly and successively filtered with a coffee filter and sterile vacuum Express Plus (0.22 µm) Milipore filtration cup. The sterilized polymer was transferred into 50-ml Falcons and

horizontally stored at  $-80^{\circ}\text{C}$  for 2 days. The frozen GelMA was lyophilized for 3 days and stored in the dark until use.

## Characterization of methacrylated gelatin hydrogel

The GelMA was dissolved in  $\text{D}_2\text{O}$  for analysis using 400-Hz nuclear magnetic resonance (Bruker AVANCE AV II-400 MHz). The degree of methacrylate substitution was determined by the formula:  $1 - (\text{lysine integration signal of GelMA} / \text{lysine integration signal of unsubstituted Gelatin}) \times 100\%$  (Brinkman et al., 2003; Nichol et al., 2010; Loessner et al., 2016). The morphology of the GelMA hydrogel was observed by scanning electron microscope (SEM). Dynamic Mechanical Analyzer (TA Instruments, Q-800, USA) was used to test the storage modulus and loss modulus of the GelMA hydrogel. The rheological properties of the GelMA hydrogel were analyzed by rheometer (MCR302, Anton Paar) (Zhou, 2021).

## Preparation of bone marrow mesenchymal stem cells–methacrylated gelatin hydrogel scaffold

The GelMA solution with a concentration of 5% was prepared by using deionized water, and a photocrosslinking agent (Irgacure 500, BASF Corporation, Germany) with a dosage of 0.25% of GelMA solution (w/v) was added. After mixing the GelMA solution with the photocrosslinking agent evenly, a mixed solution was obtained. The mixed solution was filtered through a  $0.22\text{-}\mu\text{m}$  filter membrane and mixed with BMSCs to make the cell suspension. The cell density in the suspension was  $2 \times 10^6/\text{ml}$  (Stanovici et al., 2016). The bone defect model was constructed according to the needs, and the PDMS mold of the corresponding size ( $4 \times 4 \times 5\text{ cm}$ ) was prepared according to the bone defect model. The suspension of the GelMA–BMSCs was added into the PDMS mold, and UV irradiation ( $\lambda = 365\text{ nm}$ , 40 s) was given. After crosslinking, the GelMA hydrogel bone repair scaffold containing BMSCs was obtained.

## Biocompatibility assessment

The previously prepared BMSC–GelMA hydrogel scaffolds were cultured in normal medium. LIVE/DEAD assay was applied to evaluate the cell viability at 1, 3, 7, and 14 days after culture. The hydrogel scaffolds were washed with PBS and stained with Calcein AM ( $0.5\text{ }\mu\text{l ml}^{-1}$ ) and ethidium homodimer-1 (EthD-1,  $2\text{ }\mu\text{l/ml}$ ) for 2 h at  $37^{\circ}\text{C}$ . The samples were observed under an inverted fluorescence microscope (Nikon, Japan). The number of living and dead cells in the scaffold was counted, and the percentage of living cells in the total number of cells was calculated. Cell Counting Kit-8 (CCK-8, Dojindo, Japan) was used to detect the influence of scaffolds on cell activity on days 1, 4, 7, and 14. A  $10\text{-}\mu\text{l}$  CCK8 solution was added to each well of the 96-well plate, incubated at  $37^{\circ}\text{C}$  for 2 h, and the absorbance at 450 nm was measured with a microplate analyzer (Thermo Scientific, Shanghai, China). Each experiment was repeated at least three times.

## Bone defect model construction and stent implantation

SD rats were randomly divided into four groups (16 rats in each group): group A was the model control group, group B was the GelMA hydrogel scaffold group (control group), BMSCs were in group C (control group), and group D was the GelMA hydrogel scaffold containing BMSCs (experimental group). The rats were anesthetized by intraperitoneal injection of pentobarbital, the hair of the left hind limb was cleaned, sterilized with alcohol, and was covered with a sterile dressing. A longitudinal incision was taken from the posterior middle posterior tibia, and the subcutaneous and muscular layers were incised. A 5-mm-long segmental bone defect was created with a bone saw. In group A, the intramedullary nail was used for retrograde fixation. In group B, the GelMA hydrogel scaffold was implanted and fixed with intramedullary nails. BMSC suspension was injected into the bone defect of group C. In group D, BMSC-loaded GelMA hydrogel scaffolds were implanted and fixed with intramedullary nails. The muscle, subcutaneous tissue, and skin were sewn up step by step. At weeks 4 and 8 after surgery, the bone tissue in the bone defect area was taken for histomorphological test, biomechanical property test, and micro-CT test.

## Histomorphological test

Bone tissue was taken from the bone defect area at weeks 4 and 8 after surgery, and hematoxylin–eosin (HE) staining was performed. The isolated specimens were decalcified through ethylene diamine tetraacetic acid (EDTA, Sigma, USA), dehydrated by 80, 90, and 100% ethanol, and embedded in paraffin. The specimens were then cut into  $5\text{-}\mu\text{m}$  sections and stained with hematoxylin–eosin (HE), and observed under a BX53 microscope (Olympus, Japan). The new bone and new blood vessels were quantitatively analyzed. Experimental data were expressed as mean  $\pm$  SD.

## Biomechanical performance test

On the fourth and eighth weeks after surgery, the tibia of the rats was taken for the biomechanical test. The residual soft tissue was removed, and the tibial tip was trimmed to an appropriate length so that the bone defect was located in the middle of the sample. The three-point bending test (Ruge Technology, China) was performed on the biomechanical tester to measure the bending stiffness and ultimate load to evaluate the biomechanical properties. Experimental data were expressed as mean  $\pm$  SD.

## Micro-CT detection

Bone tissue was taken from the bone defect area on the eighth week after surgery for micro-CT detection, 3D reconstruction of the bone defect area, and quantitative analysis of bone mass and bone density. Specimens were collected and fixed with 4% paraformaldehyde for micro-CT analysis. Micro-CT scanning was performed by a Quantum GX microCT imaging system (Perkin Elmer, USA) with the following settings: acquisition, 36; voxel,  $50\text{ }\mu\text{m}$ ; reconnaissance, 25. The Quantum GX software was used for 3D reconstruction. Experimental data were expressed as mean  $\pm$  SD.

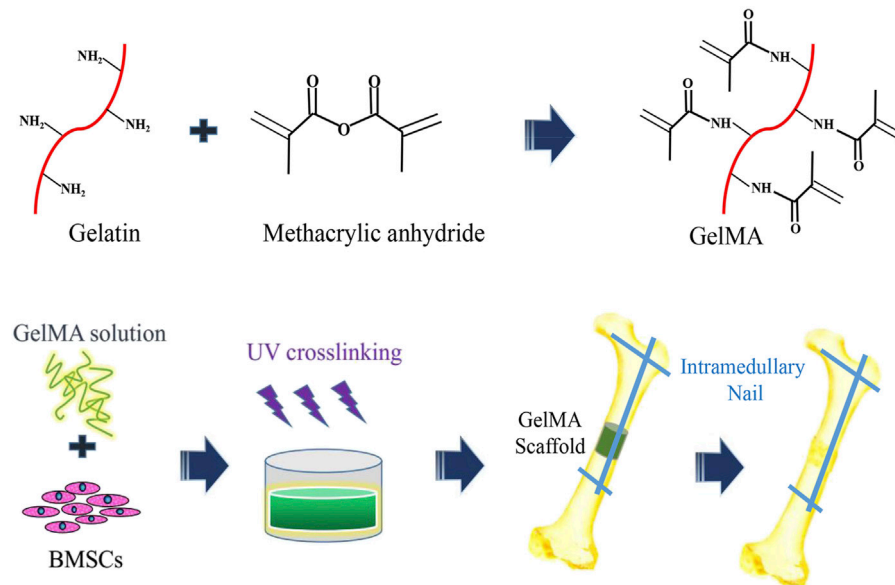


**FIGURE 1** | The schematic diagram of preparation of three-dimensional (3D) bone repair scaffolds supported by hydrogel cells and segments of bone graft defects.

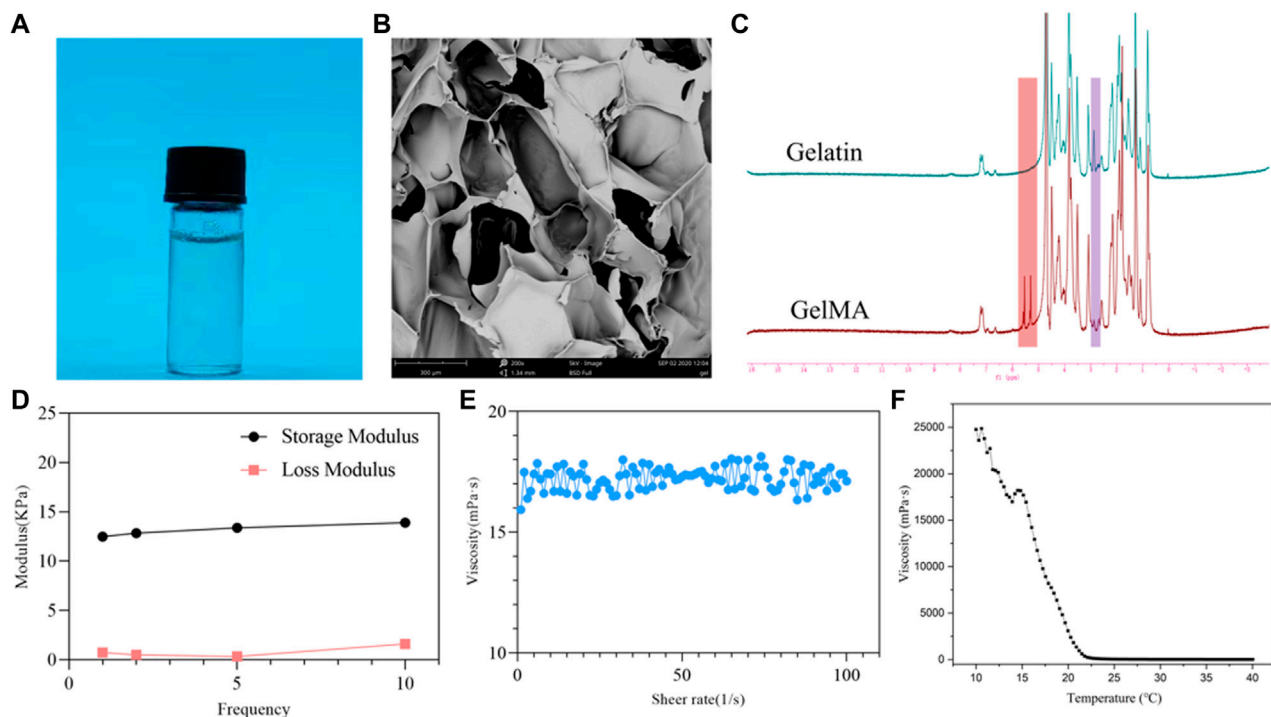


**FIGURE 2** | physicochemical properties of the methacrylated gelatin (GelMA) hydrogel. **(A)** GelMA solution; **(B)** scanning electron microscope (SEM) image of the GelMA hydrogel; **(C)** <sup>1</sup>H-MR spectra of GelMA and gelatin; **(D)** DMA analysis of GelMA hydrogel with frequency dependency; **(E)** shear thinning of GelMA solution; **(F)** the viscosity of GelMA solution from 40°C to 10°C.

## Statistical analysis

Statistical analyses were performed using Statistical Package for the Social Sciences (SPSS 19.0, IBM, New York, NY, USA). All data were expressed as the mean

value  $\pm$  standard deviation (SD). Statistical comparisons were conducted using analysis of variance (ANOVA) in which a *p*-value of less than 0.05 was considered statistically significant.



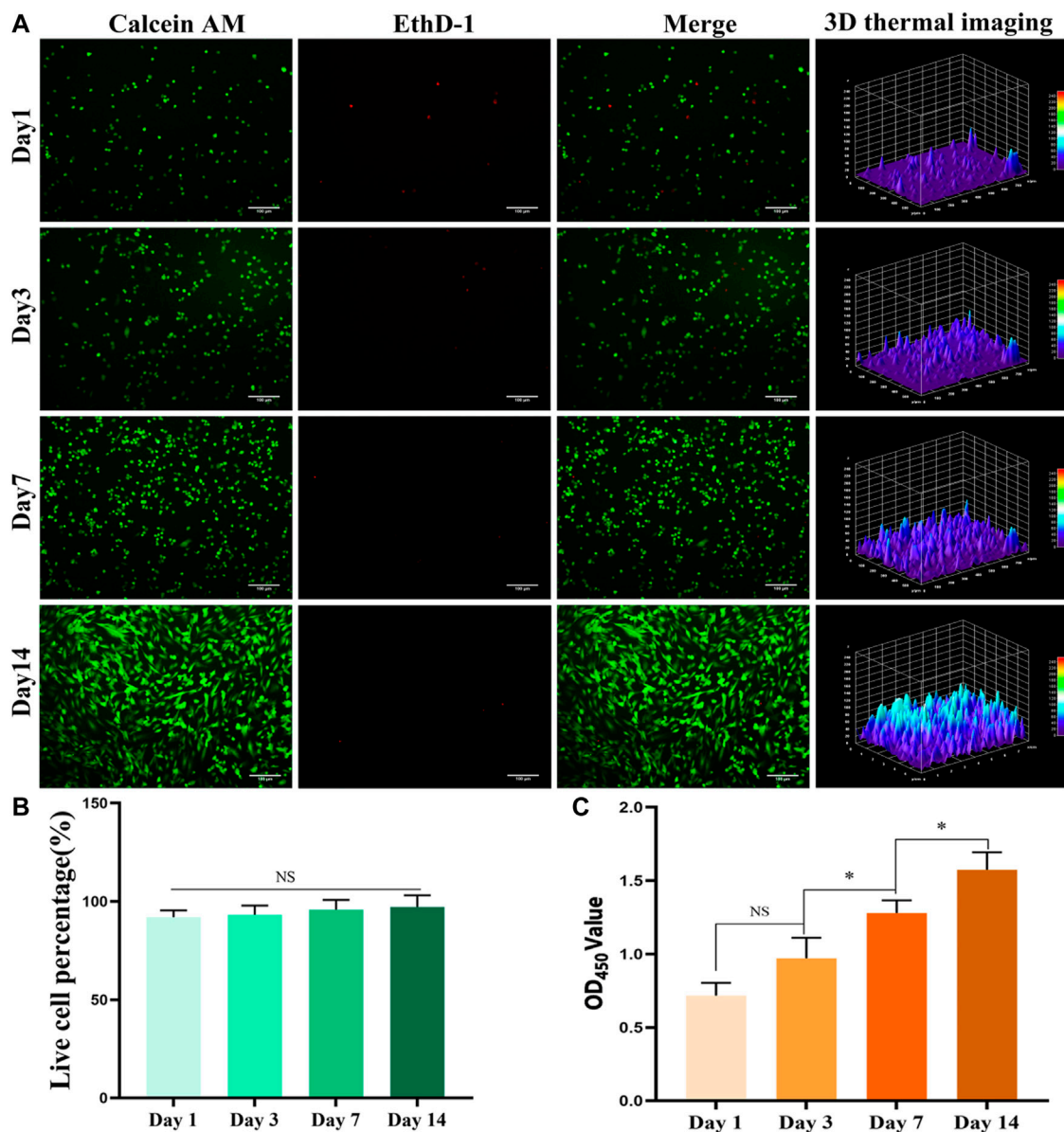


**FIGURE 3** | *In vitro* biocompatibility testing. **(A)** Live/dead staining result of bone marrow mesenchymal stem cells (BMSCs) in the hydrogel scaffold (bar = 100  $\mu$ m). **(B)** The percentage of BMSCs living cells in the total number of cells in the hydrogel scaffold. **(C)** Results of cell activity and cytotoxicity tests of BMSCs in the hydrogel scaffold for 1, 4, 7, and 14 days. \* $p < 0.05$ .

## RESULTS

### Characterization of hydrogels

The overall process of this study is shown in **Figure 1**. As shown in **Figure 2A**, the GelMA can be rapidly dissolved in deionized water. After freeze drying of the GelMA photocured hydrogel, the porous structure of the hydrogel was observed by scanning electron microscope (SEM), which can be seen in **Figure 2B**. As can be seen from **Figure 2C**, the proton peak of methacrylic acid can be observed in the range of 5–6 ppm, which indicates that the GelMA has been successfully synthesized. In addition, in the range of 2.8–2.95 ppm, it

was found that compared with the lysine proton peak of gelatin, the lysine proton peak of the GelMA was significantly weakened, indicating that the target reaction amino acid was consumed. The methacrylate substitution degree of the GelMA was calculated to be 87.6%. As shown in **Figure 2D**, the storage modulus of the GelMA hydrogel reaches 14.22 kPa at 10 Hz, and this mechanical strength can maintain the stability of the scaffold. In **Figure 2E**, as the shear rate increases from 0 to 100  $s^{-1}$ , the viscosity of the GelMA solution decreases gradually and remains stable, exhibiting shear thinning properties, which indicate that the GelMA is injectable. In **Figure 2F**, when the temperature decreases from

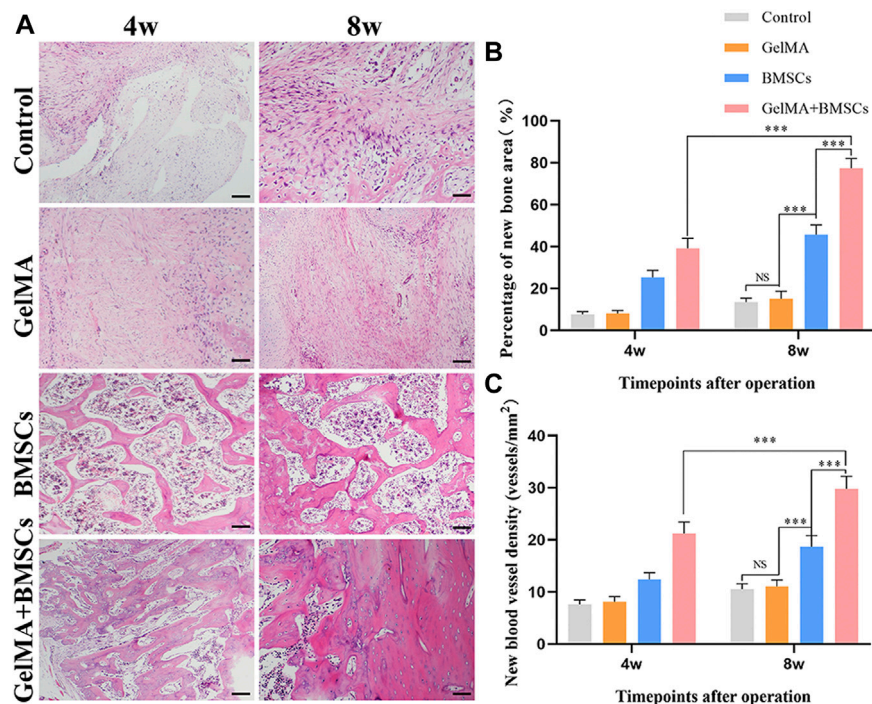


**FIGURE 4** | *In vivo* sample staining results. **(A)** Histological analysis of bone defects repaired by each group at weeks 4 and 8 after surgery (bar = 200  $\mu$ m). **(B)** The percentage of the new bone area and **(C)** the density of neovascularization in the repaired bone defect area in each group at weeks 4 and 8 after surgery. \*\*\* $p < 0.001$ .

40°C to 10°C, the viscosity of the GelMA solution increases rapidly below 22°C to the point of physical gel formation.

### Biocompatibility of hydrogels

The staining results of BMSCs with live/dead cells in the GelMA hydrogel bone repair scaffolds containing BMSCs are shown in **Figure 3A** (fluorescence staining of live/dead cells) and **Figure 3B** (percentage of the number of live cells in the total number of cells). Within 1–3 days of culture, the cells were spherical under the influence of a low adherent matrix. Over time, the cells increased and stretched, compared with the first day. Three-dimensional (3D) thermal imaging showed that fluorescence intensity increased over time. The staining results of live/dead cells showed that the survival rate of BMSCs in BMSC-loaded GelMA hydrogel bone repair scaffolds was high. After 1, 3, 7, and 14 days of culture, the number of living cells in the scaffold gradually increased, and the percentage of living cells exceeded 90%. In cell activity and toxicity tests performed on days 1, 4, 7, and 14, the results showed that the OD value increased with time (**Figure 3C**). The biocompatibility testing results showed that the GelMA hydrogel scaffold had good cell compatibility, and BMSCs could proliferate well in the scaffold.

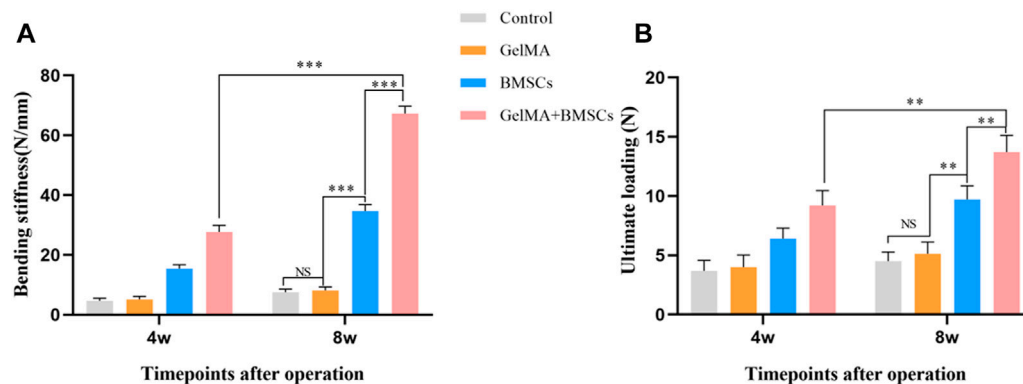
### *In vivo* repair of large-segment bone defect using the bone marrow mesenchymal stem cell-laden methacrylated gelatin hydrogels

To investigate whether the BMSC-loaded GelMA hydrogel bone repair scaffold can promote bone regeneration in the defect area,

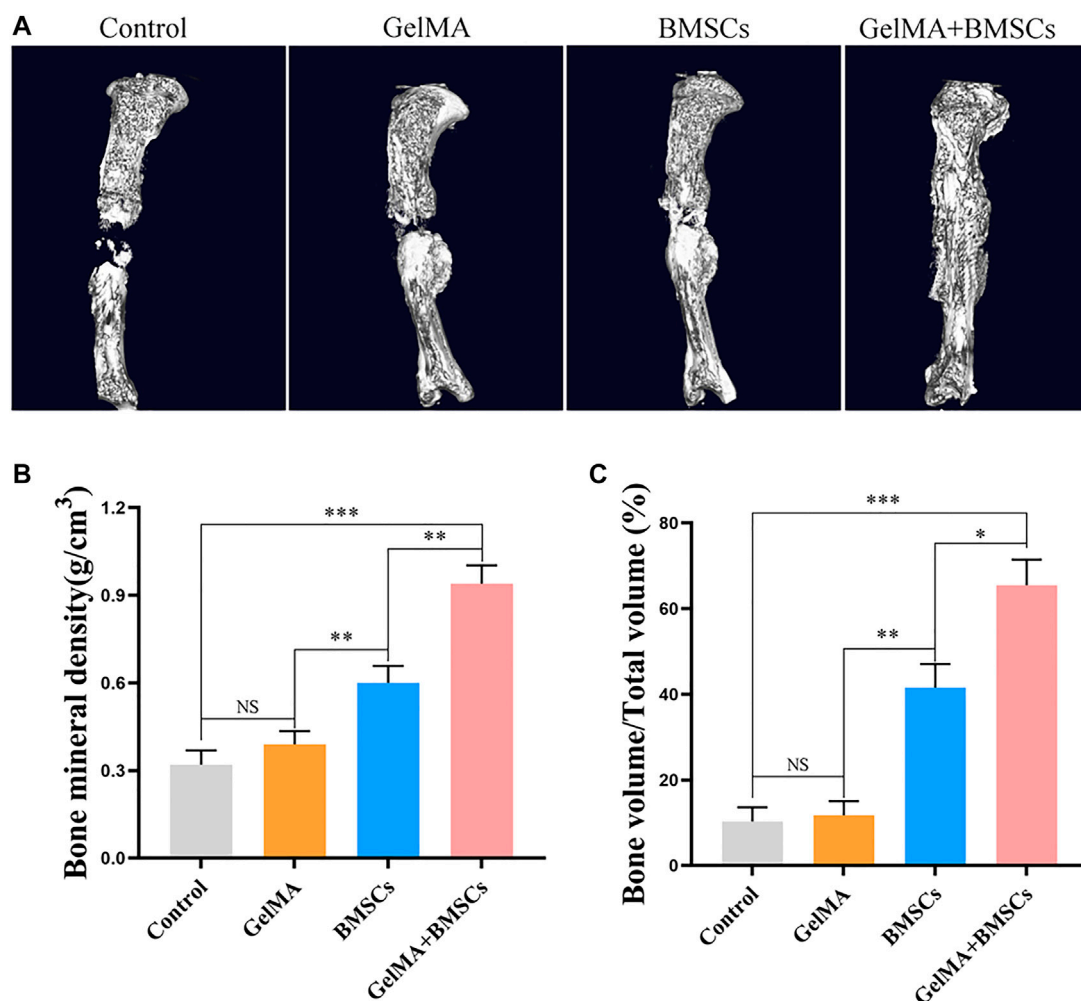
histological analysis was performed at weeks 4 and 8, respectively. **Figure 4** shows the HE staining results of bone tissue in the bone defect area. As can be seen from **Figure 4A**, bone growth in the bone defect area in the BMSC group and the BMSC-carrying GelMA hydrogel scaffold group was vigorous at the fourth and eighth weeks after surgery, and new blood vessels were observed in the regenerated bone area. At the same time, compared with the BMSC group, the BMSCs-containing GelMA hydrogel scaffold group had more new bone formation and more mature tissue structure. In contrast, in the model control group and the GelMA hydrogel scaffold group, only a small amount of new bone formation occurred in the bone defect area, accompanied by more fibrous connective tissue formation.

Image Pro-Plus 6.0 software was used for quantitative analysis of the new bone and new blood vessels. The percentage of the new bone area was calculated according to the new bone area/total defect area  $\times 100\%$ , and the density of new blood vessels was measured according to the number of new blood vessels/bone defect area. **Figures 4B, C** show that the number of new bones and the density of new blood vessels increased in each group from weeks 4 to 8. The number of new bones and density of new blood vessels in the BMSC group was significantly higher than those in the model control group and GelMA hydrogel scaffold group at each time point ( $p < 0.01$ ). However, the number of new bones and density of new blood vessels in the BMSC-carrying GelMA hydrogel scaffold group were significantly higher than those in the BMSC group ( $p < 0.05$ ). The results show that the GelMA scaffold has the ability to promote the growth of new bone, and new blood vessels, that is, it has a good ability to promote bone regeneration.





**FIGURE 5 |** The biomechanical property test result. **(A)** The flexural stiffness and **(B)** the ultimate load of the bone defect repaired by each group at weeks 4 and 8 after surgery. \*\* $p < 0.01$ , \*\*\* $p < 0.001$ .



**FIGURE 6 |** CT detection results. **(A)** The micro-CT 3D reconstruction models of bone defects repaired by each group at the eighth week after surgery. **(B–C)** The bone density and bone volume of each group at 8 weeks after surgery. \*\* $p < 0.01$ , \*\*\* $p < 0.001$ .

The biomechanical property test results are shown in **Figure 5**. According to **Figures 5A, B**, at the fourth week after surgery, the bending stiffness and ultimate load of the BMSC-loaded GelMA hydrogel scaffold group were significantly higher than those of the BMSC group ( $p < 0.05$ ), the model control group, and the GelMA hydrogel scaffold group ( $p < 0.01$ ). There was no statistically significant difference between the model control group and the GelMA hydrogel scaffold group ( $p > 0.05$ ). The biomechanical performance at week 8 was similar to that at week 4, and the difference in bending stiffness and ultimate load between the BMSC-containing GelMA hydrogel scaffold group and the BMSCs group was more significant ( $p < 0.01$ ). The experimental results show that the BMSC-loaded GelMA hydrogel bone repair scaffold can improve the mechanical strength of the defect tibia.

Micro-CT detection was performed on the bone defect area at the eighth week after surgery, and three-dimensional reconstruction was conducted. **Figure 6A** (micro-CT 3D reconstruction model) shows that the bone bridge and callus formation in BMSC-carrying GelMA hydrogel scaffold was significantly better than that in the BMSCs group, GelMA hydrogel scaffold group, and model control group. The quantitative results of bone mass (**Figure 6B**) and bone mineral density (**Figure 6C**) were consistent with the above: the mean bone mass and bone mineral density of the BMSC-loaded GelMA hydrogel scaffold group were significantly higher than that of the BMSC group alone, the GelMA hydrogel scaffold group, and the control group ( $p < 0.01$ ). There was no statistically significant difference between the GelMA hydrogel scaffold group and the control group ( $p > 0.05$ ).

## DISCUSSION

The repair of the large segmental bone defect is still a difficult problem in orthopedic clinical treatment (Wojda and Donahue, 2018). When the defect exceeds the critical size, self-healing cannot be achieved (Schemitsch, 2017). Autografts or allografts are often used to fill defects, but are limited by factors, including infection, immune response, and infectious diseases (Roseti et al., 2017). The development of bone tissue engineering shows promise in repairing large segmental bone defects (Kim et al., 2017). Hydrogels are hydrophilic polymers that are insoluble in water. After soaking in water, the weight of the hydrogel increases to several times its original dry weight (Lu et al., 2018). Hydrogels have been widely used in tissue engineering in recent years because the internal structure and composition of hydrogels are similar to the ECM (Xu et al., 2018). Hydrogels have the potential to mimic ECM in transporting nutrients and metabolites and providing an appropriate microenvironment (Ngo et al., 2018). A variety of natural and synthetic hydrogel polymers have been developed, including gelatin, alginate, fibrin, chitosan, hyaluronic acid (HA), polyethylene oxide (PEO), and polyethylene glycol (PEG) (Yang et al., 2017). Among them, GelMA-based hydrogels show great potential due to their biocompatibility and mechanical stability. Proper internal porosity is necessary for tissue-engineered materials to

maintain cell growth and nutrient transfer. The water-rich GelMA hydrogel mimics the cell matrix microenvironment, and the pore structure facilitates cell adhesion, proliferation, and growth (Shaunak et al., 2017).

In general, scaffolds should carry a mechanical load while promoting tissue regeneration (Biggemann et al., 2018; Zhang et al., 2019c). However, the mechanical properties of hydrogels are lower than that of bone tissue, so the use of hydrogels is usually limited to the areas with no or low load (Ho-Shui-Ling et al., 2018). This study confirmed that the mechanical properties of hydrogels were sufficient to support bone repair with intramedullary nails or plates. Furthermore, in this study, we detected the influence of temperature on GelMA hydrogel viscosity. The GelMA solution maintains low viscosity at room temperature and is favorable for injection. Compared with traditional prefabricated scaffolds, injectable hydrogels can fill defects of any size or shape without requiring additional surgical procedures and are easily formed by mixing with cells (Gupta et al., 2006; Ma et al., 2017).

Compared with traditional two-dimensional (2D) cell culture, three-dimensional (3D) cell culture systems better fit the physiological environment in terms of cell-cell and cell-matrix interaction and diffusion behavior (Booij et al., 2019). In 2D cell culture, the signaling molecules released by the cells are immediately diluted in a relatively larger volume of cell culture medium (Di Modugno et al., 2019). In addition, physiological gradients of signaling molecules, metabolites, and oxygen cannot be generated in 2D culture systems, whereas 3D culture can better study signaling, nutrition, and metabolism in a concentration- and site-dependent manner (Ravi et al., 2015; Xing et al., 2020). MSCs are easily extracted from bone marrow, fat, and synovium (Le et al., 2020). MSCs can be differentiated into a variety of cell lines for specific biomedical applications (Han et al., 2019). As an important MSCs-specific characteristic, differentiation potential affects the fate of MSC. MSCs from different tissue sources show different differentiation trends. Compared with adipose-derived MSCs, BMSCs show stronger osteogenic ability (Han et al., 2019). In this study, BMSCs were coated with hydrogel in a 3D environment to detect the biocompatibility of GelMA *in vitro*. BMSCs have a strong ability of regeneration and differentiation. Cell therapies using BMSCs are currently involved in more than 900 clinical trials (Kirsch et al., 2019; Wang et al., 2021). The fate of BMSCs is influenced by the microenvironment provided by the injection of hydrogels after transplantation. As an ECM analog, the injected hydrogel can affect the migration, proliferation, differentiation, and intercellular communication of stem cells (Chen et al., 2012; Ma et al., 2017). In this study, BMSCs could grow and proliferate in the GelMA hydrogel by means of *in vitro* culture, which proved that the GelMA hydrogel had good biocompatibility. In the *in vivo* experiment, with the fixation of intramedullary nails, the GelMA hydrogel-wrapped BMSCs were implanted into the bone defect site to verify its osteorepair ability. The BMSC-loaded GelMA hydrogel group was significantly superior to the other groups in both morphological and mechanical results. HE results showed that the cell-loaded GelMA hydrogels not only promoted bone regeneration but also correspondingly promoted blood vessel

regeneration, and abundant blood supply is the basis of tissue regeneration.

Due to the limitation of the mechanical properties of GelMA, GelMA is mostly used to study non-load-bearing bone (such as skull) defects or simulated periosteum (Gonçalves et al., 2021; Xiang and Cui, 1186). In these studies, the GelMA hydrogel quickly restored the integrity of the damaged bone surface. Interestingly, compared with other commonly used filling materials, such as metal and ceramic, GelMA can deposit extracellular matrix and type II collagen, which is more conducive to blood vessel and nerve regeneration (Benmassaoud et al., 2020; Xiang and Cui, 1186). Consistent with literature reports, in this study, the number of new vessels in the hydrogel stent group loaded with BMSCs was significantly higher than that in the other groups. In the repair of segmental bone defect, the two ends of the defect are completely disconnected, and the bone marrow cavity is completely exposed, so the biocompatibility of the repair material is highly required. Therefore, in the previous study, the lacunar bone defect model was used in the *in vivo* experiment of the composite scaffolds, and the repair of segmental bone defects by composite scaffolds is prone to infection and osteonecrosis (Wang et al., 2021; Zhang et al., 2021). In the segmental bone repair model in this study, the biocompatibility advantage of the GelMA was demonstrated without bone infection. In future research, the hydrogel scaffold will be optimized from the aspects of material and technology. First, to add osteogenic components, such as magnesium ion, lithium ion, and nano-hydroxyapatite. Some reports have demonstrated that hydrogels loaded with magnesium, lithium, or hydroxyapatite have enhanced mechanical strength and osteogenic induction (Wang et al., 2020a; Wang et al., 2020b; Zhu et al., 2020). Second, microneedle injection technology can be introduced to increase accuracy and efficiency (Lee et al., 2020).

In conclusion, the BMSC-carrying GelMA hydrogel scaffold has good mechanical properties and biological compatibility. Implantation of bone defects can effectively promote the regeneration of bone and blood vessels, improve the mechanical strength of bone defects, and effectively promote

the repair of bone defects. It has a good ability to promote bone regeneration and has great potential for application.

## DATA AVAILABILITY STATEMENT

The raw data supporting the conclusions of this article will be made available by the authors without undue reservation.

## ETHICS STATEMENT

The animal study was reviewed and approved by the animal management and use committee of the West China Clinical Medical College of Sichuan University.

## AUTHOR CONTRIBUTIONS

JL conducted prepared the materials and *in vivo* experiments. ML, XG, and HL conducted the *in vitro* experiments. WW wrote the original draft. PS conducted the software processing. CZ and LL reviewed and edited the manuscript.

## FUNDING

This work was partially supported by the National Key Research and Development Program of China (2018YFC1106800), the National Natural Science Foundation of China (31971251, 81874002), the Sichuan Province Science and Technology Department Projects (2016CZYD0004, 2019JDTD0008, 2019YFH0079, 2017SZ0195, 2019JDR0100, 2020JDR0054), the "111" Project (B16033), the China Postdoctoral Science Foundation (2021M692279), the National Clinical Research Center for Geriatrics, West China Hospital, Sichuan University (Y2018B22, Z20192013), and the West China Hospital Postdoctoral Research and Development Fund (2019HXBH068).

## REFERENCES

- Agarwal, R., and García, A. J. (2015). Biomaterial Strategies for Engineering Implants for Enhanced Osseointegration and Bone Repair. *Adv. Drug Deliv. Rev.* 94, 53–62. doi:10.1016/j.addr.2015.03.013
- Alcorta-Sevillano, N., Macías, I., Infante, A., and Rodríguez, C. I. (2020). Deciphering the Relevance of Bone ECM Signaling. *Cells* 9, 2630. doi:10.3390/cells9122630
- Benmassaoud, M. M., Gultian, K. A., DiCerro, M., and Vega, S. L. (2020). Hydrogel Screening Approaches for Bone and Cartilage Tissue Regeneration. *Ann. N.Y. Acad. Sci.* 1460, 25–42. doi:10.1111/nyas.14247
- Bez, M., Sheyn, D., Tawackoli, W., Avalos, P., Shapiro, G., Giacon, J. C., et al. (2017). *In Situ* bone Tissue Engineering via Ultrasound-Mediated Gene Delivery to Endogenous Progenitor Cells in Mini-Pigs. *Sci. Transl. Med.* 9, 3128. doi:10.1126/scitranslmed.aal3128
- Biggemann, J., Pezoldt, M., Stumpf, M., Greil, P., and Fey, T. (2018). Modular Ceramic Scaffolds for Individual Implants. *Acta Biomater.* 80, 390–400. doi:10.1016/j.actbio.2018.09.008
- Booij, T. H., Price, L. S., and Danen, E. H. J. (2019). 3D Cell-Based Assays for Drug Screens: Challenges in Imaging, Image Analysis, and High-Content Analysis. *SLAS DISCOVERY: Advancing Sci. Drug Discov.* 24, 615–627. doi:10.1177/2472555219830087
- Bose, S., Roy, M., and Bandyopadhyay, A. (2012). Recent Advances in Bone Tissue Engineering Scaffolds. *Trends Biotechnol.* 30, 546–554. doi:10.1016/j.tibtech.2012.07.005
- Brinkman, W. T., Nagapudi, K., Thomas, B. S., and Chaikof, E. L. (2003). Photocross-linking of Type I Collagen Gels in the Presence of Smooth Muscle Cells: Mechanical Properties, Cell Viability, and Function. *Biomacromolecules* 4, 890–895. doi:10.1021/bm0257412
- Cao, S., Zhao, Y., Hu, Y., Zou, L., and Chen, J. (2020). New Perspectives: *In-Situ* Tissue Engineering for Bone Repair Scaffold. *Composites B: Eng.* 202, 108445. doi:10.1016/j.compositesb.2020.108445
- Chen, C., Liu, F., Tang, Y., Qu, J., Cao, Y., Zheng, C., et al. (2019). Book-Shaped Acellular Fibrocartilage Scaffold with Cell-Loading Capability and Chondrogenic Inducibility for Tissue-Engineered Fibrocartilage and Bone-Tendon Healing. *ACS Appl. Mater. Inter.* 11, 2891–2907. doi:10.1021/acsami.8b20563

- Chen, F.-M., Sun, H.-H., Lu, H., and Yu, Q. (2012). Stem Cell-Delivery Therapeutics for Periodontal Tissue Regeneration. *Biomaterials* 33, 6320–6344. doi:10.1016/j.biomaterials.2012.05.048
- Cox, S. C., Thornby, J. A., Gibbons, G. J., Williams, M. A., and Mallick, K. K. (2015). 3D Printing of Porous Hydroxyapatite Scaffolds Intended for Use in Bone Tissue Engineering Applications. *Mater. Sci. Eng. C* 47, 237–247. doi:10.1016/j.msec.2014.11.024
- Cui, L., Zhang, J., Zou, J., Yang, X., Guo, H., Tian, H., et al. (2020). Electroactive Composite Scaffold with Locally Expressed Osteoinductive Factor for Synergistic Bone Repair upon Electrical Stimulation. *Biomaterials* 230, 119617. doi:10.1016/j.biomaterials.2019.119617
- Di Modugno, F., Colosi, C., Trono, P., Antonacci, G., Ruocco, G., and Nisticò, P. (2019). 3D Models in the new era of Immune Oncology: Focus on T Cells, CAF and ECM. *J. Exp. Clin. Cancer Res.* 38, 117. doi:10.1186/s13046-019-1086-2
- Fang, X., Xie, J., Zhong, L., Li, J., Rong, D., Li, X., et al. (2016). Biomimetic Gelatin Methacrylamide Hydrogel Scaffolds for Bone Tissue Engineering. *J. Mater. Chem. B* 4, 1070–1080. doi:10.1039/c5tb02251g
- Fu, X., Liu, G., Halim, A., Ju, Y., Luo, Q., and Song, G. (2019). Mesenchymal Stem Cell Migration and Tissue Repair. *Cells* 8, 784. doi:10.3390/cells8080784
- Garot, C., Bettega, G., and Picart, C. (2020). Additive Manufacturing of Material Scaffolds for Bone Regeneration: Toward Application in the Clinics. *Adv. Funct. Mater.* 31, 2006967. doi:10.1002/adfm.202006967
- Giannoudis, P. V., Harwood, P. J., Tosounidis, D., and Kanakaris, N. K. (2016). Restoration of Long Bone Defects Treated with the Induced Membrane Technique: Protocol and Outcomes. *Injury* 47 (Suppl. 6), S53–S61. doi:10.1016/S0020-1383(16)30840-3
- Gonçalves, A. M., Moreira, A., Weber, A., Williams, G. R., and Costa, P. F. (2021). Osteochondral Tissue Engineering: The Potential of Electrospinning and Additive Manufacturing. *Pharmaceutics* 13, 983. doi:10.3390/pharmaceutics13070983
- Gu, L., Zhang, J., Li, L., Du, Z., Cai, Q., and Yang, X. (2019). Hydroxyapatite Nanowire Composites Gelatin Cryogel with Improved Mechanical Properties and Cell Migration for Bone Regeneration. *Biomed. Mater.* 14, 045001. doi:10.1088/1748-605X/ab1583
- Gupta, D., Tator, C. H., and Shoichet, M. S. (2006). Fast-gelling Injectable Blend of Hyaluronan and Methylcellulose for Intrathecal, Localized Delivery to the Injured Spinal Cord. *Biomaterials* 27, 2370–2379. doi:10.1016/j.biomaterials.2005.11.015
- Haleem, A., Javaid, M., Khan, R. H., and Suman, R. (2020). 3D Printing Applications in Bone Tissue Engineering. *J. Clin. Orthopaedics Trauma* 11, S118–S124. doi:10.1016/j.jcot.2019.12.002
- Han, Y., Li, X., Zhang, Y., Han, Y., Chang, F., and Ding, J. (2019). Mesenchymal Stem Cells for Regenerative Medicine. *Cells* 8, 886. doi:10.3390/cells8080886
- Ho-Shui-Ling, A., Bolander, J., Rustom, L. E., Johnson, A. W., Luyten, F. P., and Picart, C. (2018). Bone Regeneration Strategies: Engineered Scaffolds, Bioactive Molecules and Stem Cells Current Stage and Future Perspectives. *Biomaterials* 180, 143–162. doi:10.1016/j.biomaterials.2018.07.017
- Kim, H. D., Amirthalingam, S., Kim, S. L., Lee, S. S., Rangasamy, J., and Hwang, N. S. (2017). Biomimetic Materials and Fabrication Approaches for Bone Tissue Engineering. *Adv. Healthc. Mater.* 6, 1700612. doi:10.1002/adhm.201700612
- Kirsch, M., Birnstein, L., Pepelanova, I., Handke, W., Rach, J., Seltsam, A., et al. (2019). Gelatin-Methacryloyl (GelMA) Formulated with Human Platelet Lysate Supports Mesenchymal Stem Cell Proliferation and Differentiation and Enhances the Hydrogel's Mechanical Properties. *Bioengineering* 6, 76. doi:10.3390/bioengineering6030076
- Kupikowska-Stobba, B., and Kasprzak, M. (2021). Fabrication of Nanoparticles for Bone Regeneration: New Insight into Applications of Nanoemulsion Technology. *J. Mater. Chem. B* 9, 5221–5244. doi:10.1039/d1tb00559f
- Larsen, M., Pelzer, M., Friedrich, P. F., Wood, C. M., and Bishop, A. T. (2011). Living Bone Allotransplants Survive by Surgical Angiogenesis Alone: Development of a Novel Method of Composite Tissue Allotransplantation. *J. Bone Jt. Surg Am* 93, 261–273. doi:10.2106/JBJS.G.01152
- Le, H., Xu, W., Zhuang, X., Chang, F., Wang, Y., and Ding, J. (2020). Mesenchymal Stem Cells for Cartilage Regeneration. *J. Tissue Eng.* 11, 204173142094383. doi:10.1177/2041731420943839
- Lee, K., Xue, Y., Lee, J., Kim, H. J., Liu, Y., Tebon, P., et al. (2020). A Patch of Detachable Hybrid Microneedle Depot for Localized Delivery of Mesenchymal Stem Cells in Regeneration Therapy. *Adv. Funct. Mater.* 30, 2000086. doi:10.1002/adfm.202000086
- Loessner, D., Meinert, C., Kaemmerer, E., Martine, L. C., Yue, K., Levett, P. A., et al. (2016). Functionalization, Preparation and Use of Cell-Laden Gelatin Methacryloyl-Based Hydrogels as Modular Tissue Culture Platforms. *Nat. Protoc.* 11, 727–746. doi:10.1038/nprot.2016.037
- Lu, L., Yuan, S., Wang, J., Shen, Y., Deng, S., Xie, L., et al. (2018). The Formation Mechanism of Hydrogels. *Cscr* 13, 490–496. doi:10.2174/1574888X12666170612102706
- Ma, Y., Ji, Y., Zhong, T., Wan, W., Yang, Q., Li, A., et al. (2017). Bioprinting-Based PDLSC-ECM Screening for *In Vivo* Repair of Alveolar Bone Defect Using Cell-Laden, Injectable and Photocrosslinkable Hydrogels. *ACS Biomater. Sci. Eng.* 3, 3534–3545. doi:10.1021/acsbomaterials.7b00601
- Moreno Madrid, A. P., Vrech, S. M., Sanchez, M. A., and Rodriguez, A. P. (2019). Advances in Additive Manufacturing for Bone Tissue Engineering Scaffolds. *Mater. Sci. Eng. C* 100, 631–644. doi:10.1016/j.msec.2019.03.037
- Murshed, M. (2018). Mechanism of Bone Mineralization. *Cold Spring Harb Perspect. Med.* 8, a031229. doi:10.1101/cshperspect.a031229
- Ngo, T. D., Kashani, A., Imbalzano, G., Nguyen, K. T. Q., and Hui, D. (2018). Additive Manufacturing (3D Printing): A Review of Materials, Methods, Applications and Challenges. *Composites Part B: Eng.* 143, 172–196. doi:10.1016/j.compositesb.2018.02.012
- Nichol, J. W., Koshy, S. T., Bae, H., Hwang, C. M., Yamanlar, S., and Khademhosseini, A. (2010). Cell-laden Microengineered Gelatin Methacrylate Hydrogels. *Biomaterials* 31, 5536–5544. doi:10.1016/j.biomaterials.2010.03.064
- Pepelanova, I., Kruppa, K., Scheper, T., and Lavrentieva, A. (2018). Gelatin-Methacryloyl (GelMA) Hydrogels with Defined Degree of Functionalization as a Versatile Toolkit for 3D Cell Culture and Extrusion Bioprinting. *Bioengineering* 5, 55. doi:10.3390/bioengineering5030055
- Qiao, Y., Liu, X., Zhou, X., Zhang, H., Zhang, W., Xiao, W., et al. (2020). Gelatin Templated Polypeptide Co-Cross-Linked Hydrogel for Bone Regeneration. *Adv. Healthc. Mater.* 9, 1901239. doi:10.1002/adhm.201901239
- Ravi, M., Paramesh, V., Kaviya, S. R., Anuradha, E., and Solomon, F. D. P. (2015). 3D Cell Culture Systems: Advantages and Applications. *J. Cell. Physiol* 230, 16–26. doi:10.1002/jcp.24683
- Ravindran, S., and George, A. (2014). Multifunctional ECM Proteins in Bone and Teeth. *Exp. Cel. Res.* 325, 148–154. doi:10.1016/j.yexcr.2014.01.018
- Roseti, L., Parisi, V., Petretta, M., Cavallo, C., Desando, G., Bartolotti, I., et al. (2017). Scaffolds for Bone Tissue Engineering: State of the Art and New Perspectives. *Mater. Sci. Eng. C* 78, 1246–1262. doi:10.1016/j.msec.2017.05.017
- Schemitsch, E. H. (2017). Size Matters: Defining Critical in Bone Defect Size!. *J. Orthop. Trauma* 31 (Suppl. 5), S20–S22. doi:10.1097/BOT.0000000000000978
- Shaunak, S., Dhinsa, B., and Khan, W. (2017). The Role of 3D Modelling and Printing in Orthopaedic Tissue Engineering: A Review of the Current Literature. *Cscr* 12, 225–232. doi:10.2174/1574888X11666160429122238
- Stanovici, J., Le Nail, L.-R., Brennan, M. A., Vidal, L., Trichet, V., Rosset, P., et al. (2016). Bone Regeneration Strategies with Bone Marrow Stromal Cells in Orthopaedic Surgery. *Curr. Res. Translational Med.* 64, 83–90. doi:10.1016/j.retram.2016.04.006
- Sun, M., Sun, X., Wang, Z., Guo, S., Yu, G., and Yang, H. (2018). Synthesis and Properties of Gelatin Methacryloyl (GelMA) Hydrogels and Their Recent Applications in Load-Bearing Tissue. *Polymers* 10, 1290. doi:10.3390/polym10111290
- Wade, R. J., Bassin, E. J., Gramlich, W. M., and Burdick, J. A. (2015). Nanofibrous Hydrogels with Spatially Patterned Biochemical Signals to Control Cell Behavior. *Adv. Mater.* 27, 1356–1362. doi:10.1002/adma.201404993
- Wang, W.-H., Wang, F., Zhao, H.-F., Yan, K., Huang, C.-L., Yin, Y., et al. (2020). Injectable Magnesium-Zinc Alloy Containing Hydrogel Complex for Bone Regeneration. *Front. Bioeng. Biotechnol.* 8, 617585. doi:10.3389/fbioe.2020.617585
- Wang, W., Zhang, B., Li, M., Li, J., Zhang, C., Han, Y., et al. (2021). 3D Printing of PLA/n-HA Composite Scaffolds with Customized Mechanical Properties and Biological Functions for Bone Tissue Engineering. *Composites Part B: Eng.* 224, 109192. doi:10.1016/j.compositesb.2021.109192
- Wang, Y., Cao, X., Ma, M., Lu, W., Zhang, B., and Guo, Y. (2020). A GelMA-PEGDA-nHA Composite Hydrogel for Bone Tissue Engineering. *Materials* 13, 3735. doi:10.3390/ma13173735

- Wojda, S. J., and Donahue, S. W. (2018). Parathyroid Hormone for Bone Regeneration. *J. Orthop. Res.* 36, 2586–2594. doi:10.1002/jor.24075
- Xiang, L., and Cui, W. Biomedical Application of Photo-Crosslinked Gelatin Hydrogels. *J. Leather Sci. Eng.* 3, 3. doi:10.1186/s42825-020-00043-y
- Xiao, S., Zhao, T., Wang, J., Wang, C., Du, J., Ying, L., et al. (2019). Gelatin Methacrylate (GelMA)-Based Hydrogels for Cell Transplantation: an Effective Strategy for Tissue Engineering. *Stem Cell Rev Rep* 15, 664–679. doi:10.1007/s12015-019-09893-4
- Xing, F., Zhou, C., Hui, D., Du, C., Wu, L., Wang, L., et al. (2020). Hyaluronic Acid as a Bioactive Component for Bone Tissue Regeneration: Fabrication, Modification, Properties, and Biological Functions. *Nanotechnology Rev.* 9, 1059–1079. doi:10.1515/ntrev-2020-0084
- Xu, W., Dong, S., Han, Y., Li, S., and Liu, Y. (2018). Hydrogels as Antibacterial Biomaterials. *Cpd* 24, 843–854. doi:10.2174/1381612824666180213122953
- Yang, J., Zhang, Y. S., Yue, K., and Khademhosseini, A. (2017). Cell-laden Hydrogels for Osteochondral and Cartilage Tissue Engineering. *Acta Biomater.* 57, 1–25. doi:10.1016/j.actbio.2017.01.036
- Zakhary, K. E., and Thakker, J. S. (2017). Emerging Biomaterials in Trauma. *Oral Maxill. Surg. Clin. North America* 29, 51–62. doi:10.1016/j.coms.2016.08.010
- Zhang, B., Sun, H., Wu, L., Ma, L., Xing, F., Kong, Q., et al. (2019). 3D Printing of Calcium Phosphate Bioceramic with Tailored Biodegradation Rate for Skull Bone Tissue Reconstruction. *Bio-des. Manuf.* 2, 161–171. doi:10.1007/s42242-019-00046-7
- Zhang, B., Wang, L., Song, P., Pei, X., Sun, H., Wu, L., et al. (2021). 3D Printed Bone Tissue Regenerative PLA/HA Scaffolds with Comprehensive Performance Optimizations. *Mater. Des.* 201, 109490. doi:10.1016/j.matdes.2021.109490
- Zhang, R., Ma, J., Han, J., Zhang, W., and Ma, J. (2019). Mesenchymal Stem Cell Related Therapies for Cartilage Lesions and Osteoarthritis. *Am. J. Transl Res.* 11, 6275–6289.
- Zhang, Y., Liu, X., Zeng, L., Zhang, J., Zuo, J., Zou, J., et al. (2019). Polymer Fiber Scaffolds for Bone and Cartilage Tissue Engineering. *Adv. Funct. Mater.* 29, 1903279. doi:10.1002/adfm.201903279
- Zhao, D., Zhu, T., Li, J., Cui, L., Zhang, Z., Zhuang, X., et al. (2021). Poly(lactic-co-glycolic Acid)-Based Composite Bone-Substitute Materials. *Bioactive Mater.* 6, 346–360. doi:10.1016/j.bioactmat.2020.08.016
- Zhou, C. (2021). Biofabrication (3D Bioprinting) Laboratory at Sichuan University. *Bio-Design and Manufacturing* 4, 8. doi:10.1007/s42242-020-00115-2
- Zhu, T., Cui, Y., Zhang, M., Zhao, D., Liu, G., and Ding, J. (2020). Engineered Three-Dimensional Scaffolds for Enhanced Bone Regeneration in Osteonecrosis. *Bioactive Mater.* 5, 584–601. doi:10.1016/j.bioactmat.2020.04.008

**Conflict of Interest:** The authors declare that the research was conducted in the absence of any commercial or financial relationships that could be construed as a potential conflict of interest.

**Publisher's Note:** All claims expressed in this article are solely those of the authors and do not necessarily represent those of their affiliated organizations, or those of the publisher, the editors, and the reviewers. Any product that may be evaluated in this article, or claim that may be made by its manufacturer, is not guaranteed or endorsed by the publisher.

Copyright © 2021 Li, Wang, Li, Song, Lei, Gui, Zhou and Liu. This is an open-access article distributed under the terms of the Creative Commons Attribution License (CC BY). The use, distribution or reproduction in other forums is permitted, provided the original author(s) and the copyright owner(s) are credited and that the original publication in this journal is cited, in accordance with accepted academic practice. No use, distribution or reproduction is permitted which does not comply with these terms.





# Laser Additively Manufactured Iron-Based Biocomposite: Microstructure, Degradation, and *In Vitro* Cell Behavior

Youwen Yang<sup>1</sup>, Guoqing Cai<sup>1</sup>, Mingli Yang<sup>1</sup>, Dongsheng Wang<sup>2</sup>, Shuping Peng<sup>3,4</sup>, Zhigang Liu<sup>5\*</sup> and Cijun Shuai<sup>1,6\*</sup>

<sup>1</sup>Institute of Additive Manufacturing, Jiangxi University of Science and Technology, Nanchang, China, <sup>2</sup>Key Laboratory of Construction Hydraulic Robots of Anhui Higher Education Institutes, Tongling University, Tongling, China, <sup>3</sup>School of Energy and Mechanical Engineering, Jiangxi University of Science and Technology, Nanchang, China, <sup>4</sup>NHC Key Laboratory of Carcinogenesis, The Key Laboratory of Carcinogenesis and Cancer Invasion of the Chinese Ministry of Education, School of Basic Medical Science, Central South University, Changsha, China, <sup>5</sup>School of Electrical Engineering and Automation, Jiangxi University of Science and Technology, Ganzhou, China, <sup>6</sup>State Key Laboratory of High Performance Complex Manufacturing, Central South University, Changsha, China

## OPEN ACCESS

### Edited by:

Lan Li,  
Nanjing Drum Tower Hospital, China

### Reviewed by:

Jie Chen,  
National University of Singapore,  
Singapore  
Fupo He,  
Guangdong University of Technology,  
China  
Yang Zheng,  
Tianjin Polytechnic University, China

### \*Correspondence:

Zhigang Liu  
9120030053@jxust.edu.cn  
Cijun Shuai  
shuai@csu.edu.cn  
shuai@jxust.edu.cn

### Specialty section:

This article was submitted to  
Biomaterials,  
a section of the journal  
Frontiers in Bioengineering and  
Biotechnology

**Received:** 27 September 2021

**Accepted:** 22 October 2021

**Published:** 02 December 2021

### Citation:

Yang Y, Cai G, Yang M, Wang D,  
Peng S, Liu Z and Shuai C (2021) Laser  
Additively Manufactured Iron-Based  
Biocomposite: Microstructure,  
Degradation, and *In Vitro* Cell Behavior.  
Front. Bioeng. Biotechnol. 9:783821.  
doi: 10.3389/fbioe.2021.783821

A too slow degradation of iron (Fe) limits its orthopedic application. In this study, calcium chloride (CaCl<sub>2</sub>) was incorporated into a Fe-based biocomposite fabricated by laser additive manufacturing, with an aim to accelerate the degradation. It was found that CaCl<sub>2</sub> with strong water absorptivity improved the hydrophilicity of the Fe matrix and thereby promoted the invasion of corrosive solution. On the other hand, CaCl<sub>2</sub> could rapidly dissolve once contacting the solution and release massive chloride ion. Interestingly, the local high concentration of chloride ion effectively destroyed the corrosion product layer due to its strong erosion ability. As a result, the corrosion product layer covered on the Fe/CaCl<sub>2</sub> matrix exhibited an extremely porous structure, thus exhibiting a significantly reduced corrosion resistance. Besides, *in vivo* cell testing proved that the Fe/CaCl<sub>2</sub> biocomposite also showed favorable cytocompatibility.

**Keywords:** laser additive manufacturing, iron bone implant, calcium chloride, degradation properties, cell behavior

## INTRODUCTION

In recent years, iron (Fe) has been recognized as a potential bone tissue engineering material owing to its good biocompatibility and mechanical properties (Cheng et al., 2013; Yang et al., 2020a). As compared with the other two biodegradable metals, including magnesium and zinc, Fe possesses relatively high mechanical strength and is more suitable for the repair of load-bearing bone tissue (Li et al., 2018). Fe is an essential micronutrient for the human body and participates in metabolism and various physiological functions, such as hemoglobin synthesis, metabolic enzyme activation, and immunity enhancement (Hermawan et al., 2010; Shuai et al., 2021a). As one kind of biodegradable metal, Fe can be naturally degraded and absorbed in the human body, thus avoiding secondary surgery (Spotorno et al., 2020). However, Fe degrades too slowly, which should hinder the formation and growth of new bone and even cause inflammatory reaction (Yang et al., 2018). The slow degradation is related to the formation of passive film (Sharma and Pandey, 2019). According to the theory of phase-forming film, a dense and well-covered product film could be formed on the Fe matrix as corrosion occurred (Kim et al., 2019).



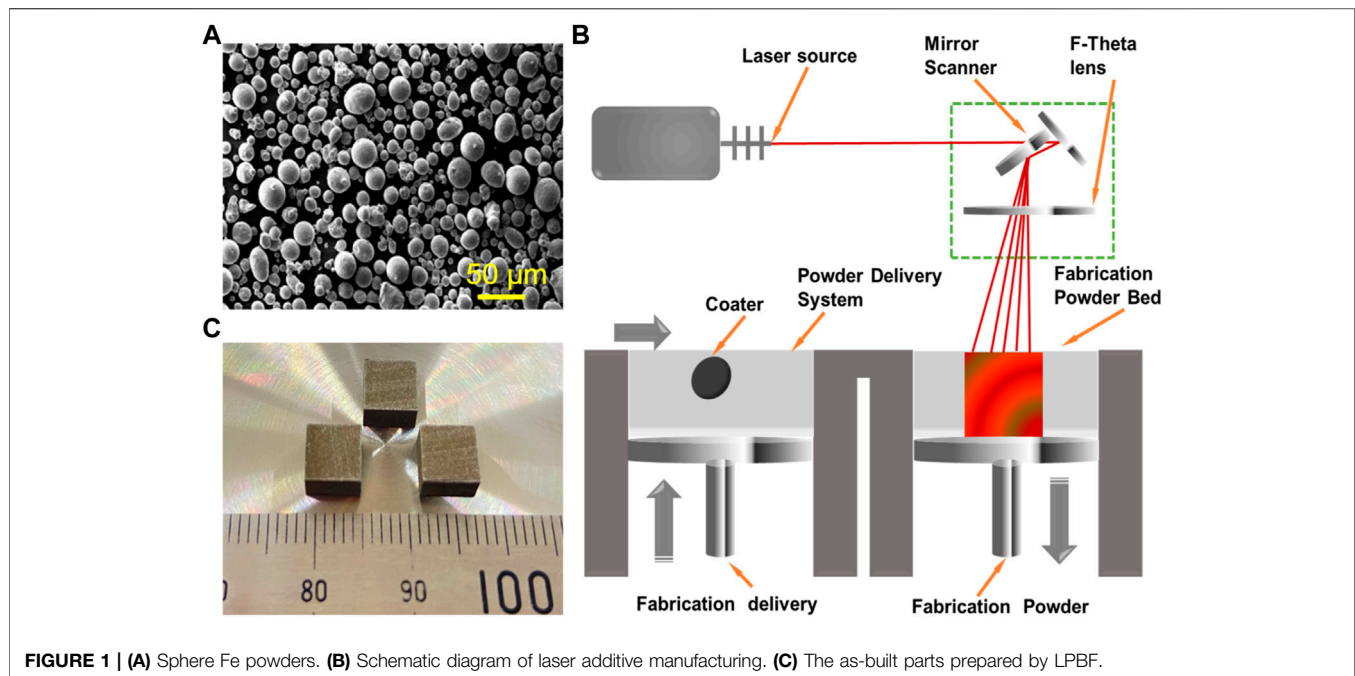


**FIGURE 1 | (A)** Sphere Fe powders. **(B)** Schematic diagram of laser additive manufacturing. **(C)** The as-built parts prepared by LPBF.

The thin film firmly combined with the Fe matrix could be regarded as an independent solid phase (Wang et al., 2020).

Destroying the passive film of a metallic surface by halogen ion breakdown is an effective way to accelerate the degradation (Yin et al., 2020). Halogen ions, such as chlorine, fluorine, and bromine ions, with strong electronegativity could penetrate into the interface between the metallic matrix and the surface film (Liu et al., 2017; Zhang et al., 2018; Gu et al., 2021). In this case, it would generate lattice expansion and resultant tensile stress at the interface, thus destroying the surface passive film. According to the research of Kong et al. (Kong et al., 2018), halogen ion could cause the relaxation of the passive film structure, so as to achieve the effect of breakdown. Wang et al. (Wang et al., 2014) found that halogen ion could change the film passive structure during the formation of the passive film, thus reducing the protective effect and accelerating the matrix corrosion. Zhou et al. (Zhou et al., 2020) also confirmed that halogen ion destroyed the passive film by potentiodynamic polarization.

In this work, calcium chloride ( $\text{CaCl}_2$ ), as a halide, was incorporated into Fe-based bone implants fabricated by laser powder bed fusion (LPBF). It was expected that  $\text{CaCl}_2$  would release Cl ion to accelerate the corrosion by attacking the passive film covered on the Fe matrix. Meanwhile, it could also offer Ca ion, one nutrient element that could promote cell proliferation and differentiation (Seol et al., 2014; Chen et al., 2020). LPBF, as additive manufacturing technology, was able to easily fabricate bone tissue engineering scaffold with a complicated pore structure and personalized outer shape, thus meeting the application requirement for different patients (Gao et al., 2021a; Shuai et al., 2021b; Yang et al., 2021). Moreover, it utilized high-energy laser beam as a heat source, which could deal with a wide range of material systems,

including metals, ceramics, polymers, and their composites (Pérez-Ruiz et al., 2021; Wang et al., 2021). Herein, the microstructure feature, degradation performance, and corrosion behavior for the Fe/ $\text{CaCl}_2$  composite were systematically studied. In addition, the biocompatibility was also evaluated synthetically to assess its potential application in bone defect repair.

## MATERIAL AND METHODS

### Preparation of the Fe/ $\text{CaCl}_2$ Powder

Sphere Fe powder (25–50 μm) and  $\text{CaCl}_2$  powder (1–3 μm) were used as raw materials, as shown in **Figure 1A**. The mixed powder containing 5 wt.% of  $\text{CaCl}_2$  was milled using a miniature planet ball mill (PULVERISETTE 6, Fritsch, Idar-Oberstein, Germany) at room temperature for 2 h. The rotation rate was 200 rpm, and the powder-to-ball weight ratio was determined at 1:10. The ball mill was suspended for half an hour every 15 min to cool down the vial. Before operation, the sealed vial was vacuumed and filled with argon (99.99% purity) aiming to avoid the oxidation. Lastly, the mixture was dried in a vacuum drying oven for 8 h at 125°C.

### LPBF of Fe-Based Biocomposite

The as-milled powder was used for laser additive manufacturing experiments. The manufacturing system consisted of a fiber laser (IPG, 500 W, Germany), a computer control system, and a building chamber filled with purity argon, as displayed in **Figure 1B**. The optimized process parameters obtained by a series of pre-experiments were as follows: laser power 110 W, scanning rate 12 mm/s, hatching space 50 μm, and layer thickness 50 μm. The laser scanning strategy was set as an alternating scanning strategy, in which the scanning vectors rotated 90°

relative to the previous layer. The typical additively manufactured parts are displayed in **Figure 1C**, and the size was 6 cm in length, 6 cm in width, and 6 cm in height.

## Microstructural Characterization

The as-built parts were grounded to 2,000 mesh utilizing SiC paper and then polished with diamond paste under the lubrication of ethanol. The microstructure was characterized utilizing a scanning electron microscope (SEM, EVO 18, Zeiss, Oberkochen, Germany) at 20 kV. The phase composition was determined utilizing an X-ray diffractometer (XRD, D8 Advance, Karlsruhe, Germany) with Cu-K $\alpha$  radiation ( $\lambda = 0.15406$  nm) at 40 kV and 40 mA. The scanning range was set at 10°–90°. The texture was investigated using an electron backscattering diffractometer (EBSD, Symmetry, Oxford Instruments, Abingdon, UK), in which the accelerating voltage varied within 12–30 kV by steps of 0.1 kV in a maximum depth range of 4–5  $\mu$ m. Before EBSD analysis, the samples were prepared by electropolishing in an ethanol solution containing 12 vol.% of water and 8 vol.% of perchloric acid. The surface hydrophilic angles were measured utilizing a contact angle measurement instrument (Shanghai Zhongchen Technology Apparatus Co., Ltd., Shanghai, China) with a 3 ml distilled water droplet suspended from the tip of the microliter syringe.

## Immersion Tests

Immersion tests were implemented to investigate the corrosion behavior. The samples were immersed in self-prepared simulated body fluid (SBF) for 7, 14, and 28 days. SBF mainly contained 142.0 mM of Na<sup>+</sup>, 5.0 mM of K<sup>+</sup>, 1.5 mM of Mg<sup>2+</sup>, 2.5 mM of Ca<sup>2+</sup>, 125.0 mM of Cl<sup>−</sup>, 327.0 mM of HCO<sup>−</sup>, 41.0 mM of HPO<sup>2−</sup>, and 40.5 mM of SO<sup>2−</sup>. After immersion, the samples were washed with distilled water. The corrosion surface was analyzed using SEM. The corrosion product after immersion for 28 days was analyzed utilizing an X-ray photoelectron spectroscopy (XPS) with a monochromatic Al K $\alpha$  radiation. High-resolution spectra were recorded at the pass energy of 12.5 eV with an energy step of 0.1 eV. The film was deeply analyzed by sputtering of argon ion beam with an energy level of 3 keV and a raster of 2  $\times$  2 mm<sup>2</sup>. The sputtering rate was 0.2 nm/s determined on SiO<sub>2</sub> standard. The samples after immersion 28 days were treated with 200 g/L of CrO<sub>3</sub> solution to remove the corrosion product. The weight loss was recorded to determine the degradation rate. Besides, the three-dimensional surface morphology was analyzed using an atomic force microscope (AFM, Verco Instruments, USA).

## Electrochemical Experiments

Electrochemical tests were performed using an electrochemical analyzer (PAR model 4,000, Princeton, Oak Ridge, TN, USA) in SBF. The three-electrode battery device was composed of platinum as counterelectrode, saturated calomel as reference electrode, and the testing sample as working electrode. The initial open-loop circuit tests were implemented for 1,800 s to achieve the voltage stability. Tafel polarization curves were obtained at a scanning rate of 1 mV/s. Electrochemical impedance spectroscopy (EIS) curves for samples with different immersing time were measured at a sinusoidal

amplitude of 10 mV with the frequency range of 1,000 kHz to 0.01 Hz. The obtained EIS curves were analyzed by ZSimpWin software. The transient time–current curves were measured from −2,000 to −1,000 mV/s at a rate of 1 mV/s. The Mott–Schottky curves were determined at a frequency of 1 kHz to evaluate the semiconductor performance of the passive film.

## In Vitro Cell Tests

Cell cytotoxicity was assessed using MG-63 cells (American Type Culture Collection, Rockville, MD, USA). Dulbecco's modified Eagle's medium (DMEM) containing 10% fetal bovine serum, 100 units/ml penicillin, and 100 mg/ml streptomycin was applied as culture medium. MG-63 cells were cultured in a 96-well plate containing culture medium for 1 day. Before the experiments, the samples were sterilized using ultraviolet light for 30 min and then immersed in culture medium for 3 days to obtain the extracts. Subsequently, the culture medium was replaced by extracts. After culture for 1, 3, and 5 days, the Calcein AM reagent was used to stain the cells for 15 min. The stained cells were observed utilizing a fluorescence microscope (BX60, Olympus, Tokyo, Japan). Besides, Cell Counting Kit-8 (CCK-8) testing was carried out to assess the cell cytotoxicity. At 1, 3, and 5 days, 10  $\mu$ l of CCK-8 reagent was dropped into each well and further incubated for 3 h. The absorbance was measured using a microplate reader at 450 nm. Meanwhile, alkaline phosphatase (ALP) staining was carried out to evaluate the differentiation ability of cells cultured for 1 week. After staining, the cells were visualized using a microscope (TE 2000U, Nikon, Tokyo, Japan).

## Statistical Analysis

In the present study, the hydrophilic angle test, immersion tests, electrochemical experiments, and cell tests were carried out at least three times for the averages. SPSS software was used to perform the statistical analysis, in which  $p < 0.05$  was recognized to be of statistical difference.

# RESULTS

## Microstructure of Additively Manufactured Biocomposite

The microstructure of the Fe and Fe/CaCl<sub>2</sub> biocomposite after etching is shown in **Figure 2A**, which clearly revealed the uniform dispersion of CaCl<sub>2</sub> in the Fe matrix. EBSD mapping further indicated that the Fe/CaCl<sub>2</sub> composite consisted of refined grains as compared with the Fe part. It was believed that the doped CaCl<sub>2</sub> pinned at the grain boundary during LPBF and interrupted the crystal growth. The corresponding XRD spectrum of the as-built parts is shown in **Figure 2B**. A strong peak corresponding to Fe (110) was clearly observed in two samples, whereas a relatively broadened peak corresponding to CaCl<sub>2</sub> (011) presented in the Fe/CaCl<sub>2</sub> composite. The hydrophilicity of the Fe and Fe/CaCl<sub>2</sub> composite was studied using contact angle measurement. As shown in **Figure 2C**, the water contact angle gradually decreased with contacting time increasing. Encouragingly, the Fe/CaCl<sub>2</sub> composite showed a significantly decreased

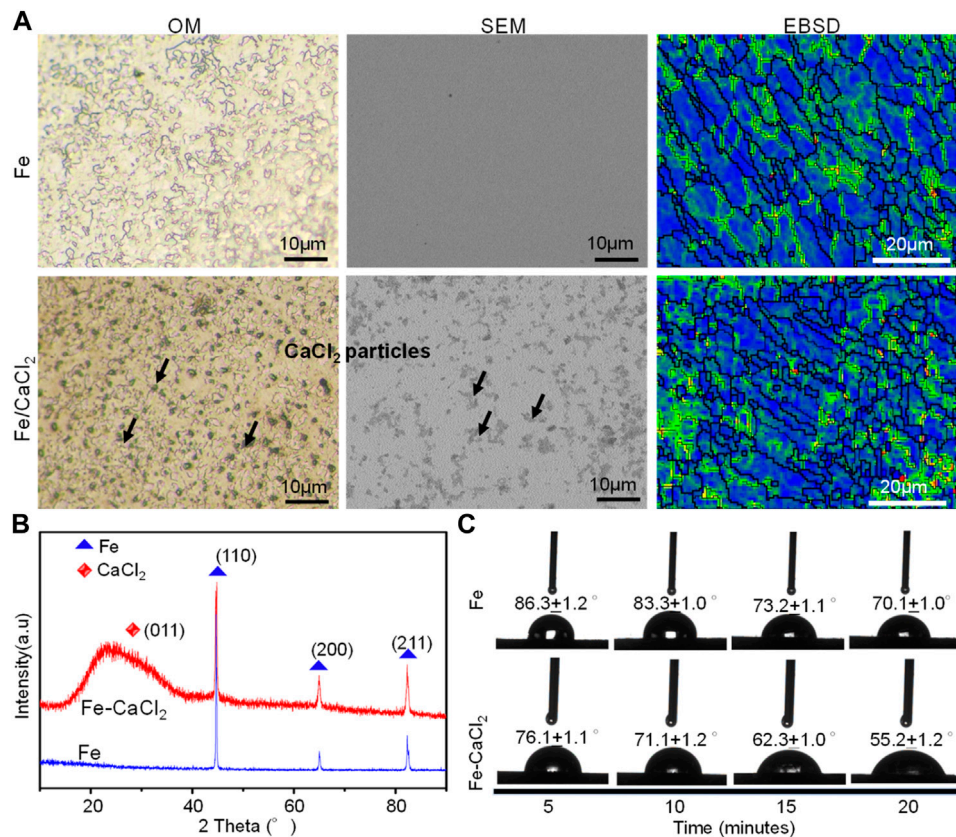


**FIGURE 2 | (A)** The microstructure, **(B)** the XRD spectrum, and **(C)** dynamic results of the hydrophilic angle test.

water contact angle of  $55.2 \pm 1.2^\circ$ , as compared with the Fe part of  $70.1 \pm 1.0^\circ$ . It was directly proved that the incorporation of CaCl<sub>2</sub> improved the surface hydrophilicity, which should be conducive to cell adhesion for the Fe-based biocomposite after implantation (Chen et al., 2018).

## Degradation Behavior in SBF

The degradation behavior of the Fe and Fe/CaCl<sub>2</sub> biocomposites was evaluated by the SBF immersion test. As shown in **Figure 3A**, the soaking liquid turned yellow turbid with immersion period gradually extending to 28 days, especially for the Fe/CaCl<sub>2</sub> composite. This was mainly attributed to the release of Fe<sup>3+</sup> ion caused by the degradation of the Fe matrix. The corresponding weight losses are displayed in **Figure 3B**. After immersion for 28 days, the weight loss rates for Fe and Fe-CaCl<sub>2</sub> were  $\sim 0.05$  and  $0.18 \text{ mg/cm}^2/\text{year}$ , respectively. Additionally, the corrosion surface was observed by SEM, as shown in **Figure 3C**. The flat corrosion surface with few corrosion products was observed for the Fe part during the whole period. Distinctively, the heavy corrosion product covered on the surface of the Fe/CaCl<sub>2</sub> composite. It should be noted that the corrosion product layer was characterized with a loosened structure and a lot of corrosion pits on it. These pits obviously became deepened and expanded with immersion time extending. As presented in **Figure 3C**, an enlarged view of SEM clearly

proved the porous structure of the corrosion film for Fe-CaCl<sub>2</sub> after 28 days' immersion.

The cross section of corrosion production covered on the Fe and Fe/CaCl<sub>2</sub> composites after immersion for 28 days is shown in **Figure 4A**. A uniform corrosion product film with a thickness of  $\sim 9.1 \mu\text{m}$  was observed for the Fe part. For the Fe/CaCl<sub>2</sub> composite, the thickness of the corrosion film increased to  $\sim 43.2 \mu\text{m}$ . The element mapping results showed that the corrosion product was mainly composed of Fe and O elements, which was also confirmed by XPS analysis. According to the scanning spectrum, the corresponding high-resolution Fe and O spectra were obtained. Spin-orbit peaks of Fe2p<sub>3/2</sub> and 2p<sub>1/2</sub> in the high-resolution Fe spectra are located at 711.4 and 724.6 eV, both of which corresponded to Fe<sub>2</sub>O<sub>3</sub> as the main corrosion product. The O1s spectrum of the Fe/CaCl<sub>2</sub> composite in the high-resolution O spectra had two new bands as compared with that of Fe. The peaks of the two bands were located at 531.0 and 529.4 eV, respectively, which were assigned to lattice oxygen and metal oxygen (Wu et al., 2020; Zhou et al., 2020).

The surface topography of the Fe and Fe/CaCl<sub>2</sub> composites with the corrosion product removed was analyzed by AFM, as shown in **Figure 5**. The surface of the Fe matrix showed only a few of small and shallow corrosion pits. In contrast, massive deep and large corrosion pits presented on the Fe/CaCl<sub>2</sub>



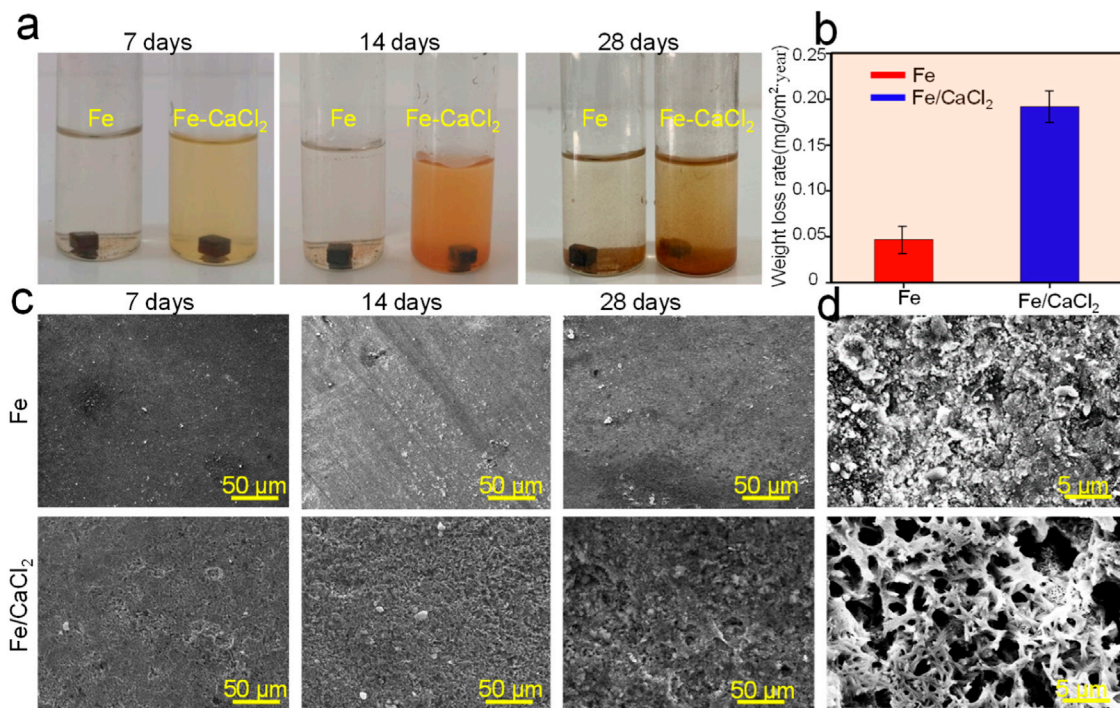


**FIGURE 3 | (A)** The photograph showing the samples immersed in SBF for 7, 14, and 28 days, **(B)** the weight loss rate, **(C)** the corresponding typical corrosion morphology, and **(D)** enlarged view of the corrosion surface.

composite. As shown in **Figure 5B**, the three-dimensional AFM images revealed that the surface roughness was only  $-0.145$  to  $0.212\ \mu\text{m}$  for the Fe part but enhanced to  $-5.5$  to  $3.8\ \mu\text{m}$  for the Fe/CaCl<sub>2</sub> composite. The curves detected on the Fe/CaCl<sub>2</sub> composite fluctuated in a larger range than those on the Fe part, as shown in **Figure 5C**, which also proved that the addition of CaCl<sub>2</sub> brought about severe pitting corrosion and destroyed the matrix.

## Electrochemical Behavior

The corrosion behavior of the Fe and Fe/CaCl<sub>2</sub> composites were further investigated by electrochemical tests. As shown in **Figure 6A**, the potentiodynamic polarization curves showed a typical anodic polarization behavior, resulting in the formation of the passivation film. After doping CaCl<sub>2</sub>, the breakdown potential of the passivation film was negatively shifted. The corrosion potential ( $E_{\text{corr}}$ ) and corrosion current density ( $i_{\text{corr}}$ ) were obtained by the Tafel region extrapolation method.  $E_{\text{corr}}$  was  $-0.75 \pm 0.1\ \text{V}$  for Fe and  $-0.94 \pm 0.2\ \text{V}$  for the Fe/CaCl<sub>2</sub> composite. However, the  $i_{\text{corr}}$  of the Fe/CaCl<sub>2</sub> composite was  $31.4 \pm 0.9\ \mu\text{A}/\text{cm}^2$ , which was significantly enhanced as compared with that of Fe ( $11.1 \pm 0.4\ \mu\text{A}/\text{cm}^2$ ).

The EIS diagrams were obtained after immersion for 7, 14, and 28 days, as shown in **Figure 6B**. The impedance arcs for the Fe parts gradually increased with immersion time extending from 7 to 28 days, which were closely related with the formation of compact passive film during corrosion. However, the impedance arcs of the Fe/CaCl<sub>2</sub> composites immersed at 7, 14, and 28 days

showed no obvious change and were significantly smaller than that of Fe. It was believed that the passive film was continuously self-destroyed, thus reducing the protection efficiency. The structure of the passive film after immersing for 7, 14, and 28 days was analyzed using equivalent circuits fitted by the EIS spectra, as exhibited in **Figure 6C**. The circuit for the Fe part indicated the existence of one time constant. It represented a compact passive film which acted as a barrier against corrosion, wherein  $R_{\text{ct}}$  and  $C_d$  were the resistance and capacitance of the passive film, respectively. Distinctively, the circuit for Fe/CaCl<sub>2</sub> composites showed the existence of two-time constants, which indicated the formation of a porous passive film. In this model, the second time constant was charge transfer reaction, which could be illustrated by the double-layer capacitance  $C_d$  and charge transfer resistance  $R_{\text{ct}}$ . The corresponding parameters obtained by fitting the EIS data are shown in **Table 1**. Obviously,  $R_{\text{ct}}$  increased with immersion time extending for the Fe part, which further proved the high resistance of the product layer and resultant protection efficiency. Meanwhile, its slight increase of  $C_d$  represented a growth of the compact passive film with a long-term stability. As for the Fe/CaCl<sub>2</sub> composite, a relatively low  $R_{\text{ct}}$  and  $C_d$  indicated its high charge transfer ability and porous product layer with poor protection efficiency (Marinenko and Foley, 1975; Darowicki and Gawel, 2017).

## In Vitro Cell Behavior

The biocompatibility of the Fe/CaCl<sub>2</sub> composite was investigated, with Fe as control. In general, the cells gradually increased with culture time increasing to 5 days, as shown in **Figure 7A**. In terms of cell morphology, a large number of cells developed pseudopodia and

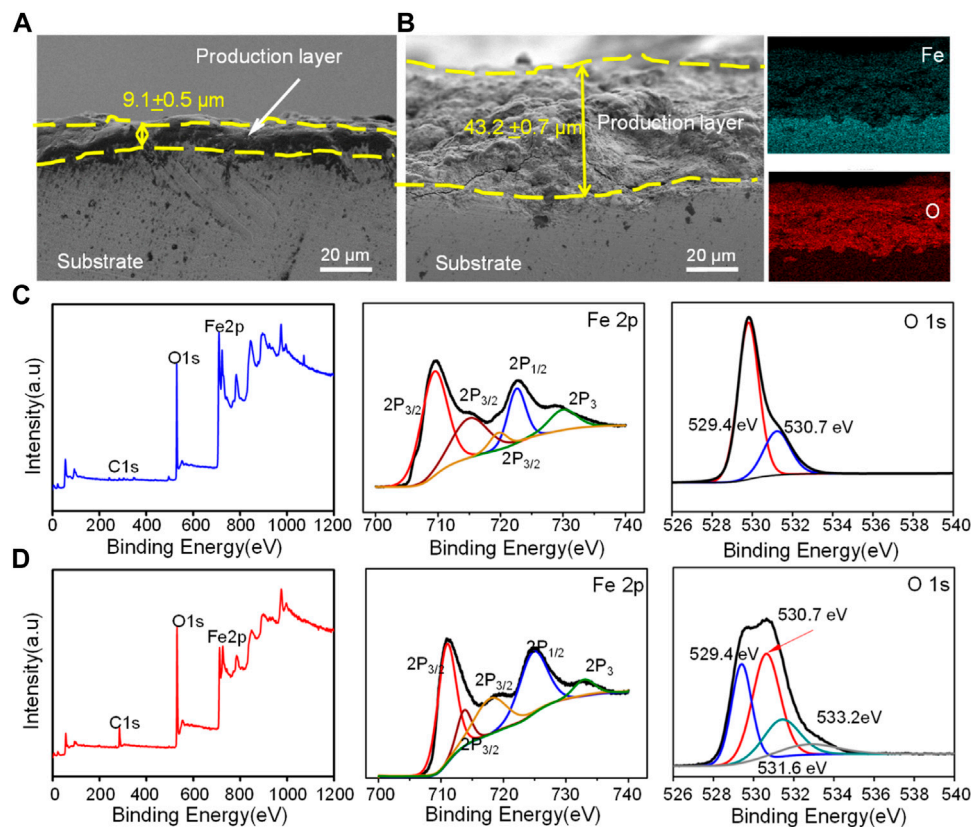


**FIGURE 4 |** The cross section of corrosion production for (A) Fe and (B) Fe/CaCl<sub>2</sub> after immersing for 28 days observed by SEM, and XPS analysis of the oxide layer for (C) Fe and (D) Fe/CaCl<sub>2</sub>, wherein the sputtering time was 10 s.

extracellular matrix at day 5. It was indicated that both the Fe/CaCl<sub>2</sub> composite and Fe exerted no obvious negative effect on cell growth. Furthermore, the cell survival rate was quantitatively analyzed by CCK-8 assay using 100% concentration extracts, as shown in **Figure 7B**. In both two groups, the cell viabilities were greater than 75%. According to ISO 10993-5-2009, the cytotoxicity was defined as grade 1, which was acceptable for bone implants (ISO, 2009). Notably, the cell viability of the Fe/CaCl<sub>2</sub> composite group was slightly higher than that of the Fe group. As shown in **Figure 7C**, the cells cultured in the Fe/CaCl<sub>2</sub> group showed intensive ALP staining as compared with the Fe group after 7 days' culture, which revealed the improvement of cell differentiation behavior. It was believed that the released Ca ion, as one of the important components for the human body, might exert a positive effect on cell growth and differentiation.

## DISCUSSION

Bone substitute was highly demanded aiming to achieve the tissue regeneration and functional reconstruction at critical defect sites (Puleo and Nanci, 1999; Li et al., 2020; Gao et al., 2021b; Qian et al., 2021). In the present study, Fe-based biocomposites were fabricated by laser additive manufacturing. Owing to the unique layer-by-layer fashion,

it easily realized the preparation of implant with high geometric complexity and interconnected microporous structure, as well as the customized shape for different patients or defect sites (An and Draughn, 1999). The typical Fe-based scaffolds fabricated by LPBF are presented in **Figure 8**. Bone tissue engineering scaffolds with different porous structures could be customized according to different needs. The other significant feature of LPBF was its rapid solidification process, which was able to tailor the microstructure (Yang et al., 2020b). Under the effect of laser irradiation, Marangoni convection was generally formed within molten pool, which effectively promoted the rearrangement of reinforcing particles (Kruth et al., 2005; Feng et al., 2021). Subsequently, the molten pool experienced a rapid solidification, namely, the fast-advancing solid-liquid interface, which could refine the grains and promote the uniform dispersion of reinforcing particles by "capture effect," as shown in **Figure 2**.

Bone implants also needed to have a degradation rate that matched the bone growth rate, so as to provide space for new bone tissue growth (Trisi et al., 2002). As previous research reported, Fe bone implants degraded too slowly, owing to its high corrosion potential and compact passive film (Cha et al., 2015). In general, a high corrosion potential represented a low corrosion tendency, whereas the compact

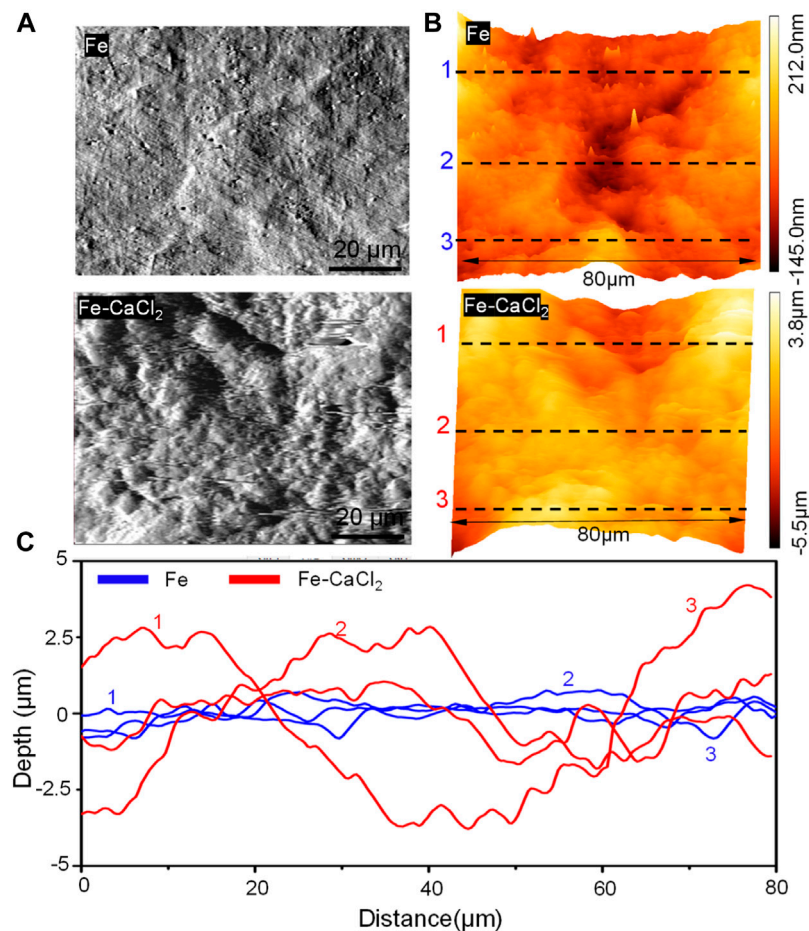


**FIGURE 5 | (A)** The AFM topography of the part surface in SBF for 28 days at 37°C, **(B)** AFM three-dimensional images, and **(C)** the derived surface roughness profiles.

passive film acted as a barrier that seriously hindered the matrix erosion (Sato and Kudo, 1971). In the present study, CaCl<sub>2</sub> as a halide was added into Fe bone implants and successfully accelerated the degradation, which was clearly proved by our immersion tests and electrochemical experiments. As shown in **Figure 4**, massive corrosion products with loose structure covered on the Fe/CaCl<sub>2</sub> composite. It was believed that the Cl ion released from the matrix resulted in the self-breakdown of the passivation film. In fact, Cl ion possessed strong electronegativity and could attach at the interface between the substrate and the passive film, thereby causing lattice expansion (Zhang et al., 2018). In this case, tensile stress was generally formed at the interface. Under this condition, the passive film located in the convex area of the interface was easily ruptured, thus forming micropores (Gao et al., 2021b). Herein, the Pilling–Bedworth ratio (PBR), defined as the ratio of the volume of oxide ( $V_{ox}$ ) and volume of metal ( $V_m$ ), was calculated to study the stress state of oxide film. According to the theory of PBR, the perfection or compactness of the oxide film could be expressed by (Zhou et al., 2010):

$$PBR = \frac{V_{ox}}{V_m} = \frac{m_{ox} \cdot \rho_m}{n \cdot A \cdot \rho_{ox}} \quad (1)$$

where  $m_{ox}$ ,  $\rho_m$ , and  $\rho_{ox}$  are the molar weight of the oxide, metal, and oxide densities, respectively.  $A$  and  $n$  are the atomic weight of the metal and the number of metal atoms in the oxide molecules, respectively. Based on XPS fitting curve analysis (**Figures 3B,C**), the calculated PBR for the Fe/CaCl<sub>2</sub> composite had a relatively small value of about 0.93 as compared with Fe (1.92) by using **Eq. 1**. It was reported that  $PBR < 1$  indicated a discontinuous and porous film with poor protection performance on the matrix (Xu and Gao, 2000; Wang et al., 2019), since it contributed to a smooth way for H<sub>2</sub>O and ions to penetrate into the oxide film. Furthermore, the uncovered Fe matrix would act as anode, whereas the porous passivation film served as cathode of corrosion battery, thus further accelerating the anodic reaction (El-Lateef et al., 2020).

On the other hand, our electrochemical experiments also proved that CaCl<sub>2</sub> reduced the corrosion resistance by means of enhancing the charge transfer ability. Usually, the charge



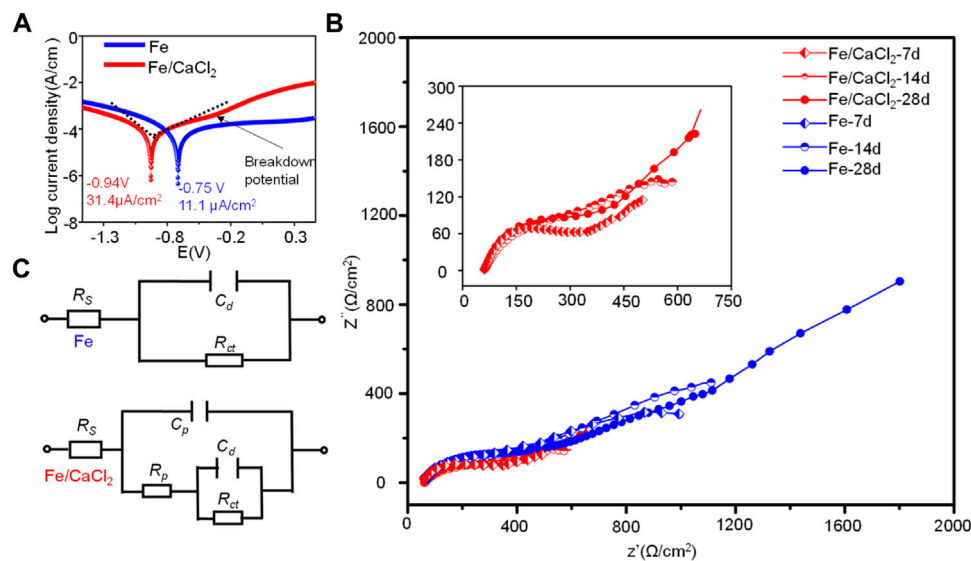


**FIGURE 6 | (A)** Tafel polarization curves for the Fe and Fe/CaCl<sub>2</sub> composites, **(B)** EIS diagrams, and **(C)** corresponding equivalent circuits after immersing for 7, 14, and 28 days.

**TABLE 1 |** Fitted parameters of EIS data for Fe/CaCl<sub>2</sub> composite and Fe.

Samples	Fe			Fe/CaCl <sub>2</sub>		
	7 days	14 days	28 days	7 days	14 days	28 days
$R_{ct}$ (Ω/cm <sup>2</sup> )	996.3	1,097.8	1,863.2	81.19	103.21	145.34
$C_d$ (μF)·10 <sup>-5</sup>	2.13	2.31	3.45	1.53	1.82	2.01

transfer ability was closely related to the structure of the passive film (Liu et al., 2020; Palaniappan et al., 2017). As shown in **Figures 9A,B**, the typical current density–time in linear and double logarithmic coordinate plots were polarized respectively at the film formation potential of 0.2 V. In the transient, the current density represented the total current resulting from the passive film formation and dissolution in SBF (Kim et al., 2018). As shown in **Figure 9A**, the initial current density decreased sharply with time extending. It was because the growth of the passive film was relatively fast as compared with the dissolution process (Heo et al., 2016). Subsequently, the current density maintained stably, indicating a balance of the formation and dissolution of the passive film. It was worth noting that the current density for the Fe/CaCl<sub>2</sub> composite was relatively high as compared with Fe, which corresponded to a weak protection ability of the passive film. Besides, the relatively high level of the current density gradually increased with time extending, which was attributed to the formation of the porous passive film (Lopes et al., 2019). As shown in **Figure 9B**, the decay rate for the Fe/CaCl<sub>2</sub> composite was much slow as compared with that of Fe, which further confirmed that the porous passive film improved the charge transfer capability (Bernède et al., 2008).

The electronic property of the passive film was further characterized by *in situ* Mott–Schottky analysis. As shown

in **Figure 9C**, the curve for the Fe/CaCl<sub>2</sub> composite exhibited a linear region with a positive slope in some potential range, which could be explained in detail by the capacitance of the passive film. According to the Mott–Schottky theory (Taveira et al., 2010), the capacitance ( $C_{sc}$ ) of passive film could be given by:

$$C_{sc}^{-2} = \frac{2}{\epsilon \epsilon_0 e N_d} \left( E - E_d - \frac{KT}{e} \right) \quad (2)$$

where  $\epsilon$  and  $N_d$  are the dielectric constant and donor density of the passive film, respectively.  $e$ ,  $E$ , and  $E_d$  correspond to the electric charge, the potential difference, and the potential in the flat band, respectively.  $K$ ,  $\epsilon_0$ , and  $T$  represent the Boltzmann constant ( $1.38 \times 10^{-23}$  J/K), the vacuum dielectric constant ( $8.854 \times 10^{-12}$  F/m), and the thermodynamic temperature in kelvin, respectively. According to **Eq. 2**, the donor concentration of the passive film increased with the increase in potential difference, as shown in **Figure 9D**. It was attributed that the movement of oxide anions increased the donor density of the whole corrosion process as passivation started (Windisch et al., 2000). In fact, the high donor density could enhance the sensitivity of the passive film to Cl ion corrosion, which accelerated the penetration and transport of Cl ions to the passive film, thereby resulting in the rapid formation of the porous passive film. In this case, the protective ability of the passive film gradually decreased, which further promoted the destruction of passive film and the corrosion of the Fe matrix (Liu and Wu, 2007; Gerling et al., 2017).

Apart from the suitable porous structure, sufficient mechanical strength, and suitable mechanical properties, bone implants also need to provide a suitable microenvironment for the growth of new tissues (Pooja et al., 2014; Li et al., 2019; Narayanan et al., 2020; Qi et al.,

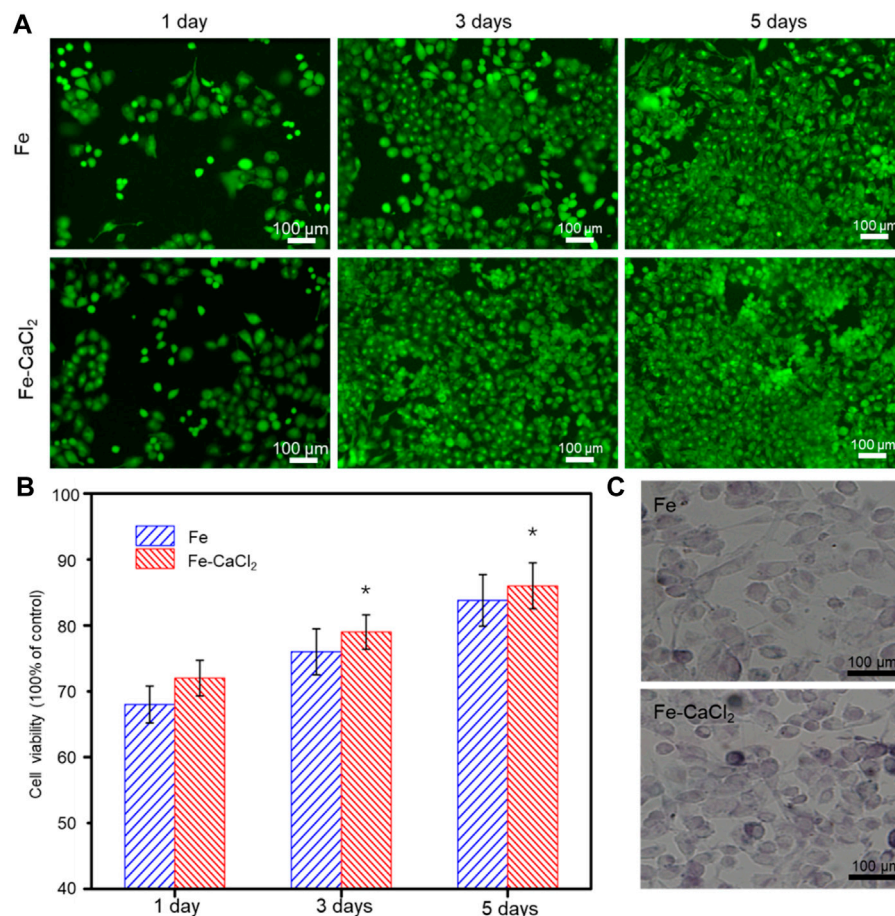


**FIGURE 7 | (A)** The cell fluorescent images after culture for 1, 3, and 5 days, and **(B)** the corresponding 100% concentration extracts using CCK-8 assay. **(C)** ALP stained cell after culture for 7 days.

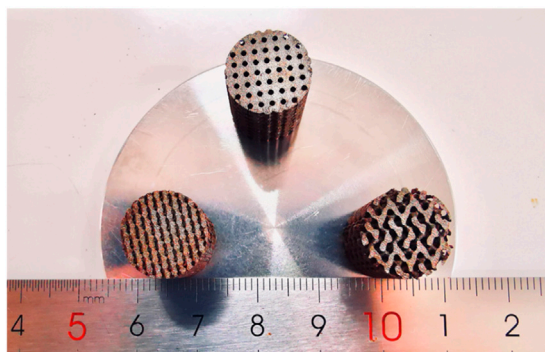


**FIGURE 8 |** Laser additively manufactured Fe-based scaffolds with porous structure.

2021). In the present study, the Fe/CaCl<sub>2</sub> biocomposite easily formed crystalline hydrate with water molecules, thereby showing a significant improvement of wettability, as shown in **Figure 2C**. Generally, the implants with favorable wettability

could quickly promote the adsorption of proteins in body fluids (Russell, 2000; He et al., 2020). As a result, numerous functional groups on proteins were able to bind to cell surface receptors, thus enhancing cell adhesion behavior. Besides, the released Ca<sup>2+</sup> ion from the Fe/CaCl<sub>2</sub> biocomposite promoted the cell growth, proliferation, and differentiation, as shown in **Figure 7**. For degradable implants, bone tissue was able to grow continuously during the process of dynamic degradation, so as to complete the repair of defect tissue and finally realize functional reconstruction (Zhao et al., 2015; He et al., 2021).

## CONCLUSION

In this study, the Fe/CaCl<sub>2</sub> biocomposite was fabricated by laser additively manufacturing. The effects of CaCl<sub>2</sub> on the microstructure, degradation behavior, and *in vitro* cell behavior were investigated. The conclusions were drawn as follows:

- 1) As compared with Fe, the surface roughness of the Fe/CaCl<sub>2</sub> composite increased to  $-5.5$  to  $3.8\ \mu\text{m}$  after immersion for 28 days. The surface film presented massive porous, and its thickness increased to  $43.2\ \mu\text{m}$ .

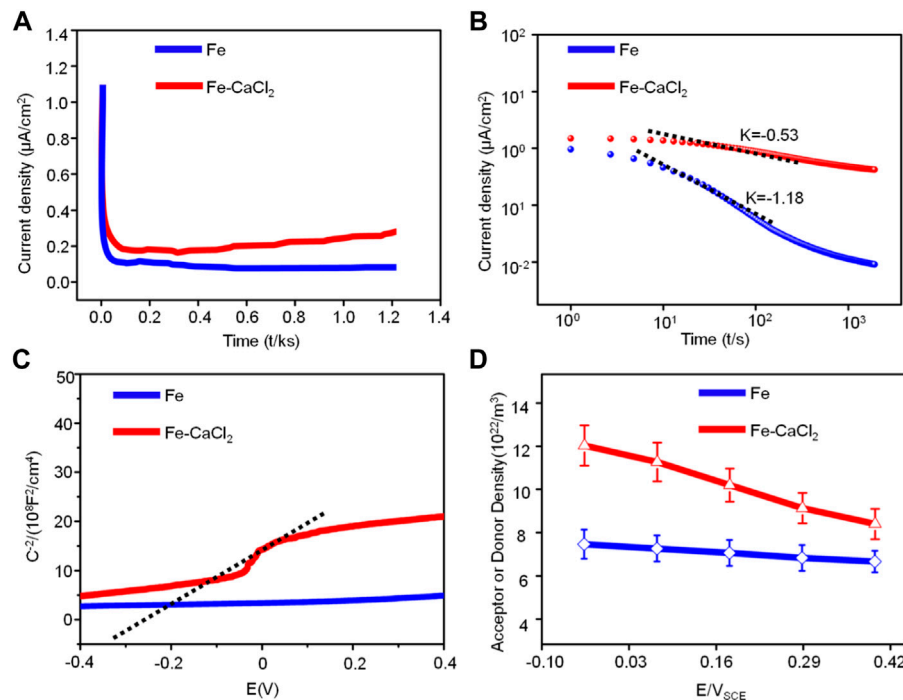


**FIGURE 9 | (A)** The current density–time in linear and **(B)** double logarithmic coordinates plots; **(C)** Mott–Schottky curves of Fe and Fe/CaCl<sub>2</sub> composite in SBF and **(D)** values of donor density.

- 2) The introduction of CaCl<sub>2</sub> led to the negative shift of breakdown potential for Fe-based implants and the increase in corrosion current to  $31.4 \pm 0.9 \mu\text{A}/\text{cm}^2$ . Besides, the current density and donor concentration of the passive film gradually increased with time, thus resulting in the enhancement of conductivity.
- 3) The uniformly distributed CaCl<sub>2</sub> decreased the water contacts of Fe-based bone implants to  $55.2 \pm 1.2^\circ$ , which improved the surface hydrophilicity and wettability. Meanwhile, Fe/CaCl<sub>2</sub> improved the cell growth and differentiation behavior, since the released Ca ion positively affected the cell response.

## DATA AVAILABILITY STATEMENT

The raw data supporting the conclusions of this article will be made available by the authors, without undue reservation.

## REFERENCES

- An, Y. H., and Draughn, R. A. (1999). *Mechanical Testing of Bone and the Bone-Implant Interface*. Boca Raton, Florida: CRC Press.
- Bernède, J. C., Cattin, L., Morsli, M., Berredjem, Y., and Cells, S. (2008). Ultra-thin Metal Layer Passivation of the Transparent Conductive Anode in Organic Solar Cells. *Solar Energ. Mater. Solar Cell* 92 (11), 1508–1515. doi:10.1016/j.solmat.2008.06.016

## AUTHOR CONTRIBUTIONS

Conceptualization, CS and YY; methodology, GC, MY; validation, CS, YY, and DW; formal analysis, SP; writing—review and editing, YY and ZL.

## FUNDING

This study was supported by the following funds: 1) National Natural Science Foundation of China (51935014, 52165043, 52105352, 82072084, 81871498); 2) Jiangxi Provincial Natural Science Foundation of China (2020ACB214004, 20202BAB214011); 3) The Provincial Key R&D Projects of Jiangxi (20201BBE51012); 4) The Project of State Key Laboratory of High Performance Complex Manufacturing; 5) China Postdoctoral Science Foundation (2020M682114); 6) Key Laboratory of Construction Hydraulic Robots of Anhui Higher Education Institutes, Tongling University (TLXYCHR-O-21YB01); and 7) Jiangsu Key Laboratory of Precision and Micro-Manufacturing Technology.

- Cha, J. Y., Pereira, M. D., Smith, A. A., Houschyar, K. S., Yin, X., Mouraret, S., et al. (2015). Multiscale Analyses of the Bone-Implant Interface. *J. Dent Res.* 94 (3), 482–490. doi:10.1177/0022034514566029
- Chen, T., Shi, P., Zhang, J., Li, Y., Tian, X., Lian, J., et al. (2018). Bioinspired Enhancement of Chitosan Nanocomposite Films via Mg-ACC Crystallization, Their Robust, Hydrophobic and Biocompatible. *Appl. Surf. Sci.* 459, 129–137. doi:10.1016/j.apsusc.2018.07.194

- Chen, Z., Nong, Y., Chen, Y., Chen, J., and Yu, B. (2020). Study on the Adsorption of OH<sup>-</sup> and CaOH<sup>+</sup> on Fe (100) Surface and Their Effect on Passivation of Steel Bar: Experiments and DFT Modelling. *Corrosion Sci.* 174, 108804. doi:10.1016/j.corsci.2020.108804
- Cheng, J., Liu, B., Wu, Y. H., and Zheng, Y. F. (2013). Comparative *In Vitro* Study on Pure Metals (Fe, Mn, Mg, Zn and W) as Biodegradable Metals. *J. Mater. Sci. Tech.* 29 (7), 619–627. doi:10.1016/j.jmst.2013.03.019
- Darowicki, K., and Gawel, L. (2017). Impedance Measurement and Selection of Electrochemical Equivalent Circuit of a Working PEM Fuel Cell Cathode. *Electrocatalysis* 8 (3), 235–244. doi:10.1007/s12678-017-0363-0
- El-Lateef, H. M. A., Albokheet, W. A., and Gouda, M. (2020). Carboxymethyl Cellulose/metal (Fe, Cu and Ni) Nanocomposites as Non-precious Inhibitors of C-Steel Corrosion in HCl Solutions: Synthesis, Characterization, Electrochemical and Surface Morphology Studies. *Cellulose* 27 (14), 8039–8057. doi:10.1007/s10570-020-03292-6
- Feng, P., Kong, Y., Liu, M., Peng, S., and Shuai, C. (2021). Dispersion Strategies for Low-Dimensional Nanomaterials and Their Application in Biopolymer Implants. *Mater. Today Nano* 15, 100127. doi:10.1016/j.mtnano.2021.100127
- Gao, C., Yao, M., Peng, S., Tan, W., and Shuai, C. (2021a). Pre-oxidation Induced *In Situ* Interface Strengthening in Biodegradable Zn/nano-SiC Composites Prepared by Selective Laser Melting. *J. Adv. Res.* doi:10.1016/j.jare.2021.09.014
- Gao, C., Zeng, Z., Peng, S., and Shuai, C. (2021b). *Magnetostriuctive Alloys: Promising Materials for Biomedical Applications*. Bioactive Materials.
- Gerling, L. G., Voz, C., Alcubilla, R., and Puigdollers, J. (2017). Origin of Passivation in Hole-Selective Transition Metal Oxides for Crystalline Silicon Heterojunction Solar Cells. *J. Mater. Res.* 32 (2), 260–268. doi:10.1557/jmr.2016.453
- Gu, J.-L., Lu, S.-Y., Shao, Y., and Yao, K.-F. (2021). Segregating the Homogeneous Passive Film and Understanding the Passivation Mechanism of Ti-Based Metallic Glasses. *Corrosion Sci.* 178, 109078. doi:10.1016/j.corsci.2020.109078
- He, F., Lu, T., Fang, X., Feng, S., Feng, S., Tian, Y., et al. (2020). Novel Extrusion-Microdrilling Approach to Fabricate Calcium Phosphate-Based Bioceramic Scaffolds Enabling Fast Bone Regeneration. *ACS Appl. Mater. Inter.* 12 (29), 32340–32351. doi:10.1021/acsami.0c07304
- He, F., Lu, T., Feng, S., Wang, Y., Huang, C., Zhang, Y., et al. (2021). Alliance of Gallium and Strontium Potently Mediates the Osteoclastic and Osteogenic Activities of  $\beta$ -tricalcium Phosphate Bioceramic Scaffolds. *Chem. Eng. J.* 412, 128709. doi:10.1016/j.cej.2021.128709
- Heo, J. S., Jo, J.-W., Kang, J., Jeong, C.-Y., Jeong, H. Y., Kim, S. K., et al. (2016). Water-Mediated Photochemical Treatments for Low-Temperature Passivation of Metal-Oxide Thin-Film Transistors. *ACS Appl. Mater. Inter.* 8 (16), 10403–10412. doi:10.1021/acsami.5b12819
- Hermawan, H., Purnama, A., Dube, D., Couet, J., and Mantovani, D. (2010). Fe-Mn Alloys for Metallic Biodegradable Stents: Degradation and Cell Viability Studies☆. *Acta Biomater.* 6 (5), 1852–1860. doi:10.1016/j.actbio.2009.11.025
- ISO (2009). *Biological Evaluation of Medical Devices—Part 5: Tests for in Vitro Cytotoxicity*. Switzerland: IOS, 10993–10995.
- Kim, J. Y., Kim, A.-Y., Liu, G., Woo, J.-Y., Kim, H., and Lee, J. K. (2018). Li<sub>4</sub>SiO<sub>4</sub>-Based Artificial Passivation Thin Film for Improving Interfacial Stability of Li Metal Anodes. *ACS Appl. Mater. Inter.* 10 (10), 8692–8701. doi:10.1021/acsami.7b18997
- Kim, M., Kim, G.-H., Lee, T. K., Choi, I. W., Choi, H. W., Jo, Y., et al. (2019). Methylammonium Chloride Induces Intermediate Phase Stabilization for Efficient Perovskite Solar Cells. *Joule* 3 (9), 2179–2192. doi:10.1016/j.joule.2019.06.014
- Kong, D., Dong, C., Wei, X., Man, C., Lei, X., Mao, F., et al. (2018). Size Matching Effect between Anion Vacancies and Halide Ions in Passive Film Breakdown on Copper. *Electrochimica Acta* 292, 817–827. doi:10.1016/j.electacta.2018.10.004
- Kruth, J. P., Mercelis, P., Van Vaerenbergh, J., Froyen, L., and Rombouts, M. J. R. P. (2005). *Binding Mechanisms in Selective Laser Sintering and Selective Laser Melting*.
- Li, J., Liu, X., Crook, J. M., and Wallace, G. G. (2020). 3D Printing of Cytocompatible Graphene/alginate Scaffolds for Mimetic Tissue Constructs. *Front. Bioeng. Biotechnol.* 8, 824. doi:10.3389/fbioe.2020.00824
- Li, L., Shi, J., Zhang, K., Yang, L., Yu, F., Zhu, L., et al. (2019). Early Osteointegration Evaluation of Porous Ti6Al4V Scaffolds Designed Based on Triply Periodic Minimal Surface Models. *J. Orthopaedic Translation* 19, 94–105. doi:10.1016/j.jot.2019.03.003
- Li, Y., Jahr, H., Lietaert, K., Pavanram, P., Yilmaz, A., Fockaert, L. I., et al. (2018). Additively Manufactured Biodegradable Porous Iron. *Acta Biomater.* 77, 380–393. doi:10.1016/j.actbio.2018.07.011
- Liu, C., and Wu, J. J. C. S. (2007). Influence of pH on the Passivation Behavior of 254SMO Stainless Steel in 3.5% NaCl Solution 49 (5), 2198–2209.
- Liu, K., He, P., Bai, H., Chen, J., Dong, F., Wang, S., et al. (2017). Effects of Dodecyltrimethylammonium Bromide Surfactant on Both Corrosion and Passivation Behaviors of Zinc Electrodes in Alkaline Solution. *Mater. Chem. Phys.* 199, 73–78. doi:10.1016/j.matchemphys.2017.06.050
- Liu, S., Fang, X., Lu, B., and Yan, D. (2020). Wide Range zero-thermal-quenching Ultralong Phosphorescence from Zero-Dimensional Metal Halide Hybrids. *Nat. Commun.* 11 (1), 4649–9. doi:10.1038/s41467-020-18482-w
- Lopes, T. S., Cunha, J. M. V., Bose, S., Barbosa, J. R. S., Borme, J., Donzel-Gargand, O., et al. (2019). Rear Optical Reflection and Passivation Using a Nanopatterned Metal/dielectric Structure in Thin-Film Solar Cells. *IEEE J. Photovoltaics* 9 (5), 1421–1427. doi:10.1109/jphotov.2019.2922323
- Marinenko, G., and Foley, R. T. (1975). Absolute Determination of the Electrochemical Equivalent and the Atomic Weight of Zinc. I. Method, Apparatus, and Preliminary Experiments. *J. Res. Natl. Bur. Stan. Sect. A* 79A (6), 737. doi:10.6028/jres.079a.030
- Narayanan, N., Jiang, C., Wang, C., Uzunalli, G., Whittern, N., Chen, D., et al. (2020). Harnessing Fiber Diameter-dependent Effects of Myoblasts toward Biomimetic Scaffold-Based Skeletal Muscle Regeneration. *Front. Bioeng. Biotechnol.* 8, 203. doi:10.3389/fbioe.2020.00203
- Palaniappan, N., Chowhan, L. R., Jothi, S., Bosco, I. G., and Cole, I. S. (2017). Corrosion Inhibition on Mild Steel by Phosphonium Salts in 1 M HNO<sub>3</sub> Aqueous Medium. *Surf. Inter.* 6, 237–246. doi:10.1016/j.surfint.2016.10.003
- Pérez-Ruiz, J. D., de Lacalle, L. N. L., Urbikain, G., Pereira, O., Martínez, S., and Bris, J. (2021). On the Relationship between Cutting Forces and Anisotropy Features in the Milling of LPBF Inconel 718 for Near Net Shape Parts. *Int. J. Machine Tools Manufacture* 170, 103801. doi:10.1016/j.ijmachtools.2021.103801
- Pooja, D., Panyaram, S., Kulhari, H., Rachamalla, S. S., and Sistla, R. (2014). Xanthan Gum Stabilized Gold Nanoparticles: Characterization, Biocompatibility, Stability and Cytotoxicity. *Carbohydr. Polym.* 110, 1–9. doi:10.1016/j.carbpol.2014.03.041
- Puleo, D. A., and Nanci, A. (1999). Understanding and Controlling the Bone-Implant Interface. *Biomaterials* 20 (23-24), 2311–2321. doi:10.1016/s0142-9612(99)00160-x
- Qi, F., Zeng, Z., Yao, J., Cai, W., Zhao, Z., Peng, S., et al. (2021). Constructing Core-Shell Structured BaTiO<sub>3</sub>@carbon Boosts Piezoelectric Activity and Cell Response of Polymer Scaffolds. *Mater. Sci. Eng. C* 126, 112129. doi:10.1016/j.msec.2021.112129
- Qian, G., Zhang, L., Wang, G., Zhao, Z., Peng, S., and Shuai, C. (2021). 3D Printed Zn-Doped Mesoporous Silica-Incorporated Poly-L-Lactic Acid Scaffolds for Bone Repair. *Int. J. Bioprinting* 7 (2). doi:10.18063/ijb.v7i2.346
- Russell, J. M. (2000). Sodium-potassium-chloride Cotransport. *Physiol. Rev.* 80, 211–276.
- Sato, N., and Kudo, K. (1971). Ellipsometry of the Passivation Film on Iron in Neutral Solution. *Electrochimica Acta* 16 (4), 447–462. doi:10.1016/0013-4686(71)85182-4
- Seol, Y. J., Park, J. Y., Jung, J. W., Jang, J., Girdhari, R., Kim, S. W., et al. (2014). Improvement of Bone Regeneration Capability of Ceramic Scaffolds by Accelerated Release of Their Calcium Ions. *Tissue Eng. Part. A* 20 (21-22), 2840–2849. doi:10.1089/ten.TEA.2012.0726
- Sharma, P., and Pandey, P. M. (2019). Corrosion Behaviour of the Porous Iron Scaffold in Simulated Body Fluid for Biodegradable Implant Application. *Mater. Sci. Eng. C* 99, 838–852. doi:10.1016/j.msec.2019.01.114
- Shuai, C., He, C., Peng, S., Qi, F., Wang, G., Min, A., et al. (2021). Mechanical Alloying of Immiscible Metallic Systems: Process, Microstructure, and Mechanism. *Adv. Eng. Mater.* 23, 2001098. doi:10.1002/adem.202001098
- Shuai, C., He, C., Peng, S., Qi, F., Wang, G., Min, A., et al. (2021). Mechanical Alloying of Immiscible Metallic Systems: Process, Microstructure, and Mechanism. *Adv. Eng. Mater.* 23 (4), 2001098. doi:10.1002/adem.202001098
- Spotorno, R., Ghiara, G., Latronico, G., Carlini, R., Mele, P., and Artini, C. J. J. O. E. M. (2020). Corrosion of the Filled Skutterudite Sm 0.1 (Fe 0.45 Ni 0.55) 4 Sb 12 by NaCl Solutions. *Electrochem. Study*, 1–9.



- Taveira, L. V., Montemor, M. F., Da Cunha Belo, M., Ferreira, M. G., and Dick, L. F. P. (2010). Influence of Incorporated Mo and Nb on the Mott-Schottky Behaviour of Anodic Films Formed on AISI 304L. *Corrosion Sci.* 52 (9), 2813–2818. doi:10.1016/j.corsci.2010.04.021
- Trisi, P., Lazzara, R., Rao, W., Rebaudi, A. J. I. J. o. P., and Dentistry, R. (2002). *Bone-implant Contact and Bone Quality: Evaluation of Expected and Actual Bone Contact on Machined and Osseointegrated Implant Surfaces*, 22.6.
- Wang, D., Deng, G.-w., Yang, Y.-q., Chen, J., Wu, W.-h., Wang, H.-l., et al. (2021). Interface Microstructure and Mechanical Properties of Selective Laser Melted Multilayer Functionally Graded Materials. *J. Cent. South. Univ.* 28 (4), 1155–1169. doi:10.1007/s11771-021-4687-9
- Wang, H., Yu, W., and Shen, S. (2019). Chemo-mechanical Coupling Effect in the High-Temperature Oxidation of Metal Materials: A Review. *Sci. China Technol. Sci.* 62 (8), 1246–1254. doi:10.1007/s11431-018-9500-y
- Wang, L., Dou, Y., Han, S., Wu, J., and Cui, Z. (2020). Influence of Sulfide on the Passivation Behavior and Surface Chemistry of 2507 Super Duplex Stainless Steel in Acidified Artificial Seawater. *Appl. Surf. Sci.* 504, 144340. doi:10.1016/j.apsusc.2019.144340
- Wang, Z. B., Hu, H. X., Liu, C. B., and Zheng, Y. G. (2014). The Effect of Fluoride Ions on the Corrosion Behavior of Pure Titanium in 0.05M Sulfuric Acid. *Electrochimica Acta* 135, 526–535. doi:10.1016/j.electacta.2014.05.055
- Windisch, C. F., Jr, Exarhos, G. J., and Technology A, S. (2000). Mott-schottky Analysis of Thin ZnO Films. *J. Vacuum Sci. Tech. A: Vacuum, Surf. Films* 18 (4), 1677–1680. doi:10.1116/1.582406
- Wu, P., Zhu, X., Xu, L., Peng, W., and Zhao, G. (2020). Effect of Stray Current Coupled with Chloride Concentration and Temperature on the Corrosion Resistance of a Steel Passivation Film. *Electrochemistry Commun.* 118, 106793. doi:10.1016/j.elecom.2020.106793
- Xu, C., and Gao, W. (2000). Pilling-Bedworth Ratio for Oxidation of Alloys. *Mater. Res. Innov.* 3 (4), 231–235. doi:10.1007/s100190050008
- Yang, C., Huan, Z., Wang, X., Wu, C., and Chang, J. (2018). 3D Printed Fe Scaffolds with HA Nanocoating for Bone Regeneration. *ACS Biomater. Sci. Eng.* 4 (2), 608–616. doi:10.1021/acsbomaterials.7b00885
- Yang, H., Jia, B., Zhang, Z., Qu, X., Li, G., Lin, W., et al. (2020). Alloying Des. biodegradable zinc as promising bone Implants load-bearing Appl. 11 (1), 1–16. doi:10.1038/s41467-019-14153-7
- Yang, Y., He, C., Dianyu E, E., Yang, W., Qi, F., Xie, D., et al. (2020). Design, Mg Bone Implant: Features, Developments and Perspectives. *Mater. Des.* 185, 108259. doi:10.1016/j.matdes.2019.108259
- Yang, Y., Lu, C., Shen, L., Zhao, Z., Peng, S., and Shuai, C. (2021). *In-situ* Deposition of Apatite Layer to Protect Mg-Based Composite Fabricated via Laser Additive Manufacturing. *J. Magnesium Alloys.* doi:10.1016/j.jma.2021.04.009
- Yin, X., Wang, H., Sun, S., and Han, E.-H. (2020). Comparative Study on the Adsorption Behaviors of O and Cl on Fe(110) Surfaces with Different Cr Content. *Mater. Today Commun.* 24, 101122. doi:10.1016/j.mtcomm.2020.101122
- Zhang, B., Wang, J., Wu, B., Guo, X. W., Wang, Y. J., Chen, D., et al. (2018). Unmasking Chloride Attack on the Passive Film of Metals. *Nat. Commun.* 9 (1), 2559–9. doi:10.1038/s41467-018-04942-x
- Zhao, J., Lai, H., Lyu, Z., Jiang, Y., Xie, K., Wang, X., et al. (2015). Hydrophilic Hierarchical Nitrogen-Doped Carbon Nanocages for Ultrahigh Supercapacitive Performance. *Adv. Mater.* 27 (23), 3541–3545. doi:10.1002/adma.201500945
- Zhou, H., Qu, J., and Cherkaoui, M. (2010). Stress-oxidation Interaction in Selective Oxidation of Cr-Fe Alloys. *Mech. Mater.* 42 (1), 63–71. doi:10.1016/j.mechmat.2009.09.007
- Zhou, S., Yan, Q., Tang, C., Mao, F., Pu, J., and Macdonald, D. D. (2020). Effect of the Chloride on Passivity Breakdown of Al-Zn-Mg alloy. *Corrosion Sci.* 163, 108254. doi:10.1016/j.corsci.2019.108254

**Conflict of Interest:** The authors declare that the research was conducted in the absence of any commercial or financial relationships that could be construed as a potential conflict of interest.

**Publisher's Note:** All claims expressed in this article are solely those of the authors and do not necessarily represent those of their affiliated organizations, or those of the publisher, the editors, and the reviewers. Any product that may be evaluated in this article, or claim that may be made by its manufacturer, is not guaranteed or endorsed by the publisher.

Copyright © 2021 Yang, Cai, Yang, Wang, Peng, Liu and Shuai. This is an open-access article distributed under the terms of the Creative Commons Attribution License (CC BY). The use, distribution or reproduction in other forums is permitted, provided the original author(s) and the copyright owner(s) are credited and that the original publication in this journal is cited, in accordance with accepted academic practice. No use, distribution or reproduction is permitted which does not comply with these terms.





# Synthesis of Silica-Based Solid-Acid Catalyst Material as a Potential Osteochondral Repair Model *In Vitro*

Rui-Min Long<sup>1†</sup>, Yan Jiang<sup>2†</sup>, Jia-Qi Guo<sup>1</sup>, Gang Ren<sup>2</sup>, Xian-Xin Guo<sup>1</sup>, Xue Xie<sup>1</sup>, Yue Wu<sup>1</sup>, Rui-Da Yan<sup>1</sup>, Zi-Zhen Lin<sup>1</sup>, Shi-Bin Wang<sup>2,3,4</sup> and Yuan-Gang Liu<sup>1,3,4\*</sup>

<sup>1</sup>College of Chemical Engineering, Huaqiao University, Xiamen, China, <sup>2</sup>College of Materials Science and Engineering, Xiamen, China, <sup>3</sup>Institute of Pharmaceutical Engineering, Huaqiao University, Xiamen, China, <sup>4</sup>Fujian Provincial Key Laboratory of Biochemical Technology, Xiamen, China

## OPEN ACCESS

### Edited by:

Lei Zhang,  
Wenzhou Medical University, China

### Reviewed by:

Xin Xiong,  
NMI Natural and Medical Sciences  
Institute, Germany  
Ting Wang,  
Southeast University, China  
Sami Sajjadifar,  
Payame Noor University, Iran  
Lihua Li,  
Jinan University, China

### \*Correspondence:

Yuan-Gang Liu  
ygliu@hqu.edu.cn

<sup>†</sup>These authors have contributed  
equally to this work

### Specialty section:

This article was submitted to  
Biomaterials,  
a section of the journal  
Frontiers in Bioengineering and  
Biotechnology

Received: 06 October 2021

Accepted: 10 November 2021

Published: 03 December 2021

### Citation:

Long R-M, Jiang Y, Guo J-Q, Ren G,  
Guo X-X, Xie X, Wu Y, Yan R-D, Lin Z-Z,  
Wang S-B and Liu Y-G (2021)  
Synthesis of Silica-Based Solid-Acid  
Catalyst Material as a Potential  
Osteochondral Repair Model *In Vitro*.  
Front. Bioeng. Biotechnol. 9:790139.  
doi: 10.3389/fbioe.2021.790139

For osteochondral damage, the pH value change of the damaged site will influence the repair efficacy of the patient. For better understanding the mechanism of the acid-base effect, the construction of *in vitro* model is undoubtedly a simple and interesting work to evaluate the influence. Here, a novel porous silica-based solid-acid catalyst material was prepared by additive manufacturing technology, exhibiting improved eliminating effects of the residue. SEM, FTIR, and TGA were used to characterize the morphology, structure, and thermal stability of the synthesized 3D material. The reaction between 4-methoxybenzyl alcohol and 3, 4-dihydro-2H-pyran was used as a template reaction to evaluate the eliminating performance of the 3D porous material. Solvents were optimized, and three reaction groups in the presence of 3D SiO<sub>2</sub>, 3D SiO<sub>2</sub>-SO<sub>3</sub>H, and 3D SiO<sub>2</sub>-NH-SO<sub>3</sub>H, as well as one without catalyst, were compared. In addition, in consideration of the complicated situation of the physiological environment *in vivo*, universality of the synthesized 3D SiO<sub>2</sub>-NH-SO<sub>3</sub>H catalyst material was studied with different alcohols. The results showed that the sulfonic acid-grafted 3D material had excellent catalytic performance, achieving a yield over 95% in only 20 min. Besides, the catalyst material can be recycled at least 10 times, with yields still higher than 90%. Such a solid catalyst material is expected to have great potential in additive manufacturing because the catalyst material is easy-recyclable, renewable and biocompatible. The 3D material with connective channels may also be utilized as an *in vitro* model for environment evaluation of osteochondral repair in the future.

**Keywords:** solid-acid catalyst material, 3D printing, SiO<sub>2</sub>, osteochondral repair, *in vitro* evaluation

## INTRODUCTION

For decades, many people suffer from various bone and cartilage damages such as arthritis. To treat these diseases, tissue engineering provides a promising and alternative method in orthopedic surgery and biomedical engineering (Wei et al., 2021a). For example, Wei et al. fabricated a 3D printed polycaprolactone scaffold modified by insulin-releasing PLGA nanoparticles for osteochondral repair, and the results indicate that both of the *in vitro* and *in vivo* studies show that the insulin-releasing scaffolds significantly improve the osteogenic differentiation of rabbit bone mesenchymal stem cells and the proliferation of

chondrocytes, and further improve the repair of cartilage and subchondral bone after 8- and 12-weeks implantation in rabbit osteochondral defects (Wei et al., 2021b). However, several factors have great influence on tissue regeneration, for example, such as the degradation of the biomaterials will result in the acid-base concentration change at the treatment site (Li et al., 2021; Xue et al., 2021), and the enrichment and diffusion of calcium ions could promote neovascularization and repair of the critical defect (Xing et al., 2021). Thus, to understand the influence of these factors is an important issue for bone and cartilage repair. *In vitro* model provides an indirect and convenient platform to assess the repair effect and scrutinize different molecular and possible therapeutic targets for better understanding the mechanisms and osteoarthritis therapeutics (Hopkins et al., 2021; Singh et al., 2021). Consequently, The aim of this work is to establish an *in vitro* model to evaluate the effect of acid-base by preparing a novel porous silica-based solid-acid catalyst material using additive manufacturing technology which may exhibit improved eliminating effects. To prepare the model, in the synthesis of some complex compounds, molecule intermediates often carry multiple functional groups, and sometimes, these functional groups react with other reactants before the intended product(s) can be formed. Therefore, protecting some functional groups of the molecule from reaction is necessary, while leaving other functional groups free to participate in the reaction (Rajkumari et al., 2017). One important example is the protection of hydroxyl groups. Until now, many ways have been discovered to achieve alcohol protection. Among these methods, ether-forming protection of hydroxyl groups (reaction of an alcohol with 3,4-dihydro-2H-pyran) is considered the most popular and convenient solution (Kumar et al., 2014; Khder et al., 2018). This is because, first, the protective agent is easier to prepare than other protective agents. Further, the corresponding ether pair reaction conditions and some reagents used, such as the format reagent, hydride, strong alkali, and other organometallic reagents, have good stability (Azzena et al., 2018). Lastly, many kinds of catalysts have been reported for tetrahydropyranlation of alcohols, including ionic liquids (Rafael et al., 2001), silica chloride (Ravindranath et al., 2001),  $\text{Al}(\text{OTf})_3$  (Williams et al., 2010), silica sulfonic acid (Shimizu et al., 2004), and modified zeolites (Narender et al., 2010; Shin et al., 2017). However, many of them have disadvantages, such as low efficiency, instability, harsh reaction conditions, and an inability to be recycle. Preparing catalysts free from these disadvantages is an important research direction (Nakhaei et al., 2019; Sajjadifar et al., 2019). According to previous work, advanced continuous porous structures help control and increase the distribution of catalytically active components, enhancing catalytic performance (Stuecker et al., 2004; Ludwig et al., 2018). However, traditional porous materials are obtained by a template method and vapor deposition, as well as others, and suffer from long preparation cycles and complicated steps (Xintong and Chang-jun, 2017). Additive manufacturing technology, also

called 3D printing, is a powerful tool for designing advanced structures (Wang et al., 2020). Silica is preferred as a carrier for its stability in most solvents, and Niknam and coworkers (Niknam et al., 2010) successfully prepared silica-bonded S-sulfonic acid (SBSSA) and employed it as a recyclable catalyst for the condensation reaction of aromatic aldehydes with 3-methyl-1-phenyl-5-pyrazolone. With continued catalyst development, Pourghasemi-Lati and colleagues (Pourghasemi-Lati et al., 2018) immobilized butane-1-sulfonic acid on magnetic  $\text{Fe}_3\text{O}_4/\text{SiO}_2$  nanoparticles for the synthesis of 5-arylidine barbituric acids and pyrano [2,3-*d*] pyrimidine derivatives. In addition, silica-based biomaterials have been widely studied in bone and cartilage tissue engineering due to high mechanical stiffness, high biocompatibility, and special bioactivities including stimulating osteogenesis and angiogenesis by enhancing corresponding gene expressions (Li et al., 2000; Du et al., 2015; Ishikawa et al., 2018). For example, silica based inorganic/organic hybrids could promote collagen Type II, Sox9 and Aggrecan production from chondrocytes (Nelson et al., 2021) or have mechanically strong and elastic characteristics (Yu et al., 2021).

Here, a new silica carrier is described, fabricated by 3D printing and combined with advanced structural perspectives. Further, chemical modifications were carried out, introducing many sulfonic acid groups, and the catalyst material was applied to hydroxyl protection reactions as model test. In addition, in consideration of the complicated situation of the physiological environment *in vivo*, universality of the synthesized material was studied. The new material is anticipated to be utilized as an *in vitro* model for environment evaluation of osteochondral repair in the future.

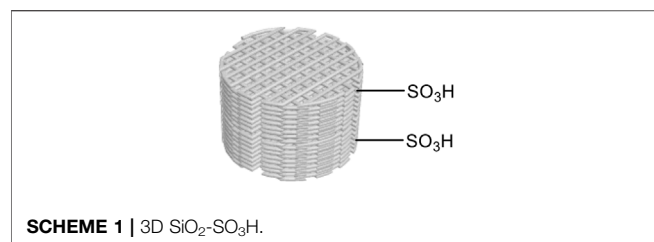
## EXPERIMENTS

### Materials and Equipment

$\text{SiO}_2$  powder (industrial grade) was provided by Delu Hardware & Plastic Co., Ltd. Chlorosulfonic acid (99% purity) was supplied by Energy Chemical. Analytical grade chemicals, including sodium alginate, ethanol, trichloromethane, dichloromethane, 3, 4-dihydro-2H-pyran, (3-chloropropyl) triethoxysilane, diethylenetriamine, 1-hexanol, 1-octanol, 1-dodecanol, 1-hexadecanol, cyclohexanol, cyclohexanemethanol, 4-methoxybenzyl alcohol, 4-chlorobenzyl alcohol, 4-bromobenzyl alcohol, and 4-methylbenzyl alcohol, were all purchased from Aladdin or Sinopharm Chemical Reagent Co., Ltd. A 3D printer (Regenovo 3D Bio-Architect -WS) was utilized to prepare the 3D model, and a furnace (Tianjin Zhong Huan, 1,600°C) was used for post-processing of the model.

### Preparation of Porous $\text{SiO}_2$

$\text{SiO}_2$  powder was first dispersed in ethanol and, then, loaded in a syringe and installed on the 3D printer. Next, the porous silica structure was printed under a pressure of 0.5 MPa and speed of



6 mm/s. Porous SiO<sub>2</sub> was obtained via a sintering process at 1,500°C. In the following research, two kinds of porous silica-based solid-acid catalysts were prepared: 3D SiO<sub>2</sub>-SO<sub>3</sub>H (catalyst 1) and 3D SiO<sub>2</sub>-NH-SO<sub>3</sub>H (catalyst 2).

### Preparation of Porous Silica-Based Solid-Acid Catalyst 1

Three-dimensional SiO<sub>2</sub> was first activated by 15 ml of 30% H<sub>2</sub>O<sub>2</sub> under 150°C to increase the number of hydroxyl groups. After drying, three pieces of 3D SiO<sub>2</sub> were mixed with chlorosulfonic acid (0.5 ml) and reacted in CHCl<sub>3</sub> (8 ml) at 0°C for 4 h. After drying in the vacuum drying oven, catalyst 1 (3D SiO<sub>2</sub>-SO<sub>3</sub>H, **Scheme 1**) was obtained.

### Preparation of Porous Silica-Based Solid-Acid Catalyst 2

A schematic diagram of the preparation of 3D SiO<sub>2</sub>-NH-SO<sub>3</sub>H is presented in **Figure 1**. Briefly, the carrier was first activated by 15 ml of 30% H<sub>2</sub>O<sub>2</sub> at 150°C to increase the number of hydroxyl groups (Díaz-Marta et al., 2018). Then, (3-chloropropyl)triethoxysilane (0.5 ml) was used to modify the surface of porous SiO<sub>2</sub>, yielding the chlorine-modified porous carrier (3D SiO<sub>2</sub>-Cl, **Scheme 2** in **Figure 1**). To obtain more sulfonic acid groups, 3D SiO<sub>2</sub>-Cl (three pieces) were put in a round-bottomed flask with diethylenetriamine (5 mmol), triethylamine (5.5 mmol), and DMF (10 ml) and reacted at 100°C for 12 h. After drying, the intermediate

product, with double terminal amino groups, was obtained (3D SiO<sub>2</sub>-NH<sub>2</sub>, **Scheme 3** in **Figure 1**). Finally, three pieces of 3D SiO<sub>2</sub>-NH<sub>2</sub> were mixed with chlorosulfonic acid (0.5 ml) in CHCl<sub>3</sub> (8 ml) for 4 h at 0°C, and then, catalyst 2 (3D SiO<sub>2</sub>-NH-SO<sub>3</sub>H, **Scheme 4** in **Figure 1**) was obtained via drying in the vacuum drying oven.

### Catalytic Reaction of the 3D Porous Catalyst

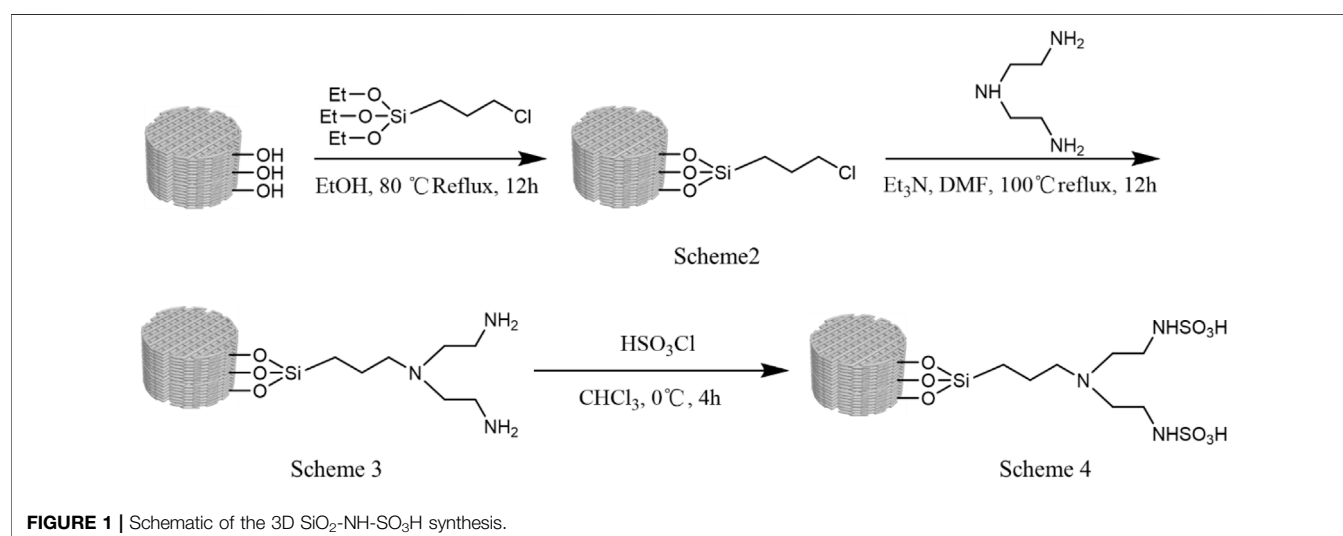
Catalytic activity was investigated via the reaction between 4-methoxybenzyl alcohol (5 mmol) and 3, 4-dihydro-2H-pyran (5.5 mmol). To begin, different solvents (10 ml) were tested, to determine the most efficient one. Further, the material, obtained via direct sulfonation of activated SiO<sub>2</sub> (3D SiO<sub>2</sub>-SO<sub>3</sub>H), was compared with 3D SiO<sub>2</sub>-NH-SO<sub>3</sub>H. Under optimized solvent conditions in the presence of 3D SiO<sub>2</sub>-NH-SO<sub>3</sub>H, different alcohols were reacted with 3, 4-dihydro-2H-pyran, and product yields and corresponding reaction times were recorded.

### Physiochemical Characterization

Scanning electron microscopy (SEM; Phenom Pro, Phenom-World Co., Ltd. Eindhoven, Netherlands) was used to observe the material micro-surface. Fourier transform infrared spectroscopy (FTIR; NICOLET IS 50, Thermo Fisher Scientific Co., Ltd. Massachusetts, United States) was utilized to determine whether the sulfonic acid group successfully grafted onto SiO<sub>2</sub>. Thermogravimetric analysis (TGA; TGA-50, Shimadzu Co., Ltd. Kyoto, Japan) was also used to confirm the molecules were grafted on 3D SiO<sub>2</sub>. Catalytic reaction products were characterized by FTIR and <sup>1</sup>H NMR spectroscopy (NMR; Advance III HD 500MHz, Bruker Technology Co., Ltd. New York, United States).

### Cytotoxicity Test

C518 cells were seeded in a 96-well plate at a density of 5 × 10<sup>3</sup> cells per well and cultured for 24 h at 37°C. Then, the medium was removed, and cells were incubated with different concentrations of sample leaching solution (12.5, 25, 50, 100, and 200 µg/ml). Cell



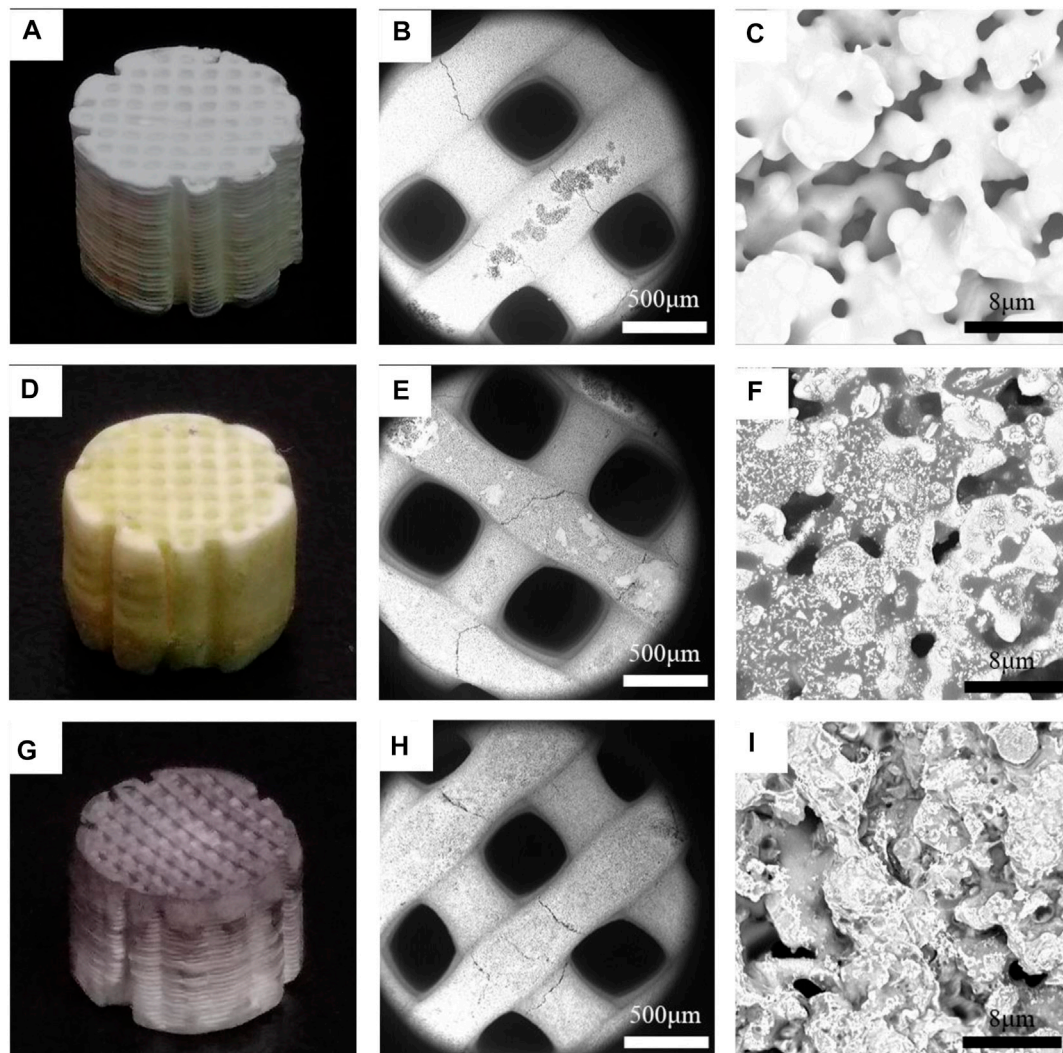


**FIGURE 2 |** Optical images of (A) 3D SiO<sub>2</sub>, (D) 3D SiO<sub>2</sub>-NH-SO<sub>3</sub>H, and (G) 3D SiO<sub>2</sub>-NH-SO<sub>3</sub>H after one catalytic cycle. SEM images of (B,C) 3D SiO<sub>2</sub>; (E,F) 3D SiO<sub>2</sub>-NH-SO<sub>3</sub>H; and (H,I) 3D SiO<sub>2</sub>-NH-SO<sub>3</sub>H after one catalytic cycle at different magnifications.

viability at 24 and 48 h was determined, respectively *via* CCK-8 assay according to the instructions provided by the manufacturer using a microplate reader under 450 nm (Spectrophotometer-1510, Thermo Fisher Scientific Co., Ltd. Massachusetts, United States). Cell viability rate was calculated according to the following formula: Cell viability (%) =  $(OD_{\text{sample}} - OD_{\text{blank}}) / (OD_{\text{control}} - OD_{\text{blank}}) \times 100$ , where control means cells with fresh medium and blank is fresh medium.

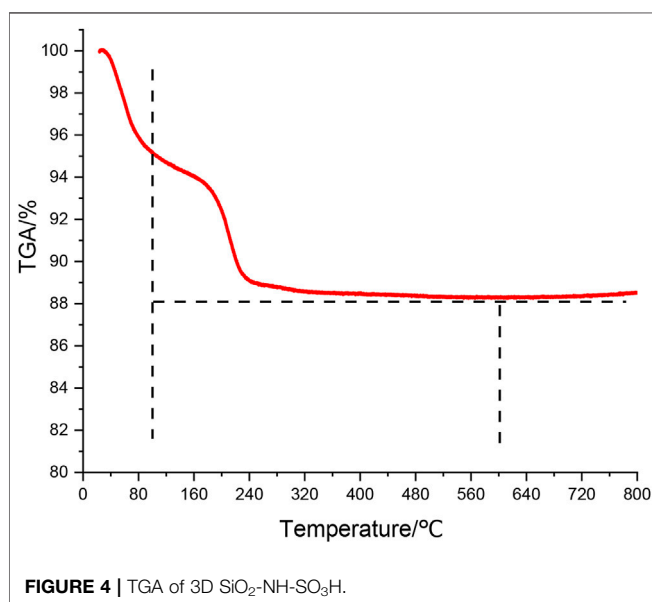
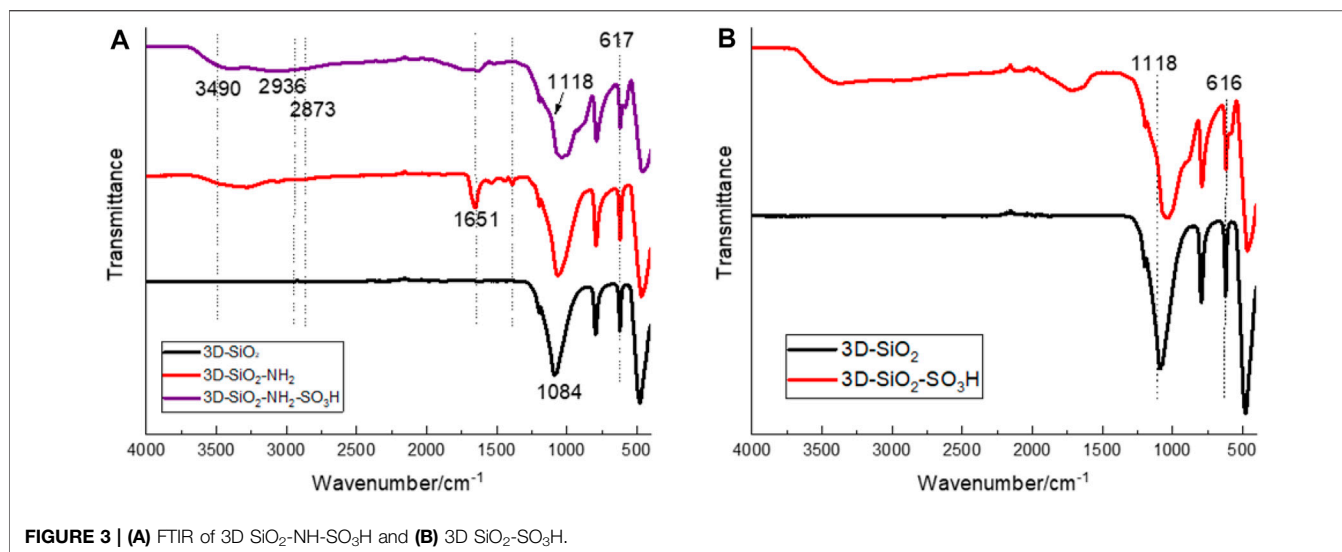
## RESULTS AND DISCUSSION

Three-dimensional SiO<sub>2</sub> was observed, together with fresh 3D SiO<sub>2</sub>-NH-SO<sub>3</sub>H, and 3D SiO<sub>2</sub>-NH-SO<sub>3</sub>H after one catalytic cycle in **Figure 2**. **Figures 2A,D,G** show optical images of as-prepared 3D SiO<sub>2</sub>, fresh 3D SiO<sub>2</sub>-NH-SO<sub>3</sub>H, and 3D SiO<sub>2</sub>-NH-SO<sub>3</sub>H which catalysed the reaction of 1-octanol with 3, 4-dihydro-2H-pyran. Compared with the white colour of the

treated, blank 3D SiO<sub>2</sub>, the surface of 3D SiO<sub>2</sub>-NH-SO<sub>3</sub>H was light yellow with some black dots, which were used for catalysing the reaction. The scanning electron microscope (SEM) images of as-prepared 3D SiO<sub>2</sub> (**Figures 2B,C**), fresh 3D SiO<sub>2</sub>-NH-SO<sub>3</sub>H (**Figures 2E,F**), and 3D SiO<sub>2</sub>-NH-SO<sub>3</sub>H after one catalytic cycle (**Figures 2H,I**) showed obvious differences. The micro-surface of the carrier and catalyst showed consequent holes, beneficial for introducing more sulfonic acid groups. Furthermore, grey parts existed on the smooth carrier surface, which could be a series of grafted molecules and sulfonic acid groups.

The presence of sulfonic acid groups on the surface of 3D porous silicon was confirmed by FTIR (**Figure 3**). The broad peak near 3,490 cm<sup>-1</sup> was assigned to N-H stretching vibrations, while the peaks at 2,936 and 2,873 cm<sup>-1</sup> were attributed to C-H stretching vibrations. The peak at 1,084 cm<sup>-1</sup> arises from the stretching vibration of Si-O-Si, but due to the overlap of S=O and





Si-O-Si characteristic peaks around 1,100 cm<sup>-1</sup>, the half-peak at 1,118 cm<sup>-1</sup> was considered to be the stretching vibration peak of S=O (Pourghasemi-Lati et al., 2018). In the low wavenumber region, some characteristic sulfonic acid peaks also overlapped with SiO<sub>2</sub>, and the peaks at 617 and 616 cm<sup>-1</sup> could be stretching vibrations of S-O.

TGA was also completed to determine the stability of the solid-acid catalyst material (Figure 4). The curve indicated that weight loss from room temperature to 100°C was a rapid, decreasing process, which may be mainly water evaporation. As the temperature continued to rise, no plateau was seen, which may indicate the material began to decompose. At about 600°C, the grafted molecules were completely decomposed.

**TABLE 1 |** Comparison of the best solvents for reaction in the presence of 3D SiO<sub>2</sub>-NH-SO<sub>3</sub>H.

Entry	Catalyst	Solvent	Yield/%
1	3D SiO <sub>2</sub> -NH-SO <sub>3</sub> H	—	86
2	3D SiO <sub>2</sub> -NH-SO <sub>3</sub> H	Acetone	87
3	3D SiO <sub>2</sub> -NH-SO <sub>3</sub> H	Acetonitrile	87
4	3D SiO <sub>2</sub> -NH-SO <sub>3</sub> H	Toluene	92
5	3D SiO <sub>2</sub> -NH-SO <sub>3</sub> H	Ethyl acetate	89
6	3D SiO <sub>2</sub> -NH-SO <sub>3</sub> H	Tetrahydrofuran	78
7	3D SiO <sub>2</sub> -NH-SO <sub>3</sub> H	Methylene chloride	96
8	—	Methylene chloride	—

Reaction conditions: 4-methoxybenzyl alcohol (5 mmol), 3, 4-dihydro-2H-pyran (5.5 mmol), and 3D SiO<sub>2</sub>-NH-SO<sub>3</sub>H (seven pieces), stirred at room temperature for 20 min.

**TABLE 2 |** Comparison of catalytic efficiency for different sulfonated catalysts.

Entry	Catalyst	Time	Yield/%
1	3D SiO <sub>2</sub> -NH-SO <sub>3</sub> H (0.5 ml ClSO <sub>3</sub> H/3 pieces)	20 min	96
2	3D SiO <sub>2</sub> -SO <sub>3</sub> H (0.5 ml ClSO <sub>3</sub> H/3 pieces)	20 min	92
3	—	24 h	—
4	3D SiO <sub>2</sub>	24 h	—

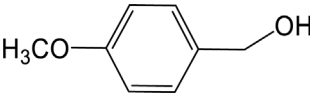
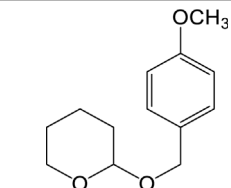
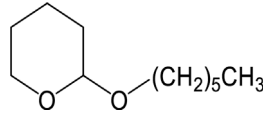
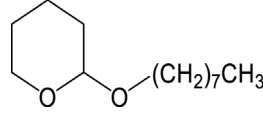
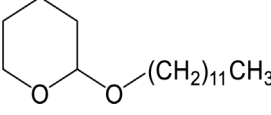
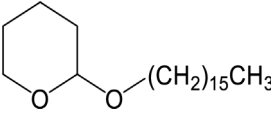
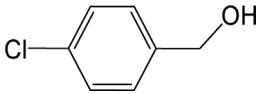
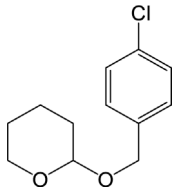
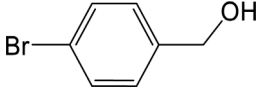
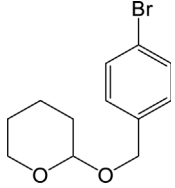
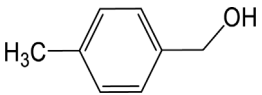
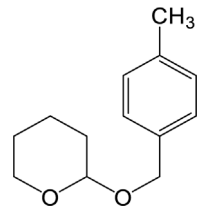
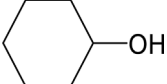
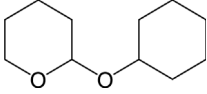
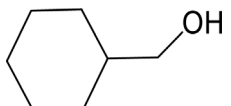
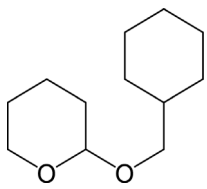
Reaction conditions: 4-methoxybenzyl alcohol (5 mmol), 3, 4-dihydro-2H-pyran (5.5 mmol), and 3D SiO<sub>2</sub> (1 piece), 3D SiO<sub>2</sub>-SO<sub>3</sub>H (1 piece), or 3D SiO<sub>2</sub>-NH-SO<sub>3</sub>H (1 piece) in CH<sub>2</sub>Cl<sub>2</sub> (8 ml). The reaction was stirred at room temperature.

To optimize reaction conditions for the synthesized material, we used the reaction of 4-methoxybenzyl alcohol and 3, 4-dihydro-2H-pyran as a template and explored the effect of different solvents on the catalytic yield in the presence of catalyst material (Table 1). In all solvents examined, methylene chloride showed the highest yield of 96% after 20 min. Furthermore, most of the non-polar solvents were promoting and exhibited better catalytic effects.

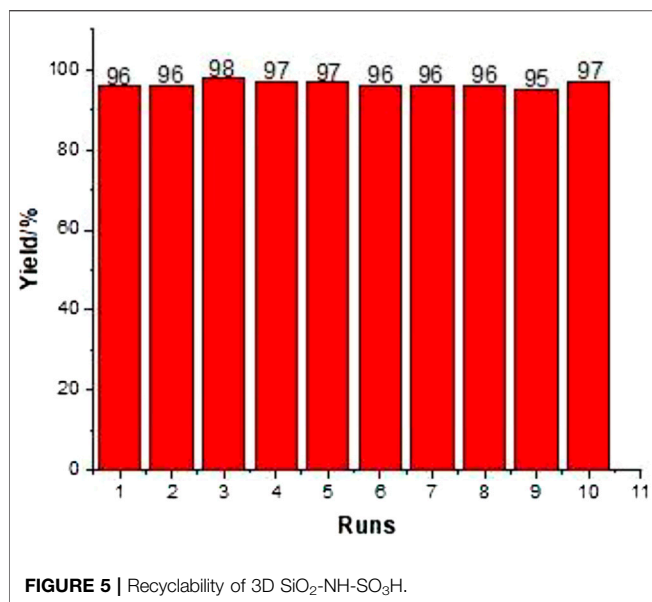
After choosing methylene chloride as the best solvent, catalyst 2 was compared with catalyst 1 by conducting catalytic



**TABLE 3** | Catalytic effects of different alcohols under the action of 3D SiO<sub>2</sub>-NH-SO<sub>3</sub>H.

Entry	Substrate	Time/min	Product	Yield/%
1		20		96
2	CH <sub>3</sub> (CH <sub>2</sub> ) <sub>5</sub> -OH	20		92
3	CH <sub>3</sub> (CH <sub>2</sub> ) <sub>7</sub> -OH	20		94
4	CH <sub>3</sub> (CH <sub>2</sub> ) <sub>11</sub> -OH	20		96
5	CH <sub>3</sub> (CH <sub>2</sub> ) <sub>15</sub> -OH	30		98
6		30		95
7		20		96
8		20		90
9		30		89
10		30		94

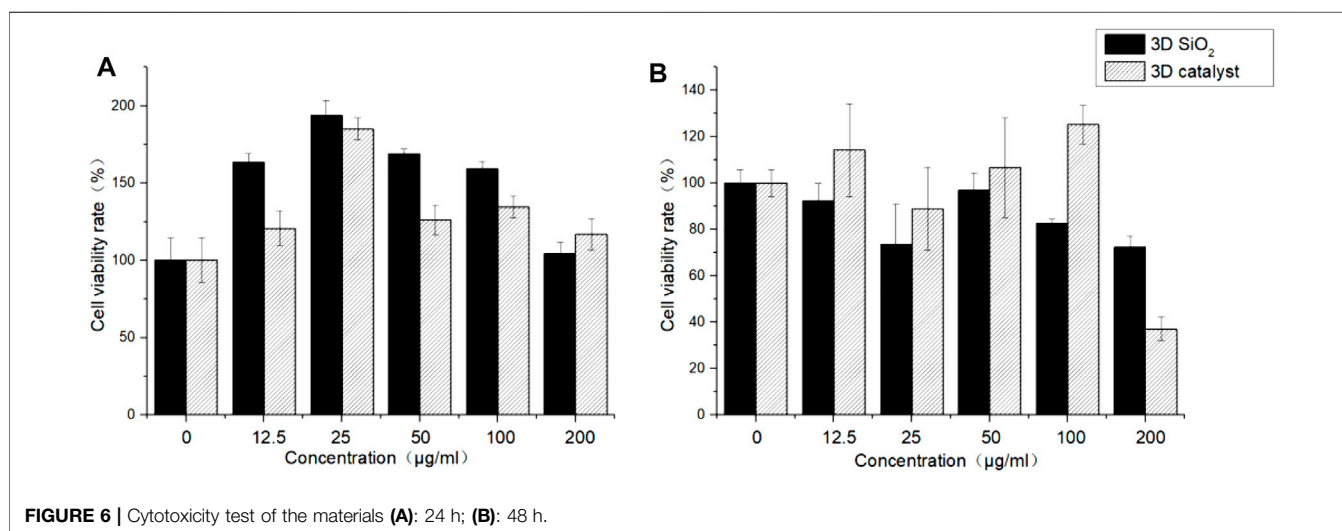
Reaction conditions: alcohol (5 mmol), 3, 4-dihydro-2H-pyran (5.5 mmol), and 3D SiO<sub>2</sub>-NH-SO<sub>3</sub>H (10 pieces), stirred at room temperature.



based solid-acid material had broad catalytic effects; many alcohol reactions were catalysed with high yields of 89% or more, with 1-hexadecanol (Entry 5) achieving a 98% yield (Table 3).

Lastly, the recyclability of 3D SiO<sub>2</sub>-NH-SO<sub>3</sub>H was investigated by the model reaction of 4-methoxybenzyl alcohol with 3, 4-dihydro-2H-pyran (Figure 5), demonstrating that the material could be used at least 10 times, while still achieving high catalytic yields. Other research also focuses on the reusable behaviour of SiO<sub>2</sub> catalyst (Kamble et al., 2021).

Meantime, in consideration of the new material is anticipated to be utilized as an *in vitro* model for osteochondral repair in the future work, the cytobiocompatibility is important because for the future evaluation, the cells must be seeded into the 3D scaffold. Thus the cytotoxicity test was performed using C518 cells as osteochondral model cell. As can be seen in Figure 6, both 3D SiO<sub>2</sub> and 3D catalyst exhibit excellent cell viability at different concentrations at 24 h, while at 48 h, the material shows limited cytotoxicity (<80%) only at high concentration (200 µg/ml), which indicates that the material is suitable for



experiments. All reaction products were detected by thin-layer chromatography (TLC) per 5 min. Table 2 shows that the reaction either did not take place or was minimal in the absence of catalyst material (Entry 3) or in the presence of 3D SiO<sub>2</sub> (Entry 4), respectively. However, high reaction yields were obtained in 20 min with both porous catalysts (Entries 1 and 2). Of the two materials, 3D SiO<sub>2</sub>-NH-SO<sub>3</sub>H exhibited a better catalytic effect, with a 96% yield, which may be due to the presence of more sulfonic acid groups compared to 3D SiO<sub>2</sub>-SO<sub>3</sub>H (Table 2).

To gain a deeper understanding of the materials' effect in protecting a series of alcohols, various alcohols were reacted with 3, 4-dihydro-2H-pyran in the presence of 3D SiO<sub>2</sub>-NH-SO<sub>3</sub>H. Catalytic reaction products were characterized by FTIR and <sup>1</sup>H NMR spectroscopy (see Supplementary Material). The experiment showed that the porous silica-

model construction *in vitro* to evaluate the potential influence of different factors.

## CONCLUSION

Some achievements have been obtained in bone and cartilage repair including clinical trial and applications when using 3D printing as an efficient tool to control the accurate microstructure of the scaffold in tissue engineering. However, the cure rate still remains a problem due to the complicated situation of the *in vivo* physiological environment, especially the microenvironment surrounding the damaged site. To study the influence of the microenvironment, a catalytic strategy was proposed to eliminate the residue of the scaffold degradation segment. In addition, an *in vitro* model will provide a simple and

practical platform to evaluate these changes. Therefore, a porous silica-based solid-acid catalyst material was successfully prepared by additive manufacturing technology and the results showed excellent catalytic performance. The catalytic strategy by constructing an *in vitro* model supplies an alternative way in environment evaluation of osteochondral repair and it also shows potential for the enzymatic catalytic research during the body's metabolism process in the future studies.

## DATA AVAILABILITY STATEMENT

The original contributions presented in the study are included in the article/**Supplementary Material**, further inquiries can be directed to the corresponding author.

## AUTHOR CONTRIBUTIONS

All authors contributed significantly to this work. YL, RL and SW conceptualized the system and designed the studies. YJ performed the experiments with assistance from JG, GR, XG,

XX, YW, RY and ZL. RL, JG and GR performed the experiments for the revision. YJ wrote the draft and finished the manuscript with assistance from YL for revision. RL wrote the revision.

## FUNDING

Financial support from the National Natural Science Foundation of China (32171337) and National Marine Economic Innovation and Development Project (16PYY007SF17) is gratefully acknowledged. This research is also supported by the Program for Innovative Research Team in Science and Technology at Fujian Province University. We also thank Instrumental Analysis Center of Huaqiao University for the support of the work.

## SUPPLEMENTARY MATERIAL

The Supplementary Material for this article can be found online at: <https://www.frontiersin.org/articles/10.3389/fbioe.2021.790139/full#supplementary-material>

## REFERENCES

- Azzena, U., Carraro, M., Modugno, G., Pisano, L., and Urtis, L. (2018). Heterogeneous Acidic Catalysts for the Tetrahydropyranlation of Alcohols and Phenols in green Ethereal Solvents. *Beilstein J. Org. Chem.* 14, 1655–1659. doi:10.3762/bjoc.14.141
- Díaz-Marta, A. S., Tubio, C. R., Carbajales, C., Fernández, C., and Coelho, A. (2018). Three Dimensional Printing in Catalysis: Combining 3D Heterogeneous Copper and Palladium Catalysts for Multicatalytic Multicomponent Reactions. *ACS Catal.* 8, 392–404. doi:10.1021/acscatal.7b02592
- Du, Y., Ge, J., Shao, Y., Ma, P. X., Chen, X., and Lei, B. (2015). Development of Silica Grafted Poly(1,8-Octanediol-Co-Citrate)s Hybrid Elastomers with Highly Tunable Mechanical Properties and Biocompatibility. *J. Mater. Chem. B* 3, 2986–3000. doi:10.1039/c4tb02089h
- Hopkins, T., Wright, K. T., Kuiper, N. J., Roberts, S., Jermin, P., Gallacher, P., et al. (2021). An *In Vitro* System to Study the Effect of Subchondral Bone Health on Articular Cartilage Repair in Humans. *Cells* 10, 1903. doi:10.3390/cells10081903
- Ishikawa, S., Iijima, K., Sasaki, K., Hashizume, M., Kawabe, M., and Otsuka, H. (2018). Cartilage Differentiation of Bone Marrow-Derived Mesenchymal Stem Cells in Three-Dimensional Silica Nonwoven Fabrics. *Appl. Sci.* 8, 1398. doi:10.3390/app8081398
- Kamble, R., Gaikwad, M., Tapare, M., Hese, S., Kadam, S., Ambhore, A., et al. (2021). DTP/SiO<sub>2</sub>: an Efficient and Reusable Heterogeneous Catalyst for Synthesis of Dihydropyrano[3,2-C]chromene-3-Carbonitrile Derivatives. *J. Appl. Organomet. Chem.* 1, 22–28. doi:10.22034/JAOC.2021.276239.1004
- Khder, A. E. R. S., Ahmed, S. A., Khairou, K. S., and Altass, H. M. (2018). Competent, Selective and High Yield of 7-Hydroxy-4-Methyl Coumarin over Sulfonated Mesoporous Silica as Solid Acid Catalysts. *J. Porous Mater.* 25, 1–13. doi:10.1007/s10934-017-0414-1
- Kumar, B., Aga, M. A., Rouf, A., Shah, B. A., and Taneja, S. C. (2014). Tetrahydropyranyl Ether (THPE) Formation in Hydroxyl Group protection and Conversion to Other Useful Functionalities. *RSC Adv.* 4, 21121–21130. doi:10.1039/c4ra02093f
- Li, S., Tallia, F., Mohammed, A. A., Stevens, M. M., and Jones, J. R. (2000). Scaffold Channel Size Influences Stem Cell Differentiation Pathway in 3-D Printed Silica Hybrid Scaffolds for Cartilage Regeneration. *Biomater. Sci.* 8, 4458–4466. doi:10.1039/c9bm01829h
- Li, X., Bian, S., Zhao, M., Han, X., Liang, J., Wang, K., et al. (2021). Stimuli-responsive Biphenyl-Tripeptide Supramolecular Hydrogels as Biomimetic Extracellular Matrix Scaffolds for Cartilage Tissue Engineering. *Acta Biomater.* 131, 128–137. doi:10.1016/j.actbio.2021.07.007
- Ludwig, T., Seckendorff, J., Troll, C., Fischer, R., Tonigold, M., Rieger, B., et al. (2018). Additive Manufacturing of Al<sub>2</sub>O<sub>3</sub>-Based Carriers for Heterogeneous Catalysis. *Chem. Ingenieur Technik* 90, 703–707. doi:10.1002/cite.201700151
- Nakhaei, A., Davoodnia, A., and Nakhaei, H. (2019). (NH<sub>4</sub>)<sub>42</sub>[MoVI<sub>72</sub>MoV<sub>60</sub>O<sub>372</sub>(CH<sub>3</sub>COO)<sub>30</sub>(H<sub>2</sub>O)<sub>72</sub>] as a Heterogeneous Reusable Catalyst for Organic Reactions: Mini-Review. *J. Chem. Rev.* 1, 139–153. doi:10.33945/SAMI/JCR.2019.2.5
- Narender, N., Suresh Kumar Reddy, K., Arun Kumar, M., Rohitha, C. N., and Kulkarni, S. J. (2010). Tetrahydropyranlation of Alcohols over Modified Zeolites. *Catal. Lett.* 134, 175–178. doi:10.1007/s10562-009-0205-7
- Nelson, M., Li, S., Page, S. J., Shi, X., Lee, P. D., Stevens, M. M., et al. (2021). 3D Printed Silica-Gelatin Hybrid Scaffolds of Specific Channel Sizes Promote Collagen Type II, Sox9 and Aggrecan Production from Chondrocytes. *Mater. Sci. Eng. C* 123, 111964. doi:10.1016/j.msec.2021.111964
- Niknam, K., Saberi, D., Sadegheyan, M., and Deris, A. (2010). Silica-bonded S-Sulfonic Acid: an Efficient and Recyclable Solid Acid Catalyst for the Synthesis of 4,4'-(arylmethylene)bis(1H-Pyrazol-5-Ols). *Tetrahedron Lett.* 51, 692–694. doi:10.1016/j.tetlet.2009.11.114
- Pourghasemi-Lati, M., Shirini, F., Alinia-Asli, M., and Rezvani, M. A. (2018). Butane-1-sulfonic Acid Immobilized on Magnetic Fe<sub>3</sub>O<sub>4</sub>@SiO<sub>2</sub>nanoparticles: A Novel and Heterogeneous Catalyst for the One-Pot Synthesis of Barbituric Acid and Pyrano[2,3-D] Pyrimidine Derivatives in Aqueous media. *Appl. Organometal Chem.* 32, e4455. doi:10.1002/aoc.4455
- Rafael, P., Celia, A., and Jesús, I. (2001). Synthesis of Enantiopure Mono- and Disubstituted Tetrahydroisoquinolines by 6-exo Radical Cyclizations. *Tetrahedron* 57, 4005–4014. doi:10.1016/S0040-4020(01)00274-5
- Rajkumari, K., Kalita, J., Das, D., and Rokhum, S. L. (2017). Magnetic Fe<sub>3</sub>O<sub>4</sub>@silica Sulfuric Acid Nanoparticles Promoted Regioselective protection/deprotection of Alcohols with Dihydropyran under Solvent-free Conditions. *RSC Adv.* 7, 56559–56565. doi:10.1039/c7ra12458a
- Ravindranath, N., Ramesh, C., and Das, B. (2001). Simple, Facile and Highly Selective Tetrahydropyranlation of Alcohols Using Silica Chloride. *Synlett* 2001, 1777–1778. doi:10.1055/s-2001-18078

- Sajjadifar, S., Hamidi, H., and Pal, K. (2019). Revisiting of boron Sulfonic Acid Applications in Organic Synthesis: Mini-Review. *J. Chem. Rev.* 1, 35–46. doi:10.33945/SAMI/JCR.2019.1.3546
- Shimizu, K.-i., Hayashi, E., Hatamachi, T., Kodama, T., and Kitayama, Y. (2004). SO<sub>3</sub>H-functionalized Silica for Acetalization of Carbonyl Compounds with Methanol and Tetrahydropyranlation of Alcohols. *Tetrahedron Lett.* 45, 5135–5138. doi:10.1016/j.tetlet.2004.04.186
- Shin, H. S., Opanasenko, M., Cabello, C. P., Ryoo, R., and Čejka, J. (2017). Surfactant-directed Mesoporous Zeolites with Enhanced Catalytic Activity in Tetrahydropyranlation of Alcohols: Effect of Framework Type and Morphology. *Appl. Catal. A: Gen.* 537, 24–32. doi:10.1016/j.apcata.2017.02.019
- Singh, Y. P., Moses, J. C., Bhardwaj, N., and Mandal, B. B. (2021). Overcoming the Dependence on Animal Models for Osteoarthritis Therapeutics - the Promises and Prospects of *In Vitro* Models. *Adv. Healthc. Mater.* 10, 2100961. doi:10.1002/adhm.202100961
- Stuecker, J. N., Miller, J. E., Ferrizz, R. E., Mudd, J. E., and Cesarano, J. (2004). Advanced Support Structures for Enhanced Catalytic Activity. *Ind. Eng. Chem. Res.* 43, 51–55. doi:10.1021/ie030291v
- Wang, C., Huang, W., Zhou, Y., He, L., He, Z., Chen, Z., et al. (2020). 3D Printing of Bone Tissue Engineering Scaffolds. *Bioactive Mater.* 5, 82–91. doi:10.1016/j.bioactmat.2020.01.004
- Wei, P., Xu, Y., Zhang, H., and Wang, L. (2021b). Continued Sustained Insulin-Releasing PLGA Nanoparticles Modified 3D-Printed PCL Composite Scaffolds for Osteochondral Repair. *Chem. Eng. J.* 422, 130051. doi:10.1016/j.cej.2021.130051
- Wei, W., Ma, Y., Yao, X., Zhou, W., Wang, X., Li, C., et al. (2021a). Advanced Hydrogels for the Repair of Cartilage Defects and Regeneration. *Bioactive Mater.* 6, 998–1011. doi:10.1016/j.bioactmat.2020.09.030
- Williams, D. B. G., Simelane, S. B., Lawton, M., and Kinfe, H. H. (2010). Efficient Tetrahydropyran and Tetrahydrofuran protection/deprotection of Alcohols and Phenols with Al(OTf)<sub>3</sub> as Catalyst. *Tetrahedron* 66, 4573–4576. doi:10.1016/j.tet.2010.04.053
- Xing, J., Peng, X., Li, A., Chen, M., Ding, Y., Xu, X., et al. (2021). Gellan Gum/alginate-Based Ca-Enriched Acellular Bilayer Hydrogel with Robust Interface Bonding for Effective Osteochondral Repair. *Carbohydr. Polym.* 270, 118382. doi:10.1016/j.carbpol.2021.118382
- Xintong, Z., and Chang-jun, L. (2017). Three-dimensional Printing for Catalytic Applications: Current Status and Perspectives. *Adv. Funct. Mater.* 27, 1701134. doi:10.1002/adfm.201701134
- Xue, X., Hu, Y., Deng, Y., and Su, J. (2021). Recent Advances in Design of Functional Biocompatible Hydrogels for Bone Tissue Engineering. *Adv. Funct. Mater.* 31, 2009432. doi:10.1002/adfm.202009432
- Yu, Y., Yu, X., Tian, D., Yu, A., and Wan, Y. (2021). Thermo-responsive Chitosan/silk Fibroin/amino-Functionalized Mesoporous Silica Hydrogels with strong and Elastic Characteristics for Bone Tissue Engineering. *Int. J. Biol. Macromolecules* 182, 1746–1758. doi:10.1016/j.ijbiomac.2021.05.166

**Conflict of Interest:** The authors declare that the research was conducted in the absence of any commercial or financial relationships that could be construed as a potential conflict of interest.

**Publisher's Note:** All claims expressed in this article are solely those of the authors and do not necessarily represent those of their affiliated organizations, or those of the publisher, the editors and the reviewers. Any product that may be evaluated in this article, or claim that may be made by its manufacturer, is not guaranteed or endorsed by the publisher.

Copyright © 2021 Long, Jiang, Guo, Ren, Guo, Xie, Wu, Yan, Lin, Wang and Liu. This is an open-access article distributed under the terms of the Creative Commons Attribution License (CC BY). The use, distribution or reproduction in other forums is permitted, provided the original author(s) and the copyright owner(s) are credited and that the original publication in this journal is cited, in accordance with accepted academic practice. No use, distribution or reproduction is permitted which does not comply with these terms.





# Analysis of Mechanical Properties and Permeability of Trabecular-Like Porous Scaffold by Additive Manufacturing

Long Chao<sup>1,2†</sup>, Chen Jiao<sup>1†</sup>, Huixin Liang<sup>2,3\*</sup>, Deqiao Xie<sup>1</sup>, Lida Shen<sup>1\*</sup> and Zhidong Liu<sup>1</sup>

<sup>1</sup>College of Mechanical and Electrical Engineering, Nanjing University of Aeronautics and Astronautics, Nanjing, China, <sup>2</sup>State Key Laboratory of Pharmaceutical Biotechnology, Division of Sports Medicine and Adult Reconstructive Surgery, Department of Orthopedic Surgery, Nanjing Drum Tower Hospital, The Affiliated Hospital of Nanjing University Medical School, Nanjing, China, <sup>3</sup>Jiangsu Engineering Research Center for 3D Bioprinting, Nanjing, China

## OPEN ACCESS

### Edited by:

Lei Zhang,  
Wenzhou Medical University, China

### Reviewed by:

Cijun Shuai,  
Central South University, China  
Youwen Yang,  
Jiangxi University of Science and  
Technology, China  
Carmen Torres,  
Loughborough University,  
United Kingdom

### \*Correspondence:

Huixin Liang  
hxtiang@nuaa.edu.cn  
Lida Shen  
ldshen@nuaa.edu.cn

<sup>†</sup>These authors have contributed  
equally to this work

### Specialty section:

This article was submitted to  
Nanobiotechnology,  
a section of the journal  
Frontiers in Bioengineering and  
Biotechnology

**Received:** 20 September 2021

**Accepted:** 17 November 2021

**Published:** 21 December 2021

### Citation:

Chao L, Jiao C, Liang H, Xie D, Shen L  
and Liu Z (2021) Analysis of  
Mechanical Properties and  
Permeability of Trabecular-Like Porous  
Scaffold by Additive Manufacturing.  
Front. Bioeng. Biotechnol. 9:779854.  
doi: 10.3389/fbioe.2021.779854

Human bone cells live in a complex environment, and the biomimetic design of porous structures attached to implants is in high demand. Porous structures based on Voronoi tessellation with biomimetic potential are gradually used in bone repair scaffolds. In this study, the mechanical properties and permeability of trabecular-like porous scaffolds with different porosity levels and average apertures were analyzed. The mechanical properties of bone-implant scaffolds were evaluated using finite element analysis and a mechanical compression experiment, and the permeability was studied by computational fluid dynamics. Finally, the attachment of cells was observed by confocal fluorescence microscope. The results show that the performance of porous structures can be controlled by the initial design of the microstructure and tissue morphology. A good structural design can accurately match the performance of the natural bone. The study of mechanical properties and permeability of the porous structure can help address several problems, including stress shielding and bone ingrowth in existing biomimetic bone structures, and will also promotes cell adhesion, migration, and eventual new bone attachment.

**Keywords:** additive manufacturing, voronoi tessellation, permeability, mechanical properties, stress shielding, bone scaffold, bionic structure

## 1 INTRODUCTION

In China, 15 million patients with bone defects need artificial bone tissue each year (Attar et al., 2018). However, the porous structure of common bone scaffolds involves various problems (Carla et al., 2018; Zhao et al., 2019), such as single morphology and insufficient osteogenesis ability. Porous scaffolds play an important role in the proliferation and differentiation of human cells. As structures for cell growth, scaffolds require a roughness surface to facilitate the attachment and proliferation of cells on the scaffolds. Moreover, porous scaffolds play an important role in nutrient transport and waste removal during cell growth. The ideal porous structure possesses bone characteristics (i.e., microstructure geometric features and mechanical, biological, and nutrient transport) to realize similar degrees of cell infiltration and diffusion (Chang et al., 2020; Falkowska et al., 2020; Ma et al., 2020; Wang et al., 2020). Trabecular-like consist of a large number of intertwined trabecular bones and match the internal bones of humans. Trabecular bones are

arranged in the same direction as that of bone stress and tension and thus can bear larger weights. It provides a template for constructing artificial bone scaffolds (Feng et al., 2017; Alias and Buenzli, 2018; Zhang et al., 2019).

Advances in medical three-dimensional printing have led to opportunities for creating complex artificial bone-implant structures (Kantaros et al., 2015; Melancon et al., 2017). Computer-aided design tools have been used to mimic scaffolding structures close to real human bone tissue. A porous structure design can be divided into rules and irregular structure, rules of porous structure modeling methods, including the unit method, the topological optimization method, and the three-cycle minimum surface method (Kumar et al., 2017; Wang et al., 2019; Rana et al., 2021). The rules of porous structures show poor biomechanics and liquidity; in addition, because small changes in the unit cell in the rules of the porous structure can lead to the internal structure of the overall change (Chen et al., 2017; Li et al., 2017; Nguyen-Van et al., 2020). Thus, the local distribution of the shape and aperture is difficult to control. Inverse modeling based on computed tomography/magnetic resonance imaging can also accurately simulate human bone tissue and prove the advantage of an irregular porous structure. However, the porous model obtained by reverse modeling is difficult to modify in the late stages (Liu et al., 2016; Ibrahim et al., 2018; Maskery et al., 2018; Onal et al., 2018; Lu et al., 2019; Ouyang et al., 2019; Samoilenko et al., 2019).

Porous structure modeling based on Voronoi tessellation has increasingly gained interest in recent years (Liang et al., 2019; Du et al., 2020; Lei et al., 2020). The structure has a large aperture distribution range because of the similarity between the designed porous structure and the complex microstructure of human bones, thus addressing the problem concerning the small aperture distribution range of regular structures. Meanwhile, by adjusting the parametric design of structures based on Voronoi tessellation, the requirements set for the mechanical properties and permeability of different porous structures are met. Currently, porous structure modeling based on Voronoi tessellation is limited by a specific modeling technique and cannot easily control the aperture and porous structure. In the current study, Voronoi tessellation is applied in the design of spongy porous structures. The design parameters of the porous structure are determined, including porosity, aperture distribution, and the relationship between mechanical properties. The porosity and average aperture of porous structures are regulated by controlling the design parameters, combined with finite element analysis, to show the applicability of the method. This study belongs to the 3D-printed Biomaterials in Osteochondral Repair. The irregular porous structure constructed by the Voronoi tessellation, porous structure is suitable for the growth of bone tissue due to its large and small pores of different shapes. The mechanical and permeability properties of trabecular-like porous scaffolds with different porosity and average apertures were analyzed. The results of the analysis are verified using a compression test and biological cell culture experiments. The research of mechanical properties and permeability of the porous structure can help address several problems, including stress

shielding and bone ingrowth in existing biomimetic bone structures. The research process is shown in **Figure 1**.

## 2 DESIGN AND METHODS

### 2.1 Design of Porous Structures

We propose a controllable irregular porous structure method based on probability balls and the Voronoi–Tessellation approach (Du et al., 2020). The software Grasshopper is used to control the irregularity of the lattice via the probability ball for design. The basic idea is to generate a regular lattice with a certain distance in the space and establish a spherical region with the regular point as the center and randomly generate a seed point in each spherical region. In accordance with the Voronoi–Tessellation principle, the random seed lattice is connected, generating a Voronoi three-dimensional framework. The characteristic parameters of irregular porous structures mainly include the average aperture ( $D$ ), porosity ( $\Phi$ ), irregularity coefficient ( $\varepsilon$ ), point spacing ( $a$ ), probability sphere radius ( $R$ ), and aperture coefficient ( $K$ ).  $K$  is the ratio of the pore area  $S_{pi}$  to the corresponding cellular surface area  $S_{ci}$ —that is,  $K = S_{ci}/S_{pi}$ .

The two factors of point spacing and irregularity coefficient only slightly affect porosity, and the porosity mainly depends on the pore size, exhibiting a strong linear relationship. The structure we designed is irregular porous structure, pore size distributed within a definite range, it is not a single value (Liang et al., 2019), so we use average aperture. To obtain a representative average aperture and a porous structure with good morphological bionic characteristics, an irregularity coefficient ranging from 0.4 to 0.5 was selected. The suitable aperture range for bone cell ingrowth is 200–1,200  $\mu\text{m}$ . With this range considered, the interval of point spacing was set to 1.5–2.5  $\mu\text{m}$ . Finally, the aperture coefficient range was set to 0.5–0.9, given that the porosity of a trabecular-like ranges from 50 to 90%. We constructed the fitting function relation (Eq. 1) to depict the relationship between porosity and average aperture and design parameters, as follows:

$$D_{avg} = -6.44375 - 95.15a - 48.375K + 448.5\varepsilon + 660 \times a \times K - 90 \times a \times \varepsilon - 6.20946 \times 10^{-13} \times K \times \varepsilon + 33.1 \times a^2 + 0.625 \times K^2 - 290 \times \varepsilon^2 \quad (1)$$

The fitted equation can be used to calculate the design parameters depending on the target average aperture. The effects of average aperture, porosity, and pore structure on the mechanical and permeability properties of porous metals were evaluated in this study. Bone integration and bone ingrowth can be facilitated and the advantages of a porous structure can be fully utilized only when the aperture is within a reasonable range. Therefore, to provide adequate space and sufficient mechanical support for cell diffusion, the aperture of the porous scaffold should be controlled as much as possible. In the design of an irregular porous mechanism based on Voronoi tessellation, irregular porous structures with different apertures were modeled under similar conditions to ensure comparability. First, the irregular porous structures exhibited porosity levels

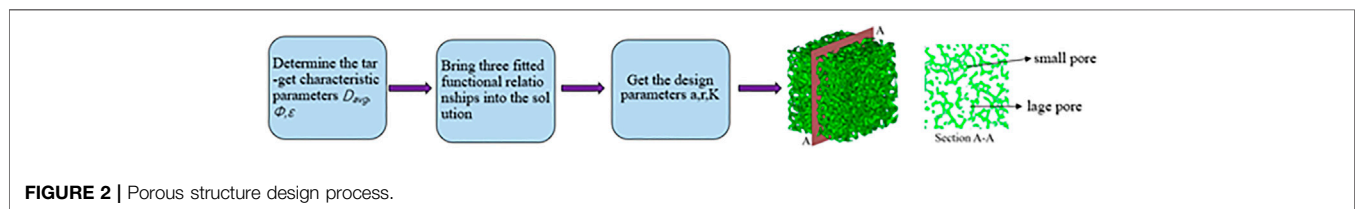
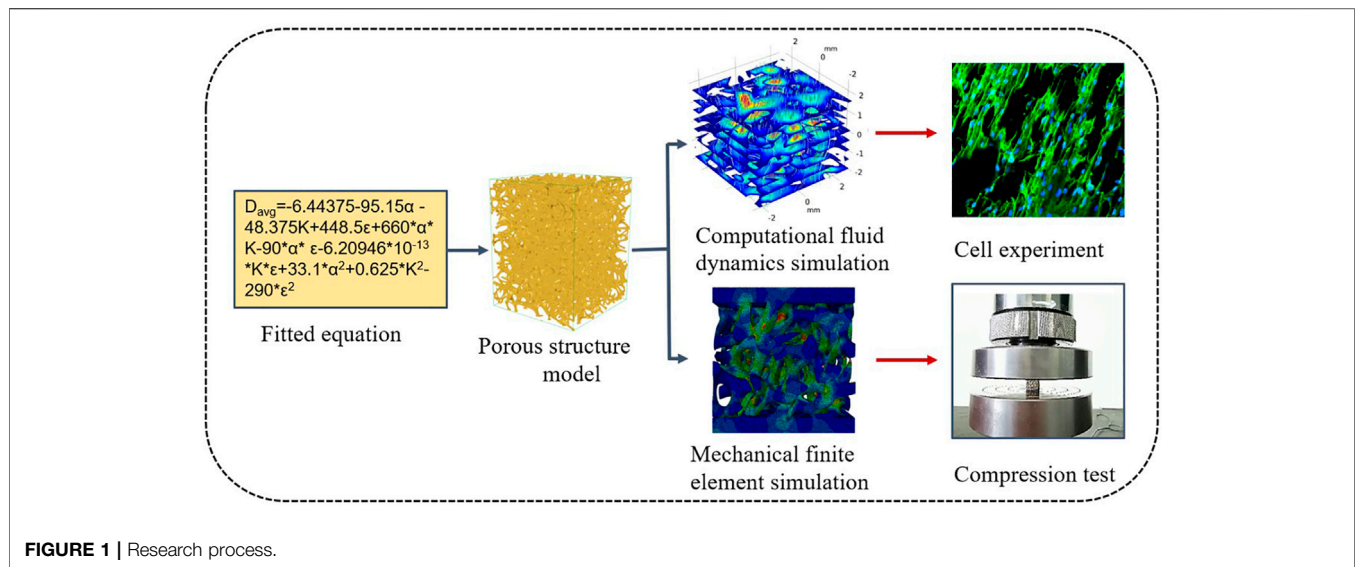


**TABLE 1 |** Design parameters of porous structure.

D	Φ (%)	K	a	r
600	70	0.66	1.43	0.64
	80	0.75	1.25	0.56
	90	0.84	1.11	0.50
700	70	0.66	1.67	0.76
	80	0.75	1.47	0.66
	90	0.84	1.31	0.59
800	70	0.66	1.91	0.86
	80	0.75	1.69	0.76
	90	0.84	1.51	0.68
900	70	0.66	2.14	0.96
	80	0.75	1.89	0.85
	90	0.84	1.69	0.76
1,000	70	0.66	2.37	1.07
	80	0.75	2.10	0.95
	90	0.84	1.88	0.85

equal to 70, 80, and 90%. Fifteen kinds of porous structure models with average apertures of 600, 700, 800, 900, and 1,000 μm were constructed. The design parameters are determined by combining the fitting formula of all characteristic and design parameters, as shown in **Figure 2**:

The solution method of design parameters is based on the function relationship between characteristic parameters and design parameters established above. Before design, the average aperture and porosity of irregular porous structure are

determined. Combining all fitting formulas of characteristic parameters and design parameters, the solution method of design parameters can be obtained as follows:

- 1) The coefficient of irregularity is between 0.4 and 0.5;
- 2) According to the porosity requirements, plug into  $\Phi = 107.87K - 1.33$  to calculate the corresponding pore size coefficient K;
- 3) According to the aperture requirements, plug into **Eq. 1** to solve the corresponding point spacing a;
- 4) According to the irregularity coefficient formula  $\varepsilon = R/a$ , the probability sphere radius R is solved;
- 5) Adopt the Voronoi tessellation structural design method to design the porous structure.

The above method can be used to design three different porosity structures, thereby determining the design parameters, as shown in **Table 1**. The irregular porous structure model obtained according to the design requirements is shown in **Figure 3A**. The printed porous structure sample is shown in **Figure 3B**.

## 2.2. Finite Element Analysis of Mechanical Properties

The study on the mechanical properties of a porous structure currently includes four major aspects: compressive strength,

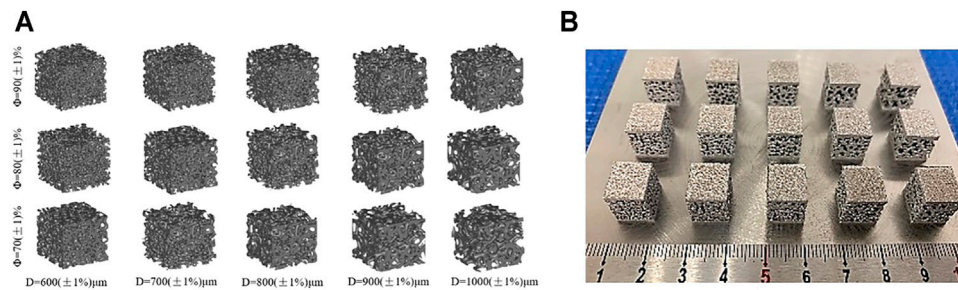


**FIGURE 3 |** Irregular porous structure model. **(A)** Design model; **(B)** Print sample.

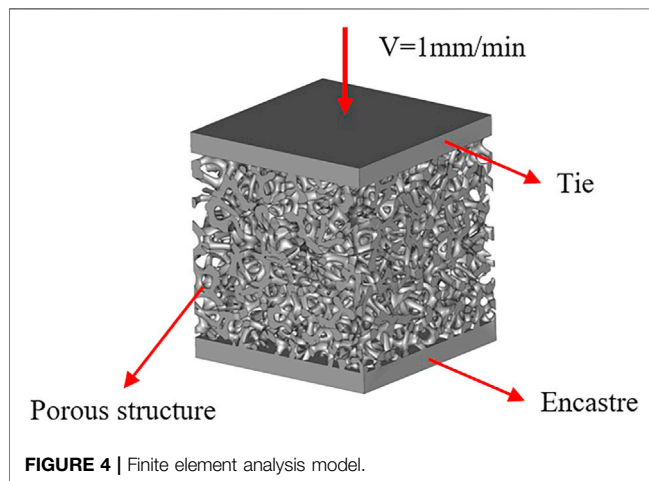


**FIGURE 4 |** Finite element analysis model.

tensile strength, bending strength, and fatigue strength (Cao et al., 2018; Qiu et al., 2018). This study mainly examines the simulation of compression testing, including the effective elastic modulus, maximum compressive strength, and stress distribution, among others. To analyze the influence of structural parameters on the mechanical properties of the designed porous structure, the commercial finite element software ABAQUS was used in the simulation of the structure. First, the model built in Grasshopper needed to be exported in the STL format, imported into the software 3-Matic to generate the volume grid, and finally exported in the INP format. The finite element simulation of the compressive strength of the porous structure is presented in **Figure 4**. The porous structures of the upper and lower sets of rigid materials, respectively, in the upper model induce a downward movement at a speed of 1 mm/min. The bottom of the model fully controlled, the other in the process of simulation, the simulation environment for the static, general motors, all models according to set the properties of the Ti-6Al-4V material. The density is 4.41 g/cm<sup>3</sup>, the elastic modulus is 110 GPa, and Poisson's ratio is 0.33.

## 2.2 Compression Test

The specimens were fabricated using an SLM machine (NCL-M2120, China) with optimized processing parameters: laser power of 130 w, scanning speed of 1,000 mm/s, and hatch

spacing of 0.08 mm. The material used was Ti-6Al-4V powder with a diameter range of 15–53 μm fifteen sets of specimens were fabricated with a height of 12 mm. The prepared porous structure was numbered (**Figure 5A**) to facilitate the experimental analysis. No support structure was used during processing to ensure the stability of the support. To facilitate the compression test, solid structures were set at the upper and lower ends of the porous structure. In the figure, both the interior and exterior appear precisely manufactured. Compression tests were performed on a mechanical testing machine (CMT5105, MTS Systems, United States). The crosshead displacement velocity was fixed at 1 mm/min. The compression experiment process is presented in **Figure 5B**.

## 2.4 Analysis of Permeability Characteristics

Computational fluid dynamics (CFD) modeling was performed using the software COMSOL. The simulation model was first determined after the porous structure was removed *via* a Boolean operation in Grasshopper (**Figure 6A**). The output was then and saved in the STL format. The software 3-MATIC was used to import the volume mesh components into COMSOL for simulation analysis.

CFD modeling is approximated by single-phase and peristaltic flow models. To simplify the simulation calculation and analysis, the deformation of the metal scaffolds is ignored during the fluid flow process. Water was assigned as the fluid domain material, with the following physical properties: temperature, 37°C (normal human body temperature); density, 1,000 kg/m<sup>3</sup>; and viscosity, 1.45 E<sup>-9</sup> MPa/s. In CFD modeling, the Reynolds number is typically used to assess the state of the fluid. The analysis object is an incompressible fluid with constant density; thus, it is defined by the Navier–Stokes equation (Wang et al., 2016; Cao et al., 2018), as shown in **Eq. 2**.

$$\rho \frac{\partial v}{\partial t} = -(\nu \cdot \nabla) \nu - \frac{1}{\rho} \nabla P + \mu \nabla^2 \nu + F \nabla \cdot \nu = 0 \quad (2)$$

where  $\rho$  is the density of the fluid (kg/m<sup>3</sup>),  $\nu$  is the speed of the fluid (m/s),  $t$  is time (s),  $\nabla$  is the operator,  $P$  is the pressure (MPa),  $\mu$  is the dynamic viscosity coefficient of the fluid, and  $F$  is the force (N).

The boundary conditions for the fluid model are presented in **Figure 6B**, with the purple section as the fluid domain, defined as the inlet boundary and the outlet boundary. The inlet velocity applied



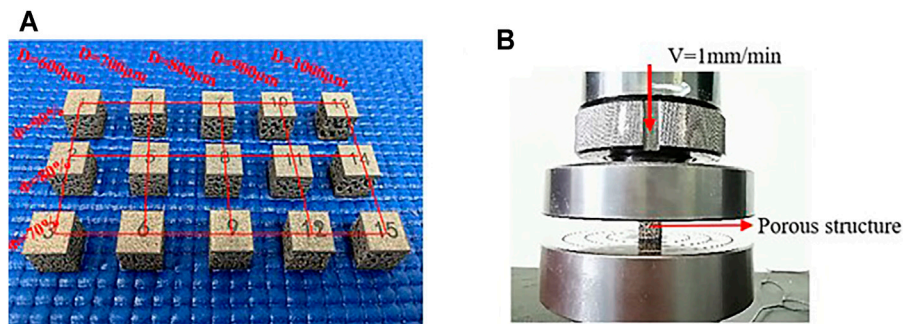


FIGURE 5 | (A) Print sample; (B) Compression test.

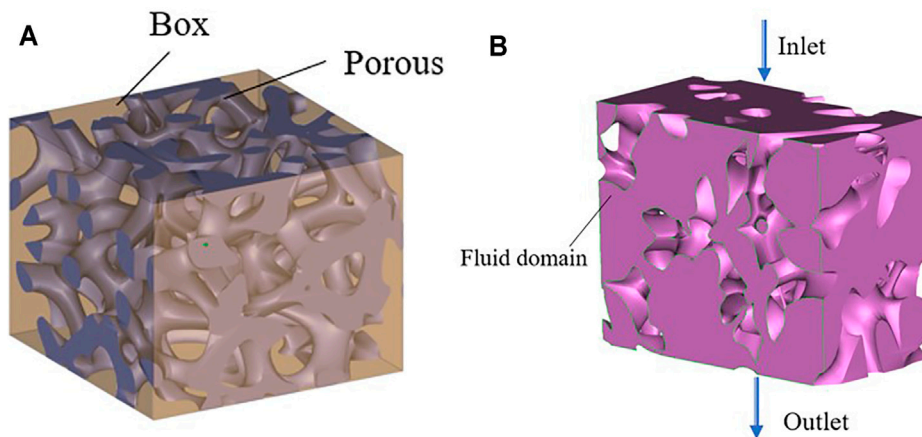


FIGURE 6 | Penetration simulation preparation process. (A) Boolean operation; (B) Fluid domain model.

to the scaffolds was 1 mm/s. The pressure at the exit is considered zero. Under the no-slip-on-the-wall assumption, the fluid flow in the bionic bone scaffolds was simulated using COMSOL.

The results report on the pressure drop, pressure gradient, porosity, outlet flow rate, and the permeability between the inlet and outlet surface of the watershed. The permeability was determined in accordance with Eq. 3 of Darcy's law, and the pressure gradient was measured using Eq. 4.

$$K = v_D \cdot \mu_d \cdot \left( \frac{L}{\Delta P_{i-0}} \right) \quad (3)$$

$$\Delta P = P_{Inlet} - P_{Outlet} \quad (4)$$

where  $K$  is the permeability,  $v_D$  is the Darcy velocity,  $u_d$  is the dynamic velocity,  $L$  is the model length, and  $P$  is the pressure gradient of the fluid domain.

## 2.5 Biocellular Culture

The prepared Ti-6Al-4V scaffold was treated before cell culture. First, the scaffold was ultrasonically rinsed for 30 min in 95% alcohol and distilled water, then soak for 24 h in a 5 M sodium hydroxide solution at 60°C, and then ultrasonically washed in distilled water for 10 min and dried for 24 h to stabilize the oxide

layer of the Ti-6Al-4V scaffold prior to cell culture. Finally, all scaffold were sterilized using high temperature and high pressure.

Osteoblasts from mice (CELL Bank MC3T3-E1, Chinese Academy of Sciences) were used to evaluate the permeability of the scaffold. The cell culture temperature was set to 37°C, and the environment contained 5% CO<sub>2</sub>. The medium used for cell culture was  $\alpha$ -MEM containing 10% fetal bovine serum and 3% penicillin–streptomycin (Gibco). The cells were seeded on sterilized samples at a density of  $5 \times 10^4$  cells/cm<sup>2</sup> in a 24-hole plate. After one, three, five and 7 days of culturing, the absorbance was measured at 450 nm using a microplate reader (Multiskan GO, Thermo Scientific, United States). According to a previously described protocol, the cells were stained with 4',6-diamidino-2-phenylindole (DAPI) for 3 h and then observed under confocal fluorescence microscope (CKX53, Olympus Corporation, Japan).

## 3 RESULTS AND DISCUSSION

### 3.1 Analysis of Mechanical Properties

#### 3.1.1 Analysis of Compression Test Results

In this study, the mechanical properties of porous bone implants include two aspects—the apparent elastic modulus ( $E$ ) and the

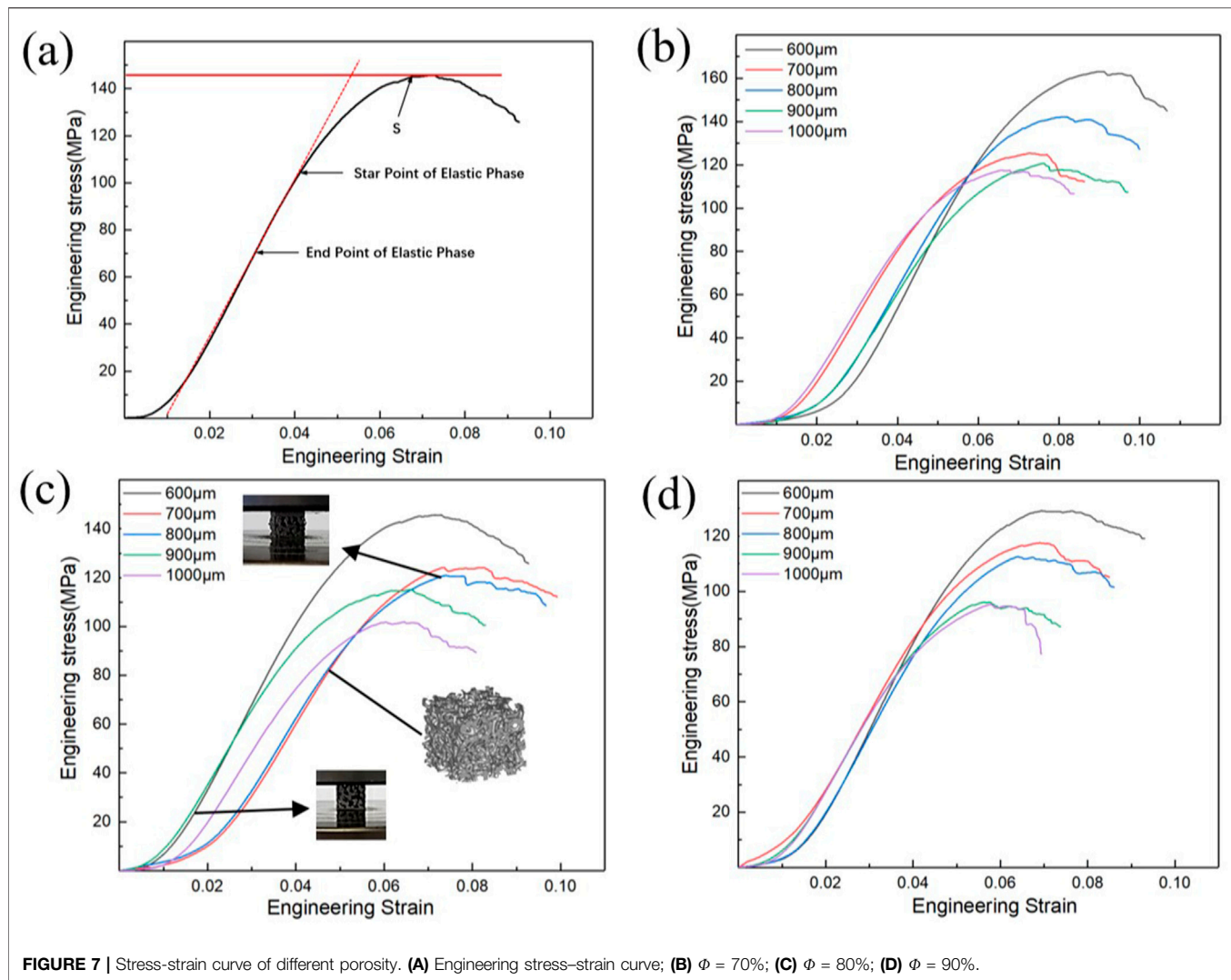


**FIGURE 7 |** Stress-strain curve of different porosity. **(A)** Engineering stress-strain curve; **(B)**  $\phi = 70\%$ ; **(C)**  $\phi = 80\%$ ; **(D)**  $\phi = 90\%$ .

ultimate compressive strength (S). E is characterized by the quasi-elastic gradient (ISO13314:2011), and S is characterized by the ultimate compressive stress. The stress-strain curve generated on the testing machine is transformed into the engineering stress-strain curve (Figure 7A). Nonlinearities are observed before the linear elastic phase of the curve. The reason is that full contact is established between the sample and the indenter during compression. The curves also show that the porous structure of titanium alloy exhibits no apparent yield behavior. The compressive strength is characterized by the ultimate compressive stress; the elastic modulus of the sample is the slope of the stress-strain curve at the elastic deformation stage; and the compressive strength is the stress corresponding to the peak of the stress-strain curve.

Mechanical properties are critical evaluation indices for the structure used in orthopedic implants (Wang et al., 2016; Zhang et al., 2018; Cai et al., 2019). The porous structure of the implant can produce a good biological reaction with the host bone *in vivo* and solve the problem of stress shielding only when its

mechanical properties meet certain conditions. Moreover, the ultimate strength of the porous structure of the implant should exceed that of the corresponding part of the human bone. Figures 7B–D show porosity levels of 70, 80, and 90%; the quasistatic compression stress-strain curve of the porous structure of a bone implant, and the mechanical deformation processes of the three groups of porous structures (Figure 7C). As shown in the figure, the compression state of the porous structure of the porosity is 80%, and the average aperture is 800 μm. The porous structure fracture occurs at maximum stress. As shown in Figure 7B, when the porosity of the porous structure is 70% and the average aperture is 600 μm, the highest stress is reached; the stress of the porous structure, as determined from the stress curves of (B–D), exceeds the stress range for the natural bone. In addition, some curves exhibit an upward-opening parabola at the start of loading, which is due to insufficient contact between the compression surface and the indenter.

Elastic modulus and compressive strength are two important parameters used to characterize the mechanical properties of

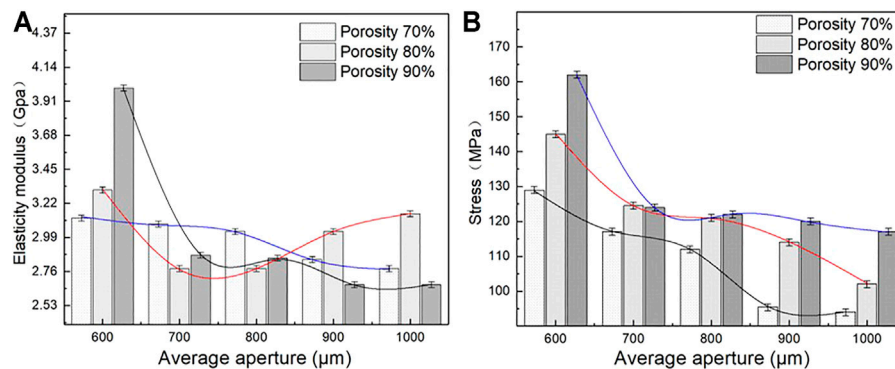


**FIGURE 8 |** Elastic modulus and Engineering stress of porous structure **(A)** Variation trend of elastic modulus; **(B)** Variation trend of engineering stress.

porous structures. The matching of the elastic modulus determines whether the structure can solve the stress shielding problem, and the compressive strength determines the maximum load that the structure can bear. **Figure 8** lists the elastic modulus and compressive strength of the sample as measured by uniaxial compression testing. As shown in **Figures 8A,B**, under different porosity levels, the elastic modulus and compressive strength of the porous structure change with the different average aperture. When the porosity is 70%, the elastic modulus and compressive strength of the porous structure tend to decrease with an increase in the average aperture. The elastic modulus and compressive strength are considerably influenced by the average aperture. When the average aperture is 600 μm, The maximum elastic modulus and compressive strength are 4 GPa and 162 MPa, respectively; when the average aperture is 1,000 μm, the minimum elastic modulus and compressive strength are 2.6 GPa and 117 MPa, respectively, when the porosity is 80%, the elastic modulus of the porous structure initially decreases and then increases with an increase in the average aperture; meanwhile, the compressive strength decreases with an increase in the average aperture. When the average aperture is 1,000 and 600 μm, the elastic modulus reaches the minimum value of 2.76 GPa and the maximum value of 3.31 GPa. When the average aperture is 600 and 1,000 μm, the maximum compressive strength reaches 145 MPa and the minimum compressive strength reaches 102 MPa. When the porosity is 90%, the elastic modulus and compressive strength of the porous structure decrease with an increase in the average aperture. The average aperture slightly affects the elastic modulus, whereas the compressive strength strongly influences the elastic modulus. When the average aperture is 600 μm, the maximum elastic modulus is 3.12 GPa and the maximum compressive strength is 129 MPa. When the average aperture is 1,000 μm, the minimum elastic modulus 2.67 GPa and the minimum compressive strength is 94 MPa. As shown in **Figures 9A,B**, under the same average aperture, the elastic modulus and compressive strength vary widely as the porosity levels changes. When the average aperture is 600 μm, the elastic modulus and compressive strength reach their maximum values. When the average aperture is 1,000 μm, the elastic modulus and

compressive strength reach their minimum values. Given different average apertures, both the elastic modulus and compressive strength are within the range of the bone tissue.

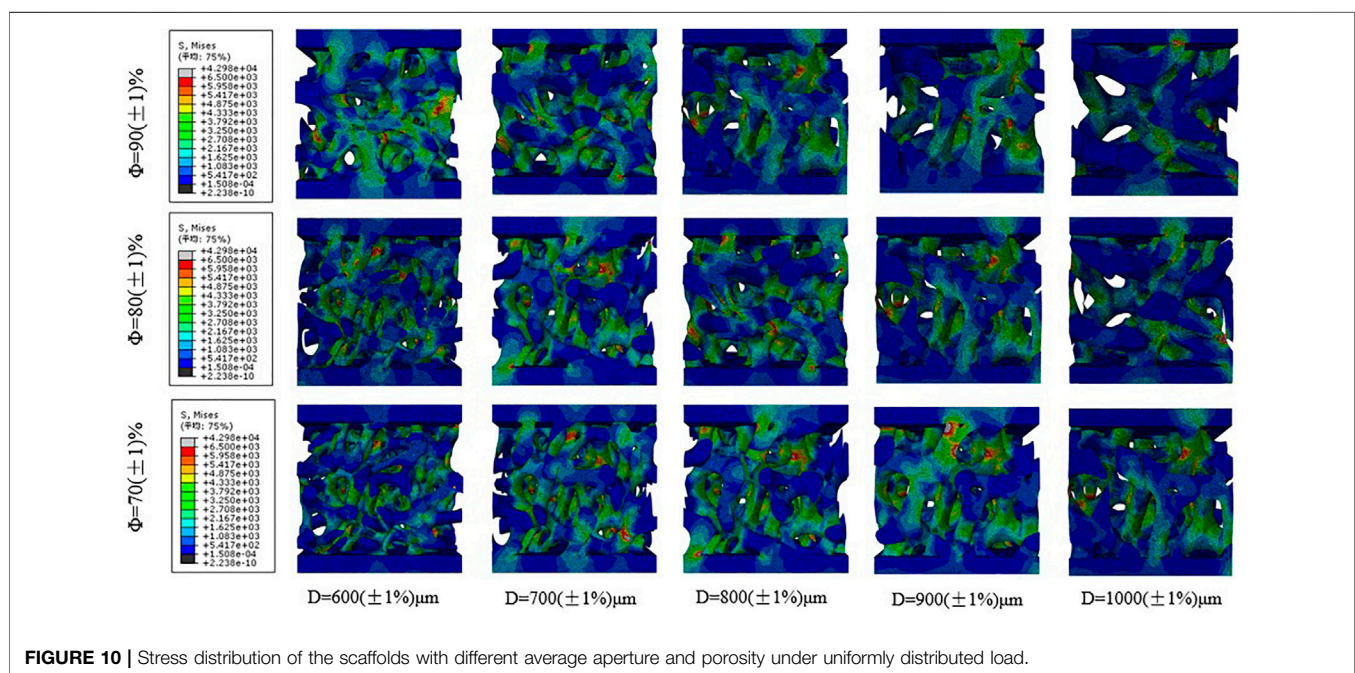
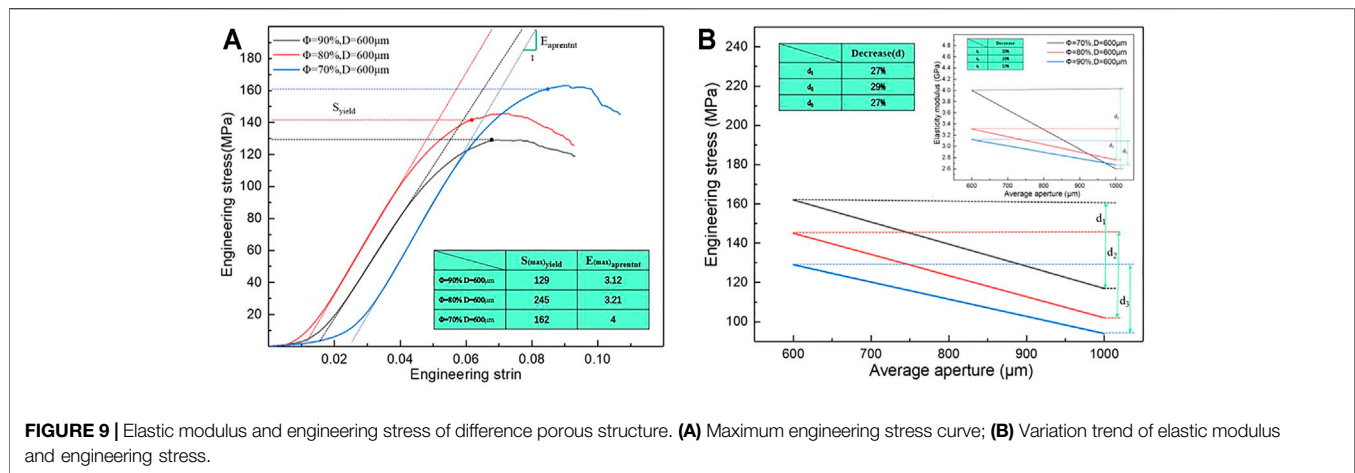
**Figure 9B** also shows the decreases in elastic modulus and compressive strength with an increase in the average aperture. When the porosity is 70%, the elastic modulus and compressive strength decrease by 33 and 27%, respectively, with a change in the average aperture; when the porosity is 80%, the elastic modulus and compressive strength decrease by 16 and 29%, respectively; when the porosity is 90%, the elastic modulus and compressive strength decrease by 10 and 27%, respectively. Under different porosity conditions, the compressive strength of the porous structure varies within a range similar to that of the average aperture, and the elastic modulus largely affects the average aperture. This finding indicates that the porosity only slightly affects the compressive strength but heavily affects the elastic modulus.

In conclusion, the porous scaffolds prepared using Ti-6Al-4V can not only substantially adjust the elastic modulus via the average aperture but also ensure high compressive strength, which shows significant potential in the application of bone scaffolds.

### 3.1.2 Mechanical Finite Element Simulation Analysis

**Figure 10** shows the stress distribution corresponding to the different average apertures of bone implants when the porosity levels are 70, 80, and 90%. As shown in the figure, the maximum Mises stress of the porous structure of bone implants is mainly concentrated at the nodes where the connecting rods of the porous structure are connected, and the randomness of the porous structure facilitates the production of fragile and brittle pore edges. With regard to bearing loads, the stress is often more concentrated on the fragile and brittle pore edges. The force can be gradually transferred via connecting rods from the loading area to the different layers of the layered slice. As shown in **Figure 9**, the smaller the average aperture, the greater the stress on the pore edge of the porous structure when the porosity level is the same; meanwhile, under different porosity conditions, the loading state of the porous structure is similar when the average aperture is the same.





Therefore, compared with the average aperture, the porosity level exerts less effect on the stress of the porous structure, which is consistent with the results of the mechanical compression test. In the design of porous structures, not only should the porosity of the porous structure be paid attention; the appropriate average aperture also needs to be ensured. Prevention of structural fracture caused by aperture distribution and reasonable control of the average aperture can effectively improve the average stress of an irregular porous structure, as well as enhance the compressive strength of the structure.

## 3.2 Permeability Analysis

### 3.2.1 Computational Fluid Dynamics Simulation

Material transport is an important index of a biomimetic bone-implant scaffold. Tissue regeneration requires continuous

absorption of nutrients via porous channels. Therefore, prediction and evaluation of the permeability and pressure drop of the structure are necessary (Peng et al., 2019; Li et al., 2020; Shuai et al., 2020; Yang et al., 2020; Yang et al., 2021; Zhang et al., 2021). After treatment, the porous structure exhibits a more bionic morphology, as shown in **Figure 11**. The porous structure similar to the trabecular bone can be simulated by changing the porosity and average aperture of the porous structure.

Fifteen groups of porous structures were analyzed by fluid dynamics simulation. Bone implants possess similar porous structures and vary in the average aperture and porosity of the structures; thus, the pressure drop and permeability of the porous structures need to be evaluated. Pressure drop and permeability are used to quantify the transmission performance between different structures. **Figure 12** presents the velocity



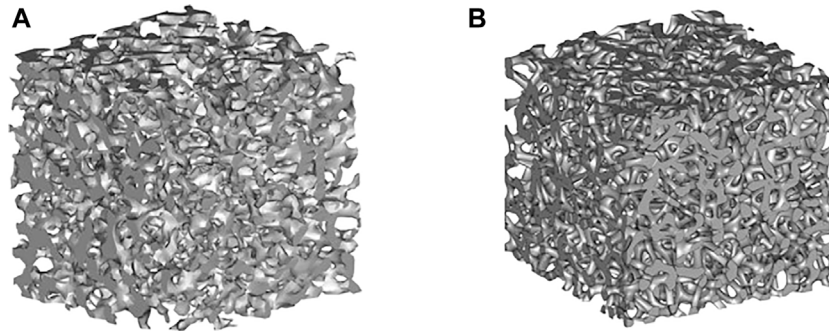


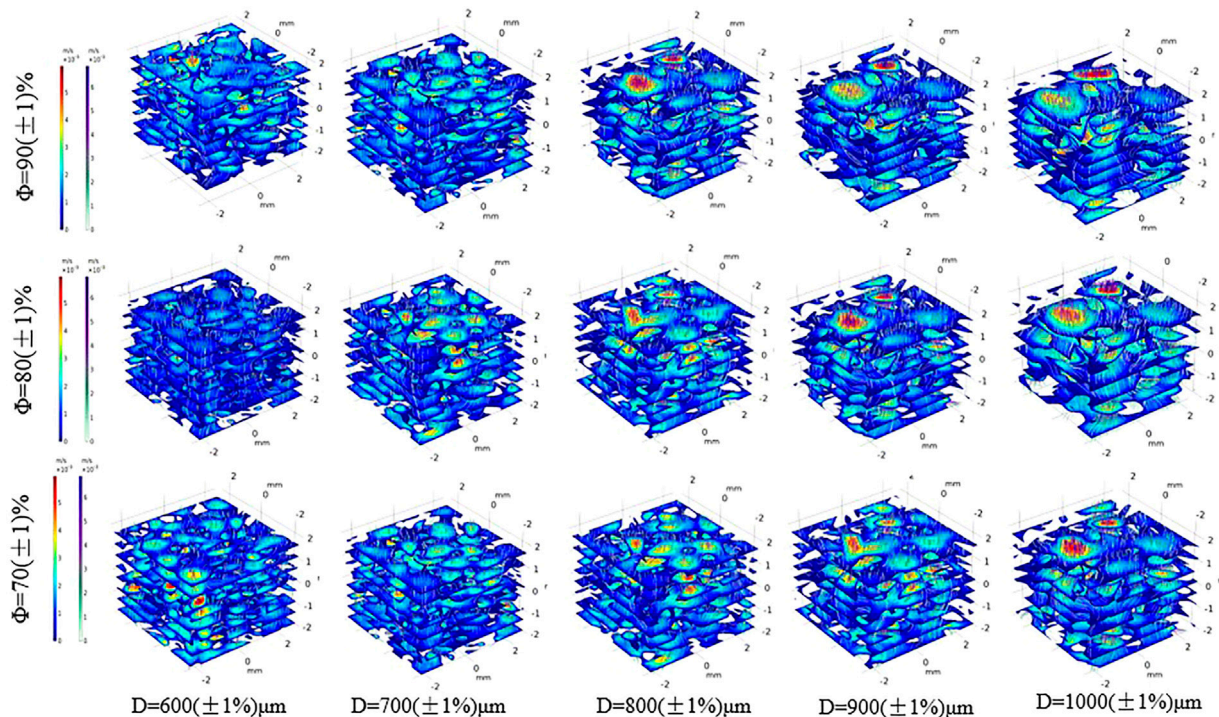
**FIGURE 11 | (A)** Trabecular structure; **(B)** Porous structure.

distribution cloud map corresponding to different average apertures determined via fluid flow simulation at porosity levels equal to 70, 80, and 90%. As shown in the figure, the porous structure of bone implants exhibits a disordered fluid velocity distribution, and the maximum velocity is normally concentrated in the area with a small aperture. Comparison of figures indicates that the velocity distribution varies between different porous structures. Under different average apertures and similar porosity levels, the pressure distribution and velocity distribution are markedly affected by average aperture and slightly influenced by porosity. The larger the average aperture, the faster the nutrient transport and cell attachment; however, a larger-than-average aperture tends to result in weak mechanical properties. The requirements for the mechanical properties of bone scaffolds cannot be satisfied; thus, the mechanical properties of different structures, as well as the cell permeability and pressure drop, should be considered.

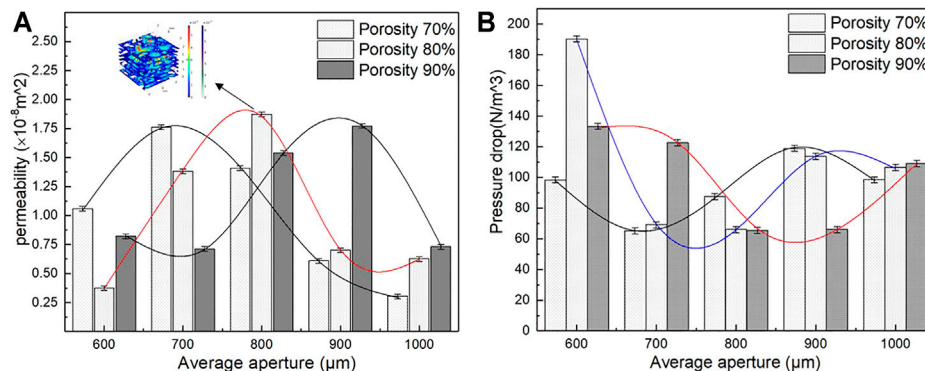
Under similar conditions, pressure drop and permeability were calculated using Eqs 3, 4. The results are shown in Figure 13. As indicated in Figure 13B, the pressure drop initially decreases and then rises with an increase in average aperture, and the small average aperture leads to a larger pressure drop and a higher flow rate. When the average aperture is 800  $\mu\text{m}$  and the porosity is 80%, the pressure drop reaches 66  $\text{N/m}^3$ , which is conducive to cell adhesion. The structure with an average aperture exceeding 800  $\mu\text{m}$  exhibits an increasing flow rate, which is not conducive to cell adsorption. As observed in Figure 13A, the permeability of the porous structure under different porosity levels increases first and then decreases with an increase in the average aperture. The main reason is that the average aperture increased, the internal surface area of the model increased, and the fluid friction increased; thus, the velocity was reduced, resulting in a decrease in permeability. When the porosity is 80%, and the average aperture is 800  $\mu\text{m}$ , the maximum permeability reaches  $1.87 \times 10^{-8} \text{ m}^2$ , which is a considerably larger value than that of the natural bone. On the basis of the aforementioned data, the permeability of the porous structure of bone implants is greater than that of the human bone. Moreover, the flow characteristics may promote tissue growth, showing great research potential and application prospects.

Figure 14A presents the cross-section of the natural bone velocity distribution cloud map, and Figure 14B shows the cross-section of the natural bone pressure cloud map. As shown in the figure, the fluid velocity is disordered, the maximum flow velocity is concentrated in the area with a small aperture, and the pressure gradually decreases from the inlet to the outlet; meanwhile, the pressure is stable in the area with a large aperture. Moreover, the permeability is  $1.50 \times 10^{-10} \text{ m}^2$ , and the pressure drop is  $4.153 \times 10^3 \text{ N/m}^3$ . Figures 14C,D present the cross-section of the velocity distribution and pressure distribution when the porosity is 80% and the average aperture is 800  $\mu\text{m}$ . In Figure 14C, the velocity distribution is the highest at the center of the inlet and outlet of the porous structure. Figure 14D shows that the pressure of the porous structure decreases gradually from the inlet to the outlet. Moreover, it decreases in the radial direction from the center to the inner boundary. This flow characteristic can be more intuitively and clearly visualized using the diagram. The high velocity at the center of the implant porous structure facilitates the migration of cells and nutrient materials deep into the scaffold. The closer to the boundary of the inner surface, the lower the velocity, which facilitates the absorption of cells and nutrients on the inner surface of the scaffold. These substances are essential for bone tissue growth and promote subsequent development.

With the special structural characteristics of irregular porous structures considered, not only are their pores randomly distributed in space, their aperture is also distributed within a certain range. Notably, this porous structure has a number of large pores distributed in space, which are less permeable and suitable for cell adhesion and proliferation; moreover, the large number of pores ensures the flow of oxygen and nutrients. Compared with that of the natural bone structure, the controllability of the porous structure design parameters of the bone implant can be controlled by adjusting the porosity and average aperture in the irregular porous scaffold. S. Gomez et al. constructed an irregular porous structure by using the Voronoi surface subdivision method. When the porosity ranged from 40 to 90%, the permeability values range from  $0.5 < K (\times 10^{-8} \text{ m}^2)$ . By contrast, the irregular porous structure in the current study had a wider permeability range and greater permeability control. The surface area of the actual porous sample after additive manufacturing tends to be larger than that of the design, and



**FIGURE 12 |** Velocity cloud map distribution of different porous structure.



**FIGURE 13 |** Permeability and pressure drop of different porous structure. **(A)** Variation trend of permeability; **(B)** Variation trend of pressure drop.

the friction of the liquid flow also increases. With these observations considered, the porous model must have a larger penetration range than that of the aforementioned, and the permeability of the porous structure with different average apertures in the figure can be met.

The average aperture not only affects the mechanical and permeability properties of the porous scaffolds, but also affects the adhesion of bone cells. Mc3t3-e1 cells were inoculated on the scaffold, after culture for 7 days, the cells attach to the walls of the scaffold was observed by confocal fluorescence microscope. In **Figure 15**, green represents the cell contour, and blue represents the nucleus. **Figure 15** shows the confocal fluorescence

microscope images of MC3T3-E1 cells (indicated by arrows) attach to the scaffold surface after incubating for 7 days. As known from the analysis of fluid dynamics, a larger average aperture and higher porosity do not indicate a higher permeability. When the average aperture is 800  $\mu\text{m}$ , **Figure 15B** shows the scaffold distribution of some larger and smaller pores, allowing more cells to be adhered, simultaneously, the maximum permeability of porous scaffolds reaches  $1.87 \times 10^{-8} \text{ m}^2$ , this permeability is greater than natural bone, resulting in a higher cell adhesion rate, more cells attach to the walls of the scaffold, and the effect of cell pseudopodia was better. In the same range, when the average aperture is 600 and

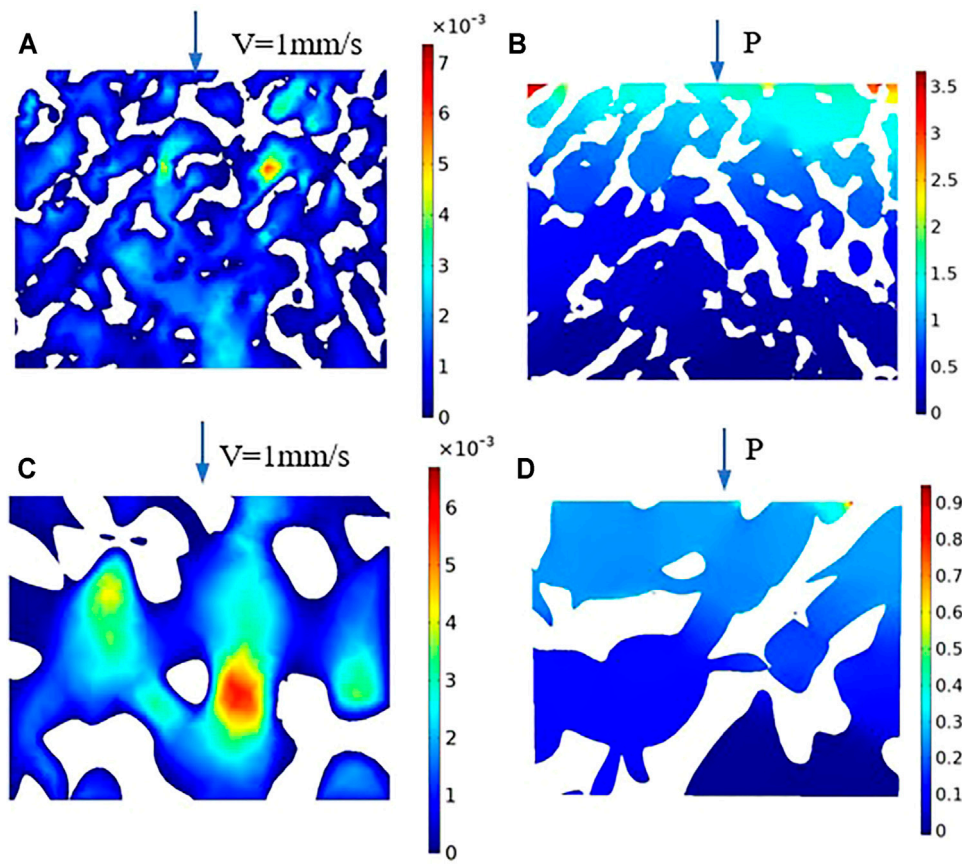


**FIGURE 14 |** Velocity and pressure section cloud diagram. **(A)** Natural bone velocity distribution cloud map; **(B)** Natural bone pressure cloud map; **(C)** Velocity distribution cloud map of the porosity is 80%; **(D)** Pressure cloud map of the porosity is 80%.

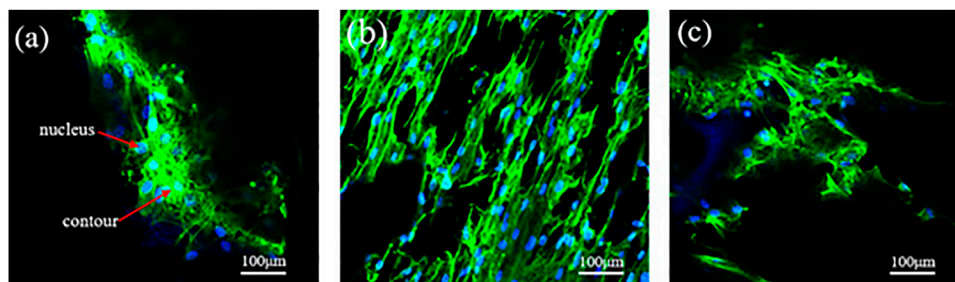


**FIGURE 15 |** Confocal fluorescence microscope images of MC3T3-E1 cells (indicated by arrows) adhered to the scaffold surface after incubating for 7 days. **(A)**  $\Phi = 80\%$ ,  $D = 600\ \mu\text{m}$ ; **(B)**  $\Phi = 80\%$ ,  $D = 800\ \mu\text{m}$ ; **(C)**  $\Phi = 80\%$ ,  $D = 1,000\ \mu\text{m}$ .

1,000  $\mu\text{m}$ , the permeability of porous scaffolds is relatively low, **Figures 15A,C** shows the cells adhere to the scaffold less than **Figure 15B**, and the effect of cell pseudopodia was not obvious.

The difference in the cell density of several groups of scaffolds in culture is mainly attributed to the difference in the local permeability of the porous structure, which can directly affect the efficiency of cell adhere to the walls of the scaffold. The permeability of porous scaffolds is related to the porosity and average aperture (Dias et al., 2012; Fan et al., 2013; Torres-

Sanchez et al., 2021b); a higher permeability indicates that the cell is subjected to less resistance when it penetrates the scaffold. Consequently, the cells adhere to the scaffold surface for a shortened time. Although the overall porosity and average aperture are roughly similar, the variation in average aperture leads to different permeability levels. The larger average aperture and higher porosity of the scaffolds can facilitate nutrient transport, address the oxygen gap, and prevent congestion; thus, it is beneficial to maintain activity and cell proliferation.



A suitable aperture range is the first prerequisite to ensure bone ingrowth, in addition to cell proliferation and differentiation. It is also the most direct and important functional parameter of the porous structure as a medical implant. Extremely large apertures and bone cells cannot adhere, resulting in bone tissue loss and poor mechanical strength. The aperture is too small for bone cells to grow in, and the tissue fluid cannot be transported efficiently.

## 4 CONCLUSION

The rational structural design of the trabecular-like porous scaffold is an important factor for the satisfactory clinical effect of the implant. Bone tissue is a three-dimensional entity with a heterogeneous structure, indicating that the ideal implant is composed of a layered structure similar to bone tissue on a multidirectional scale. In addition, the implant should have appropriate biological and biomechanical properties similar to those of the host bone and surrounding tissue. The internal pores of most porous scaffolds are identical, in contrast to the structure of real bone. Consequently, the accuracy of the complex geometry and continuity of the implant at a specific location is difficult to ensure.

The elastic modulus of natural bone is 0.1–23 GPa, and the compressive strength is 1.5–151 MPa, compared with the natural bone, the results showed that the performance index of the porous scaffolds is within and superior to the range of the natural bone, the elastic modulus of the porous structure is 2.6–4 GPa and the compressive strength is 94–162 MPa. The results reveal that the mechanical and permeability properties of the porous scaffolds of bone implants designed using the Voronoi–Tessellation method can directly depend on the porous structure of the microstructure characteristics. The simulation results are verified by the biological cell culture experiment, which shows that the irregular porous scaffolds have a wider and more uniform pore size distribution. The combination of small and large pores achieved satisfactory cell attachment efficiency. In future studies, the cell experiment will further validate the best design parameters, and the animal

implantation experiments based on the existing research will be conducted to verify the biological characteristics of porous structures.

## DATA AVAILABILITY STATEMENT

The raw data supporting the conclusion of this article will be made available by the authors, without undue reservation.

## AUTHOR CONTRIBUTIONS

LC and CJ participated in the study design, finite element analysis, data analysis, writing and editing of the manuscript. DX and HL contributed to the mechanical and permeability experiment part of this study. LS and ZL provide important guidance for the revision of the manuscript part of this paper. All authors have read and approved the final manuscript and, therefore, have full access to all the data in the study and take responsibility for the integrity and security of the data.

## FUNDING

This work was supported by the National Key R&D Program of China (2018YFB1105400), Jiangsu Provincial Key Research and Development Program (No. BE2019002) and the China Postdoctoral Science Foundation (No. 2020M671475, 2020M671455, 2020TQ0141) and Jiangsu Key Laboratory of Precision and Micro-Manufacturing Technology (2020016).

## ACKNOWLEDGMENTS

The authors also extend their science thanks to those who contributed in instructions and experiments work.

## REFERENCES

- Alias, M. A., and Buenzli, P. R. (2018). Osteoblasts Infill Irregular Pores under Curvature and Porosity Controls: a Hypothesis-Testing Analysis of Cell Behaviours. *Biomech. Model. Mechanobiol.* 17, 1357–1371. doi:10.1007/s10237-018-1031-x
- Attar, H., Ehtemam-Haghighi, S., Kent, D., and Dargusch, M. S. (2018). Recent Developments and Opportunities in Additive Manufacturing of Titanium-Based Matrix Composites: A Review. *Int. J. Machine Tools Manufacture* 133, 85–102. doi:10.1016/j.ijmachtools.2018.06.00
- Cai, Z., Liu, Z., Hu, X., Kuang, H., and Zhai, J. (2019). The Effect of Porosity on the Mechanical Properties of 3D-Printed Triply Periodic Minimal Surface (TPMS) Bioscaffold. *Bio-des. Manuf.* 2 (4), 242–255. doi:10.1007/s42242-019-00054-7
- Cao, X., Duan, S., Liang, J., Wen, W., and Fang, D. (2018). Mechanical Properties of an Improved 3D-Printed Rhombic Dodecahedron Stainless Steel Lattice Structure of Variable Cross Section. *Int. J. Mech. Sci.* 145, 53–63. doi:10.1016/j.ijmecsci.2018.07.006
- Carla, R. A., Davide, C., and Lucio, M. (2018). Implant Infections: Adhesion, Biofilm Formation and Immune Evasion. *Nat. Rev. Microbiol.* 16, 397–409. doi:10.1038/s41579-018-0019-y
- Chang, C., Huang, J., Yan, X., Li, Q., Liu, M., Deng, S., et al. (2020). Microstructure and Mechanical Deformation Behavior of Selective Laser Melted Ti6Al4V ELI alloy Porous Structures. *Mater. Lett.* 277, 128366. doi:10.1016/j.matlet.2020.128366
- Chen, S. Y., Huang, J. C., Pan, C. T., Lin, C. H., Yang, T. L., Huang, Y. S., et al. (2017). Microstructure and Mechanical Properties of Open-Cell Porous Ti-6Al-4V Fabricated by Selective Laser Melting. *J. Alloys Comp.* 713, 248–254. doi:10.1016/j.jallcom.2017.04.190
- Dias, M. R., Fernandes, P. R., Guedes, J. M., and Hollister, S. J. (2012). Permeability Analysis of Scaffolds for Bone Tissue Engineering. *J. Biomech.* 45 (6), 938–944. doi:10.1016/j.jbiomech.2012.01.019
- Du, Y., Liang, H., Xie, D., Mao, N., Zhao, J., Tian, Z., et al. (2020). Design and Statistical Analysis of Irregular Porous Scaffolds for Orthopedic Reconstruction Based on Voronoi Tessellation and Fabricated via Selective Laser Melting (SLM). *Mater. Chem. Phys.* 239, 121968. doi:10.1016/j.matchemphys.2019.121968
- Falkowska, A., Seweryn, A., and Skrodzki, M. (2020). Strength Properties of a Porous Titanium Alloy Ti6Al4V with Diamond Structure Obtained by Laser Power Bed Fusion (LPBF). *Materials* 13 (22), 5138. doi:10.3390/ma13225138
- Fan, J., Jia, X., Huang, Y., Fu, B. M., and Fan, Y. (2013). Greater Scaffold Permeability Promotes Growth of Osteoblastic Cells in a Perfused Bioreactor. *J. Tissue Eng. Regen. Med.* 9 (12), E210–E218. doi:10.1002/term.1701



- Feng, Q., Tang, Q., Liu, Y., Setchi, R., Soe, S., Ma, S., et al. (2017). Quasi-static Analysis of Mechanical Properties of Ti6Al4V Lattice Structures Manufactured Using Selective Laser Melting. *Int. J. Adv. Manuf Technol.* 94 (5-8), 2301–2313. doi:10.1007/s00170-017-0932-7
- Ibrahim, H., Jahadkbar, A., Dehghan, A., Moghaddam, N., Amerinatanz, A., and Elahinia, M. (2018). *In Vitro* Corrosion Assessment of Additively Manufactured Porous NiTi Structures for Bone Fixation Applications. *Metals* 8 (3), 164. doi:10.3390/met8030164
- Kantaros, A., Chatzidai, N., and Karalekas, D. (2015). 3D Printing-Assisted Design of Scaffold Structures. *Int. J. Adv. Manuf Technol.* 82 (1-4), 559–571. doi:10.1007/s00170-015-7386-6
- Kumar, A., Nune, K. C., and Misra, R. D. K. (2017). Design and Biological Functionality of a Novel Hybrid Ti-6 Al-4 V/hydrogel System for Reconstruction of Bone Defects. *J. Tissue Eng. Regen. Med.* 12 (4), 1133–1144. doi:10.1002/term.2614
- Lei, H.-Y., Li, J.-R., Xu, Z.-J., and Wang, Q.-H. (2020). Parametric Design of Voronoi-Based Lattice Porous Structures. *Mater. Des.* 191, 108607. doi:10.1016/j.matdes.2020.108607
- Li, J., Cui, X., Hooper, G. J., Lim, K. S., and Woodfield, T. B. F. (2020). Rational Design, Bio-Functionalization and Biological Performance of Hybrid Additive Manufactured Titanium Implants for Orthopaedic Applications: A Review. *J. Mech. Behav. Biomed. Mater.* 105, 103671. doi:10.1016/j.jmbbm.2020.103671
- Li, S., Li, X., Hou, W., Nune, K. C., Misra, R. D. K., Correa-Rodriguez, V. L., et al. (2017). Fabrication of Open-Cellular (Porous) Titanium alloy Implants: Osseointegration, Vascularization and Preliminary Human Trials. *Sci. China Mater.* 61 (4), 525–536. doi:10.1007/s40843-017-9063-6
- Liang, H., Yang, Y., Xie, D., Li, L., Mao, N., Wang, C., et al. (2019). Trabecular-like Ti-6Al-4V Scaffolds for Orthopedic: Fabrication by Selective Laser Melting and *In Vitro* Biocompatibility. *J. Mater. Sci. Techn.* 35, 1284–1297. doi:10.1016/j.jmst.2019.01.012
- Liu, Y. J., Li, S. J., Wang, H. L., Hou, W. T., Hao, Y. L., Yang, R., et al. (2016). Microstructure, Defects and Mechanical Behavior of Beta-type Titanium Porous Structures Manufactured by Electron Beam Melting and Selective Laser Melting. *Acta Materialia* 113, 56–67. doi:10.1016/j.actamat.2016.04.029
- Lu, Y., Zhao, W., Cui, Z., Zhu, H., and Wu, C. (2019). The Anisotropic Elastic Behavior of the Widely-Used Triply-Periodic Minimal Surface Based Scaffolds. *J. Mech. Behav. Biomed. Mater.* 99, 56–65. doi:10.1016/j.jmbbm.2019.07.012
- Ma, S., Song, K., Lan, J., and Ma, L. (2020). Biological and Mechanical Property Analysis for Designed Heterogeneous Porous Scaffolds Based on the Refined TPMS. *J. Mech. Behav. Biomed. Mater.* 107, 103727. doi:10.1016/j.jmbbm.2020.103727
- Maskery, I., Sturm, L., Aremu, A. O., Panesar, A., Williams, C. B., Tuck, C. J., et al. (2018). Insights into the Mechanical Properties of Several Triply Periodic Minimal Surface Lattice Structures Made by Polymer Additive Manufacturing. *Polymer* 152, 62–71. doi:10.1016/j.polymer.2017.11.049
- Melancon, D., Bagheri, Z. S., Johnston, R. B., Liu, L., Tanzer, M., and Pasini, D. (2017). Mechanical Characterization of Structurally Porous Biomaterials Built via Additive Manufacturing: Experiments, Predictive Models, and Design Maps for Load-Bearing Bone Replacement Implants. *Acta Biomater.* 63, 350–368. doi:10.1016/j.actbio.2017.09.013
- Nguyen-Van, V., Tran, P., Peng, C., Pham, L., Zhang, G., and Nguyen-Xuan, H. (2020). Bioinspired Cellular Cementitious Structures for Prefabricated Construction: Hybrid Design & Performance Evaluations. *Automation in Construction* 119, 103324. doi:10.1016/j.autcon.2020.103324
- Onal, E., Frith, J., Jurg, M., Wu, X., and Molotnikov, A. (2018). Mechanical Properties and *In Vitro* Behavior of Additively Manufactured and Functionally Graded Ti6Al4V Porous Scaffolds. *Metals* 8 (4), 200. doi:10.3390/met8040200
- Ouyang, P., Dong, H., He, X., Cai, X., Wang, Y., Li, J., et al. (2019). Hydromechanical Mechanism behind the Effect of Pore Size of Porous Titanium Scaffolds on Osteoblast Response and Bone Ingrowth. *Mater. Des.* 183, 108151. doi:10.1016/j.matdes.2019.108151
- Peng, W.-m., Liu, Y.-f., Jiang, X.-f., Dong, X.-t., Jun, J., Baur, D. A., et al. (2019). Bionic Mechanical Design and 3D Printing of Novel Porous Ti6Al4V Implants for Biomedical Applications. *J. Zhejiang Univ. Sci. B* 20 (8), 647–659. doi:10.1631/jzus.b1800622
- Qiu, H., Li, Y., Guo, T. F., Guo, X., and Tang, S. (2018). Deformation and Pattern Transformation of Porous Soft Solids under Biaxial Loading: Experiments and Simulations. *Extreme Mech. Lett.* 20, 81–90. doi:10.1016/j.eml.2018.01.008
- Rana, M., Karmakar, S. K., Pal, B., Datta, P., Roychowdhury, A., and Bandyopadhyay, A. (2021). Design and Manufacturing of Biomimetic Porous Metal Implants. *J. Mater. Res.* 36 (19), 1–11. doi:10.1557/s43578-021-00307-1
- Samoilenko, M., Seers, P., Terriault, P., and Brailovski, V. (2019). Design, Manufacture and Testing of Porous Materials with Ordered and Random Porosity: Application to Porous Medium Burners. *Appl. Therm. Eng.* 158, 113724. doi:10.1016/j.applthermaleng.2019.113724
- Shuai, C., Cheng, Y., Yang, W., Feng, P., Yang, Y., He, C., et al. (2020). Magnetically Actuated Bone Scaffold: Microstructure, Cell Response and Osteogenesis. *Composites B: Eng.* 192, 107986. doi:10.1016/j.compositesb.2020.107986
- Torres-Sanchez, C., Borgman, J. M., Sargeant, B., Bell, H., Alabort, E., Lindsay, C., et al. (2021a). Comparison of Selective Laser Melted Commercially Pure Titanium Sheet-Based Triply Periodic Minimal Surfaces and Trabecular-Like Strut-Based Scaffolds for Tissue Engineering. *Adv. Eng. Mater.*, 2100527. doi:10.1002/adem.202100527
- Torres-Sanchez, C., Norrito, M., Almushref, F. R., and Conway, P. P. (2021). The Impact of Multimodal Pore Size Considered Independently from Porosity on Mechanical Performance and Osteogenic Behaviour of Titanium Scaffolds. *Mater. Sci. Eng. C* 124, 112026. doi:10.1016/j.msec.2021.112026
- Wang, S., Liu, L., Li, K., Zhu, L., Chen, J., and Hao, Y. (2019). Pore Functionally Graded Ti6Al4V Scaffolds for Bone Tissue Engineering Application. *Mater. Des.* 168, 107643. doi:10.1016/j.matdes.2019.107643
- Wang, S., Shi, Z. a., Liu, L., Zhou, X., Zhu, L., and Hao, Y. (2020). The Design of Ti6Al4V Primitive Surface Structure with Symmetrical Gradient of Pore Size in Biomimetic Bone Scaffold. *Mater. Des.* 193, 108830. doi:10.1016/j.matdes.2020.108830
- Wang, X., Xu, S., Zhou, S., Xu, W., Leary, M., Choong, P., et al. (2016). Topological Design and Additive Manufacturing of Porous Metals for Bone Scaffolds and Orthopaedic Implants: A Review. *Biomaterials* 83, 127–141. doi:10.1016/j.biomaterials.2016.01.012
- Yang, Y., Cheng, Y., Peng, S., Xu, L., He, C., Qi, F., et al. (2021). Microstructure Evolution and Texture Tailoring of Reduced Graphene Oxide Reinforced Zn Scaffold. *Bioactive Mater.* 6 (5), 1230–1241. doi:10.1016/j.bioactmat.2020.10.017
- Yang, Y., Lu, C., Peng, S., Shen, L., Wang, D., Qi, F., et al. (2020). Laser Additive Manufacturing of Mg-Based Composite with Improved Degradation Behaviour. *Virtual Phys. Prototyping* 15, 278–293. doi:10.1080/17452759.2020.1748381
- Zhang, B., Pei, X., Zhou, C., Fan, Y., Jiang, Q., Ronca, A., et al. (2018). The Biomimetic Design and 3D Printing of Customized Mechanical Properties Porous Ti6Al4V Scaffold for Load-Bearing Bone Reconstruction. *Mater. Des.* 152, 30–39. doi:10.1016/j.matdes.2018.04.065
- Zhang, H., Jiao, C., Liu, Z., He, Z., Mengxing Ge, M., Zongjun Tian, Z., et al. (2021). 3D-printed Composite, Calcium Silicate Ceramic Doped with CaSO<sub>4</sub>·2H<sub>2</sub>O: Degradation Performance and Biocompatibility. *J. Mech. Behav. Biomed. Mater.* 121, 104642. doi:10.1016/j.jmbbm.2021.104642
- Zhang, X.-Y., Fang, G., Leeftang, S., Zadpoor, A. A., and Zhou, J. (2019). Topological Design, Permeability and Mechanical Behavior of Additively Manufactured Functionally Graded Porous Metallic Biomaterials. *Acta Biomater.* 84, 437–452. doi:10.1016/j.actbio.2018.12.013
- Zhao, L., Pei, X., Jiang, L., Hu, C., Sun, J., Xing, F., et al. (2019). Bionic Design and 3D Printing of Porous Titanium alloy Scaffolds for Bone Tissue Repair. *Composites Part B: Eng.* 162, 154–161. doi:10.1016/j.compositesb.2018.154-161

**Conflict of Interest:** The authors declare that the research was conducted in the absence of any commercial or financial relationships that could be construed as a potential conflict of interest.

**Publisher's Note:** All claims expressed in this article are solely those of the authors and do not necessarily represent those of their affiliated organizations, or those of the publisher, the editors and the reviewers. Any product that may be evaluated in this article, or claim that may be made by its manufacturer, is not guaranteed or endorsed by the publisher.

Copyright © 2021 Chao, Jiao, Liang, Xie, Shen and Liu. This is an open-access article distributed under the terms of the Creative Commons Attribution License (CC BY). The use, distribution or reproduction in other forums is permitted, provided the original author(s) and the copyright owner(s) are credited and that the original publication in this journal is cited, in accordance with accepted academic practice. No use, distribution or reproduction is permitted which does not comply with these terms.



# Porous Bioactive Prosthesis With Chitosan/Mesoporous Silica Nanoparticles Microspheres Sequentially and Sustainedly Releasing Platelet-Derived Growth Factor-BB and Kartogenin: A New Treatment Strategy for Osteoarticular Lesions

## OPEN ACCESS

### Edited by:

Lan Li,  
Nanjing Drum Tower Hospital, China

### Reviewed by:

Yong Sun,  
Sichuan University, China  
Bin Xue,  
Nanjing University, China

### \*Correspondence:

You Wang  
drwangyou@126.com

<sup>†</sup>These authors have contributed  
equally to this work

### Specialty section:

This article was submitted to  
Biomaterials,  
a section of the journal  
Frontiers in Bioengineering and  
Biotechnology

**Received:** 19 December 2021

**Accepted:** 18 January 2022

**Published:** 03 February 2022

### Citation:

Yuan Z, Lyu Z, Zhang W, Zhang J and  
Wang Y (2022) Porous Bioactive  
Prosthesis With Chitosan/Mesoporous  
Silica Nanoparticles Microspheres  
Sequentially and Sustainedly Releasing  
Platelet-Derived Growth Factor-BB  
and Kartogenin: A New Treatment  
Strategy for Osteoarticular Lesions.  
Front. Bioeng. Biotechnol. 10:839120.  
doi: 10.3389/fbioe.2022.839120

Zhiguo Yuan<sup>†</sup>, Zhuocheng Lyu<sup>†</sup>, Wei Zhang, Jue Zhang and You Wang<sup>\*</sup>

Department of Bone and Joint Surgery, Department of Orthopaedics, Renji Hospital, School of Medicine, Shanghai Jiaotong University, Shanghai, China

Osteochondral lesions represent a major clinical challenge, especially in the elderly. Traditional treatment strategies, such as arthroplasty or tissue engineering, have limitations and drawbacks. In this study, we presented a new treatment concept for the application of an innovative porous bioactive prosthesis with regenerative activity for the treatment of osteoarticular lesions. For regenerative activity, we fabricated chitosan/mesoporous silica nanoparticles (CS/MSNs) composite microspheres *via* the microfluidic method as a dual-factor carrier for the sequential release of platelet-derived growth factor BB (PDGF-BB) and kartogenin (KGN). We then integrated the factor carrier and a nondegradable polyetheretherketone (PEEK) scaffold through a surface modification technique to construct the porous sulfonated PEEK (SPK) @polydopamine (polydopamine)-CS/MSNs scaffold. We systematically evaluated the biocompatibility and biofunctionality of the SPK@PDA-CS/MSNs scaffold and implanted the scaffold in an *in vivo* cartilage defect model in rabbits. These results suggest that the SPK@PDA-CS/MSNs scaffold is biocompatible, promotes cell migration, enhances chondrogenic differentiation of BMSCs *in vitro*, and promotes cartilage regeneration *in vivo*. The porous bioactive prosthesis with regenerative activity presented first in this study may comprise a new therapeutic concept for osteoarticular lesions.

**Keywords:** bioactive scaffold, platelet-derived growth factor-BB, kartogenin, chitosan/mesoporous silica nanoparticles, osteoarticular lesions

# 1. INTRODUCTION

Osteochondral lesions are a common healthcare problem that leads to osteoarticular homeostasis imbalance, joint pain, osteoarthritis, and disability (Bruns et al., 2018; Schreiner et al., 2020). However, as the articular cartilage cannot properly self-repair due to its unique properties of avascularity, no nerves, and low cellularity, osteochondral lesions are a major clinical challenge worldwide (Carballo et al., 2017). In recent years, with advances in surgical and tissue engineering approaches for cartilage/osteochondral lesions and progressive osteoarthritis, different treatment strategies have become available (Bhattacharjee et al., 2015; Kwon et al., 2019). These strategies range from stimulation of biological regeneration to reconstruction techniques through joint surface replacement, depending on disease progression and intervention goal.

Osteoarticular treatment strategies can be divided into two main categories: 1) tissue regeneration stimulation, including microfracture (marrow stimulation) (Frehner and Benthien, 2018), osteochondral autograft/allograft (Chao and Pao, 2017), autologous chondrocyte implantation (ACI) (Krill et al., 2018), matrix-induced autologous chondrocyte implantation (MACI) (Correa Bellido et al., 2019), and autologous matrix-induced chondrogenesis (AMIC) (Tradati et al., 2020); and 2) functional replacement achievement, such as hemiarthroplasty or total joint replacement (Waldorff et al., 2013; Goodman et al., 2020). While these treatment approaches have their own indications, they also have limitations and side effects. For therapeutic strategies aimed at regenerating tissue, the first challenge is the difficulty in achieving complete tissue regeneration, as the regenerated tissue may lack the organization and biomechanics of normal cartilage (Moreira-Teixeira et al., 2011). The second obstacle is the patient's age, as many regenerative strategies are based on the patients' own regenerative potential, which is weak in elderly patients. The third challenge is that biological regeneration usually involves complicated procedures (Campos et al., 2019), which also increases the difficulty of clinical application. For functional replacement strategies, the biomechanical and wear characteristics of joint prostheses still have some disadvantages. For example, prosthesis wear problems may result in prosthetic failure due to osteolysis around the implant and fixation loosening (Affatato et al., 2008). Cobalt chromium (CoCr) hemiarthroplasty hip prostheses also fail because of pain and erosion of the acetabular cartilage (Affatato et al., 2008). Consequently, revision surgery is needed, although it is complicated, expensive, and dangerous.

Above all, the goal of complete regeneration for the treatment of osteoarticular lesions is difficult to achieve (Berthiaume et al., 2011), while joint replacement, as a final treatment, is more suitable for end-stage arthritis (Carr et al., 2012). Hence, in the present study, we propose an alternative solution, which is between "regeneration" and "replacement", for the treatment of cartilage defects in patients who are not good candidates for joint replacement and regenerative procedures.

In our previous unpublished study, we successfully fabricated a porous non-biodegradable polyetheretherketone (PEEK)-based scaffold using 3D printed technology. We observed the

physiochemical characteristics and biocompatibility of the scaffold and evaluated its feasibility and safety as a treatment for focal chondral defects in a rabbit model. In that study, we found that the compressive modulus of the 3D printed porous PEEK-based scaffold was close to that of native cartilage, and the porous sulfonated PEEK (SPK) scaffold had excellent cytocompatibility and could be beneficial for cell attachment and proliferation. The *in vivo* study also confirmed that the porous scaffold could promote tissue ingrowth and integration, and achieve cartilage function restoration to a certain extent. Even though the scaffold design was not perfect due to some drawbacks, such as no bioactive stimulator to promote cartilage regeneration, the non-biodegradable porous scaffold still had the potential to be an alternative solution for focal osteochondral lesions, especially functionalizing scaffolds with the capacity for tissue regeneration via surface modification. This can be a new treatment concept for cartilage defects because it neither aims to achieve complete tissue regeneration, nor simple prosthetic replacement, but rather takes an intermediate route between the two. Compared to the traditional treatment strategies of regeneration and replacement, the non-biodegradable porous scaffold with regenerative potential has two main advantages: 1) it can achieve faster recovery of joint function than the regenerative approaches, which require many complicated procedures; and 2) its porous characteristics and regenerative potential may produce a biological articular surface with a low coefficient of friction to avoid or reduce wear problems (Klein, 2009), which are closely associated with prosthetic failure.

In this study, we fabricated a biocompatible chitosan/mesoporous silica nanoparticles (CS/MSNs) composite microsphere via the microfluidic method as a carrier for dual-factor loading and sequential release of platelet-derived growth factor BB (PDGF-BB) and kartogenin (KGN, a small molecule that promotes chondrogenic differentiation of MSCs). Then, we introduced polydopamine (PDA) into our 3D printed porous PEEK-based scaffold system to immobilize CS/MSNs microspheres onto the pore walls of the porous scaffold with its self-polymerization and adhesion properties. In order to construct a porous bioactive prosthesis, we modified the non-biodegradable porous scaffold with CS/MSNs composite microspheres, which could sequentially release PDGF-BB and KGN, thus stimulating cartilage regeneration. Moreover, we also observed the biocompatibility and biofunctionality of the porous bioactive scaffold and evaluated its feasibility and safety as a treatment approach for focal cartilage defects in a rabbit model (Figure 1).

# 2. MATERIALS AND METHODS

## 2.1 Preparation and Characterization of Mesoporous Silica Nanoparticles (MSNs)

MSNs were fabricated using the modified Stöber method (Zhao et al., 2015). Briefly, 1.4 g cetyltrimethyl ammonium bromide (CTAB; Macklin, Shanghai, China) and 66 ml deionized water were added to a beaker, which was stirred in an 80°C water bath.

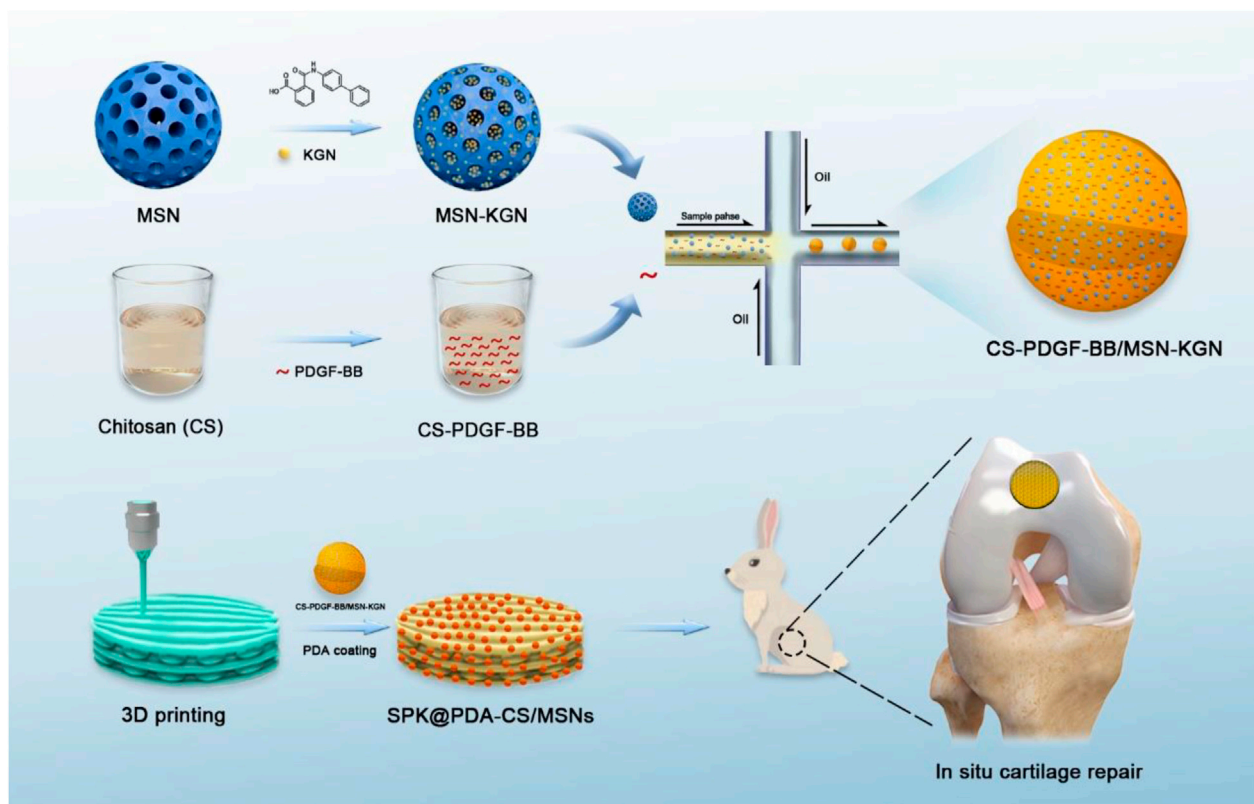


**FIGURE 1** | The schematic diagram of this study.

After the solution became clear and transparent, 20 ml ethyl acetate (Macklin, Shanghai, China) was added to the beaker, and the reaction was magnetically stirred for 30 min. Then, 14 ml 1 mol/L  $\text{NH}_4\text{OH}$  was added to the system and the reaction continued under magnetic stirring for 15 min. Next, 7.2 ml tetraethyl orthosilicate (TEOS; Macklin, Shanghai, China) was added and reacted under magnetic stirring for 6 h. Finally, the white porous silica precipitate was collected via centrifugation, washed three times with deionized water and ethanol, dried at  $60^\circ\text{C}$  for 12 h, and finally calcined at  $700^\circ\text{C}$  for 4 h to obtain MSNs. The morphology and microstructure of MSNs were observed using scanning electron microscopy (SEM; Gemini 300, Zeiss, Germany) and transmission electron microscopy (TEM; Talos F200 X, FEI, Waltham, MA, United States), and the particle size of the MSNs was measured by dynamic light scattering (DLS) using a Zetasizer (Malvern, United Kingdom).

## 2.2 Fabrication of the Microfluidic Device

The microfluidic device is comprised of a microfluidic chip and microfluidic instrumentation. The microfluidic chip (Micronit, Enschede, the Netherlands) was equipped with one inlet and one outlet, main microchannels that were approximately  $100\ \mu\text{m}$  in depth and  $200\ \mu\text{m}$  in width, and a  $50\ \mu\text{m}$  diameter nozzle. Polyethylene tubes with a  $0.5\ \text{mm}$  inner diameter were inserted as the continuous and sample phase inlets. The microfluidic instrumentation was assembled with a pressure

pump (PP), precision pressure controller (PPC), flow sensor (FS), pressure sensor (PS), and liquid storage tank (LST), which were used to pump the fluids into the microfluidic chip (**Supplementary Figure S1**).

## 2.3 Preparation of CS-MSNs Composite Microspheres

An overview of the schedule used to fabricate the CS/MSN-compromised microspheres is shown in **Figure 2A**. In brief, CS/MSNs microspheres were prepared using a microfluidic approach. First, 200 mg CS (Shanghai Bio Life Science and Technology Co., Ltd, Shanghai, China) was dissolved in 10 ml of a 0.5% acetic acid solution to form a CS solution (2% w/v). Then, 0, 0.5, 1, 5, 10, and 50 mg MSNs were added to a 10 ml chitosan solution to form different CS/MSN mixtures (CS, CS/MSNs-1, CS/MSNs-2, CS/MSNs-3, CS/MSNs-4, CS/MSNs-5), respectively, and the mixtures were ultrasonically oscillated for 10 min and filtered ( $0.22\ \mu\text{m}$  pore) to obtain a homogeneous solution (**Supplementary Figure S2**). The CS/MSNs solution, as the sample phase, was set to flow into the microfluidic chip from inlet 2 by the pumps. The oil solution was a 9:1 (v/v) mixture of octane/span 80 and acted as the continuous phase, which was injected into the microchannel from inlet 1 by the pumps, and made the CS aqueous solution form monodispersed droplets under the shear forces. Subsequently, the CS droplets were



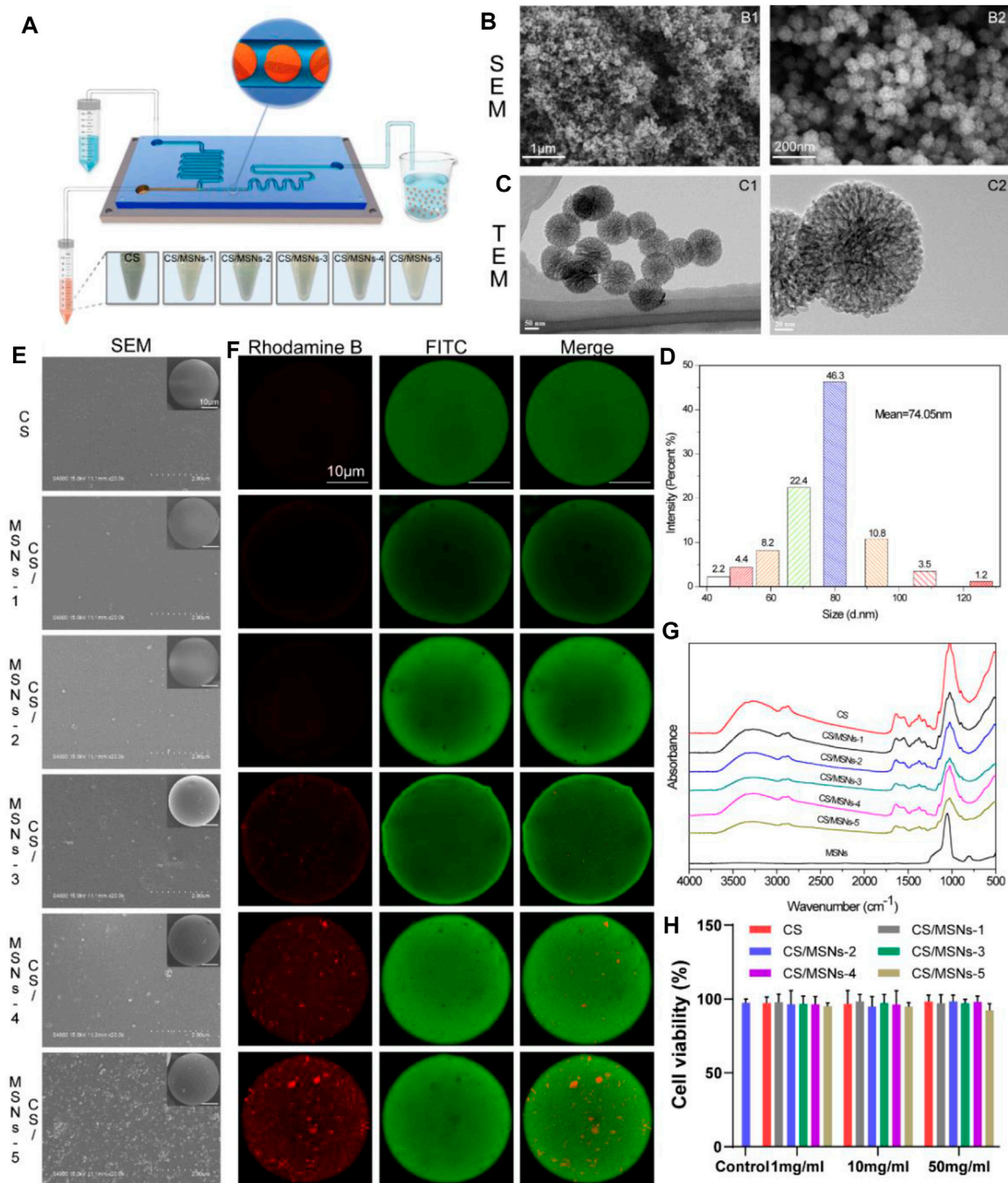


**FIGURE 2 |** Preparation and characteristics of MSNs and CS/MSNs composite microspheres. **(A)** The schematic illustration of the microfluidic chip for fabrication of CS/MSNs composite microspheres. **(B)** SEM images of MSNs. **(C)** TEM images of MSNs. **(D)** The size distribution of MSNs. **(E)** The SEM images of CS/MSNs composite microspheres. **(F)** The fluorescent images of CS/MSNs composite microspheres. **(G)** FTIR spectra of CS/MSNs composite microspheres. **(H)** Cytotoxicity of different concentrations of CS/MSNs composite microspheres (Data shows mean  $\pm$  SD,  $n = 5$ ).

dripped into cross-linking solutions (2:8 v/v mixture of 2.5% glutaraldehyde/octane) for 30 min to form CS/MSN microspheres. Then, the CS/MSN microspheres were washed twice with deionized water and ethanol. Finally, the CS/MSN microspheres were dried at 37°C under a vacuum.

## 2.4 Characterization of the CS/MSNs Composite Microspheres

The microstructure and surface morphology of the CS/MSN composite microspheres were observed using a scanning electron microscope (SEM, S-4800; Hitachi, Tokyo, Japan). Confocal laser

scanning microscopy (CLSM, Leica TCS-SP8; Heidelberg, Germany) was used to evaluate the distribution of MSNs (labeled with rhodamine B) in chitosan (labeled with FITC). The chemical structure of the CS/MSNs composite microspheres was characterized by Fourier transform infrared spectroscopy (FTIR) using a spectrometer (Nicolet Nexus 470; ThermoFisher Scientific, Waltham, MA, United States). Furthermore, X-ray diffraction (XRD) was also used to evaluate the CS/MSNs composite microspheres using an X-ray diffractometer (Ultima IV; Rigaku, Osaka, Japan) in the  $2\theta$  range of  $5-90^\circ$ .

## 2.5 *In Vitro* Cytotoxicity Evaluation of the CS-MSNs Composite Microspheres

Rabbit bone marrow mesenchymal stem cells (BMSCs) were isolated, as described in our previous study, and cultured in Dulbecco's modified Eagle's medium (DMEM; Gibco, ThermoFisher Scientific, Waltham, MA, United States) with 10% fetal bovine serum (FBS; Gibco, ThermoFisher Scientific, Waltham, MA, United States), penicillin (100 U/mL), and streptomycin (100  $\mu$ g/mL) at  $37^\circ\text{C}$  under a 5%  $\text{CO}_2$  atmosphere.

The *in vitro* cytotoxicity of the CS-MSNs composite microspheres was evaluated on BMSCs using the MTT assay. Briefly, 1 mg/mL, 10 mg/mL, and 50 mg/mL CS and CS/MSNs (CS/MSNs-1, CS/MSNs-2, CS/MSNs-3, CS/MSNs-4, CS/MSNs-5) composite microspheres were incubated in culture medium for 24 h, then the supernatant was filtered using a 0.22  $\mu\text{m}$  membrane (Millex-GP, MilliporeSigma, Burlington, MA, United States). BMSCs with a density of  $5 \times 10^3$  cells per well were seeded in 96-well plates and incubated for 24 h. Then the cells were treated with the extracts of different concentrations of CS and CS/MSNs composite microspheres for another 24 h. Subsequently, the cells were stained using the MTT assay, and the OD values were measured at 570 nm using a microplate reader (Bio-Rad Model 550; Hercules, CA, United States). Cell viability (%) was calculated as  $[\text{OD}]_{\text{sample}}/[\text{OD}]_{\text{control}} \times 100$ .

## 2.6 PDGF-BB and KGN Loading and *In Vitro* Release Study

To prepare the CS microspheres loaded with PDGF-BB, a 10 mL CS aqueous solution with 200 mg CS (2% wt) and 1 mg PDGF-BB (100 ng/mL) was used, and the fabrication procedures were performed as described above. In the case of MSNs loaded with KGN, 10 mg MSNs were added to 1 mL of 1  $\mu\text{M}$  KGN PBS solution, ultrasonicated for 5 min, and then stirred for 24 h to enable the KGN to fully impregnate the MSNs. Subsequently, MSNs-KGN was obtained by centrifugation at 15,000 rpm for 10 min. For the preparation of CS-PDGF-BB/MSNs-KGN composite microspheres, 10 mg MSNs-KGN was added to a 10 mL CS aqueous solution with 200 mg CS (2 wt%) and 1 mg PDGF-BB (100 ng/mL), and subjected to ultrasonic oscillation for 10 min to obtain a homogeneous CS/MSNs solution. The fabrication procedures of the CS-PDGF-BB/MSNs-KGN composite microspheres were performed as described above.

The *in vitro* release profiles of PDGF-BB and KGN from the CS-PDGF-BB/MSNs-KGN microspheres were compared with those of the CS-PDGF-BB microspheres and MSNs-KGN in PBS at  $37^\circ\text{C}$ . CS-

PDGF-BB/MSNs-KGN microspheres (5 mg), CS-PDGF-BB microspheres (5 mg), and MSNs-KGN (5 mg) were added to 50 mL PBS, and the mixture was shaken at 100 rpm. At the set time intervals, 100  $\mu\text{L}$  supernatant was extracted from each sample and then added to 100  $\mu\text{L}$  of fresh PBS. The PDGF-BB concentration in the supernatant was quantified using a PDGF-BB ELISA Kit (Neobioscience, Shenzhen, China), and the KGN concentration was quantified by HPLC.

## 2.7 Preparation of the 3D Printed Porous PEEK Scaffold and SPK@PDA-CS/MSNs Scaffold

The PEEK scaffolds were fabricated using a fused filament fabrication (FFF) 3D printer, according to our previous study. The printing parameters of the scaffold, such as strut size (nozzle size), pore size, layer height, and dimensions, were set to the following: 250  $\mu\text{m}$  strut size, 400  $\mu\text{m}$  pore size, 1 mm layer height, and  $\varnothing 4 \text{ mm} \times 1 \text{ mm}$  dimensions.

The sulfonated PEEK scaffold (SPK) was fabricated as follows. The PEEK scaffolds were treated with concentrated sulfuric acid (98 wt%), subjected to ultrasonic oscillation for 30 s, and then washed with deionized water for 6 h.

CS/MSNs composite microspheres (containing PDGF-BB and KGN) were immobilized in the SPK scaffold using the PDA coating method. The SPK scaffolds were immersed in Tris-HCl buffered solution (pH 8.5) with 2 mg/mL dopamine and 20 mg/mL CS/MSNs microspheres (containing PDGF-BB and KGN) under magnetic stirring for 4 h (termed SPK@PDA-CS/MSNs), and the samples without CS/MSNs microspheres were denoted as SPK@PDA.

## 2.8 Characterization of SPK@PDA-CS/MSNs Scaffold

### 2.8.1 Scanning Electron Microscopy (SEM)

The surface morphologies of PEEK, SPK, SPK@PDA, and SPK@PDA-CS/MSNs scaffolds were observed using an emission scanning electron microscope (SEM, Hitachi S-4800; Hitachi, Tokyo, Japan). The prepared specimens were dried and coated with gold prior to the SEM observation.

### 2.8.2 Hydrophilic Property

We used the water contact angle (WCA) to evaluate the surface hydrophilicity of the scaffolds via a contact angle goniometer (JY-82B; Kruss DSA, Hamburg, Germany) at room temperature. Deionized water (2  $\mu\text{L}$ ) was dropped on the surface of the samples, left for 3 s, and observed using a video contact angle system. Five repeated measurements were performed on each specimen to provide an average.

## 2.9 Biocompatibility of the SPK@PDA-CS/MSNs Scaffold

### 2.9.1 Cell Adhesion

Rabbit BMSCs were obtained and cultured as described previously. Each of these PEEK, SPK, SPK@PDA, and SPK@

PDA-CS/MSNs scaffolds were seeded with  $5 \times 10^4$  cells. After culturing for 6, 12, and 24 h, the cell-scaffold complexes were collected. The cells in the scaffold were measured using a Cell Counting Kit-8 (CCK-8, Beyotime, Shanghai, China) assay, and the OD values of these specimens were measured at 450 nm using a microplate reader (Synergy HT; Bio-Tek Co., Winooski, VT, United States).

### 2.9.2 Live/Dead Staining

The cytocompatibility of the PEEK, SPK@PDA, and SPK@PDA-CS/MSNs scaffolds was assessed using a live/dead assay kit (Beyotime, Shanghai, China) according to the manufacturer's instructions. After 3 and 7 days of culture, the cell/scaffold complex was collected and washed with phosphate buffered saline (PBS) twice, and then treated with calcein AM and propidium iodide (PI) (Beyotime) for 0.5 h. Subsequently, the specimens were washed with PBS twice and then observed using a fluorescence confocal microscope (Leica SP8, Wetzlar, Germany). Furthermore, all procedures were performed in a dark room.

### 2.9.3 Cytoskeletal Observations

The morphology of cells on the PEEK, SPK@PDA, and SPK@PDA-CS/MSNs scaffolds was evaluated by cytoskeletal observations using F-actin staining. After 3 days of culture, cells on different samples were fixed with paraformaldehyde (4% v/v) for 30 min, washed twice with PBS, and stained with FITC-phalloidin (Solarbio, Beijing, China) for 40 min. After washing with PBS twice, the cells were treated with 4',6-diamidino-2-phenylindole (DAPI; Beyotime, Shanghai, China) for 10 min, and then observed using a Leica SP8 fluorescence confocal microscope.

## 2.10 In Vitro Cell Migration Evaluation of the SPK@PDA-CS/MSNs Scaffold

We used the transwell chemotactic migration system (Corning, Corning, NY, United States) to evaluate the recruitment ability of PDGF-BB released from the SPK@PDA-CS/MSNs scaffold. In brief,  $5 \times 10^4$  BMSCs were seeded in the upper chamber of the transwell plate, and the SPK@PDA and SPK@PDA-CS/MSNs scaffolds were placed in the lower chamber. After 24 h of culture, the transwell membrane was scraped on the upper surface to remove the cells, and the migrated cells on the lower side were fixed in 4% paraformaldehyde, stained with crystal violet, imaged using an optical microscope (Olympus Corporation, Japan), and quantitatively evaluated using the Imaris software.

## 2.11 Chondrogenic Differentiation Evaluation of the SPK@PDA-CS/MSNs Scaffold

**2.11.1 Chondrogenic Differentiation in BMSCs Pellets**  
We evaluated the chondrogenic differentiation capacity of KGN released from the SPK@PDA-CS/MSNs scaffold using a transwell system (Corning, NY, United States). First,  $5 \times 10^5$  BMSCs were placed into a 15 ml centrifuge tube, centrifuged at 250 g for 5 min, and then cultured for 2 days to form BMSC pellets. The same transwell plate used in the cell migration experiment was also

used in the chondrogenic differentiation experiment. The pellets were transferred to the fresh upper well of the transwell plate, and the SPK@PDA-CS/MSNs scaffold was positioned in the lower well. The chondrogenic culture medium (Cyagen, Santa Clara, CA, United States) in the transwell plate was exchanged every 3 days. After 21 days of culture, the pellets were photographed and analyzed.

### 2.11.2 Histological and Immunohistochemical Examination

After culturing for 21 days, the pellets were harvested, fixed in 4% paraformaldehyde for 2 days, dehydrated, embedded, and sectioned into 7  $\mu$ m slices. These sections were stained with hematoxylin-eosin (HE), Alcian blue (AB), and Safranin O/Fast Green (SO/FG). The sections were then subjected to immunohistochemical (IHC) analysis for collagen II (primary antibody Col II 1:100; Abcam, Boston, MA, United States). Immunohistochemical staining was performed as described in our previous study (Yuan et al., 2021).

### 2.11.3 GAG/DNA

After 21 days of culture, the pellets were harvested and assayed for DNA and GAG content. The DNA of the pellets was extracted using a genomic DNA kit (TIANamp, Beijing, China), and then quantified using a PicoGreen DNA assay kit (Invitrogen, Carlsbad, CA, United States). The GAG content of the pellets was measured using a tissue GAG total content 1,9-dimethylmethylene blue (DMMB) colorimetric kit (Genmed Scientific Inc, Shanghai, China). The GAG secreted by the cells was standardized using GAG/DNA.

### 2.11.4 RT-PCR

We evaluated the expression of cartilage-related genes SRY-Box Transcription Factor 9 (SOX9), aggrecan, collagen I, and collagen II in the pellets of the SPK@PDA-CS/MSNs and SPK@PDA groups using real-time polymerase chain reaction (RT-PCR) experiments. In brief, RNA was extracted using TRIzol (Sigma-Aldrich, St. Louis, MO, United States) and transcribed into complementary DNA (cDNA) using a ReverTra Ace kit (Toyobo, Osaka, Japan). Gene expression was quantified by quantitative reverse transcription polymerase chain reaction (qRT-PCR) using a LightCycler 480 system (Roche Applied Science, Indianapolis, IN, United States). The primers used in this study are shown in **Supplementary Table S1**, and glyceraldehyde-3-phosphate dehydrogenase (GAPDH) was used as a reference gene.

## 2.12 In Vivo Animal Studies

### 2.12.1 Surgical Procedure

Animal studies were approved by the Institutional Animal Care and Use Committee of Renji Hospital, which was affiliated with Shanghai Jiao Tong University Medical College. Twenty-four adult New Zealand white rabbits were used in this study and were randomly allocated into three groups: SPK@PDA-CS/MSNs, SPK@PDA, and the control group. A  $\varnothing 4$  mm  $\times$  1 mm cylinder defect was fashioned using a punch in the femoral trochlear to create a cartilage defect model of the rabbits. In



the SPK@PDA-CS/MSNs group, the defect was treated with the SPK@PDA-CS/MSNs scaffold (containing PDGF-BB and KGN), whereas in the SPK@PDA group, the defect was treated with the SPK@PDA scaffold. The defect was left untreated in the control group. Postoperatively, the rabbits were administered antibiotics to prevent infection and were left free to move in the cages. The rabbits were euthanized at 1 and 3 months after surgery and were prepared for analysis.

### 2.12.2 Macroscopic Observations

The femoral condyles were harvested and photographed at 1 and 3 months after surgery. The macroscopic observations in the different groups were semi-quantitatively analyzed via the macroscopic scoring system from Goebel et al. (Goebel et al., 2012; Madry et al., 2020), which was performed by two blinded experienced investigators. The scoring details were presented in **Supplementary Table S2**.

### 2.12.3 Histological Examination

The femoral condyles were harvested at 1 and 3 months postoperatively, fixed in 4% paraformaldehyde for 2 days, decalcified with ethylenediaminetetraacetic acid (EDTA, Servicebio, Wuhan, Hubei, China), dehydrated, embedded, and sectioned into 7  $\mu\text{m}$  slices. The sections were stained with HE and toluidine blue (TB). The sections were also subjected to IHC staining for collagen II as described above.

### 2.12.4 Biochemical Assays for GAG and Collagen

We evaluated the GAG content of the repaired tissue using a tissue GAG total content DMMB colorimetric kit (GenMed, Shanghai, China). The total collagen content of the repaired tissue was measured using a hydroxyproline assay kit (Nanjing Jiancheng Bioengineering Institute, Nanjing, China) according to the manufacturer's instructions.

### 2.12.5 RT-PCR

To further evaluate cartilage regeneration, we used RT-PCR to evaluate the expression of the cartilage-related genes SOX9, aggrecan, collagen I, and collagen II. RNA was extracted, reverse-transcribed, and quantified, as described above. The primer sequences are listed in **Supplementary Table S1**, and GAPDH was used as an internal control.

## 2.13 Statistical Analysis

Statistical analysis was performed with Tukey's multiple comparison tests, as well as one-way analysis of variance (ANOVA), using GraphPad Prism 9 (GraphPad Software, Inc, La Jolla, CA, United States). All data were expressed as the mean  $\pm$  standard deviation (SD), and the significance of the difference was set at  $p < .05$ .

## 3. RESULTS

### 3.1 Characterization of MSNs and CS/MSNs Composite Microspheres

As shown in **Figure 2B**, the morphology of the MSNs was observed using SEM. It could be seen that the MSNs were

nanoscale particles. The internal pore structure of the MSNs was observed using TEM. We confirmed that the MSNs were monodisperse and possessed a highly porous structure and sufficient space for the adsorption of biomolecules, such as KGN (**Figure 2C**). The particle size distribution of the MSNs was measured using dynamic light scattering (DLS), as shown in **Figure 2D**. The particle size was approximately 74 nm, and it was mainly distributed between 68 and 92 nm.

Moreover, different amounts of MSNs (0.5, 1, 5, 10, and 50 mg) were added to 10 ml chitosan solution, and then ultrasonically oscillated for 10 min to form a homogeneous CS/MSNs (CS/MSNs-1, CS/MSNs-2, CS/MSNs-3, CS/MSNs-4, and CS/MSNs-5) mixture solution. As shown in **Supplementary Figure S2**, CS/MSNs-1, CS/MSNs-2, CS/MSNs-3, and CS/MSNs-4 mixture solutions were homogeneous, while there were some sediments in the CS/MSNs-5 mixture solution, indicating that 50 mg MSNs cannot disperse completely in a 10 ml chitosan solution. Next, different CS/MSN composite microspheres were prepared from a chitosan mixed solution by the microfluidic method.

Subsequently, the CS/MSN composite microspheres were characterized by SEM, fluorescence labeling, FTIR, and XRD. As shown in **Figure 2E**, SEM was used to observe the surface morphology of the CS/MSN composite microspheres. It can be seen that the structures of the CS/MSNs composite microspheres were significantly different, and the distribution of the MSNs in the CS/MSNs composite microspheres increased as the MSNs concentration increased. Furthermore, we utilized fluorescence labeling (MSNs labeled with rhodamine B, and CS marked with FITC) to observe the internal structure of CS/MSNs composite microspheres, as shown in **Figure 2F**. The CLSM results showed that the MSN content in the CS/MSNs composite microspheres increased with the addition of MSNs, and MSNs aggregation was evident in the CS/MSNs-5 group, which was consistent with the results of SEM.

The main chemical groups of CS microspheres, CS/MSNs composite microspheres, and MSNs could be evaluated from the FTIR spectra, as shown in **Figure 2G**. For the CS microspheres, the characteristic peaks were at  $2,872\text{ cm}^{-1}$  (C-H stretching vibration),  $1,634\text{ cm}^{-1}$  (C=O stretching vibration),  $1,550\text{ cm}^{-1}$  (N-H stretching vibration), and  $1,024\text{ cm}^{-1}$  (C-O stretching vibration). The characteristic absorption peak of MSNs at  $806\text{ cm}^{-1}$  (Si-O-Si stretching vibration) was weakened in the spectra of the CS/MSNs composite microspheres, which may mean that the MSNs were dispersed into the CS matrix. For the CS/MSNs composite microspheres, the main characteristic peaks were also observed at  $2,872\text{ cm}^{-1}$ ,  $1,634\text{ cm}^{-1}$ ,  $1,550\text{ cm}^{-1}$ , and  $1,024\text{ cm}^{-1}$ , which were similar to those of the CS microspheres. Furthermore, the CS microspheres, CS/MSNs composite microspheres, and MSNs were characterized by XRD, as shown in **Supplementary Figure S3**. The characteristic diffraction peak of the CS microspheres was at  $2\theta = 19.94^\circ$  (hydrated crystalline). MSNs appeared as an intense reflection peak at  $2\theta = 21.6^\circ$ . With the addition of the MSNs, the characteristic reflection peak of the CS/MSNs composite microspheres was similar to that of the CS microspheres, indicating that the MSNs were dispersed in the CS matrix.



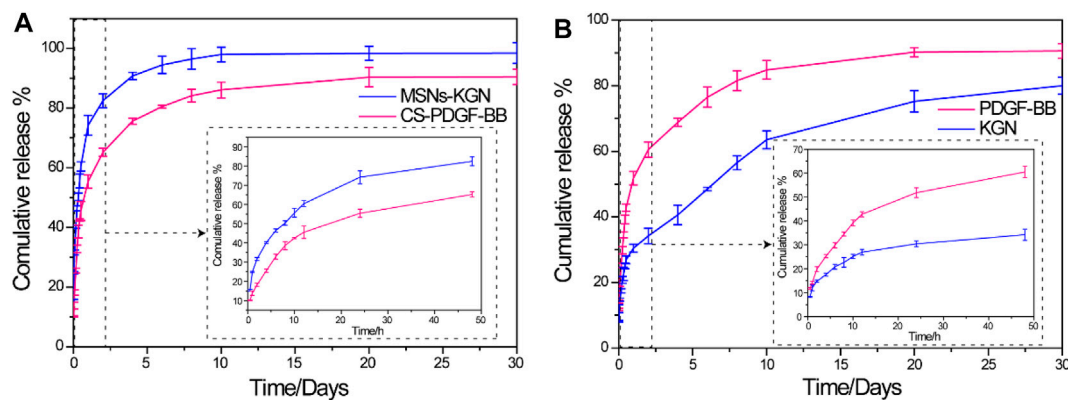


**FIGURE 3 | (A)** *In vitro* release profiles of KGN from MSNs and PDGF-BB from CS in PBS solution. **(B)** *In vitro* release profiles of PDGF-BB and KGN from CS/MSNs composite microspheres. Date was shown as mean  $\pm$  SD,  $n = 3$ .

Next, we assessed the cytotoxicity of the CS microspheres and CS/MSNs composite microspheres at 1 mg/ml, 10 mg/ml, and 50 mg/ml using BMSCs by MTT assay. **Figure 2H** shows the cell viability of BMSCs treated with the extracts of CS microspheres and CS/MSNs composite microspheres at 1 mg/ml, 10 mg/ml, and 50 mg/ml, respectively. The cell viability of CS/MSNs composite microspheres was approximately the same as that of the CS microspheres and the control group; the cell viability of the different samples was above 90%, indicating that CS and CS/MSNs would be safe as drug delivery carriers. As for the five different CS/MSNs composite microspheres (CS/MSNs-1, CS/MSNs-2, CS/MSNs-3, CS/MSNs-4, and CS/MSNs-5), the SEM and CLSM results also confirmed that, with the addition of the MSNs, the distribution of the MSNs in the CS/MSNs composite microspheres increased. In contrast, in CS/MSNs-5, the MSNs aggregation could be observed. Similarly, the CS/MSNs-5 mixture solution contained some sediments, indicating that 50 mg MSNs could not disperse completely in a 10 ml chitosan solution. Therefore, we chose CS/MSNs-4 as a drug delivery carrier.

### 3.2 *In Vitro* Release of PDGF-BB and KGN

The PDGF-BB and KGN release profiles of the MSNs loaded with KGN, CS microspheres loaded with PDGF-BB, and CS/MSNs composite microspheres loaded with PDGF-BB and KGN *in vitro* were investigated using ELISA kits and HPLC (**Figure 3**). For the KGN release from the MSNs, which was showed in **Figure 3A**, there was a rapid release of 74% of the total KGN released from the MSNs on the first day, after which the release rate slowed and reached approximately 98% of the total KGN released after 10 days. For the PDGF-BB release from the CS microspheres loaded with PDGF-BB, there was still an initial burst release, with nearly 55% of the total PDGF-BB released on the first day; subsequently, the release slowed and approximately 86% was released after 10 days. In contrast, the drug release behavior of the composite microspheres was completely different from that of the pure MSNs and CS microspheres, as shown in **Figure 3B**. The release of KGN from CS/MSNs composite microspheres (loaded with PDGF-BB and KGN) was sustained and controlled, with a

comparatively slow release of 30% on the first day, and then sustainably released for as long as 3 weeks. The PDGF-BB release from CS/MSNs composite microspheres was sharp compared with KGN, with 51% released on the first day, and nearly 84% released at 10 days, whereas approximately 40% of the total KGN was retained after 10 days. The results indicated that PDGF-BB and KGN were sequentially released from the CS/MSNs composite microspheres. According to the literatures (Charnay et al., 2004; Zhao et al., 2015), drugs (KGN in this study) were loaded in the pore walls of the MSNs and were usually located in the center of the MSNs. As for the CS/MSNs composite microspheres, the KGN first traveled to the surface of the MSNs and entered the CS matrix, then passed through the CS matrix, lengthening the diffusion route, whereas the PDGF-BB diffused directly out of the CS matrix. Therefore, the sequential release behavior of PDGF-BB and KGN from the CS/MSNs composite microspheres could be attributed to the characteristic composite structure of the CS/MSNs.

### 3.3 Characterization of the SPK@PDA-CS/MSNs Scaffold

We evaluated the microstructure and hydrophilicity of the PEEK, SPK, SPK@PDA, and SPK@PDA-CS/MSNs scaffolds using SEM and the water contact angle (WCA). As shown in **Figure 4A**, **Supplementary Figure S4**, the morphology observation of the different scaffolds was conducted using general observation and SEM. The PEEK scaffold had a smooth surface, while the SPK and SPK@PDA scaffolds were rougher, which was mainly attributed to the sulfonation treatment and PDA coating. The SEM results also confirmed that the CS/MSNs composite microspheres could be immobilized in the SPK@PDA-CS/MSNs scaffold by the PDA coating method. **Figure 4B** shows the water angles of the prepared scaffolds and confirmed that these surface modification methods altered the surface wettability of the scaffolds. The sulfonation treatment changed the hydrophilicity of the PEEK scaffold from  $68.2 \pm 1.5^\circ$  (PEEK) to  $77.9 \pm 1.1^\circ$  (SPK), whereas the PDA coating enhanced the hydrophilicity of SPK from  $77.9 \pm 1.1^\circ$  to  $58.6 \pm 1.9^\circ$ . After the

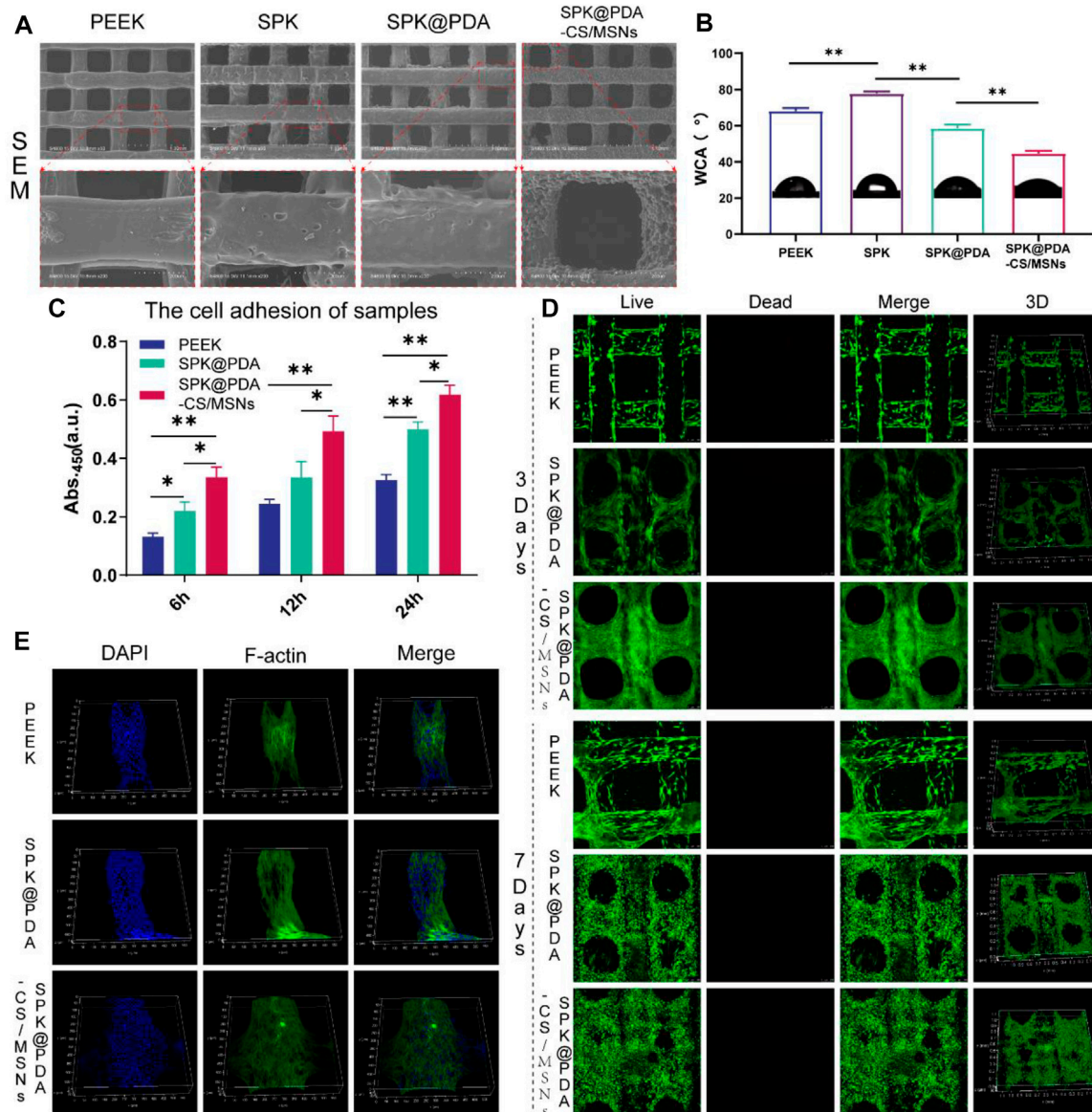


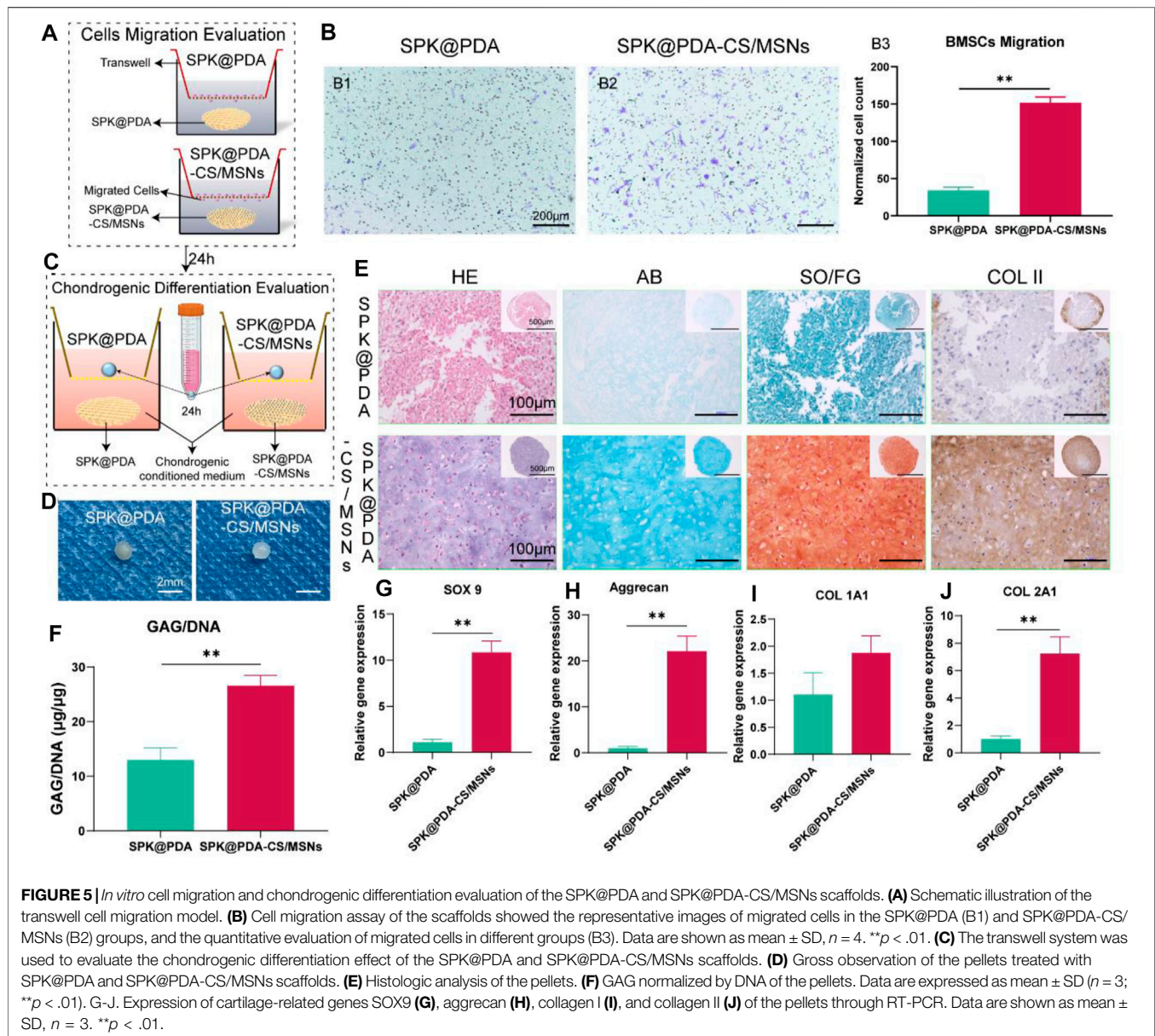
**FIGURE 4 |** The properties and cytocompatibility of the prepared scaffolds. **(A)** The SEM images of the PEEK, SPK, SPK@PDA, and SPK@PDA-CS/MSNs scaffolds. **(B)** The water contact angle (WCA) of the prepared specimens. **(C)** The cell adhesion of the PEEK, SPK@PDA, and SPK@PDA-CS/MSNs scaffolds. Data are presented as mean  $\pm$  SD,  $n = 5$ ,  $*p < .05$ ,  $**p < .01$ . **(D)** Live/Dead staining. **(E)** Three-dimensional fluorescence images of BMSCs on the scaffolds for 3 days of culture.

deposition of CS/MSNs composite microspheres in the scaffold, the contact water angles further decreased to  $44.7 \pm 1.4^\circ$ .

### 3.4 Cytocompatibility of the SPK@PDA-CS/MSNs Scaffold

The cytocompatibility of the prepared specimens, including the PEEK, SPK@PDA, and SPK@PDA-CS/MSNs scaffolds, was evaluated via a cell adhesion assay, live/dead staining, and cytoskeletal staining. The cell adhesion of the scaffolds was evaluated using the CCK-8 kit, and the results in **Figure 4C** demonstrate that the cell attachment capacity of the SPK@PDA-

CS/MSNs scaffold was superior to that of the PEEK and SPK@PDA scaffolds. We then assessed the cell growth of the BMSCs on the PEEK, SPK@PDA, and SPK@PDA-CS/MSNs scaffolds through live/dead staining after culturing them for 3 and 7 days. As shown in **Figure 4D**, most of the BMSCs on the three different scaffolds were alive after 3 and 7-days culture, and there was an increase in cells on the scaffolds as the culture time increased. In addition, there were more cells on the SPK@PDA-CS/MSNs scaffolds than that on the PEEK and SPK@PDA scaffolds. Furthermore, we observed the morphology of the cells on the three scaffolds after 3-days culture through cytoskeletal staining, which is shown in **Figure 4E**,



**Supplementary Figure S5.** The BMSCs were spread well on all three scaffolds, while there were more well-spread cells on the SPK@PDA-CS/MSNs scaffold compared to the PEEK and SPK@PDA scaffolds. Therefore, all the experiments demonstrated that the SPK@PDA-CS/MSNs scaffold had superior cytocompatibility and biocompatibility.

### 3.5 *In Vitro* Cell Migration

The chemotactic capacity of the SPK@PDA-CS/MSNs scaffold (containing PDGF-BB and KGN) was evaluated *via* a transwell system, as shown in **Figure 5A**. The BMSCs traversing the transwell membrane were identified and quantified by crystal violet staining, and the results are shown in **Figure 5B**. The number of migrating cells in the SPK@PDA-CS/MSNs group was significantly higher than that in the SPK@PDA group, confirming

the recruitment capacity of PDGF-BB released from the SPK@PDA-CS/MSNs scaffold.

### 3.6 *In Vitro* Chondrogenic Differentiation Evaluation

We evaluated the chondrogenic differentiation capacity of the SPK@PDA and SPK@PDA-CS/MSNs scaffolds in the BMSC pellet culture using the transwell system (**Figure 5C**). As shown in **Figures 5D,E**, the pellet treated with SPK@PDA-CS/MSNs after a 21-days culture was more transparent than that in the SPK@PDA group. The HE results showed that there were plenty of chondrocyte-like cells and cartilage lacuna in the pellet treated with SPK@PDA-CS/MSNs, whereas the SPK@PDA-treated pellet showed abundant spindle-shaped cells and a



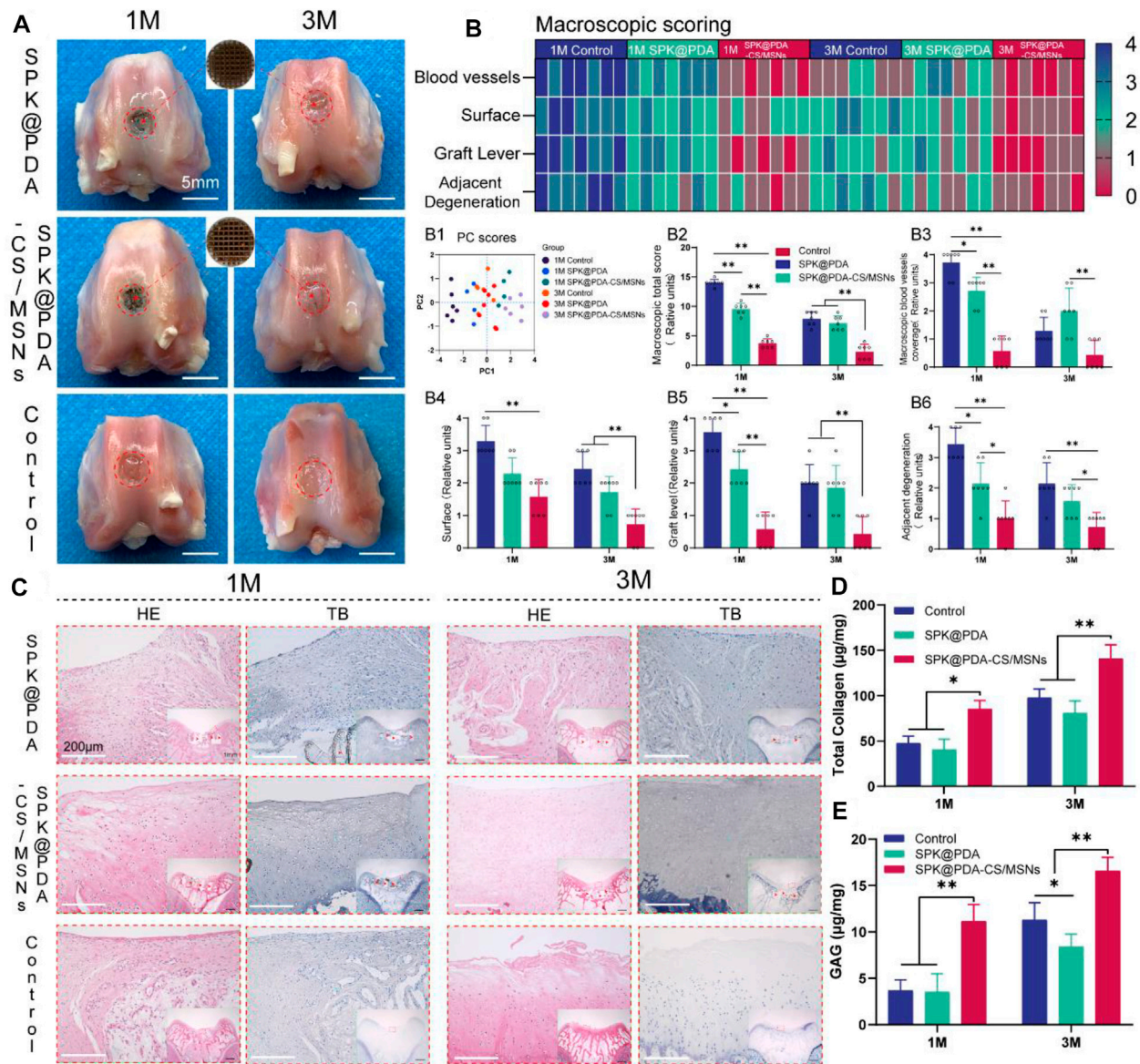


**FIGURE 6 |** Gross observation and histological analysis of cartilage defects treated with SPK@PDA and SPK@PDA-CS/MSNs scaffolds at 1 and 3 months after surgery. **(A)** Gross morphology of the repaired tissue. **(B)** Heat map of the macroscopic scoring system. B1. Principal component analysis of the macroscopic score. B2. Total macroscopic score comparison of different groups. B3-6. Comparison of variables in different groups, including blood-vessel coverage (B3), surface (B4), graft level (B5), and adjacent cartilage degeneration (B6). Data are shown as mean  $\pm$  SD,  $n = 7$ ,  $p < 0.05$ ,  $^{**}p < .01$ . **(C)** Hematoxylin-eosin (HE) and toluidine blue (TB) staining of the repaired tissue at 1 and 3 months after surgery, red arrows indicate residual PEEK scaffold. **(D,E)** Total collagen and GAG content of the repaired tissue at 1 and 3 months after surgery. Data are shown as mean  $\pm$  SD,  $n = 3$ ,  $p < 0.05$ ,  $^{**}p < .01$ .

loose structure. The AB and SO/FG staining showed greater intensity in the pellets treated with SPK@PDA-CS/MSNs than in those treated with SPK@PDA. Moreover, the GAG per DNA content of the pellet treated with SPK@PDA-CS/MSNs increased significantly compared with that of the SPK@PDA-treated pellet, which was consistent with the histological results (Figure 5F). We then evaluated the expression of chondrogenic differentiation-related genes, including SOX 9 (Figure 5G), aggrecan (Figure 5H), collagen I (Figure 5I), and collagen II (Figure 5J),

in the pellets treated with SPK@PDA and SPK@PDA-CS/MSNs by RT-PCR. The expression of SOX 9, aggrecan, and collagen II increased significantly in the pellet treated with SPK@PDA-CS/MSNs compared to those treated with SPK@PDA, while only slight changes were observed in the collagen I expression of the pellets treated with SPK@PDA and SPK@PDA-CS/MSNs, with no statistical significance. These results demonstrated that the chondrogenic differentiation capacity of the BMSC pellets was enhanced by treatment with SPK@PDA-CS/MSNs.



### 3.7 In Vivo Cartilage Repair Studies

To evaluate the effect of the SPK@PDA and SPK@PDA-CS/MSNs scaffolds on cartilage regeneration, we implanted them into a cartilage defect model of rabbits and observed cartilage regeneration at 1 and 3 months after surgery, using gross observation, histology, biochemical assays, and RT-PCR. Macroscopically, there was no obvious inflammatory reaction in any of the SPK@PDA, SPK@PDA-CS/MSNs, and control groups, and some neo-tissue could be seen in the SPK@PDA and SPK@PDA-CS/MSNs groups, while the smoothness of the repair area, graft level, and adjacent cartilage degeneration varied in the SPK@PDA, SPK@PDA-CS/MSNs, and control groups (**Figure 6A**). We then semi-quantitatively evaluated the repair effect of the cartilage defect treated with the SPK@PDA and SPK@PDA-CS/MSNs scaffolds *via* macroscopic cartilage repair scoring (**Figure 6B**). As shown in **Figure 6B1-7**, the scoring of macroscopic cartilage repair showed a significantly improved repair effect in the SPK@PDA-CS/MSNs group compared to that of the SPK@PDA and control groups. The individual parameters of blood vessel presence, surface, graft level, and adjacent cartilage degeneration of the repair tissue of defects treated with SPK@PDA-CS/MSNs were superior to those of the SPK@PDA and control groups.

The histological findings according to HE and TB staining are showed in **Figure 6C**, which revealed that application of the SPK@PDA-CS/MSNs scaffold significantly improved the repair effect of the cartilage defect relative to the SPK@PDA and control groups. We then evaluated the total collagen and GAG content of the repair tissue using a biochemical assay, as shown in **Figures 6D,E**, which revealed that application of the SPK@PDA-CS/MSNs scaffold significantly increased the collagen and GAG contents of the repair tissue relative to the SPK@PDA and control groups, which was consistent with the histological findings. Furthermore, the immunohistochemistry analysis of collagen II also showed that application of the SPK@PDA-CS/MSNs significantly increased collagen II staining intensity compared to the SPK@PDA and control groups at 1 and 3 months after surgery (**Figure 7A**).

RT-PCR with mRNA isolated from the repair tissue was used to evaluate the expression of cartilage-related genes, including SOX 9 (**Figure 7B**), aggrecan (**Figure 7C**), collagen II (**Figure 7D**), and collagen I (**Figure 7E**). The gene expression of SOX 9, aggrecan, and collagen II in the SPK@PDA-CS/MSNs group were higher than those in the SPK@PDA and control groups at 1 and 3 months after surgery, respectively, while the collagen I expression of the repair tissue in the SPK@PDA-CS/MSNs group was only higher than that in the control group at 1 month after surgery. Other groups only showed slight changes, which were not statistically significant.

## 4. DISCUSSION

In the present study, we propose a new therapeutic concept for osteoarticular lesions. This is different from the traditional tissue engineering strategy aimed at complete regeneration and the prosthesis replacement strategy aimed at pure functional

replacement, because it utilizes a porous prosthesis with regenerative activity. Compared with the traditional “regeneration” and “replacement” strategies, the porous prosthetic strategy with induced regenerative activity may have two major advantages, one being its faster functional recovery ability that can quickly accommodate the needs of patients for early functional recovery compared to the regeneration strategy; the second being its ability to promote partial cartilage biological regeneration to restore the biological friction mechanism of the articular cartilage surface.

In order to evaluate the strategy of porous prostheses with regenerative activity, we first fabricated a drug delivery system based on MSNs and chitosan (CS) using a microfluidic method, which has the ability to sequentially and sustainably release PDGF-BB and KGN. We evaluated the physicochemical properties and cytotoxicity of different CS/MSNs composite microspheres and chose the CS/MSNs-4 mixture as the drug delivery carrier for PDGF-BB and KGN because of its superior structural characteristics. We then observed the release behavior of PDGF-BB and KGN from CS/MSNs composite microspheres and confirmed that the CS/MSNs delivery system could sequentially and sustainably release PDGF-BB and KGN. This may be due to the extended transport path required for KGN release, which involves diffusion from the MSNs to the CS matrix and travel across the CS matrix, while the PDGF-BB diffuses directly from the CS matrix. Subsequently, we constructed a 3D porous PEEK scaffold following our previous study and performed surface modification on the scaffold through sulfonation treatment, and then immobilized the CS/MSNs composite microspheres (containing PDGF-BB and KGN) in the SPK scaffold through PDA coating to fabricate the SPK@PDA-CS/MSNs scaffold. We investigated the microstructure and hydrophilicity of these scaffolds via SEM and WCA, which demonstrated that the SPK@PDA-CS/MSNs scaffold had an excellent pore structure and a hydrophilic surface. We then evaluated the cytocompatibility of the prepared scaffolds and confirmed that the SPK@PDA-CS/MSNs scaffold could promote BMSC adhesion, spread, and growth, and was biocompatible. We assessed the biofunctionalities of the scaffolds for cell chemotactic ability and chondrogenic differentiation capacity through the transwell system, and the results confirmed that the SPK@PDA-CS/MSNs scaffold (containing PDGF-BB and KGN) had the capacity to recruit BMSCs and promote chondrogenic differentiation of BMSCs.

In this study, we successfully fabricated a porous bioactive prosthesis with excellent biocompatibility and superior biofunctionalities for BMSC recruitment and chondrogenic differentiation capacity *in vitro*. We then implanted the scaffold into the cartilage defect model of rabbits and evaluated its feasibility and safety at 1 and 3 months after surgery. The gross observations and histological results confirmed that the SPK@PDA-CS/MSNs scaffold could effectively fill the cartilage defects and promote biological regeneration of the cartilage located inside and on the surface of the porous scaffold, which may have the potential to restore the biological lubrication of the articular cartilage surface. We then

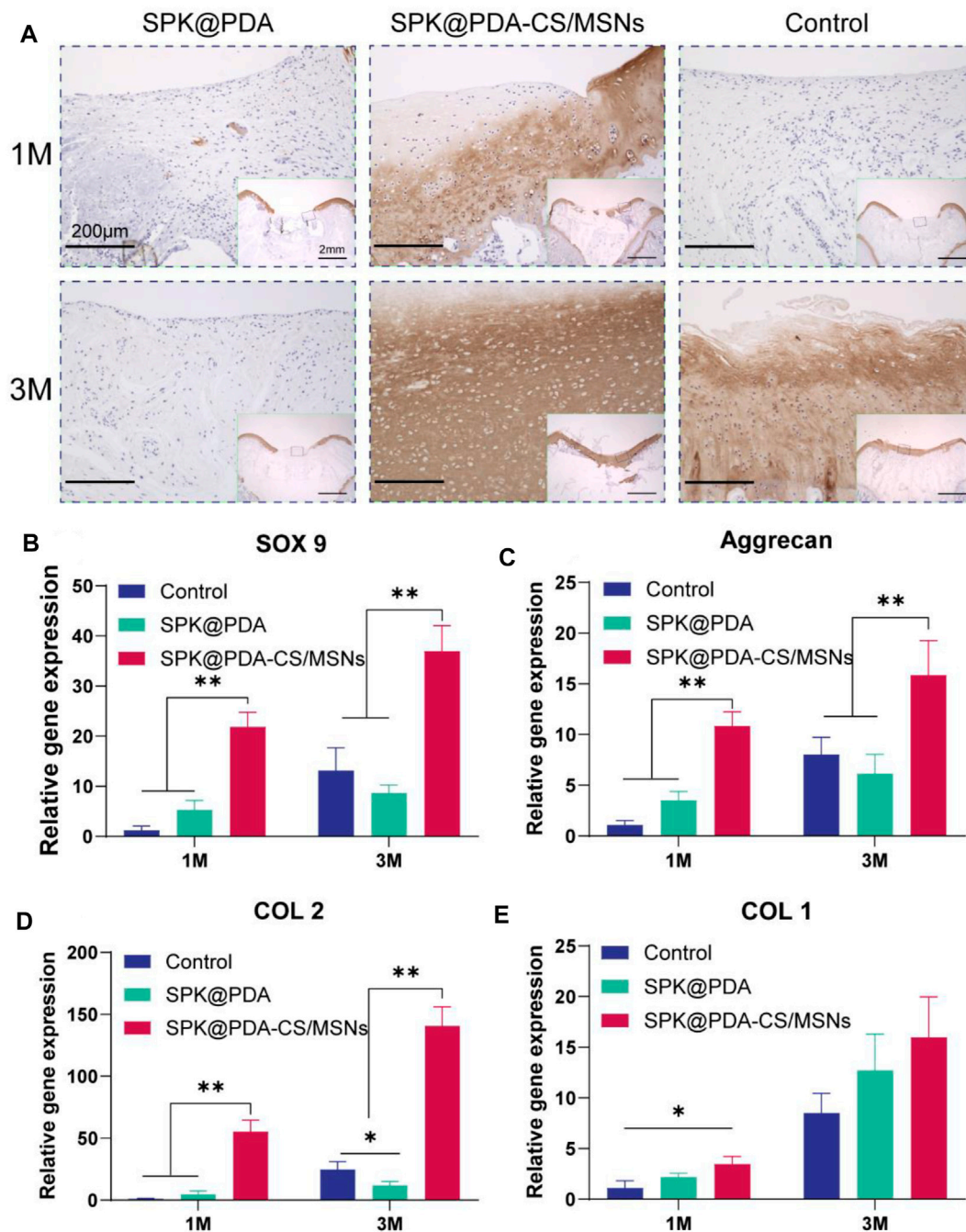
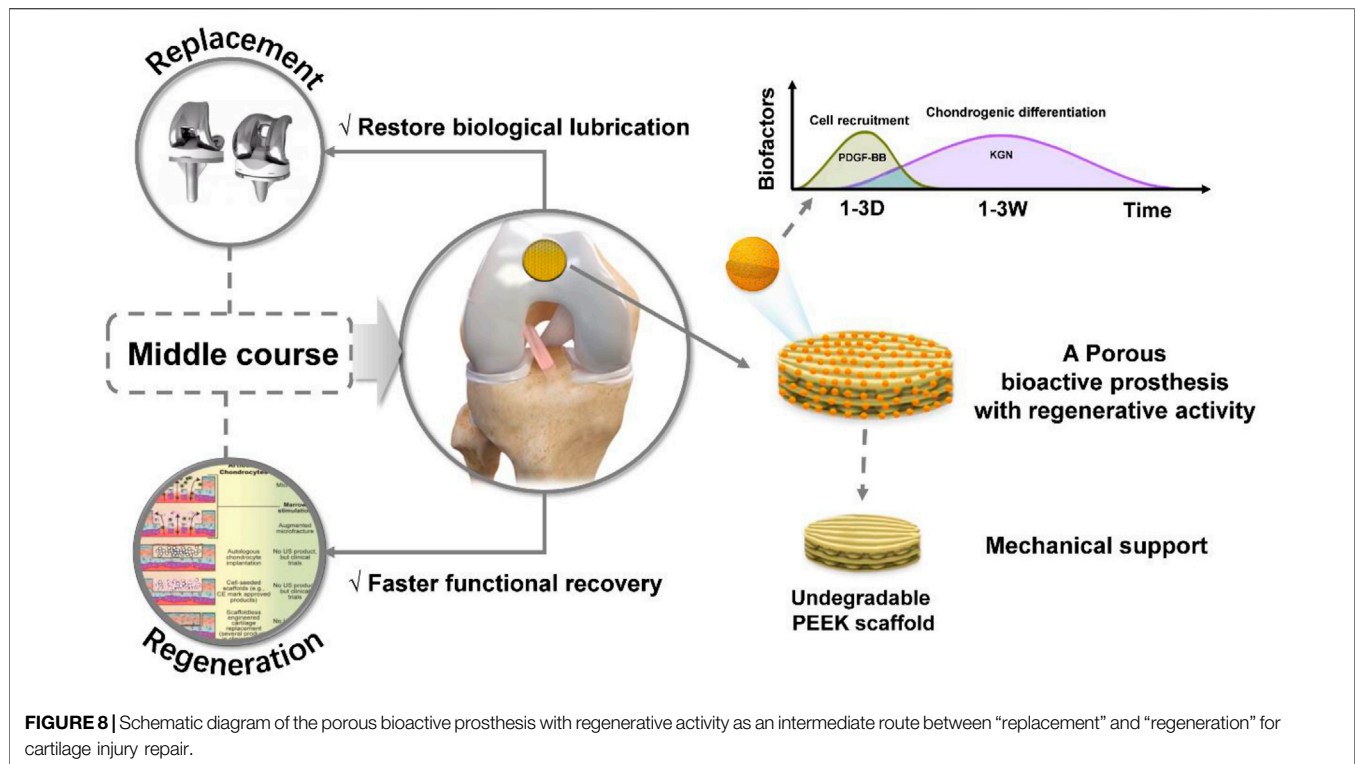


**FIGURE 7 |** Immunohistochemical staining and RT-PCR analysis for cartilage repair. **(A)** Immunohistochemical staining with collagen II of the repaired tissue at 1 and 3 months after surgery. **(B–E)** Expression of related genes, SOX9 **(B)**, aggrecan **(C)**, collagen II **(D)**, and collagen I **(E)** of the repaired tissue at 1 and 3 months after surgery. Data are showed as mean ± SD,  $n = 3$ . \* $p < .05$ , \*\* $p < .01$ .

quantitatively analyzed the collagen and GAG content of the repaired tissue through biochemical assays and RT-PCR, and these results suggested that the SPK@PDA-CS/MSNs scaffold could promote cartilage regeneration *in vivo*, which was consistent with the histological results.

To the best of our knowledge, this is the first study to propose a new concept of a porous bioactive prosthesis for articular cartilage lesions, and to systematically evaluate the feasibility of the porous bioactive prosthesis with induced regeneration activity for articular cartilage damage repair. Of course, this



was only a relatively elementary study, and there were some limitations and drawbacks. First, the animal model was not optimal, as the regenerative potential of rabbits was greater than that of large animals, such as sheep, which should be investigated in a future study. Second, we did not present the tribological properties of the porous scaffold, which may not have a high coefficient of friction under compressive stress and lubrication of the joint fluid. Third, we did not assess the functional and tribological properties of the repaired tissue in this study, although it would be difficult to perform in rabbits, it would be meaningful for assessing the feasibility of the porous prostheses, and it will be performed in our next large animal experiment. Finally, this was only a preliminary study on the new therapeutic concept for cartilage lesions, and before clinical application can occur, many *in vitro* and *in vivo* experiments are needed to further verify the feasibility and safety of this therapeutic concept.

In this study, as shown in **Figure 8**, we proposed a porous bioactive prosthesis strategy as a new middle course between “replacement” and “regeneration” for osteoarticular lesions. To achieve the bioactivity of the porous prosthesis in inducing cartilage regeneration, we fabricated a drug delivery system using a microfluidic chip, which could sequentially and sustainably release a cell chemotactic factor, PDGF-BB, and a chondrogenic differentiation cytokine, KGN, and then integrated the drug carrier and a porous PEEK scaffold to construct a porous bioactive prosthesis with regenerative activity. We also evaluated the feasibility of using a porous bioactive prosthesis for cartilage lesions and found that the bioactive prosthesis could induce cartilage regeneration to promote fast functional recovery and

restore the biological friction mechanism of the articular cartilage surface. In view of the difficulty in achieving complete cartilage regeneration and the side effects of joint replacement, the porous bioactive prosthesis strategy may become a new treatment for cartilage injury in the near future.

## 5 CONCLUSION

In this study, we first fabricated a drug delivery system (CS/MSNs composite microspheres loaded with PDGF-BB and KGN) based on MSNs and CS using a microfluidic chip, which could sequentially and sustainably release PDGF-BB and KGN. Then, we integrated the CS/MSNs composite microspheres loaded with PDGF-BB and KGN and a 3D printed porous PEEK scaffold to construct the SPK@PDA-CS/MSNs scaffold, a porous bioactive prosthesis with regenerative activity. We systematically evaluated the biocompatibility and biofunctionality of the SPK@PDA-CS/MSNs scaffold through *in vitro* and *in vivo* experiments and confirmed that the SPK@PDA-CS/MSNs scaffold was biocompatible, enhanced chondrogenic differentiation of BMSCs *in vitro*, and promoted cartilage regeneration *in vivo*. The application of a porous bioactive prosthesis may represent a new treatment for cartilage injury.

## DATA AVAILABILITY STATEMENT

The original contributions presented in the study are included in the article/**Supplementary Material**, further inquiries can be directed to the corresponding author.



## ETHICS STATEMENT

The animal study was reviewed and approved by Animal studies were approved by the Institutional Animal Care and Use Committee of Renji Hospital, which is affiliated with Shanghai Jiao Tong University Medical College.

## AUTHOR CONTRIBUTIONS

ZY: writing original draft, investigation, data curation, formal analysis, and visualization. ZL: data curation, formal analysis, and software; WZ: investigation and visualization. JZ: data curation, methodology and formal analysis. YW: conceptualization, supervision and project administration.

## REFERENCES

- Affatato, S., Spinelli, M., Zavalloni, M., Mazzega-Fabbro, C., and Viceconti, M. (2008). Tribology and Total Hip Joint Replacement: Current Concepts in Mechanical Simulation. *Med. Eng. Phys.* 30, 1305–1317. doi:10.1016/j.medengphys.2008.07.006
- Berthiaume, F., Maguire, T. J., and Yarmush, M. L. (2011). Tissue Engineering and Regenerative Medicine: History, Progress, and Challenges. *Annu. Rev. Chem. Biomol. Eng.* 2, 403–430. doi:10.1146/annurev-chembioeng-061010-114257
- Bhattacharjee, M., Coburn, J., Centola, M., Murab, S., Barbero, A., Kaplan, D. L., et al. (2015). Tissue Engineering Strategies to Study Cartilage Development, Degeneration and Regeneration. *Adv. Drug Deliv. Rev.* 84, 107–122. doi:10.1016/j.addr.2014.08.010
- Bruns, J., Werner, M., and Habermann, C. (2018). Osteochondritis Dissecans: Etiology, Pathology, and Imaging with a Special Focus on the Knee Joint. *Cartilage* 9, 346–362. doi:10.1177/1947603517715736
- Campos, Y., Almirall, A., Fuentes, G., Bloem, H. L., Kaijzel, E. L., and Cruz, L. J. (2019). Tissue Engineering: An Alternative to Repair Cartilage. *Tissue Eng. B: Rev.* 25, 357–373. doi:10.1089/ten.teb.2018.0330
- Carballo, C. B., Nakagawa, Y., Sekiya, I., and Rodeo, S. A. (2017). Basic Science of Articular Cartilage. *Clin. Sports Med.* 36, 413–425. doi:10.1016/j.csm.2017.02.001
- Carr, A. J., Robertsson, O., Graves, S., Price, A. J., Arden, N. K., Judge, A., et al. (2012). Knee Replacement. *The Lancet* 379, 1331–1340. doi:10.1016/s0140-6736(11)60752-6
- Chao, J., and Pao, A. (2017). Restorative Tissue Transplantation Options for Osteochondral Lesions of the Talus. *Orthop. Clin. North America* 48, 371–383. doi:10.1016/j.joc.2017.03.008
- Charnay, C., Bégu, S., Tourné-Péteilh, C., Nicole, L., Lerner, D. A., and Devoisselle, J. M. (2004). Inclusion of Ibuprofen in Mesoporous Templated Silica: Drug Loading and Release Property. *Eur. J. Pharmaceutics Biopharmaceutics* 57, 533–540. doi:10.1016/j.ejpb.2003.12.007
- Correa Bellido, P., Wadhwani, J., and Gil Monzo, E. (2019). Matrix-induced Autologous Chondrocyte Implantation Grafting in Osteochondral Lesions of the Talus: Evaluation of Cartilage Repair Using T2 Mapping. *J. Orthopaedics* 16, 500–503. doi:10.1016/j.jor.2019.04.002
- Frehner, F., and Benthien, J. P. (2018). Microfracture: State of the Art in Cartilage Surgery? *Cartilage* 9, 339–345. doi:10.1177/1947603517700956
- Goebel, L., Orth, P., Müller, A., Zurakowski, D., Bucker, A., Cucchiari, M., et al. (2012). Experimental Scoring Systems for Macroscopic Articular Cartilage Repair Correlate with the MOCART Score Assessed by a High-Field MRI at 9.4 T - Comparative Evaluation of Five Macroscopic Scoring Systems in a Large Animal Cartilage Defect Model. *Osteoarthritis and Cartilage* 20, 1046–1055. doi:10.1016/j.joca.2012.05.010
- Goodman, S. B., Wimmer, M. A., and Ploeg, H. L. (2020). Recent Advances in Total Joint Replacement. *J. Orthop. Res.* 38, 1413. doi:10.1002/jor.24734
- Klein, J. (2009). Repair or Replacement--A Joint Perspective. *Science* 323, 47–48. doi:10.1126/science.1166753

All authors contributed to the article and approved the submitted version.

## FUNDING

This study was supported by the National Key R&D Program of China (Grant Nos. 2016YFC1101802).

## SUPPLEMENTARY MATERIAL

The Supplementary Material for this article can be found online at: <https://www.frontiersin.org/articles/10.3389/fbioe.2022.839120/full#supplementary-material>

- Krill, M., Early, N., Everhart, J. S., and Flanagan, D. C. (2018). Autologous Chondrocyte Implantation (ACI) for Knee Cartilage Defects. *JBJS Rev.* 6, e5. doi:10.2106/jbjs.rvw.17.00078
- Kwon, H., Brown, W. E., Lee, C. A., Wang, D., Paschos, N., Hu, J. C., et al. (2019). Surgical and Tissue Engineering Strategies for Articular Cartilage and Meniscus Repair. *Nat. Rev. Rheumatol.* 15, 550–570. doi:10.1038/s41584-019-0255-1
- Madry, H., Gao, L., Rey-Rico, A., Venkatesan, J. K., Müller-Brandt, K., Cai, X., et al. (2020). Thermosensitive Hydrogel Based on PEO-PPO-PEO Poloxamers for a Controlled *In Situ* Release of Recombinant Adeno-Associated Viral Vectors for Effective Gene Therapy of Cartilage Defects. *Adv. Mater.* 32, e1906508. doi:10.1002/adma.201906508
- Moreira-Teixeira, L. S., Georgi, N., Leijten, J., Wu, L., and Karperien, M. (2011). Cartilage Tissue Engineering. *Endocr. Dev.* 21, 102–115. doi:10.1159/000328140
- Schreiner, A. J., Stoker, A. M., Bozynski, C. C., Kuroki, K., Stannard, J. P., and Cook, J. L. (2020). Clinical Application of the Basic Science of Articular Cartilage Pathology and Treatment. *J. Knee Surg.* 33, 1056–1068. doi:10.1055/s-0040-1712944
- Tradati, D., De Luca, P., Maione, A., Ubaldi, F. M., Volpi, P., de Girolamo, L., et al. (2020). AMIC-autologous Matrix-Induced Chondrogenesis Technique in Patellar Cartilage Defects Treatment: A Retrospective Study with a Mid-term Follow-Up. *J. Clin. Med.* 9. doi:10.3390/jcm9041184
- Waldorff, E. I., Roessler, B. J., Zachos, T. A., Miller, B. S., McHugh, J., and Goldstein, S. A. (2013). Preclinical Evaluation of a Novel Implant for Treatment of a Full-Thickness Distal Femoral Focal Cartilage Defect. *The J. Arthroplasty* 28, 1421–1429. doi:10.1016/j.arth.2012.11.020
- Yuan, Z., Lyu, Z., Liu, X., Zhang, J., and Wang, Y. (2021). Mg-BGNs/DCECM Composite Scaffold for Cartilage Regeneration: A Preliminary *In Vitro* Study. *Pharmaceutics* 13. doi:10.3390/pharmaceutics13101550
- Zhao, X., Hu, C., Pan, G., and Cui, W. (2015). Pomegranate-Structured Electrospun Microspheres for Long-Term Controlled Drug Release. *Part. Part. Syst. Charact.* 32, 529–535. doi:10.1002/ppsc.201400199

**Conflict of Interest:** The authors declare that the research was conducted in the absence of any commercial or financial relationships that could be construed as a potential conflict of interest.

**Publisher's Note:** All claims expressed in this article are solely those of the authors and do not necessarily represent those of their affiliated organizations, or those of the publisher, the editors, and the reviewers. Any product that may be evaluated in this article, or claim that may be made by its manufacturer, is not guaranteed or endorsed by the publisher.

Copyright © 2022 Yuan, Lyu, Zhang, Zhang and Wang. This is an open-access article distributed under the terms of the Creative Commons Attribution License (CC BY). The use, distribution or reproduction in other forums is permitted, provided the original author(s) and the copyright owner(s) are credited and that the original publication in this journal is cited, in accordance with accepted academic practice. No use, distribution or reproduction is permitted which does not comply with these terms.





# 3D Printing for Bone-Cartilage Interface Regeneration

Jialian Xu<sup>1†</sup>, Jindou Ji<sup>2†</sup>, Juyang Jiao<sup>1†</sup>, Liangjun Zheng<sup>1</sup>, Qimin Hong<sup>1</sup>, Haozheng Tang<sup>1</sup>, Shutao Zhang<sup>1</sup>, Xinhua Qu<sup>1\*</sup> and Bing Yue<sup>1\*</sup>

<sup>1</sup>Department of Bone and Joint Surgery, Renji Hospital, School of Medicine, Shanghai Jiao Tong University, Shanghai, China,

<sup>2</sup>The First Clinical Medical College, Shandong University of Traditional Chinese Medicine, Jinan, China

## OPEN ACCESS

### Edited by:

Lan Li,  
Nanjing Drum Tower Hospital, China

### Reviewed by:

Quanyi Guo,  
Chinese PLA General Hospital, China  
Sheng Zhao,  
Zhejiang University, China

### \*Correspondence:

Xinhua Qu  
xinhua\_qu@126.com  
Bing Yue  
advbmp2@163.com

<sup>†</sup>These authors share first authorship

### Specialty section:

This article was submitted to  
Biomaterials,  
a section of the journal  
Frontiers in Bioengineering and  
Biotechnology

**Received:** 04 December 2021

**Accepted:** 25 January 2022

**Published:** 14 February 2022

### Citation:

Xu J, Ji J, Jiao J, Zheng L, Hong Q,  
Tang H, Zhang S, Qu X and Yue B  
(2022) 3D Printing for Bone-Cartilage  
Interface Regeneration.  
Front. Bioeng. Biotechnol. 10:828921.  
doi: 10.3389/fbioe.2022.828921

Due to the vasculature defects and/or the avascular nature of cartilage, as well as the complex gradients for bone-cartilage interface regeneration and the layered zonal architecture, self-repair of cartilage and subchondral bone is challenging. Currently, the primary osteochondral defect treatment strategies, including artificial joint replacement and autologous and allogeneic bone graft, are limited by their ability to simply repair, rather than induce regeneration of tissues. Meanwhile, over the past two decades, three-dimension (3D) printing technology has achieved admirable advancements in bone and cartilage reconstruction, providing a new strategy for restoring joint function. The advantages of 3D printing hybrid materials include rapid and accurate molding, as well as personalized therapy. However, certain challenges also exist. For instance, 3D printing technology for osteochondral reconstruction must simulate the histological structure of cartilage and subchondral bone, thus, it is necessary to determine the optimal bioink concentrations to maintain mechanical strength and cell viability, while also identifying biomaterials with dual bioactivities capable of simultaneously regenerating cartilage. The study showed that the regeneration of bone-cartilage interface is crucial for the repair of osteochondral defect. In this review, we focus on the significant progress and application of 3D printing technology for bone-cartilage interface regeneration, while also expounding the potential prospects for 3D printing technology and highlighting some of the most significant challenges currently facing this field.

**Keywords:** 3D printing, bone repair, chondral regeneration, reconstructive implant, regenerative medicine

## 1 INTRODUCTION

During activities such as walking, kneeling, rotating and jumping, the knee joint is subjected to compression, shear and tension forces from the whole body, where the bone-chondral interface serves as a transitional interface between viscoelastic cartilage and solid bone, maintaining structural stability (Hoemann et al., 2012). Osteochondral damage (OCD) disrupts the integrity and stability of the bone-cartilage interface as it includes not only the articular cartilage but also the underlying subchondral bone (Madry et al., 2010). OCD is often caused by trauma, cancer, and joint inflammation, such as osteoarthritis (OA) (Mano and Reis, 2007). As we age, the natural wear and tear of cartilage tissue often leads to OA, which can evolve into OCD and is difficult to effectively treat, with many patients continuing to suffer from pain that can impede even simple daily tasks, such as walking, and can progress to physical disability (Glyn-Jones et al., 2015; Sacitharan, 2019). OA affects 7% of the global

population (~500 million people) and is significantly more common in women than men (Mandl, 2019; Hunter et al., 2020).

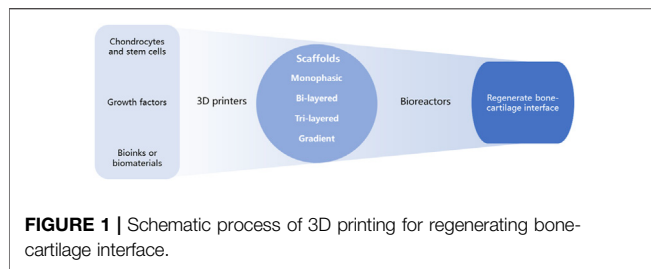
Damage or degeneration at the bone-cartilage interface due to osteochondral defects is difficult to self-heal and often requires external therapies due to the complex structural features of the osteochondral structure. Common surgical treatments for OCD occurring in large areas currently used in clinical practice include autologous chondrocyte implantation (ACI) (Kubosch et al., 2018; Schuette et al., 2021), osteochondral allograft transplantation (OCA) (Gilat et al., 2021) and matrix-induced autologous chondrocyte implantation (MACI) (Gao et al., 2019). Each of these treatment strategies has demonstrated a certain level of success. Autologous bone has good ability to induce osteogenesis and integrate with defect area, but there is a scarcity of available OCA donors (Moatshe and LaPrade, 2020), and OCA surgery will have adverse effects on the donor-site (Hishimura et al., 2019). ACI and MACI have valuable advantages such as good biocompatibility, small trauma, quick recovery after operation and reconstruction of tissue function. However, ACI or MACI involves two separate surgeries, which increases a greater risk of severe graft site infections that has been reported by Gobbi et al. (2020). Therefore, an eminent push toward the development of new treatment options that possess better treatment effects and less disadvantages. High expectations are given to the 3D bioprint technology.

In recent years, 3D bioprinting, an additive manufacturing technology, has reformed the field of regenerative medicine and tissue engineering (TE). To date, 3D printing technology has been implemented in anatomical tissue models, medical devices, elucidation of biological mechanisms, TE scaffolds, and drug delivery routes (Murphy and Atala, 2014; Ventola, 2014; Schweiger et al., 2016; Liaw and Guvendiren, 2017). 3D bioprinting is an integrated process that requests consideration of different design factors, including imaging (CT or MRI), modeling (computer-aided design (CAD), computer-aided manufacturing tools, and mathematical modeling), printer selection, bioink selection (natural or synthetic), culture conditions (differentiated or undifferentiated cells, growth factors, and extracellular matrix (ECM)), and 3D construct development (Cui et al., 2017). Bone-cartilage interface regeneration involves the cartilage and subchondral bone. Indeed, this technology has been clinically applied to assist in OCAs (Okoroha et al., 2018; Huutilainen et al., 2019; Russo et al., 2021) via 3D scanning and printing of the defect site to determine the size of patient-specific allograft plugs prior to grafting. However, a single 3D printed scaffold for bone or cartilage does not achieve the goal of osteochondral interface regeneration. A full understanding of the structure and composition of bone and cartilage, as well as of the reconstruction process is necessary to achieve regeneration of the osteochondral interface via 3D printing. The osteochondral interface is a specialized area that connects two tissues with different biochemical and mechanical properties. The transition of mechanical loads between cartilage and bone owe to osteochondral interface structure (Yang and Temenoff, 2009). The osteochondral interface is typically <1 mm and contains

three orders of magnitude (quantum) of mechanical strength differences in addition to gradient variations in growth factor concentrations and cell differentiation. For 3D printing, the scaffold must achieve a spatially graded mechanical and chemical mimicry in the sub-millimeter range, which in turn complicates the design of the scaffold and its subsequent selection of cells and growth factors, as each region has different optimal conditions. Therefore, to successfully regenerate the osteochondral interface, the interdependent nature of the interfacial structures must be considered to attain the best balance of mechanical and biological properties.

Based on the speedy development of TE and regenerative medicine, various 3D printing regeneration plans have been schemed for osteochondral interface. The scaffold is the fundamental basis for 3D printed regenerative osteochondral interfaces, hence, good biodegradability and histocompatibility must be achieved in scaffold materials (Fu et al., 2018). Currently, natural materials (Bonani et al., 2018), synthetic materials (Frassica and Grunlan, 2020), ceramics (Wen et al., 2017), glass (Brauer, 2015), and composite materials (Turnbull et al., 2018), are used to construct scaffolds. Additionally, the method of material binding significantly impacts the structural strength of, and cell attachment to, the scaffold (Aisenbrey et al., 2018; Gao et al., 2020). Based on the multilayered hybrid structure of osteochondral bone, 3D printing research has focused on efforts to form layered structures that mimic the natural osteochondral interface. For example, Li et al. (2018b) designed a hybrid scaffold of hydroxyapatite (HAP), polylactic-co-glycolic acid (PLGA), and extracted bovine cartilage matrix that adequately mimicked the natural tissue structure. The healing of damaged tissues requires effective cell implantation and survival, thus, the ability of cells to be delivered on 3D-printed scaffolds and, subsequently, adhere and survive at the targeted site, improves the success of tissue regeneration (Cui et al., 2020). Specific cells have the potentiality to differentiate into target cells. For example, mesenchymal stem cells (MSCs) can differentiate into chondrocytes *in vitro*, while transforming growth factors (TGF), and growth factor (GF) signaling, are responsible for regulating the differentiation of mesenchymal cells into chondrocytes and the eventual formation of cartilage tissue (Foster et al., 2015). Additionally, the culture substrate must effectively promote cell proliferation, delay chondrocyte dedifferentiation without further ossification (i.e., endochondral ossification), and suppress the expression of genes involved in chondrocyte hypertrophy (Yang et al., 2018). To achieve this, 3D printing of regenerative osteochondral interfaces often includes growth factors, transforming growth factors, among other materials (ECM, metal ions, etc.) (Deng et al., 2018; Saha et al., 2013). Considering that the bone-cartilage interface structure is surrounded by cartilage and subchondral bone, all of which have their own structural layers, current research is concentrated on the development of multi-factor combinations and advanced delivery methods for reliable osteochondral tissue regeneration (Han et al., 2015).

Bone-cartilage interface regeneration has been neglected due to its complexity. With the importance of the bone-cartilage revealed, many researchers have started to focus on it. Thus,



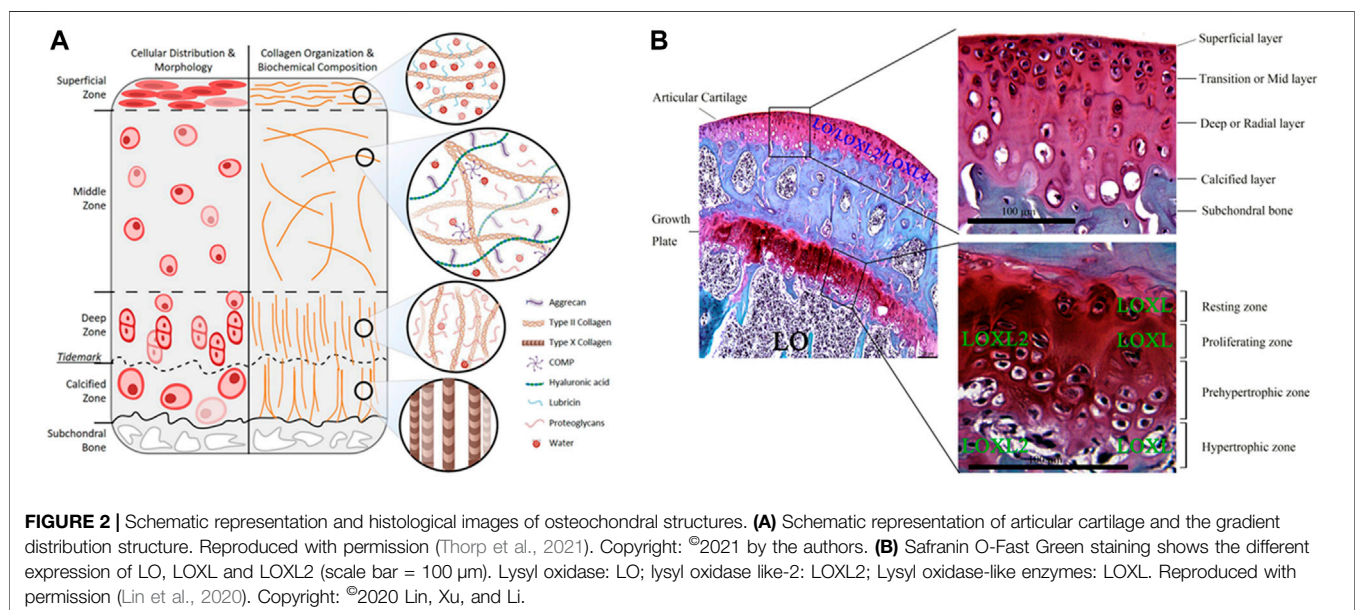
compared with the previous reviews, we want to have a comprehensive summary about the 3D printing for bone-cartilage interface regeneration and update the advanced progress. This review highlights new developments regarding materials, cells, signaling molecules, and the latest scaffold designs for 3D printing at the osteochondral interface by providing an overview of osteochondral structures, OCD, and repair mechanisms of osteochondral structures. We then present the current challenges and future directions in this field to support the development of effective 3D printing methods for osteochondral interface regeneration (Figure 1).

## 2 OSTEOCHONDRAL

### 2.1 Organizational Structure

Osteochondral tissue comprises the cartilage layer, bone-cartilage interface, and subchondral bone (Figure 2). The cartilage in the uppermost layer is essential for joint function since it is responsible for lubrication, protection, and weight-bearing. Damage to cartilage caused by frictional forces can lead to degenerative lesions that destroy the osteochondral interface and extend to the subchondral bone. Cartilage is distributed

throughout the body, such as in the external ear, nose, tracheal walls, ends of helper bones, and between the bones of the spinal roots. There are three types of cartilage: hyaline cartilage, fibrocartilage, and elastic cartilage, of which the hyaline cartilage is the most widely distributed in the body, and contains the articular cartilage. The articular cartilage is an interconnective tissue that covers the epiphyseal surface of the joint. It is a biphasic medium containing approximately 80% water, contains no nerves or blood and lymphatic vessels, incapable of self-regeneration, and has only a single cell type, the chondrocytes (Jiang and Tuan, 2015; Armiento et al., 2018). Chondrocytes primarily produce ECM and balance its content, thereby maintaining the microenvironment around the cartilage. Although cartilage composition may seem simple, its complex biomolecular roles, multilayered hierarchical structure, and specific tissue functions hinder its regeneration. The structure and content of the cartilage's ECM is a major determinant of normal function, while its components play different, but related roles (Krishnan and Grodzinsky, 2018). The proteoglycans of ECM make up about 5%–10% wet weight of cartilage tissue, while proteoglycans are dominated by aggrecan, which contains high levels of glycosaminoglycans (GAGs), including HA and chondroitin sulfate. GAGs are negatively charged and attract cations, creating ion-induced osmotic swelling, while the large amount of water absorbed provides the ECM with compressive stiffness, which significantly contributes to the weight-bearing mechanism of articular cartilage (Katta et al., 2008; Moshtagh et al., 2018). Collagen fiber is another important source of organizational strength, which is primarily composed of collagen type II. Nevertheless, the IV, VI, IX, X, XI, XII, XIII, and XIV account for only a small part of the mature matrix, but they have specific biological functions as well as act a pivotal part in the mechanical properties, organization, and shape of articular cartilage (Luo et al., 2017). The collagen fibril network contains



numerous GAG chains and proteoglycan-bound aggregates of 300 MDa, interlaced by structured collagen (Athanasios et al., 2009; Bajpayee and Grodzinsky, 2017).

Articular cartilage is highly organized and consists of four zones: superficial (tangential), intermediate (transitional), deep (radial), and calcified (Carballo et al., 2017). Numerous cells of the articular cartilage, ECM, and collagen fibers are anisotropic, especially in the superficial zone, where collagen fibers have a preferential orientation (Hossain et al., 2020), which is the main obstacle in regenerating the osteochondral interface.

The superficial zone, located at the surface, has the following distinct structural features: 1) Collagen fibers are aligned parallel to the joint surface and have lower proteoglycan content and fixed charge density compared with deeper tissues. 2) Contains an extensive network of elastic fibers roughly aligned with the collagen fibers in a plane parallel to the surface. 3) The superficial chondrocytes are disk-like shaped. 4) The ECM contains elastin and lipids. 5) SFZ cells produce a protein responsible for joint lubrication, which is encoded by *PRG4* and helps to protect the articular cartilage (Rolauffs et al., 2010; Mansfield et al., 2015; Xuan et al., 2019). The largest region, the middle zone, has rounded central chondrocytes; the type II collagen (Col II) is randomly distributed in the ECM (Amanatullah et al., 2014). The middle zone withstand compression and recover from the impact on the articular surface owing to these properties. The deep zone is distinct from the surface zone, with spherical chondrocytes, collagen fibers aligned obliquely to the articular surface, and a lower cell content but higher compression modulus. The border between the calcified and deep zones forms a distinctive line on the transverse light microscopic sections, called the tidemark, which marks the transition from the deep zone to the calcified zone (Mansfield and Winlove, 2012). The calcified zone contains a small number of mast cells (Diederichs et al., 2018) capable of secreting type X collagen (Kirsch and von der Mark, 1991), the mineralizing enzyme alkaline phosphatase (ALP), the HAp binding protein osteopontin, and MMP13 (Gannon et al., 1991; Hoemann et al., 2012). Collagen fibers in the calcified areas are arranged in an arch shape and contribute to the reinforcement of cartilage tissue. The strong interadhesion and intermediate stiffness of calcified cartilage facilitate load transfer, prevent cartilage delamination, and serve as a transition between plastic cartilage and stiff subchondral bone.

The subchondral bone, located beneath the cartilage, is formed by the subchondral plate and a 6 mm layer of trabeculae (also known as the subarticular spongiosa) (Henrotin et al., 2012). The subchondral bone plate is immediately below the calcified cartilage layer and a thin cortical layer (Milz and Putz, 1994). The articular cartilage separates from the bone marrow on account of a unit formed by the two mineralized layers of the subchondral plate form (Madry et al., 2010). The subchondral plate is a permeable structure with distinct pores that provide a direct link between the articular cartilage and subchondral tuberosity. Arterial and venous vessels and nerves penetrate the channels and send tiny branches into the calcified cartilage. Vessels distribution depends not only on the amount of intra-articular stress, but also on the stress variations in

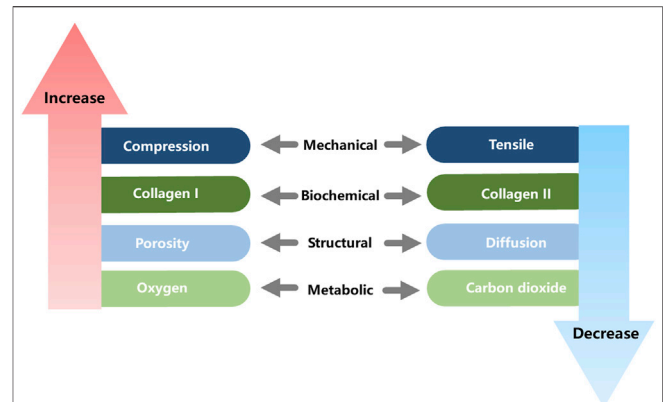


**FIGURE 3 |** Gradient change of osteochondral properties.

different joints (Holmdahl and Ingelmark, 1950; Madry et al., 2010). The subchondral cancellous bone is more porous, while the volume, density, and stiffness are lower than those of the cortical plate (Sharma et al., 2013). The permeability of both provides nutrition and timely physiological and pathological feedback to the cartilage. The thickness of the subchondral bone plate varies depending on the joint, while there is a regional specificity in the thickness and density distribution of the subchondral bone plate. The resulting bone trabeculae are referred to as “supporting trabeculae” (Madry et al., 2010). Cartilage is the load-bearing and protective structure of joints. However, cartilage cannot bear weight alone due to its limited regenerative capacity, whereas subchondral bone is considered a weight-bearing structure with good regenerative capacity. Thus, the osteochondral unit should be used to withstand physiological loads, allowing physiological and structural balance (Hoechel et al., 2012; Goyal et al., 2017). Meanwhile, the sodium citrate (SC) bone acts as a dynamic component of the OC unit, transmitting forces through the joint and adapting to its mechanical demands (Hoechel et al., 2012). The specific structure of the subchondral bone helps to minimize and redistribute axial forces, cushion shock through deformation and during stress transmission to avoid excessive stress damage to the cartilage. After loading, the subchondral bone can be regulated, by the blood vessels and nerves between the pores, to induce the release of joint fluid, proteoglycans, and fibers (Goyal et al., 2017). Subchondral bone is also a repository of stem cells, with subchondral bone providing undifferentiated bone marrow stem cells as the sole source for new chondrocyte generation. Various growth factors are also provided by subchondral bone, and play an active role in cartilage healing and remodeling (Goyal et al., 2017).

Many of the functional properties of the joint arise from the unique gradient structure of the osteochondral unit (Figure 3). From the tip (cartilage) to the base (bone), the following changes occur: biomechanical compression and elastic modulus gradually increase, while hydrostatic pressure and viscous modulus gradually decrease. Additionally, hydroxyapatite (HAp) and collagen type I (Col I) contents gradually increase, while water and collagen type II (Col II) gradually decrease. Structurally,



vascularity, permeability and porosity gradually increase. In terms of bioelectricity, piezoelectricity and pyroelectricity gradually increase, while flow potential, dielectric constant and diffusion potential gradually decrease. Finally, metabolically, glucose and oxygen contents gradually increase, while carbon dioxide and lactic acid gradually decrease (Zhou et al., 2020).

## 2.2 Osteochondral Defects

Avascular articular cartilage cannot form blood clots nor does it engage in necrosis, inflammation, repair, or remodeling, all of which are required for healing injured tissues. As such, articular cartilage has a limited intrinsic healing and repair capacity, and mature chondrocytes are not sufficient to produce adequate ECM (Carballo et al., 2017). With age, chondrocyte apoptosis, water content, and proteoglycan size decrease within the ECM, leaving articular cartilage highly vulnerable to damage (Sophia Fox et al., 2009). In addition, anti-inflammatory treatments, diabetes, and menopause have been shown to disrupt cartilage structure and affect cartilage stiffness, leading to greater susceptibility to cartilage destruction. As the lack of continuous collagen fibers of the transition from calcified cartilage zone to subchondral bone plate, the bone-cartilage interface is more fragile than the transition within the cartilage zone in the structural property. Thus, the bone-cartilage interface is susceptible to damage when the cartilage is damaged. In healthy bones, a balance exists between bone resorption and deposition in response to dynamic adaptation to mechanical loading. In Osteochondral Defects (OCD), this balance is disrupted, leading to changes in the structure of the subchondral trabeculae (T bone), including increased thickness of the subchondral bone plate, formation of new bony structures at the joint edges (osteophytes), and development of subchondral bone cysts (Goldring and Goldring, 2010; Loeser et al., 2012; Funck-Brentano and Cohen-Solal, 2015; Tuerlings et al., 2021).

Cartilage defects can be classified, using various methods, according to severity, width, and depth, according to different methods. The most popular approach is to group patients based on the Outerbridge classification system, which classifies cartilage areas on a 0–IV scale. Grade 0: healthy cartilage; Grade I: softened and swollen cartilage, usually requiring probes or other instruments for diagnosis; Grade II: partial-thickness defect with a defect  $\leq 1.5$  cm in diameter or reaching the subchondral bone; Grade III: cartilage defect  $> 1.5$  cm in diameter or reaching the subchondral bone; Grade IV: exposure of the subchondral bone (Outerbridge, 1961; Outerbridge, 1964; Slaterry and Kweon, 2018). Alternative grading systems that can accurately assess the degree of cartilage damage, include the International Cartilage Repair Society (ICRS), Oswestry Arthroscopy Score (OAS) (van den Borne et al., 2007), Histology/Histochemistry Grading System (HHGS), and Osteoarthritis Research Society International (OARSI) Cartilage Histopathology Assessment System (OOCAS) (Custers et al., 2007).

## 2.3 Osteochondral Repair Mechanisms

Cartilage heals through chondrocyte secretion of ECM and fibrosis. Subchondral bone remodeling is an important regulatory mechanism by which bone tissue adapts to changes

in the local biological microenvironment and mechanical stimuli, and includes, in sequence, the resorption phase (initiation/activation of bone remodeling at a specific site), reversal phase (bone resorption and simultaneous recruitment of MSCs and osteoprogenitor cells), and osteogenic phase [osteoblast differentiation and function (osteoid synthesis), and quiescent phase (completion of bone-like mineralization and bone reconstruction)]. During remodeling, bone resorption and bone formation are coupled, and the synergistic activity of osteoclasts and osteoblasts promotes the resorption of old bone tissue and subsequent new bone formation (Feng and McDonald, 2011). The mechanism of OCD healing has been studied in several animal models, and Shapiro et al. (1993) described the sequence of healing a 3 mm diameter OCD in the femoral rotor of a rabbit, including fibrin production, mesenchymal cell aggregation, cartilage formation, and bone formation. The mechanism of osteochondral repair in sheep is endochondral ossification, however, unlike rabbits, no evidence of MSC recruitment was found for OCD healing in the sheep model (Lydon et al., 2019).

## 3 3D PRINTING

### 3.1 Bioinks

Bioink is the base material for scaffold formation and are generally flowable liquids that can be easily squeezed and rapidly solidified, retaining their shape by physical or chemical stimulation (Dai et al., 2020). The porous structure, adjustable mechanical properties, and high water content can provide an appropriate environment for different cells to mimic the ECM. Furthermore, these inks can be easily loaded with bioactive molecules and cells to assist the adhesion, proliferation, and differentiation of target cells (Ozbolat and Hospodiuk, 2016).

#### 3.1.1 Natural Bioinks

Natural bioinks have a high water content, good biocompatibility and biodegradability, and the ability to transport metabolic waste and nutrients, which are critical for *in vivo* applications. When liquid-like natural inks undergo gelation, the loaded cells can be encapsulated in a three-dimensional structure. Natural bioinks used for osteochondral interface regeneration include collagen (Marques et al., 2019), gelatin (Echave et al., 2019), silk fibroin (Ni et al., 2020), silk sericin (Naskar et al., 2021), fibrin (Nulty et al., 2021), keratin (Shavandi et al., 2017), chitosan (Shouei et al., 2021), alginate (Chen et al., 2018), HA (Yontar et al., 2019), and gellan gum (Choi et al., 2020) among other polysaccharides. However, the drawbacks of natural bioinks are their weak mechanical properties and antigenicity. Crosslinking can make up for these shortcomings (Lin et al., 2021), the common crosslinking strategies including light (Lee et al., 2020), UV (Frieß et al., 2021), energy electron irradiation (Tang et al., 2021) and enzymatically crosslinking (Wu et al., 2022) methods. Therefore, most natural bioinks used for 3D printing have improved mechanical properties by crosslinking (physically or chemically) and compounding synthetic polymers (Chawla et al., 2020). Alternatively, gelatin methacrylate (GelMA) is a

photosensitive biohydrogel material obtained from methacrylic anhydride and gelatin that is often used for bone-cartilage repair (Gao et al., 2021) as a common alternative to natural bioinks.

The decellularized osteochondral ECM is also the focus of current research. Lin et al. (2018) prepared a decellularized ECM scaffold with natural components (mainly collagen) and three-dimensional tissue structures with good biocompatibility *in vitro* and *in vivo*. In this study, the biphasic scaffold was nearly devoid of angiogenesis, avoiding endochondral ossification due to vascular invasion into the cartilage region, and also had the ability to promote MSC proliferation and differentiation, as well as low immunogenicity, thus, successfully promoting regeneration of osteochondral tissue.

### 3.1.2 Synthetic Bioinks

The wide variety of synthetic bioinks allows for diverse chemical and mechanical applications. Sequence modification can modulate the degradation rate of biodegradable polymers and influence the material properties of bioink solubilization and gelation (Austin and Rosales, 2019). Popular biodegradable synthetic bioinks include poly (caprolactone) (PCL), PLGA, and poly (lactic acid) (PLA) (Critchley et al., 2020). Although synthetic bioinks have stronger mechanical properties and printability than natural bioinks, they also have poor biocompatibility and biodegradability. Therefore, future research strategies should focus on establishing an effective combination of natural and synthetic bioinks to exploit the advantages of both materials, while providing possibilities for osteochondral regeneration solutions. Indeed, Guo et al. (2021) recently published a study on PCL-peptide complexes, in which they employed aqueous click conjugation to combine acetylene-capped PCL and peptides with different chemical characteristics and different chemical and biological origins. They then performed multi-material segmental printing using melt extrusion printing to generate a PCL-peptide scaffold obtained by  $\mu$ CT that maintained good printability. Moreover, *in vitro*, the scaffolds incorporating different tissue-specific peptides showed strong bioactivity and effectively promoted osteogenic or chondrogenic ECM deposition of bone marrow-derived MSCs (BM-MSCs) (Guo et al., 2021).

### 3.1.3 Bioceramics, Bioglass and Biological Composites

Bioceramics were originally developed for the repair, reconstruction, and replacement of diseased hard tissues (e.g., teeth and bone) and were later adapted for artificial heart valves, artificial tendons, etc. Bioceramics promote biomineralization and have the advantages of good wear resistance, osteoconductivity, corrosion resistance, hard surface, oxidation resistance, and low coefficient of friction (Hasan et al., 2013). Bioceramics can be further divided into natural and synthetic bioceramics, that is, bioinert ceramics (e.g.,  $\text{Al}_2\text{O}_3$ ,  $\text{ZrO}_2$ , etc.), bioactive glasses (e.g., dense hydroxyapatite), glass ceramics, and bioresorbable calcium phosphate substrates (Pina et al., 2018). Previous studies have showed that ceramics, such as HAp, or other calcium phosphate (Ca-P) ceramics (including tricalcium phosphate, (TCP)) or bioactive glasses, play an important role in

the promotion of the formation of bone-like apatite layers on the surface of scaffolds upon implantation. This is considered a positive feature of bioceramic bone binding, which improves the stability of implant fixation (Mano and Reis, 2007). In addition, the surface of bioceramic scaffolds can absorb osteoinductive factors and/or ions and continuously release them to modulate the surrounding environment, promoting the differentiation of MSCs and thus bone formation *in vivo* (Ma et al., 2018).

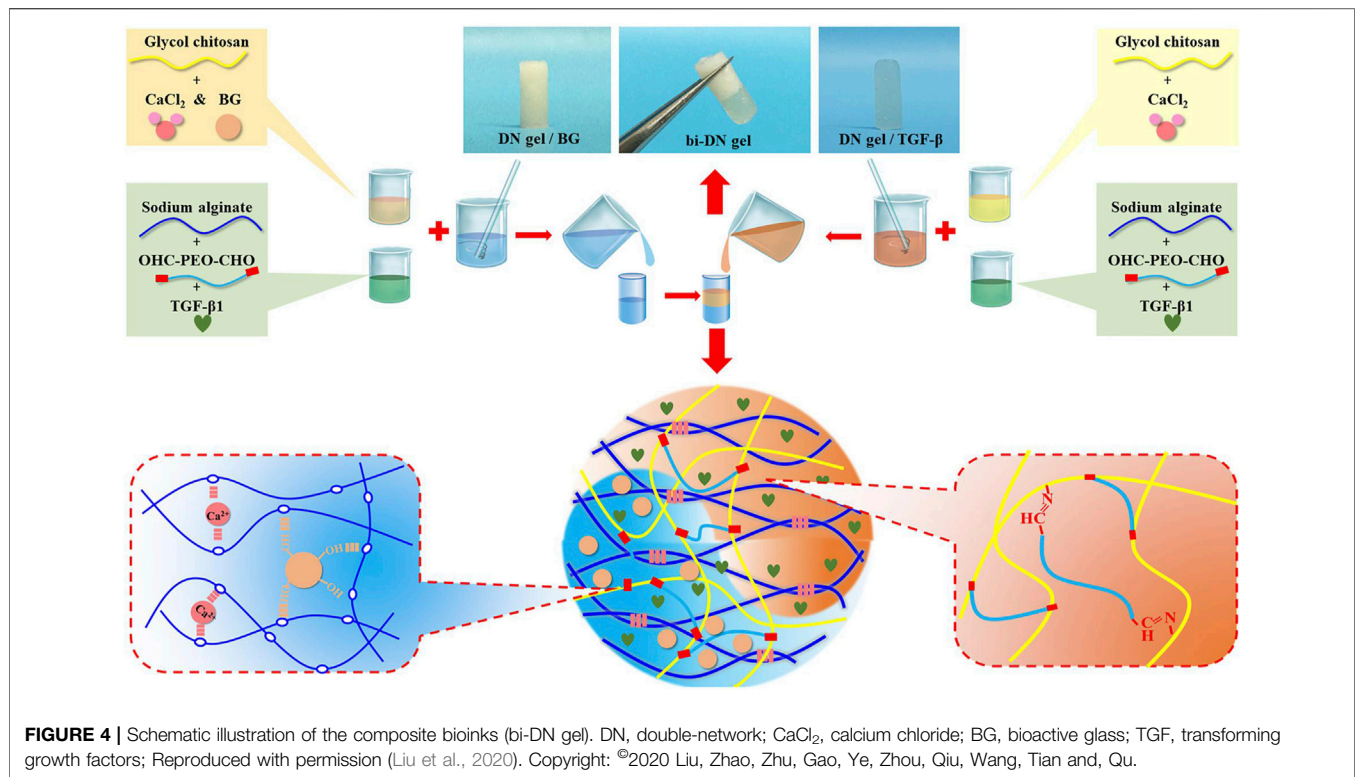
$\beta$ -TCP is one of the most widely used and effective bioceramics and has good osteoconductive and osteoinductive properties. Kosik-Kozioł et al. (2019) investigated the effect of different concentrations of TCP on the efficiency of UV-induced crosslinking of GelMA and concluded that 0.5% w/v  $\beta$ -TCP was optimal for forming ideally shaped scaffolds with calcified cartilage development-related biological properties at the optimal concentration (Kosik-Kozioł et al., 2019).

The addition of silicon (Si) (Yu et al., 2018), strontium (Sr) (Deng et al., 2018), Molybdenum (Mo) (Dang et al., 2018), lithium (Li) (Chen et al., 2019), Copper (Cu) (Lin et al., 2019), or other elements, can also improve the biological properties of scaffolds. Biological composites are the most suitable option for treatment of osteochondral interface injuries (Figure 4). Biocomposites exhibit excellent mechanical properties and bionic properties owing to their highly organized, heterogeneous structure across various length scales (Rajasekharan et al., 2017). Indeed, You et al. (2018) obtained ALG/HAP composites by homogeneous dispersion of HA in sodium alginate (ALG) hydrogel using SC. The ALG/HAP composite scaffold promoted chondrocyte secretion of type X collagen and increased ALP activity and mineral deposition (You et al., 2018). We believe that composites that combine the advantages of different materials will be the key for developing effective 3D printing strategies for regenerative osteochondral interfaces.

## 3.2 Chondrocytes and Mesenchymal Stem Cells

When creating a scaffold for osteochondral interface regeneration, the addition of specific cells to the scaffold can alter the way the surrounding tissues interact with the scaffold, which in sequence can affect the way the overall healing occurs. Scaffolds often carry several cellular components, the most common of which used for osteochondral interface regeneration are chondrocytes and stem cells. Chondrocytes are tissue-specific cells and, in diseased articular cartilage, do not proliferate sufficiently. Thus, chondrocytes adhering to the scaffold can help regenerate functional cartilage tissue at the defect site. Meanwhile, stem cells can self-renew and differentiate into multiple mature cell types; among these, MSCs are the most promising for osteochondral repair as they can differentiate into bone or cartilage under specific induction conditions (Vasiliadis and Galanis, 2020).

Chondrocytes are often used to study the effect of scaffolds on chondrocyte proliferation and maturation *in vitro* (Deng et al., 2018), and to place chondrocytes in scaffolds to help regenerate



cartilage tissue. Experiments were mostly performed with bovine (Wuest et al., 2018), rabbit (Zhou et al., 2017), rat (Bao et al., 2020) and human (Takahashi et al., 2018) origin chondrocytes. Primary monolayer chondrocyte cultures can generate numerous Col II and cartilage-specific proteoglycans (Perka et al., 2000). Primary culture chondrocytes are of limited origin, however, multiple *in vitro* passages cause them to lose their phenotype and convert to fibroblasts, reducing Col II expression and increasing type I collagen expression at the mRNA and protein levels. Sliogeryte et al. (2016) monitored innovatively isolated primary chondrocytes (P0) and cells of the first generation (P1) cultured in monolayer culture for 9 days. They found that monolayer culture and dedifferentiation strengthen membrane-actin cortex adhesion and increase cortical F-actin organization and ERM protein expression (Sliogeryte et al., 2016). These changes influence chondrocyte functions, including migration, endocytosis, and differentiation (Sliogeryte et al., 2016).

As such, research has focused on isolating primary chondrocytes from cartilage. However, chondrocytes are usually digested with collagenase to facilitate complete isolation, which can be detrimental to the cells. That is, too much or too little collagenase can lead to failure or low yield (Lepage et al., 2019). Hence, in a study conducted by Muhammad et al. (2019), a protocol for chondrocyte isolation was optimized using trypsin-ethylenediaminetetraacetic acid (EDTA), collagenase II in Hank's balanced salt solution (HBSS), and collagenase II in Dulbecco's modified Eagle medium/Nutrient Mixture F-12 (DMEM/F-12) for chondrocyte isolation. They found that collagenase II in HBSS retained the chondrogenic phenotype, especially proteoglycan expression (Muhammad

et al., 2019). Meanwhile, for chondrocyte dedifferentiation, Jeyakumar et al. (2017) demonstrated the positive effect of platelet-rich plasma (PRP) on proliferation and redifferentiation of dedifferentiated chondrocytes, and concluded that the standard usage of 10% FCS could be replaced with 10% PRP.

In addition, many researchers have used MSCs as seed cells. BM-MSCs were the first MSCs used for bone and cartilage repair, however, collection of autologous BM-MSCs was highly invasive for the patient. Alternatively, adipose-derived mesenchymal stem cells (AMSCs) are relatively noninvasive, easy to obtain, and have demonstrated differentiation potential in specific settings (Yamasaki et al., 2019). Human turbinate-derived mesenchymal stromal cells (hTMSCs) are MSCs with chondrogenic, osteogenic, and lipogenic differentiation potential (Hwang et al., 2012). hTMSCs were used by Shim et al. as seed cells encapsulated in cucurbit [6] uril (CB)/1,6-diaminohexane (DAH)-supramolecular HA in a multilayer 3D scaffold. hTMSCs with ALP, collagen I (Col I), and osterix (Osx) were not significantly expressed, whereas the expression of aggrecan (ACAN), collagen type II (Col II), and SRY-related high-mobility-group box 9 (Sox-9) was enhanced (Shim et al., 2016).

Umbilical cord blood mesenchymal stem cells (UCB-MSCs) have the general characteristics of MSCs. However, unlike hTMSCs and BM-MSCs, UCB-MSCs have the highest amplification potential and possess osteogenic and chondrogenic differentiation capacity, without adipogenic differentiation capacity. Moreover, UCB-MSCs exhibit lower expression of immunogenic markers (CD105 and CD90), are



easily accessible from cord blood, and their use is not ethically controversial. Indeed, Zheng et al. (2019) demonstrated that UCB-MSC xenografts contributed to osteochondral repair in a rabbit model.

### 3.3 Growth Factors

Chondrocytes carried by the stent or migrating from the tissue surrounding the damaged site usually produce fibrocartilage tissue in the absence of growth factors, rather than the ideal hyaline cartilage tissue. Growth factors are naturally occurring substances, such as hormones or proteins that can cue and expedite cell growth in a certain direction and are useful. In osteochondral regeneration, specific growth factors can induce the differentiation of stem cells into chondrocytes. For example, factors such as bone morphogenetic proteins (BMPs), insulin-like growth factors (IGFs), and transforming growth factors (TGFs) have been shown to promote the differentiation of stem cells into cartilage or osteogenesis (Mora-Boza and Lopez-Donaire, 2018). Vascular endothelial growth factor (VEGF) and BMP-4 promote angiogenesis for nutrient transport, oxygen exchange, waste transport, etc. (Lee et al., 2020). The synthesis and modification of collagen in chondrocytes are controlled by the metabolism of HIF-1 $\alpha$  (Stegen et al., 2019). Growth factors can also influence the physical properties of nascent cartilage tissues. And there is an interesting phenomenon that the expression of BMP requires the expression of SOX genes, which in turn promotes the expression of SOX genes during chondrogenesis. Within a rabbit model of OCD in the patellar groove, the addition of TGF- $\beta$ 1 and IGF-1 induces BM-MSCs to differentiate into chondrocytes and increase matrix synthesis, enabling the formation of smooth-surfaced hyaline cartilage at the defect site (Gugjoo et al., 2020).

PRP is a concentrate prepared from fresh blood by low-speed centrifugation and contains large amounts of autologous growth factors, including platelet-derived growth factor (PDGF), TGF- $\beta$ , IGF, epidermal growth factor (EGF), and VEGF. PRP stimulates chondrocyte proliferation and promotes the production of therapeutic cells in cartilage tissues. In addition, PRP induces autocrine growth factors to promote cartilage healing (Chang et al., 2018). Jiang et al. (2021) suggested that PRP can promote osteochondral regeneration by promoting the polarization of M2 macrophages. Accordingly, they prepared PRP-GelMA hydrogel scaffolds inoculated with rabbit BMSCs and observed an increase in M2 macrophage, which had an anti-inflammatory effect and provided a favorable environment for osteochondral regeneration (Jiang et al., 2021).

Recently, Vainieri et al. (2020) investigated the effects of 50 and 100 ng/ml PDGF-BB, chemokine ligand 5 (CCL5/RANTES), and stromal cell-derived factor-1 (SDF-1) on the migration of bone marrow mesenchymal stem cells (BMSCs) *in vitro*; the migration distance of BMSCs in three-dimensional spheroids was examined by confocal microscopy. All groups, save for 100 ng/ml RANTES, promoted BMSC migration *in vitro*, with 50 ng/ml PDGF-BB being the most effective (Vainieri et al., 2020).

BMP-2 and VEGF can promote osteogenesis and angiogenesis at the osteochondral interface. However, they are natural macromolecules that are unstable and expensive. As an

alternative, Wang et al. (2021) proposed that synthetic osteogenic peptide (OP) and angiogenic peptide (AP) could be used. Indeed, scaffolds containing AP and OP exhibited rapid release of AP and sustained release of OP inducing significant vascularity and new bone formation, respectively (Wang et al., 2021). Furthermore, since the osteochondral interface involves both cartilage and subchondral bone, researchers have focused on the use of biphasic scaffolds carrying osteogenic and chondrogenic peptides, respectively. For instance, osteogenic peptide/TGF- $\beta$ 1 (Wang et al., 2020) and HA bind (hyaluronic acid-binding peptide)/E3 (mineralizing peptide) (Camacho et al., 2021) have been successfully used for osteochondral tissue regeneration.

Collectively, these studies suggest that growth factors act a crucial part in influencing the effectiveness of stem cells in regenerating tissues. In addition to typical growth factors, biomolecules with different functions have great potential. For example, Zhu et al. (2020) compared polyethylene glycol diacrylate (PEGDA)/ECM scaffolds with PEGDA/ECM/honokiol (an inflammatory phytochemical) scaffolds, and found the honokiol group showed significantly enhanced osteochondral regeneration 4 and 8 weeks postoperatively in rat model (Zhu et al., 2020).

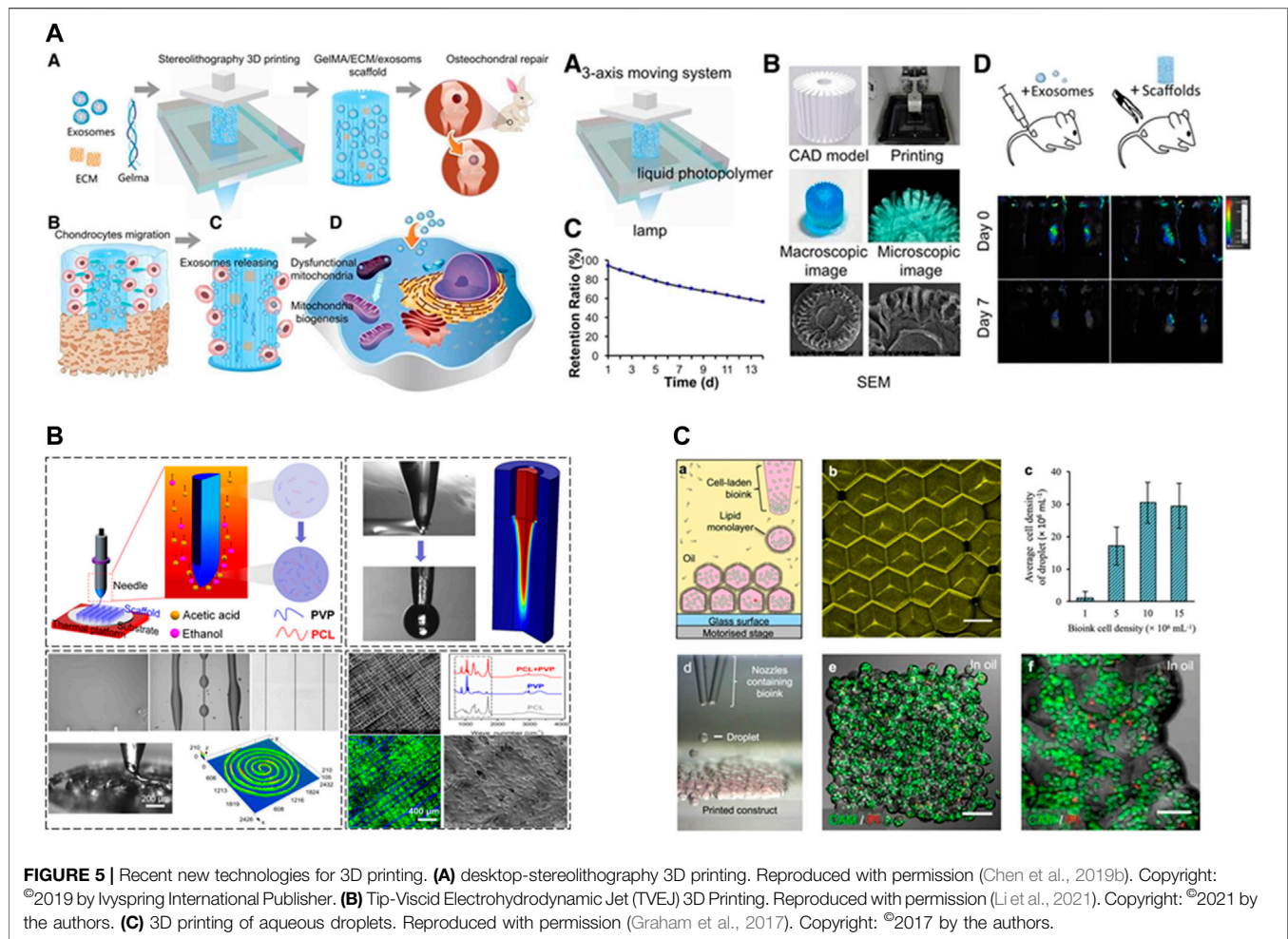
Johnson et al. (2012) identified a small molecule, kartogenin, that promotes cartilage production by inducing the transformation of MSCs into chondrocytes. Kartogenin interrupts the interaction between filamin A (FLNA) and CBF- $\beta$  and controls the expression of a family of proteins that play key roles in musculoskeletal development. Topical administration of kartogenin to mice with osteoarthritis-like symptoms, triggered the development of cartilage. (Johnson et al., 2012). Moreover, Zhao et al. (2020) prepared KGN-encapsulating PLGA microspheres using a solid-oil-water double solvent evaporation technique, complexed with CECM scaffolds containing TGF- $\beta$ 3, and demonstrated that the scaffold prolonged the activity of KGN and supported the adhesion, proliferation, and chondrogenic differentiation of BMSCs *in vitro*. Moreover, Zhao et al. (2020) reported the successful integration of new cartilage at the defect site with surrounding tissues in a rabbit femoral condylar cartilage defect model. This study provided novel insights regarding the generation of scaffolds with kartogenin, however, no positive synergy was observed between kartogenin and TGF- $\beta$ 3 (Zhao et al., 2020).

Finally, considering that ECM exosomes act a pivotal part in intercellular mitochondrial communication (Singh et al., 2017), Chen et al. (2019b) prepared a 3D printed cartilage ECM/GelMA/extracellular body scaffold with radial channels via desktop stereolithography. They found that ECM exosomes could restore chondrocyte mitochondrial dysfunction in a rabbit OCD model possibly associated with 10.3% of its internal mitochondria-associated proteins (Chen et al., 2019b).

### 3.4 Scaffold Design and Machining

The role of the scaffold in the development of osteochondral tissue is to provide a shape for tissue regeneration and to load cells and bioactive factors. The advent of three-dimensional printing (3DP) technology has made it possible to fabricate highly





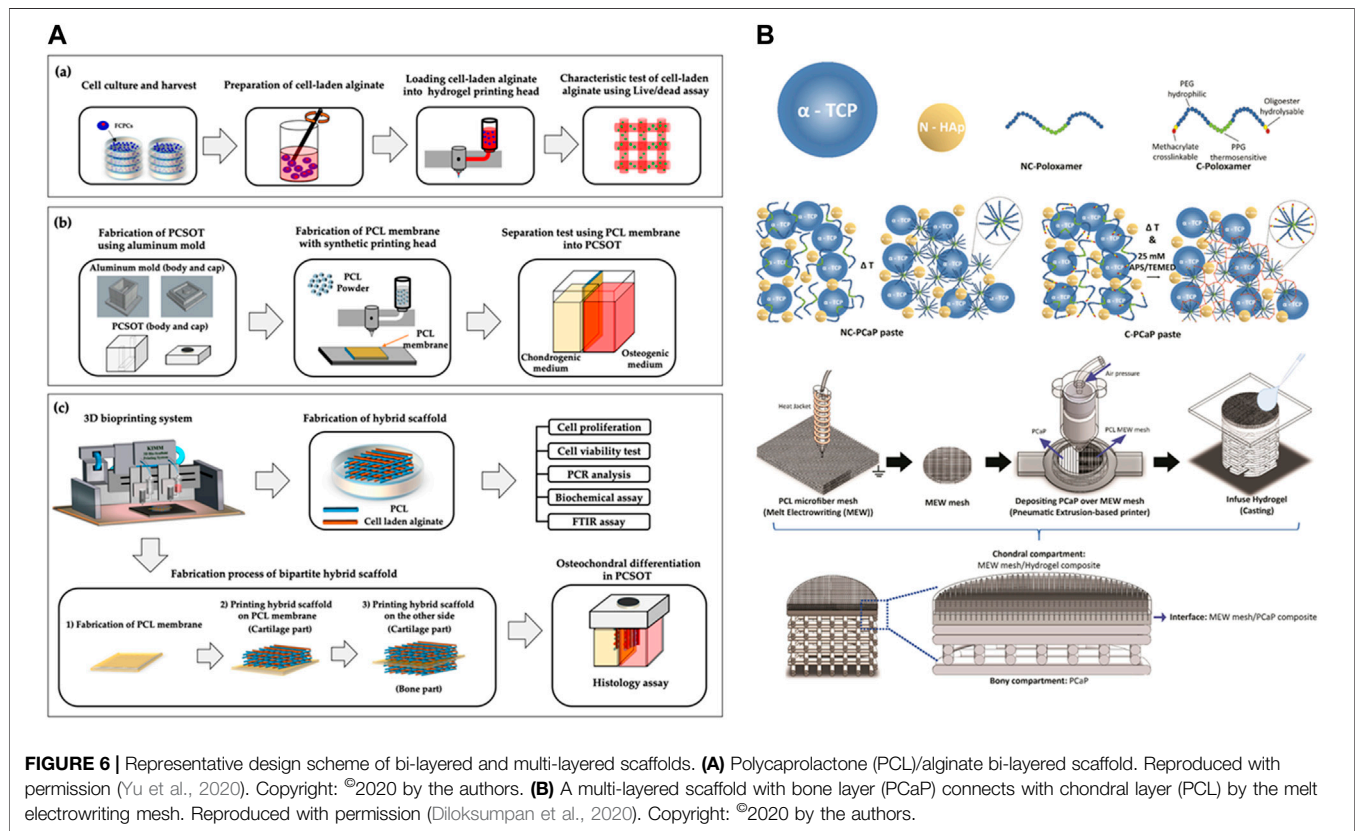
complex scaffolds (Figure 5). An ideal scaffold must possess an appropriate pore size, interconnectivity, and surface topography, biocompatibility, vascularity, biodegradability, non-cytotoxicity, good mechanical and rheological properties, as well as a simple and economical preparation process.

### 3.4.1 3D Printing Techniques

The most commonly used 3D printing technologies are fused deposition modeling (Distler et al., 2020), stereolithography (SLA) (Kumar and Kim, 2020), selective laser sintering (Zeng et al., 2020), inkjet (Li et al., 2020), 3D plotting (Seok et al., 2020) and LOM (Luong et al., 2018).

Mellor et al. (2017) pioneered the combination of electrospinning and 3D printing technologies to obtain a scaffold with the advantages of both. During implantation into a porcine osteochondral defect model, the nanofiber composite scaffold obtained by electrospinning alone was prone to delamination, whereas the composite micro/nanofiber scaffold did not peel off during culture, and the cells proliferated stably on days 1, 4, 7, and 21 (Mellor et al., 2017). Additionally, Graham et al. (2017) designed a novel droplet-based 3D printing technique that printed  $\leq 200 \mu\text{m}$  high-resolution 3D geometrically shaped ovine MSCs. After 5 weeks of *in vitro* culture, the printed oMSCs

differentiated into chondrogenic lineage cells, generating cartilage-like structures with Col II (Graham et al., 2017). Still further, Schoonraad et al. (2021) utilized digital light processing-based stereolithography (DLP) to print a bilayer scaffold. The prepared photoresins were printed in CAD files as  $25 \mu\text{m}$  layers, irradiated at  $\lambda = 405 \text{ nm}$  for 6 s followed by a brief rinse with 100% ethanol to remove redundant resin, and then heat cured in an oven at  $120^\circ\text{C}$  under vacuum for 1 h (Schoonraad et al., 2021). Li et al. (2021) investigated the application of tip-viscid electrohydrodynamic jet printing (TVEJ) for osteochondral regeneration. TVEJ utilizes a combination of thermal, flow, and electric fields to prepare PCL/PVP composite osteochondral scaffolds by viscous tip jets generated at the tip of the needle; the solvent evaporation rate was adjusted to allow flexible control of various printing patterns and structural resolution. The biocompatibility of the scaffold was demonstrated by *in vitro* culture of murine MC3T3-E1 Subclone14 cartilage cells with cell survival rates of 84%, 88%, and 91% after 1, 2, and 3 days, respectively (Li et al., 2021). Idaszek et al. (2019) designed a multi-material deposition system based on a microfluidic platform with a hybrid chamber and proved its feasibility for depositing continuous gradients of cells and materials in 3D structures with high shape fidelity, appropriate porosity, and cell viability (Idaszek et al., 2019).



When stem cells are used for tissue regeneration, the compression and shearing of cells by the scaffold can lead to cell damage or death (Manoukian et al., 2018). The loss modulus ( $G''$ ), energy storage modulus ( $G'$ ) and loss angle tangent ( $G''/G'$ ) are the main parameters that determine the results of extrusion uniformity, extrudability, and structural integrity printing (Chen et al., 2020). The loss angle tangent is inversely proportional to the extrusion pressure. As excessive squeeze pressure can damage cells loaded in bioinks, extrusion pressure should be controlled to maintain cell viability at the lowest possible loss rate (Abdollahiyan et al., 2020). Moreover, pore shape and porosity affect the permeability/diffusivity, degradation rate, and elastic modulus of the scaffold. Zhang et al. (2020a) investigated the effect of porosity and pore shape on the mechanical properties of the scaffold using a finite element method, and concluded that the Young's modulus (overall mechanical properties of the scaffold) decreases with increasing porosity of the scaffold (Zhang et al., 2020a). Additionally, Reed et al. (2016) fabricated highly porous, hydrophilic chitosan-alginate (Ch-Al) scaffolds by 3DP and directional freezing, resulting microchannels parallel to the Z-axis and lamellar pores with 300  $\mu\text{m}$  long and 50  $\mu\text{m}$  in diameter. A porous pore zone with a diameter of 100  $\mu\text{m}$  was visible in the bottom 500  $\mu\text{m}$  of the scaffold, with a complete transition from the lamellar to the spherical pore zone (Reed et al., 2016).

In the development of osteochondral tissue scaffolds, new or combined 3D printing strategies are developed or improved to obtain reproducible bionic structures with controlled porosity,

composed of different materials, spatially organized, and capable of delivering cells and growth factors in a controlled manner. Such scaffolds are designed to address specific aspects of osteochondral tissue, namely vascularization, deposition of calcium phosphate in predefined areas, directing regeneration in certain directions (by gradient delivery of factors or anisotropic porous structures), development of different tissues (i.e., OCD), or inhibition of calcification and cell adhesion.

### 3.4.2 Monophasic Scaffolds

3D printing has long been used in osteochondral interface regeneration with monophasic scaffolds representing the earliest standard technique (Figure 6). Single-phase scaffolds use a single material with a single structure and porosity throughout; the same cell types and bioactive factors are distributed within the scaffold to accommodate the shape of the defect area. Studies of single-phase scaffolds have shown that they support the attachment and proliferation of chondrocytes and osteoblasts. However, due to the complex tissue composition and structure of the osteochondral interface, monophasic scaffolds do not simulate both cartilage and subchondral bone, let alone tidemark and cement lines.

### 3.4.3 Bi-Layered, Tri-Layered Scaffolds

Current research focuses on hierarchical scaffolds, including bi-layered, tri-layered, and gradient layers (Zhou et al., 2019; Mancini et al., 2020).

Thunsiri et al. (2020) designed a bilayer biologically active biomaterial scaffold with a cartilage (AC) layer consisting of polylactic acid (PLA) and polycaprolactone (PCL) hybrid fibers printed in 3D and freeze-dried with chitosan (CS)/filamentous fibers (SF), as well as a bone layer consisting of PLA, PCL, and HA. Analysis of the mechanical properties showed that following culture of the AC layer scaffold with the human fetal osteoblast cell line hFOB1.19, and the B layer scaffold with SW1353 chondrocyte-like cells, increased cell survival was observed in the AC and B layers, indicating that the presence of bioactive substances (CS and SF) promotes cell proliferation (Thunsiri et al., 2020).

Natarajan et al. (2021) printed a turbid solution containing PCL, PLGA, and chondroitin sulfate at a ratio of 65:30:5 at different filling densities to form a gradient cartilage layer. They used a dissolved-adhesion technology to bond the cartilage layer to the calcified layer to obtain a biphasic scaffold with simultaneous osteogenic differentiation potential. The resulting scaffold had a stable and continuous connection between the two layers at the interface. Moreover, approximately 35% of the bilayer scaffold (BLS) degraded after 3 months of immersion in PBS with synchronized precipitation and dissolution processes. Furthermore, by analyzing the viability of rabbit AMSCs, 3D printed scaffolds (i.e., PCL/PLGA/CS, PCL/PLGA/ $\beta$ -TCP, BLS) were found to have more live cells and fewer dead cells with no change in cell morphology after 3 days of culture. After 7 days of culture, the proliferation of AMSCs on composite scaffolds was significantly increased ( $p < 0.05$ ) compared to that of the control. After 28 days of culture in the differentiation medium, AMSCs were active on the bilayer scaffold, and cells cultured on the scaffold containing CS and  $\beta$  had higher metabolic activity than those cultured in the control group. Most importantly, the CS- and  $\beta$ -TCP-containing BLS supported the differentiation of AMSCs into bone and cartilage cell lineages. At days 7 and 14, the ALP activity of BLS was significantly higher than that of the control ( $p < 0.05$ ). On day 28, the GAG, collagen, and calcium contents of BLS were higher than those in the control ( $p < 0.01$ ). Moreover, the expression of chondrocyte/bone marker genes (collagen II, aggrecan, hyaluronan synthase 2, SOX 9), and osteogenic-specific genes (bone sialoprotein, osteocalcin, and osterix) was significantly upregulated in the BLS group (Natarajan et al., 2021).

Meanwhile, it is also important to consider the banded (zonal) structure of natural articular cartilage. Accordingly, Mancini et al. designed a scaffold with two layers of a thiol-ene cross-linkable HA/poly (glycidol) hybrid hydrogel [HA-SH/P (AGE-co-G)]. Articular cartilage progenitor cells (ACPC) and MSCs of superficial cartilage origin were added to the top and bottom layers, respectively. These layers were then mounted on 3D-printed poly ( $\epsilon$ -caprolactone) (PCL) bone anchors, which were secured by reinforcing fibers protruding from the bone anchors onto the cartilage portion of the construct. Six months after implantation of the composite scaffold into an equine model, the mean compressive modulus of the repaired tissue in the banded group was  $147.5 \pm 40.7$  kPa, which was significantly higher than that of the non-banded construct ( $96.9 \pm 33.0$  kPa,  $p < 0.05$ ), however, lower than that of the natural cartilage ( $495.9 \pm$

174.0 kPa). Moreover, both the banded and non-banded groups formed fibrocartilage and produced primarily Col I rather than Col II and GAG, which may be related to the failure of MSC proliferation. At 6 months, both MSCs and ACPCs had disappeared leaving only host cells at the defect site, thus, fibrocartilage may be generated via host self-healing (Mancini et al., 2020). These findings may promote seed cell survival, adhesion, proliferation, and differentiation by culturing seed cells in a bioreactor or by adding appropriate growth factors.

Li et al. (2018b) designed a bionic three-layer fibrous-hydrogel scaffold and used a low-temperature 3D bioprinter to fabricate a three-dimensional bone and calcified layer scaffold with PLGA and  $\beta$ -TCP composite. The resulting product comprised a cartilage matrix from bovine articular cartilage using cell-free technology and freeze-drying technique. Li et al. (2018b) used the “lysis-adhesion technique” to fix the three layers together to obtain a stable three-layer bionic scaffold. MSCs were inoculated *in vitro*, and were found to adhere to all scaffold layers. Moreover, the number of cells in the scaffold increased with time, and cell proliferation was stable during the plateau period from day 7–11. These results confirmed the biocompatibility of the scaffold, while the introduced calcified layer served as the role of bone-cartilage interface, achieving the expected isolation. However, considering the insufficient sample size and lack of animal model in this study, these findings require further investigation to demonstrate their feasibility and identify potential biological relationships (Li et al., 2018).

The upper interface between the CCZ and hyaline cartilage is called the tidemark, while the lower interface between the CCZ and subchondral bone is the cement line. In most studies of 3D printed regenerative osteochondral interfaces, little attention has been paid to the tidemark, which is difficult to induce after scaffold implantation. However, Mellor et al. (2020) and Nordberg et al. (2021) adopted the electrospinning technique to add a tidemark layer between the bone and cartilage layers. Their results demonstrated that the tidemark inhibits cell migration between the subchondral bone and cartilage, thereby preventing the invasion of cartilage by subchondral bone forming vessels (Mellor et al., 2020; Nordberg et al., 2021).

#### 3.4.4 Gradient Design of the Scaffolds

Osteochondral units are tissues that contain bone, cartilage, and transitional layers with gradient-based mechanical and biological properties. Therefore, a gradient-based scaffold design is essential for encapsulating the properties of musculoskeletal and other heterogeneous tissues (Bittner et al., 2018). Continuous gradient scaffolds more closely mimic natural OC tissue, as no distinct interface exists between each layer (Zhang et al., 2020b). However, in biphasic or multiphase interfaces the fixation between different interfaces may be unstable *in vivo*, thus, failing to mimic the original interface structure of osteochondral tissue, which is a gradual transition from soft cartilaginous tissue to hard subchondral bone, with biological, physicochemical, and anatomical gradients in the process.

Previous studies have suggested that parathyroid hormone (PTH) inhibits chondrocyte hypertrophy and facilitates articular hyaline chondrogenesis. Deng et al. (2021) used silk fibroin (SF)



grafted with PTH by sulfonated SMCC (SF-PTH), covalently immobilized methacrylic anhydride (SF-MA), and photo-crosslinkable gelatin methacryloyl (GMA) for gradient strengthening of the scaffold based on natural mechanical strength. BMSCs were co-cultured separately *in vitro* with four bioinks (10% GM, 10% GM-5% SF, 10% GM-5% SF-MA, and 10% GM-5% SF-PTH). All four bioinks had good biocompatibility, while GM + SF-PTH ink inhibited the hypertrophy of cultured chondrocytes. After implantation of GM + SF-PTH/GM + SF-MA scaffolds in rabbit distal femoral talar sulcus defects, higher macroscopic scores, and fewer specific markers of chondrocyte hypertrophy, were observed compared with controls, demonstrating that this mechanically graded bioprinted biphasic scaffold can effectively promote regeneration of osteochondral defects, while PTH helps maintain the phenotype of hyaline cartilage (Deng et al., 2021).

Radhakrishnan et al. (2018) compared the effects of biphasic (nHA or CHS) and gradient (nHA + CHS) hydrogel scaffolds on *in vivo* osteochondral regeneration in a rabbit osteochondral defect model. The gradient group (8 weeks) had complete closure of the defect, showing good tissue coverage, while the other groups retained defects. Moreover, histological analysis revealed the formation of tidemark, collagen and GAG deposition in the neoplastic matrix, as well as the presence of hyaline cartilage, the characteristic matrix, chondrocytes, and osteoblasts. mCT further revealed mineralized new tissue formation and confinement to the defect area with a high bone density gradient (cartilage:  $0.42 \pm 0.07$  g/cc, bone density:  $0.64 \pm 0.08$  g/cc). In addition, biomechanical studies showed that the gradient group load for failure ( $378 \pm 56$  N) was significantly higher than that of the other groups. Thus, this bionic gradient hydrogel scaffold has the potential to promote osteochondral regeneration (Radhakrishnan et al., 2018).

Gao et al. (2019a) strengthened GelMA hydrogels by cleavable poly (N-acryloyl 2-glycine) (PACG) with dynamic hydrogen bonding and obtained hydrogels with high compressive strength (12.4 MPa) and compressive modulus (837 kPa). Moreover, bioactive glass (BG) can improve ALP activity, as well as the proliferation and differentiation of hBMSCs. Thus, the top layer of the generated hydrogel was doped with BG as the cartilage layer. Additionally, considering that  $Mn^{2+}$  can promote the cartilage differentiation of hBMSCs, the bottom layer of the hydrogel was doped with  $Mn^{2+}$  as the bone layer. The two layers were then fixed by UV light irradiation. The resulting bilayer biohybrid gradient hydrogel scaffold was evaluated using a rat model. The PAG-Mn-BG scaffold provided important template guidance and mechanical support, while further accelerating the regeneration of subchondral bone. Furthermore, the microscopic morphology of the repaired cartilage was smooth and homogeneous, with no significant difference from normal cartilage; that is, the scaffold enhanced both articular cartilage and subchondral bone repair and promoted the repair of osteochondral tissue at the defect site (Gao et al., 2019a).

In addition to biomechanical gradients, bioactive signal gradients are critical for regeneration at the osteochondral interface. SPIONs coupled with heparin produce a glycosylated corona that forms an agarose gel that stably encapsulates the

BMP-2 gradient, which can effectively isolate and release growth factors. For example, a human HMSC stent pre-loaded with BMP-2 gradients released from the hydrogel over 28 days of culture, stimulated osteogenic gene expression and tissue mineralization. The resulting tissue exhibited a cartilaginous zone, rich in Col II and GAG, with transitioning to a mineralized bone zone exhibiting a broad distribution of  $\beta$ -TCP and HAP (Li et al., 2018a).

To date, many 3DP scaffolds have been fabricated to encapsulate the gradient properties of the bone-cartilage interface. Attempts have been made to mimic the chemical, mechanical, and biochemical structures, as well as the electrical gradients at the bone-cartilage interface. However, few scaffold materials with gradient metabolic properties have been developed. At the bone-cartilage interface, the vascularity is not distributed uniformly, thus, cells at different sites differ in terms of metabolic demand. Khorshidi and Karkhaneh (2021) designed a scaffold with oxygen-releasing particles from PLA and calcium peroxide. A gradient mixing chamber was employed to load the particles in a gradient manner into a hydrogel precursor solution of functionalized pectin and sericin. The chemical, morphological, and structural changes in the thickness of the composites were evaluated using microscopic and spectroscopic analyses. The particle concentration gradually increased from approximately 10% w/w over time and approached approximately 30% w/w by the end of the preparation process. SEM photographs of the composite cross-sections confirmed a gradual increase in the particle density from the lower surface to the upper surface. Meanwhile, spectral analysis confirmed that the scaffold was capable of releasing oxygen as a component, that is, calcium peroxide. Oxygen measurements of continuous cross-sections showed a gradual increase in oxygen production of the composite from the lowest to highest point. Microscopic and spectroscopic analyses confirmed the increase in particle content over the thickness of the scaffold. In addition, the scaffold cross-sections produced different amounts of oxygen and showed oxygen release behavior with depth (Khorshidi and Karkhaneh, 2021).

These innovative gradients are designed to promote hyaline cartilage formation by accelerating early subchondral bone regeneration and tight integration with the surrounding host site.

### 3.4.5 Scaffold-Free Bioprinting

Stent implantation poses a myriad of problems, thus, the use of stentless bioprinting eliminates many of these complications while providing better intercellular interactions and long-term functions. Breathwaite et al. (2019) and Grogan et al. (2020) produced cellular microspheroids using MSCs to demonstrate the feasibility of cell-free scaffolds *in vitro* and in a rabbit osteochondral defect model, respectively. Meanwhile, Brown et al. (2021) used scaffold-free, self-assembling neocartilage as the chondral phase. They then compared the compressive strength of HAP, following introduction of HAP with 55% porosity with that of 0.95 MPa 32 at two neocartilage maturation stages (day 4 and 10). Osteochondral gross analysis, neocartilage and osteochondral histology, osteochondral interdigitation, neocartilage biochemistry, and



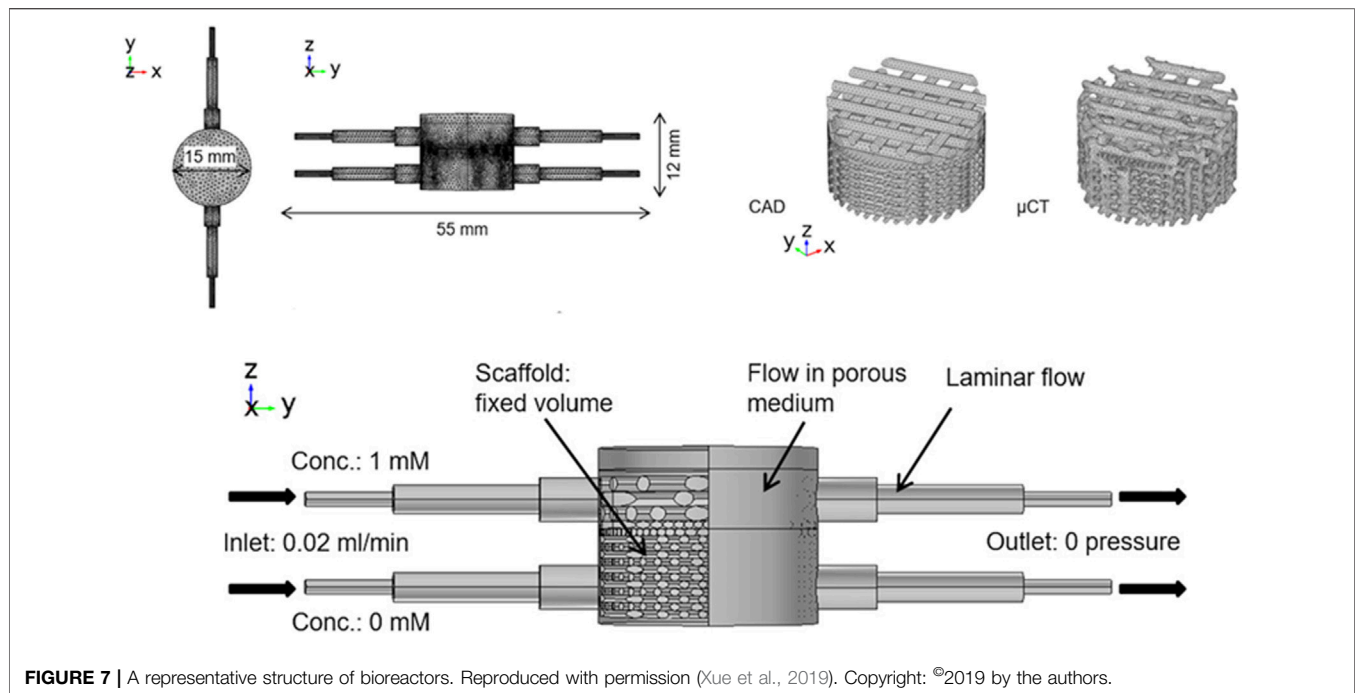


**FIGURE 7** | A representative structure of bioreactors. Reproduced with permission (Xue et al., 2019). Copyright: ©2019 by the authors.

neocartilage mechanics were then assessed. The early osteochondral assembly interface resulted in a 243-fold increase in shear modulus, a 4.9-fold increase in ultimate shear strength, a 244% increase in interface interdigitation depth, and a 438% increase in interdigitation frequency compared to late assembly (Brown et al., 2021).

### 3.5 Bioreactors

Even with the perfect combination of scaffolds, growth factors, and cells, osteochondral constructs may lack mass transfer of oxygen, nutrients, waste, and metabolites (Ravichandran et al., 2018). In *in vitro* cultures, cells are often loaded unevenly onto, and within, the scaffold, and cell viability and proliferation are heterogeneous throughout the graft. However, the flow state generated within the bioreactor helps overcome the limitations of oxygen diffusion in tissue-engineered grafts, while promoting cell transfer, providing critical physical and chemical cues for tissue regeneration, and helping restore the essential site properties of the original tissue, all of which is critical for maintaining cell survival and uniform cell distribution in the graft (Gadjanski, 2018). Biomechanical stimulation categories include direct compression, hydrostatic pressure, shear bioreactors, “low-shear” systems, and hybrid bioreactors that incorporate multiple loading regimes. Mechanical compression and shear forces represent the primary sources of physical stress affecting cartilage and subchondral bone.

Studies have shown that bioreactors (Figure 7) that can provide direct compression can stimulate chondrocytes and increase the synthesis of proteoglycans and collagen to enhance their mechanical properties. Fluid shear utilizes fluids to generate shear force between osteochondral constructs to increase the transfer of waste and nutrients during culture.

Meanwhile, low-shear systems can be used to stimulate cells in the matrix, while still allowing the cells to retain their chondrocyte phenotype.

Data from computer modeling can be used to understand the correlation between physical stimuli and cellular responses to bone and cartilage formation, thereby, saving money and time required for *in vitro* and *in vivo* studies. Xue et al. (2019) proposed an osteochondral culture system using a flow rate of 0.02 ml/min and adding 1 (cartilage matrix) and 0 mM (osteogenic medium) concentration with no pressure at the outlet, inducing an average fluid-induced shear stress of approximately 0.03 and 0.28 MPa in the cartilage and bone layers. Bilayer PLA scaffolds loaded with ATDC5 and MC3T3-E1 cells cultured in this system for 7 days showed a significant increase in metabolic activity and cell number compared to CAD scaffolds. ATDC5 cells dominated the upper segment, while MC3T3-E1 cells dominated the lower segment. Moreover, the cells effectively attached to the collagen and PLA struts of the scaffold, thus, demonstrating the viability of the system (Xue et al., 2019). However, this system is not only applicable to *in vitro* culture of osteochondral bone, but also for the cytotoxicity and response monitoring of clinical drugs.

Nichols et al. optimized a new bioreactor capable of optical monitoring within 3D structures (Nichols et al., 2018). Yu et al. (2020) designed and developed a polydimethylsiloxane coculture system for osteochondral tissue (PCSOT). The body of PCSOT consists of a PCL membrane divided into two separate chambers, allowing cells to be exposed to different culture media using different chondrogenic and osteogenic media, thereby, providing a suitable osteochondral differentiation environment that allows FCPC to differentiate into osteochondral tissue (Yu et al., 2020). Current research is focused on unifying the design of bioreactors for effective osteochondral graft culture.

**TABLE 1 |** Current clinical translational results of 3D printing for OCD regeneration in big animal models.

Materials	Cell/molecules type	Scaffold structure	Development	Result	References
RGD- $\gamma$ alginates, PCL	FPSCs, chondrocytes, BMSCs	Bi-phasic	In caprine models	After 6 months of implantation, osteochondral tissues were generated significantly. However, limited Safranin-O staining suggested the cartilage template have undergone endochondral ossification. One animal's implantation failed	Critchley et al. (2020)
—	AT-MSCs	Scaffold free	In mini-pig models	After 3 months of operation, percentage RV and MOCART scores had significant differences compared with the control group. After 6 months of operation, the gross scores were higher than the control group but without statistical differences	Yamasaki et al. (2019)
HA-SH/P (AGE-co-G), PCL	ACPCs, MSCs	Tri-phasic	In equine models	Observed promising results of bone regeneration in equine models. However, the cartilage regeneration was worse than the natural OCD groups	Mancini et al. (2020)
PCL, collagen type I gel	hASC	Tri-phasic	In porcine models	The scaffold reinforced with intermediate electrospun layer had better performance and operational convenience than the single PCL scaffold	Mellor et al. (2017)
PCL, TCP, dECM	hASC	Bi-phasic	In porcine models	The scaffolds promoted the regeneration of osteochondral tissues compared with the open lesion groups. Scaffold loaded with hASC scored best ICR II grading among all groups. Adding a tidemark layer performed as a boundary line to separate the cartilage and bone	Nordberg et al. (2021)

*GelMA, gelatin methacrylate; ECM, extracellular matrix; MSC, mesenchymal stem cell; PCL, polycaprolactone; FPSCs, fat pad derived stem/stromal cells; BMSCs, bone marrow derived stem cells; AT-MSCs, adipose tissue-derived mesenchymal stem cells; ACPC, articular cartilage progenitor cells; HA-SH/P(AGE-co-G), thiol-ene cross-linkable hyaluronic acid/poly(glycidol) hybrid hydrogel; hASC, human adipose-derived stem cells; TCP,  $\beta$ -tricalcium phosphate.*

## 4 DISCUSSION AND FUTURE DIRECTIONS

With the development of 3DP technology and a deeper understanding of osteochondral structure, researchers began to consider the feasibility of applying 3DP to regenerate OCD, from simply repairing articular cartilage to subchondral bone and smooth bone-cartilage interfaces. Initially, natural materials were the first choice for constructing scaffolds; however, their disadvantages could not be avoided. Currently, composites based on natural and artificial polymers are the dominant research directions. Due to the location of the bone-cartilage interface, regenerating the bone-cartilage interface must consider both articular cartilage and subchondral bone. Although the approach based on monophasic scaffolds has become obsolete, many research groups have developed bilayer and triple-layer scaffolds that mimic the osteochondral cartilage and bone layering structure (or tidemark and calcified cartilage area). These scaffolds have also been combined with tissue-specific cells (osteoblasts for bone, chondrocytes for cartilage) or MSCs (BMSCs, hTSMCs, AMSCs, and UCB-MSCs) and appropriate growth factors are then selected to promote migration, proliferation, and differentiation of the seed cells to form osteochondral tissue. The development of mechanical gradient scaffolds with a structure mimicking osteochondral tissue and bio-gradient scaffolds with graded release of bioactive factors is promising for establishing the formation of osteochondral interfaces. Bioreactor culture further facilitates homogeneous nutrient transfer, providing key physical and chemical cues for tissue regeneration and promoting osteochondral tissue formation. 3D scanning (Li et al., 2017) and robot-assisted 3D bioprinting (Lipskas et al., 2019; Ma et al., 2020) are viable options. In the last 5 years,

many combinations have been proposed and have been successful. However, some key challenges remain, including how to differentiate different tissues (bone and cartilage) while regenerating the bone-cartilage interface so that the regenerated tissue structurally and functionally mimics the native tissue. Animal models are also vital for clinical translation. Although small animals like rats and rabbits have the advantages of lost cost, but for the consideration of defect size and surgical difficulty, researchers should focus more on the big animal models for the evaluation of 3D printing Scaffolds' clinical prospects (Table 1). In addition, clinical applications face many regulatory and commercial challenges while needing to accommodate the automation and volume of composite scaffold printing.

## AUTHOR CONTRIBUTIONS

JX, JiJ, and JuJ wrote the draft manuscript. LZ, SZ, HT, and QH performed the literature review and data collection. BY and XQ conceived the general idea and revised the manuscript. All authors contributed to the article and approved the submitted version.

## FUNDING

This work was supported by the National Natural Science Foundation of China (Grant No. 82172464, 82172453, and 81972086); National Key Research and Development Project of China (Grant No. 2020YFC1107500 and 2020YFC1107503); The Shanghai Rising-Star Program (21QA1405500); Shanghai "Rising Stars of Medical Talent" Youth Development Program (Youth

Medical Talents—Specialist Program) (Grant No. 2019-72); “Technology Innovation Action Plan” Key Project of Shanghai Science and Technology Commission (Grant No. 19411962800);

Shanghai municipal education commission—Gaofeng clinical medicine grant support (Grant No. 20161423); NSFC Advancing Targeted Projects (RJT)-JX-005, RJT22-RC-011).

## REFERENCES

- Abdollahiyan, P., Oroojalian, F., Mokhtarzadeh, A., and Guardia, M. (2020). Hydrogel-Based 3D Bioprinting for Bone and Cartilage Tissue Engineering. *Biotechnol. J.* 15, 2000095. doi:10.1002/biot.202000095
- Aisenbrey, E. A., Tomaschke, A., Kleinjan, E., Muralidharan, A., Pascual-Garrido, C., McLeod, R. R., et al. (2018). A Stereolithography-Based 3D Printed Hybrid Scaffold for *In Situ* Cartilage Defect Repair. *Macromol. Biosci.* 18, 1700267. doi:10.1002/mabi.201700267
- Amanatullah, D. F., Yamane, S., and Reddi, A. H. (2012). Distinct Patterns of Gene Expression in the Superficial, Middle and Deep Zones of Bovine Articular Cartilage. *J. Tissue Eng. Regen. Med.* 8, a–n. doi:10.1002/term.1543
- Armiento, A. R., Stoddart, M. J., Alini, M., and Eglin, D. (2018). Biomaterials for Articular Cartilage Tissue Engineering: Learning from Biology. *Acta Biomater.* 65, 1–20. doi:10.1016/j.actbio.2017.11.021
- Athanasios, K. A., Darling, E. M., and Hu, J. C. (2009). Articular Cartilage Tissue Engineering. *Synth. Lectures Tissue Eng.* 1, 1–182. doi:10.2200/S00212ED1V01Y200910TIS003
- Austin, M. J., and Rosales, A. M. (2019). Tunable Biomaterials from Synthetic, Sequence-Controlled Polymers. *Biomater. Sci.* 7, 490–505. doi:10.1039/c8bm01215f
- Bajpayee, A. G., and Grodzinsky, A. J. (2017). Cartilage-targeting Drug Delivery: Can Electrostatic Interactions Help? *Nat. Rev. Rheumatol.* 13, 183–193. doi:10.1038/nrrheum.2016.210
- Bao, J., Chen, Z., Xu, L., Wu, L., and Xiong, Y. (2020). Rapamycin Protects Chondrocytes against IL-18-induced Apoptosis and Ameliorates Rat Osteoarthritis. *Aging* 12, 5152–5167. doi:10.18632/aging.102937
- Bittner, S. M., Guo, J. L., Melchiorri, A., and Mikos, A. G. (2018). Three-dimensional Printing of Multilayered Tissue Engineering Scaffolds. *Mater. Today* 21, 861–874. doi:10.1016/j.mattod.2018.02.006
- Bonani, W., Singhatanadgige, W., Pornanong, A., and Motta, A. (2018). Natural Origin Materials for Osteochondral Tissue Engineering. *Adv. Exp. Med. Biol.* 1058, 3–30. doi:10.1007/978-3-319-76711-6\_1
- Brauer, D. S. (2015). Bioactive Glasses-Structure and Properties. *Angew. Chem. Int. Ed.* 54, 4160–4181. doi:10.1002/anie.201405310
- Breathwaite, E. K., Weaver, J. R., Murchison, A. C., Treadwell, M. L., Odanga, J. J., and Lee, J. B. (2019). Scaffold-free Bioprinted Osteogenic and Chondrogenic Systems to Model Osteochondral Physiology. *Biomed. Mater.* 14, 065010. doi:10.1088/1748-605X/ab4243
- Brown, W. E., Huang, B. J., Hu, J. C., and Athanasios, K. A. (2021). Engineering Large, Anatomically Shaped Osteochondral Constructs with Robust Interfacial Shear Properties. *NPJ Regen. Med.* 6, 42. doi:10.1038/s41536-021-00152-0
- Camacho, P., Behre, A., Fainor, M., Seims, K. B., and Chow, L. W. (2021). Spatial Organization of Biochemical Cues in 3D-Printed Scaffolds to Guide Osteochondral Tissue Engineering. *Biomater. Sci.* 9, 6813–6829. doi:10.1039/d1bm00859e
- Carballo, C. B., Nakagawa, Y., Sekiya, I., and Rodeo, S. A. (2017). Basic Science of Articular Cartilage. *Clin. Sports Med.* 36, 413–425. doi:10.1016/j.csm.2017.02.001
- Chang, N.-J., Erdenekhyag, Y., Chou, P.-H., Chu, C.-J., Lin, C.-C., and Shie, M.-Y. (2018). Therapeutic Effects of the Addition of Platelet-Rich Plasma to Biointerfaces and Early Rehabilitation Exercise on Articular Cartilage Repair. *Am. J. Sports Med.* 46, 2232–2241. doi:10.1177/0363546518780955
- Chawla, D., Kaur, T., Joshi, A., and Singh, N. (2020). 3D Bioprinted Alginate-Gelatin Based Scaffolds for Soft Tissue Engineering. *Int. J. Biol. Macromolecules* 144, 560–567. doi:10.1016/j.ijbiomac.2019.12.127
- Chen, L., Deng, C., Li, J., Yao, Q., Chang, J., Wang, L., et al. (2019a). 3D Printing of a Lithium-Calcium-Silicate crystal Bioscaffold with Dual Bioactivities for Osteochondral Interface Reconstruction. *Biomaterials* 196, 138–150. doi:10.1016/j.biomaterials.2018.04.005
- Chen, P., Xia, C., Mo, J., Mei, S., Lin, X., and Fan, S. (2018). Interpenetrating Polymer Network Scaffold of Sodium Hyaluronate and Sodium Alginate Combined with Berberine for Osteochondral Defect Regeneration. *Mater. Sci. Eng. C* 91, 190–200. doi:10.1016/j.msec.2018.05.034
- Chen, P., Zheng, L., Wang, Y., Tao, M., Xie, Z., Xia, C., et al. (2019b). Desktop-stereolithography 3D Printing of a Radially Oriented Extracellular Matrix/mesenchymal Stem Cell Exosome Bioink for Osteochondral Defect Regeneration. *Theranostics* 9, 2439–2459. doi:10.7150/thno.31017
- Chen, Y., Xiong, X., Liu, X., Cui, R., Wang, C., Zhao, G., et al. (2020). 3D Bioprinting of Shear-Thinning Hybrid Bioinks with Excellent Bioactivity Derived from Gellan/alginate and Thixotropic Magnesium Phosphate-Based Gels. *J. Mater. Chem. B* 8, 5500–5514. doi:10.1039/d0tb00060d
- Choi, J. H., Kim, N., Rim, M. A., Lee, W., Song, J. E., and Khang, G. (2020). Characterization and Potential of a Bilayered Hydrogel of Gellan Gum and Demineralized Bone Particles for Osteochondral Tissue Engineering. *ACS Appl. Mater. Inter.* 12, 34703–34715. doi:10.1021/acsami.0c10415
- Critchley, S., Sheehy, E. J., Cuniffe, G., Diaz-Payno, P., Carroll, S. F., Jeon, O., et al. (2020). 3D Printing of Fibre-Reinforced Cartilaginous Templates for the Regeneration of Osteochondral Defects. *Acta Biomater.* 113, 130–143. doi:10.1016/j.actbio.2020.05.040
- Cui, C., Kim, D.-O., Pack, M. Y., Han, B., Han, L., Sun, Y., et al. (2020). 4D Printing of Self-Folding and Cell-Encapsulating 3D Microstructures as Scaffolds for Tissue-Engineering Applications. *Biofabrication* 12, 045018. doi:10.1088/1758-5090/aba502
- Cui, H., Nowicki, M., Fisher, J. P., and Zhang, L. G. (2017). 3D Bioprinting for Organ Regeneration. *Adv. Healthc. Mater.* 6, 1601118. doi:10.1002/adhm.201601118
- Custers, R. J. H., Creemers, L. B., Verbout, A. J., van Rijen, M. H. P., Dhert, W. J. A., and Saris, D. B. F. (2007). Reliability, Reproducibility and Variability of the Traditional Histologic/Histochemical Grading System vs the New OARSI Osteoarthritis Cartilage Histopathology Assessment System. *Osteoarthritis and cartilage* 15, 1241–1248. doi:10.1016/j.joca.2007.04.017
- Dai, W., Sun, M., Leng, X., Hu, X., and Ao, Y. (2020). Recent Progress in 3D Printing of Elastic and High-Strength Hydrogels for the Treatment of Osteochondral and Cartilage Diseases. *Front. Bioeng. Biotechnol.* 8, 604814. doi:10.3389/fbioe.2020.604814
- Dang, W., Wang, X., Li, J., Deng, C., Liu, Y., Yao, Q., et al. (2018). 3D Printing of Mo-Containing Scaffolds with Activated Anabolic Responses and Bi-lineage Bioactivities. *Theranostics* 8, 4372–4392. doi:10.7150/thno.27088
- Deng, C., Yang, J., He, H., Ma, Z., Wang, W., Zhang, Y., et al. (2021). 3D Bio-Printed Biphasic Scaffolds with Dual Modification of Silk Fibroin for the Integrated Repair of Osteochondral Defects. *Biomater. Sci.* 9, 4891–4903. doi:10.1039/d1bm00535a
- Deng, C., Zhu, H., Li, J., Feng, C., Yao, Q., Wang, L., et al. (2018). Bioactive Scaffolds for Regeneration of Cartilage and Subchondral Bone Interface. *Theranostics* 8, 1940–1955. doi:10.7150/thno.23674
- Diederichs, S., Renz, Y., Hagmann, S., Lotz, B., Seebach, E., and Richter, W. (2018). Stimulation of a Calcified Cartilage Connecting Zone by GDF-5-Augmented Fibrin Hydrogel in a Novel Layered Ectopic *In Vivo* Model. *J. Biomed. Mater. Res.* 106, 2214–2224. doi:10.1002/jbm.b.34027
- Diloksumpan, P., de Ruijter, M., Castilho, M., Gbureck, U., Vermonden, T., van Weeren, P. R., et al. (2020). Combining Multi-Scale 3D Printing Technologies to Engineer Reinforced Hydrogel-Ceramic Interfaces. *Biofabrication* 12, 025014. doi:10.1088/1758-5090/ab69d9
- Distler, T., Fournier, N., Grünwald, A., Polley, C., Seitz, H., Detsch, R., et al. (2020). Polymer-Bioactive Glass Composite Filaments for 3D Scaffold Manufacturing by Fused Deposition Modeling: Fabrication and Characterization. *Front. Bioeng. Biotechnol.* 8, 552. doi:10.3389/fbioe.2020.00552
- Echave, M. C., Hernández-Moya, R., Iturriga, L., Pedraz, J. L., Lakshminarayanan, R., Dolatshahi-Pirouz, A., et al. (2019). Recent Advances in Gelatin-Based Therapeutics. *Expert Opin. Biol. Ther.* 19, 773–779. doi:10.1080/14712598.2019.1610383

- Feng, X., and McDonald, J. M. (2011). Disorders of Bone Remodeling. *Annu. Rev. Pathol. Mech. Dis.* 6, 121–145. doi:10.1146/annurev-pathol-011110-130203
- Foster, N. C., Henstock, J. R., Reinwald, Y., and El Haj, A. J. (2015). Dynamic 3D Culture: Models of Chondrogenesis and Endochondral Ossification. *Birth Defect Res. C* 105, 19–33. doi:10.1002/bdrc.21088
- Frassica, M. T., and Grunlan, M. A. (2020). Perspectives on Synthetic Materials to Guide Tissue Regeneration for Osteochondral Defect Repair. *ACS Biomater. Sci. Eng.* 6, 4324–4336. doi:10.1021/acsbomaterials.0c00753
- Frief, F. V., Hu, Q., Mayer, J., Gemmer, L., Presser, V., Balzer, B. N., et al. (2021). Nanoporous Block Copolymer Membranes with Enhanced Solvent Resistance via UV-Mediated Cross-Linking Strategies. *Macromol. Rapid Commun.* 1, 2100632. doi:10.1002/marc.202100632
- Fu, N., Dong, T., Meng, A., Meng, Z., Zhu, B., and Lin, Y. (2018). Research Progress of the Types and Preparation Techniques of Scaffold Materials in Cartilage Tissue Engineering. *Cscr* 13, 583–590. doi:10.2174/1574888x12666170718152611
- Funck-Brentano, T., and Cohen-Solal, M. (2015). Subchondral Bone and Osteoarthritis. *Curr. Opin. Rheumatol.* 27, 420–426. doi:10.1097/bor.0000000000000181
- Gadjanski, I. (2018). Mimetic Hierarchical Approaches for Osteochondral Tissue Engineering. *Adv. Exp. Med. Biol.* 1058, 143–170. doi:10.1007/978-3-319-76711-6\_7
- Gannon, J. M., Walker, G., Fischer, M., Carpenter, R., Thompson, R. C., Jr., and Oegema, T. R., Jr. (1991). Localization of Type X Collagen in Canine Growth Plate and Adult Canine Articular Cartilage. *J. Orthop. Res.* 9, 485–494. doi:10.1002/jor.1100090404
- Gao, F., Xu, Z., Liang, Q., Li, H., Peng, L., Wu, M., et al. (2019a). Osteochondral Regeneration with 3D-Printed Biodegradable High-Strength Supramolecular Polymer Reinforced-Gelatin Hydrogel Scaffolds. *Adv. Sci.* 6, 1900867. doi:10.1002/advs.201900867
- Gao, J., Ding, X., Yu, X., Chen, X., Zhang, X., Cui, S., et al. (2021). Cell-Free Bilayered Porous Scaffolds for Osteochondral Regeneration Fabricated by Continuous 3D-Printing Using Nascent Physical Hydrogel as Ink. *Adv. Healthc. Mater.* 10, 2001404. doi:10.1002/adhm.202001404
- Gao, L., Orth, P., Cucchiari, M., and Madry, H. (2019b). Autologous Matrix-Induced Chondrogenesis: A Systematic Review of the Clinical Evidence. *Am. J. Sports Med.* 47, 222–231. doi:10.1177/0363546517740575
- Gao, Q., Xie, C., Wang, P., Xie, M., Li, H., Sun, A., et al. (2020). 3D Printed Multi-Scale Scaffolds with Ultrafine Fibers for Providing Excellent Biocompatibility. *Mater. Sci. Eng. C* 107, 110269. doi:10.1016/j.msec.2019.110269
- Gilat, R., Haunschild, E. D., Huddleston, H., Parvareh, K. C., Chahla, J., Yanke, A. B., et al. (2021). Osteochondral Allograft Transplantation of the Knee in Adolescent Patients and the Effect of Physal Closure. *Arthrosc. J. Arthroscopic Relat. Surg.* 37, 1588–1596. doi:10.1016/j.arthro.2020.12.204
- Glyn-Jones, S., Palmer, A. J. R., Agricola, R., Price, A. J., Vincent, T. L., Weinans, H., et al. (2015). Osteoarthritis. *The Lancet* 386, 376–387. doi:10.1016/s0140-6736(14)60802-3
- Gobbi, A., Lane, J. G., and Dallo, I. (2020). Editorial Commentary: Cartilage Restoration-What Is Currently Available? *Arthrosc. J. Arthroscopic Relat. Surg.* 36, 1625–1628. doi:10.1016/j.arthro.2020.04.001
- Goldring, M. B., and Goldring, S. R. (2010). Articular Cartilage and Subchondral Bone in the Pathogenesis of Osteoarthritis. *Ann. New York Acad. Sci.* 1192, 230–237. doi:10.1111/j.1749-6632.2009.05240.x
- Goyal, D., Goyal, A., and Adachi, N. (2017). “Subchondral Bone: Healthy Soil for the Healthy Cartilage,” in *Bio-orthopaedics: A New Approach*. Editors A. Gobbi, J. Espregueira-Mendes, J. G. Lane, and M. Karahan (Springer Berlin Heidelberg), 479–486. doi:10.1007/978-3-662-54181-4\_38
- Graham, A. D., Olof, S. N., Burke, M. J., Armstrong, J. P. K., Mikhailova, E. A., Nicholson, J. G., et al. (2017). High-Resolution Patterned Cellular Constructs by Droplet-Based 3D Printing. *Sci. Rep.* 7, 7004. doi:10.1038/s41598-017-06358-x
- Grogan, S. P., Dorthé, E. W., Glembocki, N. E., Gaul, F., and D’Lima, D. D. (2020). Cartilage Tissue Engineering Combining Microspheroid Building Blocks and Microneedle Arrays. *Connect. Tissue Res.* 61, 229–243. doi:10.1080/03008207.2019.1617280
- Gugioo, M. B., AmaralAbdelbaset-Ismail, A., Abdelbaset-Ismail, A., Aithal, H. P., Kinjavdekar, P., Kumar, G. S., et al. (2020). Allogeneic Mesenchymal Stem Cells and Growth Factors in Gel Scaffold Repair Osteochondral Defect in Rabbit. *Regenerative Med.* 15, 1261–1275. doi:10.2217/rme-2018-0138
- Guo, J. L., Diaz-Gomez, L., Xie, V. Y., Bittner, S. M., Jiang, E. Y., Wang, B., et al. (2021). Three-Dimensional Printing of Click Functionalized, Peptide Patterned Scaffolds for Osteochondral Tissue Engineering. *Bioprinting* 22, e00136. doi:10.1016/j.bprint.2021.e00136
- Han, F., Zhou, F., Yang, X., Zhao, J., Zhao, Y., and Yuan, X. (2015). A Pilot Study of Conically Graded Chitosan-Gelatin Hydrogel/PLGA Scaffold with Dual-Delivery of TGF-β1 and BMP-2 for Regeneration of Cartilage-Bone Interface. *J. Biomed. Mater. Res.* 103, 1344–1353. doi:10.1002/jbm.b.33314
- Hasan, M. S., Ahmed, I., Parsons, A. J., Rudd, C. D., Walker, G. S., and Scotchford, C. A. (2013). Investigating the Use of Coupling Agents to Improve the Interfacial Properties between a Resorbable Phosphate Glass and Poly(lactic Acid Matrix). *J. Biomater. Appl.* 28, 354–366. doi:10.1177/0885328212453634
- Henrotin, Y., Pesesse, L., and Sanchez, C. (2012). Subchondral Bone and Osteoarthritis: Biological and Cellular Aspects. *Osteoporos. Int.* 23 (Suppl. 8), 847–851. doi:10.1007/s00198-012-2162-z
- Hishimura, R., Onodera, T., Hontani, K., Baba, R., Homan, K., Matsubara, S., et al. (2019). Osteochondral Autograft Transplantation Technique Augmented by an Ultrapurified Alginate Gel Enhances Osteochondral Repair in a Rabbit Model. *Am. J. Sports Med.* 47, 468–478. doi:10.1177/0363546518817527
- Hoehel, S., Wirz, D., and Müller-Gerbl, M. (2012). Density and Strength Distribution in the Human Subchondral Bone Plate of the Patella. *Int. Orthopaedics (Sicot)* 36, 1827–1834. doi:10.1007/s00264-012-1545-2
- Hoemann, C., Lafantaisie-Favreau, C.-H., Lascau-Coman, V., Chen, G., and Guzmán-Morales, J. (2012). The Cartilage-Bone Interface. *J. Knee Surg.* 25, 085–098. doi:10.1055/s-0032-1319782
- Holmdahl, D. E., and Ingelmark, B. E. (1950). The Contact between the Articular Cartilage and the Medullary Cavities of the Bone. *Acta orthopaedica Scand.* 20, 156–165. doi:10.3109/17453675009043414
- Hossain, M. J., Noori-Dokht, H., Karnik, S., Alyafei, N., Joukar, A., Trippel, S. B., et al. (2020). Anisotropic Properties of Articular Cartilage in an Accelerated *In Vitro* Wear Test. *J. Mech. Behav. Biomed. Mater.* 109, 103834. doi:10.1016/j.jmbmm.2020.103834
- Hunter, D. J., March, L., and Chew, M. (2020). Osteoarthritis in 2020 and beyond: a Lancet Commission. *The Lancet* 396, 1711–1712. doi:10.1016/s0140-6736(20)32230-3
- Huotilainen, E., Salmi, M., and Lindahl, J. (2019). Three-dimensional Printed Surgical Templates for Fresh Cadaveric Osteochondral Allograft Surgery with Dimension Verification by Multivariate Computed Tomography Analysis. *The Knee* 26, 923–932. doi:10.1016/j.knee.2019.05.007
- Hwang, S. H., Kim, S. Y., Park, S. H., Choi, M. Y., Kang, H. W., Seol, Y.-J., et al. (2012). Human Inferior Turbinate. *Otolaryngol. Head Neck Surg.* 147, 568–574. doi:10.1177/0194599812447172
- Idaszek, J., Costantini, M., Karlsen, T. A., Jaroszewicz, J., Colosi, C., Testa, S., et al. (2019). 3D Bioprinting of Hydrogel Constructs with Cell and Material Gradients for the Regeneration of Full-Thickness Chondral Defect Using a Microfluidic Printing Head. *Biofabrication* 11, 044101. doi:10.1088/1758-5090/ab2622
- Jeyakumar, V., Niculescu-Morza, E., Bauer, C., Lacza, Z., and Nehrer, S. (2017). Platelet-Rich Plasma Supports Proliferation and Redifferentiation of Chondrocytes during *In Vitro* Expansion. *Front. Bioeng. Biotechnol.* 5, 75. doi:10.3389/fbioe.2017.00075
- Jiang, G., Li, S., Yu, K., He, B., Hong, J., Xu, T., et al. (2021). A 3D-Printed PRP-GelMA Hydrogel Promotes Osteochondral Regeneration through M2 Macrophage Polarization in a Rabbit Model. *Acta Biomater.* 128, 150–162. doi:10.1016/j.actbio.2021.04.010
- Jiang, Y., and Tuan, R. S. (2015). Origin and Function of Cartilage Stem/progenitor Cells in Osteoarthritis. *Nat. Rev. Rheumatolrheumatology* 11, 206–212. doi:10.1038/nrrheum.2014.200
- Johnson, K., Zhu, S., Tremblay, M. S., Payette, J. N., Wang, J., Bouchez, L. C., et al. (2012). A Stem Cell-Based Approach to Cartilage Repair. *Science* 336, 717–721. doi:10.1126/science.1215157
- Katta, J., Stapleton, T., Ingham, E., Jin, Z. M., and Fisher, J. (2008). The Effect of Glycosaminoglycan Depletion on the Friction and Deformation of Articular Cartilage. *Proc. Inst. Mech. Eng. H* 222, 1–11. doi:10.1243/09544119JHEM325
- Khorshidi, S., and Karkhaneh, A. (2021). A Hydrogel/particle Composite with Gradient in Oxygen Releasing Microparticle for Oxygenation of the Cartilage-To-Bone Interface: Modeling and Experimental Viewpoints. *Mater. Sci. Eng. C* 118, 111522. doi:10.1016/j.msec.2020.111522



- Kirsch, T., and von der Mark, K. (1991). Ca<sup>2+</sup>-binding Properties of Type X Collagen. *FEBS Lett.* 294, 149–152. doi:10.1016/0014-5793(91)81363-d
- Kosik-Kozioł, A., Costantini, M., Mróz, A., Idaszek, J., Heljak, M., Jaroszewicz, J., et al. (2019). 3D Bioprinted Hydrogel Model Incorporating  $\beta$ -tricalcium Phosphate for Calcified Cartilage Tissue Engineering. *Biofabrication* 11, 035016. doi:10.1088/1758-5090/ab15cb
- Krishnan, Y., and Grodzinsky, A. J. (2018). Cartilage Diseases. *Matrix Biol.* 71–72, 51–69. doi:10.1016/j.matbio.2018.05.005
- Kubosch, E. J., Lang, G., Furst, D., Kubosch, D., Izadpanah, K., Rolaufts, B., et al. (2018). The Potential for Synovium-Derived Stem Cells in Cartilage Repair. *Cscr* 13, 174–184. doi:10.2174/1574888x12666171002111026
- Kumar, H., and Kim, K. (2020). Stereolithography 3D Bioprinting. *Clifton, N.J.* 2140, 93–108. doi:10.1007/978-1-0716-0520-2\_6
- Lee, M., Rizzo, R., Surman, F., and Zenobi-Wong, M. (2020a). Guiding Lights: Tissue Bioprinting Using Photoactivated Materials. *Chem. Rev.* 120, 10950–11027. doi:10.1021/acs.chemrev.0c00077
- Lee, S. S., Kim, J. H., Jeong, J., Kim, S. H. L., Koh, R. H., Kim, I., et al. (2020b). Sequential Growth Factor Releasing Double Cryogel System for Enhanced Bone Regeneration. *Biomaterials* 257, 120223. doi:10.1016/j.biomaterials.2020.120223
- Lepage, S. I. M., Sharma, R., Dukoff, D., Stalker, L., LaMarre, J., and Koch, T. G. (2019). Gene Expression Profile Is Different between Intact and Enzymatically Digested Equine Articular Cartilage. *Cartilage* 12, 222–225. doi:10.1177/1947603519833148
- Li, C., Armstrong, J. P., Pence, I. J., Kit-Anan, W., Puetzer, J. L., Correia Carreira, S., et al. (2018a). Glycosylated Superparamagnetic Nanoparticle Gradients for Osteochondral Tissue Engineering. *Biomaterials* 176, 24–33. doi:10.1016/j.biomaterials.2018.05.029
- Li, K., Wang, D., Zhang, F., Wang, X., Chen, H., Yu, A., et al. (2021). Tip-Viscid Electrohydrodynamic Jet 3D Printing of Composite Osteochondral Scaffold. *Nanomaterials* 11, 2694. doi:10.3390/nano11102694
- Li, L., Yu, F., Shi, J., Shen, S., Teng, H., Yang, J., et al. (2017). *In Situ* repair of Bone and Cartilage Defects Using 3D Scanning and 3D Printing. *Sci. Rep.* 7, 9416. doi:10.1038/s41598-017-10060-3
- Li, X., Liu, B., Pei, B., Chen, J., Zhou, D., Peng, J., et al. (2020). Inkjet Bioprinting of Biomaterials. *Chem. Rev.* 120, 10793–10833. doi:10.1021/acs.chemrev.0c00008
- Li, Z., Jia, S., Xiong, Z., Long, Q., Yan, S., Hao, F., et al. (2018b). 3D-printed Scaffolds with Calcified Layer for Osteochondral Tissue Engineering. *J. Biosci. Bioeng.* 126, 389–396. doi:10.1016/j.jbiosc.2018.03.014
- Liaw, C.-Y., and Guvendiren, M. (2017). Current and Emerging Applications of 3D Printing in Medicine. *Biofabrication* 9, 024102. doi:10.1088/1758-5090/aa7279
- Lin, R., Deng, C., Li, X., Liu, Y., Zhang, M., Qin, C., et al. (2019). Copper-incorporated Bioactive Glass-Ceramics Inducing Anti-inflammatory Phenotype and Regeneration of Cartilage/bone Interface. *Theranostics* 9, 6300–6313. doi:10.7150/tno.36120
- Lin, W., Xu, L., and Li, G. (2020). Molecular Insights into Lysyl Oxidases in Cartilage Regeneration and Rejuvenation. *Front. Bioeng. Biotechnol.* 8, 359. doi:10.3389/fbioe.2020.00359
- Lin, X., Chen, J., Qiu, P., Zhang, Q., Wang, S., Su, M., et al. (2018). Biphasic Hierarchical Extracellular Matrix Scaffold for Osteochondral Defect Regeneration. *Osteoarthritis and cartilage* 26, 433–444. doi:10.1016/j.joca.2017.12.001
- Lin, X., Zhang, L., and Duan, B. (2021). Polyphenol-mediated Chitin Self-Assembly for Constructing a Fully Naturally Resourced Hydrogel with High Strength and Toughness. *Mater. Horiz.* 8, 2503–2512. doi:10.1039/D1MH00878A
- Lipskas, J., Deep, K., and Yao, W. (2019). Robotic-Assisted 3D Bio-Printing for Repairing Bone and Cartilage Defects through a Minimally Invasive Approach. *Sci. Rep.* 9, 3746. doi:10.1038/s41598-019-38972-2
- Liu, B., Zhao, Y., Zhu, T., Gao, S., Ye, K., Zhou, F., et al. (2020). Biphasic Double-Network Hydrogel with Compartmentalized Loading of Bioactive Glass for Osteochondral Defect Repair. *Front. Bioeng. Biotechnol.* 8, 752. doi:10.3389/fbioe.2020.00752
- Loeser, R. F., Goldring, S. R., Scanzello, C. R., and Goldring, M. B. (2012). Osteoarthritis: a Disease of the Joint as an Organ. *Arthritis Rheum.* 64, 1697–1707. doi:10.1002/art.34453
- Luo, Y., Sinkeviciute, D., He, Y., Karsdal, M., Henrotin, Y., Mobasheri, A., et al. (2017). The Minor Collagens in Articular Cartilage. *Protein Cell* 8, 560–572. doi:10.1007/s13238-017-0377-7
- Luong, D. X., Subramanian, A. K., Silva, G. A. L., Yoon, J., Cofer, S., Yang, K., et al. (2018). Laminated Object Manufacturing of 3D-Printed Laser-Induced Graphene Foams. *Advanced materials (Deerfield Beach, Fla.)* 30, e1707416. doi:10.1002/adma.201707416
- Lydon, H., Getgood, A., and Henson, F. M. D. (2019). Healing of Osteochondral Defects via Endochondral Ossification in an Ovine Model. *Cartilage* 10, 94–101. doi:10.1177/1947603517713818
- Ma, H., Feng, C., Chang, J., and Wu, C. (2018). 3D-printed Bioceramic Scaffolds: From Bone Tissue Engineering to Tumor Therapy. *Acta Biomater.* 79, 37–59. doi:10.1016/j.actbio.2018.08.026
- Ma, K., Zhao, T., Yang, L., Wang, P., Jin, J., Teng, H., et al. (2020). Application of Robotic-Assisted *In Situ* 3D Printing in Cartilage Regeneration with HAMA Hydrogel: An *In Vivo* Study. *J. Adv. Res.* 23, 123–132. doi:10.1016/j.jare.2020.01.010
- Madry, H., van Dijk, C. N., and Mueller-Gerbl, M. (2010). The Basic Science of the Subchondral Bone. *Knee Surg. Sports Traumatol. Arthrosc.* 18, 419–433. doi:10.1007/s00167-010-1054-z
- Mancini, I. A. D., Schmidt, S., Brommer, H., Pouran, B., Schäfer, S., Tessmar, J., et al. (2020). A Composite hydrogel-3D Printed Thermoplast Osteochondral Anchor as Example for a Zonal Approach to Cartilage Repair: *In Vivo* Performance in a Long-Term Equine Model. *Biofabrication* 12, 035028. doi:10.1088/1758-5090/ab94ce
- Mandl, L. A. (2019). Osteoarthritis Year in Review 2018: Clinical. *Osteoarthritis and cartilage* 27, 359–364. doi:10.1016/j.joca.2018.11.001
- Mano, J. F., and Reis, R. L. (2007). Osteochondral Defects: Present Situation and Tissue Engineering Approaches. *J. Tissue Eng. Regen. Med.* 1, 261–273. doi:10.1002/term.37
- Manoukian, O. S., Dieck, C., Milne, T., Dealy, C. N., Rudraiah, S., and Kumbar, S. G. (2018). Nanomaterials/Nanocomposites for Osteochondral Tissue. *Adv. Exp. Med. Biol.* 1058, 79–95. doi:10.1007/978-3-319-76711-6\_4
- Mansfield, J. C., Bell, J. S., and Winlove, C. P. (2015). The Micromechanics of the Superficial Zone of Articular Cartilage. *Osteoarthritis and cartilage* 23, 1806–1816. doi:10.1016/j.joca.2015.05.030
- Mansfield, J. C., and Peter Winlove, C. (2012). A Multi-Modal Multiphoton Investigation of Microstructure in the Deep Zone and Calcified Cartilage. *J. Anat.* 220, 405–416. doi:10.1111/j.1469-7580.2012.01479.x
- Marques, C. F., Diogo, G. S., Pina, S., Oliveira, J. M., Silva, T. H., and Reis, R. L. (2019). Collagen-based Bioinks for Hard Tissue Engineering Applications: a Comprehensive Review. *J. Mater. Sci. Mater. Med.* 30, 32. doi:10.1007/s10856-019-6234-x
- Mellor, L. F., Huebner, P., Cai, S., Mohiti-Asli, M., Taylor, M. A., Spang, J., et al. (2017). Fabrication and Evaluation of Electrospun, 3D-Bioplot, and Combination of Electrospun/3D-Bioplot Scaffolds for Tissue Engineering Applications. *Biomed. Res. Int.* 2017, 1–9. doi:10.1155/2017/6956794
- Mellor, L. F., Nordberg, R. C., Huebner, P., Mohiti-Asli, M., Taylor, M. A., Efrid, W., et al. (2020). Investigation of Multiphasic 3D-bioplot Scaffolds for Site-specific Chondrogenic and Osteogenic Differentiation of Human Adipose-derived Stem Cells for Osteochondral Tissue Engineering Applications. *J. Biomed. Mater. Res.* 108, 2017–2030. doi:10.1002/jbm.b.34542
- Milz, S., and Putz, R. (1994). Quantitative Morphology of the Subchondral Plate of the Tibial Plateau. *J. Anat.* 185 ( Pt 1) (Pt 1), 103–110.
- Moatshe, G., and LaPrade, R. F. (2020). Editorial Commentary: Knee Lateral Femoral Osteochondral Allografts Are Not Recommended for Medial Femoral Condylar Defects: If the Shoe Doesn't Fit, Don't Wear It!. *Arthroscopy : the journal of arthroscopic & related surgery : official publication of the Arthroscopy Association of North America and the International Arthroscopy Association* 36, 2909–2910. doi:10.1016/j.arthro.2020.09.029
- Mora-Boza, A., and Lopez-Donaire, M. L. (2018). Preparation of Polymeric and Composite Scaffolds by 3D Bioprinting. *Adv. Exp. Med. Biol.* 1058, 221–245. doi:10.1007/978-3-319-76711-6\_10
- Moshagh, P. R., Korthagen, N. M., van Rijen, M. H. P., Castelein, R. M., Zadpoor, A. A., and Weinans, H. (2018). Effects of Non-enzymatic Glycation on the Micro- and Nano-Mechanics of Articular Cartilage. *J. Mech. Behav. Biomed. Mater.* 77, 551–556. doi:10.1016/j.jmbm.2017.09.035

- Muhammad, S. A., Nordin, N., Hussin, P., Mehat, M. Z., Tan, S. W., and Fakurazi, S. (2019). Optimization of Protocol for Isolation of Chondrocytes from Human Articular Cartilage. *Cartilage* 13, 872S–884S. doi:10.1177/1947603519876333
- Murphy, S. V., and Atala, A. (2014). 3D Bioprinting of Tissues and Organs. *Nat. Biotechnol.* 32, 773–785. doi:10.1038/nbt.2958
- Naskar, D., Sapru, S., Ghosh, A. K., Reis, R. L., Dey, T., and Kundu, S. C. (2021). Nonmulberry Silk Proteins: Multipurpose Ingredient in Bio-Functional Assembly. *Biomed. Mater.* 16, 062002. doi:10.1088/1748-605X/ac20a0
- Natarajan, A. B. M., Sivasdas, V. P. D., and Nair, P. D. P. D. (2021). 3D-printed Biphasic Scaffolds for the Simultaneous Regeneration of Osteochondral Tissues. *Biomed. Mater.* 16, 054102. doi:10.1088/1748-605X/ac14cb
- Ni, T., Liu, M., Zhang, Y., Cao, Y., and Pei, R. (2020). 3D Bioprinting of Bone Marrow Mesenchymal Stem Cell-Laden Silk Fibroin Double Network Scaffolds for Cartilage Tissue Repair. *Bioconj. Chem.* 31, 1938–1947. doi:10.1021/acs.bioconjchem.0c00298
- Nichols, D. A., Sondh, I. S., Litte, S. R., Zunino, P., and Gottardi, R. (2018). Design and Validation of an Osteochondral Bioreactor for the Screening of Treatments for Osteoarthritis. *Biomed. Microdevices* 20, 18. doi:10.1007/s10544-018-0264-x
- Nordberg, R. C., Huebner, P., Schuchard, K. G., Mellor, L. F., Shirwaiker, R. A., Lobo, E. G., et al. (2021). The Evaluation of a Multiphasic 3D -bioprinted Scaffold Seeded with Adipose Derived Stem Cells to Repair Osteochondral Defects in a Porcine Model. *J. Biomed. Mater. Res.* 109, 2246–2258. doi:10.1002/jbm.b.34886
- Nulty, J., Burdis, R., and Kelly, D. J. (2021). Biofabrication of Prevascularised Hypertrophic Cartilage Microtissues for Bone Tissue Engineering. *Front. Bioeng. Biotechnol.* 9, 661989. doi:10.3389/fbioe.2021.661989
- Okoroha, K. R., Evans, T. J., Stephens, J. P., Makhni, E. C., and Moutzouras, V. (2018). Three-dimensional Printing Improves Osteochondral Allograft Placement in Complex Cases. *Knee Surg. Sports Traumatol. Arthrosc.* 26, 3601–3605. doi:10.1007/s00167-018-4849-y
- Outerbridge, R. E. (1964). Further Studies on the Etiology of Chondromalacia Patellae. *The J. Bone Jt. Surg. Br. volume* 46-B, 179–190. doi:10.1302/0301-620x.46b2.179
- Outerbridge, R. E. (1961). The Etiology of Chondromalacia Patellae. *The J. Bone Jt. Surg. Br. volume* British volume 43-b, 752–757. doi:10.1302/0301-620x.43b4.752
- Ozolat, I. T., and Hospodiuk, M. (2016). Current Advances and Future Perspectives in Extrusion-Based Bioprinting. *Biomaterials* 76, 321–343. doi:10.1016/j.biomaterials.2015.10.076
- Perka, C., Spitzer, R.-S., Lindenhayn, K., Sittlinger, M., and Schultz, O. (2000). Matrix-mixed Culture: New Methodology for Chondrocyte Culture and Preparation of Cartilage Transplants. *J. Biomed. Mater. Res.* 49, 305–311. doi:10.1002/(sici)1097-4636(20000305)49:3<305:aid-jbm2>3.0.co;2-9
- Pina, S., Rebelo, R., Correlo, V. M., Oliveira, J. M., and Reis, R. L. (2018). Bioceramics for Osteochondral Tissue Engineering and Regeneration. *Adv. Exp. Med. Biol.* 1058, 53–75. doi:10.1007/978-3-319-76711-6\_3
- Radhakrishnan, J., Manigandan, A., Chinnaswamy, P., Subramanian, A., and Sethuraman, S. (2018). Gradient Nano-Engineered *In Situ* Forming Composite Hydrogel for Osteochondral Regeneration. *Biomaterials* 162, 82–98. doi:10.1016/j.biomaterials.2018.01.056
- Rajasekharan, A. K., Bordes, R., Sandström, C., Ekh, M., and Andersson, M. (2017). Hierarchical and Heterogeneous Bioinspired Composites-Merging Molecular Self-Assembly with Additive Manufacturing. *Small* 13, 1700550. doi:10.1002/smll.201700550
- Ravichandran, A., Liu, Y., and Teoh, S.-H. (2018). Review: Bioreactor Design towards Generation of Relevant Engineered Tissues: Focus on Clinical Translation. *J. Tissue Eng. Regen. Med.* 12, e7–e22. doi:10.1002/term.2270
- Reed, S., Lau, G., Delattre, B., Lopez, D. D., Tomsia, A. P., and Wu, B. M. (2016). Macro- and Micro-designed Chitosan-Alginate Scaffold Architecture by Three-Dimensional Printing and Directional Freezing. *Biofabrication* 8, 015003. doi:10.1088/1758-5090/8/1/015003
- Rolauffs, B., Muehleman, C., Li, J., Kurz, B., Kuettner, K. E., Frank, E., et al. (2010). Vulnerability of the Superficial Zone of Immature Articular Cartilage to Compressive Injury. *Arthritis Rheum.* 62, 3016–3027. doi:10.1002/art.27610
- Russo, R., Guastafierro, A., Della Rotonda, G., Viglione, S., Ciccirelli, M., Fiorentino, F., et al. (2021). Osteochondral Allograft Transplantation for Complex Distal Humeral Fractures Assisted by 3D Computer Planning and Printing Technology: Technical Note. *Eur. J. Orthop. Surg. Traumatol.* 1, 1. doi:10.1007/s00590-021-03118-6
- Sacitharan, P. K. (2019). Ageing and Osteoarthritis. *Sub-cellular Biochem.* 91, 123–159. doi:10.1007/978-981-13-3681-2\_6
- Saha, S., Kundu, B., Kirkham, J., Wood, D., Kundu, S. C., and Yang, X. B. (2013). Osteochondral Tissue Engineering In Vivo: a Comparative Study Using Layered Silk Fibroin Scaffolds From Mulberry and Nonmulberry Silkworms. *PloS one* 8, e80004. doi:10.1371/journal.pone.0080004
- Schoonraad, S. A., Fischenich, K. M., Eckstein, K. N., Crespo-Cuevas, V., Savard, L. M., Muralidharan, A., et al. (2021). Biomimetic and Mechanically Supportive 3D Printed Scaffolds for Cartilage and Osteochondral Tissue Engineering Using Photopolymers and Digital Light Processing. *Biofabrication* 13, 044106. doi:10.1088/1758-5090/ac23ab
- Schuette, H. B., Kraeutler, M. J., Schrock, J. B., and McCarty, E. C. (2021). Primary Autologous Chondrocyte Implantation of the Knee versus Autologous Chondrocyte Implantation after Failed Marrow Stimulation: A Systematic Review. *Am. J. Sports Med.* 49, 2536–2541. doi:10.1177/0363546520968284
- Schweiger, J., Beuer, F., Stimmelmayer, M., Edelhoff, D., Magne, P., and Güth, J. F. (2016). Histo-anatomic 3D Printing of Dental Structures. *Br. Dent J.* 221, 555–560. doi:10.1038/sj.bdj.2016.815
- Seok, J. M., Rajangam, T., Jeong, J. E., Cheong, S., Joo, S. M., Oh, S. J., et al. (2020). Fabrication of 3D Plotted Scaffold with Microporous Strands for Bone Tissue Engineering. *J. Mater. Chem. B* 8, 951–960. doi:10.1039/c9tb02360g
- Shapiro, F., Koide, S., and Glimcher, M. J. (1993). Cell Origin and Differentiation in the Repair of Full-Thickness Defects of Articular cartilageThe Journal of Bone and Joint Surgery. *J. Bone Jt. Surg.* 75, 532–553. doi:10.2106/00004623-199304000-00009
- Sharma, A., Jagga, S., Lee, S.-S., and Nam, J.-S. (2013). Interplay between Cartilage and Subchondral Bone Contributing to Pathogenesis of Osteoarthritis. *Ijms* 14, 19805–19830. doi:10.3390/ijms141019805
- Shavandi, A., Silva, T. H., Bekhit, A. A., and Bekhit, A. E.-D. A. (2017). Keratin: Dissolution, Extraction and Biomedical Application. *Biomater. Sci.* 5, 1699–1735. doi:10.1039/c7bm00411g
- Shim, J.-H., Jang, K.-M., Hahn, S. K., Park, J. Y., Jung, H., Oh, K., et al. (2016). Three-dimensional Bioprinting of Multilayered Constructs Containing Human Mesenchymal Stromal Cells for Osteochondral Tissue Regeneration in the Rabbit Knee Joint. *Biofabrication* 8, 014102. doi:10.1088/1758-5090/8/1/014102
- Shouir, K. R., El-Desouky, N., Rashad, M. M., Ahmed, M. K., Janowska, I., and El-Kemary, M. (2021). Chitosan Based-Nanoparticles and Nanocapsules: Overview, Physicochemical Features, Applications of a Nanofibrous Scaffold, and Bioprinting. *Int. J. Biol. Macromolecules* 167, 1176–1197. doi:10.1016/j.ijbiomac.2020.11.072
- Singh, B., Modica-Napolitano, J. S., and Singh, K. K. (2017). Defining the Momio: Promiscuous Information Transfer by mobile Mitochondria and the Mitochondrial Genome. *Semin. Cancer Biol.* 47, 1–17. doi:10.1016/j.semcancer.2017.05.004
- Slattery, C., and Kweon, C. Y. (2018). Classifications in Brief: Outerbridge Classification of Chondral Lesions. *Clin. Orthop. Relat. Res.* 476, 2101–2104. doi:10.1007/s11999-0000000000000255
- Sligeryte, K., Botto, L., Lee, D. A., and Knight, M. M. (2016). Chondrocyte Dedifferentiation Increases Cell Stiffness by Strengthening Membrane-Actin Adhesion. *Osteoarthritis and cartilage* 24, 912–920. doi:10.1016/j.joca.2015.12.007
- Sophia Fox, A. J., Bedi, A., and Rodeo, S. A. (2009). The Basic Science of Articular Cartilage: Structure, Composition, and Function. *Sports health* 1, 461–468. doi:10.1177/1941738109350438
- Stegen, S., Laperre, K., Eelen, G., Rinaldi, G., Fraisl, P., Torrekens, S., et al. (2019). HIF-1α Metabolically Controls Collagen Synthesis and Modification in Chondrocytes. *Nature* 565, 511–515. doi:10.1038/s41586-019-0874-3
- Takahashi, T., Sato, M., Toyoda, E., Maehara, M., Takizawa, D., Maruki, H., et al. (2018). Rabbit Xenogeneic Transplantation Model for Evaluating Human Chondrocyte Sheets Used in Articular Cartilage Repair. *J. Tissue Eng. Regen. Med.* 12, 2067–2076. doi:10.1002/term.2741
- Tang, Z., Chulanova, E., Küllmer, M., Winter, A., Picker, J., Neumann, C., et al. (2021). Photoactive Ultrathin Molecular Nanosheets with Reversible Lanthanide Binding Terpyridine Centers. *Nanoscale* 13, 20583–20591. doi:10.1039/d1nr05430a

- Thorp, H., Kim, K., Kondo, M., Maak, T., Grainger, D. W., and Okano, T. (2021). Trends in Articular Cartilage Tissue Engineering: 3D Mesenchymal Stem Cell Sheets as Candidates for Engineered Hyaline-like Cartilage. *Cells* 10, 643. doi:10.3390/cells10030643
- Thunsiri, K., Pitjarnit, S., Pothacharoen, P., Pruksakorn, D., Nakkiew, W., and Wattanachariya, W. (2020). The 3D-Printed Bilayer's Bioactive-Biomaterials Scaffold for Full-Thickness Articular Cartilage Defects Treatment. *Materials* 13, 3417. doi:10.3390/ma13153417
- Tuerlings, M., Hoolwerff, M., Houtman, E., Suchiman, E. H. E. D., Lakenberg, N., Mei, H., et al. (2021). RNA Sequencing Reveals Interacting Key Determinants of Osteoarthritis Acting in Subchondral Bone and Articular Cartilage: Identification of IL11 and CHADL as Attractive Treatment Targets. *Arthritis Rheumatol.* 73, 789–799. doi:10.1002/art.41600
- Turnbull, G., Clarke, J., Picard, F., Riches, P., Jia, L., Han, F., et al. (2018). 3D Bioactive Composite Scaffolds for Bone Tissue Engineering. *Bioactive Mater.* 3, 278–314. doi:10.1016/j.bioactmat.2017.10.001
- Vainieri, M. L., Lolli, A., Kops, N., D'Atri, D., Eglin, D., Yayon, A., et al. (2020). Evaluation of Biomimetic Hyaluronic-Based Hydrogels with Enhanced Endogenous Cell Recruitment and Cartilage Matrix Formation. *Acta Biomater.* 101, 293–303. doi:10.1016/j.actbio.2019.11.015
- van den Borne, M. P. J., Rajmakers, N. J. H., Vanlauwe, J., Victor, J., de Jong, S. N., Bellemans, J., et al. (2007). International Cartilage Repair Society (ICRS) and Oswestry Macroscopic Cartilage Evaluation Scores Validated for Use in Autologous Chondrocyte Implantation (ACI) and Microfracture. *Osteoarthritis and cartilage* 15, 1397–1402. doi:10.1016/j.joca.2007.05.005
- Vasiliadis, A. V., and Galanis, N. (2020). Human Bone Marrow-Derived Mesenchymal Stem Cells from Different Bone Sources: a Panorama. *Stem Cell Investig* 7, 15. doi:10.21037/sci-2020-013
- Ventola, C. L. (2014). Medical Applications for 3D Printing: Current and Projected Uses. *P T* 39, 704–711.
- Wang, C., Lai, J., Li, K., Zhu, S., Lu, B., Liu, J., et al. (2021). Cryogenic 3D Printing of Dual-Delivery Scaffolds for Improved Bone Regeneration with Enhanced Vascularization. *Bioactive Mater.* 6, 137–145. doi:10.1016/j.bioactmat.2020.07.007
- Wang, C., Yue, H., Huang, W., Lin, X., Xie, X., He, Z., et al. (2020). Cryogenic 3D Printing of Heterogeneous Scaffolds with Gradient Mechanical Strengths and Spatial Delivery of Osteogenic peptide/TGF- $\beta$ 1 for Osteochondral Tissue Regeneration. *Biofabrication* 12, 025030. doi:10.1088/1758-5090/ab7ab5
- Wen, Y., Xun, S., Haoye, M., Baichuan, S., Peng, C., Xuejian, L., et al. (2017). 3D Printed Porous Ceramic Scaffolds for Bone Tissue Engineering: a Review. *Biomater. Sci.* 5, 1690–1698. doi:10.1039/c7bm00315c
- Wu, T., Liu, C., and Hu, X. (2022). Enzymatic Synthesis, Characterization and Properties of the Protein-Polysaccharide Conjugate: A Review. *Food Chem.* 372, 131332. doi:10.1016/j.foodchem.2021.131332
- Wuest, S., Calio, M., Wernas, T., Tanner, S., Giger-Lange, C., Wyss, F., et al. (2018). Influence of Mechanical Unloading on Articular Chondrocyte Dedifferentiation. *Ijms* 19, 1289. doi:10.3390/ijms19051289
- Xuan, F., Yano, F., Mori, D., Chijimatsu, R., Maenohara, Y., Nakamoto, H., et al. (2019). Wnt/ $\beta$ -catenin Signaling Contributes to Articular Cartilage Homeostasis through Lubricin Induction in the Superficial Zone. *Arthritis Res. Ther.* 21, 247. doi:10.1186/s13075-019-2041-5
- Xue, R., Chung, B., Tamaddon, M., Carr, J., Liu, C., and Cartmell, S. H. (2019). Osteochondral Tissue Coculture: An *In Vitro* and *In Silico* Approach. *Biotechnol. Bioeng.* 116, 3112–3123. doi:10.1002/bit.27127
- Yamasaki, A., Kunitomi, Y., Murata, D., Sunaga, T., Kuramoto, T., Sogawa, T., et al. (2019). Osteochondral Regeneration Using Constructs of Mesenchymal Stem Cells Made by Bio Three-dimensional Printing in Mini-pigs. *J. Orthop. Res.* 37, 1398–1408. doi:10.1002/jor.24206
- Yang, P. J., and Temenoff, J. S. (2009). Engineering Orthopedic Tissue Interfaces. *Tissue Eng. B: Rev.* 15, 127–141. doi:10.1089/ten.teb.2008.0371
- Yang, Y., Lin, H., Shen, H., Wang, B., Lei, G., and Tuan, R. S. (2018). Mesenchymal Stem Cell-Derived Extracellular Matrix Enhances Chondrogenic Phenotype and Cartilage Formation by Encapsulated Chondrocytes *In Vitro* and *In Vivo*. *Acta Biomater.* 69, 71–82. doi:10.1016/j.actbio.2017.12.043
- Yontar, N. S., Aslan, L., Can, A., and Ogut, T. (2019). One Step Treatment of Talus Osteochondral Lesions with Microfracture and Cell Free Hyaluronic Acid Based Scaffold Combination. *Acta orthopaedica et traumatologica turcica* 53, 372–375. doi:10.1016/j.aott.2019.04.002
- You, F., Chen, X., Cooper, D. M. L., Chang, T., and Eames, B. F. (2018). Homogeneous Hydroxyapatite/alginate Composite Hydrogel Promotes Calcified Cartilage Matrix Deposition with Potential for Three-Dimensional Bioprinting. *Biofabrication* 11, 015015. doi:10.1088/1758-5090/aaf44a
- Yu, J., Lee, S., Choi, S., Kim, K. K., Ryu, B., Kim, C.-Y., et al. (2020). Fabrication of a Polycaprolactone/Alginate Bipartite Hybrid Scaffold for Osteochondral Tissue Using a Three-Dimensional Bioprinting System. *Polymers* 12, 2203. doi:10.3390/polym12102203
- Yu, X., Zhao, T., Qi, Y., Luo, J., Fang, J., Yang, X., et al. (2018). *In Vitro* Chondrocyte Responses in Mg-Doped Wollastonite/Hydrogel Composite Scaffolds for Osteochondral Interface Regeneration. *Sci. Rep.* 8, 17911. doi:10.1038/s41598-018-36200-x
- Zeng, H., Pathak, J. L., Shi, Y., Ran, J., Liang, L., Yan, Q., et al. (2020). Indirect Selective Laser Sintering-Printed Microporous Biphasic Calcium Phosphate Scaffold Promotes Endogenous Bone Regeneration via Activation of ERK1/2 Signaling. *Biofabrication* 12, 025032. doi:10.1088/1758-5090/ab78ed
- Zhang, B., Guo, L., Chen, H., Ventikos, Y., Narayan, R. J., and Huang, J. (2020a). Finite Element Evaluations of the Mechanical Properties of Polycaprolactone/hydroxyapatite Scaffolds by Direct Ink Writing: Effects of Pore Geometry. *J. Mech. Behav. Biomed. Mater.* 104, 103665. doi:10.1016/j.jmbbm.2020.103665
- Zhang, B., Huang, J., and Narayan, R. J. (2020b). Gradient Scaffolds for Osteochondral Tissue Engineering and Regeneration. *J. Mater. Chem. B* 8, 8149–8170. doi:10.1039/d0tb00688b
- Zhao, Y., Zhao, X., Zhang, R., Huang, Y., Li, Y., Shan, M., et al. (2020). Cartilage Extracellular Matrix Scaffold with Kartogenin-Encapsulated PLGA Microspheres for Cartilage Regeneration. *Front. Bioeng. Biotechnol.* 8, 600103. doi:10.3389/fbioe.2020.600103
- Zheng, P., Hu, X., Lou, Y., and Tang, K. (2019). A Rabbit Model of Osteochondral Regeneration Using Three-Dimensional Printed Polycaprolactone-Hydroxyapatite Scaffolds Coated with Umbilical Cord Blood Mesenchymal Stem Cells and Chondrocytes. *Med. Sci. Monit.* 25, 7361–7369. doi:10.12659/MSM.915441
- Zhou, B., Chen, D., Xu, H., and Zhang, X. (2017). Proliferation of Rabbit Chondrocyte and Inhibition of IL-1 $\beta$ -induced Apoptosis through MEK/ERK Signaling by Statins. *In Vitro Cell.Dev.Biol.-Animal* 53, 124–131. doi:10.1007/s11626-016-0086-1
- Zhou, L., Gjym, V. O., Malda, J., Stoddart, M. J., Lai, Y., Richards, R. G., et al. (2020). Innovative Tissue-Engineered Strategies for Osteochondral Defect Repair and Regeneration: Current Progress and Challenges. *Adv. Healthc. Mater.* 9, 2001008. doi:10.1002/adhm.202001008
- Zhou, X., Esworthy, T., Lee, S.-J., Miao, S., Cui, H., Plesiniak, M., et al. (2019). 3D Printed Scaffolds with Hierarchical Biomimetic Structure for Osteochondral Regeneration. *Nanomedicine: Nanotechnology, Biol. Med.* 19, 58–70. doi:10.1016/j.nano.2019.04.002
- Zhu, S., Chen, P., Chen, Y., Li, M., Chen, C., and Lu, H. (2020). 3D-Printed Extracellular Matrix/Polyethylene Glycol Diacrylate Hydrogel Incorporating the Anti-inflammatory Phytochemical Honokiol for Regeneration of Osteochondral Defects. *Am. J. Sports Med.* 48, 2808–2818. doi:10.1177/0363546520941842

**Conflict of Interest:** The authors declare that the research was conducted in the absence of any commercial or financial relationships that could be construed as a potential conflict of interest.

**Publisher's Note:** All claims expressed in this article are solely those of the authors and do not necessarily represent those of their affiliated organizations, or those of the publisher, the editors and the reviewers. Any product that may be evaluated in this article, or claim that may be made by its manufacturer, is not guaranteed or endorsed by the publisher.

Copyright © 2022 Xu, Ji, Jiao, Zheng, Hong, Tang, Zhang, Qu and Yue. This is an open-access article distributed under the terms of the Creative Commons Attribution License (CC BY). The use, distribution or reproduction in other forums is permitted, provided the original author(s) and the copyright owner(s) are credited and that the original publication in this journal is cited, in accordance with accepted academic practice. No use, distribution or reproduction is permitted which does not comply with these terms.



# A Novel Adjustable EndoButton Fixation Assisted by 3D Printing Technology for Tibiofibular Syndesmosis Injury: A Biomechanical Study

Lei Zhang<sup>1,2,3,4†</sup>, Junjie Xu<sup>5†</sup>, Xiangyu Tang<sup>5†</sup>, Xin Zhou<sup>1,2,3,4</sup>, Bingkun Li<sup>1,2,3</sup> and Guoyou Wang<sup>1,2,3,4\*</sup>

<sup>1</sup>Department of Orthopedics, The Affiliated Traditional Chinese Medicine Hospital of Southwest Medical University, Luzhou, China, <sup>2</sup>Center for Orthopedic Diseases Research, The Affiliated Traditional Chinese Medicine Hospital of Southwest Medical University, Luzhou, China, <sup>3</sup>Specialist Workstation in Luzhou, Luzhou, China, <sup>4</sup>Clinical Base of The Affiliated Traditional Chinese Medicine Hospital of Southwest Medical University, Guangdong Province Medical 3D Printing Application Transformation Engineering Technology Research Center, Luzhou, China, <sup>5</sup>School of Clinical Medicine, Southwest Medical University, Luzhou, China

## OPEN ACCESS

### Edited by:

Changchun Zhou,  
Sichuan University, China

### Reviewed by:

Elisabetta M. Zanetti,  
University of Perugia, Italy  
Zhihong Dong,  
Chengdu University, China  
Yu-Cong Zou,  
Southern Medical University, China

### \*Correspondence:

Guoyou Wang  
wang-guoyou1981@163.com

<sup>†</sup>These authors have contributed  
equally to this work and share first  
authorship

### Specialty section:

This article was submitted to  
Biomaterials,  
a section of the journal  
Frontiers in Bioengineering and  
Biotechnology

**Received:** 12 October 2021

**Accepted:** 21 February 2022

**Published:** 10 March 2022

### Citation:

Zhang L, Xu J, Tang X, Zhou X, Li B and  
Wang G (2022) A Novel Adjustable  
EndoButton Fixation Assisted by 3D  
Printing Technology for Tibiofibular  
Syndesmosis Injury: A  
Biomechanical Study.  
Front. Bioeng. Biotechnol. 10:793866.  
doi: 10.3389/fbioe.2022.793866

**Purpose:** The recommendations for surgical fixation of tibiofibular syndesmosis injuries are increasingly challenging for many clinical orthopedists, as international consensus has not been published for the optimal treatment of the injury. Thus, we have created a 3D-printed navigation template for a precise bone tunnel and a novel adjustable EndoButton fixation (NAE) for the ideal treatment. The purpose of this research was to evaluate the accuracy of the 3D-printed navigation template and explore the biomechanical performance of the NAE technique by comparing it with the intact syndesmosis, screw technique, and TightRope (TR) technique.

**Methods:** Twenty-four human cadaveric legs were randomly allocated to four groups: the NAE group ( $n = 6$ ), TR group ( $n = 6$ ), screw group ( $n = 6$ ), and intact group ( $n = 6$ ). A personalized navigation template based on computed tomography scans was designed, and 3D printing models were generated for the distal tibiofibular syndesmosis. The NAE, TR, and screw group were performed via 3D-printed navigation template, respectively. All groups were tested under increasing loading forces including axial loading (from 100 N to 700 N) and torsional loading (from 1 N to 5 N), which were performed in different ankle positions. The displacements of the tibiofibular syndesmosis were analyzed using the Bose Electroforce 3510-AT biomechanical testing equipment.

**Results:** Surgical fixations were conducted successfully through a 3D-printed navigation template. Both in axial or torsional loading experiments, no statistically significant difference was observed in the displacements among the NAE, TR, and intact groups in most situations ( $p > 0.05$ ), whereas the screw group demonstrated obviously smaller displacements than the abovementioned three groups ( $p < 0.05$ ).

**Conclusion:** The 3D printing technology application may become beneficial and favorable for locating and making the bone tunnel. Also, the NAE fixation provides the performance



of complete ligaments; it also restores physiologic micromotion and avoids insufficient or excessive reduction when compared to the TR and screw technique. This may offer a new fixation for the treatment of tibiofibular syndesmosis injuries that is desirable for clinical promotion.

**Keywords:** 3D printing, navigation template, tibiofibular syndesmosis, biomechanics, EndoButton

## INTRODUCTION

The separation of the distal tibiofibular syndesmosis is a common orthopaedic injury that is usually associated with 1–20% of all ankle sprains and 13% of ankle fractures in patients (Egol et al., 2010; Liu et al., 2018; Shimozone et al., 2019; Corte-Real and Caetano, 2021). Inappropriate treatment of syndesmosis injuries could result in ankle instability, stiffness, and poor functional performance and ultimately lead to traumatic osteoarthritis (Krähenbühl et al., 2019). Therefore, it is necessary to search for an ideal treatment when dealing with syndesmotic injuries. For most unstable syndesmosis injuries, with ankle fractures, patients are advised to be treated operatively (van Dijk et al., 2016). Various therapies have been used in clinical practices for years; however, the optimal surgical fixation is still controversial (Teramoto et al., 2011). Although screw fixation is one of the most common methods, it does not respect the dynamic properties, and there still exist some inevitable complications, including screw loosening and breakage and a high risk of reoperation for screw removal (McBryde et al., 1997; Jurkowitsch et al., 2016; Azoulay et al., 2020). More recently, most surgical fixations for syndesmosis diastasis have been operated with the flexible fixation method involving the suture button (Chen et al., 2019; Alastuey-López et al., 2021). Based on suture button design, TightRope (TR) has become a relatively new operation which provides accurate reduction and anatomical maintenance (Qu et al., 2017). However, the TR system fixation also brings about several new potential complications, which include knot infection and looseness (Xie et al., 2018; Pang et al., 2019).

Consequently, to solve these issues, a novel adjustable EndoButton (NAE) has been introduced with the benefit of

being knotless and efficient. In particular, the design behind this innovation is to adjust the length of the loop and the force of reduction intraoperatively according to individual therapy (Weng et al., 2020). In our technique, the EndoButton and the loop formed a ring-shaped system that makes the new fixation stable (**Figure 1A**). With an adjustable serration device, our EndoButton can change the position of special grooves and protrusions by sliding the regulation holes (**Figure 1B**), so as to find a suitable force to restore the anatomical relationship of syndesmosis with a controllable range between the minimum and maximum adjustment (**Figure 1C**). Eventually, the NAE can be adjusted prior to, during, or after fixation of the tibiofibular syndesmosis injury. Virtual 3D models of the NAE and real product are displayed in **Figure 2**. However, precise placement of the NAE in the distal tibiofibular syndesmosis remains a challenging job that is highly crucial for fixation success. To date, three-dimensional (3D) printing models based on individualized navigation templates have been popular in orthopedic surgery (Jastifer and Gustafson, 2017; Guo et al., 2019; Li et al., 2020). Compared to traditional surgical techniques, the 3D-printed navigation template promotes the accuracy of implant insertion and considers the biomechanical parameters of a specific patient. However, rare is the clinical application in the tibiofibular syndesmosis injury.

Thus, in this study, we designed a 3D-printed navigation template to improve the accuracy of drilling in the tibiofibular syndesmosis during implantation, and cadaveric specimens were used to compare the biomechanical differences between the NAE and two different implants for the treatment of syndesmosis injuries.

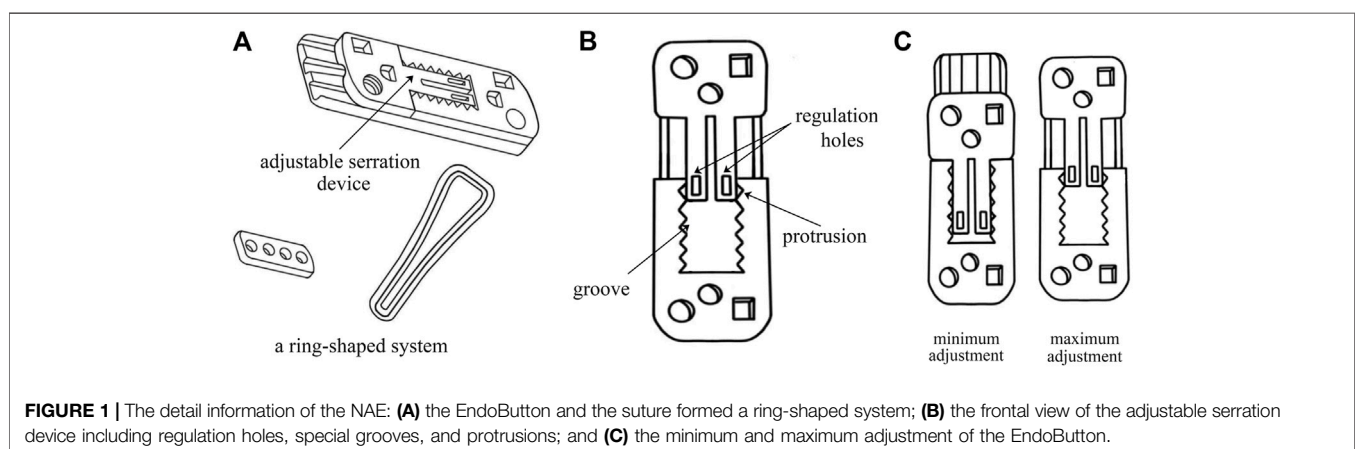


**FIGURE 1 |** The detail information of the NAE: **(A)** the EndoButton and the suture formed a ring-shaped system; **(B)** the frontal view of the adjustable serration device including regulation holes, special grooves, and protrusions; and **(C)** the minimum and maximum adjustment of the EndoButton.

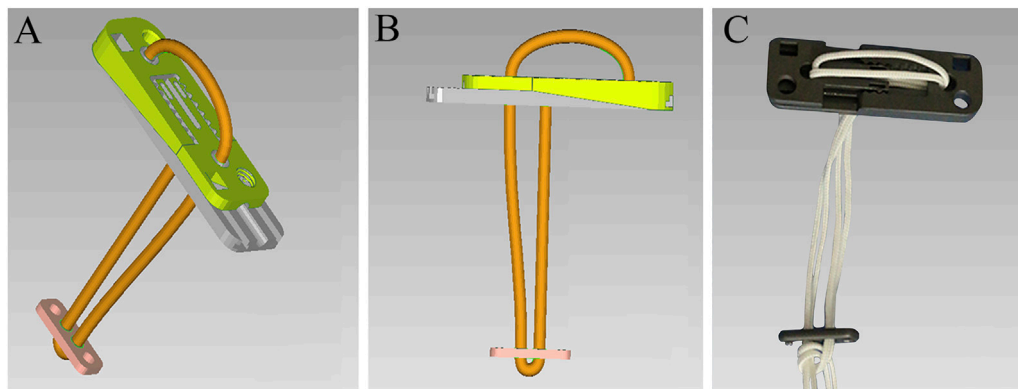


**FIGURE 2 |** Virtual 3D models of the NAE (A) and (B) and real product (C).

## MATERIALS AND METHODS

### Ethics Statement

This research was approved by the medical ethics committee of The Affiliated Traditional Chinese Medicine Hospital of Southwest Medical University (No. KY2018043).

### Specimens and Grouping

A total of 24 human leg specimens (12 males and 12 females) were included in this study, and the mean age of the specimens was 43.2 years (in the range of 28–62 years). The specimens were chosen from the School of Basic Medical Sciences, Southern Medical University, Guangzhou, China. All of them had been observed carefully by X-ray and CT examinations to confirm their normality. Cadaveric specimens with ankle abnormalities, fractures, ligament lesions, or other serious associated injuries were excluded, and included specimens showed no damage to the tibia, fibula, and ligaments. All cadavers were randomly allocated to four groups: the NAE group (Delta Medical, Beijing, China,  $n = 6$ ), TR group (Arthrex, Naples, FL,  $n = 6$ ), screw group (Delta Medical, Beijing, China,  $n = 6$ ), and intact group ( $n = 6$ ).

### Design and 3D-Printed Navigation Template

All cadaveric specimens underwent thin-slice CT scanning, and image data were collected from a 64-row spiral CT scan (Siemens, Germany, 120 kV, 120 mAs, 0.6 mm slices,  $256 \times 256$ ). The DICOM format files of image data were imported into Mimics 21.0 (Materialise, Belgium). In the 3D visualization interface of the Mimics software, the 3D models of the tibiofibular syndesmosis were reconstructed via the Calculate 3D tool and saved as Standard Triangulation Language (STL) format files. Then, the bone plane of the syndesmosis is marked and cut on the 3D model to copy the virtual bone tunnel of fixation surgery. The “Create cylinder” function was used to create a cylinder with the same diameter as the Kirschner wire. By adjusting the length and direction of the virtual Kirschner wire, the position of the bone tunnel was determined along the bone cutting plane. Based on Boolean subtraction, a personalized navigation template was

established with holes for drilling guidance. This template design was exported as an STL file and then printed by using a 3D printer (MakerBot Replicator 2, MakerBot Industries, United States) with polylactic acid (PLA). The following process settings were standardized: extruder temperature 215°C, chamber temperature 24°C, primary layer height 0.2 mm, infill 2%, support infill 20%, and maximum overhang without support 60%. Then, a 1:1 physical model of the template was fabricated with PLA. Finally, we placed the 3D-printed navigation template and fixed it on the cadaveric specimens to assist the syndesmosis drilling (Figure 3).

### Specimen Preparation and Surgical Approaches for Different Fixations

In order to prepare for surgical procedures, the fresh specimens were tested at room temperature and kept wet with normal saline throughout the study. The skin, fascia, muscles, and soft tissues, including the periosteum, were removed carefully, and finally, the tibiofibular syndesmosis was exposed completely. Then, the distal tibiofibular syndesmosis was removed to simulate syndesmosis injury models (except for the intact group).

For the NAE group, tibiofibular syndesmosis was secured with the assistance of a patellar clamp in the position of slight dorsiflex ( $5^\circ$ ). Then, after the 3D-printed navigation template was placed and fixed, a 1.5 mm Kirschner wire was used to make a bone tunnel, drilling from the fibula to the tibia. Then, the template was removed, and the Kirschner wire was placed to assist the knotless loop passing through the bone tunnel. The suture on the fibular side crossed the connecting holes of the adjustable button first, via the bone tunnel. The suture on the tibial side crossed the connecting holes of the fixed button. When finishing the ring-shaped system, the fixed button was pulled on the tibia while the adjustable button was attached to the fibula (as shown in Figure 4). Typically, the length of knotless suture was changed depending on every specimen's shape by sliding the regulation holes in the adjustable serration device.

For the TR group, this construction consists of two cortical buttons connected by two loops. The surgical method was

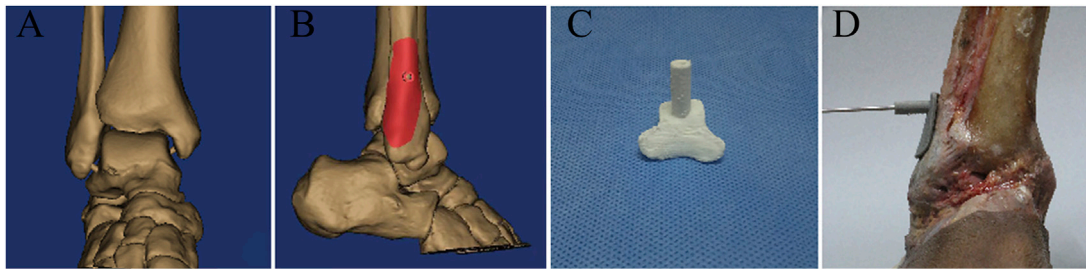


**FIGURE 3 |** (A) 3D model of the ankle joint based on CT reconstruction; (B) digital navigation template according to the 3D model; (C) 3D-printed navigation template for tibiofibular syndesmosis; and (D) the bone tunnel was established with the guidance of a 3D-printed navigation template.

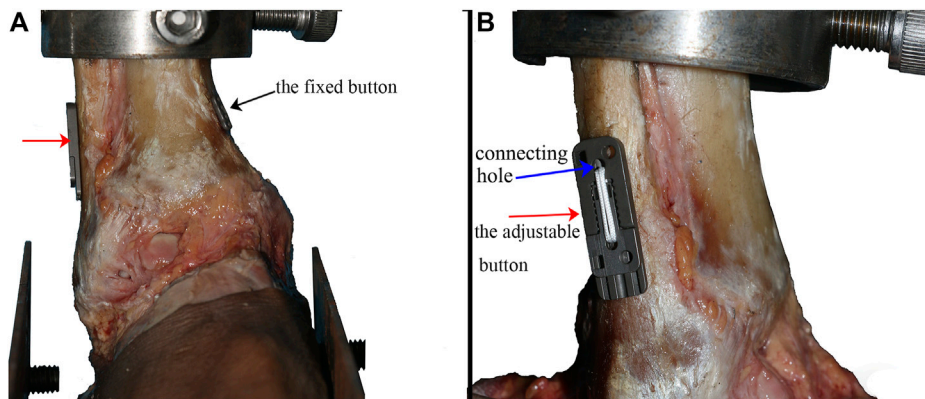


**FIGURE 4 |** Specimen fixed with the NAE (the black arrow showed the fixed button, the red arrow showed the adjustable button, and the blue arrow showed the connecting holes in the adjustable button) (A) observed from the front side and (B) observed from the fibula side.

basically similar to the NAE. The difference, however, was that a knot was needed after fixation to make a circle.

For the screw group, a hole was drilled with the navigation template, and a 3.5 mm screw crossed the hole from the fibular side to the tibia side. Care must be taken to ensure that the screw on each specimen is threaded through the four layers of the tibia and fibula cortex.

## Biomechanical Study

All biomechanical experiments were conducted using the Bose 3510-AT Electro Force biomechanical testing equipment (Bose Corporation, MN, United States) and the Win Test Digital Control System linked to the equipment for transmitting the input and output parameters. This test system had a maximum dynamic load of 7.5 kN, a dynamic displacement of 25 mm, and a test frequency from static to 100 Hz. The cadaveric specimens were rigidly secured to a footplate using a clamping facility, and each ankle was connected to the equipment (as shown in **Figure 5**). Additionally, the KA-300 grating ruler (Lokshun, Guangzhou, China) was placed on the tibia side and fibula side with an aim of measuring the displacements. The resolution of the KA-300 grating ruler was 1/5  $\mu\text{m}$ .

For the axial loading experiment, the human cadaveric specimens were tested in five different positions: neutral

position, plantar flexion ( $15^\circ$ ), dorsiflexion ( $10^\circ$ ), valgus ( $15^\circ$ ), and varus ( $10^\circ$ ), and the load was exerted along the long axis of the tibia, respectively. Every specimen's long axis of the tibia must be aligned with the internal/external rotational servomotor, and its transverse bimalleolar axis was supposed to be aligned with the plantar flexion/dorsiflexion axis of the foot plate. The axial loading ranged from 0 to 700 N, and it was applied to all specimens by increasing the speed of 10 N/s steadily by using the biomechanical machine. Before the initial loading, a preloading of 250 N was exerted and slowly pulled out to all the specimens; additionally, ligaments were kept fresh and moist all the time. The data of displacement was acquired for every 20 N increase in the force loading at a frequency of 0.1 Hz, with the load-displacement curve recorded by using the KA-300 grating ruler. Before each load, the limit bar of the KA-300 grating ruler should be adjusted to be close to one end of the syndesmosis. In addition, the data display of the grating ruler was cleared before each load experiment. When reaching the upper limit, the loading was slowly released to the initial value.

For the torsional loading experiment, internal/external rotation torque was applied only in the neutral position. In addition, each specimen was mounted in the same way as in

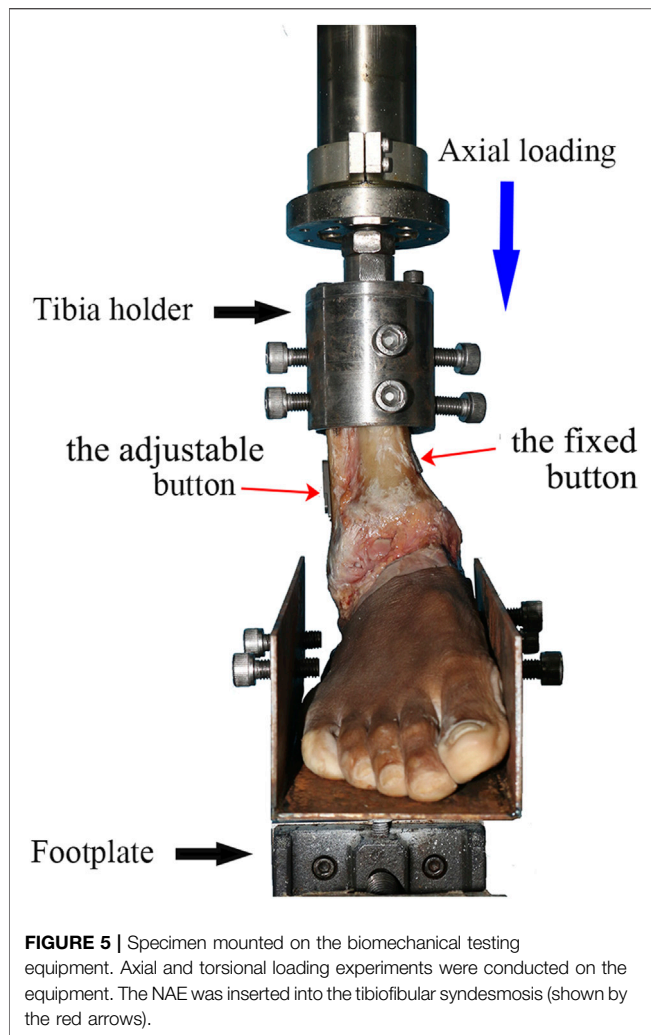


**FIGURE 5 |** Specimen mounted on the biomechanical testing equipment. Axial and torsional loading experiments were conducted on the equipment. The NAE was inserted into the tibiofibular syndesmosis (shown by the red arrows).

the previous experiment. The axial loading was from 0 to 300 N, and the rotation torque was forced on all specimens from 0 to 5 Nm at a speed of 0.1 Nm/s. Before the initial loading, a 2 Nm preloading force was applied and slowly pulled out to all the specimens. The displacement data were acquired when adding 1 N to the torsional loading, and the frequency was 0.1 Hz, with the load–displacement curve recorded by using the KA-300 grating ruler.

The abovementioned experiments were supposed to be performed three times repeatedly with an interval of 2 min. The sampling results were the average of three times.

## Statistical Analysis

Quantitative values were presented as mean  $\pm$  SD. The Anderson–Darling test was used to test the normal distribution, and the Fisher test was used to test the homogeneity of variance. Single-factor analysis of variance (ANOVA) was adopted to detect the difference among the four groups. Data analysis was carried out by the SPSS 20.0 package (SPSS Inc., Chicago, IL, United States), and the level of significance was set at  $p < 0.05$ .

## RESULTS

### Tibiofibular Syndesmosis Drilling

A total of 18 navigation templates (NAE, TR, and screw groups) were created via 3D printing technology. In each of the abovementioned three groups, the bone tunnel was drilled accurately and successfully via a 3D-printed navigation template, with no need for repeat drilling.

### Displacement in an Axial Loading Experiment

As found in Table 1, in most situations (neutral, dorsiflexion, valgus, and varus, except 300 N in the plantar flexion position), the screw group demonstrated smaller displacements than any of the other three groups of all seven testing points (100–700 N) ( $p < 0.05$ ). Moreover, we found a statistically non-significant difference in the displacements among the NAE, TR, and intact groups at most of these testing points (except 100, 400, 600, and 700 N in the varus position, the TR and NAE groups were smaller than the intact group).

### Displacement in the Torsional Loading Experiment

As found in Table 2, in the internal and external rotation, the screw group was smaller than the NAE, TR, and intact groups for all five testing points in the displacement comparison (1–5 Nm) (except for 2 Nm in the external rotation) ( $p < 0.05$ ). In addition, the comparison among the NAE, TR, and intact groups was represented without a statistically significant difference of all five testing points (1–5 Nm) (except for 1 Nm in the internal rotation) ( $p < 0.05$ ).

## DISCUSSION

The major advantages of syndesmosis fixation with the NAE technique are achieving a flexible system, adjusting the length of the knotless loop and the force of reduction, and decreasing procedure complications as far as possible. Furthermore, the improved NAE technique has allowed for accurate drilling with the assistance of 3D printing technology. With the increasing availability of 3D printing, it is becoming popular to assist the surgeon in orthopedic surgery by creating navigation templates and 3D models (Deng et al., 2016). In traditional surgery, limited surgical view makes it challenging to establish a precise bone tunnel during the drilling procedure. It is unknown whether the 3D-printed navigation template may promote the accuracy of drilling in the clinical application of the syndesmosis injury so far. In this study, the personalized 3D-printed navigation template was designed and applied. Finally, the results have shown that the real bone tunnel was accurate, and syndesmosis fixations were conducted successfully along with the guidance of the special navigation templates in the NAE, TR, and screw groups. Apparently, the feasibility of adopting a 3D-printed navigation template in syndesmosis fixation requires evaluation



**TABLE 1** | Displacement in different ankle positions.

Fixation	Ankle position	Displacement under different axial loading forces (mm)						
		100 N	200 N	300 N	400 N	500 N	600 N	700 N
Intact	Neutral position	10.504 ± 3.732	11.396 ± 3.842	12.522 ± 4.076	13.063 ± 4.089	13.508 ± 4.094	13.903 ± 4.076	14.157 ± 4.004
	Dorsiflexion	10.012 ± 2.119	10.790 ± 2.186	11.798 ± 2.297	12.260 ± 2.336	12.507 ± 2.328	12.595 ± 2.278	12.893 ± 2.280
	Plantar flexion	10.067 ± 3.083	11.294 ± 3.502	12.209 ± 3.57	13.085 ± 3.804	14.011 ± 4.078	14.027 ± 4.021	15.313 ± 4.440
	Varus	9.304 ± 1.228	10.758 ± 2.228	11.547 ± 2.383	12.625 ± 2.569	12.731 ± 2.623	13.555 ± 2.577	14.157 ± 2.665
	Valgus	9.975 ± 1.535	11.352 ± 1.683	12.112 ± 1.69	12.696 ± 1.701	13.001 ± 1.67	13.408 ± 1.642	13.767 ± 1.614
Screw	Neutral position	4.899 ± 1.561 <sup>a</sup>	5.397 ± 1.557 <sup>a</sup>	5.807 ± 1.567 <sup>a</sup>	6.393 ± 1.591 <sup>a</sup>	6.992 ± 1.632 <sup>a</sup>	7.768 ± 1.634 <sup>a</sup>	8.208 ± 1.655 <sup>a</sup>
	Dorsiflexion	4.420 ± 1.374 <sup>a</sup>	5.175 ± 1.580 <sup>a</sup>	5.889 ± 1.564 <sup>a</sup>	6.265 ± 1.648 <sup>a</sup>	6.710 ± 1.738 <sup>a</sup>	7.385 ± 1.820 <sup>a</sup>	7.951 ± 2.100 <sup>a</sup>
	Plantar flexion	4.617 ± 1.584 <sup>a</sup>	5.218 ± 1.728 <sup>a</sup>	5.942 ± 1.910	6.596 ± 1.881 <sup>a</sup>	7.158 ± 1.926 <sup>a</sup>	7.744 ± 2.107 <sup>a</sup>	8.402 ± 2.050 <sup>a</sup>
	Varus	5.131 ± 1.471 <sup>a</sup>	5.611 ± 1.499 <sup>a</sup>	5.963 ± 1.502 <sup>a</sup>	6.420 ± 1.494 <sup>a</sup>	6.714 ± 1.440 <sup>a</sup>	7.159 ± 1.410 <sup>a</sup>	7.621 ± 1.477 <sup>a</sup>
	Valgus	5.037 ± 1.966 <sup>a</sup>	5.258 ± 1.867 <sup>a</sup>	5.760 ± 1.966 <sup>a</sup>	6.150 ± 1.936 <sup>a</sup>	6.450 ± 1.906 <sup>a</sup>	6.600 ± 1.790 <sup>a</sup>	6.928 ± 1.749 <sup>a</sup>
Novel EndoButton	Neutral position	8.592 ± 2.050 <sup>b</sup>	9.654 ± 1.918 <sup>b</sup>	10.302 ± 2.000 <sup>b</sup>	10.851 ± 2.061 <sup>b</sup>	11.287 ± 2.092 <sup>b</sup>	11.682 ± 2.117 <sup>b</sup>	12.005 ± 2.104 <sup>b</sup>
	Dorsiflexion	8.164 ± 2.531 <sup>b</sup>	9.107 ± 3.154 <sup>b</sup>	9.804 ± 3.399 <sup>b</sup>	10.378 ± 3.475 <sup>b</sup>	10.847 ± 3.510 <sup>b</sup>	11.256 ± 3.538 <sup>b</sup>	11.610 ± 3.561 <sup>b</sup>
	Plantar flexion	7.785 ± 1.285 <sup>b</sup>	8.818 ± 1.159 <sup>b</sup>	9.653 ± 1.198	10.221 ± 1.321 <sup>b</sup>	10.736 ± 1.520 <sup>a,b</sup>	11.173 ± 1.714 <sup>b</sup>	12.706 ± 2.093 <sup>b</sup>
	Varus	7.126 ± 0.831 <sup>a, b</sup>	8.813 ± 1.788 <sup>b</sup>	9.561 ± 1.820 <sup>b</sup>	10.136 ± 1.827 <sup>a, b</sup>	10.646 ± 1.850 <sup>b</sup>	11.105 ± 1.865 <sup>a, b</sup>	11.53 ± 1.915 <sup>a, b</sup>
	Valgus	7.571 ± 3.602	8.358 ± 3.878	8.929 ± 3.989	9.402 ± 4.044	9.866 ± 4.099	10.235 ± 4.096	10.609 ± 4.095
Tightrope	Neutral position	8.524 ± 3.019 <sup>b</sup>	9.672 ± 3.321 <sup>b</sup>	10.353 ± 3.452 <sup>b</sup>	10.889 ± 3.493 <sup>b</sup>	11.369 ± 3.567 <sup>b</sup>	11.474 ± 3.578 <sup>b</sup>	11.913 ± 3.648 <sup>b</sup>
	Dorsiflexion	7.778 ± 1.995 <sup>b</sup>	8.870 ± 1.368 <sup>b</sup>	9.749 ± 1.039 <sup>b</sup>	10.629 ± 0.928 <sup>b</sup>	11.225 ± 0.732 <sup>b</sup>	11.722 ± 0.617 <sup>b</sup>	12.332 ± 0.660 <sup>b</sup>
	Plantar flexion	8.744 ± 2.006 <sup>b</sup>	9.498 ± 1.864 <sup>b</sup>	10.703 ± 1.863	11.475 ± 1.782 <sup>b</sup>	11.933 ± 1.624 <sup>b</sup>	12.622 ± 1.794 <sup>b</sup>	13.626 ± 2.883 <sup>b</sup>
	Varus	5.705 ± 1.692 <sup>a</sup>	6.342 ± 3.088	8.85 ± 1.471 <sup>a, b</sup>	9.786 ± 1.573 <sup>a, b</sup>	10.442 ± 1.592 <sup>a, b</sup>	11.021 ± 1.538 <sup>a, b</sup>	11.611 ± 1.517 <sup>a, b</sup>
	Valgus	9.121 ± 2.660 <sup>b</sup>	10.450 ± 3.086 <sup>a</sup>	11.455 ± 3.499 <sup>b</sup>	12.322 ± 3.781 <sup>b</sup>	12.575 ± 3.922 <sup>b</sup>	13.005 ± 4.022 <sup>b</sup>	13.848 ± 4.213 <sup>b</sup>

<sup>a</sup>Significant difference compared with the intact group ( $p < 0.05$ ).<sup>b</sup>Significant difference compared with the screw group ( $p < 0.05$ ).

**TABLE 2** | Displacement in internal and external rotation.

Fixation	Rotation	Displacement under different torques (mm)				
		1 N	2 N	3 N	4 N	5 N
Intact	Internal	6.227 ± 0.943	6.280 ± 0.940	6.316 ± 0.936	6.414 ± 0.905	6.635 ± 0.798
	External	8.195 ± 0.484	8.255 ± 0.477	8.280 ± 0.544	8.346 ± 0.537	8.392 ± 0.513
Screw	Internal	3.376 ± 0.395 <sup>a</sup>	3.426 ± 0.400 <sup>a</sup>	3.498 ± 0.382 <sup>a</sup>	3.563 ± 0.380 <sup>a</sup>	3.636 ± 0.420 <sup>a</sup>
	External	5.351 ± 0.384 <sup>a</sup>	5.401 ± 0.393 <sup>a</sup>	5.455 ± 0.391 <sup>a</sup>	5.507 ± 0.389 <sup>a</sup>	5.574 ± 0.396 <sup>a</sup>
Novel EndoButton	Internal	5.330 ± 0.923 <sup>a b</sup>	6.440 ± 0.422 <sup>b</sup>	6.584 ± 0.349 <sup>b</sup>	6.717 ± 0.313 <sup>b</sup>	6.780 ± 0.302 <sup>b</sup>
	External	7.033 ± 1.229 <sup>b</sup>	7.342 ± 1.208 <sup>b</sup>	7.472 ± 1.175 <sup>b</sup>	7.668 ± 1.193 <sup>b</sup>	7.864 ± 1.238 <sup>b</sup>
Tightrope	Internal	4.442 ± 0.116 <sup>a b</sup>	4.451 ± 0.114 <sup>a b</sup>	4.478 ± 0.118 <sup>a b</sup>	4.524 ± 0.161 <sup>a b</sup>	4.564 ± 0.198 <sup>a b</sup>
	External	7.152 ± 1.456 <sup>b</sup>	7.229 ± 1.490	7.317 ± 1.484 <sup>b</sup>	7.402 ± 1.507 <sup>b</sup>	7.559 ± 1.561 <sup>b</sup>

<sup>a</sup>Significant difference compared with the intact group ( $p < 0.05$ ).

<sup>b</sup>Significant difference compared with the screw group ( $p < 0.05$ ).

and exploration before clinical applications. Nevertheless, the long-term clinical effects and procedure complications need to be explored in further studies (Xie et al., 2014).

This study investigated the stability and flexibility of the tibiofibular syndesmosis using three different fixation techniques in cadaveric specimens. The results showed that, in axial and torsional loading experiments, the screw group revealed smaller displacements than any of the other three groups in most conditions. This obviously indicated that screw fixation constrained the physiological motion of the tibiofibular syndesmosis compared with the intact model, and the screw technique became too rigid, providing excessive fixation strength. Owing to a rigid system, Kaiser et al. (2021) suggested that screw fixation may be a good option in cases of severe or multiple syndesmotic injuries with unstable fracture comminution. Moreover, technical considerations about screw fixation still remain without clear standards for the location, diameter, orientation, and number of screws inserted (Peek et al., 2014). Surprisingly, among the NAE, TR, and intact groups, a non-significant difference was found statistically in most situations, which meant that these two fixations achieved similar dynamic stability as the intact syndesmosis. Because of the suture button design, NAE and TR allow fibular movement relative to the tibia in the physiological range. Westermann et al. (2014) found that flexible fixation reduced the risk of malreduction and achieved a self-reduction in restoring the anatomical relationship of the distal tibia-fibula. Many studies have reported that flexible fixation is superior to screw fixation when it comes to clinical efficacy and overall postoperative complications (Doll et al., 2020; Gan et al., 2020). However, there are still some shortcomings in the TR technique. For instance, a knot is needed in traditional TR fixation, but because of the knot, suture loosening and knot irritation occur sometimes, making the fixation unstable. While the suture is knotted, the length of the suture cannot be adjusted, and finally, it may cause insufficient or excessive reduction, leading to looseness and hardware removal (Fantry et al., 2017). Naqvi et al. presented a removal rate of 22% in a 2.5-year follow-up study. Also, in a 5-year retrospective case, five patients needed hardware removal owing to persistent knot irritation in 19 patients (26%). In other words, the TR

fixation is not perfect and personalized (Naqvi et al., 2012; Förschner et al., 2017).

Accordingly, the NAE is with the goal of retaining the advantages of the TR and screw and improving the disadvantages of them. According to the findings in the study, the NAE fixation might serve the same purpose as TR fixation and complete ligament effect, which means it could provide physiologic stabilization of the ankle joint. With a ring-shaped system, there are no risks of screw removal, loosening, and knot irritation. The second operation for fixation removal is unnecessary (Wei et al., 2021). More importantly, the length of the suture is changeable because of the adjustable serration device, enabling a personalized project according to every patient's requirements. With a simple construction, it is easy for surgeons to master our novel technique, which can shorten operation time and improve efficiency (Wang et al., 2018).

The current study also has several limitations. First, one limitation was that the study was unable to simulate the effects of living muscle and soft tissue on ankle joint stability because of cadaver specimens. Then, the implant failure tests were not performed in the experiments, so the maximum strengths of the three devices were unknown. Furthermore, large clinical trials are needed to prove the effectiveness of the NAE method. In addition, both the suture and tissues are likely to undergo creep behavior, which means that the measured gap could grow as time passes. Finally, there are frictional forces which could potentially result in suture wear and tearing. For these reasons, further tests could be performed in the future in order to take into account both creep and fatigue behavior, taking advantage of the experimental setup introduced here where sutures are tested on site; therefore, it is possible to best reproduce the actual suture behavior.

In general, the NAE is an effective method for distal tibiofibular syndesmosis injury. This new technique offers physiologic stabilization of the syndesmosis and retains stability and flexibility, which is the same as complete ligaments. In particular, the adjustable length of the knotless loop makes it possible for individualized therapy, and clearly, without a knot, the NAE will decrease the risk of suture loosening and knot irritation. This may offer a new fixation for the treatment of tibiofibular syndesmosis injuries that is desirable for clinical promotion.

## DATA AVAILABILITY STATEMENT

The original contributions presented in this study are included in the article/Supplementary Material, further inquiries can be directed to the corresponding author.

## ETHICS STATEMENT

The studies involving human participants were reviewed and approved by the medical ethics committee of The Affiliated Traditional Chinese Medicine Hospital of Southwest Medical University (No. KY2018043). The patients/participants provided their written informed consent to participate in this study.

## AUTHOR CONTRIBUTIONS

The conception and study design were put forward by LZ. Interpretation of the data and drafting of the article were performed by JX and XT. Acquisition of figures was conducted by XT. Acquisition of data and data analysis were

conducted by BL. GW and XZ made the critical revisions to the manuscript. All authors approved the final version of the manuscript.

## FUNDING

This work was supported by the Health Commission of Sichuan Province Science and Research Project (Popularization and Application Project), grant number: 20PJ143, Luzhou People's Government-Southwest Medical University Shi-zhen Zhong Academician Talent Team Sub-project, grant number: 2018zszysrctdxm, and Southwest Medical University Research Project, grant number: 2020ZRQNA045.

## ACKNOWLEDGMENTS

The authors are very grateful to Southern Medical University for providing specimens. They would like to thank all the projects for providing funding.

## REFERENCES

- Alastuey-López, D., Seral, B., and Pérez, M. Á. (2021). Biomechanical Evaluation of Syndesmotom Fixation Techniques via Finite Element Analysis: Screw vs. Suture Button. *Comp. Methods Programs Biomed.* 208, 106272. doi:10.1016/j.cmpb.2021.106272
- Azoulay, V., Briot, J., Mansat, P., Swider, P., and Bonneville, N. (2020). Mechanical Behavior of Screw versus Endobutton for Coracoid Bone-Block Fixation. *Orthopaedics Traumatol. Surg. Res.* 106, 1089–1093. doi:10.1016/j.otsr.2020.03.035
- Chen, B., Chen, C., Yang, Z., Huang, P., Dong, H., and Zeng, Z. (2019). To Compare the Efficacy between Fixation with Tightrope and Screw in the Treatment of Syndesmotom Injuries: A Meta-Analysis. *Foot Ankle Surg.* 25, 63–70. doi:10.1016/j.fas.2017.08.001
- Corte-Real, N., and Caetano, J. (2021). Ankle and Syndesmosis Instability: Consensus and Controversies. *EFORT Open Rev.* 6, 420–431. doi:10.1302/2058-5241.6.210017
- Deng, T., Jiang, M., Lei, Q., Cai, L., and Chen, L. (2016). The Accuracy and the Safety of Individualized 3D Printing Screws Insertion Templates for Cervical Screw Insertion. *Comp. Assist. Surg.* 21, 143–149. doi:10.1080/24699322.2016.1236146
- Doll, J., Waizenegger, S., Bruckner, T., Schmidmaier, G., Wolf, S. I., and Fischer, C. (2020). Differences in Gait Analysis and Clinical Outcome after TightRope or Screw Fixation in Acute Syndesmosis Rupture: Study Protocol for a Prospective Randomized Pilot Study. *Trials* 21, 606. doi:10.1186/s13063-020-04550-5
- Egol, K. A., Pahl, B., Walsh, M., Tejwani, N. C., Davidovitch, R. I., and Koval, K. J. (2010). Outcome after Unstable Ankle Fracture: Effect of Syndesmotom Stabilization. *J. Orthop. Trauma* 24, 7–11. doi:10.1097/BOT.0b013e3181b1542c
- Fantry, A. J., O'Donnell, S. W., Born, C. T., and Hayda, R. A. (2017). Deep Infections after Syndesmotom Fixation with a Suture Button Device. *Orthopaedics* 40, 541–545. doi:10.3928/01477447-20161229-02
- Förschner, P. F., Beitzel, K., Imhoff, A. B., Buchmann, S., Feuerriegel, G., Hofmann, F., et al. (2017). Five-Year Outcomes after Treatment for Acute Instability of the Tibiofibular Syndesmosis Using a Suture-Button Fixation System. *Orthopaedic J. Sports Med.* 5, 232596711770285–232596711770287. doi:10.1177/2325967117702854
- Gan, K., Xu, D., Hu, K., Wu, W., and Shen, Y. (2020). Dynamic Fixation Is superior in Terms of Clinical Outcomes to Static Fixation in Managing Distal Tibiofibular Syndesmosis Injury. *Knee Surg. Sports Traumatol. Arthrosc.* 28, 270–280. doi:10.1007/s00167-019-05659-0
- Guo, Y., Tian, G., Zlotolow, D. A., Tian, W., Zhong, W., and Sun, L. (2019). A Cadaveric Study on the Accuracy of an Individualized Guiding Template to Assist Scaphoid Fixation Using Computed Tomography and 3-Dimensional Printing. *J. Hand Surg.* 44, e1–251. doi:10.1016/j.jhsa.2018.06.017
- Jastifer, J. R., and Gustafson, P. A. (2017). Three-Dimensional Printing and Surgical Simulation for Preoperative Planning of Deformity Correction in Foot and Ankle Surgery. *J. Foot Ankle Surg.* 56, 191–195. doi:10.1053/j.jfas.2016.01.052
- Jurkowsky, J., Dall'Ara, E., Quadlbauer, S., Pezzeti, C., Jung, I., Pahr, D., et al. (2016). Rotational Stability in Screw-Fixed Scaphoid Fractures Compared to Plate-Fixed Scaphoid Fractures. *Arch. Orthop. Trauma Surg.* 136, 1623–1628. doi:10.1007/s00402-016-2556-z
- Kaiser, P. B., Bejarano-Pineda, L., Kwon, J. Y., DiGiovanni, C. W., and Guss, D. (2021). The Syndesmosis, Part II. *Orthop. Clin. North America* 52, 417–432. doi:10.1016/j.ocl.2021.05.011
- Krähenbühl, N., Weinberg, M. W., Hintermann, B., Haller, J. M., Saltzman, C. L., and Barg, A. (2019). Surgical Outcome in Chronic Syndesmotom Injury: A Systematic Literature Review. *Foot Ankle Surg.* 25, 691–697. doi:10.1016/j.fas.2018.08.008
- Li, Z., Xu, D., Li, F., Liu, M., Xu, G., and Yang, M. (2020). Design and Application of a Novel Patient-specific 3D Printed Drill Navigational Guiding Template in Percutaneous Thoracolumbar Pedicle Screw Fixation: A Cadaveric Study. *J. Clin. Neurosci.* 73, 294–298. doi:10.1016/j.jocn.2020.01.083
- Liu, G. T., Ryan, E., Gustafson, E., VanPelt, M. D., Raspovic, K. M., Lalli, T., et al. (2018). Three-Dimensional Computed Tomographic Characterization of Normal Anatomic Morphology and Variations of the Distal Tibiofibular Syndesmosis. *J. Foot Ankle Surg.* 57, 1130–1136. doi:10.1053/j.jfas.2018.05.013
- McBryde, A., Chiasson, B., Wilhelm, A., Donovan, F., Ray, T., and Bacilla, P. (1997). Syndesmotom Screw Placement: a Biomechanical Analysis. *Foot Ankle Int.* 18, 262–266. doi:10.1177/107110079701800503
- Naqvi, G. A., Cunningham, P., Lynch, B., Galvin, R., and Awan, N. (2012). Fixation of Ankle Syndesmotom Injuries. *Am. J. Sports Med.* 40, 2828–2835. doi:10.1177/0363546512461480
- Pang, E. Q., Bedigrew, K., Palanca, A., Behn, A. W., Hunt, K. J., and Chou, L. (2019). Ankle Joint Contact Loads and Displacement in Syndesmosis Injuries Repaired with Tightropes Compared to Screw Fixation in a Static Model. *Injury* 50, 1901–1907. doi:10.1016/j.injury.2019.09.012

- Peek, A. C., Fitzgerald, C. E., and Charalambides, C. (2014). Syndesmosis Screws: How many, what Diameter, where and Should They Be Removed? A Literature Review. *Injury* 45, 1262–1267. doi:10.1016/j.injury.2014.05.003
- Qu, J.-t., Shi, G.-h., Wang, Y.-c., Li, J., Dong, J.-w., and Hu, Y. (2017). An Alternative Strategy for Treatment of Distal Tibiofibular Syndesmotic Disruption: A Technical Note. *J. Foot Ankle Surg.* 56, 1087–1090. doi:10.1053/j.jfas.2017.04.010
- Shimozono, Y., Hurley, E. T., Myerson, C. L., Murawski, C. D., and Kennedy, J. G. (2019). Suture Button versus Syndesmotic Screw for Syndesmosis Injuries: A Meta-Analysis of Randomized Controlled Trials. *Am. J. Sports Med.* 47, 2764–2771. doi:10.1177/0363546518804804
- Teramoto, A., Suzuki, D., Kamiya, T., Chikenji, T., Watanabe, K., and Yamashita, T. (2011). Comparison of Different Fixation Methods of the Suture-Button Implant for Tibiofibular Syndesmosis Injuries. *Am. J. Sports Med.* 39, 2226–2232. doi:10.1177/0363546511413455
- van Dijk, C. N., Longo, U. G., Loppini, M., Florio, P., Maltese, L., Ciuffreda, M., et al. (2016). Conservative and Surgical Management of Acute Isolated Syndesmotic Injuries: ESSKA-AFAS Consensus and Guidelines. *Knee Surg. Sports Traumatol. Arthrosc.* 24, 1217–1227. doi:10.1007/s00167-016-4017-1
- Wang, L., Zhang, Y., Song, Z., Chang, H., Tian, Y., and Zhang, F. (2018). A Novel Method of Using Elastic Bionic Fixation Device for Distal Tibiofibular Syndesmosis Injury. *Int. Orthopaedics (Sicot)* 42, 2219–2229. doi:10.1007/s00264-018-3869-z
- Wei, X.-K., Jing, G.-W., Shu, Y., Tong, J., and Wang, J.-H. (2021). Self-made Wire-Rope Button Plate: A Novel Option for the Treatment of Distal Tibiofibular Syndesmosis Separation. *J. Orthop. Surg. (Hong Kong)* 29, 230949902097521–230949902097526. doi:10.1177/2309499020975215
- Weng, Q., Lin, C., Liu, Y., Dai, G., Lutchooman, V., and Hong, J. (2020). Biomechanical Analysis of a Novel Syndesmotic Plate Compared with Traditional Screw and Suture Button Fixation. *J. Foot Ankle Surg.* 59, 522–528. doi:10.1053/j.jfas.2019.07.025
- Westermann, R. W., Rungprai, C., Goetz, J. E., Femino, J., Amendola, A., and Phisitkul, P. (2014). The Effect of Suture-Button Fixation on Simulated Syndesmotic Malreduction: a Cadaveric Study. *J. Bone Jt. Surg.* 96, 1732–1738. doi:10.2106/JBJS.N.00198
- Xie, B., Jing, Y.-f., Xiang, L.-b., Zhou, D.-p., and Tian, J. (2014). A Modified Technique for Fixation of Chronic Instability of the Distal Tibiofibular Syndesmosis Using a Wire and Button. *J. Foot Ankle Surg.* 53, 813–816. doi:10.1053/j.jfas.2014.05.006
- Xie, L., Xie, H., Wang, J., Chen, C., Zhang, C., Chen, H., et al. (2018). Comparison of Suture Button Fixation and Syndesmotic Screw Fixation in the Treatment of Distal Tibiofibular Syndesmosis Injury: A Systematic Review and Meta-Analysis. *Int. J. Surg.* 60, 120–131. doi:10.1016/j.ijsu.2018.11.007

**Conflict of Interest:** The authors declare that the research was conducted in the absence of any commercial or financial relationships that could be construed as a potential conflict of interest.

**Publisher's Note:** All claims expressed in this article are solely those of the authors and do not necessarily represent those of their affiliated organizations, or those of the publisher, the editors, and the reviewers. Any product that may be evaluated in this article, or claim that may be made by its manufacturer, is not guaranteed or endorsed by the publisher.

Copyright © 2022 Zhang, Xu, Tang, Zhou, Li and Wang. This is an open-access article distributed under the terms of the Creative Commons Attribution License (CC BY). The use, distribution or reproduction in other forums is permitted, provided the original author(s) and the copyright owner(s) are credited and that the original publication in this journal is cited, in accordance with accepted academic practice. No use, distribution or reproduction is permitted which does not comply with these terms.





# Injectable Photo-Crosslinked Bioactive BMSCs-BMP2-GelMA Scaffolds for Bone Defect Repair

Senlin Chai<sup>1†</sup>, Jianhao Huang<sup>2†</sup>, Abdurahman Mahmut<sup>1</sup>, Bin Wang<sup>3</sup>, Yao Yao<sup>1</sup>, Xiaofeng Zhang<sup>1</sup>, Zaikai Zhuang<sup>1</sup>, Chunmei Xie<sup>4</sup>, Zhihong Xu<sup>1\*</sup> and Qing Jiang<sup>1,5\*</sup>

<sup>1</sup>State Key Laboratory of Pharmaceutical Biotechnology, Division of Sports Medicine and Adult Reconstructive Surgery, Department of Orthopedic Surgery, Nanjing Drum Tower Hospital, The Affiliated Hospital of Nanjing University Medical School, Nanjing, China, <sup>2</sup>Department of Orthopedics, Jinling Hospital, The First School of Clinical Medicine, Southern Medical University, Nanjing, China, <sup>3</sup>The First Affiliated Hospital of Zhejiang University School of Medicine, Hangzhou, China, <sup>4</sup>Hangzhou Lancet Robotics Company Ltd, Hangzhou, China, <sup>5</sup>Jiangsu Engineering Research Center for 3D Bioprinting, Nanjing, China

## OPEN ACCESS

### Edited by:

Lei Zhang,  
Wenzhou Medical University, China

### Reviewed by:

Lei Yang,  
University of Chinese Academy of  
Sciences, China  
Youwen Yang,  
Jiangxi University of Science and  
Technology, China

### \*Correspondence:

Zhihong Xu  
xuzhihongjoint@hotmail.com  
Qing Jiang  
qingj@njnu.edu.cn

<sup>†</sup>These authors have contributed  
equally to this work

### Specialty section:

This article was submitted to  
Biomaterials,  
a section of the journal  
Frontiers in Bioengineering and  
Biotechnology

Received: 14 February 2022

Accepted: 07 March 2022

Published: 24 March 2022

### Citation:

Chai S, Huang J, Mahmut A, Wang B,  
Yao Y, Zhang X, Zhuang Z, Xie C, Xu Z  
and Jiang Q (2022) Injectable Photo-  
Crosslinked Bioactive BMSCs-BMP2-  
GelMA Scaffolds for Bone  
Defect Repair.  
Front. Bioeng. Biotechnol. 10:875363.  
doi: 10.3389/fbioe.2022.875363

Injectable hydrogels offer a new therapy option for irregular bone deformities. Based on gelatin methacryloyl (GelMA), bone marrow mesenchymal stem cells (BMSCs), and bone morphogenetic protein 2 (BMP2), we created a photo-crosslinked composite bioactive scaffold. The composite scaffolds had appropriate mechanical properties for stem cells adhesion and proliferation, as well as good biocompatibility and the ability to stimulate BMSCs osteogenic differentiation *in vitro*. The synergistic effect of BMSCs and BMP2 enabled the composite bioactive scaffold to exhibit higher osteogenic potential *in vivo* than scaffolds loaded alone with BMSCs or BMP2, according to imaging and histology studies. In conclusion, by promoting the osteogenic differentiation of BMSCs, the composite bioactive scaffold based on BMSCs-BMP2-GelMA has demonstrated remarkable application potential in bone regeneration and bone defects repair.

**Keywords:** GelMA, BMSCs, BMP2, scaffold, photo-crosslinked, osteogenic differentiation, bone defect

## INTRODUCTION

Bone damage and defects caused by trauma, osteoporosis, tumor, and osteoarthritis can easily lead to bone nonunion and limb dysfunction, which seriously reduce the life quality of patients (Ren et al., 2018; Zou et al., 2020). Bone graft surgery is frequently required to treat nonunion fractures and large bone defects that are difficult to mend on their own (Pape et al., 2010). In bone defect repair procedures, autologous cancellous bone, allogeneic bone grafts, polymer materials, and periosteal induction materials based on metallic and inorganic non-metallic materials are now used (Wang and Yeung 2017; Yang et al., 2022). Insufficient supply of bone grafts and the inability of metal materials to combine with human tissues are inevitable problems in the application of graft materials in bone repair (Rupp et al., 2021). Many promising natural proteins or polysaccharide-based biopolymers, such as alginate, hyaluronic acid, bacterial cellulose, and gelatin, which have good biocompatibility have been widely used as raw material for bone regeneration grafts (Ferreira et al., 2020; Li L. et al., 2021; Xue et al., 2021). Gelatin methacryloyl (GelMA) is a popular biomaterial for bone, cartilage, and vessel tissue regeneration because of its biocompatibility, biodegradability, strong hydrophilicity, and structural, mechanical, and biological qualities that are similar to natural bone (Jiang et al., 2021; Ngan et al., 2021).

Bone marrow mesenchymal stem cells (BMSCs) have osteogenic differentiation potential and promote bone regeneration, and are widely used in fracture and bone defect repair (Arthur and Gronthos, 2020). Currently, stem cells are injected directly into the treatment region using a syringe,

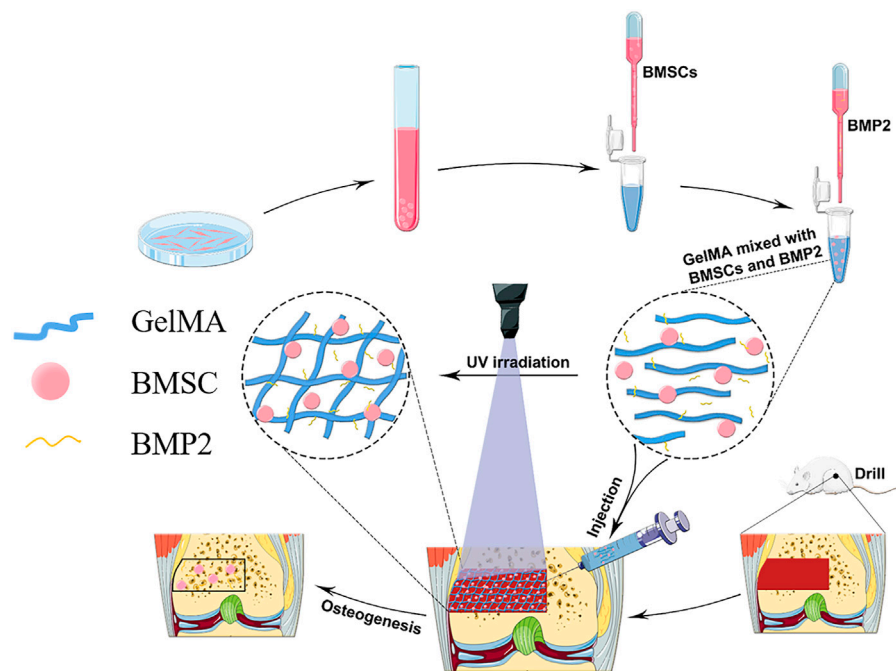


**FIGURE 1** | A schematic diagram of the preparation of bioactive BMSCs-BMP2-GelMA scaffold and the experimental procedure.

which reduces the amount of harm produced by surgical procedures. Low retention and engraftment of directly injected cells, on the other hand, remain important roadblocks to effective clinical translation. GelMA scaffold contains an arginine-glycine-aspartic acid (RGD) peptide sequence, reported to improve cells adhesion, proliferation through integrin (Yoon et al., 2019; Sun et al., 2021). This property makes GelMA hydrogel a good carrier for encapsulating stem cells and growth factors, which eliminates cell membrane damage caused by mechanical shear forces and a lack of a stable 3D microenvironment during stem cell injection (Li J. et al., 2021). Zhao et al. wrapped bone marrow mesenchymal stem cells (BMSCs) in photo-crosslinkable GelMA microspheres. BMSCs encapsulated in microspheres show enhanced cell proliferation and osteogenesis (Zhao et al., 2016). Bone morphogenetic protein 2 (BMP2), a member of the transforming growth factor- $\beta$  (TGF- $\beta$ ) superfamily of growth factors, promotes migration and osteogenic differentiation of mesenchymal stem cells (Katagiri and Watabe, 2016). Although BMP2 has been approved by the FDA for clinical use, the high concentration local application can cause complications such as heterotopic mineralization and inflammation (Dickerman et al., 2007). Samorezov et al. developed a GelMA hydrogel-based BMP2 delivery system that allows for long-term BMP2 release at low local concentrations. The data showed that sustained-release delivery of BMP2 can promote osteogenic differentiation *in vitro* more than free BMP2 in the culture medium (Samorezov et al., 2016).

When BMSCs were placed into the bone defect, the complex inflammatory microenvironment caused BMSCs to become fibrotic and lose their ability to develop into osteogenic cells (Shi et al., 2020). A topic that needs to be explored is how to constantly trigger the osteogenic development of mesenchymal stem cells in the scaffold under the complex interior environment

of bone defects. We combined the strategy of BMP2 retardation and delivery of BMSCs in a GelMA hydrogel scaffold. We hypothesized that the synergistic effects of stem cells and growth factors in biomaterials could promote bone defect repair and better bone regeneration than previous scaffolds loaded with only osteoblast or cytokines. In addition, GelMA concentrations reported range from 5 to 20%, and the appropriate concentrations of GelMA hydrogel scaffolds for loading stem cells and cytokines need to be screened (Yin et al., 2018; Dong et al., 2021).

In this study, a GelMA hydrogel scaffold loaded with stem cells is combined with a strategy of slow-release BMP2 to form BMSCs-BMP2-GelMA photo-crosslinked bioactive scaffolds for bone repair (Figure 1). By selecting the proper GelMA concentration, scaffold materials with good pore sizes, mechanical properties, and sustain-released capacity were obtained. Subsequently, the biocompatibility and the ability of the composite bioactive scaffold to promote osteogenic differentiation of BMSCs were examined *in vitro*. Finally, the *in vivo* biosafety and ability to promote bone regeneration of the composite bioactive scaffold were verified in a rat distal femoral bone defect model.

## MATERIALS AND METHODS

### Materials

SPF male SD rats (2 and 6 weeks) were obtained from Nanjing Medical University. Animal experiments were approved by the Animal Ethics Committee of Nanjing Drum Tower Hospital. GelMA was purchased from Cure Gel Co. Photo-initiator (PI)

2959, human recombinant bone morphogenetic protein 2 (BMP2) was purchased from Sigma-Aldrich. F12 basal medium (F12-MEM) and fetal bovine serum (FBS) were purchased from Gibco. Osteogenic differentiation medium was purchased from Cyagen. Live/dead cell staining kit, Alizarin Red S and Masson's Trichrome Stain Kit were purchased from Solarbio. Anti-Osteopontin antibody (ab63856) and Anti-Osteocalcin antibody (ab93876) were purchased from Abcam.

## Cell Culture

Rat bone marrow-derived stem cells (BMSCs) were isolated from the bone marrow of SD rats (2 weeks old, male) according to our previous work (Zhang et al., 2021). BMSCs were cultured in F12-MEM medium containing 10% v/v fetal bovine serum (FBS) and 1% v/v penicillin-streptomycin solution at 37°C under 5% CO<sub>2</sub>. The culture medium was replaced every 3 days, and the cells were harvested and passaged after reaching 90% confluence. Experiments were carried out on cells from the third passage.

## Generation of Bioactive Scaffolds

The GelMA solution and the photo-initiator were mixed in PBS, filtered through a 0.22 µm filter. BMSCs ( $2 \times 10^5$ /mL) and BMP2 (100 ng/ml) were added to the mixed solution respectively. The hydrogel was photo-crosslinked under ultraviolet light (365 nm, 100 mW cm<sup>-2</sup>) for 30 s to form a hydrogel. The hydrogel scaffold was washed repeatedly with fresh PBS to clean the hydrogel monomers and photo-crosslinking agents. The GelMA hydrogel scaffolds containing BMSCs and BMP2 were called composite bioactive scaffolds.

## Scaffold Characterization and Analysis of the Sustained-Release Rate

The surface pore size of the hydrogel scaffold was measured by Scanning electron microscope (SEM) and image J. The hydrogel scaffold was prepared into a cylinder with a diameter of 8 mm and a height of 4 mm. The maximum compressive strength and Young's modulus of hydrogel scaffolds were determined with the Instron material test system (Instron, USA) at a compressive speed of 0.5 mm/min. The viscoelasticity of hydrogel scaffolds was determined with an RS6000 parallel plate rheometer (HAAKE, German). To estimate the release kinetics of proteins from bioactive scaffolds, scaffolds were fabricated by 100 ng/ml Rhodamine B in GelMA solution. The photo-crosslinked scaffolds were soaked in PBS. The images were taken with a fluorescence microscope (Zeiss, USA) every 24 h. The composite scaffold sample loaded with BMP2 was immersed in 1 ml PBS and placed on a shaker platform at 37°C. From the 0th h, 500 µL of PBS was taken out every 24 h and supplemented with an equal amount of fresh PBS. The BMP2 ELISA kit was used to determine the concentration of BMP2 in PBS, and the cumulative release concentration was calculated.

## Live and Dead Staining

Live/Dead viability kit (Solarbio, China) was used according to the manufacturer's instructions. The bioactive scaffold was washed 3 times with PBS, then stained with Calcein AM

(green) and propidium iodide (red) at 37°C for 30 mins, washed three times with PBS. The images were taken with a fluorescence microscope (Zeiss, USA). For each scaffold, z-serial images were taken at three different locations with optical sectioning, and the background signals were eliminated with structural illumination. Live and dead cells were counted in ImageJ software. Live cell percentage was calculated by using the equation:

$$\text{Live cell (\%)} = [(\text{live cell number}) / (\text{total cell number})] * 100\%$$

## Osteogenic Differentiation *In Vitro*

BMSCs were respectively co-cultured with BMSCs-GelMA scaffolds and BMSCs-BMP2-GelMA scaffolds. After 14 days of osteogenic induction, the total RNA of the co-cultured BMSCs and BMSCs in scaffolds were extracted. Quantitative real-time PCR was performed with the corresponding primers (as listed in Table 1.), SYBR Green PCR kit (Takara) at a total volume of 20 µL, and an ABI Step One Plus real-time PCR system (Applied Biosystems). Each sample was made in triplicate, and the relative mRNA expression level was quantified by the housekeeping gene β-Actin and calculated using the 2<sup>-ΔΔCT</sup> method.

BMSCs-GelMA scaffolds and BMSCs-BMP2-GelMA scaffolds were co-cultured with BMSCs in osteogenic media for 21 days. After fixation with 4% paraformaldehyde for 20 min, the scaffolds and co-cultured BMSCs were washed 3 times with deionized water and immersed in 1% (w/v) Alizarin Red S (pH = 4.2) at room temperature for 30 min. After washing off the dye with deionized water, scaffolds were cut into thin slices and transferred to a glass slide for microscopic observation. Image J software was used to calculate the area of the stained positive area.

## Establishment of Femur Model and Photo-Crosslinking of Scaffolds *In Vivo*

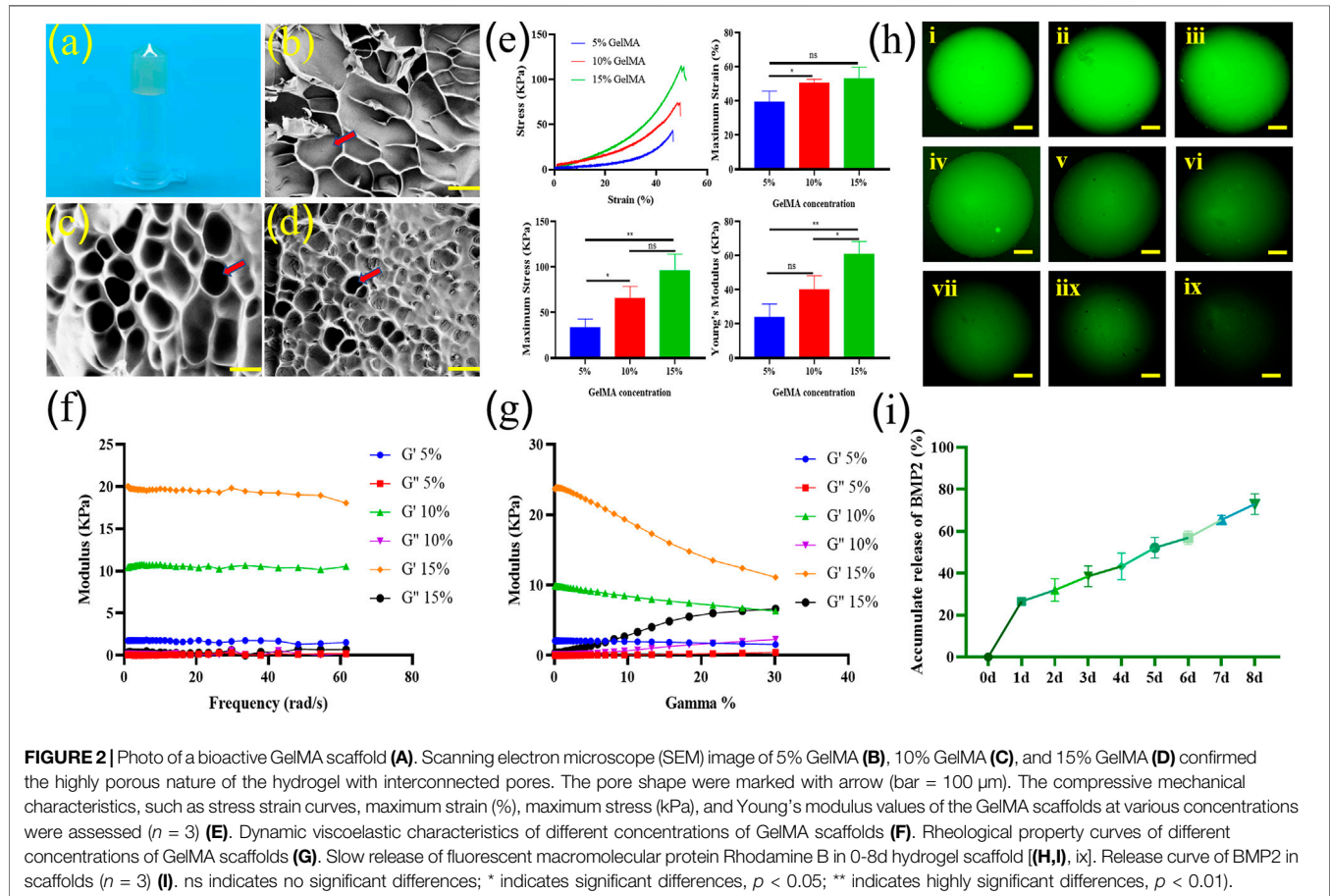
Animal experiments were approved by the Animal Ethics Committee of Nanjing Drum Tower Hospital. SD rats (6 weeks old, male) were housed in standard aseptic conditions. After acclimatizing for 1 week, the rats were anesthetized with isoflurane, and their distal femurs were pierced with an electric drill of diameter 3 mm to induce a bone defect with a diameter of 3 mm and a depth of 2 mm. The rats were randomly assigned to the saline group (Shame), photo-crosslinked GelMA loaded with BMSCs group (BMSCs-GelMA), photo-crosslinked GelMA loaded with BMP2 group (BMP2-GelMA), photo-crosslinked GelMA loaded with BMSCs and BMP2 groups (BMSCs-BMP2-GelMA) (*n* = 7 each), and the injured sites were accordingly injected with 20 µL saline or the corresponding GelMA respectively for UV cross-linking (365 nm, 100 mW cm<sup>-2</sup>) for 30 s. The wound was gently washed with saline and the incision was sutured.

## Radiological and Histological Assessment

Eight weeks after the operation, the rats were killed by overdose anesthesia. Femoral specimens were collected. Micro-CT was used to scan the distal femur of the rats. Calculate the

**TABLE 1** | Primer sequences used for RT-qPCR analysis in the present study.

Gene symbol	Forward primer (5'-3')	Reverse primer (3'-5')
COL1	GCTCCTCTTAGGGGCCACT	CCACGTCTCACCATTGGGG
ALP	CCAACTCTTTTGTGCCAGAGA	GGCTACATTGGTGTGAGCTTTT
$\beta$ -Actin	CATGTACGTTGCTATCCAGGC	CTCCTTAATGTACGCACGAT



proportion of bone tissue volume (BV/TV), trabecular thickness (Tb.Th), trabecular number (Tb.N) and trabecular separation (Tb.Sp) ( $n = 3$ ). For histological evaluation, the femur was fixed in 4% paraformaldehyde for 24 h, decalcified with 10% ethylenediaminetetraacetic acid (EDTA) at 37°C for 4 weeks. The femur was dehydrated through a serial alcohol gradient, embedded in paraffin, and cut into 5  $\mu$ m thick sections for HE Staining, Masson staining, immunohistochemical staining (IHC) according to the previous report (Liu et al., 2017; Tandon et al., 2019). The images were analyzed by Image-J.

## Statistical Analysis

All analysis data are expressed as the mean  $\pm$  standard deviation of three independent experiments. Statistical analysis was performed by SPSS 20 (IBM) and GraphPad Prism Software. GraphPad Prism Software was used to draw all the charts. An

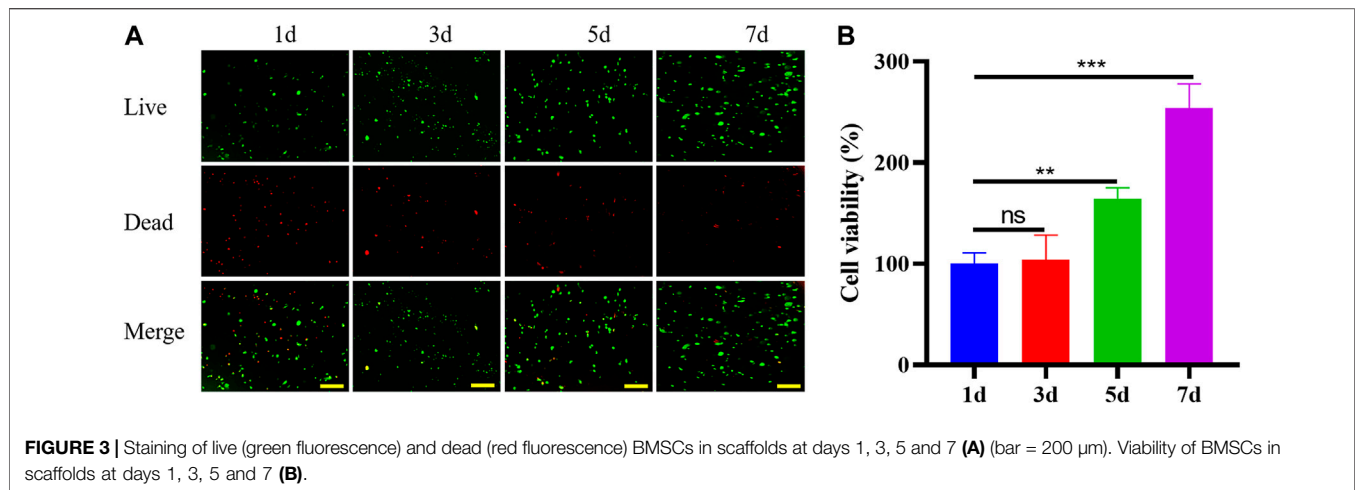
independent *T*-test, assuming unequal variances, was used for the analysis of differences between groups, and analysis of variance was used for the analysis of differences within groups. A *p*-value  $< 0.05$  was considered statistically significant.

## RESULTS

### Physical and Mechanical Properties of GelMA Hydrogel Scaffolds

After photo-crosslinking, hydrogels can form a stable solid form for subsequent experiments (Figure 2A). Scanning electron microscope results and Image J analysis showed that 5% w/v GelMA scaffolds formed a loose surface structure with a pore size of 180–240  $\mu$ m (Figure 2B). The pore size of the 10% w/v GelMA scaffold is 90–130  $\mu$ m (Figure 2C), and the pore size of the 15%





w/v GelMA scaffold is 40–60 μm (Figure 2D). The compressive mechanical characteristics of the GelMA scaffolds at various concentrations were assessed (Figure 2E). As expected, the stress-strain curves of the scaffolds showed that the mechanical properties of the hydrogels increased with the increase of GelMA concentration. The compressive maximum strain of the scaffolds had a range of 40–60%. The compressive maximum stress of GelMA scaffolds with 5, 10, and 15% concentrations were  $33.63 \pm 7.57$  kPa,  $66.16 \pm 10.13$  kPa, and  $96.65 \pm 14.15$  kPa, respectively. The Young's modulus of GelMA scaffolds with 5, 10, and 15% concentrations were  $24.07 \pm 6.18$  kPa,  $40.47 \pm 6.36$  kPa, and  $60.97 \pm 6.07$  kPa, respectively. According to the dynamic viscoelastic properties data, the storage modulus ( $G'$ ) was highly bigger than the loss modulus ( $G''$ ) for all concentration hydrogels, indicating that these scaffolds are all highly structured (Figure 2F). The rheological property curves indicated that all hydrogel scaffolds possessed shear-thinning behavior in the measured shear rate range (Figure 2G).

The sustained release rate of macromolecular proteins in the composite hydrogel scaffold was detected by the green fluorescence of model drug Rhodamine b and Elisa results of BMP2. The release of macromolecular proteins exceeded 20% on the first day. This may be related to the fact that the macromolecular protein adhesion to the surface of the hydrogel scaffold will be washed away by PBS in the subsequent operation. Within 1 week, the release of macromolecular protein and BMP2 were close to 75%, indicating that the composite scaffold we synthesized was more in line with the application requirements of sustained-release BMP2 (Figures 2H,I).

### Biocompatibility of GelMA Scaffolds

To determine the biocompatibility of GelMA hydrogel as an injectable photo-crosslinked bone regeneration bioactive scaffold, the viability of BMSCs was evaluated by quantifying the live and dead cells encapsulated inside the GelMA scaffold using live/dead assay (Figure 3A). The cell viability on the first day was about 68%, due to inevitable factors such as ultraviolet (UV) light irradiation and mechanical stress during operation. After

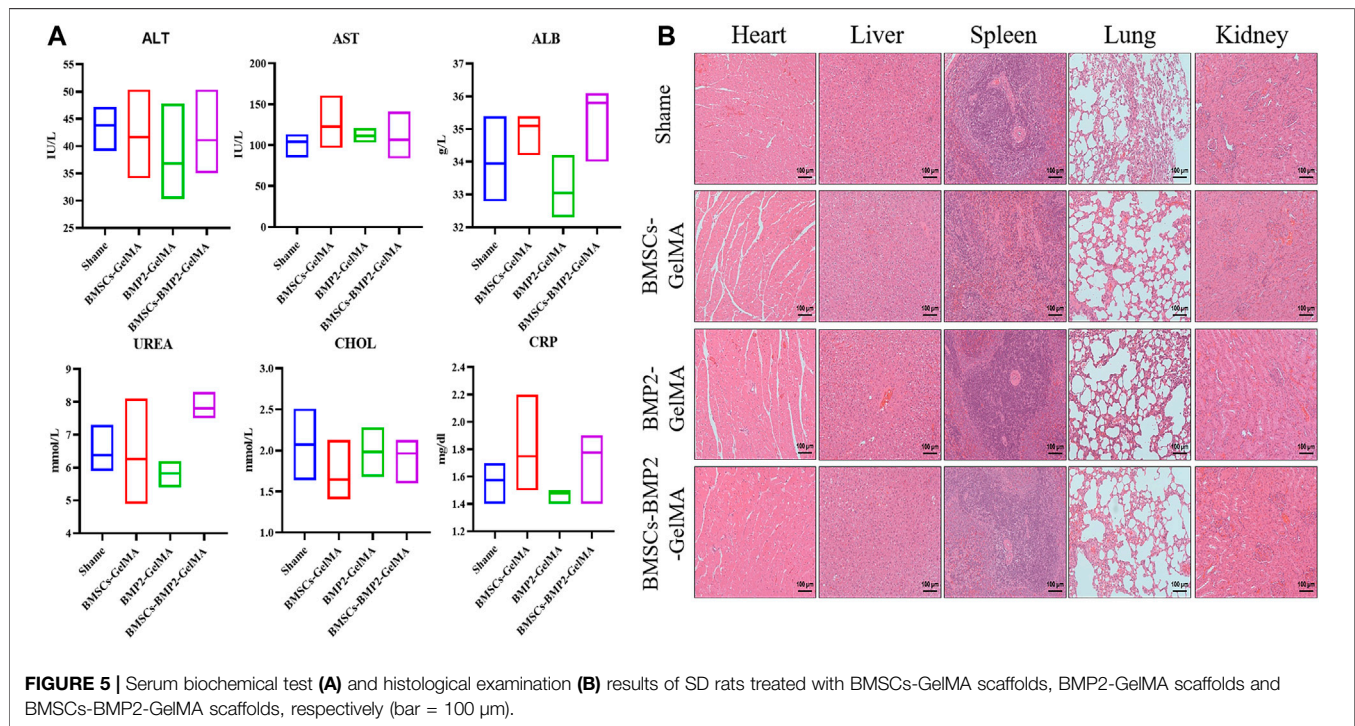
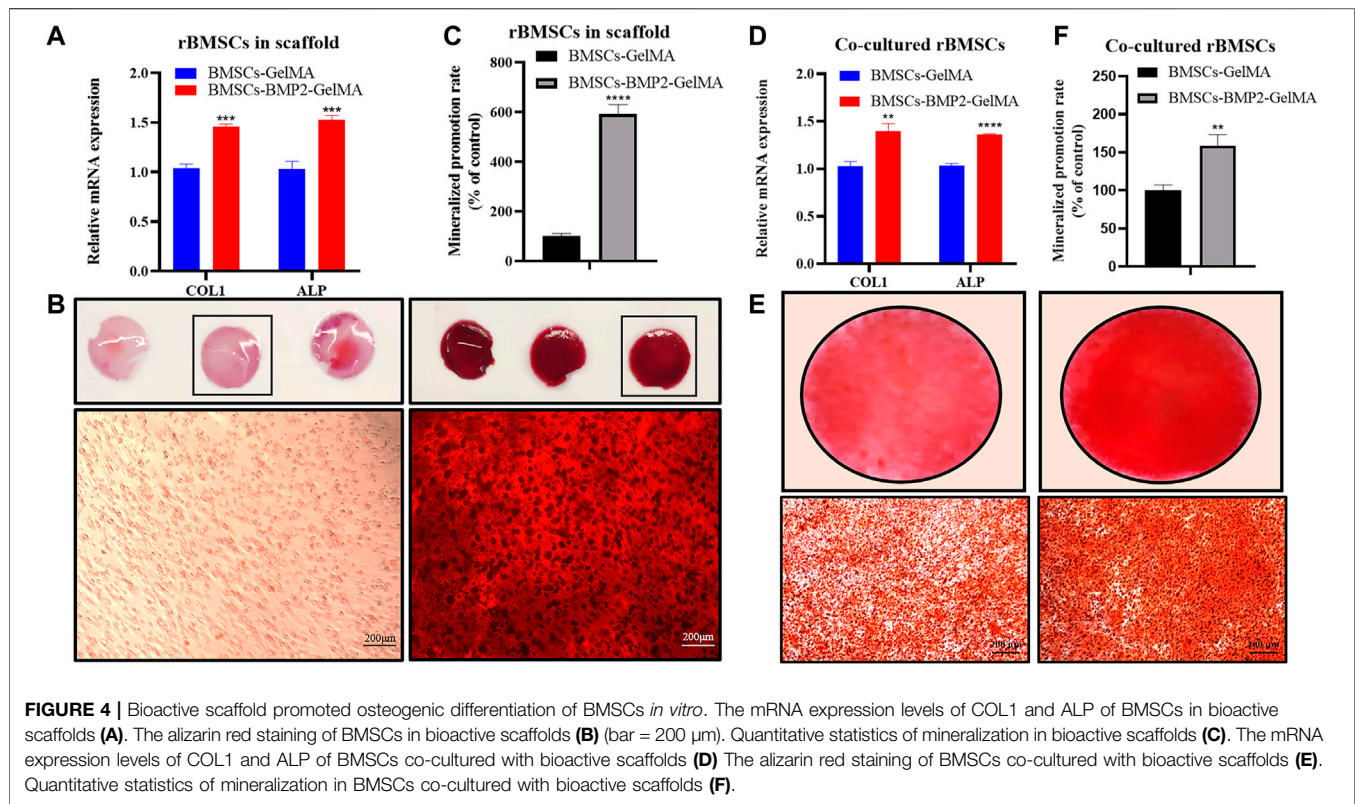
7 days of culture, BMSCs proliferated and migrated in hydrogel scaffolds, indicating that the photo-crosslinked scaffolds had good biocompatibility and were suitable for cell survival and growth (Figure 3B).

### Osteogenic Differentiation of BMSCs *In Vitro*

To investigate the effect of the bioactive scaffold micro-environment on the osteogenic differentiation of BMSCs in scaffolds and co-cultured BMSCs, the expression of osteogenic related genes, such as collagen type I (COL1), alkaline phosphatase (ALP) which can be used to evaluate the degree of osteogenic differentiation were detected by RT-qPCR (Sun et al., 2015). After 14 days of osteoblast induction, the expression levels of COL1 and ALP in BMSCs in the BMSCs-BMP2-GelMA group were higher than those in the BMSCs-GelMA group (Figure 4A). After 21 days of osteoblast induction, the results of Alizarin Red Staining (ARS) showed that there were more red-brown calcium nodules in BMSCs-BMP2-GelMA scaffolds than BMSCs-GelMA scaffolds (Figures 4B,C). It was observed that BMSCs co-cultured with BMSCs-BMP2-GelMA scaffolds showed relatively higher ALP and COL1 expression levels compared with BMSCs co-cultured with BMSCs-GelMA scaffolds (Figure 4D). Furthermore, the results from ARS performed to examine the mineralized nodules formation of BMSCs co-cultured with bioactive scaffolds, revealed that the BMSCs-BMP2-GelMA group had more calcium nodules than the BMSCs-GelMA group (Figures 4E,F). The sustained release of BMP2 in the scaffold continuously induces the osteogenic differentiation of stem cells inside and outside the scaffold, which has a better potential for repairing bone defects.

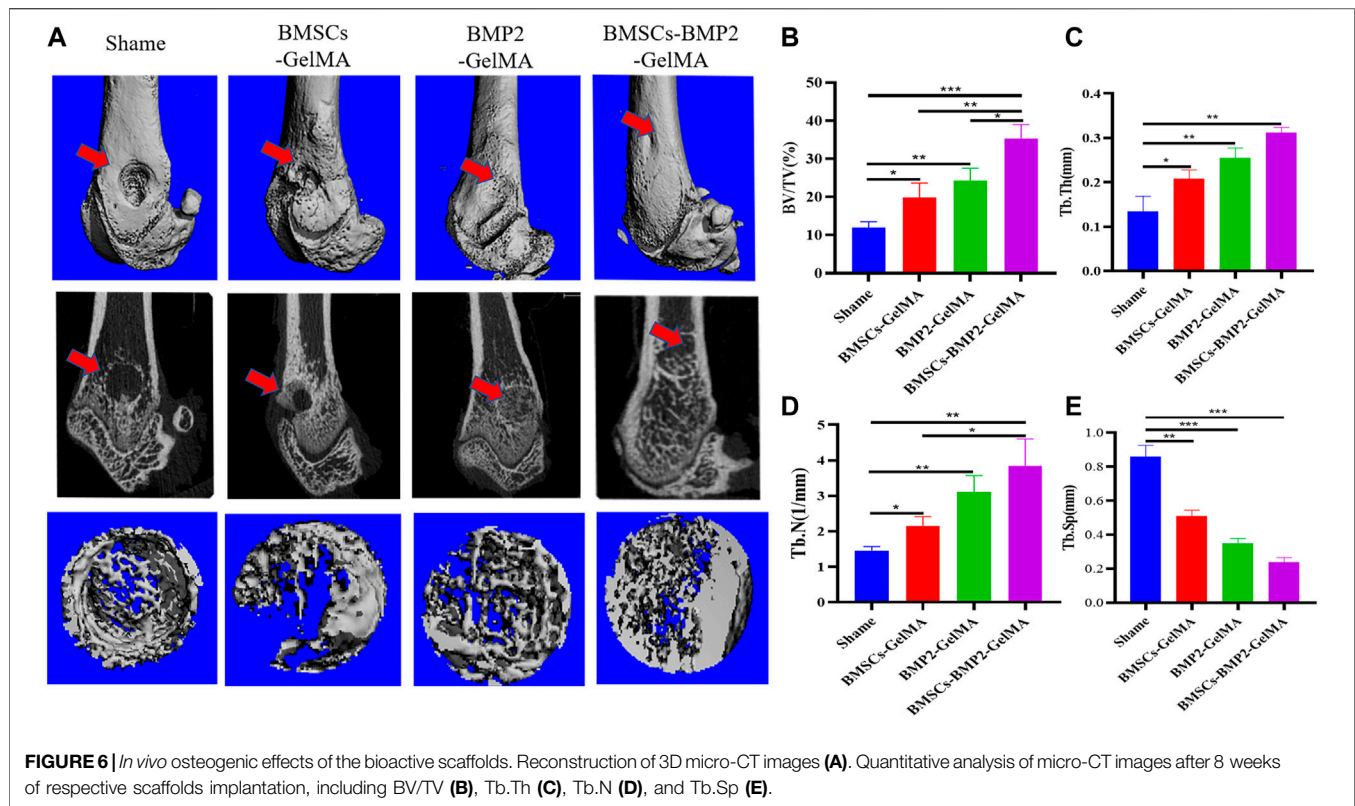
### The Biosafety of Bioactive Scaffolds *In Vivo*

The biosafety of bioactive scaffolds was evaluated by analyzing the serum indexes and organ sections from Sprague-Dawley (SD) rats. The serum biochemical test results demonstrated that alanine aminotransferase (ALT), aspartate aminotransferase



(AST), albumin (ALB), urea, cholesterol, and C-reactive protein (CRP) were all within the normal range (Figure 5A). In addition, histological examination showed

that the heart, liver, spleen, lung, and kidney collected from SD rats treated with bioactive scaffolds exhibited no obvious inflammation or damage (Figure 5B).



## Micro-Computed Tomography Scanning and Analysis

Micro-CT was used to scan rat femur specimens to observe the repair of bone defects. From the perspective of the 3D reconstruction of the defect site, 8 weeks after the operation, only a small amount of new bone tissue was formed in the control group. There were more new bone tissues in the BMSCs-GelMA group, BMP2-GelMA group, and BMSCs-BMP2-GelMA group than the control group. Among them, The BMSCs-BMP2-GelMA group had the most bone tissue at the distal femoral defect and the smallest defect area (Figure 6A). To further quantify the new bone tissue, the proportion of bone tissue volume (BV/TV) (Figure 6B), trabecular thickness (Tb.Th) (Figure 6C), trabecular number (Tb.N) (Figure 6D), and trabecular separation (Tb.Sp) (Figure 6E) in the defect area were calculated (Table 2.). The BV/TV, Tb.Th and Tb.N of the BMSCs-GelMA group, BMP2-GelMA group, and BMSCs-BMP2-GelMA group were significantly higher than those of the control group, and the difference was statistically significant ( $p < 0.05$ ). The BV/TV, Tb.Th and Tb.N of the BMSCs-BMP2-GelMA group was the highest among the four groups. The Tb.Sp of the BMSCs-BMP2-GelMA group, on the other hand, was the lowest of the four and statistically different from the other three ( $p < 0.05$ ). This indicated that the bioactive scaffolds carrying seed cells and cytokines like BMP2 have a better promoting effect on the formation of new bone tissue in bone defects, and the combined use of BMP2 and BMSCs has better osteogenic effects than the two alone.

## Histological Examination of Rat Femurs

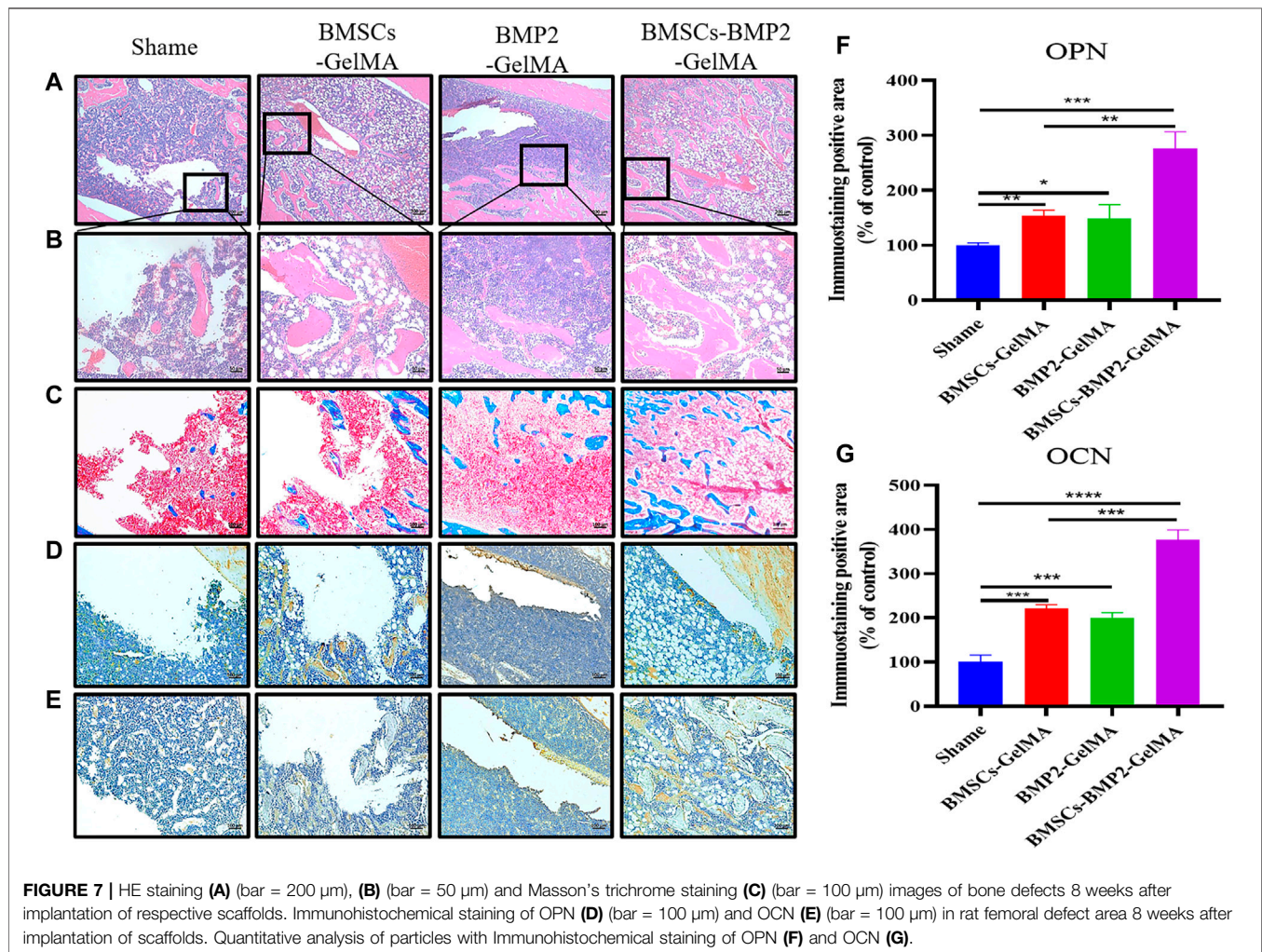
Eight weeks after surgery, the regenerated bone tissue in the defect area was further examined by histological analysis. The H&E staining results were consistent with the micro-CT reconstruction results. Compared with the control group, more connective tissue and new bone tissue were observed in the BMSCs-GelMA group, BMP2-GelMA group, and BMSCs-BMP2-GelMA group under high magnification (Figure 7A and Figure 7B). The bone defect treated with BMSCs-BMP2-GelMA scaffolds was mostly filled with newly formed bone. In the results of Masson's trichrome staining, collagen tissue of bone was stained blue while other tissues were stained red. The area of new bone tissue in the BMSCs-GelMA group, BMP2-GelMA group, and BMSCs-BMP2-GelMA group was higher than that of the control group. The area of new bone tissue in the BMSCs-BMP2-GelMA group was higher than that of the BMSCs-GelMA group and BMP2-GelMA group (Figure 7C).

Immunohistochemical staining was performed on late osteogenic differentiation markers: osteopontin (OPN) (Figure 7D) and osteocalcin (OCN) (Figure 7E) to evaluate the expression of osteogenic proteins and osteogenic potential in different groups (Byambaa et al., 2017). As shown in the figure, only a few positive staining cells were seen around the defect in the control group, and more positive staining areas were seen around the defect in the BMSCs-GelMA group, BMP2-GelMA group, and BMSCs-BMP2-GelMA group. The image analysis software was used to further evaluate the number of positive staining cells for OPN (Figure 7F) and OCN (Figure 7G). The results showed that the expression of



**TABLE 2 |** Results of rat bone trabeculae parameters at bone defects (Mean  $\pm$  SEM).

	Shame	BMSCs-GelMA	BMP2-GelMA	BMSCs-BMP2-GelMA
BV/TV (%)	11.92 $\pm$ 1.31	19.83 $\pm$ 3.16	24.24 $\pm$ 2.72	35.41 $\pm$ 2.96
Tb.Th (mm)	0.13 $\pm$ 0.03	0.21 $\pm$ 0.02	0.25 $\pm$ 0.02	0.31 $\pm$ 0.01
Tb.N (1/mm)	1.46 $\pm$ 0.09	2.15 $\pm$ 0.21	3.11 $\pm$ 0.38	3.85 $\pm$ 0.61
Tb.Sp (mm)	0.86 $\pm$ 0.05	0.51 $\pm$ 0.03	0.35 $\pm$ 0.03	0.24 $\pm$ 0.02



OPN and OCN in different groups had similar trends. The number of positive staining cells in the BMSCs-GelMA group, BMP2-GelMA group, and BMSCs-BMP2-GelMA group were significantly higher than that of the control ( $p < 0.05$ ). There was no significant difference in the number of positive staining cells between the BMSCs-GelMA group and the BMP2-GelMA group ( $p > 0.05$ ). The number of positive staining cells in the BMSCs-BMP2-GelMA group was significantly higher than that in the BMSCs-GelMA group and BMP2-GelMA group ( $p < 0.05$ ). The results showed that the composite bio-scaffolds containing stem cells and bone-promoting factors have the strongest bone-promoting ability in these four groups.

## DISCUSSION

This study demonstrated that the photo-crosslinked BMSCs-BMP2-GelMA bioactive hydrogel scaffold effectively promotes BMSCs osteogenic differentiation and bone tissue regeneration, and validated the biosafety of the composite scaffold *in vivo* and *in vitro* experiments. BMP2 and BMSCs in GelMA hydrogel scaffolds showed good synergistic effects in encouraging bone defect repair.

In this study, we injected a GelMA solution with a homogeneous mixture of BMSCs and BMP2 into the bone defect area to form a hydrogel scaffold by UV crosslinking. The mechanical properties of the scaffold affect the



proliferation, adhesion, and migration of cells in the scaffold (Hölzl et al., 2016). MSCs cultured in a harder matrix (Elastic Substrate 25–40 kPa) were morphologically similar to osteoblasts (Engler et al., 2006). The compressive maximum strain, compressive maximum stress, and Young's modulus all increased with increasing GelMA concentration. The Young's modulus of the 10% GelMA scaffold was  $40.47 \pm 6.36$  kPa, which is very close to the appropriate range for promoting MSC osteogenic differentiation as described above, 25–40 kPa. Consistent with previous reports, osteogenic differentiation was increased on stiffer matrices (Young's modulus of  $42.1 \pm 3.2$  kPa) compared to a hydrogel with Young's modulus of  $7.0 \pm 1.2$  kPa, as shown by gene expression of OPN et al. and mineralization (Shih et al., 2011). As the GelMA concentration increased, the pore size on the surface and inside the hydrogel decreased. The smaller pore size was not conducive to the proliferation and migration of BMSCs (McBeth et al., 2017; Yin et al., 2018). Therefore, 10% GelMA hydrogel was chosen for the subsequent cell experiments.

Bioresorbable scaffolds, seed cells, and growth factors are the three main elements of tissue engineering materials. Wu et al. prepared cell-laden GelMA microspheres by microfluidics synchronous crosslinked technology to promote tissue regeneration in a murine bone defect model (Wu et al., 2020). The survival rate of BMSCs in our bioactive scaffolds was higher at day 1 compared to BMSCs in microspheres, which may be related to the damage to cells during microsphere preparation. On day 7, the proliferation of BMSCs in microspheres and BMSCs in active scaffolds was close. This indicated that BMSCs exhibit good survival and proliferation in the bioactive scaffold, which is the basis for osteogenic differentiation of BMSCs. GelMA hydrogel scaffolds can also provide a more stable microenvironment for stem cells to thrive in, as well as the potential to differentiate into osteoblasts. BMP2 remained active in photo-crosslinking hydrogel scaffolds, stimulated DNA synthesis and cell replication, and stimulated osteogenic differentiation of BMSCs inside and outside the scaffolds. The loose and porous GelMA hydrogel scaffolds showed good effects on the sustained release of BMP2, with BMP2 release approaching 75% within a week. Reprogramming of osteogenic genes can be achieved by the addition of soluble induction factors during the first week of culture, but the effect of matrix elasticity on cell osteogenic differentiation is more pronounced after many weeks of culture (Engler et al., 2006). In the complex inflammatory environment of the bone defect area, the active scaffold provided a relatively stable microenvironment and adhesion sites for BMSCs. And the active scaffold released about 70% of the BMP2 in the first week, which continuously stimulated the adhesion and osteogenic differentiation of BMSCs inside and outside the scaffold. In the subsequent weeks, the stiffness and elasticity of the scaffold may play a greater role in promoting osteogenesis.

The FDA approved the clinical use of rhBMP2 in 2002, and it is still the only commercially available treatment as an alternative to bone transplants (James et al., 2016). It has been hypothesized

that supraphysiological amounts of BMP-2 are the main cause of significant adverse reactions such as inflammation and swelling (Halloran et al., 2020). Clinical evidence demonstrated that BMP2 injections also lead to an increased rate of osteoporotic and microfractures (Tannoury and An, 2014). The series of adverse effects associated with direct BMP2 injection has limited the clinical use of BMP2. Serological examinations and pathological examinations showed that neither low concentrations of slow-release BMP2 nor metabolites of GelMA hydrogel induced local and systemic inflammatory responses in rats. Sustained release of BMP2 from the bioactive scaffold induced osteogenic differentiation of BMSCs both inside and outside the scaffold and no significant adverse effects were observed *in vitro*. Animal experimental results showed that the BMSCs-BMP2-GelMA scaffold had the strongest bone defect repair among the four groups, which was superior to the BMSCs-GelMA scaffold and the BMP2-GelMA scaffold. This meant that scaffolds with combined application of seed cells and cytokines had a better chance of repairing bone defects. Achieving high viability implantation of MSCs and controlled slow release of BMP2 at the site of bone defects by tissue engineering techniques is an effective strategy to solve current clinical problems.

This study has several limitations. Firstly, BMP2 in the bioactive scaffold was released by simple diffusion and the degradation of the hydrogel, and the rate of BMP2 slow-release lacked regulation. Follow-up studies could further regulate the retention time of BMP2 *in vivo* through proteins with significant affinity for BMP2, or microparticle and microneedle encapsulation. Secondly, when investigating the mechanical properties of GelMA hydrogels, just the time point when the hydrogel was originally formed was measured. The changes in the physical properties of the hydrogel scaffolds with cell proliferation and mineralization in the hydrogel were still unclear. Finally, the sample size of animal experiments should be further expanded.

In summary, the composite bioactive scaffolds based on GelMA, BMSCs, and BMP2 were successfully prepared by photo-crosslinking. By forming hydrogel scaffolds *in situ* at the bone defects site, it provided a suitable carrier for the proliferation and migration of BMSCs and the sustained release of BMP2. The results demonstrated that, compared with the previous simple scaffold, the composite bioactive scaffold promoted the osteogenic differentiation of BMSCs in the scaffold and co-cultured *in vitro*, and showed stronger promotion of new bone tissue formation in the rat femoral defect model. Hence, this photo-crosslinked bioactive scaffolds with superior biocompatibility and osteogenic activity *in vitro* and *in vivo* can act as a promising graft for the treatment of irregular bone defects.

## DATA AVAILABILITY STATEMENT

The raw data supporting the conclusions of this article will be made available by the authors, without undue reservation.

## ETHICS STATEMENT

The animal study was reviewed and approved by Animal Ethics Committee of Nanjing Drum Tower Hospital.

## AUTHOR CONTRIBUTIONS

Conceptualization, SC and JH; methodology, SC and JH; software, SC and AM; validation, BW, YY, and XZ; formal analysis, AM; investigation, SC and AM; data curation, ZZ and CX; writing—original draft preparation, SC; writing—review and editing, ZX and QJ; visualization, SC and

JH; supervision, YY; project administration, ZX and QJ; funding acquisition, ZX and QJ. All authors have read and agreed to the published version of the manuscript.

## FUNDING

This work was supported by Natural Science Foundation of Jiangsu Province (BK20200121, BK20202013), China Postdoctoral Science Foundation (2020M671454), Key Program of NSFC (81730067), Major Project of NSFC (81991514).

## REFERENCES

- Arthur, A., and Gronthos, S. (2020). Clinical Application of Bone Marrow Mesenchymal Stem/Stromal Cells to Repair Skeletal Tissue. *Int. J. Mol. Sci.* 21 (24). doi:10.3390/ijms21249759
- Byambaa, B., Annabi, N., Yue, K., Trujillo-de Santiago, G., Alvarez, M. M., Jia, W., et al. (2017). Bioprinted Osteogenic and Vasculogenic Patterns for Engineering 3D Bone Tissue. *Adv. Healthc. Mater.* 6 (16). doi:10.1002/adhm.201700015
- Dickerman, R. D., Reynolds, A. S., Morgan, B. C., Tompkins, J., Cattorini, J., and Bennett, M. (2007). rh-BMP-2 Can Be Used Safely in the Cervical Spine: Dose and Containment Are the Keys!. *Spine J.* 7, 508–509. doi:10.1016/j.spinee.2007.03.003
- Dong, L., Bu, Z., Xiong, Y., Zhang, H., Fang, J., Hu, H., et al. (2021). Facile Extrusion 3D Printing of Gelatine methacrylate/Laponite Nanocomposite Hydrogel with High Concentration Nanoclay for Bone Tissue Regeneration. *Int. J. Biol. Macromolecules* 188, 72–81. doi:10.1016/j.ijbiomac.2021.07.199
- Engler, A. J., Sen, S., Sweeney, H. L., and Discher, D. E. (2006). Matrix Elasticity Directs Stem Cell Lineage Specification. *Cell* 126 (4), 677–689. doi:10.1016/j.cell.2006.06.044
- Ferreira, F. V., Otoni, C. G., De France, K. J., Barud, H. S., Lona, L. M. F., Cranston, E. D., et al. (2020). Porous Nanocellulose Gels and Foams: Breakthrough Status in the Development of Scaffolds for Tissue Engineering. *Mater. Today* 37, 126–141. doi:10.1016/j.mattod.2020.03.003
- Halloran, D., Durbano, H. W., and Nohe, A. (2020). Bone Morphogenetic Protein-2 in Development and Bone Homeostasis. *J. Dev. Biol.* 8 (3). doi:10.3390/jdb8030019
- Hölzl, K., Lin, S., Tytgat, L., Van Vlierberghe, S., Gu, L., and Ovsianikov, A. (2016). Bioink Properties before, during and after 3D Bioprinting. *Biofabrication* 8. doi:10.1088/1758-5090/8/3/032002
- James, A. W., LaChaud, G., Shen, J., Asatrian, G., Nguyen, V., Zhang, X., et al. (2016). A Review of the Clinical Side Effects of Bone Morphogenetic Protein-2. *Tissue Eng. B: Rev.* 22 (4), 284–297. doi:10.1089/ten.teb.2015.0357
- Jiang, G., Li, S., Yu, K., He, B., Hong, J., Xu, T., et al. (2021). A 3D-Printed PRP-GelMA Hydrogel Promotes Osteochondral Regeneration through M2 Macrophage Polarization in a Rabbit Model. *Acta Biomater.* 128, 150–162. doi:10.1016/j.actbio.2021.04.010
- Katagiri, T., and Watabe, T. (2016). Bone Morphogenetic Proteins. *Cold Spring Harb Perspect. Biol.* 8 (6). doi:10.1101/cshperspect.a021899
- Li, J., Wang, W., Li, M., Song, P., Lei, H., Gui, X., et al. (2021). Biomimetic Methacrylated Gelatin Hydrogel Loaded with Bone Marrow Mesenchymal Stem Cells for Bone Tissue Regeneration. *Front. Bioeng. Biotechnol.* 9, 770049. doi:10.3389/fbioe.2021.770049
- Li, L., Shi, J., Ma, K., Jin, J., Wang, P., Liang, H., et al. (2021). Robotic *In Situ* 3D Bio-Printing Technology for Repairing Large Segmental Bone Defects. *J. Adv. Res.* 30, 75–84. doi:10.1016/j.jare.2020.11.011
- Liu, H., Zhu, R., Liu, C., Ma, R., Wang, L., Chen, B., et al. (2017). Evaluation of Decalcification Techniques for Rat Femurs Using HE and Immunohistochemical Staining. *Biomed. Res. Int.* 2017, 9050754. doi:10.1155/2017/9050754
- McBeth, C., Lauer, J., Ottersbach, M., Campbell, J., Sharon, A., and Sauer-Budge, A. F. (2017). 3D Bioprinting of GelMA Scaffolds Triggers mineral
- Deposition by Primary Human Osteoblasts. *Biofabrication* 9 (1), 015009. doi:10.1088/1758-5090/aa53bd
- Ngan, C. G. Y., Quigley, A., Williams, R. J., O'Connell, C. D., Blanchard, R., Boyd-Moss, M., et al. (2021). Matured Myofibers in Bioprinted Constructs with *In Vivo* Vascularization and Innervation. *Gels* 7 (4). doi:10.3390/gels7040171
- Pape, H. C., Evans, A., and Kobbe, P. (2010). Autologous Bone Graft: Properties and Techniques. *J. Orthop. Trauma* 24 (Suppl. 1), S36–S40. doi:10.1097/BOT.0b013e3181cec4a1
- Ren, B., Chen, X., Du, S., Ma, Y., Chen, H., Yuan, G., et al. (2018). Injectable Polysaccharide Hydrogel Embedded with Hydroxyapatite and Calcium Carbonate for Drug Delivery and Bone Tissue Engineering. *Int. J. Biol. Macromolecules* 118 (Pt A), 1257–1266. doi:10.1016/j.ijbiomac.2018.06.200
- Rupp, M., Kerschbaum, M., Klute, L., Frank, L., and Alt, V. (2021). Knochentransplantation Oder Biomaterial? *Unfallchirurg* 124 (2), 146–152. doi:10.1007/s00113-020-00861-z
- Samorezov, J. E., Headley, E. B., Everett, C. R., and Alsberg, E. (2016). Sustained Presentation of BMP-2 Enhances Osteogenic Differentiation of Human Adipose-Derived Stem Cells in Gelatin Hydrogels. *J. Biomed. Mater. Res.* 104 (6), 1387–1397. doi:10.1002/jbm.a.35668
- Shi, Z., Wang, Q., Zhang, Y., and Jiang, D. (2020). Extracellular Vesicles Produced by Bone Marrow Mesenchymal Stem Cells Attenuate Renal Fibrosis, in Part by Inhibiting the RhoA/ROCK Pathway, in a UUO Rat Model. *Stem Cell Res Ther* 11 (1), 253. doi:10.1186/s13287-020-01767-8
- Shih, Y.-R. V., Tseng, K.-F., Lai, H.-Y., Lin, C.-H., and Lee, O. K. (2011). Matrix Stiffness Regulation of Integrin-Mediated Mechanotransduction during Osteogenic Differentiation of Human Mesenchymal Stem Cells. *J. Bone Miner Res.* 26 (4), 730–738. doi:10.1002/jbmr.278
- Sun, J., Li, J., Li, C., and Yu, Y. (2015). Role of Bone Morphogenetic Protein-2 in Osteogenic Differentiation of Mesenchymal Stem Cells. *Mol. Med. Rep.* 12 (3), 4230–4237. doi:10.3892/mmr.2015.3954
- Sun, Q., Shen, Z., Liang, X., He, Y., Kong, D., Midgley, A. C., et al. (2021). Progress and Current Limitations of Materials for Artificial Bile Duct Engineering. *Materials* 14 (23), 7468. doi:10.3390/ma14237468
- Tandon, A., Singh, A., Shetty, D., and Juneja, S. (2019). Tetrachromic VOF/Masson's Trichrome/H and E Stains: Unmasking Their Usability in Differential Stromal Hard Tissue Staining. *Indian J. Pathol. Microbiol.* 62 (1), 67–72. doi:10.4103/ijpm.ijpm\_242\_18
- Tannoury, C. A., and An, H. S. (2014). Complications with the Use of Bone Morphogenetic Protein 2 (BMP-2) in Spine Surgery. *Spine J.* 14 (3), 552–559. doi:10.1016/j.spinee.2013.08.060
- Wang, W., and Yeung, K. W. K. (2017). Bone Grafts and Biomaterials Substitutes for Bone Defect Repair: A Review. *Bioactive Mater.* 2 (4), 224–247. doi:10.1016/j.bioactmat.2017.05.007
- Wu, J., Li, G., Ye, T., Lu, G., Li, R., Deng, L., et al. (2020). Stem Cell-Laden Injectable Hydrogel Microspheres for Cancellous Bone Regeneration. *Chem. Eng. J.* 393, 124715. doi:10.1016/j.cej.2020.124715
- Xue, B., Gu, J., Li, L., Yu, W., Yin, S., Qin, M., et al. (2021). Hydrogel tapes for Fault-Tolerant strong Wet Adhesion. *Nat. Commun.* 12, 7156. doi:10.1038/s41467-021-27529-5
- Yang, Y., Cheng, Y., Yang, M., Qian, G., Peng, S., Qi, F., et al. (2022). Semicoherent Strengthens Graphene/zinc Scaffolds. *Mater. Today Nano* 17, 100163. doi:10.1016/j.mtnano.2021.100163

- Yin, J., Yan, M., Wang, Y., Fu, J., and Suo, H. (2018). 3D Bioprinting of Low-Concentration Cell-Laden Gelatin Methacrylate (GelMA) Bioinks with a Two-step Cross-Linking Strategy. *ACS Appl. Mater. Inter.* 10 (8), 6849–6857. doi:10.1021/acsami.7b16059
- Yoon, Y., Jung, T., Afan Shahid, M., Khan, I. U., Kim, W. H., and Kweon, O. K. (2019). Frozen-thawed Gelatin-Induced Osteogenic Cell Sheets of Canine Adipose-Derived Mesenchymal Stromal Cells Improved Fracture Healing in Canine Model. *J. Vet. Sci.* 20 (6), e63. doi:10.4142/jvs.2019.20.e63
- Zhang, Y., Li, Y., Liao, W., Peng, W., Qin, J., Chen, D., et al. (2021). Citrate-Stabilized Gold Nanorods-Directed Osteogenic Differentiation of Multiple Cells. *Ijn* 16, 2789–2801. doi:10.2147/ijn.s299515
- Zhao, X., Liu, S., Yildirimer, L., Zhao, H., Ding, R., Wang, H., et al. (2016). Injectable Stem Cell-Laden Photocrosslinkable Microspheres Fabricated Using Microfluidics for Rapid Generation of Osteogenic Tissue Constructs. *Adv. Funct. Mater.* 26 (17), 2809–2819. doi:10.1002/adfm.201504943
- Zou, Z., Wang, L., Zhou, Z., Sun, Q., Liu, D., Chen, Y., et al. (2021). Simultaneous Incorporation of PTH(1-34) and Nano-Hydroxyapatite into Chitosan/Alginate Hydrogels for Efficient Bone Regeneration. *Bioact Mater.* 6 (6), 1839–1851. doi:10.1016/j.bioactmat.2020.11.021

**Conflict of Interest:** CX was employed by the Hangzhou Lancet Robotics Company Ltd.

The remaining authors declare that the research was conducted in the absence of any commercial or financial relationships that could be construed as a potential conflict of interest.

**Publisher's Note:** All claims expressed in this article are solely those of the authors and do not necessarily represent those of their affiliated organizations, or those of the publisher, the editors and the reviewers. Any product that may be evaluated in this article, or claim that may be made by its manufacturer, is not guaranteed or endorsed by the publisher.

Copyright © 2022 Chai, Huang, Mahmut, Wang, Yao, Zhang, Zhuang, Xie, Xu and Jiang. This is an open-access article distributed under the terms of the Creative Commons Attribution License (CC BY). The use, distribution or reproduction in other forums is permitted, provided the original author(s) and the copyright owner(s) are credited and that the original publication in this journal is cited, in accordance with accepted academic practice. No use, distribution or reproduction is permitted which does not comply with these terms.



# Preparation of BMP-2/PDA-BCP Bioceramic Scaffold by DLP 3D Printing and its Ability for Inducing Continuous Bone Formation

Ziyang Yang<sup>1,2</sup>, Li Xie<sup>2\*</sup>, Boqing Zhang<sup>3</sup>, Gang Zhang<sup>1</sup>, Fangjun Huo<sup>2</sup>, Changchun Zhou<sup>3</sup>, Xi Liang<sup>2</sup>, Yujiang Fan<sup>3</sup>, Weidong Tian<sup>2\*</sup> and Yinghui Tan<sup>1\*</sup>

<sup>1</sup>Department of Stomatology, Xinqiao Hospital, Third Military Medical University, Chongqing, China, <sup>2</sup>State Key Laboratory of Oral Diseases and National Clinical Research Center for Oral Diseases and Engineering Research Center of Oral Translational Medicine, Ministry of Education and National Engineering Laboratory for Oral Regenerative Medicine, West China Hospital of Stomatology, Sichuan University, Chengdu, China, <sup>3</sup>National Engineering Research Center for Biomaterials, Sichuan University, Chengdu, China

## OPEN ACCESS

### Edited by:

Roman Surmenev,  
Tomsk Polytechnic University, Russia

### Reviewed by:

Xiong Lu,  
Southwest Jiaotong University, China  
ZuFu Lu,  
The University of Sydney, Australia

### \*Correspondence:

Yinghui Tan  
tanyh1962@outlook.com  
Li Xie  
samuel0121@163.com  
Weidong Tian  
drtwd@sina.com

### Specialty section:

This article was submitted to  
Biomaterials,  
a section of the journal  
Frontiers in Bioengineering and  
Biotechnology

Received: 14 January 2022

Accepted: 16 February 2022

Published: 06 April 2022

### Citation:

Yang Z, Xie L, Zhang B, Zhang G, Huo F, Zhou C, Liang X, Fan Y, Tian W and Tan Y (2022) Preparation of BMP-2/PDA-BCP Bioceramic Scaffold by DLP 3D Printing and its Ability for Inducing Continuous Bone Formation. *Front. Bioeng. Biotechnol.* 10:854693. doi: 10.3389/fbioe.2022.854693

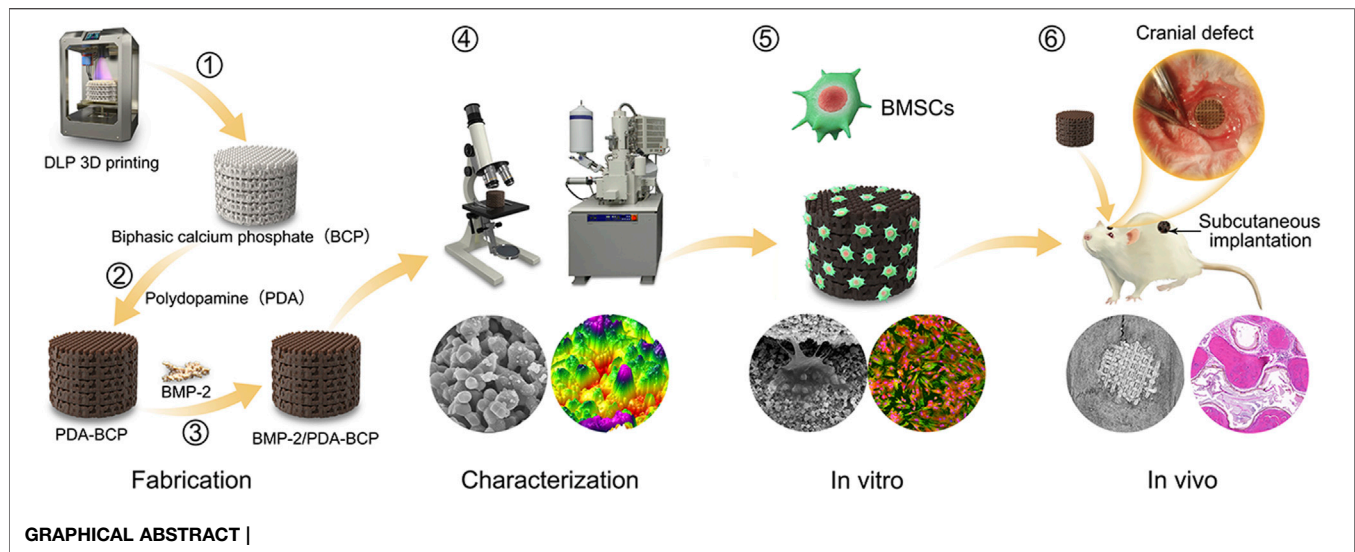
Digital light processing (DLP)-based 3D printing is suitable to fabricate bone scaffolds with small size and high precision. However, the published literature mainly deals with the fabrication procedure and parameters of DLP printed bioceramic scaffold, but lacks the subsequent systematic biological evaluations for bone regeneration application. In this work, a biphasic calcium phosphate (BCP) macroporous scaffold was constructed by DLP-based 3D printing technique. Furthermore, bone morphogenetic protein-2 (BMP-2) was facily incorporated into this scaffold through a facile polydopamine (PDA) modification process. The resultant scaffold presents an interconnected porous structure with pore size of ~570  $\mu\text{m}$ , compressive strength (~3.6 MPa), and the self-assembly Ca-P/PDA nanocoating exhibited excellent sustained-release property for BMP-2. Notably, this BMP-2/PDA-BCP scaffold presents favorable effects on the adhesion, proliferation, osteogenic differentiation, and mineralization of bone marrow stromal cells (BMSCs). Furthermore, *in vivo* experiments conducted on rats demonstrated that the scaffolds could induce cell layer aggregation adjacent to the scaffolds and continuous new bone generation within the scaffold. Collectively, this work demonstrated that the BMP-2/PDA-BCP scaffold is of immense potential to treat small craniofacial bone defects in demand of high accuracy.

**Keywords:** bone regeneration, DLP 3D printing, biphasic calcium phosphate, polydopamine, bone morphogenetic protein-2 (BMP-2)

## 1 INTRODUCTION

Bone tissue defects caused by trauma, infection, cancer, congenital diseases, and other reasons are increasingly common worldwide, which will greatly affect normal life and life quality of the patients (Green et al., 2017; Aghali, 2021). Nowadays, commonly used bone grafts to treat bone defects include autografts (gold standard), allografts, and xenografts. However, autografts and allografts are both restricted by issues of donor tissue availability, donor site morbidity, and anatomic shape mismatch, while both allografts and xenografts present shortcomings with immune response complications, risk of disease transmission, and lack of osteogenetic properties (Panagopoulos





et al., 2017; Shang et al., 2021). These issues have driven great research enthusiasm into new, cost-effective, and clinical-transformable strategies to treat critical-sized bone defects (Xie et al., 2021; Zhu et al., 2021).

With the advent of tissue engineering science and technology, tissue-engineered bone scaffolds are promising alternative choices for treatment of bone defects (Tan et al., 2021). Understandably, an ideal bone scaffold is expected to possess these properties (Ricciardi and Bostrom, 2013): 1) a match between the shape and size of the scaffold with the irregular and customized recipient site; 2) adequate porosity for new bone growth and new vessels; 3) mechanical properties consistent with the surrounding native bone; 4) cytocompatibility and biocompatibility of the scaffold; and 5) osteoconductivity and osteoinductivity of the scaffold materials. Therefore, a variety of biomaterials and manufacturing methods have been developed to fabricate patient-specific bone scaffolds in the past decades for repairing bone defects (Fu et al., 2021; Zhang et al., 2021; Zhao et al., 2021).

During the last decade, great progress has been achieved using 3D printing technologies to construct macroporous bioceramic scaffolds, thereby revolutionizing the traditional treatments of bone defects (Wen et al., 2017; Zhang L et al., 2019). Based on medical imaging data, 3D printing enables the mold-free fabrication of patient-specific bone substitutes with complex configuration directly from bioceramic powders and precise design of the structures at the macro- and micro-scales. Various 3D printing methods, including fused deposition modeling (FDM), selective laser sintering (SLS), stereolithography (SLA), and digital light processing (DLP)-based 3D printing, have been used for bone scaffold fabrication (Lee et al., 2018; Lin et al., 2019; Charbonnier et al., 2021). Compared with other 3D printing techniques, the DLP-based 3D printing has prominent advantages of high print resolution and fast print speed (Hong et al., 2020), which is suitable for printing scaffolds with small size and high precision. In regard of some bone defects in specific anatomic sites, e.g.,

cranial and maxillofacial bones, bone scaffold with small-size, shape-irregularity, and high-precision should be used, to recover a high-standard of functional or aesthetic appearance (Shen et al., 2020). In these cases, DLP-based 3D printing holds high promise.

Nowadays, DLP-based 3D printing is widely used to fabricate hydrogel scaffolds (Gong et al., 2020) and there are comparatively less reports to fabricate bioceramic scaffolds. For bioceramic scaffold fabrication, bioceramic powders should first be prepared in slurry type combined with photocurable resin as 3D printing inks (Kim et al., 2020). After DLP-based 3D printing, the scaffold subsequently should be thermally processed to remove the organic resin and obtain the final bioceramic scaffold. There are several reports regarding preparing DLP-printed bone scaffolds using hydroxyapatite (HA),  $\beta$ -tricalcium phosphate ( $\beta$ -TCP), and calcium silicate bioceramics (Shao et al., 2017; Zhang J et al., 2019; Schmidleithner et al., 2019). Zhang et al. (2020) recently prepared a structurally diversified Haversian bone-mimicking scaffold via DLP-based 3D printing using bioceramic  $\text{Ca}_2\text{MgSi}_2\text{O}_7$ , which is hard to fabricate through the FDM printing method. However, the existing published reports mainly dealt with the fabrication process and parameters of DLP printed bioceramic scaffold, but lack the subsequent systematic biological evaluations for bone regeneration application (Li et al., 2021). Recently, there is a growing interest in developing HA/ $\beta$ -TCP biphasic calcium phosphate (BCP) bioceramics as bone scaffolding materials because they are more effective in bone regeneration than pure HA or pure  $\beta$ -TCP, and have a controllable degradation rate (Kim and Park, 2020). However, there is rarely published literature reporting DLP-based printed BCP scaffolds in bone tissue engineering applications.

On the other hand, not only the customized shape and interconnected pores but hierarchical porous structures and biological properties (both osteoconductivity and osteoinductivity) of bone scaffolds are critical factors affecting cell behavior and osteogenic performance (Feng et al., 2021). Compared to scaffolds with a smooth surface, scaffolds with a

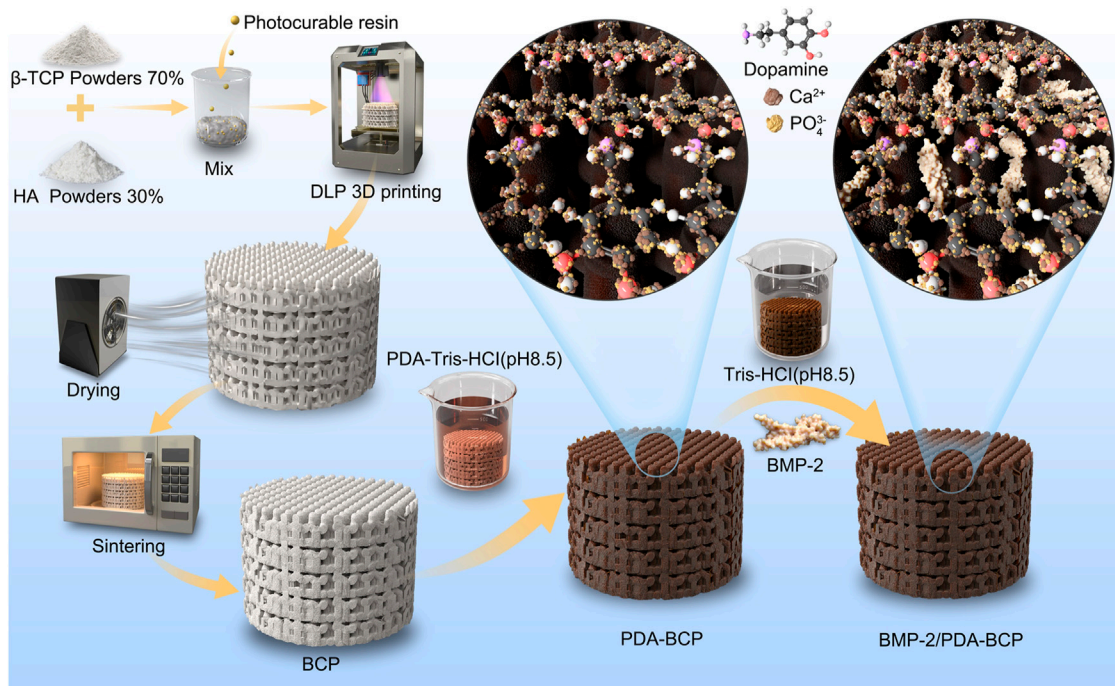


**FIGURE 1** | Schematic diagram of DLP 3D printing, modification of PDA, and grafting of BMP-2. DLP: digital light processing; PDA: polydopamine; BMP-2: bone morphogenetic protein-2.

porous surface structure in micro/nano-sized scale were found to be beneficial (Zhu et al., 2017). In addition, bone morphogenetic proteins (BMPs), particularly BMP-2, are capable of inducing the osteogenic differentiation of mesenchymal stem cells (MSCs) and accelerating bone regeneration in the clinic, showing excellent osteoinductivity (Zhou et al., 2018). However, the control over the surface morphology of the scaffold struts and the *in situ* delivery of bioactive agents appear difficult directly through DLP 3D printing, which calls for subsequent surface modification treatment.

Owing to the satisfactory biocompatibility, biodegradability, and substrate independent, mussel-inspired polydopamine (PDA) modification has great potential for further surface modification of 3D porous scaffolds (Liu et al., 2014). Ma et al. (2016) reported that a uniformly self-assembled Ca-P/PDA nanolayer was deposited on a  $\text{Ca}_7\text{Si}_2\text{P}_2\text{O}_{16}$  bioceramic scaffold fabricated by FDM printing. Furthermore, the formed self-assembled Ca-P/PDA composite nanolayer significantly enhances the attachment, proliferation, alkaline phosphate (ALP) activity, and bone-related gene expression of rabbit bone mesenchymal stem cells (rBMSCs). Besides, self-assembled PDA coating can also act as growth factors (GFs) delivery vehicle, which can adhere strongly to almost every kind of biomolecule owing to copious catechol moieties (Ryu et al., 2018). As far as we know, DLP-based printed BCP bioceramic scaffold with a GF-delivery PDA nanocoating has not been reported yet.

Based on the above background, we reported the fabrication of a DLP-based 3D printed BCP bioceramic scaffold with self-

assembly PDA modification and BMP-2 incorporation. Collectively, we proposed a novel bone tissue scaffold with comprehensive properties including designable macroporous structures, suitable bioceramic substrates, and osteogenic ability. The physicochemical properties of the PDA-modified scaffold, including surface topography, surface roughness, hydrophilicity, and mechanical strength are characterized. Also, the sustained release behavior of BMP-2 on the PDA-BCP scaffold was assessed. A schematic diagram of the fabrication procedure of porous scaffolds is shown in **Figure 1**. Then, the cell attachment, viability, proliferation, and osteogenic differentiation of BMSCs were systematically evaluated. We finally evaluated its bone regeneration capacity in a rat cranial bone defect model via micro-CT and histomorphometric analysis.

## 2 MATERIALS AND METHODS

### 2.1 Fabrication of the DLP-Based 3D Printed BCP Scaffold

The 3D structures of the scaffolds were designed by Materialize 3-matic software to obtain the 3D stereolithography (STL) files. With a mass ratio of 7:3,  $\beta$ -tricalcium phosphate ( $\beta$ -TCP) powders and hydroxyapatite (HA) powders were mixed and ball milled with a mass fraction of 25% photosensitive resin to obtain the precursor slurry. The bioceramic powders were supplied by the Engineering Research Center for Biomaterials of Sichuan University.

The precursor slurry was printed and cross-linked by a DLP-based 3D printer (AdMaflex 130Plus, AdMatec, Netherlands) following the STL files. The exposure time was 300 ms and the single-layer scanning time was 20 s for each 50- $\mu$ m thick slice. The wavelength of the light source was 400 nm. After printing, the samples were detached from the prototyping platform and washed by ultrasonication and further washed in alcohol for 15 min to remove the uncured resin and the solid bottom of the scaffolds were then removed. The green bodies of the BCP scaffolds were then sintered in a muffle furnace to obtain the pure bioceramic scaffolds. The sintering procedure was described as follows: first heated to 800°C at a rate of 5°C/min and kept for 2.7 h, then heated to 1100°C at a rate of 5°C/min for 5 h, and finally cooled to room temperature naturally in the furnace. Porous scaffolds with the preset pore sizes of 300  $\mu$ m, 600  $\mu$ m, 800  $\mu$ m, and 1000  $\mu$ m were fabricated. The size of each printed scaffold before and after sintering was measured by vernier caliper and the shrinkage rates were calculated.

## 2.2 Preparation and Characterization of PDA-Coated BCP Scaffolds

To prepare a self-assembled Ca-P/PDA nanolayer on the surface of the BCP bioceramic scaffold, dopamine hydrochloride (Aladdin, China) was first dissolved in 10 mM Tris-HCl buffer (pH 8.5) at a concentration of 2 mg/ml, 4 mg/ml, and 8 mg/ml, respectively. BCP scaffolds were soaked in Tris-dopamine solution for 24 h at 37°C in a 100-rpm oscillator. The samples were denoted as 2PDA-BCP, 4PDA-BCP, and 8PDA-BCP, respectively. After soaking, the samples were rinsed in ultrapure water three times and dried at 60°C overnight.

The gross images, surface microstructure, surface chemical composition, and surface roughness of the bare BCP scaffold and PDA-BCP scaffolds were characterized by stereoscopic microscope (SZX2, Olympus, Japan), scanning electron microscopy (SEM, SU8220, Hitachi, Japan), atomic force microscopy (AFM, Dimension Icon, Bruker, Germany), energy-dispersive spectroscopy (EDS, SU8220, Hitachi, Japan), and Fourier transform infrared spectroscopy (FTIR, Nicolet iN10, ThermoFisher, Massachusetts, United States). The hydrophilicity of scaffolds was detected by investigating with a water contact angle tester (DSA30, KRÜSS, Germany).

The released calcium (Ca) and phosphorus (P) ionic concentrations from the scaffolds were examined by inductively coupled plasma optical emission spectroscopy (ICP-OES). The scaffolds were soaked in the Tris-HCl solution (pH = 7.4) with a mass/volume ratio of 50 mg/ml at 37°C under constant agitation at 100 rpm. After 1, 3, and 7 d, the supernatants were collected for detection.

The compressive strength of the scaffolds was assessed by applying a vertical load on the samples using a universal testing machine (UTM, AGS-X, Shimadzu, Japan), all tests were implemented at a strain rate of 1 mm/min. The stiffness of specimens was obtained from the curve.

## 2.3 BMP-2 Loading and Release Profile Detection

The scaffolds were sterilized by epoxy ethane in advance. BMP-2 solution was prepared by dissolving the BMP-2 (Human BMP2 Protein [Recombinant His], LSBio, United States) in 10 mM Tris-HCl buffer (pH 8.5). Each of the scaffolds (BCP, 2PDA-BCP, 4PDA-BCP, and 8PDA-BCP) was immersed in 250 ng/ml BMP-2 solution for 24, 48, and 72 h, respectively. After that, the supernatants were collected, and the amount of unattached BMP-2 was quantified by ELISA assay using a human bone morphogenetic protein two ELISA kit according to the manufacturer's instructions (Jingmei Biotechnology, China). The adsorbed BMP-2 on the scaffolds was then calculated.

To investigate the *in vitro* release profiles of BMP-2 from BCP and PDA-BCP scaffolds, each scaffold was immersed in 1 ml of 250 ng/ml BMP-2 solution and incubated for 48 h under aseptic conditions at 37°C. Then, the scaffolds were washed gently with PBS and stored at -20°C for later use. Then they were incubated in 500  $\mu$ L PBS at 37°C in an incubator. The total release medium was taken out and frozen at -80°C at Day 1, 3, 5, 7, 10, 14, 21, 28, and 35, and replaced with an equal amount of fresh PBS solution. The quantitative measurement of the BMP-2 in the supernatants was performed using an ELISA Kit as mentioned above. The release curve was calculated in terms of the cumulative release percentage of BMP-2 (%) with incubation time. A standard curve was generated using known concentration (0.25–8 ng/ml).

## 2.4 *In vitro* Cell Responses of BMSCs on Scaffolds

### 2.4.1 Isolation and Culture of BMSCs

All the procedures were under a protocol approved by the Ethics Committee, West China School of Stomatology, Sichuan University, China. BMSCs were isolated from long bones of SD rats according to the previous literature (Boregowda et al., 2016). The cells were cultured in 90%  $\alpha$ -minimum essential medium ( $\alpha$ -MEM; HyClone) containing 10% fetal bovine serum (Gibco, a product line of Thermo Fisher Scientific, Waltham, MA, United States), 100 IU/ml penicillin, and 100  $\mu$ g/ml streptomycin. The medium was changed every 3 d and adherent cells were passaged until 80–90% confluence was achieved. Third-passage cells were used for subsequent experiments.

### 2.4.2 Cellular Viability, Proliferation, and Apoptosis of BMSCs on Scaffolds

The qualitative assessment on the cell viability of BMSCs was evaluated using the Live/Dead assay kit (keyGEN bioTECH, Jiangsu, China) after being cultured for 1 d and 4 d. In brief, a Live/Dead staining solution contained 2  $\mu$ M Calcein AM and 8  $\mu$ M propidium iodide (PI) was prepared in PBS, with Calcein AM detecting live cell and PI for dead cell identification. The samples were incubated with the staining solution at 37°C for 30 min, then they were washed again with PBS three times, and stained cells were imaged under a confocal laser scanning microscope (CLSM, Olympus FV1200, Olympus Corporation,



Japan). Live cell numbers were measured in three randomly selected images of each sample using NIH ImageJ 1.52i software.

On the hand, BMSCs were seeded on scaffolds in 48-well plates at a density of  $1 \times 10^4$  cells/well and cultured for 1, 4, and 7 d. At each time point, 40  $\mu$ l of CCK-8 solution mixed with 400  $\mu$ l culture medium was added to each well and the plates were incubated for 2.5 h. Then, 110  $\mu$ l aliquot was taken from each well and transferred to a fresh 96-well plate. The absorbance values were read at 450 nm ( $n = 3$ ) using a microplate reader (Spectrophotometer; ThermoFisher, Massachusetts, United States).

For the apoptosis assay, the scaffolds were placed to the upper chamber of the transwell and nearly  $1 \times 10^5$  cells/well were cultured on the lower chamber for 7 d. The cells were trypsinized and the cell suspension was centrifuged. BMSCs seeded on culture dishes without scaffolds were prepared as a blank control. The cells were stained using an Annexin V-FITC/PI Apoptosis assay Kit (Absin, Shanghai, China) following the manufacturer's instructions and analyzed using a BD Accuri C6 Flow Cytometer ( $n = 3$ ).

### 2.4.3 Cell Adhesion on Scaffolds

For the evaluation of cell attachment, BMSCs with a density of  $1 \times 10^5$  cells/well were seeded on BCP, PDA-BCP, BMP-2-BCP, and BMP-2/PDA-BCP scaffolds. After cultured for 1 d, the scaffolds were rinsed with PBS three times and fixed with 4% paraformaldehyde for 4 h. Then the fixative was removed by washing with PBS, followed by sequential dehydration in graded ethanol. The specimens were dried in hexamethyldisilane (HMDS) for 30 min before coating with gold for SEM analysis. The morphology of the attached cells was observed under SEM.

Meanwhile, cells cultured on scaffolds for 7 d were stained and observed under CLSM. The fixed cells were stained with phalloidin 647 Conjugate (1:1,000, Absin) for F-actin and DAPI (1:1,000, Sigma) for cell nuclei. Three random images were selected for measurement of mean gray value using ImageJ software.

## 2.5 Effect of Scaffolds on the Osteogenic Differentiation of BMSCs

### 2.5.1 ALP Activity and ALP Staining of BMSCs on Scaffolds

The ALP activity assay and ALP staining were performed to evaluate the osteogenic differentiation of BMSCs. There were  $5 \times 10^4$  cells seeded onto each scaffold and placed in a 48 well plate and cultured for 4, 7, and 14 d. After cell lysis, the supernatant was centrifuged and used for the ALP kit detection (Beyotime, Shanghai, China) according to the manufacturer's instruction. The results were normalized to the total protein content, which was measured by BCA protein assay kit (KeyGen, China).

For ALP staining, BMSCs with a density of  $5 \times 10^4$  cells/well were seeded on each pristine well (transwell of 12 wells). After 24 h, the medium was exchanged with osteogenic medium. ALP staining was evaluated after incubation for 10 d and performed by an ALP staining kit (Beyotime biotechnology, Shanghai, China). Briefly, the cell-seeded wells were fixed with 4% paraformaldehyde at room temperature for 15 min. After washing with PBS carefully, 5-Bromo-4-Chloro-3-Indolyl-Phosphate/Nitro-Blue-

**TABLE 1 |** List of qRT-PCR primers.

Target cDNA	Primer sequence (5'-3')
GAPDH-Forward	GACATGCCGCTGGAGAAAC
GAPDH-Reverse	AGCCCAGGATGCCCTTTAGT
Runx2- Forward	CTTCGTGAGCGTCCATCAGTTCC
Runx2-Reverse	TCCATCAGCGTCAACACCATCATTC
OCN- Forward	ACTCTGAGTCTGACAAAGCCTTCATG
OCN-Reverse	GGCTCCAAGTCCATTGTTGAGGTAG
COL 1- Forward	CGAGTCACACCGGAACCTTG
COL 1-Reverse	CCAATGTCCAAGGGAGCCAC
OPN- Forward	AACACTCAGATGCTGTAGCCACTTG
OPN-Reverse	GCTTTTCATTGGAGTTGCTTGAAGAG

Tetrazolium (BCIP/NBT) staining solution was added to ensure that the sample was fully covered. The samples were incubated for 30 min in the dark at room temperature. The reaction was terminated after washing with PBS 1–2 times, and the cell staining images were observed under an inverted microscope (Olympus, Tokyo, Japan).

### 2.5.2 Calcium Deposition and Mineralization Detection

The effect of the scaffolds on extracellular mineralization was detected on Day 21 of osteogenic induction. In short, medium was removed, gently washed with PBS 3 times, and fixed with 4% paraformaldehyde at room temperature for 15 min. After being washed with deionized water 3 times, 0.2% alizarin red solution was added for 30 min at room temperature. The plates were washed by deionized water 3 times, images were taken with digital cameras (EOS550D, Canon, Japan). In addition, the calcium nodules area was conducted in three random fields using ImageJ software. After the images were collected, 10% cetylpyridinium chloride (Sangon Biotech, Shanghai, China) (1 g with 10 m LDD water, shaken well in a shaker at 37°C to form a transparent solution) was incubated in the dark for 30 min, and 100  $\mu$ l was transferred to a 96-well plate to test the OD value at 560 nm.

### 2.5.3 Osteogenic-Related Gene Expression

The osteogenic-related mRNA expression of BMSCs, including runt-related transcription factor 2 (Runx-2), osteocalcin (OCN), collagen type 1 (Col-1), and osteopontin (OPN), on the scaffolds was determined by real-time quantitative PCR. Cells with density of  $1 \times 10^6$  cells/well were seeded onto each scaffold, which was placed in 6-well plates. The cells were incubated in osteogenic induction medium for 4, 7, and 10 d. The osteogenic medium contained 10 mM  $\beta$ -glycerol phosphate, 0.2 mM ascorbic acid, 0.01  $\mu$ M 1,25-dihydroxy vitamin D3, 10<sup>-8</sup> M dexamethasone. After the preset time point, Trizol Reagent® (Invitrogen Pty Ltd., Australia) solution was used to extract the total RNA according to the manufacturer's instructions. Relative expression levels for each gene were normalized against the cycle threshold (Ct) value of the house keeping gene (GAPDH) and determined by using the delta Ct ( $\Delta$ Ct) method. Each sample was performed in triplicate. The primer sequences used are described in **Table 1**.



### 2.5.4 Immunofluorescence Images for Osteocalcin and Osteopontin Expression

BMSCs were cultured in osteogenic medium in the presence of each scaffold as described above. After 14 days, cells were fixed with 4% paraformaldehyde solution, washed with PBS, and stored at 4°C until cytochemistry labeling. Cells were permeabilized with 0.2% (v/v) Triton X-100 for 20 min and nonspecific binding blocked with a 5% BSA solution (Solarbio, China). Then they were incubated overnight at 4°C with the primary antibodies osteocalcin (GTX13418, GeneTex) and osteopontin (AF0227, Affinity), respectively. Then, the cells were washed with PBS and incubated with appropriate Fluor-coupled secondary antibodies for 1 h. Nuclei were counter-stained with DAPI. The cells were thoroughly washed with PBS before observation under CLSM.

## 2.6 Animal Experiments

### 2.6.1 Animal Surgery Procedure

Eight-week-old male SD rats with a weight of  $280 \pm 20$  g were obtained from the Sichuan University Animal Center (Sichuan, China). All procedures concerning animal use were under a protocol approved by the Research Ethics Committee, West China Hospital of Stomatology of Sichuan University. Briefly, the animals were anesthetized by an intraperitoneal injection of 3% pentobarbital (1 ml/kg). Subsequently, rats were randomly divided into five groups: 1) BCP scaffold, 2) PDA-BCP scaffold, 3) BMP-2-BCP scaffold, 4) BMP-2/PDA-BCP scaffold, and 5) Control (without any scaffold). The scaffolds were immersed in 1 ml of 2500 ng/ml BMP-2 solution and incubated for 48 h under aseptic conditions at 37°C for the *in vivo* experiments. The scaffolds were subcutaneously implanted at the dorsum area of the SD rats for 1 and 4 weeks to study the *in vivo* biocompatibility and possible ectopic osteogenic ability. For the critical defect bone regeneration evaluation, a full-thickness calvarial bone defect (diameter: 8 mm) was created using a slow-speed dental drill. These rats were sacrificed under general anesthesia after 4, 8, and 12 weeks of implantation. The specimens, containing the cranial defect and 3–5 mm peripheral cortical bone adjacent to the defect, were harvested and fixed in 4% paraformaldehyde for further micro-computed tomography (micro-CT) and histological analysis.

### 2.6.2 Micro-CT Imaging and Osteogenic Analysis

New bone formation was examined using high-resolution micro-CT (SkyScan 1176 desktop X-ray micro-CT system, Bruker, Billerica, MA, United States). The voltage was set to 80 kV and the current was 300  $\mu$ A, with aluminum and cuprum filtration. 3D views of the region of interest were reconstructed by NRecon cone beam reconstruction software (Skyscan Company), and the threshold was optimized to isolate bone tissues and scaffolds. A cylinder area of 8 mm in diameter and 1.5 mm in height of the skull containing scaffolds was selected as the region of interest. The ratio of bone volume to total volume (BV/TV) and number of bone trabeculae (Tb.N) in the bone defects were calculated by using the auxiliary histomorphometric software (Ctan, Belgium).

### 2.6.3 Histological and Immunohistochemical Analysis

After micro-CT analysis, the harvested samples were fixed in 4% paraformaldehyde for 2 weeks and then were decalcified using 10% EDTA solution (pH 7.4) at 4°C for 4 weeks. 5- $\mu$ m thick sections were prepared and stained with hematoxylin and eosin (H&E) or Masson's trichrome according to the manufacturers' instructions. The sections were observed using a Panoramic MIDI II pathological section scanner (3DHISTECH, Ltd., Budapest, Hungary). At least five slices of Masson's trichrome stain for each group were analyzed. The area ratios of new bone were calculated in the NIH ImageJ 1.52i software. Immunohistochemistry (IHC) of OCN was performed to evaluate bone matrix deposition.

## 2.7 Statistical Analysis

Statistical analysis was conducted using GraphPad Prism 9.0.0 Software (GraphPad Software Inc.). All data were expressed as means  $\pm$  standard deviations (SD) and were analyzed using two-way ANOVA followed by a Turkey HSD post-hoc test, differences with *p*-values ( $^*p < 0.05$ ,  $^{**}p < 0.01$ ,  $^{***}p < 0.001$ ) were considered statistically significant. All quantifications were done with ImageJ 1.52 software on high resolution images.

## 3 RESULTS

### 3.1 Fabrication and Characterization of PDA-Modified 3D-Printed BCP Scaffolds

#### 3.1.1 Fabrication and Microstructure of DLP-Printed BCP Scaffold

BCP scaffolds with different designed pore sizes (300, 600, 800, 1000  $\mu$ m) could be fabricated through DLP-based 3D printing technology and a followed sinter treatment (**Supplementary Figure S1A**). The shrinkage rates after sintering were about 17–21% (**Supplementary Figures S1B, C**). Scaffolds with designed pore size of 600  $\mu$ m were chosen in the following experiments. The 3D printed disc-shape BCP scaffold was  $7.8 \pm 0.2$  mm in diameter,  $1.5 \pm 0.1$  mm in height (**Supplementary Figure S1D**). As shown in stereoscopic and SEM images (**Figure 2A**), the scaffold possessed a porous structure with inter-layered and regular 90–90° layer-by-layer pattern. The aperture was  $\sim 570 \pm 20$   $\mu$ m, the structure width was  $\sim 500$   $\mu$ m, and the porosity was  $\sim 67.3\%$ . At high-magnification SEM images, the syncretic micro-scale crystal grains could be observed with size about  $1.2 \pm 0.3$   $\mu$ m.

#### 3.1.2 Preparation and Physicochemical Properties of PDA-BCP Scaffolds

The 3D-printed BCP scaffolds were then treated in DA-Tris-HCl solution with different concentrations (2, 4, and 8 mg/ml) for 24 h to obtain a self-assembly PDA layer on the scaffold surfaces. Optical stereo images (**Figures 2B–D**) showed that the PDA-BCP scaffolds turned from white to brown and the color became darker with the increase of the concentration. The SEM images of PDA-BCP scaffolds showed that newly formed spherical precipitations, size ranging from 200–400 nm, could be found on both the surfaces and cross-sectional surface, which were

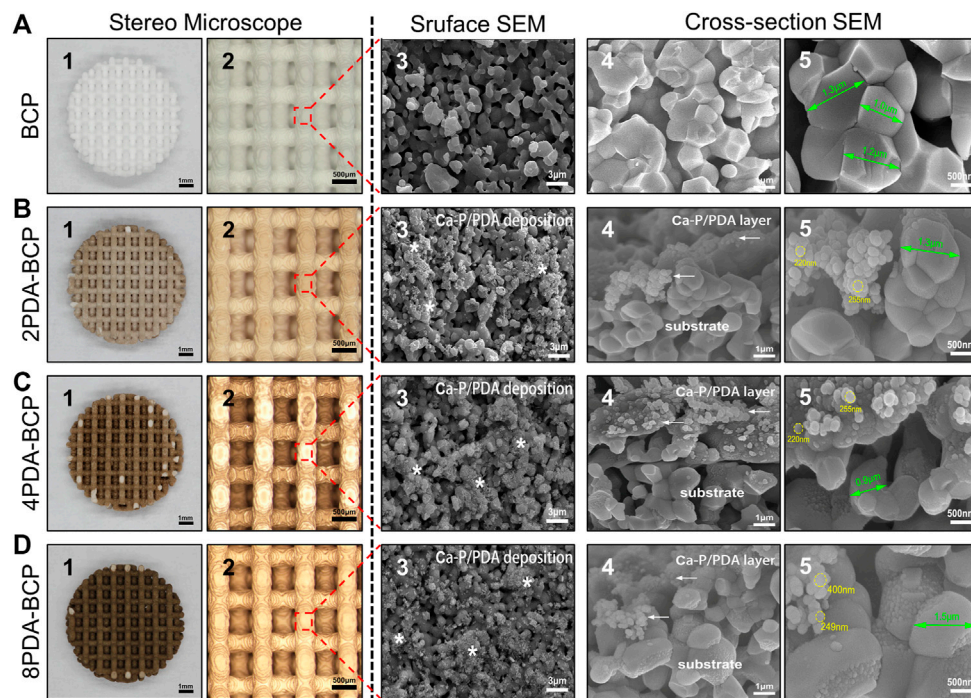


**FIGURE 2 |** Macroscopic morphology, surface microstructures, and cross-section morphologies of 3D printed scaffolds and PDA modification scaffolds on stereo microscope and scanning electron microscope. **(A)** BCP. **(B)** 2PDA-BCP. **(C)** 4PDA-BCP. **(D)** 8PDA-BCP. The white stars indicate deposition composed of Ca-P/PDA, the white arrows indicate the PDA layer and amorphous Ca-P nanoparticles. The grain size of BCP (green arrows), the size of new formation amorphous Ca-P nanoparticles (yellow circle). Scale bars = 1 mm, 500  $\mu$ m, 3  $\mu$ m, 1  $\mu$ m, 500 nm.

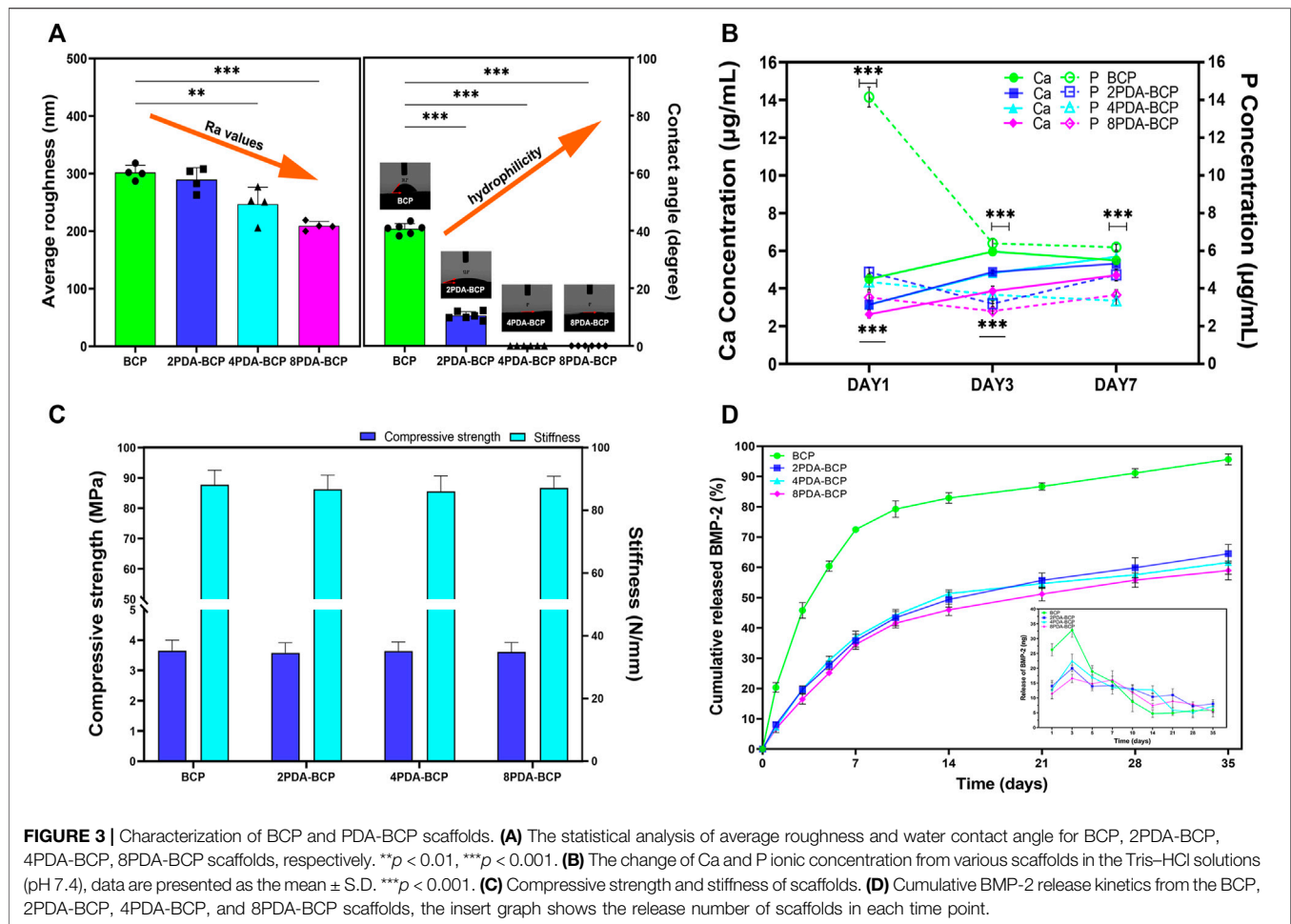
different from the pristine BCP crystallites. Besides, these newly formed crystals deposited on the scaffold surface can also be observed in the AFM images (**Supplementary Figure S2**). Also, FTIR spectra (**Supplementary Figure S3**) showed that all scaffolds exhibited vibrations of PO<sub>4</sub><sup>3-</sup> groups ranging from 960 to 1035 cm<sup>-1</sup> ascribed to HA and TCP (Lee et al., 2017). For PDA-BCP scaffolds, FTIR peaks at 3379 cm<sup>-1</sup> were corresponded to -OH and N-H groups and a range of characteristic peaks at 1500–1615 cm<sup>-1</sup> were assigned to different N-H bands, which were identified from dopamine and polydopamine (Li et al., 2014). Furthermore, the EDS analysis showed that the Ca/P ratio on the bare BCP scaffold surface was 1.538, while the Ca/P ratios of the newly formed precipitates on PDA-BCP scaffolds ranged between 1.604 and 1.640 (**Supplementary Figure S4**). Collectively, these results suggested that a layer of calcium-phosphate (Ca-P)/polydopamine (PDA) was uniformly formed on the BCP scaffold (Feng et al., 2020).

The Ra values calculated from AFM data were 302 nm, 290 nm, 247 nm, and 209 nm for the BCP, 2PDA-BCP, 4PDA-BCP, and 8PDA-BCP respectively, indicating that the surface roughness of the scaffolds decreased gradually with the increase of PDA concentration (**Figure 3A**). The surface hydrophilicity of the BCP scaffold was improved after PDA modification (**Figure 3A**). The water contact angle (WCA) values of BCP

and 2PDA-BCP scaffolds were  $40.6 \pm 1.8^\circ$  and  $10.5 \pm 1.4^\circ$ , respectively, while the 4PDA-BCP and 8PDA-BCP scaffolds were superhydrophilic with WCA of  $0^\circ$ . In addition, the ion solubility of the scaffolds is detected. As shown in **Figure 3B**, the concentrations of Ca<sup>2+</sup> and PO<sub>4</sub><sup>3-</sup> ion dissolved from PDA-BCP scaffolds were significantly lower than that from the bare BCP scaffold. The average values of compressive strength and stiffness of the BCP and PDA-BCP scaffolds were about 3.6 MPa and 86 N/mm, respectively (**Figure 3C**). The results also indicated that PDA modifications have no adverse effect on the compressive strength and stiffness of the BCP scaffolds.

### 3.1.3 BMP-2 Adsorption and Release Behavior

BMP-2 loading behaviors on BCP and PDA-BCP scaffolds were presented in **Supplementary Figure S5**. After 48 h, significantly more BMP-2 was immobilized (173.05 ng) on the 2PDA-BCP scaffold surfaces compared with that on the bare BCP scaffold (129.05 ng), while there is no significant difference among the three PDA-BCP scaffolds. The release kinetics of the BMP-2 from the scaffolds was investigated by ELISA assay. The release profiles of BMP-2 from the three PDA-BCP scaffolds exhibited similar trends and all showed a sustained release behavior with negligible burst release during the observed 35 d (**Figure 3D**). The cumulative released ratio of BMP-2 from the 2PDA-BCP scaffold was about 64.5% after 35 d. In contrast, the BMP-2



showed a burst release from the BCP scaffold within the initial 7 d. In the following experiments, 2PDA-BCP scaffold was chosen since it can meet the requirements for bone scaffold application as revealed by the above physicochemical and BMP-2 delivery properties.

### 3.2 In vitro Studies of PDA-Modified 3D-Printed BCP Scaffolds

#### 3.2.1 Cell Viability, Morphology, and Proliferation

The viability of BMSCs was qualitatively identified by live/dead fluorescent cell staining and observed by CLSM. As shown in **Figure 4A**, cells on all scaffolds displayed high viability, with almost no dead cells found in the images after 1 and 4 d of culture. In addition, the density of live cells on PDA-modified scaffolds was higher than that on bare BCP scaffolds (**Figure 4B**). Furthermore, the flow cytometry results (**Supplementary Figures S6A, B**) showed that the live cell ratios were all nearly 80% on the four kinds of scaffolds after incubation for 7 d, further demonstrating the excellent cell cytocompatibility of the scaffolds.

The adhesion and morphology of BMSCs on the scaffolds were further evaluated by SEM and CLSM (**Figures 4C,D**). After 24 h

of culture, cells could be observed to adhere and spread well on all scaffolds, showing flattened polygonal shapes and pseudopodia extension. In addition, many spreading cells exhibited on all the scaffolds on Day 7 after seeding (**Figure 4D**). Cells on the BMP-2/PDA-BCP scaffold were significantly more than those in the bare BCP scaffold (**Figure 4E**). Consistently, the BMP-2/PDA-BCP scaffold exhibited a higher proliferation rate compared with the bare BCP scaffold (**Figure 4F**). Additionally, cells on the PDA-BCP scaffold seemed to proliferate faster compared with the bare BCP scaffold, although with no significant difference on Day 7.

#### 3.2.2 Osteogenic Differentiation and Mineralization

ALP staining and ALP activity assay were used to monitor osteogenic differentiation of BMSCs on the scaffolds. The most intense ALP staining was observed in BMP-2/PDA-BCP scaffold among all the groups, followed by BMP-2-BCP scaffold (**Figure 5A**). As shown in **Figure 5B**, BMSCs on BMP-2/PDA-BCP scaffold exhibited the highest ALP activity. Also, cells on BMP-2-BCP and PDA-BCP scaffolds exhibited higher ALP activity compared with the bare BCP scaffold. The mineralization of BMSCs was examined by alizarin red staining of calcium nodules after 21 days of culture (**Figure 5C**). It was found that the calcium nodule area of the



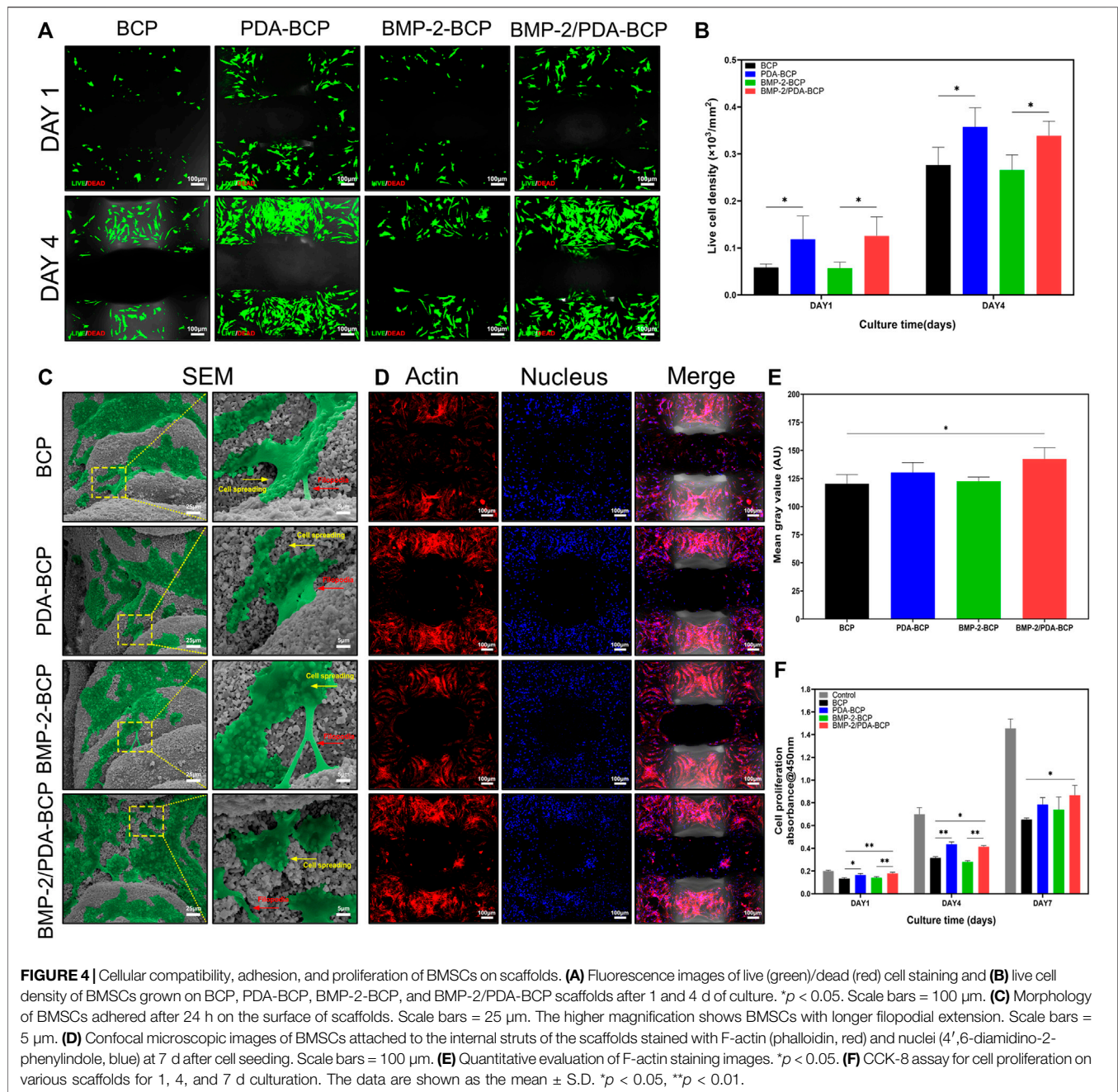


**FIGURE 4 |** Cellular compatibility, adhesion, and proliferation of BMSCs on scaffolds. **(A)** Fluorescence images of live (green)/dead (red) cell staining and **(B)** live cell density of BMSCs grown on BCP, PDA-BCP, BMP-2-BCP, and BMP-2/PDA-BCP scaffolds after 1 and 4 d of culture. \* $p < 0.05$ . Scale bars = 100  $\mu\text{m}$ . **(C)** Morphology of BMSCs adhered after 24 h on the surface of scaffolds. Scale bars = 25  $\mu\text{m}$ . The higher magnification shows BMSCs with longer filopodial extension. Scale bars = 5  $\mu\text{m}$ . **(D)** Confocal microscopic images of BMSCs attached to the internal struts of the scaffolds stained with F-actin (phalloidin, red) and nuclei (4',6-diamidino-2-phenylindole, blue) at 7 d after cell seeding. Scale bars = 100  $\mu\text{m}$ . **(E)** Quantitative evaluation of F-actin staining images. \* $p < 0.05$ . **(F)** CCK-8 assay for cell proliferation on various scaffolds for 1, 4, and 7 d cultivation. The data are shown as the mean  $\pm$  S.D. \* $p < 0.05$ , \*\* $p < 0.01$ .

BMP-2/PDA-BCP group was the largest, followed by the BMP-2-BCP group (Figure 5D). The OD values of dissolved alizarin red staining was well agreed with the results of calcium nodules counting (Figure 5E).

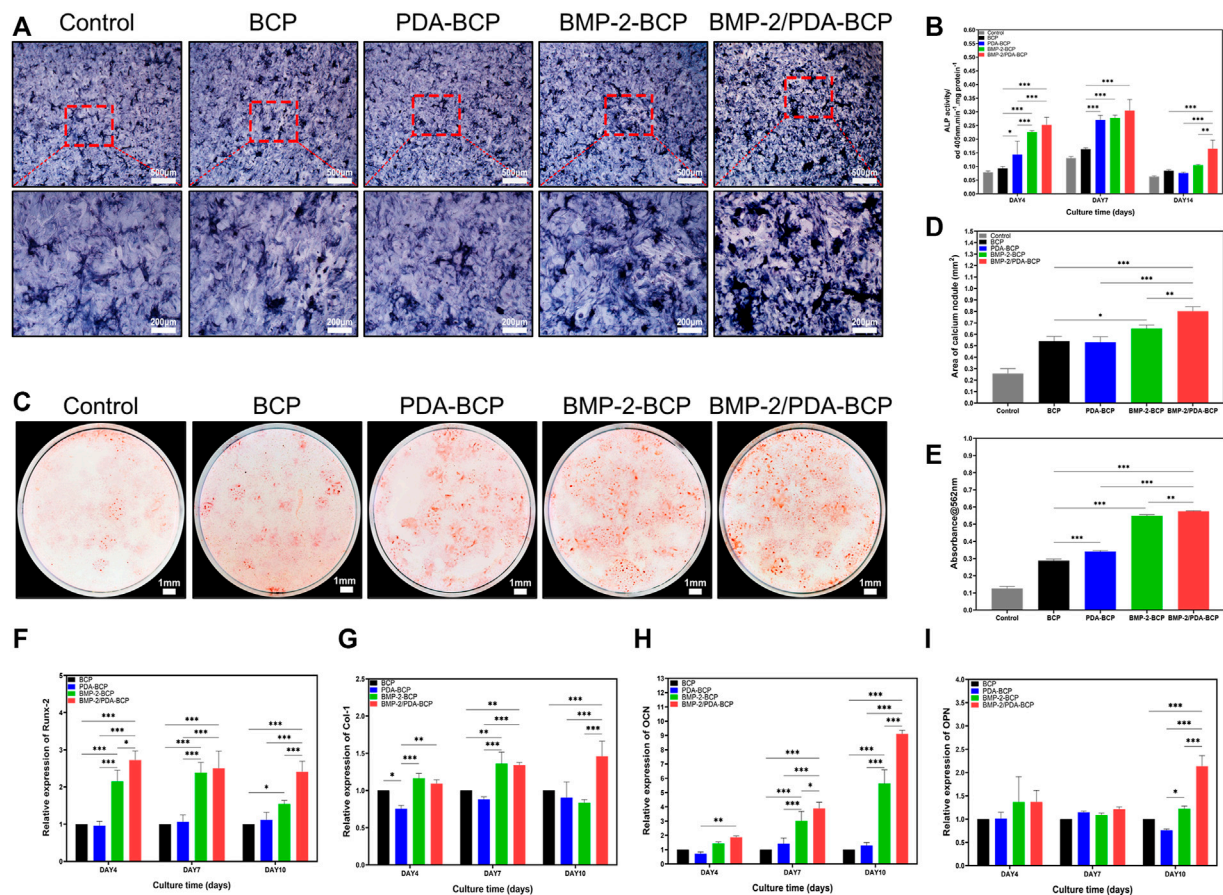
The qRT-PCR results of relative mRNA expression levels of osteogenic genes were displayed in Figures 5F–I. Generally, the BMP-2/PDA-BCP scaffold augmented the highest expression of OCN, Runx-2, and Col-1 on Day 4, 7, and 10. In addition, the BMP-2-BCP scaffold exhibited significant higher expression level of Runx-2 and OCN compared with PDA-BCP and BCP scaffolds on all time intervals. Also, the immunofluorescence staining of osteogenic-related proteins (OCN and OPN) (Supplementary

Figure S7) was the most pronounced on the BMP-2/PDA-BCP scaffold over the other groups, followed by the BMP-2-BCP scaffold.

### 3.3 *In vivo* Biocompatibility and Osteogenesis of BMP-2/PDA-BCP Scaffold

The results of subcutaneous implantation showed that all the scaffolds displayed good biocompatibility *in vivo*, without obvious inflammatory cells infiltration (Figure 6). Also, no obvious ectopic bone tissue formation could be found within all the scaffolds. Notably, an interesting phenomenon can be





**FIGURE 5 |** Effect of scaffolds on the osteogenic differentiation of BMSCs *in vitro*. (A) Representative microscopic images of ALP staining results for BMSCs after cultivation with scaffolds for 10 d. Scale bars = 500  $\mu$ m, 200  $\mu$ m. (B) The ALP activity was normalized by the total cell protein (OD 560 nm) of each sample at Days 4, 7, and 14 after seeding. (C) Representative digital images of alizarin red S staining of cells cultured in osteoinductive conditional medium for 21 d. Scale bars = 1 mm. (D) Quantification of alizarin red S staining area on various scaffolds from Figure 5C by ImageJ software. (E) Results of quantifying the amount of alizarin red S. Data are presented as the mean  $\pm$  S.D. \*\*\* $p$  < 0.001, \*\* $p$  < 0.01, \* $p$  < 0.05. qRT-PCR of osteogenic gene expression in BMSCs at 4, 7, and 10 d after seeding onto BCP, PDA-BCP, BMP-2-BCP, and BMP-2/PDA-BCP scaffolds under osteoinductive conditions, including (F) Runx-2, (G) Col-1, (H) OCN, and (I) OPN. \* $p$  < 0.05, \*\* $p$  < 0.01 and \*\*\* $p$  < 0.001.

observed that there are several layers of fibroblast-like cells formed adjacent to the scaffolds with PDA nanocoating on Week one and Week 4. Comparatively, a thinner cell layer formed alongside the BMP-2/BCP scaffold at 4 weeks, while the bare BCP scaffold did not show such phenomenon.

3D micro-CT data of calvarial bone defect repair in SD rats are presented in Figure 7A. In all four groups, the newly formed bone increased in volume from 4 to 12 weeks. The most amount of new bone was generated in the BMP-2/PDA-BCP group, followed by the BMP-2-BCP group. On Week 12, bone volume/total volume (BV/TV) and trabecular number (Tb.N) values of the BMP-2/PDA-BCP group were the largest among all the groups (Figures 7B,C).

H&E staining revealed progressive bone formation in four groups from 8 to 12 weeks (Figure 8A). The newly formed bone tissues seemed the largest in amount for the BMP-2/PDA-BCP group. Notably, continuous new bone generated alongside the

struct interspace (marked with green dotted lines) of PDA-BCP and BMP-2/PDA-BCP scaffolds, while such phenomenon cannot be observed in other scaffolds. In addition, the new bone tissue of the BMP-2-BCP and PDA-BCP scaffolds was more than the bare BCP scaffold. Consistent with H&E images, Masson staining images of 12 weeks showed that the BMP-2/PDA-BCP group obtained the greatest new bone ingrowth (Figure 8B), which is further proved by statistical result of new bone area (Supplementary Figure S8A). Similarly, continuous new bones could also be observed alongside the structure interspace (marked with green dotted lines) of PDA-BCP and BMP-2/PDA-BCP scaffolds. As shown in Supplementary Figure S8B, immunohistochemical images showed that the BMP-2/PDA-BCP group exhibited the highest expression levels of OCN, followed by the BMP-2-BCP group. The positively stained region of OCN was distributed in the extracellular matrix, especially in bone tissue.

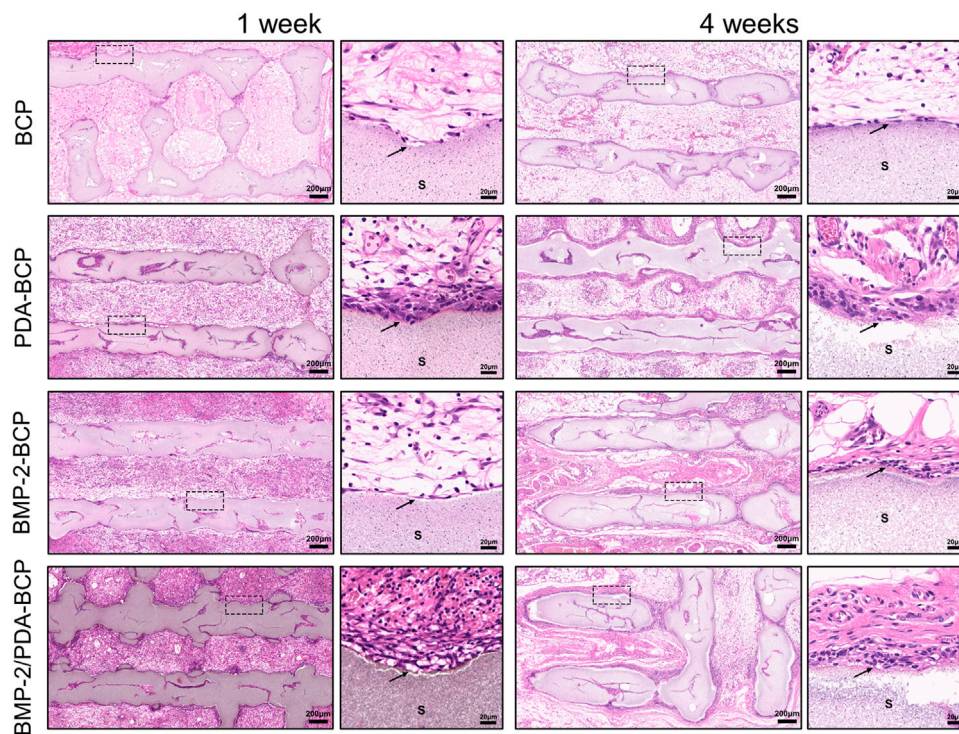


**FIGURE 6 |** Histological evaluation of the precursor cells infiltration in the ectopic osteogenesis model of SD rats after 1 and 4 weeks. Original magnification  $\times 50$ ,  $\times 500$ ; scale bar = 200  $\mu\text{m}$ , 20  $\mu\text{m}$ . Black arrows: cell adhesion layer, S: scaffolds.

## 4 DISCUSSION

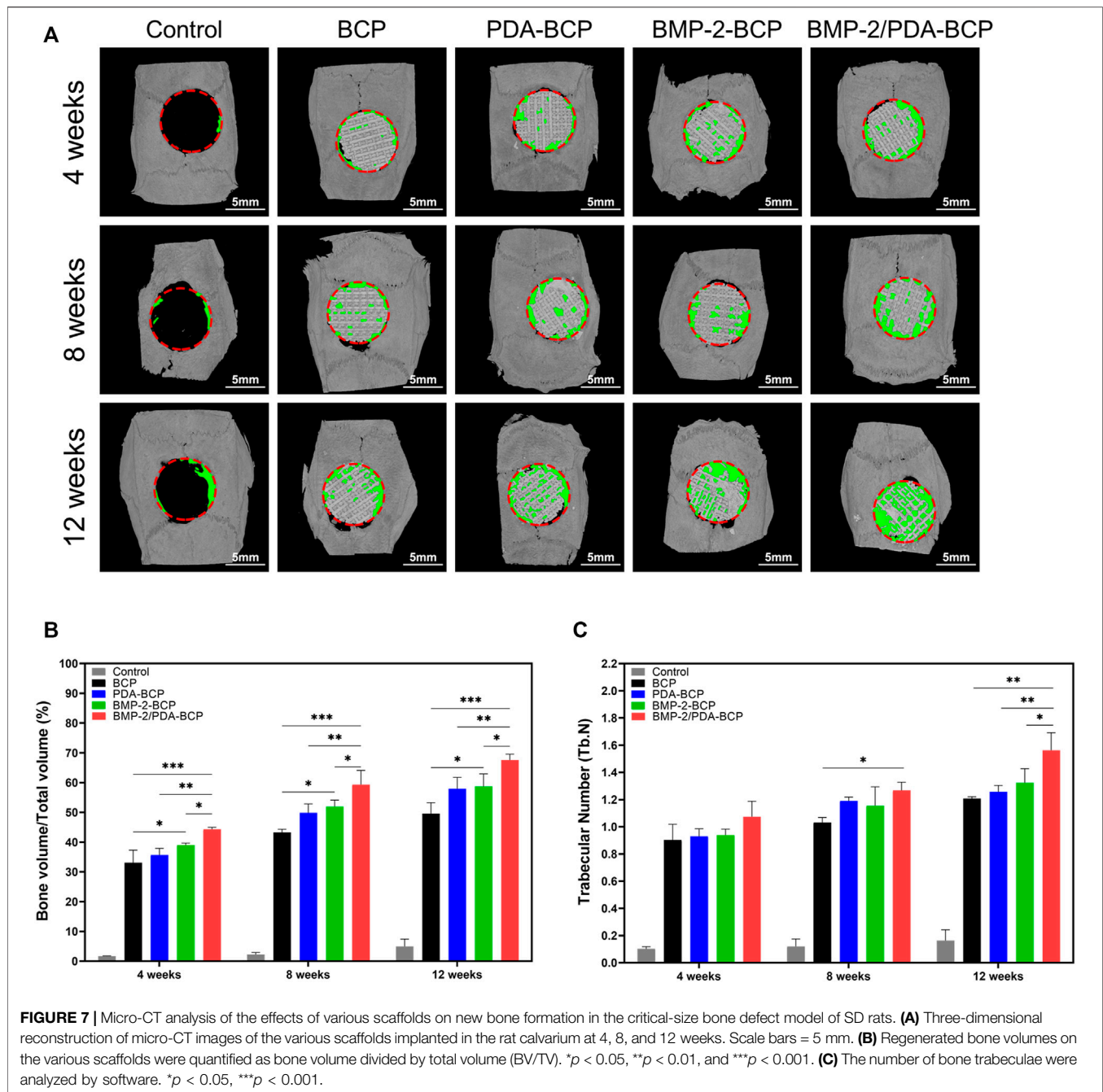
Owing to its high accuracy and fast speed, DLP-based 3D printing shows great application potential in fabrication of bioceramic bone scaffold for bone defects with small size and complex structure. But until now, comprehensive design and systematic biological evaluation about DLP-printed bioceramic scaffold are relatively less reported. In this study, we successfully fabricated 3D interconnected porous BCP scaffolds by DLP-based printing technique and further obtained a self-assembled Ca-P/PDA nanolayer, which can sustainably release BMP-2 protein. Through systematic physicochemical characterization, BMSCs evaluation, and *in vivo* experiments, the BMP-2/PDA-BCP scaffold exhibited excellent biocompatibility and enhancement effect on accelerating bone regeneration in continuous new bones formation.

3D printing based on the DLP technique is one of the attractive technologies suitable for preparation of high-performance porous bioceramics. This technique has the advantages of fast-forming speed, template-free, high-tunability, and high precision. It allows adequate control of accurate and versatile structure, which is relatively challenging for other fabrication methods (Roseti et al., 2017; Zeng et al., 2018). The size error between the designed model and the actual printing scaffolds can be guaranteed by setting a compensation error value induced by shrinking rates (Supplementary Figure

S1). The DLP-printed BCP scaffold had no obvious deformation after sintering and the high-interconnected pores could enhance mass transfer and benefit cellular penetration and tissue ingrowth (Tang et al., 2019). Additionally, the PDA-modification had no adverse effect on the mechanical strength of the scaffold. The compressive strengths of the PDA-BCP scaffolds were comparable with that of cancellous bone and thus were sufficient for non-load bearing bone regeneration (Morgan et al., 2018).

The SEM, FTIR, and EDS results together demonstrated the formation of Ca-P/PDA composite nanolayer on the BCP scaffold surfaces, which is consistent with the study published by Wu et al. and the formation mechanism was also clarified in that literature (Wu et al., 2014). Briefly, the formation mechanism of a Ca-P/PDA composite nanolayer involved two steps: 1) the addition of DA to Tris-HCl solution decreases the pH value and accelerates Ca and P ionic dissolution from the crystal boundaries of BCP ceramics; and 2) DA is polymerized to form self-assembled PDA film and, at the same time, Ca-P nanoparticles are mineralized with the assistance of PDA, in which the formation of PDA occurs simultaneously with Ca-P mineralization, and eventually a self-assembled Ca-P/PDA nanolayer forms. In addition, the EDS results (Supplementary Figure S4) revealed that the Ca/P ratio of the Ca-P deposits assembled on the PDA-BCP scaffold (Ca/P: 1.607–1.640) are higher than that of the pristine BCP scaffold (Ca/P: 1.538). Thus,





it is speculated that the unstable  $\beta$ -TCP phase (Ca/P: 1.5) in BCP scaffold transforms into more stable HA phase (Ca/P: 1.67) (Lee et al., 2014).

The surface roughness values and the wettability of the scaffolds changed after PDA modification. The Ra values decreased after PDA modification and decreased with the dopamine concentration. It is possible because the Ca-P/PDA deposits may fill some microscale cavities in the scaffold. In contrast to our observations, surface roughness increase due to PDA modification has been reported in previous literature (Wu et al., 2014). However, the PDA coating was deposited on  $\beta$ -TCP

discs with relatively smoother surfaces. Superhydrophilicity were mainly related to the Ca-P/PDA nanolayer, which contained abundant hydrophilic groups (NH<sub>2</sub>- and OH-) as well as nanostructures (Lynge et al., 2015; Qiu et al., 2018). Most studies have found that hydrophilic surfaces tend to enhance the early stages of osteoblast adhesion, proliferation, differentiation, and bone mineralization compared to hydrophobic surfaces (Wang et al., 2019; Lee et al., 2020; Wu et al., 2020). In addition, the dissolution rates of Ca and P ions from the PDA-BCP scaffold were slowed down, probably due to the physical diffusion barrier of the PDA coating and the

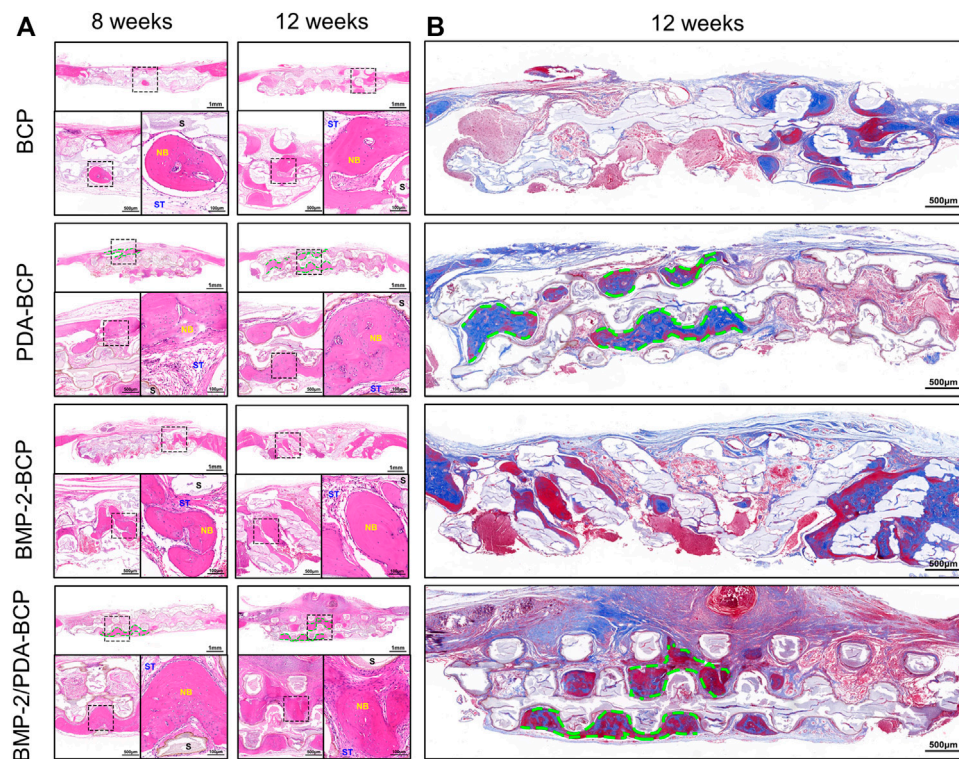


**FIGURE 8 |** Histological evaluation of new bone formation in the critical-size bone defect model of SD rats after 8 and 12 weeks. **(A)** Representative full image of H&E staining of cranial bone defects. Original magnification: 10 $\times$ , 30 $\times$ , 100 $\times$ ; scale bar = 1 mm, 500  $\mu$ m, 100  $\mu$ m. Green dotted line: continuous new bones; NB: newly formed bone; ST: soft tissue; S: scaffolds. **(B)** Full images of Masson's trichrome staining of decalcified bone in the defect area. Original magnification  $\times$ 20; scale bar = 500  $\mu$ m.

promotion of the secondary mineralization induced by PDA layer (Kaushik et al., 2020). Additionally, the long-term (35 d) sustained-release of BMP-2 was achieved through PDA layer immobilization. Compared with physical adsorption and other chemical conjunction techniques, the PDA chemistry is rather cost-effective, versatile, and suitable for growth factors delivery of 3D porous scaffolds (Cheng et al., 2019). It is considered that primary amine group of BMP-2 can covalently and non-covalently bind to the catechol/quinone groups in the PDA (Hauser et al., 2020).

Taken together of all the *in vitro* and *in vivo* results (Figures 4–8), we can generally conclude that the PDA-BCP scaffolds have advantages compared with BCP scaffold in BMSCs viability, adhesion, and proliferation, and new bone formation. These improvements should be related to the comprehensive property enhancement induced by PDA coating, including nanostructures, superhydrophilicity, and chemical groups of PDA. Previous studies have considered that PDA coating will increase serum proteins adsorption, which further favor cell adhesion (Meng et al., 2020; Wang et al., 2020). Jo et al. (2013) and Lee et al. (2016) demonstrated that PCL scaffolds modified with PDA facilitates cell proliferation and migration. In addition, different from PDA coating on polymer scaffold, the as-prepared Ca-P/PDA coating also exhibited a nano-sized porous topography and

it has been widely accepted that hierarchical porous structure is beneficial for BMSCs behaviors and *in vivo* osteogenesis (Xu et al., 2016).

Notably, cell layers were densely distributed alongside the PDA-modified scaffolds in the subcutaneous implantation experiments. The possible explanation is that the PDA coating improved cell adhesion and proliferation, which has been demonstrated by *in vitro* cell experiments. Additionally, continuous new bones formed alongside the struct interspace for PDA-modified scaffolds in rat cranial defects. These two phenomena might have close association. To the best of our knowledge, this is the first report on these phenomena for PDA-coated scaffold, and the underlying mechanism needs to be studied in the future. The BMP-2/PDA-BCP scaffold possessed the best osteogenic performances, which must be ascribed to the synergistic effect of the 3D structure of the scaffold, the BCP bioceramic, Ca-P/PDA nanocoating, and sustained-release of BMP-2. These factors together composed a favorable osteogenic microenvironment. Thanks to the DLP-based 3D printing technology, the porous BCP ceramic scaffold possessed a macroporous structure with interconnected pores, which is beneficial for oxygen and nutrient transportation, as well as bone tissue formation and blood vessels ingrowth. The chemical and phase composition of BCP bioceramics are similar with natural bone, which is crucial for its bioactivity



and osteoconductivity. As mentioned above, the PDA modification endowed the scaffold with nano-sized topography, superhydrophilicity, and chemical groups of PDA, which facilitate BMSCs viability, adhesion, and proliferation. BMP-2 is currently the only Food and Drug Administration (FDA)-approved osteoinductive growth factor used as a bone graft substitute. Additionally, the good “secondary reaction” characteristics of PDA coating enable it to deliver BMP-2 effectively and release slowly *in vivo*, continuously acting on the osteogenic site, further enhancing the osteogenic ability of the scaffold. Collectively, these factors play a synergistic and positive role in the change of local microenvironment which can facilitate bone regeneration. We plan to carry out research on DLP-based 3D printed scaffold for repairing small-sized maxillofacial bone defects in large animal models for future transformation.

## 5 CONCLUSION

Porous DLP-printed BCP bioceramic scaffolds coated with polydopamine/BMP-2 were successfully fabricated. The scaffold exhibits an interconnected porous structure with a pore size of  $\sim 570\ \mu\text{m}$  and acceptable compressive strength ( $\sim 3.6\ \text{MPa}$ ) that matched with load-free cancellous bone. Additionally, a uniform Ca-P/PDA nanocoating was formed on the whole external and internal surface of the scaffold, which endowed the scaffold with superhydrophilicity and BMP-2 delivery and sustained-release abilities.

Furthermore, BMSCs showed improved cell viability, adhesion, proliferation, osteogenic differentiation, and mineralization on BMP-2/PDA-BCP scaffolds compared with bare BCP scaffold. *In vivo* results of subcutaneous implantation and cranial defect repair on SD rats demonstrated that the PDA coating induced cell aggregation nearby the coating and continuous lamellar new bone formation within the scaffold. Taken together, this study provided a promising strategy to fabricate bone substitute scaffolds for enhanced bone regeneration for bone defects in demand for high precision and small size.

## REFERENCES

- Aghali, A. (2021). Craniofacial Bone Tissue Engineering: Current Approaches and Potential Therapy. *Cells* 10 (11), 2993. doi:10.3390/cells10112993
- Boregowda, S. V., Krishnappa, V., and Phinney, D. G. (2016). Isolation of Mouse Bone Marrow Mesenchymal Stem Cells. *Methods Mol. Biol.* 1416, 205–223. doi:10.1007/978-1-4939-3584-0\_11
- Charbonnier, B., Hadida, M., and Marchat, D. (2021). Additive Manufacturing Pertaining to Bone: Hopes, Reality and Future Challenges for Clinical Applications. *Acta Biomater.* 121, 1–28. doi:10.1016/j.actbio.2020.11.039
- Cheng, C.-H., Chen, Y.-W., Kai-Xing Lee, A., Yao, C.-H., and Shie, M.-Y. (2019). Development of Mussel-Inspired 3D-Printed Poly (Lactic Acid) Scaffold Grafted with Bone Morphogenetic Protein-2 for Stimulating Osteogenesis. *J. Mater. Sci. Mater. Med.* 30, 78. doi:10.1007/s10856-019-6279-x
- Feng, C., Wu, Y., Cao, Q., Li, X., Zhu, X., and Zhang, X. (2021). Effect of Hydrothermal Media on the *In-Situ* Whisker Growth on Biphasic Calcium Phosphate Ceramics. *Jpn* 16, 147–159. doi:10.2147/ijn.s280130

## DATA AVAILABILITY STATEMENT

The original contributions presented in the study are publicly available. This data can be found here: <https://www.ncbi.nlm.nih.gov/sra/>, PRJNA791405.

## ETHICS STATEMENT

The animal study was reviewed and approved by The Ethics Committee, West China School of Stomatology, Sichuan University, China.

## AUTHOR CONTRIBUTIONS

All authors listed have made a substantial, direct, and intellectual contribution to the work and approved it for publication.

## FUNDING

This study was supported by the Clinical Technology Innovation Cultivation Project of the Third Military Medical University (grant number CX2019JS108), the National Key R and D Program of China (grant number 2017YFA0104800), the National Natural Science Foundation of China (grant number 81970968), the Clinical major innovative characteristic Technology Project of the Second Affiliated Hospital of the Third Military Medical University (grant number 2018JSLC0022), and the Science and Technology Project of Sichuan University (grant number 2016CZYD0004-21).

## SUPPLEMENTARY MATERIAL

The Supplementary Material for this article can be found online at: <https://www.frontiersin.org/articles/10.3389/fbioe.2022.854693/full#supplementary-material>

- Feng, P., Peng, S., Shuai, C., Gao, C., Yang, W., Bin, S., et al. (2020). *In Situ* Generation of Hydroxyapatite on Biopolymer Particles for Fabrication of Bone Scaffolds Owning Bioactivity. *ACS Appl. Mater. Inter.* 12, 46743–46755. doi:10.1021/acsami.0c13768
- Fu, Y., Cui, S., Luo, D., and Liu, Y. (2021). Novel Inorganic Nanomaterial-Based Therapy for Bone Tissue Regeneration. *Nanomaterials (Basel)* 11 (3), 789. doi:10.3390/nano11030789
- Gong, L., Li, J., Zhang, J., Pan, Z., Liu, Y., Zhou, F., et al. (2020). An Interleukin-4-Loaded Bi-layer 3D Printed Scaffold Promotes Osteochondral Regeneration. *Acta Biomater.* 117, 246–260. doi:10.1016/j.actbio.2020.09.039
- Green, D. W., Ben-Nissan, B., Yoon, K. S., Milthorpe, B., and Jung, H.-S. (2017). Natural and Synthetic Coral Natural and Synthetic Coral Biomineralization for Human Bone Revitalization. *Trends Biotechnol.* 35, 43–54. doi:10.1016/j.tibtech.2016.10.003
- Hauser, D., Septiadi, D., Turner, J., Petri-Fink, A., and Rothen-Rutishauser, B. (2020). From Bioinspired Glue to Medicine: Polydopamine as a Biomedical Material. *Materials (Basel)* 13 (7), 1730. doi:10.3390/ma13071730
- Hong, H., Seo, Y. B., Kim, D. Y., Lee, J. S., Lee, Y. J., Lee, H., et al. (2020). Digital Light Processing 3D Printed Silk Fibroin Hydrogel for Cartilage Tissue Engineering. *Biomaterials* 232, 119679. doi:10.1016/j.biomaterials.2019.119679

- Jo, S., Kang, S. M., Park, S. A., Kim, W. D., Kwak, J., and Lee, H. (2013). Enhanced Adhesion of Preosteoblasts inside 3DPCL Scaffolds by Polydopamine Coating and Mineralization. *Macromol. Biosci.* 13, 1389–1395. doi:10.1002/mabi.201300203
- Kaushik, N., Nhat Nguyen, L., Kim, J. H., Choi, E. H., and Kumar Kaushik, N. (2020). Strategies for Using Polydopamine to Induce Biomineralization of Hydroxyapatite on Implant Materials for Bone Tissue Engineering. *Int. J. Mol. Sci.* 21 (18), 6544. doi:10.3390/ijms21186544
- Kim, J. W., Yang, B. E., Hong, S. J., Choi, H. G., Byeon, S. J., Lim, H. K., et al. (2020). Bone Regeneration Capability of 3D Printed Ceramic Scaffolds. *Int. J. Mol. Sci.* 21 (14), 4837. doi:10.3390/ijms21144837
- Kim, S. E. S. E., and Park, K. (2020). Recent Advances of Biphasic Calcium Phosphate Bioceramics for Bone Tissue Regeneration. *Adv. Exp. Med. Biol.* 1250, 177–188. doi:10.1007/978-981-15-3262-7\_12
- Lee, G. H., Makkar, P., Paul, K., and Lee, B. (2017). Development of BMP-2 Immobilized Polydopamine Mediated Multichannelled Biphasic Calcium Phosphate Granules for Improved Bone Regeneration. *Mater. Lett.* 208, 122–125. doi:10.1016/j.matlet.2017.05.017
- Lee, H. A., Park, E., and Lee, H. (2020). Polydopamine and its Derivative Surface Chemistry in Material Science: A Focused Review for Studies at KAIST. *Adv. Mater.* 32 (35), e1907505. doi:10.1002/adma.201907505
- Lee, J. B., Maeng, W. Y., Koh, Y. H., and Kim, H. E. (2018). Porous Calcium Phosphate Ceramic Scaffolds with Tailored Pore Orientations and Mechanical Properties Using Lithography-Based Ceramic 3D Printing Technique. *Materials (Basel)* 11 (9), 1711. doi:10.3390/ma11091711
- Lee, S. J., Lee, D., Yoon, T. R., Kim, H. K., Jo, H. H., Park, J. S., et al. (2016). Surface Modification of 3D-Printed Porous Scaffolds via Mussel-Inspired Polydopamine and Effective Immobilization of rhBMP-2 to Promote Osteogenic Differentiation for Bone Tissue Engineering. *Acta Biomater.* 40, 182–191. doi:10.1016/j.actbio.2016.02.006
- Lee, W.-H., Loo, C.-Y., and Rohanizadeh, R. (2014). A Review of Chemical Surface Modification of Bioceramics: Effects on Protein Adsorption and Cellular Response. *Colloids Surf. B: Biointerfaces* 122, 823–834. doi:10.1016/j.colsurfb.2014.07.029
- Li, Y., Shi, Y., Duan, S., Shan, D., Wu, Z., Cai, Q., et al. (2014). Electrospun Biodegradable Polyorganophosphazene Fibrous Matrix with Poly(dopamine) Coating for Bone Regeneration. *J. Biomed. Mater. Res.* 102, 3894–3902. doi:10.1002/jbm.a.35065
- Li, Y., Wu, R., Yu, L., Shen, M., Ding, X., Lu, F., et al. (2021). Rational Design of Nonstoichiometric Bioceramic Scaffolds via Digital Light Processing: Tuning Chemical Composition and Pore Geometry Evaluation. *J. Biol. Eng.* 15, 1. doi:10.1186/s13036-020-00252-3
- Lin, K., Sheikh, R., Romanazzo, S., and Roohani, I. (2019). 3D Printing of Bioceramic Scaffolds-Barriers to the Clinical Translation: From Promise to Reality, and Future Perspectives. *Materials (Basel)* 12 (17), 2660. doi:10.3390/ma12172660
- Liu, Y., Ai, K., and Lu, L. (2014). Polydopamine and its Derivative Materials: Synthesis and Promising Applications in Energy, Environmental, and Biomedical fields. *Chem. Rev.* 114, 5057–5115. doi:10.1021/cr400407a
- Lyng, M. E., Schattling, P., and Städler, B. (2015). Recent Developments in Poly(dopamine)-Based Coatings for Biomedical Applications. *Nanomedicine* 10, 2725–2742. doi:10.2217/nnm.15.89
- Ma, H., Luo, J., Sun, Z., Xia, L., Shi, M., Liu, M., et al. (2016). 3D Printing of Biomaterials with Mussel-Inspired Nanostructures for Tumor Therapy and Tissue Regeneration. *Biomaterials* 111, 138–148. doi:10.1016/j.biomaterials.2016.10.005
- Meng, X., Zhang, J., Chen, J., Nie, B., Yue, B., Zhang, W., et al. (2020). KR-12 Coating of Polyetheretherketone (PEEK) Surface via Polydopamine Improves Osteointegration and Antibacterial Activity *In Vivo*. *J. Mater. Chem. B* 8, 10190–10204. doi:10.1039/d0tb01899f
- Morgan, E. F., Unnikrisnan, G. U., and Hussein, A. I. (2018). Bone Mechanical Properties in Healthy and Diseased States. *Annu. Rev. Biomed. Eng.* 20, 119–143. doi:10.1146/annurev-bioeng-062117-121139
- Panagopoulos, G. N., Mavrogenis, A. F., Mauffrey, C., Lesenský, J., Angelini, A., Megalokonomos, P. D., et al. (2017). Intercalary Reconstructions after Bone Tumor Resections: a Review of Treatments. *Eur. J. Orthop. Surg. Traumatol.* 27, 737–746. doi:10.1007/s00590-017-1985-x
- Qiu, W.-Z., Yang, H.-C., and Xu, Z.-K. (2018). Dopamine-assisted Co-deposition: An Emerging and Promising Strategy for Surface Modification. *Adv. Colloid Interf. Sci.* 256, 111–125. doi:10.1016/j.cis.2018.04.011
- Ricciardi, B. F., and Bostrom, M. P. (2013). Bone Graft Substitutes: Claims and Credibility. *Semin. Arthroplasty* 24, 119–123. doi:10.1053/j.sart.2013.07.002
- Roseti, L., Parisi, V., Petretta, M., Cavallo, C., Desando, G., Bartolotti, I., et al. (2017). Scaffolds for Bone Tissue Engineering: State of the Art and New Perspectives. *Mater. Sci. Eng. C* 78, 1246–1262. doi:10.1016/j.msec.2017.05.017
- Ryu, J. H., Messersmith, P. B., and Lee, H. (2018). Polydopamine Surface Chemistry: A Decade of Discovery. *ACS Appl. Mater. Inter.* 10, 7523–7540. doi:10.1021/acsami.7b19865
- Schmidleithner, C., Malferrari, S., Palgrave, R., Bomze, D., Schwentenwein, M., and Kalaskar, D. M. (2019). Application of High Resolution DLP Stereolithography for Fabrication of Tricalcium Phosphate Scaffolds for Bone Regeneration. *Biomed. Mater.* 14, 045018. doi:10.1088/1748-605x/ab279d
- Shang, F., Yu, Y., Liu, S., Ming, L., Zhang, Y., Zhou, Z., et al. (2021). Advancing Application of Mesenchymal Stem Cell-Based Bone Tissue Regeneration. *Bioactive Mater.* 6, 666–683. doi:10.1016/j.bioactmat.2020.08.014
- Shao, H., Ke, X., Liu, A., Sun, M., He, Y., Yang, X., et al. (2017). Bone Regeneration in 3D Printing Bioactive Ceramic Scaffolds with Improved Tissue/material Interface Pore Architecture in Thin-wall Bone Defect. *Biofabrication* 9 (2), 025003. doi:10.1088/1758-5090/aa663c
- Shen, C., Witek, L., Flores, R. L., Tovar, N., Torroni, A., Coelho, P. G., et al. (2020). Three-Dimensional Printing for Craniofacial Bone Tissue Engineering. *Tissue Eng. A* 26, 1303–1311. doi:10.1089/ten.tea.2020.0186
- Tan, B., Tang, Q., Zhong, Y., Wei, Y., He, L., Wu, Y., et al. (2021). Biomaterial-based Strategies for Maxillofacial Tumour Therapy and Bone Defect Regeneration. *Int. J. Oral Sci.* 13, 9. doi:10.1038/s41368-021-00113-9
- Tang, Q., Hu, Z., Jin, H., Zheng, G., Yu, X., Wu, G., et al. (2019). Microporous Polysaccharide Multilayer Coated BCP Composite Scaffolds with Immobilised Calcitriol Promote Osteoporotic Bone Regeneration Both *In Vitro* and *In Vivo*. *Theranostics* 9, 1125–1143. doi:10.7150/thno.29566
- Wang, P., Yu, T., Lv, Q., Li, S., Ma, X., Yang, G., et al. (2019). Fabrication of Hydroxyapatite/hydrophilic Graphene Composites and Their Modulation to Cell Behavior toward Bone Reconstruction Engineering. *Colloids Surf. B: Biointerfaces* 173, 512–520. doi:10.1016/j.colsurfb.2018.10.027
- Wang, X., Peng, X., Yue, P., Qi, H., Liu, J., Li, L., et al. (2020). A Novel CPC Composite Cement Reinforced by Dopamine Coated SCPP Fibers with Improved Physicochemical and Biological Properties. *Mater. Sci. Eng. C* 109, 110544. doi:10.1016/j.msec.2019.110544
- Wen, Y., Xun, S., Haoye, M., Baichuan, S., Peng, C., Xuejian, L., et al. (2017). 3D Printed Porous Ceramic Scaffolds for Bone Tissue Engineering: a Review. *Biomater. Sci.* 5, 1690–1698. doi:10.1039/c7bm00315c
- Wu, C., Han, P., Liu, X., Xu, M., Tian, T., Chang, J., et al. (2014). Mussel-inspired Bioceramics with Self-Assembled Ca-P/polydopamine Composite Nanolayer: Preparation, Formation Mechanism, Improved Cellular Bioactivity and Osteogenic Differentiation of Bone Marrow Stromal Cells. *Acta Biomater.* 10, 428–438. doi:10.1016/j.actbio.2013.10.013
- Wu, L., Zhou, C., Zhang, B., Lei, H., Wang, W., Pu, X., et al. (2020). Construction of Biomimetic Natural Wood Hierarchical Porous-Structure Bioceramic with Micro/Nanowhisker Coating to Modulate Cellular Behavior and Osteoinductive Activity. *ACS Appl. Mater. Inter.* 12, 48395–48407. doi:10.1021/acsami.0c15205
- Xie, C., Ye, J., Liang, R., Yao, X., Wu, X., Koh, Y., et al. (2021). Advanced Strategies of Biomimetic Tissue-Engineered Grafts for Bone Regeneration. *Adv. Healthc. Mater.* 10 (14), e2100408. doi:10.1002/adhm.202100408
- Xu, M., Zhai, D., Xia, L., Li, H., Chen, S., Fang, B., et al. (2016). Hierarchical Bioceramic Scaffolds with 3D-Plotted Macropores and Mussel-Inspired Surface Nanolayers for Stimulating Osteogenesis. *Nanoscale* 8, 13790–13803. doi:10.1039/c6nr01952h
- Zeng, Y., Yan, Y., Yan, H., Liu, C., Li, P., Dong, P., et al. (2018). 3D Printing of Hydroxyapatite Scaffolds with Good Mechanical and Biocompatible Properties by Digital Light Processing. *J. Mater. Sci.* 53, 6291–6301. doi:10.1007/s10853-018-1992-2
- Zhang, J., Huang, D., Liu, S., Dong, X., Li, Y., Zhang, H., et al. (2019). Zirconia Toughened Hydroxyapatite Biocomposite Formed by a DLP 3D Printing Process for Potential Bone Tissue Engineering. *Mater. Sci. Eng. C* 105, 110054. doi:10.1016/j.msec.2019.110054
- Zhang, J., Jiang, Y., Shang, Z., Zhao, B., Jiao, M., Liu, W., et al. (2021). Biodegradable Metals for Bone Defect Repair: A Systematic Review and

- Meta-Analysis Based on Animal Studies. *Bioactive Mater.* 6, 4027–4052. doi:10.1016/j.bioactmat.2021.03.035
- Zhang, L., Yang, G., Johnson, B. N., and Jia, X. (2019). Three-dimensional (3D) Printed Scaffold and Material Selection for Bone Repair. *Acta Biomater.* 84, 16–33. doi:10.1016/j.actbio.2018.11.039
- Zhang, M. M., Lin, R., Wang, X., Xue, J., Deng, C., Feng, C., et al. (2020). 3D Printing of Haversian Bone-Mimicking Scaffolds for Multicellular Delivery in Bone Regeneration. *Sci. Adv.* 6 (12), eaaz6725. doi:10.1126/sciadv.aaz6725
- Zhao, D., Zhu, T., Li, J., Cui, L., Zhang, Z., Zhuang, X., et al. (2021). Poly(lactic-co-glycolic Acid)-Based Composite Bone-Substitute Materials. *Bioactive Mater.* 6, 346–360. doi:10.1016/j.bioactmat.2020.08.016
- Zhou, P., Wu, J., Xia, Y., Yuan, Y., Zhang, H., Xu, S., et al. (2018). Loading BMP-2 on Nanostructured Hydroxyapatite Microspheres for Rapid Bone Regeneration. *Ijn* 13, 4083–4092. doi:10.2147/ijn.s158280
- Zhu, G., Zhang, T., Chen, M., Yao, K., Huang, X., Zhang, B., et al. (2021). Bone Physiological Microenvironment and Healing Mechanism: Basis for Future Bone-Tissue Engineering Scaffolds. *Bioactive Mater.* 6, 4110–4140. doi:10.1016/j.bioactmat.2021.03.043
- Zhu, Y., Zhang, K., Zhao, R., Ye, X., Chen, X., Xiao, Z., et al. (2017). Bone Regeneration with Micro/nano Hybrid-Structured Biphasic Calcium Phosphate Bioceramics at Segmental Bone Defect and the Induced Immunoregulation of MSCs. *Biomaterials* 147, 133–144. doi:10.1016/j.biomaterials.2017.09.018
- Conflict of Interest:** The authors declare that the research was conducted in the absence of any commercial or financial relationships that could be construed as a potential conflict of interest.
- Publisher's Note:** All claims expressed in this article are solely those of the authors and do not necessarily represent those of their affiliated organizations, or those of the publisher, the editors, and the reviewers. Any product that may be evaluated in this article, or claim that may be made by its manufacturer, is not guaranteed or endorsed by the publisher.

Copyright © 2022 Yang, Xie, Zhang, Zhang, Huo, Zhou, Liang, Fan, Tian and Tan. This is an open-access article distributed under the terms of the Creative Commons Attribution License (CC BY). The use, distribution or reproduction in other forums is permitted, provided the original author(s) and the copyright owner(s) are credited and that the original publication in this journal is cited, in accordance with accepted academic practice. No use, distribution or reproduction is permitted which does not comply with these terms.



# A Biomimetic Platelet-Rich Plasma-Based Interpenetrating Network Printable Hydrogel for Bone Regeneration

Shijia Tang<sup>1†</sup>, Lin Wang<sup>1†</sup>, Yunyang Zhang<sup>2</sup> and Feimin Zhang<sup>1\*</sup>

<sup>1</sup>Jiangsu Province Key Laboratory of Oral Diseases, Department of Prosthodontics, The Affiliated Stomatological Hospital of Nanjing Medical University, Nanjing, China, <sup>2</sup>Center of Modern Analysis, Nanjing University, Nanjing, China

## OPEN ACCESS

### Edited by:

Lan Li,  
Nanjing Drum Tower Hospital, China

### Reviewed by:

Ming-Guo Ma,  
Beijing Forestry University, China  
Xiao Jiang,  
North Carolina State University,  
United States

### \*Correspondence:

Feimin Zhang  
fmzhang@njmu.edu.cn

<sup>†</sup>These authors have contributed  
equally to this work and share first  
authorship

### Specialty section:

This article was submitted to  
Biomaterials,  
a section of the journal  
Frontiers in Bioengineering and  
Biotechnology

**Received:** 01 March 2022

**Accepted:** 25 March 2022

**Published:** 12 April 2022

### Citation:

Tang S, Wang L, Zhang Y and Zhang F  
(2022) A Biomimetic Platelet-Rich  
Plasma-Based Interpenetrating  
Network Printable Hydrogel for  
Bone Regeneration.  
Front. Bioeng. Biotechnol. 10:887454.  
doi: 10.3389/fbioe.2022.887454

Repair of bone defects caused by trauma or diseases is the primary focus of prosthodontics. Hydrogels are among the most promising candidates for bone tissue regeneration due to their unique features such as excellent biocompatibility, similarities to biological tissues, and plasticity. Herein, we developed a type of novel biomimetic interpenetrating polymeric network (IPN) hydrogel by combining methacrylated alginate and 4-arm poly (ethylene glycol)-acrylate (4A-PEGAc) through photo-crosslinking. Platelet-rich plasma (PRP), a patient-specific source of autologous growth factors, was incorporated into the hydrogel, and thereafter the hydrogels were biological mineralized by simulated body fluid (SBF). Physical properties of hydrogels were comprehensively characterized. *In vitro* studies demonstrated that the incorporation of PRP and biomineralization promoted the biocompatibility of hydrogel. Strikingly, the osteogenic bioactivities, including ALP activity, mineralized nodule formation, and expression of osteogenic markers were found substantially enhanced by this biomineralized PRP-hydrogel. Finally, a rabbit model of bone defect was employed to assess *in vivo* bone regeneration, micro-CT analysis showed that the biomineralized PRP-hydrogels could significantly accelerate bone generation. We believed that this novel biomineralized PRP-incorporated IPN hydrogel could be promising scaffolds for bone tissue regeneration.

**Keywords:** platelet-rich plasma, interpenetrating polymeric network hydrogel, osteogenic differentiation, bone regeneration, biomineralization

## INTRODUCTION

Repair of bone defects is the primary focus of prosthodontics, especially with an increasing demand for bone grafts to heal bone defects due to trauma or diseases (Schneider et al., 2009). Although autografts and allografts remain commonly used clinically for the reparation of large bone defects, such approaches still have some drawbacks. For example, autografts could cause a secondary injury when obtaining donor tissue, while allografts pose a potential risk of pathogen transmission and immune rejection (Fleming et al., 2000; Lei et al., 2019; Busch et al., 2021). With the development of biotechnology, bone tissue engineering (BTE), which is expected to overcome these shortcomings, might provide a new tool for the treatment of bone defects (Zheng et al., 2022). The next-generation engineered bone tissues aim at mimicking physiological tissue morphology and functions by generating more complex and structurally organized implants (Hofmann et al., 2007). The scaffold is one of the



critical components in BTE. It acts as a temporary substrate or template as well as a carrier of biochemical factors, which can provide cells with both anchorage sites and appropriate physical (e.g., mechanical properties) and biochemical stimulation (e.g., cytokine, chemokine), therefore supporting cell growth and maintaining cell functions. In particular, the architecture of scaffold provides spatially mechanical stimulation to cells and defines the final shape of the newly formed bone (Schmid et al., 2019). Therefore, the outcome of bone tissue regeneration strategies is dependent, to a large extent, on the performance of scaffolds (Wang et al., 2007; Seok et al., 2021).

There are several kinds of biomaterials, including hydrogels, biological ceramics and collagen that have been developed as promising scaffolds for BTE (Huang et al., 2021; Li et al., 2021; Wang et al., 2021). Among them, hydrogels possess highly hydrated polymer networks, numerous functions towards cells and have been extensively utilized as bone substitute in the field of tissue engineering (Rastogi and Kandasubramanian 2019). Hydrogels are also good space filling agents (flexibility in fitting in any application site), delivery vehicles for bioactive molecules (controllability pore size in the polymer network), and three-dimensional culture matrices (Drury and Mooney 2003; Tan et al., 2005; Ma et al., 2020). All these advantages make hydrogels a promising candidate for using in bone tissue engineering scaffolds. Recently, interpenetrating network (IPN) hydrogels with two or more networks have attracted considerable attention in the field of BTE due to the enhanced mechanical strength and toughness (Scalet et al., 2021; Zou et al., 2021). There are several studies that have demonstrated that the mechanical performance of IPN hydrogels was far superior compared with either of the “parent” networks (Ingavle et al., 2016). However, the application of IPN hydrogels is still limited since the inability to provide cells with proper microenvironment, such as lack of cell adhesion sites and therefore unable to induce bone regeneration. Therefore, it is highly desirable and a great challenge to prepare IPN hydrogels-based scaffolds with excellent biological activities for bone tissue regeneration.

We hypothesized this lack of cell compatibility can be substantially improved by combining synthetic IPN hydrogels and bioactive agents, including nanocrystalline hydroxyapatite (nHAp), calcium phosphate and growth factors (Li C. et al., 2020; Dabiri et al., 2021). Among them, growth factors are essential for successful bone regeneration and their importance has been shown in the previous study (Boyle et al., 2013; Wu et al., 2020). Platelet-rich plasma (PRP) is a mixture of highly concentrated platelets and associated growth factors, including platelet derived growth factor (PDGF), vascular endothelial growth factor (VEGF), transforming growth factor- $\beta$  (TGF- $\beta$ ), fibroblast growth factor (FGF) and insulin-like growth factors I (IGF-I) (Foster et al., 2009; Franchini et al., 2018). Numerous studies have shown the effectiveness and versatility of PRP in regeneration/repair of skin, cartilage and bone (Hom 1995; Rodriguez et al., 2013). Particularly in the case of bone regeneration, PRP-based scaffolds were demonstrated to be capable of enhancing bone density/mineralization, vascularization and osteogenesis (Rai et al., 2007; Zhou et al., 2021).

In the present study, we fabricated a novel biomimetic PRP-incorporated methacrylated alginate/4Arm-PEGAc IPN hydrogels through photo-crosslinking upon exposure to long-wave UV light and further biological mineralized through exposure to native calcium ions in simulated body fluid (SBF). Cell proliferation and adhesion were measured to investigate their biological activities using BMSCs. After that, Alkaline phosphatase (ALP) activity level, Alizarin red staining, expression of osteogenic-related genes and proteins were detected to investigate their osteogenic bioactivities. Moreover, the IPN hydrogels were surgically implanted to a rabbit condyle defects for *in vivo* bone regeneration assessment. We believe that the biomineralized PRP-incorporated IPN hydrogel can be used as promising scaffolds for bone tissue regeneration.

## MATERIALS AND METHODS

### Materials

Rabbit bone marrow mesenchymal stem cells were purchased from Cyagen Co. Ltd. (GuangZhou, China). Sodium alginate, methacrylic anhydride, 2-hydroxy4'-(2-hydroxyethoxy)-2-methylpropiophenone (Irgacure 2959, 98%) and sodium hydroxide (NaOH) were purchased from Sigma-Aldrich Co. Ltd. (MO, United States). 4-arm poly (ethylene glycol) acrylate was provided by Sinopeg Biotech Co. Ltd. (China). Ultrapure water was obtained from a Millipore Auto-pure system. All reagents were used without further purification.

### Synthesis of Methacrylated Alginate

The methacrylated alginate was prepared according to a reported study (Choi et al., 2021). Briefly, ALG was dissolved with 20 ml of deionized water to produce a 2% (w/v) solution at 37°C overnight. Then, 20 ml of methacrylic anhydride was added dropwise to the system, and the solution was continuously stirred magnetically at room temperature for 3 days, with the pH periodically adjusted to 7 with aqueous NaOH (5 M). After the 3-days reaction period, the resulting solution was poured into 100 ml of ethanol (pre-chilled in advance at -20°C) to precipitate the ALG-MA product for about 8 h at RT. Finally, the precipitate was vacuum filtered, washed three times with ethanol, oven dried at 37°C, and stored at -20°C until use. From the addition of methacrylic anhydride, all the synthesis steps were carried out under dark conditions.

### PRP Preparation

The PRP was prepared according to a reported study (Faramarzi et al., 2018). Briefly, rabbit ear margin vein blood was centrifuged at 250 g for 15 min to separate red blood cells from plasma. The upper plasma phase, including the interface, was centrifuged at 1600 g for 60 min to pellet the platelets. The upper three-quarters of the plasma phase were discarded to retain the remaining one-quarter. The obtained PRP was then stored at -80°C until further use. Further platelet activation was performed by repeated freeze-thaw cycles in subsequent experiments.

## Preparation and Structural Characterization of Hydrogels

To generate hydrogels, alginate-methacrylic anhydride was dissolved separately in PBS (PRP group: 10% PRP [v/v]-ALGMA) to achieve a concentration of 1.67% (w/v) in borosilicate vials, combined with four arm-PEG at twice the solution's mass, and incubated in a 37°C water bath until complete dissolution. The resulting solutions were added with I2959 (1% (w/v)). Then, 180  $\mu$ L of the resulting solution was solidified in PDMS molds (diameter, 1.3 mm; height, 1 mm) to form sheets and subjected to UV-light irradiation for 90 s at 365 nm. Finally, these hydrogel disks were soaked in dopamine (2 mg/ml) and collagen for 60 s after being submerged in PBS or SBF for 24 h to remove the excess unreacted monomer. For *in vitro* experiments, all hydrogel disks were sterilized by ethylene oxide.

## Nuclear Magnetic Resonance ( $^1\text{H}$ NMR) Spectroscopy

The samples were examined before and after the ALG-MA grafting reaction on a solid-state NMR spectrometer, and  $^1\text{H}$  NMR spectra were obtained and analyzed for comparison. Magnetic field intensity was 9.4 T, with a maximum speed of 10 kHz.

## Fourier Transform Infrared Spectroscopy

The material was dried in the oven, mixed with potassium bromide (KBr) powder and ground into a transparent flake with a mass ratio of 1:100 of KBr powder. Spectral analysis of the sample was performed by FTIR, at a resolution of 4  $\text{cm}^{-1}$  and an instrument scan range of 400–4,000  $\text{cm}^{-1}$ .

## Swelling Ratio Measurement

PBS-PRP (-), PBS-PRP (+), SBF-PRP (-) and SBF-PRP (+) hydrogels were fabricated and lyophilized. After measuring the lyophilized weight, the lyophilized hydrogels were immersed in PBS or SBF at room temperature, removed at certain time intervals, and weighed again after wiping off the surface water with filter papers until they were completely swollen and the weight would not increase further. The swelling ratio was calculated by the following equation: swelling ratio (Q) =  $W_s/W_l$ , where  $W_s$  is the weight of a fully swollen sample and  $W_l$  is the weight of the corresponding lyophilized sample. Four replicates were used in this experiment.

## Mechanical Test

For compressive mechanical testing, hydrogels were produced in a cylindrical shape (height: 10 mm, diameter: 10 mm). The compressive test was performed on a Trapezium X-type tester (Shimadzu Corporation, Japan). The horizontal head of the mechanical testing machine was set to move at a speed of 1 mm/min. The end of the sample was fixed with a metal clamp, and then a force gradient of 0.25 N/min was applied, starting from 2 mN preload until the sample fractured. The stress-strain curve was generated for each sample, and the maximum fracture point was recorded to calculate the strain

results. The Young's modulus could be obtained by calculating the slope of stress-strain curve in their initial linear part. The energy dissipation of hydrogels was obtained by calculating the area of compression-relaxation cycles. Triplicate assays were performed thrice. The rheology properties of the hydrogels were measured using a Thermo Scientific Haake Mars 40, where the strain-sweep mode at a strain amplitude range of 0.01%–10% at a frequency of 6.28 rad/s and the frequency-sweep mode at a frequency of 1 rad/s to 60 rad/s with 1% strain. For recovery-mode,  $G'$  and  $G''$  were measured with a strain of 0.1% and a frequency of 6.28 rad/s for 300 s, followed by the strain was set to 300% and the frequency of 100 Hz for 60 s, and subsequently switched back to 0.1% strain and 6.28 rad/s to monitor the recovery of mechanical properties for 300 s.

## SBF Immersion and Scanning Electron Microscopy

SBF was prepared by adding 700 ml of deionized water to a 1000 ml beaker, followed by 7.996 g of NaCl, 0.350 g of  $\text{NaHCO}_3$ , 0.224 g of KCl, 0.228 g of  $\text{K}_2\text{HPO}_4 \cdot 3\text{H}_2\text{O}$ , 0.305 g of  $\text{MgCl}_2 \cdot 6\text{H}_2\text{O}$ , 4 ml of 10 mol/L HCl, 0.278 g of  $\text{CaCl}_2$  and 0.071 g of  $\text{NaSO}_4$ . After full dissolution, 6.057 g of  $(\text{CH}_2\text{OH})_3\text{CNH}_2$  was added carefully dropwise, i.e., less than 1 g at a time. Then, 300 ml of deionized water was added and pH was adjusted to 7 with HCl. To investigate the apatite forming ability of hydrogels, fabricated SBF-PRP (-) and SBF-PRP (+) hydrogels were placed in a 12-well plate filled with 1 ml of SBF solution and incubated at 37°C for 5 days. Collected samples were washed with deionized water and lyophilized before characterizing the formed apatite by scanning electron microscopy (SEM). The microstructures and cross sections of hydrogels were captured at 3 kV by energy dispersive X-ray spectroscopy (EDS) at 8 kV.

## Kinetics of TGF- $\beta$ Release From PRP-Incorporated Hydrogels

The PRP-incorporated hydrogels [PBS-PRP (+), SBF-PRP (+)] were placed in a 12-well plate filled with 1 ml of PBS at 37°C. At pre-determined time intervals over 14 days, the PBS were taken out for measuring the amount of released TGF- $\beta$  by ELISA assay and re-added the fresh PBS.

## Cell Experiments

### Cell Culture

Rabbit bone marrow mesenchymal stem cells (rBMSCs) were used in cell culture studies. The cells were incubated in DMEM with 10% (v/v) fetal bovine serum and 1% (v/v) penicillin/streptomycin (Gibco) at 37°C in a humidified incubator in the presence of 5%  $\text{CO}_2$ . The studies were carried out with four experimental groups, including the PBS-PRP (-), PBS-PRP (+), SBF-PRP (-) and SBF-PRP (+) groups. The four groups of hydrogels were placed in twelve-well plates separately, and then 1 ml of complete medium was added per well for pre-culture. At 80–90% confluence, the cells were trypsinized and resuspended at  $1 \times 10^5$  cells/ml. Then, 500- $\mu$ L cell suspensions were seeded in each group (50000 cells/well), and the culture medium was changed every 2 days. The morphology of BMSCs was observed under an inverted microscope (LEICA DMIL) on bright field and the LAS V4.12 software was used for imaging.

## Cell Viability Detection

Cell proliferation rate was assessed with CCK-8 (E1CK-000208; Enogene Biotech., Nanjing, China). Four groups of hydrogels were cut to fit 96-well plates, and 5,000 cells in 20  $\mu$ L medium were seeded in each well. The original medium was discarded after 1, 3, 5, and 7 days of culture, respectively. Complete medium containing 10% CCK-8 solution was added to each well and placed in an incubator for 4 h. A microplate reader (BioTek ELx808) was used to detect absorbance at 450 nm.

## Observation of Cell Morphology

The morphological features of BMSCs on PBS-PRP (-), PBS-PRP (+), SBF-PRP (-) and SBF-PRP (+) hydrogels were observed by confocal laser scanning microscopy respectively. Cells were washed with PBS twice and incubated with phalloidin and DAPI in a dark environment.

## Live/Dead Staining

After 24 h of culture, hydrogels with BMSCs were transferred to confocal dishes and washed with PBS. Then, fluorescein diacetate (FDA)/propidium iodide (PI) mixture was applied for live/dead staining. Cells were observed and imaged with a laser scanning confocal microscope (LSM710; Zeiss, Germany) at 488 nm for living cells and 565 nm for dead cells.

## Immunofluorescent Staining

After 7 days of osteogenic differentiation, the expression of RUNX2 in BMSCs cultured on PBS-PRP (-), PBS-PRP (+), SBF-PRP (-) and SBF-PRP (+) hydrogels was detected by IF staining. Briefly, cells were fixed with 4% paraformaldehyde at 4°C and permeabilized with 0.5% Triton X-100. After permeabilization for 10 min, cells were washed three times with PBS and blocked with 3% BSA for 30 min. Diluted anti-RUNX2 primary antibodies were added and incubated overnight at 4°C. Subsequently, cells were rinsed three times with PBST (PBS +0.1% Tween 20) and subjected to further incubation with Alexa Fluor 565-conjugated secondary antibodies for 1 h in the dark at room temperature. Fluorescence images were captured under a confocal microscope.

## ALP Activity Assay and ALP Staining

BMSCs were seeded as described above. After incubation in osteogenic induction medium for 7 days, cells in four groups of hydrogels were harvested separately for analysis. ALP activity was assessed with the ALP/ALP assay kit (A059-2-2, Boqiao Biotech, Nanjing, China) according to the manufacturer's instructions, normalized to total protein concentration detected with BCA Protein Assay Kit (PT0001, Leagene, Beijing, China). BCIP/NBT Alkaline Phosphatase Color Development Kit (C3206, Beyotime, Shanghai, China) was applied for ALP staining after 7 days of osteogenic induction. Cells were fixed with 4% paraformaldehyde and stained according to the manufacturer's instructions.

## Alizarin Red S Staining

Cells were incubated with leach liquor of four group of hydrogels, after 21 days of osteogenic differentiation, ARS staining was

performed with 1% ARS (pH 4.2, Leagene, Beijing, China) after fixation with 4% paraformaldehyde. After incubation at RT for 5 min, cells were rinsed with PBS and imaged. Further quantification of calcium mineralization was detected by immersing the stained cells in 10% (w/v) cetyl pyridinium chloride for 1 h, and the absorbance was measured using a plate reader at 562 nm.

## RNA Isolation and Quantitative Real-Time Polymerase Chain Reaction

Total RNA was extracted from BMSCs with Cell/Bacteria Kit (Tiangen Biotech Co., Ltd., Beijing, China) after 24 h of culture in complete medium and 14 days of culture in osteogenic medium respectively. qRT-PCR primers were shown in **Supplementary Table S2**. GAPDH was used as a reference, and quantitative real-time PCR was performed on an ABI 7900 Real-Time PCR System (Thermo Fisher Scientific) with TB Green Premix Ex Taq II (RR820A; Takara Bio Inc., Japan) according to the manufacturer's instructions. Relative expression levels were calculated by the  $2^{-\Delta\Delta C_t}$  method, and each analysis included three to five replicates.

## Western Blot

Western blot was performed as previously described (Liu et al., 2021), with primary antibodies targeting BMP2, OPN, COL1, ALP, TUBULIN, and GAPDH (Tanon 5200).

## Animal Experiments

Twelve Male Newland rabbits with an average weight of 4 kg were obtained from the Laboratory Animal Center of Drum Tower Hospital affiliated to the Medical School of Nanjing University (China). All experimental protocols were approved by the ethics committee of Drum Tower Hospital affiliated to the Medical School of Nanjing University, and performed according to the Institutional Animal Care and Use Committee (IACUC) guidelines.

## Femur Condyle Defect Model

New Zealand rabbits were anesthetized with propofol and lidocaine, followed by the establishment of a 5-mm defect in the lateral femur. Then, SBF-PRP (+) and SBF-PRP (-) hydrogels were implanted in the experimental and control groups, respectively. No operation was performed in the blank control group. Femur condyles were harvested at eight postoperative weeks for further bone tissue regeneration evaluation.

## Micro-CT Analysis and 3D Reconstruction

The harvested femur condyles were scanned on a vivaCT 80 system (V6.5-3 Scanco Medical, Bruettisellen, Switzerland). The operating voltage and current were 45 KeV and 145  $\mu$ A, respectively. Bone mineral densities and relevant bone trabecula parameters were obtained according to micro-CT data. Three-dimensional models of the harvested femur condyles were reconstructed with MIMICS 19.0 (Materialise, Leuven, Belgium).

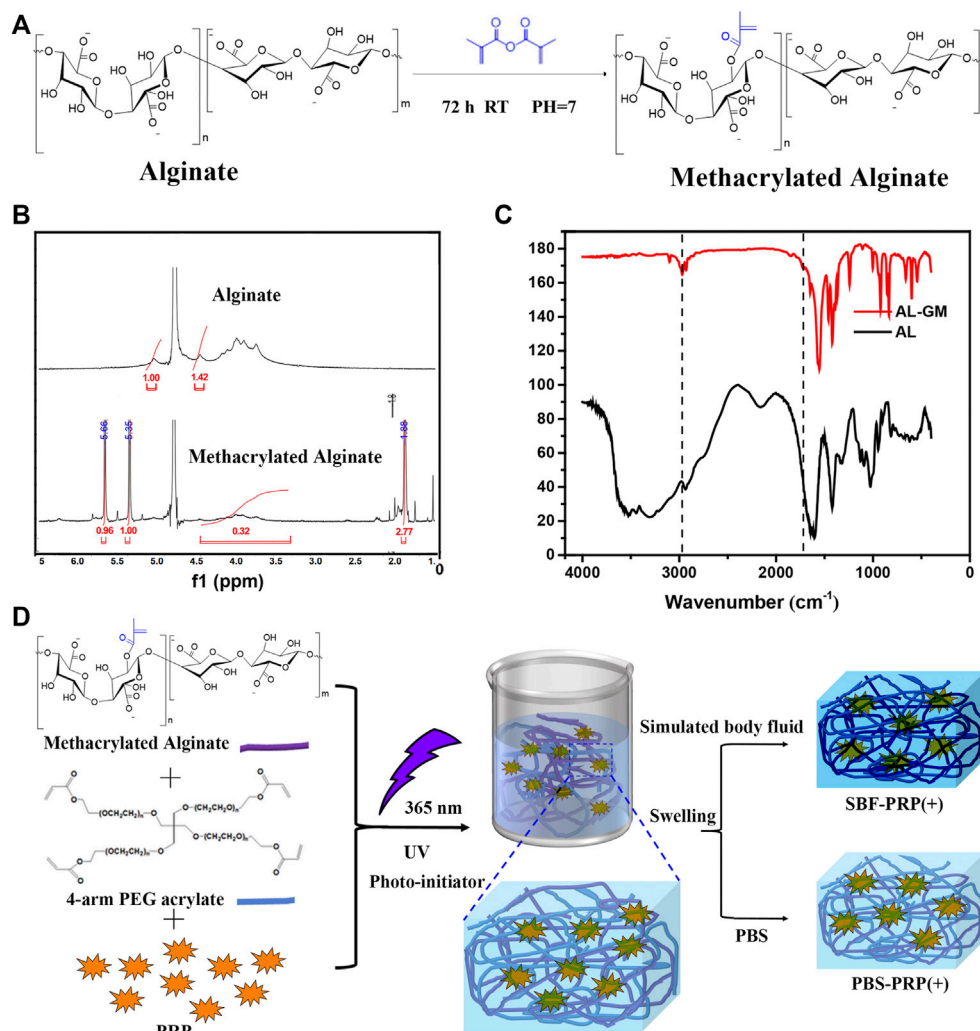


**FIGURE 1** | Preparation of IPN M-ALG/PEG hydrogels. **(A)** Reaction schemes, **(B)**  $^1\text{H}$ -NMR spectra and **(C)** FTIR spectra of M-ALG. **(D)** Schematic of preparation process of IPN M-ALG/PEG hydrogels alone or combine with PRP.

## Statistical Analysis

All experiments were performed with three replicates unless otherwise stated. Data are mean  $\pm$  SD. Statistical analysis was performed with the Origin software (8.5 version). Asterisks in statistical analysis indicate statistically significant differences between the control and experimental groups (\* $p < 0.05$ ; \*\* $p < 0.01$ ; \*\*\* $p < 0.005$ ; \*\*\*\* $p < 0.001$ ).

## RESULTS AND DISCUSSION

### Design of the PRP-Hydrogel

Methacrylated alginate (M-ALG) was synthesized from the reaction between the hydroxyl group of alginate and the epoxy group of methacrylic anhydride under alkaline conditions, the mechanisms of which include epoxide ring-opening, carbodiimide chemistry and transesterification (Araiza-Verduzco et al., 2020). The reaction is schematically shown in

Figure 1A, and the structures of neat ALG and M-ALG were confirmed by  $^1\text{H}$  NMR spectroscopy in  $\text{D}_2\text{O}$  (Figure 1B), depicting characteristic peaks between 3.50 and 5.20 ppm from both neat ALG and M-ALG due to their saccharide units. As expected, the spectrum of M-ALG displayed distinctive peaks corresponding to the vinyl (5.35 and 5.66 ppm) and methyl (1.80 ppm) hydrogens of methacrylate grafted groups, consistent with previous reports (Wang et al., 2015). Of note, these peaks could slightly shift due to different chemical environments (Burdick et al., 2005). Furthermore, the chemical structures of neat ALG and M-ALG were characterized by FTIR. As shown in Figure 1C, M-ALG' spectrum exhibited two additional bands compared with that of ALG (arrows): occurrence of  $-\text{CH}$  stretching bands ( $2980\text{--}2850\text{ cm}^{-1}$ ) and appearance of a shoulder ( $1721\text{ cm}^{-1}$ ), which were attributed to stretching vibrations of the aliphatic chains'  $-\text{CH}$  groups and the esters'  $\text{C}=\text{O}$  group, respectively. Both groups were due to the grafting of methacrylate units (Mugnaini



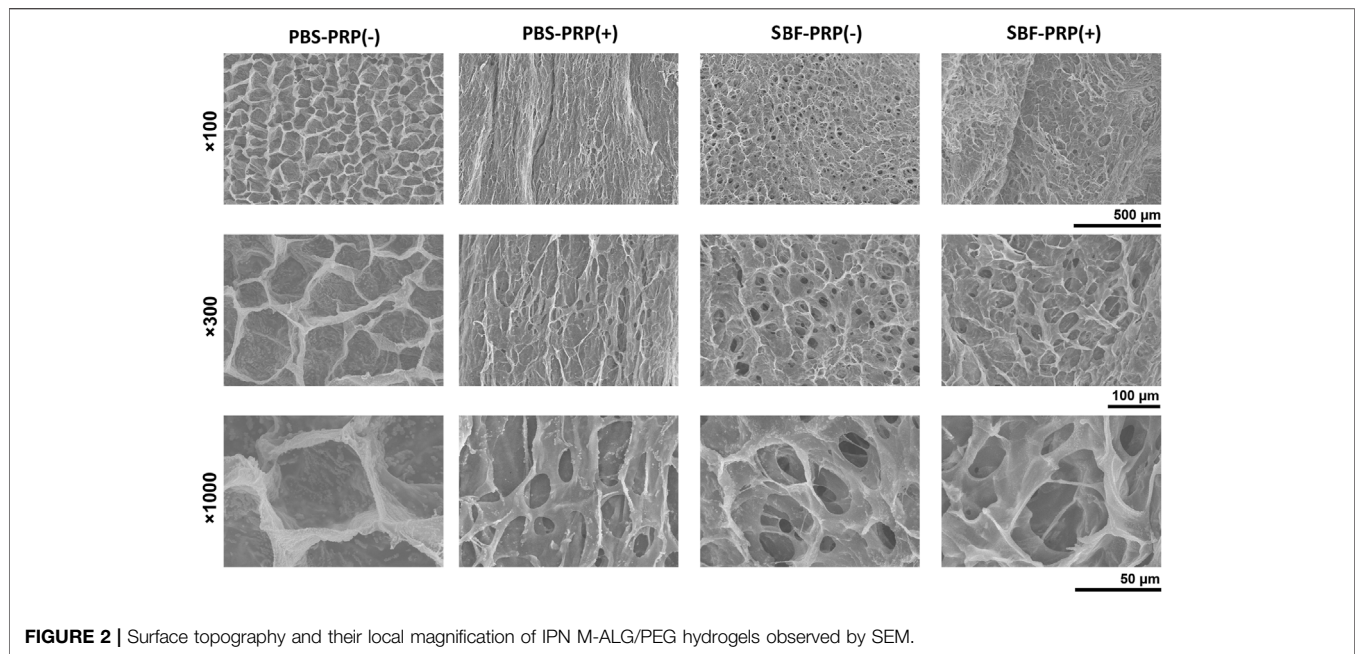


**FIGURE 2 |** Surface topography and their local magnification of IPN M-ALG/PEG hydrogels observed by SEM.

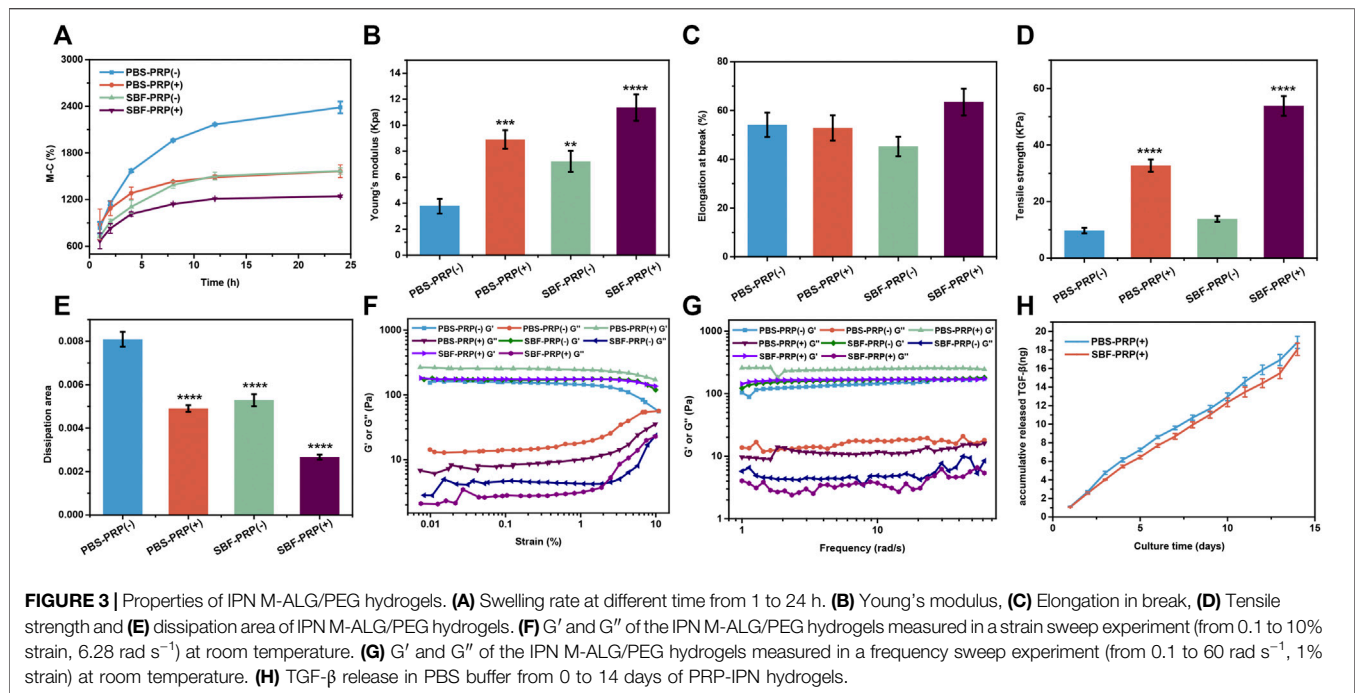
et al., 2021) (chemical structures in **Figure 1A**). These results confirmed that methacrylate was successfully grafted to neat ALG.

PRP-incorporated interpenetrating polymeric network (IPN) hydrogels were synthesized through free radical polymerization reaction under UV-light irradiation in the presence of PRP (**Figure 1D**). Covalent crosslinks between M-ALG (methacrylate groups) and 4-Armed PEG-ACLT (acrylate groups) were formed after this reaction, where a biocompatible photoinitiator (I2959) was used to induce fluid-solid phase transformations. Tetra-functionalized PEG and M-ALG crosslinkers were used due to their high crosslinking efficiency, and the addition of PRP improved biological activities (Andersen et al., 2021; Xu et al., 2021). The as-prepared hydrogels were further crosslinked by exposure to SBF that contained  $\text{Ca}^{2+}$  to interact with ALG, forming mineralized PRP-incorporated IPN hydrogels. Photographs of as-prepared hydrogels, including PBS-PRP (-), PBS-PRP (+), SBF-PRP (-) and SBF-PRP (+) were shown in **Supplementary Figure S1**, depicting the hydrogel turning pale yellow after the incorporation of PRP. As expected, the volume of the hydrogel alone or combined with PRP biomaterialized by SBF was smaller than that of the corresponding hydrogel treated with PBS, indicating that biological mineralization hindered the swelling of hydrogels. In addition, lyophilized PRP-incorporated IPN hydrogels were morphologically characterized by SEM. As illustrated in **Figure 2**, all IPN hydrogels had a porous structure with a pore size of about 20–50  $\mu\text{m}$ . Different from the uniform pore size in the PBS-PRP (-) group, pore size in the PBS-PRP (+) group was slightly discrepant, and its surface appears clearly cross-linked fibers, indicating the formation of a platelet activation-dependent fibrin network which is consistent with the results of previous studies (Qian et al., 2022). In contrast to the PBS-PRP (-) group, hydrogel pores in the mineralized group are smaller while the pore wall thickness is significantly increased, which is related to

the presence of more crosslinks within the scaffold of the mineralized group. Furthermore, EDS mapping based on SEM images was also present to verify the biological mineralization between  $\text{Ca}^{2+}$  in SBF and ALG. As shown in **Supplementary Figure S2** and **Supplementary Table S1**, all IPN hydrogels contained O, Na, Cl and K. Meanwhile, Ca was only present in SBF-PRP (-) and SBF-PRP (+), which was attributed to successful biological mineralization. In particular, we expected the porous microstructures are suitable for containing of cells, thereby accommodating a large number of cells and facilitating multiple cellular functions, including cell attachment, proliferation and differentiation (Li L. et al., 2020; Huang et al., 2021).

## Physicochemical Properties of the PRP-Hydrogel

It is known that bioactive materials used as bone repair scaffolds should possess several features, including high surface area/volume ratio, proper mechanical properties, excellent biocompatibility and enhanced osteoconductivity (Dong et al., 2019; Wang et al., 2020). By achieving these, scaffolds can provide cells with an appropriate three-dimensional (3D) environment, enabling cells to exert normal functions such as proliferation and migration, and subsequently support the newly formed bone (Sun et al., 2016; Zhu et al., 2021). Hence, the physicochemical properties of the as-prepared IPN hydrogels were assessed. Swelling rate, one of the most important properties that can reflect the crosslinking degree, affinity toward  $\text{H}_2\text{O}$  molecules, ionization degree of functional groups and properties of swelling medium such as ionic strength and temperature (Kim et al., 2013) were firstly measured. As shown in **Figure 3A**, swelling rate decreased after the biological mineralization process, suggesting ionic crosslinking between  $\text{Ca}^{2+}$  and ALG occurred. Furthermore, we also studied the compressive mechanical properties of as-

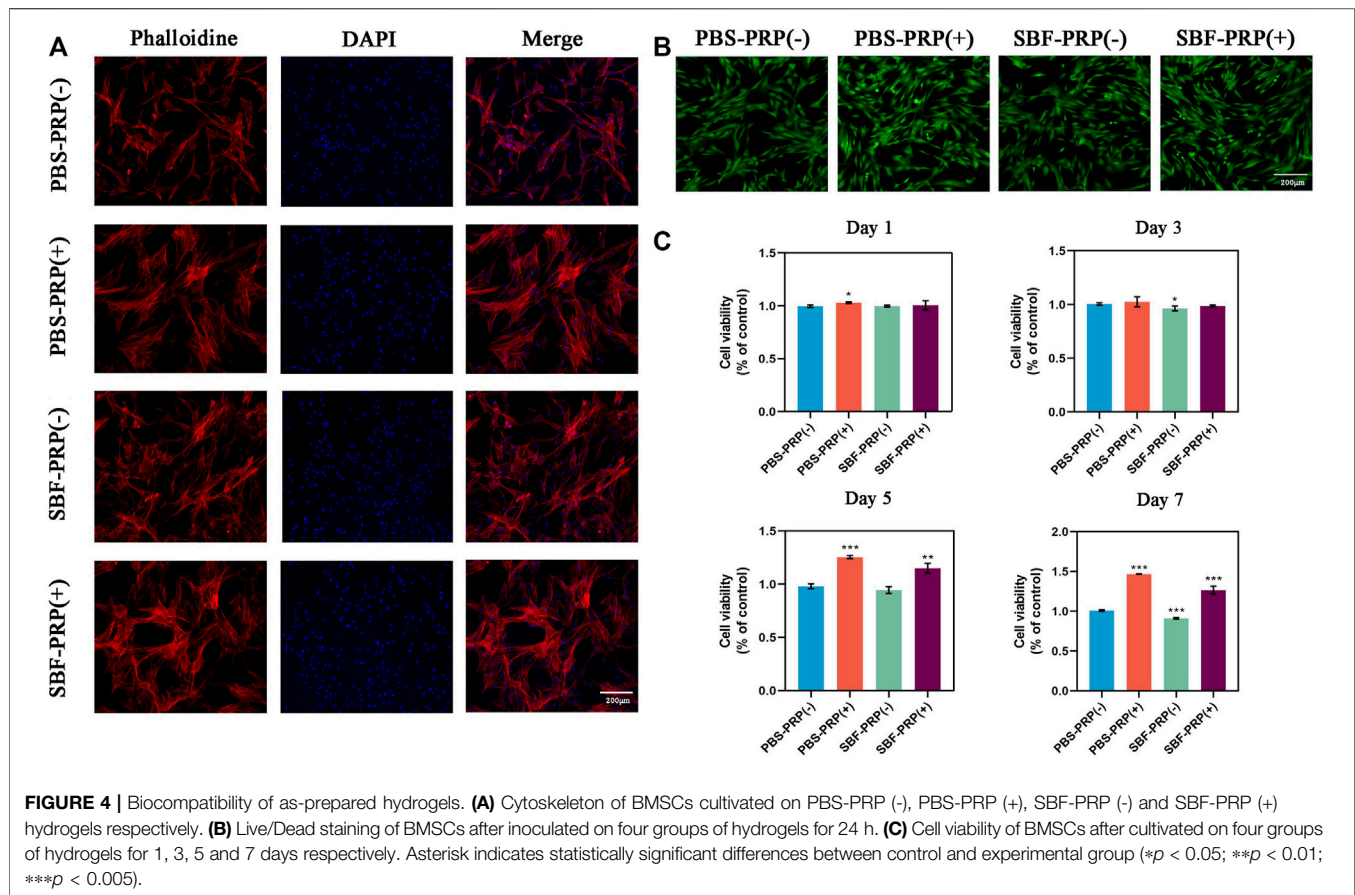


prepared IPN M-ALG/PEG hydrogels by standard mechanical tests. The obtained stress-strain curves based on the compression-crack test were shown in **Supplementary Figure S3A**, which indicated that SBF-PRP (+) demonstrated the enhanced Young's modulus ( $11.36 \pm 1.02 \text{ Kpa}$ ) compared with the other hydrogels (**Figure 3B**). Strikingly, the elongations at break (**Figure 3C**) and tensile strength (**Figure 3D**) of hydrogels increased after the PRP incorporation and the biological mineralization, which substantially improved the load bearing ability of the hydrogel. Furthermore, the energy dissipation levels of hydrogels were investigated through compression-relaxation cycles under 50% strain. As shown in **Supplementary Figure S3B**, all hydrogels demonstrated slight energy dissipation, with no significant difference among them, which could be attributed to the rupture of physical cross-linkers. As expected, the calculated dissipation of hydrogels (**Figure 3E**) was significantly decreased after the incorporation of PRP and the biological mineralization process. The fast recovery ability of hydrogels was then tested by applying continuous compression-relaxation cycles for 10 cycles (**Supplementary Figure S3C**). The results revealed that the tensile strength of each cycle was slightly decreased but remained at more than 85% after 10 continuous cycles, suggesting the remarkably fast recovery ability of IPN hydrogels. In next, the rheological properties of the as-prepared hydrogels were investigated. Strain-dependent oscillatory shear rheology (**Figure 3F**) exhibited a strain at yield strength of 10%, which was the cross point of  $G'$  and  $G''$ , representing the transition of the hydrogel from solid to liquid state. Besides, the frequency-sweep test (**Figure 3G**) demonstrated that the storage modulus ( $G'$ ) was larger than the loss modulus ( $G''$ ), suggesting that the fabricated hydrogels exhibited a solid-like

behavior. Furthermore, step-strain measurements (**Supplementary Figure S4**) demonstrated that all hydrogels were destroyed partly and subsequently recovered completely and rapidly from a strain of 300%–0.1% for four cycles of breaking and reforming, revealing the dominant elastic nature of these hydrogels. Furthermore, the accumulative release of TGF- $\beta$  from PRP-incorporated IPN hydrogels was investigated in phosphate buffer saline (PBS) over an incubation period of 14 days, which was quantified by enzyme-linked immuno sorbent assay (ELSA). The obtained release curves are shown in **Figure 3H**, sustained release of TGF- $\beta$  over the investigated period could be observed for both PBS-PRP (+) and SBF-PRP (+). As expected, SBF-PRP (+) demonstrated relatively slower release due to the biological mineralization layer partly prevented the release of TGF- $\beta$ . These results indicated that the as-prepared PRP-incorporated IPN hydrogels possess substantially improved mechanical strength and sustained release of growth factor, constituting potential repair scaffolds for bone tissue regeneration.

## Proliferation and Attachment of BMSCs on the PRP-Hydrogel

The physical characterization of the scaffold was followed by cytocompatibility assessment *in vitro*. It is known that the integration of scaffolds with the natural bone by forming the apatite layer on its surface *in vivo* can be simulated *in vitro* by scaffold incubation in SBF (Lewandowska-Łańcucka et al., 2019). Considering the possible *in vivo* application of this scaffold in BTE, *in vitro* biomineralization of the PRP-hydrogel scaffold was performed using SBF. Subsequently,



the cytocompatibility of scaffolds was assessed by co-incubating with cells and measuring cell viability, cell proliferation and cell adhesion assays. Cell morphology on different groups was depicted in **Figure 4A**. As demonstrated, cells can well spread, survive, and maintain their spindle-shaped morphology on the hydrogels, suggesting the excellent cytocompatibility of both non-mineralized and mineralized scaffolds (**Figure 4B**). It is worth to mention that higher cell attachment was found after 24 h of cell incubation on both non-mineralized and mineralized scaffolds in the presence of PRP compared with the control group. Also, cell morphology observation on all four groups after 48 h incubation was obtained by optical microscopy and confocal microscopy (**Supplementary Figure S6**). These results demonstrated that the incorporation of PRP facilitates cell adhesion. In order to further evaluate the effect of PRP on cell adhesion, RT-PCR was performed to detect the expression of integrin  $\beta 1$ , which is a classic transmembrane receptor that mediate the attachment between a cell and its surroundings. RT-PCR primer of integrin  $\beta 1$  was shown in revised **Supplementary Table S2**. BMSCs were cultivated on PBS-PRP (-), PBS-PRP (+), SBF-PRP (-) and SBF-PRP (+) hydrogels for 24 h and then collected respectively. Then the relative expression of integrin  $\beta 1$  was detected by RT-PCR. As shown in the revised **Supplementary Figure S5**, cells seeded on the PRP-containing hydrogels exhibit higher expression of integrin

$\beta 1$ , with or without the presence of SBF. This is consistent with our previous results obtained by cytoskeleton staining in **Figure 4A**. Cell proliferation on the scaffolds was further quantified by the CCK-8 assay after 1, 3, 5, and 7 days of cell culture, respectively. As shown in **Figure 4C**, nearly no significant difference was observed at 1 and 3 days and the numerical results were shown in **Supplementary Table S3**. Surprisingly, PRP-incorporated IPN hydrogel scaffolds had a higher cell proliferation rate than the neat hydrogel scaffolds after 5 and 7 days of culture ( $p < 0.05$ ), which indicated that the incorporation of PRP into the alginate/ethylene-glycol hydrogel greatly promotes BMSC proliferation. In general, multiple studies have consistently confirmed that PRP increase cell proliferation *in vitro* (Gentile and Garcovich 2020), and this effect is mainly attributed to the release of growth factors from platelets (Martino et al., 2011). In this study, benefiting from the novel double-network structure of the hydrogel scaffold, biomolecules from PRP could more readily penetrate the scaffold and be continuously released without being affected by the mineralization of scaffolds.

### Effects of the PRP-Hydrogel on Osteogenic Differentiation of BMSCs

ALP activity and ARS staining intensity were detected after seeding of BMSCs. Higher ALP activity (**Figures 5A,C**) and ARS



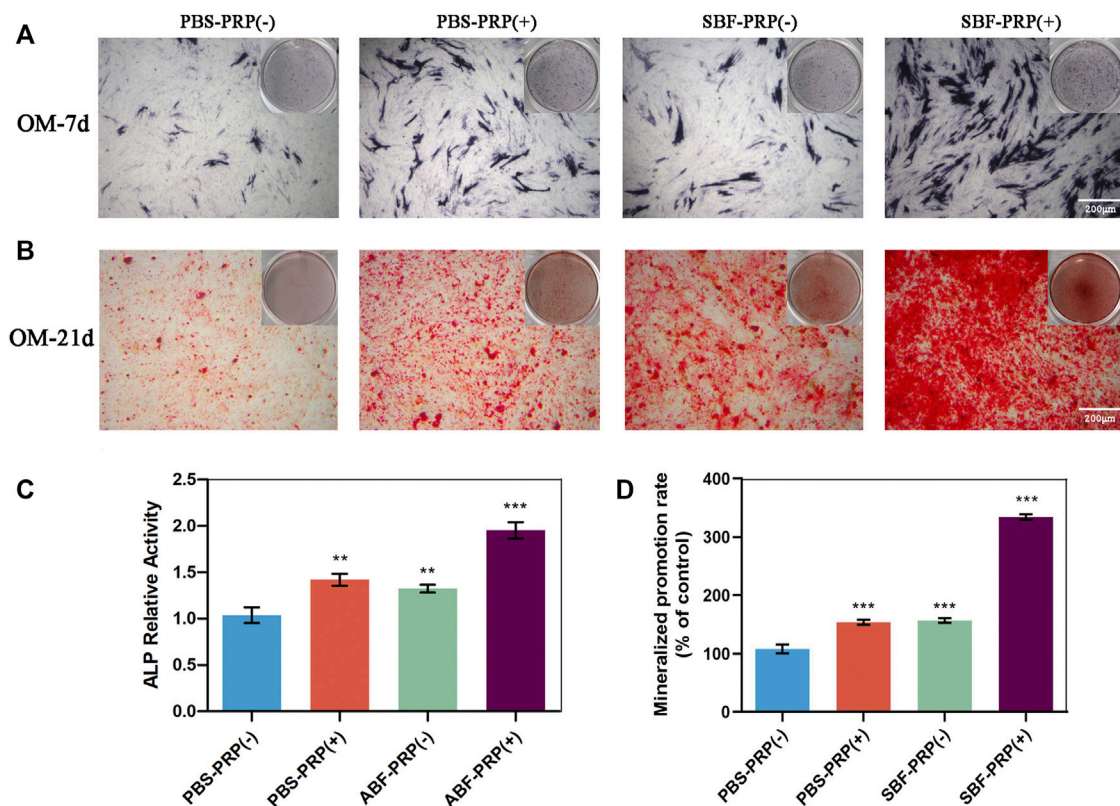


**FIGURE 5 |** ALP activity and calcium nodule production of BMSCs. **(A)** ALP staining of BMSCs after osteogenic differentiation for 7 days. **(B)** Alizarin red staining of BMSCs after osteogenic differentiation for 21 days. **(C)** ALP activity level of BMSCs after osteogenic differentiation for 7 days. **(D)** Quantification of Alizarin red staining in **(B)**. (\* $p < 0.05$ ; \*\* $p < 0.01$ ; \*\*\* $p < 0.005$ ).

intensity (**Figures 5B,D**) were quantitatively and statistically found on the BMSCs cultured on mineralized PRP-containing substrate compared with others, indicating an increased osteogenic differentiation capacity. We then cultured BMSCs on scaffolds and analyzed RUNX2 expression by immunofluorescence (IF) (**Figure 6**). Increased amount of RUNX2-positive cells were observed in the SBF-PRP (+) group compared with the other groups. Furthermore, we analyzed the expression levels of common osteogenesis markers (Tang et al., 2017), including BMP2, OPN, ALP and COL-I, and found that osteogenesis-related genes were significantly upregulated at both mRNA and protein levels in BMSCs cultured on the mineralized PRP-hydrogel scaffold (**Figure 7**). The raw data of western blot analysis was shown in **Supplementary Figure S7** and semi quantitative analysis of western blot was shown in **Supplementary Figure S8**. These data demonstrated that PRP and mineralization of the scaffold synergistically promote osteogenic differentiation in BMSCs. However, the osteogenic effects of PRP are complex. Some studies have suggested that PRP may facilitate bone formation in combination with MSCs from different species; others have shown that PRP decreases the osteogenic differentiation of MSCs (Gruber et al., 2004; Felka et al., 2010). This is probably because PRP highly varies from donor to donor, and each PRP preparation may differ in the

concentrations of proteins and growth factors (Lim et al., 2013). Recent research reported that PRP, in a certain concentration range, promotes cell proliferation at the early stage of differentiation, but causes no impairment of osteogenic differentiation in BMSCs (Xu et al., 2015; Xie et al., 2020). This is partly consistent with our findings that PRP had a positive effect on the proliferation of BMSCs on PRP-hydrogel scaffolds whether mineralized or not, and stimulated the osteogenic differentiation of BMSCs, particularly those cultured on the mineralized PRP-hydrogel. It is known that differentiation and proliferation represent dichotomous aspects of cellular function, and proliferation is frequently associated with differentiation (Schröder et al., 2009; Zheng et al., 2021a; Zheng et al., 2021b). A possible explanation for our findings is the sustained release of PRP from the hydrogel, which has a beneficial effect on cell proliferation and the early stage of osteogenesis. Furthermore, the biomineralization of scaffolds has been shown to considerably promote osteogenic differentiation of stem cells (Kim et al., 2021). Because the PRP-hydrogel mineralizes in a manner similar to biological mineralization, this scaffold modification significantly enhanced osteogenic differentiation of BMSCs. Summary results of the abovementioned studies lead to the conclusion that such synergistic effects of physical structures, the double-network structure/biomineralization of



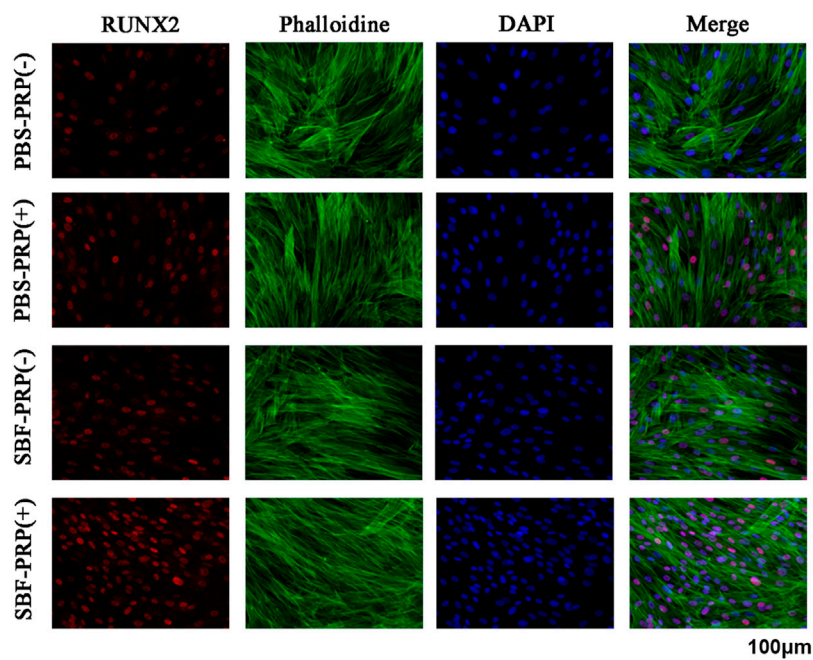
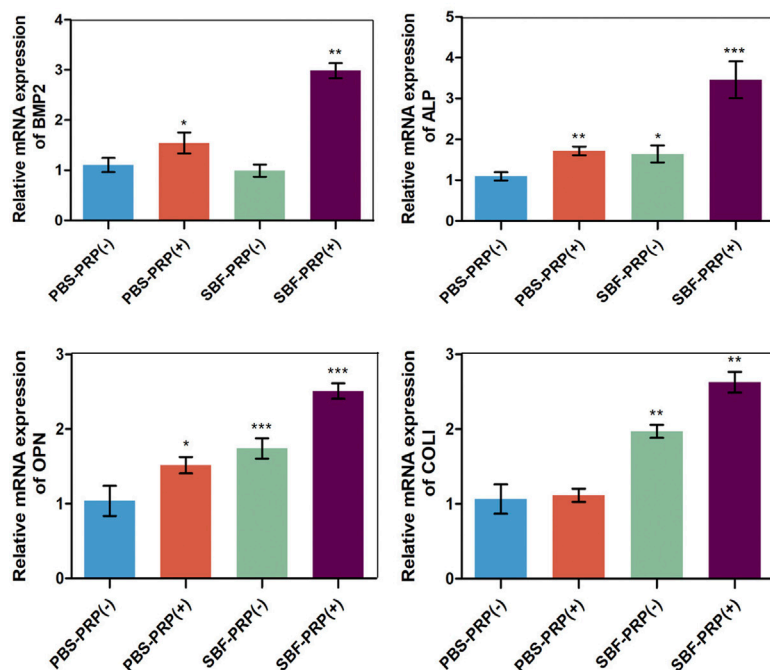


**FIGURE 6** | RUNX2 expression of BMSCs cultivated on PBS-PRP (-), PBS-PRP (+), SBF-PRP (-) and SBF-PRP (+) hydrogels. RUNX2, F-actin and nuclear were visualized by RUNX2-specific antibodies (red), rhodamine phalloidin (green) and DAPI (blue) respectively.

**A**



**B**

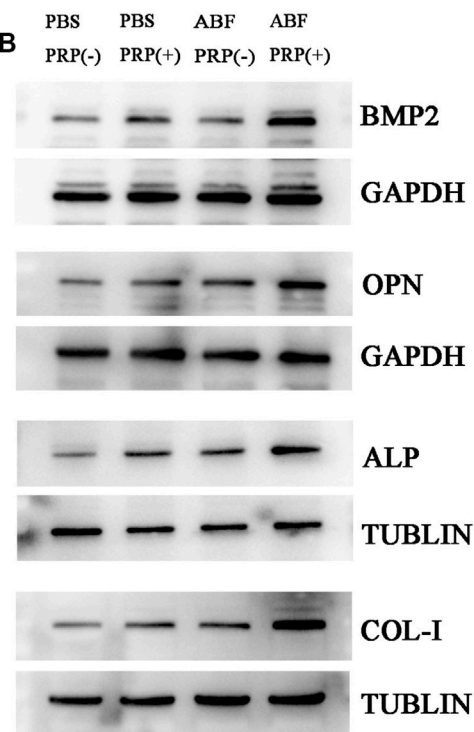
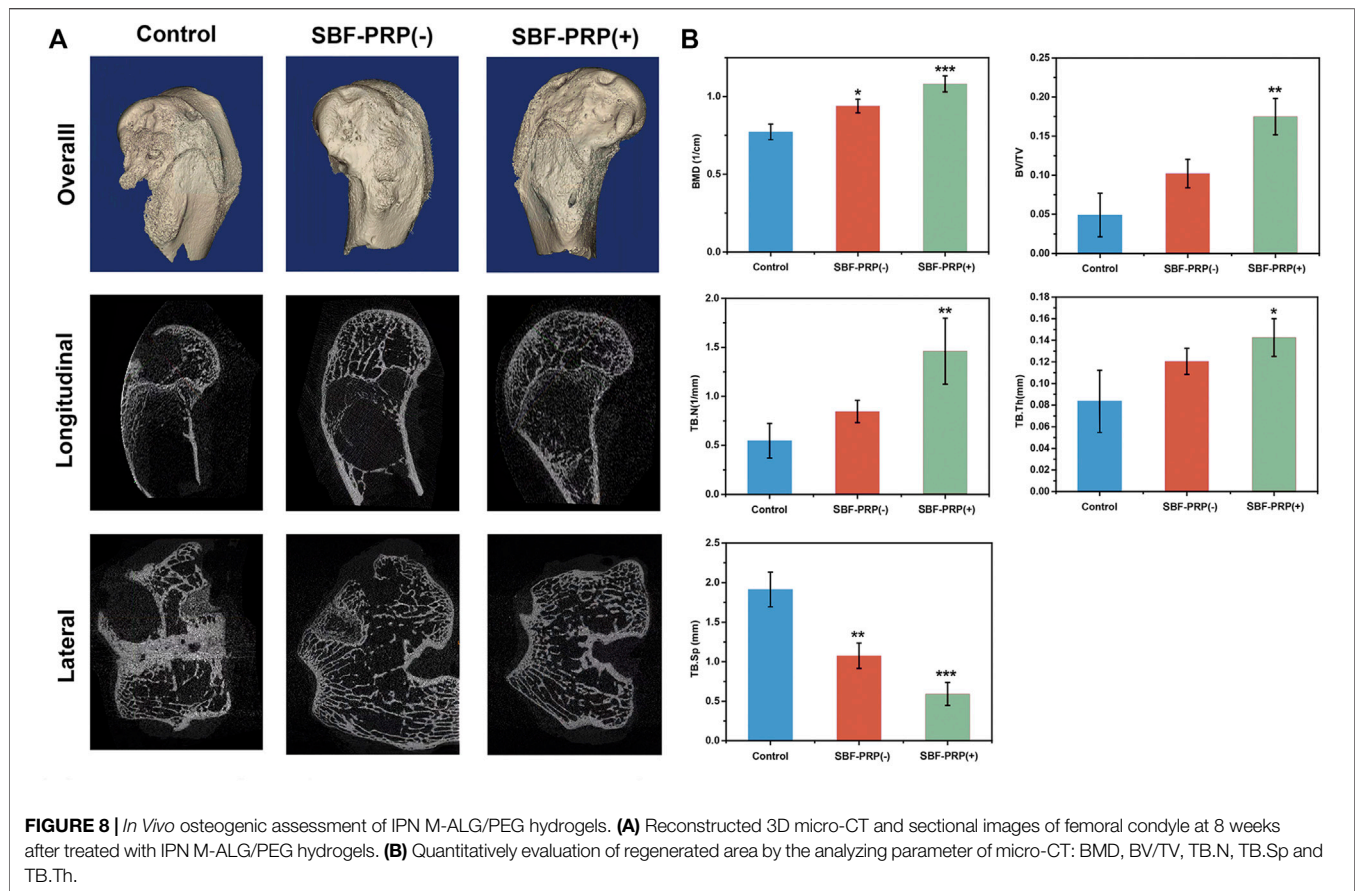


**FIGURE 7** | Osteogenic gene and protein expression of BMSCs. **(A)** RT-PCR analysis of BMP2, OPN, ALP and COL1 in BMSCs after 14 days cultivation on PBS-PRP (-), PBS-PRP (+), SBF-PRP (-) and SBF-PRP (+) hydrogels. **(B)** Western blot analysis of BMP2, OPN, ALP and COL1 in BMSCs cultivated on PBS-PRP (-), PBS-PRP (+), SBF-PRP (-) and SBF-PRP (+) hydrogels. \* $p < 0.05$  \*\* $p < 0.01$  \*\*\* $p < 0.001$  (Student's t-test). Data are presented as mean  $\pm$  SD ( $n \geq 3$ ).



scaffolds, and molecular supplements (PRP) could significantly promote osteogenesis and subsequent bone regeneration.

### ***In vivo* Osteogenic Effects of the PRP-Hydrogel**

*In vitro* investigations have shown that SBF-PRP (+) hydrogel exhibited excellent biocompatibility and mechanical strength, and enhanced osteogenic activities. This prompted us to assess the *in vivo* bone regeneration performance of the fabricated hydrogels. Hence, we further evaluated the bone repair ability hydrogel with or without SBF-PRP in a rabbit model of femoral 5-mm defect (Zhang et al., 2021). SBF-PRP (-) and SBF-PRP (+) hydrogels were directly implanted into the femur defects of rabbits. For comparison, no operation was performed after creating the bone defects. At 2 months after the implantation of hydrogels, femurs were harvested and firstly observed by micro-CT. The reconstructed three-dimensional (3D) and sectional images of femoral condyles were shown in **Figure 8A**, indicating that there was still a large defect in the control group, while treatment with the SBF-PRP (+) hydrogel exhibited more newly formed cancellous bone compared with the SBF-PRP (-) group. For quantitative analysis, BMD, bone volume per total volume (BV/TV) and the trabecular parameters of the cancellous bone, including trabecular number (Tb.N), trabecular thickness (Tb.Th) and trabecular Spacing (Tb.Sp) were assessed and the

results were shown in **Figure 8B**. BMD in the control group was  $0.77 \pm 0.05 \text{ cm}^{-1}$ , while the SBF-PRP (+) group had a value of  $1.08 \pm 0.05 \text{ cm}^{-1}$ , which was higher than that of the SBF-PRP (-) group. A similar trend was observed for BV/TV. As for trabecular parameters, Tb.N and Tb.Th were significantly increased after treatment with the SBF-PRP (+) hydrogel compared with the SBF-PRP (-) and control groups, while Tb.Sp was significantly decreased. These results confirmed that the SBF-PRP (+) hydrogel accelerates bone regeneration *in vivo*. Similar trends were observed in Masson staining. Taken together, these results suggested that the PRP-incorporated IPN hydrogels can rapidly and effectively promote bone regeneration.

### **SUMMARY**

In summary, we reported a novel PRP-incorporated IPN hydrogel, which fabricated by combining M-ALG and 4A-PEGAc through photo-crosslinking upon exposure to long-wave UV light and ionic crosslinked through exposure to native calcium ions in SBF. The as-prepared hydrogels exhibited expected improvement in terms of morphological and mechanical properties after PRP incorporation and biological mineralization. *In vitro* studies demonstrated that the incorporation of PRP endowed the hydrogels with excellent biocompatibility and osteogenic bioactivity, as evident by enhanced ALP activity, mineralized nodule formation, and osteogenic gene

and protein expression. *In vivo* studies confirmed that the PRP-incorporated IPN hydrogels showed great ability in inducing bone regeneration. Taken together, it is anticipated that the PRP-incorporated biomineralized IPN hydrogels might be promising scaffolds for bone tissue regeneration.

## DATA AVAILABILITY STATEMENT

The original contributions presented in the study are included in the article/**Supplementary Material**, further inquiries can be directed to the corresponding author.

## ETHICS STATEMENT

The animal study was reviewed and approved by the ethics committee of Nanjing Medical University.

## REFERENCES

- Andersen, C., Wragg, N. M., Shariatadeh, M., and Wilson, S. L. (2021). The Use of Platelet-Rich Plasma (PRP) for the Management of Non-union Fractures. *Curr. Osteoporos. Rep.* 19, 1–14. doi:10.1007/s11914-020-00643-x
- Araiza-Verduzco, F., Rodríguez-Velázquez, E., Cruz, H., Rivero, I. A., Acosta-Martínez, D. R., Pina-Luis, G., et al. (2020). Photocrosslinked Alginate-Methacrylate Hydrogels with Modulable Mechanical Properties: Effect of the Molecular Conformation and Electron Density of the Methacrylate Reactive Group. *Materials (Basel)* 13, 534. doi:10.3390/ma13030534
- Boyle, A. J., Sweeney, R. M., and McAuley, D. F. (2013). Pharmacological Treatments in ARDS; a State-Of-The-Art Update. *BMC Med.* 11, 166. doi:10.1186/1741-7015-11-166
- Burdick, J. A., Chung, C., Jia, X., Randolph, M. A., and Langer, R. (2005). Controlled Degradation and Mechanical Behavior of Photopolymerized Hyaluronic Acid Networks. *Biomacromolecules* 6, 386–391. doi:10.1021/bm049508a
- Busch, A., Jäger, M., Mayer, C., and Sowislok, A. (2021). Functionalization of Synthetic Bone Substitutes. *Int. J. Mol. Sci.* 22, 4412. doi:10.3390/ijms22094412
- Choi, C., Kim, S., and Cha, C. (2021). Dual-functional Alginate Crosslinker: Independent Control of Crosslinking Density and Cell Adhesive Properties of Hydrogels via Separate Conjugation Pathways. *Carbohydr. Polym.* 252, 117128. doi:10.1016/j.carbpol.2020.117128
- Dabiri, S. M. H., Samiei, E., Shojaei, S., Karperien, L., Khun Jush, B., Walsh, T., et al. (2021). Multifunctional Thermoresponsive Microcarriers for High-Throughput Cell Culture and Enzyme-free Cell Harvesting. *Small* 17, e2103192. doi:10.1002/sml.202103192
- Dong, H., Zheng, L., Yu, P., Zhang, P., Wu, Y., Huang, C., et al. (2019). Characterization and Application of Lignin-Carbohydrate Complexes from Lignocellulosic Materials as Antioxidants for Scavenging *In Vitro* and *In Vivo* Reactive Oxygen Species. *ACS Sust. Chem. Eng.* 8, 256–266. doi:10.1021/acsschemeng.9b05290
- Drury, J. L., and Mooney, D. J. (2003). Hydrogels for Tissue Engineering: Scaffold Design Variables and Applications. *Biomaterials* 24, 4337–4351. doi:10.1016/s0142-9612(03)00340-5
- Faramarzi, N., Yazdi, I. K., Nabavinia, M., Gemma, A., Fanelli, A., Caizzzone, A., et al. (2018). Patient-Specific Bioinks for 3D Bioprinting of Tissue Engineering Scaffolds. *Adv. Healthc. Mater.* 7, e1701347. doi:10.1002/adhm.201701347
- Felka, T., Schäfer, R., De Zwart, P., and Aicher, W. K. (2010). Animal Serum-free Expansion and Differentiation of Human Mesenchymal Stromal Cells. *Cytotherapy* 12, 143–153. doi:10.3109/14653240903470647
- Fleming, J. E., Jr., Cornell, C. N., and Muschler, G. F. (2000). Bone Cells and Matrices in Orthopedic Tissue Engineering. *Orthop. Clin. North America* 31, 357–374. doi:10.1016/s0030-5898(05)70156-5
- Foster, T. E., Puskas, B. L., Mandelbaum, B. R., Gerhardt, M. B., and Rodeo, S. A. (2009). Platelet-Rich Plasma. *Am. J. Sports Med.* 37, 2259–2272. doi:10.1177/0363546509349921
- Franchini, M., Cruciani, M., Mengoli, C., Marano, G., Pupella, S., Veropalumbo, E., et al. (2018). Efficacy of Platelet-Rich Plasma as Conservative Treatment in Orthopaedics: a Systematic Review and Meta-Analysis. *Blood Transfus.* 16, 502–513. doi:10.2450/2018.0111-18
- Gentile, P., and Garcovich, S. (2020). Systematic Review-The Potential Implications of Different Platelet-Rich Plasma (PRP) Concentrations in Regenerative Medicine for Tissue Repair. *Int. J. Mol. Sci.* 21, 5702. doi:10.3390/ijms21165702
- Gruber, R., Karreth, F., Kandler, B., Fuerst, G., Rot, A., Fischer, M. B., et al. (2004). Platelet-released Supernatants Increase Migration and Proliferation, and Decrease Osteogenic Differentiation of Bone Marrow-Derived Mesenchymal Progenitor Cells Underin Vitroconditions. *Platelets* 15, 29–35. doi:10.1080/09537100310001643999
- Hofmann, S., Hagenmüller, H., Koch, A. M., Müller, R., Vunjak-Novakovic, G., Kaplan, D. L., et al. (2007). Control of *In Vitro* Tissue-Engineered Bone-like Structures Using Human Mesenchymal Stem Cells and Porous Silk Scaffolds. *Biomaterials* 28, 1152–1162. doi:10.1016/j.biomaterials.2006.10.019
- Hom, D. B. (1995). Growth Factors in Wound Healing. *Otolaryngol. Clin. North. Am.* 28, 933–953. doi:10.1016/s0030-6665(20)30461-8
- Huang, C., Dong, J., Zhang, Y., Chai, S., Wang, X., Kang, S., et al. (2021). Gold Nanoparticles-Loaded Polyvinylpyrrolidone/Ethylcellulose Coaxial Electrospun Nanofibers with Enhanced Osteogenic Capability for Bone Tissue Regeneration. *Mater. Des.* 212, 110240. doi:10.1016/j.matdes.2021.110240
- Ingavle, G., Avadhanam, V., Zheng, Y., Liu, C., and Sandeman, S. (2016). Biomineralized Interpenetrating Network Hydrogels for Bone Tissue Engineering. *Bioinspired, Biomimetic and Nanobiomaterials* 5, 12–23. doi:10.1680/jbibn.15.00013
- Kim, B., Hong, D., and Chang, W. V. (2013). Swelling and Mechanical Properties of pH-Sensitive Hydrogel Filled with Polystyrene Nanoparticles. *J. Appl. Polym. Sci.* 130, 3574–3587. doi:10.1002/app.39544
- Kim, J. W., Han, Y. S., Lee, H. M., Kim, J. K., and Kim, Y. J. (2021). Effect of Morphological Characteristics and Biomineralization of 3D-Printed Gelatin/Hyaluronic Acid/Hydroxyapatite Composite Scaffolds on Bone Tissue Regeneration. *Int. J. Mol. Sci.* 22, 6794. doi:10.3390/ijms22136794
- Lei, X., Gao, J., Xing, F., Zhang, Y., Ma, Y., and Zhang, G. (2019). Comparative Evaluation of the Physicochemical Properties of Nano-Hydroxyapatite/collagen and Natural Bone Ceramic/collagen Scaffolds and Their Osteogenesis-Promoting Effect on MC3T3-E1 Cells. *Regen. Biomater.* 6, 361–371. doi:10.1093/rb/rbz026

## AUTHOR CONTRIBUTIONS

FZ proposed the idea. ST and LW did the experiments. YZ helped the ICP measurement.

## FUNDING

This work was supported by grants from the National Key Research and Development Project (2021YFA1201302), the National Natural Science Foundation of China (81870807).

## SUPPLEMENTARY MATERIAL

The Supplementary Material for this article can be found online at: <https://www.frontiersin.org/articles/10.3389/fbioe.2022.887454/full#supplementary-material>



- Lewandowska-Łańcucka, J., Gilarska, A., Buła, A., Horak, W., Łatkiewicz, A., and Nowakowska, M. (2019). Genipin Crosslinked Bioactive Collagen/chitosan/hyaluronic Acid Injectable Hydrogels Structurally Amended via Covalent Attachment of Surface-Modified Silica Particles. *Int. J. Biol. Macromol.* 136, 1196–1208. doi:10.1016/j.ijbiomac.2019.06.184
- Li, C., Guo, C., Fitzpatrick, V., Ibrahim, A., Zwierstra, M. J., Hanna, P., et al. (2020a). Design of Biodegradable, Implantable Devices towards Clinical Translation. *Nat. Rev. Mater.* 5, 61–81. doi:10.1038/s41578-019-0150-z
- Li, L., Shi, J., Ma, K., Jin, J., Wang, P., Liang, H., et al. (2021). Robotic *In Situ* 3D Bio-Printing Technology for Repairing Large Segmental Bone Defects. *J. Adv. Res.* 30, 75–84. doi:10.1016/j.jare.2020.11.011
- Li, L., Zhang, K., Wang, T., Wang, P., Xue, B., Cao, Y., et al. (2020b). Biofabrication of a Biomimetic Supramolecular-Polymer Double Network Hydrogel for Cartilage Regeneration. *Mater. Des.* 189, 108492. doi:10.1016/j.matdes.2020.108492
- Lim, H.-P., Mercado-Pagan, A. E., Yun, K.-D., Kang, S.-S., Choi, T.-H., Bishop, J., et al. (2013). The Effect of rhBMP-2 and PRP Delivery by Biodegradable  $\beta$ -tricalcium Phosphate Scaffolds on New Bone Formation in a Non-through Rabbit Cranial Defect Model. *J. Mater. Sci. Mater. Med.* 24, 1895–1903. doi:10.1007/s10856-013-4939-9
- Liu, L., Li, X., Wu, H., Tang, Y., Li, X., and Shi, Y. (2021). The COX10-AS1/miR-641/E2F6 Feedback Loop Is Involved in the Progression of Glioma. *Front. Oncol.* 11, 648152. doi:10.3389/fonc.2021.648152
- Ma, K., Zhao, T., Yang, L., Wang, P., Jin, J., Teng, H., et al. (2020). Application of Robotic-Assisted *In Situ* 3D Printing in Cartilage Regeneration with HAMA Hydrogel: An *In Vivo* Study. *J. Adv. Res.* 23, 123–132. doi:10.1016/j.jare.2020.01.010
- Martino, M. M., Tortelli, F., Mochizuki, M., Traub, S., Ben-David, D., Kuhn, G. A., et al. (2011). Engineering the Growth Factor Microenvironment with Fibronectin Domains to Promote Wound and Bone Tissue Healing. *Sci. Transl. Med.* 3, 100ra89. doi:10.1126/scitranslmed.3002614
- Mugnaini, G., Rosta, C., Poggi, G., and Bonini, M. (2021). Photopolymerizable Pullulan: Synthesis, Self-Assembly and Inkjet Printing. *J. Colloid Interf. Sci.* 592, 430–439. doi:10.1016/j.jcis.2021.02.074
- Qian, B., Yang, Q., Wang, M., Huang, S., Jiang, C., Shi, H., et al. (2022). Encapsulation of Lyophilized Platelet-Rich Fibrin in Alginate-Hyaluronic Acid Hydrogel as a Novel Vascularized Substitution for Myocardial Infarction. *Bioactive Mater.* 7, 401–411. doi:10.1016/j.bioactmat.2021.05.042
- Rai, B., Oest, M. E., Dupont, K. M., Ho, K. H., Teoh, S. H., and Guldberg, R. E. (2007). Combination of Platelet-Rich Plasma with Polycaprolactone-Tricalcium Phosphate Scaffolds for Segmental Bone Defect Repair. *J. Biomed. Mater. Res.* 81A, 888–899. doi:10.1002/jbm.a.31142
- Rastogi, P., and Kandasubramanian, B. (2019). Review of Alginate-Based Hydrogel Bioprinting for Application in Tissue Engineering. *Biofabrication* 11, 042001. doi:10.1088/1758-5090/ab331e
- Rodriguez, I., Sell, S., McCool, J., Saxena, G., Spence, A., and Bowlin, G. (2013). A Preliminary Evaluation of Lyophilized Gelatin Sponges, Enhanced with Platelet-Rich Plasma, Hydroxyapatite and Chitin Whiskers for Bone Regeneration. *Cells* 2, 244–265. doi:10.3390/cells2020244
- Scalet, J. M., Suekama, T. C., Jeong, J., and Gehrke, S. H. (2021). Enhanced Mechanical Properties by Ionomeric Complexation in Interpenetrating Network Hydrogels of Hydrolyzed Poly (N-Vinyl Formamide) and Polyacrylamide. *Gels* 7, 80. doi:10.3390/gels7030080
- Schmid, J., Schwarz, S., Fischer, M., Sudhop, S., Clausen-Schaumann, H., Schieker, M., et al. (2019). A Laser-Cutting-Based Manufacturing Process for the Generation of Three-Dimensional Scaffolds for Tissue Engineering Using Polycaprolactone/Hydroxyapatite Composite Polymer. *J. Tissue Eng.* 10, 2041731419859157. doi:10.1177/2041731419859157
- Schneider, O. D., Weber, F., Brunner, T. J., Loher, S., Ehrbar, M., Schmidlin, P. R., et al. (2009). *In Vivo* and *In Vitro* Evaluation of Flexible, Cottonwool-like Nanocomposites as Bone Substitute Material for Complex Defects. *Acta Biomater.* 5, 1775–1784. doi:10.1016/j.actbio.2008.11.030
- Schröder, K., Wandzioch, K., Helmcke, I., and Brandes, R. P. (2009). Nox4 Acts as a Switch between Differentiation and Proliferation in Preadipocytes. *Arterioscler Thromb. Vasc. Biol.* 29, 239–245. doi:10.1161/ATVBAHA.108.174219
- Seok, J. M., Choe, G., Lee, S. J., Yoon, M.-A., Kim, K.-S., Lee, J. H., et al. (2021). Enhanced Three-Dimensional Printing Scaffold for Osteogenesis Using a Mussel-Inspired Graphene Oxide Coating. *Mater. Des.* 209, 109941. doi:10.1016/j.matdes.2021.109941
- Sun, W., Xue, B., Li, Y., Qin, M., Wu, J., Lu, K., et al. (2016). Polymer-Supramolecular Polymer Double-Network Hydrogel. *Adv. Funct. Mater.* 26, 9044–9052. doi:10.1002/adfm.201603512
- Tan, J., Gemeinhart, R. A., Ma, M., and Mark Saltzman, W. (2005). Improved Cell Adhesion and Proliferation on Synthetic Phosphonic Acid-Containing Hydrogels. *Biomaterials* 26, 3663–3671. doi:10.1016/j.biomaterials.2004.09.053
- Tang, S., Hu, K., Sun, J., Li, Y., Guo, Z., Liu, M., et al. (2017). High Quality Multicellular Tumor Spheroid Induction Platform Based on Anisotropic Magnetic Hydrogel. *ACS Appl. Mater. Inter.* 9, 10446–10452. doi:10.1021/acsami.6b15918
- Wang, H., Gong, S., Lin, Z., Fu, J., Xue, S., Huang, J., et al. (2007). *In Vivo* biocompatibility and Mechanical Properties of Porous Zein Scaffolds. *Biomaterials* 28, 3952–3964. doi:10.1016/j.biomaterials.2007.05.017
- Wang, P., Yin, B., Dong, H., Zhang, Y., Zhang, Y., Chen, R., et al. (2020). Coupling Biocompatible Au Nanoclusters and Cellulose Nanofibrils to Prepare the Antibacterial Nanocomposite Films. *Front. Bioeng. Biotechnol.* 8, 986. doi:10.3389/fbioe.2020.00986
- Wang, X., Hao, T., Qu, J., Wang, C., and Chen, H. (2015). Synthesis of Thermal Polymerizable Alginate-GMA Hydrogel for Cell Encapsulation. *J. Nanomater.* 2015, 970619. doi:10.1155/2015/970619
- Wang, X., Tang, S., Chai, S., Wang, P., Qin, J., Pei, W., et al. (2021). Preparing Printable Bacterial Cellulose Based Gelatin Gel to Promote *In Vivo* Bone Regeneration. *Carbohydr. Polym.* 270, 118342. doi:10.1016/j.carbpol.2021.118342
- Wu, J., Liu, Y., Cao, Q., Yu, T., Zhang, J., Liu, Q., et al. (2020). Growth Factors Enhanced Angiogenesis and Osteogenesis on Polydopamine Coated Titanium Surface for Bone Regeneration. *Mater. Des.* 196, 109162. doi:10.1016/j.matdes.2020.109162
- Xie, Y., Chen, M., Chen, Y., Xu, Y., Sun, Y., Liang, J., et al. (2020). Effects of PRP and LyPRP on Osteogenic Differentiation of MSCs. *J. Biomed. Mater. Res.* 108, 116–126. doi:10.1002/jbm.a.36797
- Xu, F. T., Li, H. M., Yin, Q. S., Liang, Z. J., Huang, M. H., Chi, G. Y., et al. (2015). Effect of Activated Autologous Platelet-Rich Plasma on Proliferation and Osteogenic Differentiation of Human Adipose-Derived Stem Cells *In Vitro*. *Am. J. Transl. Res.* 7, 257–270.
- Xu, H.-H., Li, S.-M., Fang, L., Xia, C.-J., Zhang, P., Xu, R., et al. (2021). Platelet-rich Plasma Promotes Bone Formation, Restrains Adipogenesis and Accelerates Vascularization to Relieve Steroids-Induced Osteonecrosis of the Femoral Head. *Platelets* 32, 950–959. doi:10.1080/09537104.2020.1810221
- Zhang, Y., Wang, P., Mao, H., Zhang, Y., Zheng, L., Yu, P., et al. (2021). PEGylated Gold Nanoparticles Promote Osteogenic Differentiation in *In Vitro* and *In Vivo* Systems. *Mater. Des.* 197, 109231. doi:10.1016/j.matdes.2020.109231
- Zheng, L., Lu, G., Pei, W., Yan, W., Li, Y., Zhang, L., et al. (2021a). Understanding the Relationship between the Structural Properties of Lignin and Their Biological Activities. *Int. J. Biol. Macromolecules* 190, 291–300. doi:10.1016/j.ijbiomac.2021.08.168
- Zheng, L., Yu, P., Zhang, Y., Wang, P., Yan, W., Guo, B., et al. (2021b). Evaluating the Bio-Application of Biomacromolecule of Lignin-Carbohydrate Complexes (LCC) from Wheat Straw in Bone Metabolism via ROS Scavenging. *Int. J. Biol. Macromolecules* 176, 13–25. doi:10.1016/j.ijbiomac.2021.01.103
- Zheng, L., Zhuang, Z., Li, Y., Shi, T., Fu, K., Yan, W., et al. (2022). Bone Targeting Antioxidative Nano-Iron Oxide for Treating Postmenopausal Osteoporosis. *Bioactive Mater.* 14, 250–261. doi:10.1016/j.bioactmat.2021.11.012
- Zhou, X., Chen, J., Sun, H., Wang, F., Wang, Y., Zhang, Z., et al. (2021). Spatiotemporal Regulation of Angiogenesis/osteogenesis Emulating Natural Bone Healing cascade for Vascularized Bone Formation. *J. Nanobiotechnol.* 19, 420. doi:10.1186/s12951-021-01173-z
- Zhu, Y., Goh, C., and Shrestha, A. (2021). Biomaterial Properties Modulating Bone Regeneration. *Macromol. Biosci.* 21, e2000365. doi:10.1002/mabi.202000365
- Zou, M., Sun, J., and Xiang, Z. (2021). Induction of M2-type Macrophage Differentiation for Bone Defect Repair via an Interpenetration Network Hydrogel with a GO-Based Controlled Release System. *Adv. Healthc. Mater.* 10, e2001502. doi:10.1002/adhm.202001502



**Conflict of Interest:** The authors declare that the research was conducted in the absence of any commercial or financial relationships that could be construed as a potential conflict of interest.

The handling editor LL declared a shared parent affiliation with the authors at the time of review.

**Publisher's Note:** All claims expressed in this article are solely those of the authors and do not necessarily represent those of their affiliated organizations, or those of the publisher, the editors, and the reviewers. Any product that may be evaluated in

this article, or claim that may be made by its manufacturer, is not guaranteed or endorsed by the publisher.

*Copyright © 2022 Tang, Wang, Zhang and Zhang. This is an open-access article distributed under the terms of the Creative Commons Attribution License (CC BY). The use, distribution or reproduction in other forums is permitted, provided the original author(s) and the copyright owner(s) are credited and that the original publication in this journal is cited, in accordance with accepted academic practice. No use, distribution or reproduction is permitted which does not comply with these terms.*



# Osteogenesis of Iron Oxide Nanoparticles-Labeled Human Precartilaginous Stem Cells in Interpenetrating Network Printable Hydrogel

Wei Liao<sup>1,2†</sup>, Jingwei Lu<sup>3†</sup>, Qianjin Wang<sup>4</sup>, Sen Yan<sup>5</sup>, Yan Li<sup>5</sup>, Yibo Zhang<sup>4</sup>, Peng Wang<sup>4</sup>, Qing Jiang<sup>4,6\*</sup> and Ning Gu<sup>2,5\*</sup>

<sup>1</sup>Children's Hospital of Nanjing Medical University, Nanjing, China, <sup>2</sup>School of Biomedical Engineering and Informatics, Nanjing Medical University, Nanjing, China, <sup>3</sup>Department of Orthopedics, Jinling School of Clinical Medicine, Nanjing Medical University, Jinling Hospital, Nanjing, China, <sup>4</sup>State Key Laboratory of Pharmaceutical Biotechnology, Department of Sports Medicine and Adult Reconstructive Surgery, Nanjing Drum Tower Hospital, The Affiliated Hospital of Nanjing University Medical School, Nanjing, China, <sup>5</sup>State Key Laboratory of Bioelectronics, Jiangsu Key Laboratory for Biomaterials and Devices, School of Biological Sciences and Medical Engineering, Southeast University, Nanjing, China, <sup>6</sup>Nanjing Drum Tower Hospital Clinical College of Nanjing Medical University, Nanjing, China

## OPEN ACCESS

### Edited by:

Lei Zhang,  
Wenzhou Medical University, China

### Reviewed by:

Chuan-Ling Si,  
Tianjin University of Science and  
Technology, China  
Zigang Ge,  
Peking University, China

### \*Correspondence:

Qing Jiang  
qingj@njmu.edu.cn  
Ning Gu  
guning@seu.edu.cn

<sup>†</sup>These authors have contributed  
equally to this work

### Specialty section:

This article was submitted to  
Biomaterials,  
a section of the journal  
Frontiers in Bioengineering and  
Biotechnology

Received: 09 February 2022

Accepted: 05 April 2022

Published: 29 April 2022

### Citation:

Liao W, Lu J, Wang Q, Yan S, Li Y,  
Zhang Y, Wang P, Jiang Q and Gu N  
(2022) Osteogenesis of Iron Oxide  
Nanoparticles-Labeled Human  
Precartilaginous Stem Cells in  
Interpenetrating Network  
Printable Hydrogel.  
Front. Bioeng. Biotechnol. 10:872149.  
doi: 10.3389/fbioe.2022.872149

Smart biomaterials combined with stem cell-based therapeutic strategies have brought innovation in the field of bone tissue regeneration. However, little is known about precartilaginous stem cells (PCSCs), which can be used as seed cells and incorporated with bioactive scaffolds for reconstructive tissue therapy of bone defects. Herein, iron oxide nanoparticles (IONPs) were employed to modulate the fate of PCSCs, resulting in the enhanced osteogenic differentiation potential both *in vitro* and *in vivo*. PCSCs were isolated from the ring of La-Croix extracted from polydactylism patient and identified through immunohistochemically staining using anti-FGFR-3 antibodies. Potential toxicity of IONPs toward PCSCs was assessed through cell viability, proliferation, and attachment assay, and the results demonstrated that IONPs exhibited excellent biocompatibility. After that, the effects of IONPs on osteogenic differentiation of PCSCs were evaluated and enhanced ALP activity, formation of mineralized nodule, and osteogenic-related genes expressions could be observed upon IONPs treatment. Moreover, *in vivo* bone regeneration assessment was performed using rabbit femur defects as a model. A novel methacrylated alginate and 4-arm poly (ethylene glycol)-acrylate (4A-PEGAc)-based interpenetrating polymeric printable network (IPN) hydrogel was prepared for incorporation of IONPs-labeled PCSCs, where 4A-PEGAc was the common component for three-dimensional (3D) printing. The implantation of IONPs-labeled PCSCs significantly accelerated the bone formation process, indicating that IONPs-labeled PCSCs could endow current scaffolds with excellent osteogenic ability. Together with the fact that the IONPs-labeled PCSCs-incorporated IPN hydrogel (PCSCs-hydrogels) was biosafety and printable, we believed that PCSCs-hydrogels with enhanced osteogenic bioactivity could enrich the stem cell-based therapeutic strategies for bone tissue regeneration.

**Keywords:** iron oxide nanoparticles, human precartilaginous stem cells, osteogenic activity, interpenetrating network hydrogel, bone regeneration

## 1 INTRODUCTION

Repair of large bone defects caused by trauma, disease, or tumor resection has become a fundamental challenge in the field of orthopedics (Stahl and Yang, 2021). Currently, autologous or allogeneic bone grafts are considered as the most appropriate materials for the treatment of large bone defects but come with some limitations such as infection, possible fracture, and limited bone availability (Brink, 2021). To overcome these shortcomings, functional tissue engineering bone grafts, containing osteoblast or stem cells, growth factor, and bioactive materials, are considered as promising alternatives that have attracted a great deal of interest from researchers and focuses on regenerative strategies for large bone defects (Battafarano et al., 2021; Chansaenroj et al., 2021). Recently, stem cell-based therapeutic strategies have attracted considerable attention in the field of bone tissue regeneration due to their excellent osteogenic potential, superior biocompatibility, low immunogenicity, and ease of accessibility (Shang et al., 2021). In addition to their differentiation potential, stem cells also have ability to regulate other cells' function and systemic inflammatory condition through cell-cell interaction to enhance their therapeutic efficacy (Sui et al., 2019). This was an advantage for bone repair using stem cell-based therapeutic strategies.

There are several kinds of stem cells, including embryonic stem cells (ESCs), bone marrow mesenchymal stem cells (BMSCs), and adipose-derived mesenchymal stem cells (ADSCs), which have been used as seed cells of tissue engineering for substitute therapies of bone defects (Kim et al., 2011; Pan et al., 2016; Du et al., 2021; Mende et al., 2021). Although the current stem cell-based therapeutic strategies exhibited potential capacity for bone tissue regeneration they still have some limitations in terms of difficulty in isolation, purification, and manipulation of stem cell fate. Apart from these stem cells, precartilaginous stem cells (PCSCs), a kind of adult stem cells that can be isolated from the peripheral layer of the epiphyseal organ with a perichondrial mesenchyme in embryo limbs (the ring of La-Croix), have strong proliferation ability and differentiation potential (You et al., 2011). There are accumulating evidence that PCSCs exhibit excellent chondrogenic activity and have been extensively utilized as seed cells for reconstructive tissue therapy of cartilage defects due to their excellent chondrogenic ability (Guo et al., 2013; Pan et al., 2016). However, little is known about their osteogenic ability when they were employed as seed cells for bone defects repair. Therefore, it is highly desirable and a great challenge to investigate their osteogenic potential, enriching the stem cell-based therapeutic strategies for bone tissue regeneration.

To date, the compounds with capability to promote cell differentiation have been investigated in different bio-fields (Huang C et al., 2018; Pei et al., 2020; Wang et al., 2021). While, there are some application issues for the compounds in bio-fields, such as the tanglesome extraction process, instability of bio-activity, and bio-toxicity (Gu et al., 2021; Yang et al., 2021; Hu et al., 2022). Comparing to the compounds, nanomaterials have attracted considerable attention in the bio-field due to their distinct physicochemical properties, superior

biocompatibility, and manipulation of stem cell fate (Zhang et al., 2021b; Huang et al., 2021). Recent studies suggested that magnetic iron oxide nanoparticles (IONPs) demonstrated great potential for versatile biomedical applications, especially stem cell therapy and bone tissue engineering (Hu et al., 2018; Soto et al., 2021). IONPs can facilitate osteogenic differentiation of stem cells *via* supporting transduction of dynamic mechanical stimulation, which is of great requirement for bone tissue regeneration (Henstock et al., 2014). Our previous study suggested that IONPs could promote osteogenic differentiation of human bone-derived mesenchymal stem cells (hBMSCs), and mechanism exploration *via* gene microarray assay and bioinformatics analysis exhibited that IONPs could activate the mitogen-activated protein kinase (MAPK) signal pathway (Wang et al., 2016). Incorporation of IONPs could also endow current bone repair scaffolds fabricated by electrostatic spinning and 3D-printing scaffolds with enhanced osteogenic performance both *in vitro* and *in vivo*. Hence, IONPs may endow PCSCs with great osteogenic bioactivity and subsequently used as seed cells for bone tissue regeneration.

To load the nanomaterials to achieve the excellent performance, the scaffolds and polymer matrices have been fabricated by various technologies (Huang et al., 2020; Liu et al., 2021; Xu et al., 2021). Scaffold materials have attracted considerable attention in stem cell-based therapeutic strategies for bone tissue regeneration due to their ability to hold stem cells for several cellular functions such as cell attachment, proliferation, and differentiation (Chen et al., 2019). There are numerous scaffolds, including hydrogels, acellular tissue matrix, and collagen, which have been used in bone tissue regeneration. Among these materials, hydrogels have been extensively utilized as bone repair scaffolds due to their good biocompatibility, favorable mechanical properties, suitable degradation rate, and superior biological activities (e.g., osteoconductivity and osteoinductivity) (Li et al., 2020). Hydrogels have the ability to hold and retain stem cells at the bone repair site, adaptively fill the lesion cavity, optimize the microenvironment, and mediate the directional growth of stem cells (Bai et al., 2018). Particularly, the physicochemical properties of hydrogels can be adjusted by varying the component and crosslinking methods. Recently, interpenetrating polymeric network (IPN) hydrogels with two or more crosslinked polymers are considered as a simple and easily feasible route to improve cell spreading and proliferation inside hydrogels (Geng et al., 2012). Therefore, IONPs-labeled PCSCs-incorporated IPN hydrogels could be used as promising repair scaffolds for bone tissue regeneration.

In the present study, PCSCs were successfully isolated and identified through immunohistochemically staining using anti-FGFR-3 antibodies. Subsequently, the effects of IONPs on biocompatibility and osteogenic differentiation of PCSCs were comprehensively investigated. Moreover, novel IPN hydrogel was employed as scaffold for holding IONPs-labeled PCSCs for *in vivo* bone regeneration assessment. Together with the fact that the IPN hydrogel was printable and could be used for 3D printing, we believed that IONPs-

labeled PCSCs with enhanced osteogenic bioactivity could enrich the stem cell-based therapeutic strategies for bone tissue regeneration.

## 2 MATERIALS AND METHODS

### 2.1 Materials and Reagents

Collagenase type I, sodium alginate, methacrylic anhydride, and 2-hydroxy-4'-(2-hydroxyethoxy)-2-methylpropiophenone (Irgacure 2959, 98%) were obtained from Sigma-Aldrich Co. Ltd. (MO, United States). 4-arm poly (ethylene glycol) acrylate was provided by Sinopeg Biotech Co. Ltd. (China). Cell Counting Kit-8 was from Bimake (United States). Ultrapure water was achieved from a Millipore auto-pure system. All reagents were used without further purification.

### 2.2 Culture and Identifying Precartilaginous Stem Cells

PCSCs were isolated individually from the ring of La-Croix extracted for polydactylism patient (age range 0.5–1 year) by collagenase type I (Zhang et al., 2020), which was approved by the ethics committee of Children's Hospital affiliated to the Nanjing Medical University. Briefly, the ring of La-Croix, encompassing the lucent epiphyseal disk of embryo limbs, was precisely dissected under the operating microscope, followed by washing with phosphate-buffered saline (PBS) for three times. After that, the tissue was cut into fragments (1 mm×1 mm) digested with collagenase type I (1 mg/ml) for 12 h at 37°C in 5% CO<sub>2</sub>. After filtered by a 100-mesh aperture sieve, the obtained PCSCs were cultured in growth medium at 37°C in 5% CO<sub>2</sub>. The obtained PCSCs (passages 2 and 6) were used in subsequent experiments. For cells identification, the PCSCs were seeded into a 6-well plate containing poly-L-lysine-coated cover slips at a density of 5×10<sup>4</sup> per well. After 3 days culture, the slips were immunohistochemically stained using anti-FGFR-3 antibodies [a specific marker for precartilaginous stem cells (Robinson et al., 1999)].

### 2.3 Iron Oxide Nanoparticles Synthesis and Characterization

IONPs were prepared according to a classic chemical co-precipitation method using polyglucose-sorbitol-carboxymethyl ether (PSC) as a stabilizer (Zheng L et al., 2021). Briefly, PSC (100 mg) was dissolved in 5 ml ultrapure water and the mixed solution was purified by argon for at least 5 min to remove the oxygen. After that, FeCl<sub>3</sub> (30 mg) and FeCl<sub>2</sub> (15 mg) were dissolved in 10 ml ultrapure water and the mixed solution was added to the reaction system, followed by the addition of ammonium hydroxide (500 mg, 28% w/v) under vigorous stirring at 80°C for 30 min. The obtained IONPs were collected and dialyzed using membrane tubing (MWCO = 3000) to remove the free PSC. As for characterization, the morphology of IONPs was characterized by transmission electron microscopy (TEM, JEOL 1200EX). The

hydrodynamic size of IONPs was measured by dynamic light scattering (DLS) (Malvern Zetasizer Nano ZS90, United Kingdom).

## 2.4 Cell Experiment

### 2.4.1 Cell Culture

The PCSCs were cultured at 37°C with 5% CO<sub>2</sub> in growth medium (DMEM medium containing 10% fetal bovine serum and 1% penicillin/streptomycin). For osteogenic induction, the culture medium was replaced by osteogenic medium (growth medium supplemented with 0.1 μM dexamethasone, 50 μg/ml ascorbic acid, and 10 mM β-glycerophosphate). The culture medium was replaced every 3 days.

### 2.4.2 Cellular Uptake Observation of Iron Oxide Nanoparticles by Prussian Blue Staining

After seeded in 24-well plates (1×10<sup>5</sup> cells per well) and cultured for 24 h, the PCSCs were incubated with various amount of IONPs (Fe concentration: 50, 100, and 200 mg/ml) for 24 h, collected, and fixed with 4% (v/v) formaldehyde (PFA) and a Perl's blue staining assay was performed to determine the internalization of IONPs. After that, the cells were observed by an inverted optical microscope (Olympus IMT-2, Tokyo, Japan).

### 2.4.3 Cell Viability

The toxicity of IONPs toward PCSCs was assessed using a standard Cell Counting Kit-8 (CCK-8) assay (Zhang et al., 2021a). In brief, PCSCs were seeded in 96-well plates (1×10<sup>4</sup> cells per well) before various amount of IONPs (Fe concentration: 50, 100, and 200 mg/ml) were added. To test the cytotoxicity, 10 μl CCK-8 was added and cultured for another 1 h. Cell viability was detected according to the OD value observed by a microplate reader (Multiskan GO, Thermo Fisher Scientific, United States).

### 2.4.4 Live/Dead Staining

After treated with IONPs (100 mg/ml) for 3 days, PCSCs were harvested, washed with PBS for three times, and stained with calcein-AM/PI (Solarbio, China). Fluorescence images were observed using an inverted optical microscope (Olympus IMT-2, Tokyo, Japan).

### 2.4.5 Alkaline Phosphatase and Alizarin Red S Staining

PCSCs treated with IONPs (100 mg/ml) were harvested after osteogenic induction for 14 days (ALP staining) and 21 days (ARS staining). The cells were stained using the BCIP/NBT alkaline phosphatase color development kit (Beyotime, China) and 5% ARS staining solution (Sigma, United States) according to the manufacturer's instructions, respectively, followed by the observation using an inverted optical microscope (Olympus IMT-2, Tokyo, Japan).

### 2.4.6 Real-Time Quantitative PCR

PCSCs were cultured in a 6-well plate (3×10<sup>5</sup> cells per well) for 24 h, followed by the treatment of IONPs (100 mg/ml) for 3 days. After that, total RNA was isolated using an RNA-Quick Purification Kit (Yishan Biotech, Shanghai, China) and cDNA was generated using a HiScript II Q RT SuperMix according to



the manufacturer's instructions. Finally, the quantitative PCR was detected using a ChamQ™ SYBR Color qPCR Master Mix (Vazyme Biotech). **Supplementary Table S1** listed the forward and reverse primers of the investigated osteogenic-related genes.

## 2.5 Preparation of Interpenetrating Polymeric Network Hydrogel for Holding Precartilaginous Stem Cells

An interpenetrating polymeric network based on photo-crosslinking of methacrylated alginate and 4-arm poly (ethylene glycol)-acrylate (4A-PEGAc) was constructed for holding PCSCs, where methacrylated alginate was synthesized according to a reported study (Araiza-Verduzco et al., 2020). In brief, 100 mg methacrylated alginate and 50 mg 4A-PEGAc were dissolved in 5 ml PBS at 37°C for 1 h, followed by the addition of I2959 (1% (w/v)). After that, PCSCs were already incorporated with IONPs *in vitro* to acquire great osteogenic activity, followed by the transfer 500 µl of the mixed solution containing  $1 \times 10^6$  IONPs-incorporated PCSCs to a flat-bottomed 1-ml tube and subjected UV-light irradiation (365 nm) for 90 s. The as-prepared PCSCs-incorporated hydrogel was submerged in PBS at 37°C for 1 h and implanted to femur condyle defect of rabbit for *in vivo* bone regeneration assessment.

## 2.6 Animal Experiment

All experimental protocols were approved by the ethics committee of Drum Tower Hospital affiliated to the Medical School of Nanjing University, and performed according to the Institutional Animal Care and Use Committee (IACUC) guidelines.

### 2.6.1 The Femur Condyle Defect Model

A total of 12 male Newland rabbits (3.5 kg) were enrolled in the study and randomly divided into three groups (control group, neat hydrogel group, and PCSCs-hydrogels group). Bilateral femur condyle defect (high: 3 mm, diameter: 5 mm) was made, followed by the implantation of hydrogels and the defects in the control group remained blank. All rabbits were sacrificed at week 12 post-operation for *in vivo* bone regeneration assessment.

### 2.6.2 Micro-CT Analysis

The high-resolution micro-CT scanner (Scanco Medical, Switzerland) was used to evaluate the *in vivo* bone regeneration, where bone mineral density (BMD), bone volume/total volume (BV/TV), trabecular number (TB.N), trabecular separation (TB.Sp), and trabecular thickness (TB.Th) were quantified. A commercial software MIMICS19.0 (Materialise, Leuven, Belgium) was used to generate 3D models of the harvested femurs.

### 2.6.3 Histological Analysis

After fixed with formalin at 4°C for 24 h, the harvested femur condyles were decalcified using 15% ethylene diamine tetra-acetic acid (EDTA) for 28 days. After that, the decalcified femur condyles were embedded in paraffin and sectioned at 5 µm of

hematoxylin and eosin (H&E) and Masson's trichrome staining. The histological analysis of major organs (heart, liver, spleen, lung, and kidney) followed the same process except for the decalcification process.

## 2.7 Statistical Analysis

All experiments were performed with three replicates unless otherwise stated. Data are mean  $\pm$  standard deviation. Statistical analysis was performed with Origin software (8.5 version). Asterisks in statistical analysis indicate statistically significant differences between the control and experimental groups (\* $p < 0.05$ ; \*\* $p < 0.01$ ; and \*\*\* $p < 0.005$ ).

## 3 RESULTS

### 3.1 Isolation and Identification of Precartilaginous Stem Cells

PCSCs were isolated individually from the ring of La-Croix extracted for polydactylism patient (age range 0.5–3 years) by collagenase type I, the process of which was shown in **Figure 1A**. It could be seen that the PCSCs grow well under a light microscope. In addition, fibroblast growth factor receptor 3 (FGFR-3), a specific marker for precartilaginous stem cells was used to identify the PCSCs (Robinson et al., 1999), where human bone marrow-derived mesenchymal stem cells (hBMSCs) were used as control. As shown in **Figure 1B**, the immunofluorescence staining results for PCSCs demonstrated the positive expression of FGFR-3. In contrast, almost no FGFR-3-positive expression was found in hBMSCs (**Figure 1C**). These results unarguably confirmed that the isolated cells were PCSCs, which could be used for further *in vitro* osteogenic differentiation and *in vivo* bone regeneration assessment.

### 3.2 Preparation and Characterization of Iron Oxide Nanoparticles

IONPs were synthesized by a classic chemical co-precipitation method (Chen et al., 2018). The as-prepared IONPs solution displayed dark brown color (**Figure 2A**, inset). Characterizations of IONPs were performed using TEM and DLS. TEM images (**Figure 2A**) demonstrated that the obtained IONPs exhibited dimensional homogeneity and excellent dispersity. The statistical average size (**Figure 2B**) of the iron oxide cores were  $7.14 \pm 0.68$  nm. In addition, the hydrodynamic size (**Figure 2C**) of IONPs was 34.9 nm, the value of which was larger than their physical size due to the hydrated PSC shell. The polydispersity index (P.I.) was 0.229, indicating the excellent monodispersity. It was also demonstrated that the zeta potential (**Figure 2D**) of IONPs was  $-41.69$  mV, and the negatively charged value was attributed to the numerous carboxyl of PSC (Yu et al., 2020). It should be mentioned that the synthetic route of PSC-coated IONPs exactly followed the technology of ferumoxytol, which is the only inorganic nano-drug approved by the Food and Drug Administration (FDA) for

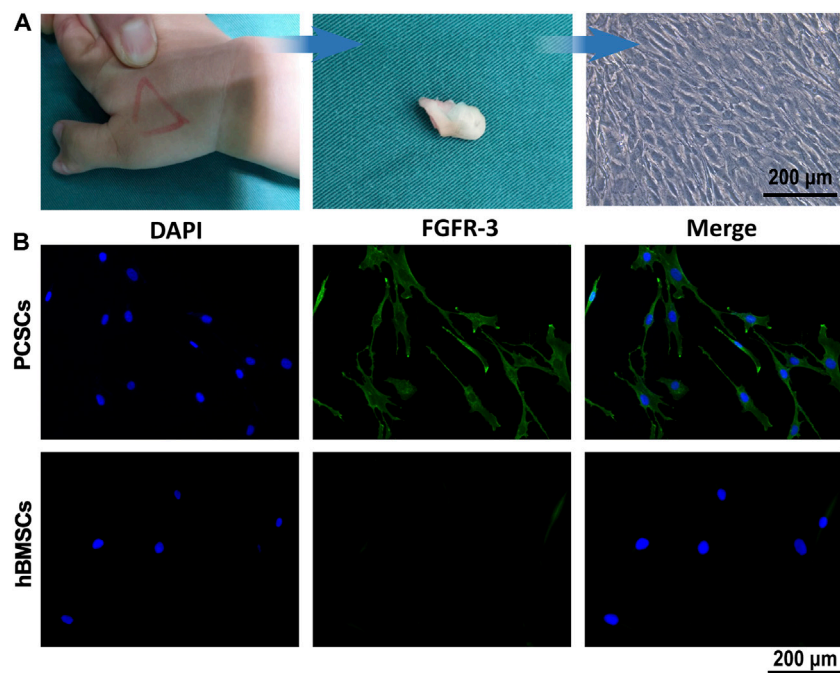


**FIGURE 1 |** Isolation and identification of PCSCs. **(A)** Process of isolation of PCSCs from the ring of La-Croix extracted from polydactylism patient. **(B)** Representative images of immunostaining for DAPI (blue) and FGFR-3 (green), and hBMSCs were used as control.

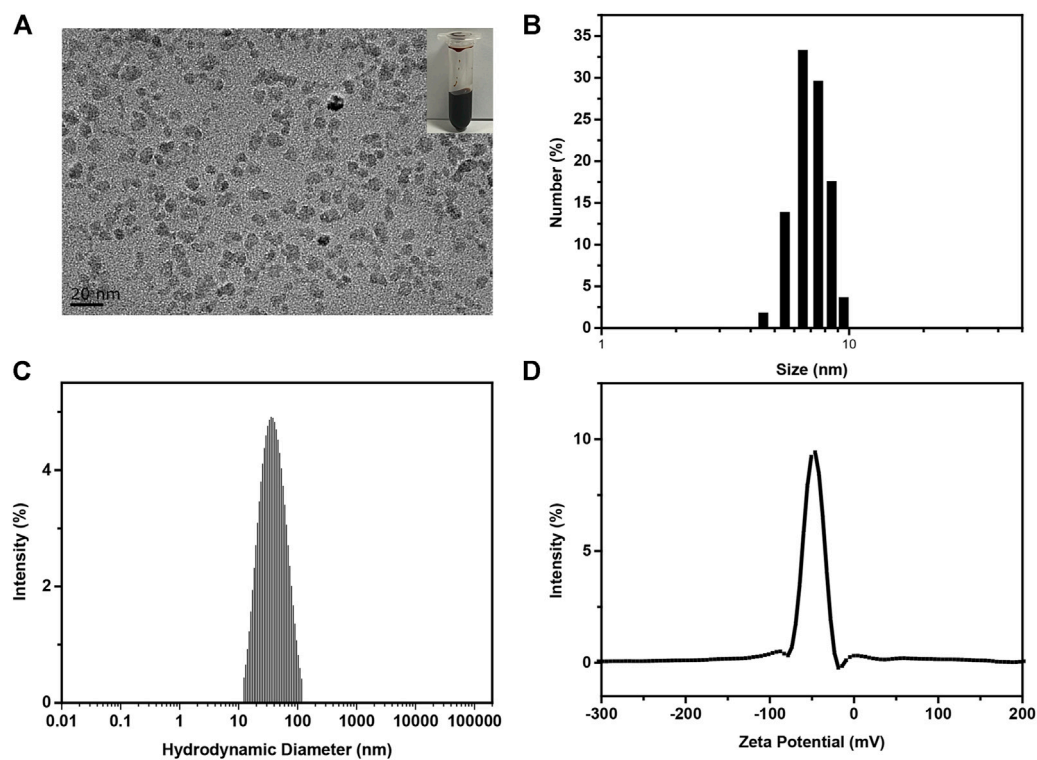


**FIGURE 2 |** Preparation and characterization of IONPs. **(A)** Typical TEM image, **(B)** statistical size distribution according to **(A-C)** hydrodynamic diameter, **(D)** zeta potential of as-prepared PSC-coated IONPs.

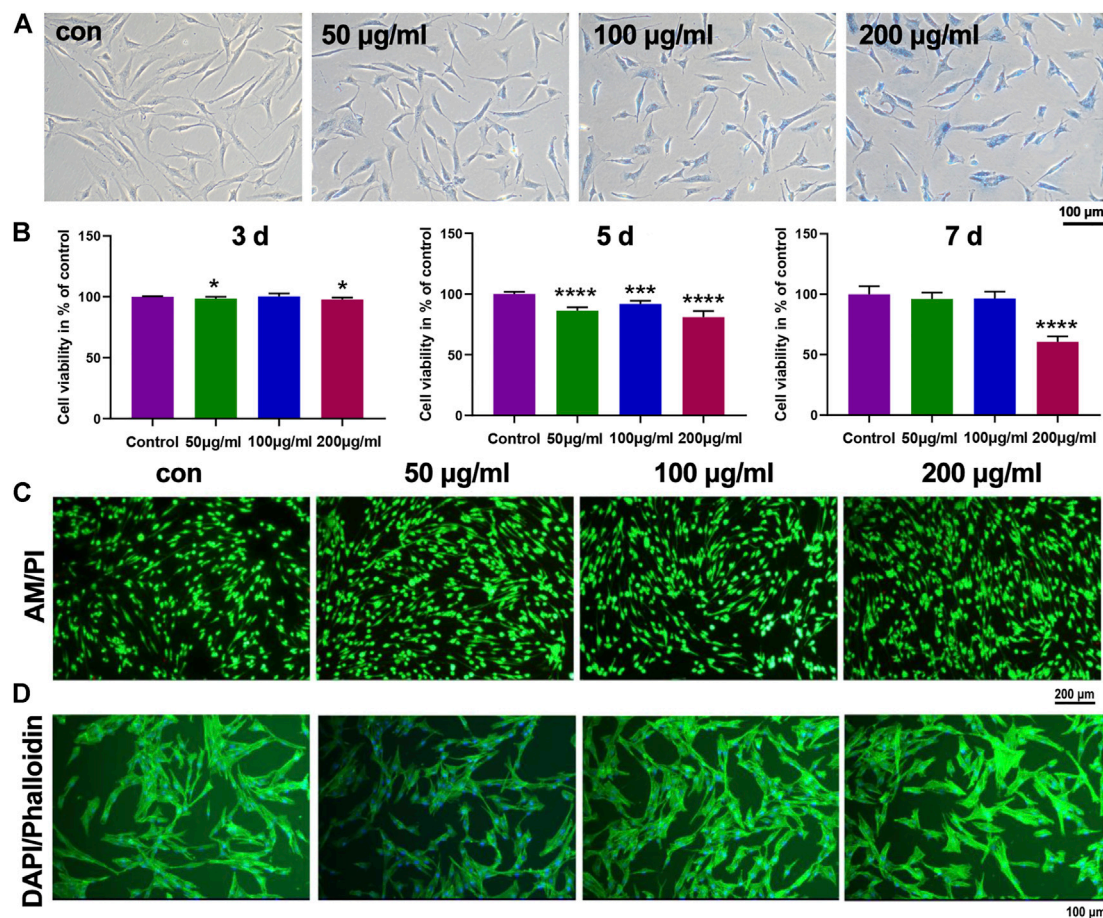


**FIGURE 3 |** *In vitro* biocompatibility and cellular uptake of IONPs on PCSCs. **(A)** Prussian blue staining of PCSCs treated with IONPs with various concentrations (50, 100, and 200 µg/ml). **(B)** Cell viability of PCSCs after incubated with IONPs (concentration: 50, 100, and 200 µg/ml) for 3, 5, and 7 days. Representative scan of **(C)** live/dead staining (green- and red-labeled cells denote living and dead cells, respectively) and **(D)** cytoskeleton staining of PCSCs after treated with IONPs with various concentration (50, 100, and 200 µg/ml), respectively. Asterisk indicates statistically significant differences between the control and experience groups (\* $p < 0.05$ ; \*\*\* $p < 0.005$ ; and \*\*\*\* $p < 0.001$ ).

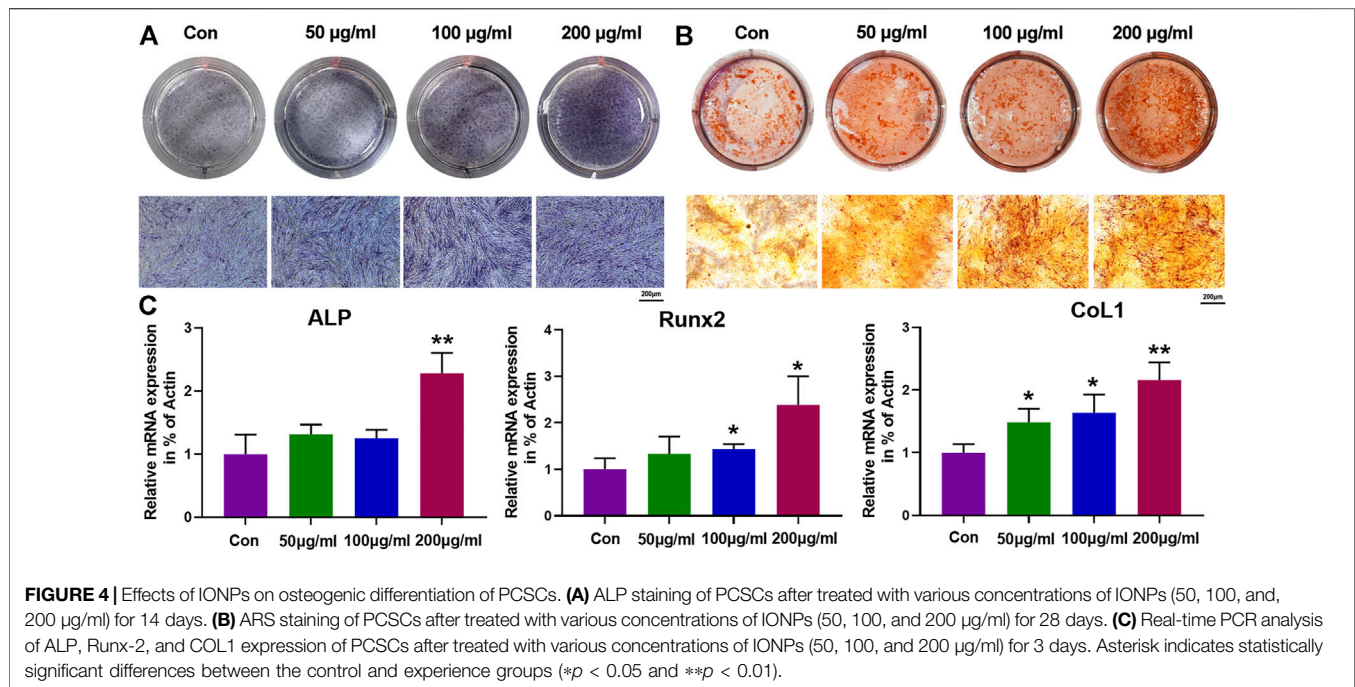
clinical applications. Hence, IONPs we used in our study were of great biosecurity, potentially translatable, and could be used to investigate their biological effects on PCSCs.

### 3.3 *In Vitro* Biocompatibility and Cellular Uptake of Iron Oxide Nanoparticles on Precartilaginous Stem Cells

It has been widely reported that the cytomembrane of biological cells is negatively charged due to the hydrophilic phosphonyl group of phospholipid bilayer (Huang B et al., 2018). Hence, the negatively charged PSC-coated IONPs might hardly be taken by cells, limiting their interactions with biological cells. Hence, we employed positively charged poly-L-lysine to modify IONPs using a reported method (Sun et al., 2021). Effects of IONPs on cell viability and cellular uptake of PCSCs were first studied. As shown in **Figure 3A**, the Prussian blue staining results demonstrated that the cellular uptake of IONPs by PCSCs was obviously enhanced with the concentration of IONPs increased

from 50 to 200 µg/ml. The biocompatibilities of IONPs with various concentrations toward PCSCs were further investigated using Cell Counting Kit-8 (CCK8) at 3, 5, and 7 days (**Figure 3B**). IONPs of all three concentrations demonstrated no obvious cytotoxicity toward PCSCs after 3 and 5 days' treatment with the viability exceeding 80%. However, after treated with IONPs (200 µg/ml) for 7 days, obvious decrease of cell viability could be observed, resulting in the apparent toxicity. Hence, 100 µg/ml could be considered as a proper concentration for further osteogenic assessment. To further verify their potential toxicity to PCSCs, live/dead staining was employed, and the results were exhibited in **Figure 3C**. Nearly all the PCSCs were alive (green fluorescence) after treated with IONPs at all investigated concentrations. The effect of IONPs on attachment of PCSCs was assessed using phalloidine/DAPI staining (**Figure 3D**), where it could be seen that PCSCs spread out with their filopodia extended. These results indicated that IONPs were biocompatible toward PCSCs and could be used to further assess their biological activity.





### 3.4 Effects of Iron Oxide Nanoparticles on Osteogenic Differentiation of Precartilaginous Stem Cells

Osteogenic differentiation is a crucial process for biological cells when it was used as a osteogenic bioactive agent for bone tissue regeneration, where alkaline phosphatase (ALP) activity and formation of mineralized nodule are two significant signals for the early and final stages process of osteogenic differentiation, respectively (Zhang et al., 2017). Hence, the effects of IONPs on osteogenic differentiation of PCSCs were further assessed using ALP and alizarin red S (ARS) staining. As shown in **Figure 4A,B**, IONPs demonstrated a dose-dependent effect in increasing ALP activity and mineralized nodule formation. In addition, the expression of osteogenic-related genes, including ALP, runt-related transcription factor 2 (Runx2), and collagen type 1 (COL1) were determined using real-time PCR in PCSCs treated with IONPs (100 µg/ml) for 3 days. As illuminated in **Figure 4C**, the expression of these osteogenic-related genes were significantly upregulated after treated with IONPs, where high concentration IONPs (200 µg/ml) exhibited the strongest effect on accelerating the osteogenic-related genes expression of PCSCs. Taken together, these results confirmed that IONPs showed the positive effect on facilitating osteogenic differentiation of PCSCs.

### 3.5 Preparation and Characterization of Precartilaginous Stem Cells-Hydrogels

To further investigate the *in vivo* bone regeneration ability of IONPs-labeled PCSCs when used as a osteogenic bioactive agent, smart scaffolds with several advantages, including excellent biocompatibility, porous microstructures, and appropriate mechanical properties should be used for holding

PCSCs (Zheng J et al., 2021). Among these scaffolds, hydrogels with three-dimensional culture matrices have been widely used as space filling agents (flexibility in fitting in any application site) and delivery vehicles for bioactive molecules (controllability pore size in the polymer network) (Ma et al., 2021). In our study, novel biomimetic interpenetrating polymeric network (IPN) hydrogel constructed by methacrylated alginate (MLA) and 4-arm poly (ethylene glycol)-acrylate (4A-PEGAc) through photo-crosslinking upon exposure to long-wave UV light was used as scaffold to hold PCSCs for bone regeneration assessment. The morphology of lyophilized IPN hydrogel was characterized by SEM and the results are shown in **Figure 5A**. It could be seen that our prepared IPN hydrogel demonstrated a porous microstructure with a pore size of around 30–50 nm, facilitating several cellular functions such as cell attachment, proliferation, and differentiation (Ajadary et al., 2021). Moreover, physicochemical properties of IPN hydrogel, including swelling rate, mechanical, and rheological properties were further measured. As shown in **Figure 5B**, the IPN hydrogel swelled to its maximum swelling ratio of about 2100% within 24 h. The excellent swelling property might make our hydrogel suitable for *in vivo* applications. The compressive mechanical properties of our as-prepared hydrogel were detected using standard mechanical tests. According to the results of compression-crack test (**Figure 5C**) and compression-relaxation cycles test (**Figure 5D**), the compressive modulus of IPN hydrogel was 210 Pa and the gels can compress a strain of more than 55%, indicating excellent load-bearing ability. In addition, only slight energy dissipation could be observed, suggesting that the as-prepared exhibited reliable mechanical properties. In addition, rheological properties were further measured and the results of



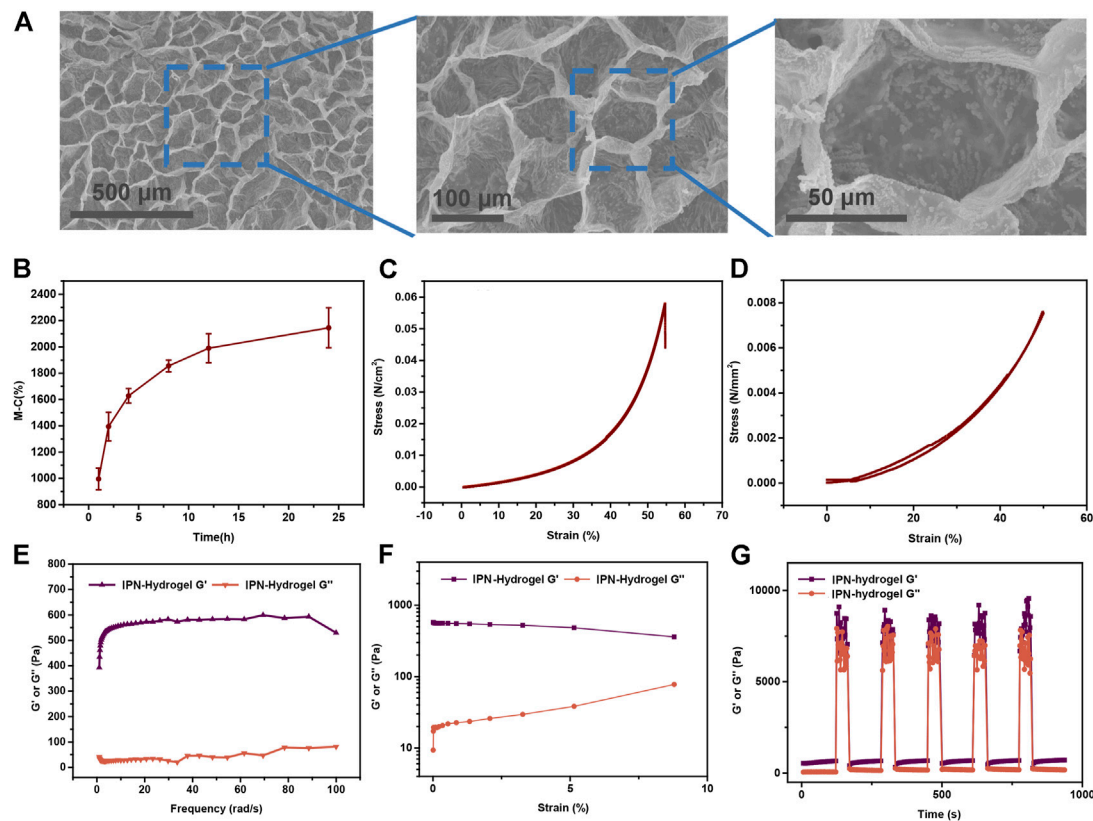


**FIGURE 5 |** Preparation and characterization of PCSCs-hydrogels. **(A)** Surface topography and their local magnification of lyophilized PCSCs-hydrogels observed by SEM. **(B)** Swelling rate at different time from 1 to 24 h. **(C)** Uniaxial stress–strain curves under compression until cracking. **(D)** Uniaxial compression–relaxation curves. **(E)**  $G'$  and  $G''$  of hydrogels measured in a strain sweep experiment (from 0.1 to 10% strain, 6.28 rad s<sup>-1</sup>) at room temperature. **(F)**  $G'$  and  $G''$  of the hydrogels measured in a frequency sweep experiment (from 0.1 to 60 rad s<sup>-1</sup>, 1% strain) at room temperature. **(G)** Hydrogels in a destroy–recovery experiment at room temperature. The frequency and strain were set to the frequency of 100 Hz and amplitude of 300% to destroy the coordination interactions and switched back to a frequency of 6.28 rad s<sup>-1</sup> and amplitude of 0.1% to monitor recovery of the mechanical properties.

frequency-sweep test, strain-sweep test, and step-strain test are demonstrated in **Figures 5E–G**, respectively. It could be seen that as-prepared IPN hydrogel demonstrated a solid-like behavior [ $G'$  was larger than the loss modulus ( $G''$ )] and dominant elastic property (partly destroyed and subsequently completely recovered). All these features suggested that our IPN hydrogel with excellent physicochemical properties could be employed as scaffold for holding IONPs-labeled PCSCs for bone tissue regeneration.

### 3.6 *In Vivo* Bone Regeneration Assessment of Iron Oxide Nanoparticles-Labeled Precartilaginous Stem Cells-Hydrogels

*In vivo* bone regeneration performance of IONPs-labeled PCSCs were finally assessed using a rabbit model of 5 mm femoral defect, where IPN hydrogel was used as scaffold for holding PCSCs. IONPs-labeled PCSCs-hydrogels (height: 5 mm and diameter: 5 mm) were directly implanted into the femur defects of rabbits and neat IPN hydrogels were used as control. After 3 months of implantation, femurs of rabbits were harvested and comprehensively characterized by micro-CT and histological

analysis. Micro-CT data (**Figure 6A**), including the reconstructed three-dimensional (3D) model, lateral and longitudinal sectional images exhibited that more newly formed bone could be observed around the bone defect area in the PCSCs-hydrogels group compared with that in the neat hydrogel and control groups. Furthermore, quantitative bone density analysis of newly formed bone, including bone mineral density (BMD), bone volume per total volume (BV/TV), and the trabecular parameters of the cancellous bone such as trabecular thickness (TB.Th), trabecular number (TB.N), and trabecular spacing (TB.Sp) were performed according to the micro-CT data. As demonstrated in **Figure 6B**, the values of BMD and BV/TV were significantly increased in the PCSCs-hydrogels group compared with a neat hydrogel group, indicating that PCSCs played an important role in accelerating bone formation. Further trabecular results exhibited the increased TB.Th and TB.N values and the decreased TB.Sp after treated with IONPs-labeled PCSCs-hydrogels by following the similar trend with the BMD. Furthermore, histological analysis (H&E and Masson staining) was also used to assess the bone regeneration performance. As shown in **Figure 6C**, more newly formed bone and trabecula could be observed in the PCSCs-hydrogel

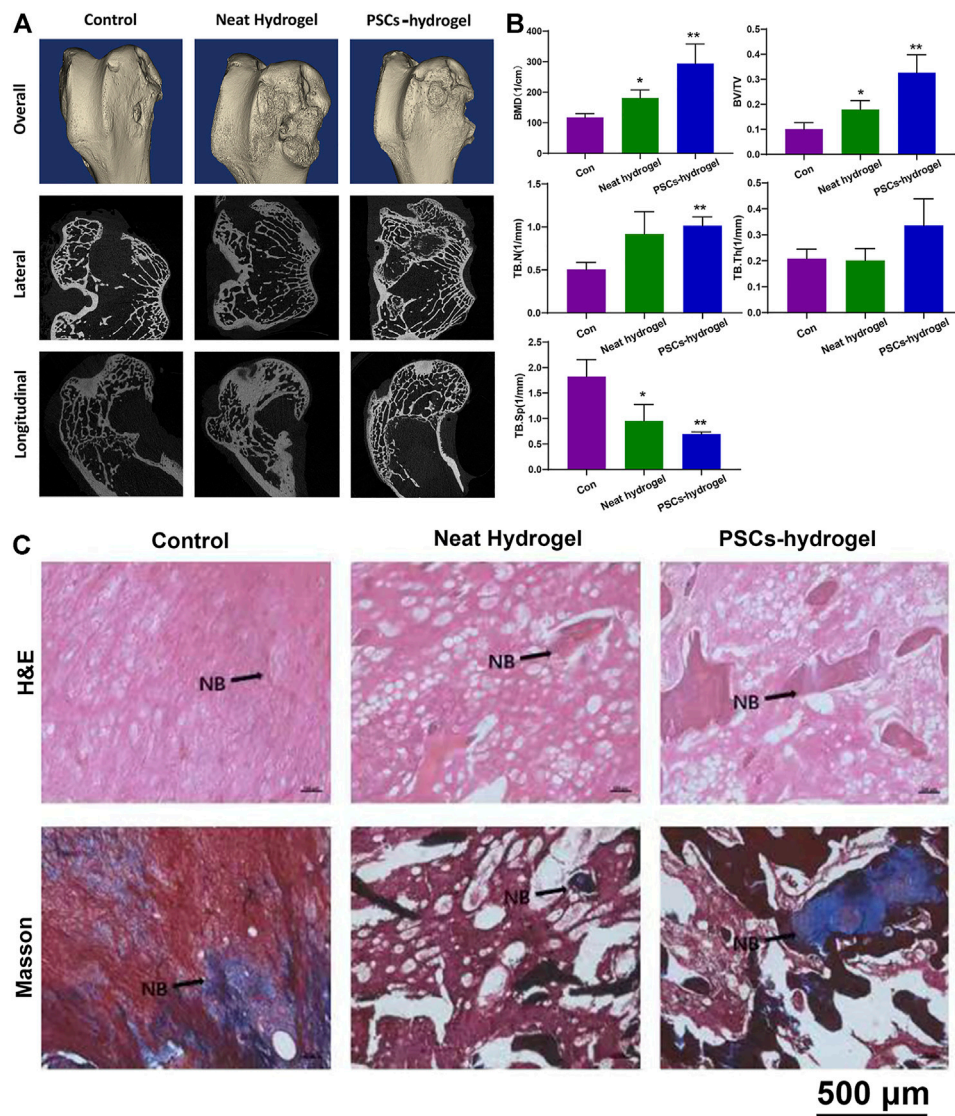


**FIGURE 6** | *In vivo* bone regeneration assessment of PCSCs-hydrogels. **(A)** Reconstructed 3D micro-CT and sectional images of femoral condyle after treated with PCSCs-hydrogels for 12 weeks. **(B)** Quantitative evaluation of the regenerated area by analyzing the parameter of micro-CT: BMD, BV/TV, TBN, TB.Sp, and TB.Th. **(C)** H&E and Masson staining images of bone defect implanted with neat hydrogel and PCSCs-hydrogel. Abbreviation: NB, newly formed bone. Asterisk indicates statistically significant differences between the control and experience groups (\* $p < 0.05$  and \*\* $p < 0.01$ ).

group compared with that in the neat hydrogel and control groups with only fibrotic connective tissues. Finally, the *in vivo* biosafety of our IONPs-labeled PCSCs-hydrogels was detected using histopathological analysis. Major organs, including heart, liver, spleen, lung, and kidney were collected from the rabbits that were implanted IONPs-labeled PCSCs-hydrogels and neat hydrogel for 3 months and histopathologically examined through hematoxylin and eosin (H&E) and Masson staining. As shown in **Supplementary Figure S1**, no obvious damage or inflammation of these tissue slices could be observed in all the investigated groups, indicating that both IPN hydrogels and IONPs-labeled PCSCs were of great biocompatibility.

## 4 DISCUSSION

Stem cell-based therapeutic strategies are considered to be very promising platforms for bone tissue regeneration, among which PCSCs has been the focus of significant interest due to their potential regenerative capacity to transform themselves into a crowd of different cells (Luo et al., 2012). Although, PCSCs showed excellent chondrogenic ability but little is known about their osteogenic ability when they were employed as seed cells for bone defects repair. Recent investigations demonstrated that nanomaterials, especially IONPs could modulate the fate of stem cells and interactions between nanomaterials and stem cells have taken into serious

consideration in facilitating stem cell-based therapeutic strategies for bone tissue regeneration (Wang et al., 2020). In this study, we have isolated PCSCs from the ring of La-Croix extracted for polydactylism patient and observed that IONPs could promote osteogenic differentiation of PCSCs. Subsequently, IONPs-labeled PCSCs-incorporated IPN hydrogel was extensively utilized as repair scaffolds for bone tissue regeneration and the results indicated that IONPs-labeled PCSCs could accelerate the bone repair process rapidly and efficiently.

There are two common methods to obtain somatic stem cells 1) directional differentiation of embryonic stem cells (ESC) (Wichterle et al., 2002) and 2) *in vitro* isolation and cultivation of the desired stem cells in specific tissue (Eberle et al., 2013). The method 1) has some limitations in terms of complex condition for directional differentiation of ESC. In our study, PCSCs were isolated individually and identified using FGFR-3. The positive expression of FGFR-3 unarguably confirmed that the isolated cells were PCSCs. Subsequently, IONPs were prepared by a classic chemical co-precipitation method and the obtained IONPs were of low polydispersion, which guaranteed the reproducibility of their biological effect.

To assess the bio-toxicity of IONPs, the viability and adhesion of PCSCs cultured with IONPs (50, 100, and 200 µg/ml) were detected. The results demonstrated that IONPs with the concentration lower than 100 µg/ml were non-toxic toward PCSCs, in agreement with previous reports (Wang et al., 2017). Based on the biocompatibility results, the effects of IONPs on osteogenic differentiation of PCSCs at concentrations of 50, 100, and 200 µg/ml. The ALP activity level (an important indicator for osteoblast differentiation) and formation of mineralized nodule were considered as two specific stages of osteogenic differentiation (Mohamed-Ahmed et al., 2018). In our study, after treated with IONPs (especially at a concentration of 200 µg/ml), the ALP activity level and mineralization were significantly enhanced, indicating the high osteogenic potential. The osteogenic-related genes, including ALP, Runx2, and COL1 were further detected to verify their osteogenic ability, where Runx2 was considered as an early master regulator for the initiation of osteogenesis that regulate the osteogenic-related genes such as COL1 and ALP (Komori, 2018). The results showed that all these genes were upregulated after treated with IONPs, which matched well with the aforementioned ALP activity level and mineralization results. Hence, IONPs could be used to induce osteogenic differentiation of PCSCs and IONPs-labeled PCSCs with enhanced osteogenic activity could be further used for *in vivo* bone tissue regeneration.

Smart biomaterials such as hydrogels, nanofibrils, and biological ceramics have proven incredibly beneficial as scaffold for bone tissue regeneration due to their adjustable nanostructure, excellent biocompatibility, biodegradability, proper mechanical properties, enhanced osseointegration capability and superior biological activities (Yue et al., 2015; Huang et al., 2020; De France et al., 2021). Among these biomaterials, hydrogels with additional advantages such as printability have attracted considerable attention. Numerous of materials have been used to construct bioactive hydrogels for

bone tissue regeneration. Alginate, a naturally occurring biopolymer, has been widely used design materials for bone tissue regeneration due to their attractive properties such as biocompatibility, biodegradability, antibacterial activity, hydrophilicity, and nontoxicity (Hernández-González et al., 2020). Previous study demonstrated that alginate could be methacrylated and the obtained ionic and photo-crosslinked alginate-methacrylate hydrogels showed modulable mechanical properties (Araiza-Verduzco et al., 2020). PEG-based hydrogels with great printability have been the focus of significant interest in designing multifunctional scaffolds for bone tissue regeneration, where PGE was the common components for photo-crosslinked three-dimensional (3D) printing. In our study, MLA/4A-PEGAc IPN hydrogel was prepared through photo-crosslinking and ionic-crosslinking. The as-prepared IPN hydrogel possessed porous nanostructure and proper mechanical properties and could be used to incorporate IONPs-labeled PCSCs for bone tissue regeneration assessment. As for the *in vitro* results, both micro-CT and histological analysis indicated that the implantation of IONPs-labeled PCSCs significantly accelerated the process of bone formation, indicating that IONPs-labeled PCSCs could endow current bone repair scaffolds with excellent osteogenic activity.

## 5 SUMMARY

This study is the first report of osteogenesis of PCSCs induced by IONPs, which is evidenced by an enhanced ALP activity level, mineralized matrix nodules, and osteogenic-related gene expressions. Further *in vivo* therapeutic performance of bone defect repair could be obtained by incorporation of IPN hydrogel as scaffold. Together with the fact that the IONPs-labeled PCSCs-incorporated IPN hydrogel was of great printability, biosafety, and improvement of cell spreading and proliferation, we believed that this PCSCs-based scaffolds could enrich the stem cell-based therapeutic strategies for bone tissue regeneration.

## DATA AVAILABILITY STATEMENT

The original contributions presented in the study are included in the article/**Supplementary Material**, further inquiries can be directed to the corresponding authors.

## ETHICS STATEMENT

The studies involving human participants were reviewed and approved by the ethics committee of Children's Hospital affiliated to the Nanjing Medical University. Written informed consent to participate in this study was provided by the participants' legal guardian/next of kin. The animal study was reviewed and approved by the ethics committee of Drum Tower Hospital affiliated to the Medical School of Nanjing University, and performed according to the Institutional Animal Care and Use Committee (IACUC) guidelines.



## AUTHOR CONTRIBUTIONS

NG and QJ proposed the idea. WL and JL performed the experiments. SY and QW helped the cell experiment. PW and YZ helped the animal experiment.

## FUNDING

The research was supported by the grant received from the National Key Research and Development Program of China (2017YFA0104302), the Key Project of the National Natural Science Foundation of China (51832001), the National Natural Science Innovative Research Group Project of China

## REFERENCES

- Ajdary, R., Tardy, B. L., Mattos, B. D., Bai, L., and Rojas, O. J. (2021). Plant Nanomaterials and Inspiration from Nature: Water Interactions and Hierarchically Structured Hydrogels. *Adv. Mater.* 33, e2001085. doi:10.1002/adma.202001085
- Araiza-Verduzco, F., Rodríguez-Velázquez, E., Cruz, H., Rivero, I. A., Acosta-Martínez, D. R., Pina-Luis, G., et al. (2020). Photocrosslinked Alginate-Methacrylate Hydrogels with Modulable Mechanical Properties: Effect of the Molecular Conformation and Electron Density of the Methacrylate Reactive Group. *Materials (Basel)* 13, 534. doi:10.3390/ma13030534
- Bai, X., Gao, M., Syed, S., Zhuang, J., Xu, X., and Zhang, X.-Q. (2018). Bioactive Hydrogels for Bone Regeneration. *Bioactive Mater.* 3, 401–417. doi:10.1016/j.bioactmat.2018.05.006
- Battafarano, G., Rossi, M., De Martino, V., Marampon, F., Borro, L., Secinaro, A., et al. (2021). Strategies for Bone Regeneration: From Graft to Tissue Engineering. *Int. J. Mol. Sci.* 22, 1128. doi:10.3390/ijms22031128
- Brink, O. (2021). The Choice between Allograft or Demineralized Bone Matrix Is Not Unambiguous in Trauma Surgery. *Injury* 52 (Suppl. 2), S23–s28. doi:10.1016/j.injury.2020.11.013
- Chansaenroj, A., Yodmuang, S., and Ferreira, J. N. (2021). Trends in Salivary Gland Tissue Engineering: From Stem Cells to Secretome and Organoid Bioprinting. *Tissue Eng. B: Rev.* 27, 155–165. doi:10.1089/ten.teb.2020.0149
- Chen, B., Sun, J., Fan, F., Zhang, X., Qin, Z., Wang, P., et al. (2018). Ferumoxylol of Ultrahigh Magnetization Produced by Hydrocooling and Magnetically Internal Heating Co-precipitation. *Nanoscale* 10, 7369–7376. doi:10.1039/c8nr00736e
- Chen, L., Deng, C., Li, J., Yao, Q., Chang, J., Wang, L., et al. (2019). 3D Printing of a Lithium-Calcium-Silicate crystal Bioscaffold with Dual Bioactivities for Osteochondral Interface Reconstruction. *Biomaterials* 196, 138–150. doi:10.1016/j.biomaterials.2018.04.005
- De France, K., Zeng, Z., Wu, T., and Nyström, G. (2021). Functional Materials from Nanocellulose: Utilizing Structure-Property Relationships in Bottom-Up Fabrication. *Adv. Mater.* 33, e2000657. doi:10.1002/adma.202000657
- Du, F., Wang, Q., Ouyang, L., Wu, H., Yang, Z., Fu, X., et al. (2021). Comparison of Concentrated Fresh Mononuclear Cells and Cultured Mesenchymal Stem Cells from Bone Marrow for Bone Regeneration. *Stem Cell Transl Med* 10, 598–609. doi:10.1002/sctm.20-0234
- Eberle, I., Moslem, M., Henschler, R., and Cantz, T. (2013). Engineered MSCs from Patient-specific iPS Cells. *Adv. Biochem. Eng. Biotechnol.* 130, 1–17. doi:10.1007/10\_2012\_156
- Geng, X., Mo, X., Fan, L., Yin, A., and Fang, J. (2012). Hierarchically Designed Injectable Hydrogel from Oxidized Dextran, Amino Gelatin and 4-arm Poly(ethylene Glycol)-Acrylate for Tissue Engineering Application. *J. Mater. Chem.* 22, 25130–25139. doi:10.1039/c2jm34737g
- Gu, J., Guo, M., Huang, C., Wang, X., Zhu, Y., Wang, L., et al. (2021). Titanium Dioxide Nanoparticle Affects Motor Behavior, Neurodevelopment and Axonal Growth in Zebrafish (*Danio rerio*) Larvae. *Sci. Total Environ.* 754, 142315. doi:10.1016/j.scitotenv.2020.142315
- (61821002). The National Natural Science Foundation of China (81802135), the International Cooperation and Exchange of National Natural Science Foundation (NSFC 81420108021), Key Program of NSFC (81730067), Science and Technology Development Fund of Nanjing Medical University (NMUB2020103).
- Guo, X., Chu, X., Li, W., Pan, Q., and You, H. (2013). Chondrogenic Effect of Precartilaginous Stem Cells Following NLS-TAT Cell Penetrating Peptide-Assisted Transfection of Eukaryotic hTGFβ3. *J. Cel. Biochem.* 114, 2588–2594. doi:10.1002/jcb.24606
- Henstock, J. R., Rotherham, M., Rashidi, H., Shakesheff, K. M., and El Haj, A. J. (2014). Remotely Activated Mechanotransduction via Magnetic Nanoparticles Promotes Mineralization Synergistically with Bone Morphogenetic Protein 2: Applications for Injectable Cell Therapy. *Stem Cell Transl Med* 3, 1363–1374. doi:10.5966/sctm.2014-0017
- Hernández-González, A. C., Téllez-Jurado, L., and Rodríguez-Lorenzo, L. M. (2020). Alginate Hydrogels for Bone Tissue Engineering, from Injectables to Bioprinting: A Review. *Carbohydr. Polym.* 229, 115514. doi:10.1016/j.carbpol.2019.115514
- Hu, S., Zhou, Y., Zhao, Y., Xu, Y., Zhang, F., Gu, N., et al. (2018). Enhanced Bone Regeneration and Visual Monitoring via Superparamagnetic Iron Oxide Nanoparticle Scaffold in Rats. *J. Tissue Eng. Regen. Med.* 12, e2085–e2098. doi:10.1002/term.2641
- Hu, Y., Yan, B., Chen, Z. S., Wang, L., and Tang, W. (2022). Recent Technologies for the Extraction and Separation of Polyphenols in Different Plants: A Review. *J. Renew. Mater.* 10, 1471–1490. doi:10.32604/jrm.2022.018811
- Huang, B., Tan, Z., Bohinc, K., and Zhang, S. (2018). Interaction between Nanoparticles and Charged Phospholipid Membranes. *Phys. Chem. Chem. Phys.* 20, 29249–29263. doi:10.1039/c8cp04740e
- Huang, C., Dong, H., Zhang, Z., Bian, H., and Yong, Q. (2020). Procuring the Nano-Scale Lignin in Prehydrolyzate as Ingredient to Prepare Cellulose Nanofibril Composite Film with Multiple Functions. *Cellulose* 27, 9355–9370. doi:10.1007/s10570-020-03427-9
- Huang, C., Dong, J., Zhang, Y., Chai, S., Wang, X., Kang, S., et al. (2021). Gold Nanoparticles-Loaded Polyvinylpyrrolidone/Ethylcellulose Coaxial Electrospun Nanofibers with Enhanced Osteogenic Capability for Bone Tissue Regeneration. *Mater. Des.* 212, 110240. doi:10.1016/j.matdes.2021.110240
- Huang, C., Tang, S., Zhang, W., Tao, Y., Lai, C., Li, X., et al. (2018). Unveiling the Structural Properties of Lignin-Carbohydrate Complexes in Bamboo Residues and its Functionality as Antioxidants and Immunostimulants. *ACS Sust. Chem. Eng.* 6, 12522–12531. doi:10.1021/acssuschemeng.8b03262
- Kim, M. J., Park, J. S., Kim, S., Moon, S.-H., Yang, H. N., Park, K.-H., et al. (2011). Encapsulation of Bone Morphogenic Protein-2 with Cbfa1-Overexpressing Osteogenic Cells Derived from Human Embryonic Stem Cells in Hydrogel Accelerates Bone Tissue Regeneration. *Stem Cell Dev.* 20, 1349–1358. doi:10.1089/scd.2010.0311
- Komori, T. (2018). Runx2, an Inducer of Osteoblast and Chondrocyte Differentiation. *Histochem. Cel Biol* 149, 313–323. doi:10.1007/s00418-018-1640-6
- Li, C., Guo, C., Fitzpatrick, V., Ibrahim, A., Zwierstra, M. J., Hanna, P., et al. (2020). Design of Biodegradable, Implantable Devices towards Clinical Translation. *Nat. Rev. Mater.* 5, 61–81. doi:10.1038/s41578-019-0150-z
- Liu, H., Du, H., Zheng, T., Liu, K., Ji, X., Xu, T., et al. (2021). Cellulose Based Composite Foams and Aerogels for Advanced Energy Storage Devices. *Chem. Eng. J.* 426, 130817. doi:10.1016/j.cej.2021.130817

## SUPPLEMENTARY MATERIAL

The Supplementary Material for this article can be found online at: <https://www.frontiersin.org/articles/10.3389/fbioe.2022.872149/full#supplementary-material>



- Luo, W., Fan, J., and Ye, C. (2012). Proliferation and Chondrogenic Differentiation of Precartilaginous Stem Cells in Self-Assembling Peptide Nanofiber Scaffolds. *Zhongguo Xiu Fu Chong Jian Wai Ke Za Zhi* 26, 1505–1511.
- Ma, C., Liu, Q., Peng, Q., Yang, G., Jiang, M., Zong, L., et al. (2021). Biomimetic Hybridization of Janus-like Graphene Oxide into Hierarchical Porous Hydrogels for Improved Mechanical Properties and Efficient Solar Desalination Devices. *ACS Nano* 15, 19877–19887. doi:10.1021/acsnano.1c07391
- Mende, W., Götzl, R., Kubo, Y., Pufe, T., Ruhl, T., and Beier, J. P. (2021). The Role of Adipose Stem Cells in Bone Regeneration and Bone Tissue Engineering. *Cells* 10, 975. doi:10.3390/cells10050975
- Mohamed-Ahmed, S., Fristad, I., Lie, S. A., Suliman, S., Mustafa, K., Vindenes, H., et al. (2018). Adipose-derived and Bone Marrow Mesenchymal Stem Cells: a Donor-Matched Comparison. *Stem Cell Res Ther* 9, 168. doi:10.1186/s13287-018-0914-1
- Pan, Q., Li, W., Yuan, X., Rakhmanov, Y., Wang, P., Lu, R., et al. (2016). Chondrogenic Effect of Cell-Based Scaffold of Self-Assembling Peptides/PLGA-PLL Loading the hTGFβ3 Plasmid DNA. *J. Mater. Sci. Mater. Med.* 27, 19. doi:10.1007/s10856-015-5631-z
- Pei, W., Chen, Z. S., Chan, H. Y. E., Zheng, L., Liang, C., and Huang, C. (2020). Isolation and Identification of a Novel Anti-protein Aggregation Activity of Lignin-Carbohydrate Complex from *Chionanthus Retusus* Leaves. *Front. Bioeng. Biotechnol.* 8, 573991. doi:10.3389/fbioe.2020.573991
- Robinson, D., Hasharoni, A., Cohen, N., Yayon, A., Moskowitz, R. M., and Nevo, Z. (1999). Fibroblast Growth Factor Receptor-3 as a Marker for Precartilaginous Stem Cells. *Clin. orthopaedics Relat. Res.* 367, S163–S175. doi:10.1097/00003086-199910001-00018
- Shang, F., Yu, Y., Liu, S., Ming, L., Zhang, Y., Zhou, Z., et al. (2021). Advancing Application of Mesenchymal Stem Cell-Based Bone Tissue Regeneration. *Bioactive Mater.* 6, 666–683. doi:10.1016/j.bioactmat.2020.08.014
- Soto, P. A., Vence, M., Piñero, G. M., Coral, D. F., Usach, V., Muraca, D., et al. (2021). Sciatic Nerve Regeneration after Traumatic Injury Using Magnetic Targeted Adipose-Derived Mesenchymal Stem Cells. *Acta Biomater.* 130, 234–247. doi:10.1016/j.actbio.2021.05.050
- Stahl, A., and Yang, Y. P. (2021). Regenerative Approaches for the Treatment of Large Bone Defects. *Tissue Eng. Part B: Rev.* 27, 539–547. doi:10.1089/ten.teb.2020.0281
- Sui, B.-D., Hu, C.-H., Liu, A.-Q., Zheng, C.-X., Xuan, K., and Jin, Y. (2019). Stem Cell-Based Bone Regeneration in Diseased Microenvironments: Challenges and Solutions. *Biomaterials* 196, 18–30. doi:10.1016/j.biomaterials.2017.10.046
- Sun, C., Zhang, A. D., Chen, H. H., Bian, J., and Liu, Z. J. (2021). Magnet-targeted Delivery of Bone Marrow-Derived Mesenchymal Stem Cells Improves Therapeutic Efficacy Following Hypoxic-Ischemic Brain Injury. *Neural Regen. Res.* 16, 2324–2329. doi:10.4103/1673-5374.310942
- Wang, P., Ma, S., Ning, G., Chen, W., Wang, B., Ye, D., et al. (2020). Entry-Prohibited Effect of kHz Pulsed Magnetic Field upon Interaction between SPIO Nanoparticles and Mesenchymal Stem Cells. *IEEE Trans. Biomed. Eng.* 67, 1152–1158. doi:10.1109/tbme.2019.2931774
- Wang, Q., Chen, B., Cao, M., Sun, J., Wu, H., Zhao, P., et al. (2016). Response of MAPK Pathway to Iron Oxide Nanoparticles *In Vitro* Treatment Promotes Osteogenic Differentiation of hBMSCs. *Biomaterials* 86, 11–20. doi:10.1016/j.biomaterials.2016.02.004
- Wang, Q., Chen, B., Ma, F., Lin, S., Cao, M., Li, Y., et al. (2017). Magnetic Iron Oxide Nanoparticles Accelerate Osteogenic Differentiation of Mesenchymal Stem Cells via Modulation of Long Noncoding RNA INZEB2. *Nano Res.* 10, 626–642. doi:10.1007/s12274-016-1322-4
- Wang, R., Zheng, L., Xu, Q., Xu, L., Wang, D., Li, J., et al. (2021). Unveiling the Structural Properties of Water-Soluble Lignin from Gramineous Biomass by Autohydrolysis and Its Functionality as a Bioactivator (Anti-inflammatory and Antioxidative). *Int. J. Biol. Macromolecules* 191, 1087–1095. doi:10.1016/j.ijbiomac.2021.09.124
- Wichterle, H., Lieberam, I., Porter, J. A., and Jessell, T. M. (2002). Directed Differentiation of Embryonic Stem Cells into Motor Neurons. *Cell* 110, 385–397. doi:10.1016/s0092-8674(02)00835-8
- Xu, T., Du, H., Liu, H., Liu, W., Zhang, X., Si, C., et al. (2021). Advanced Nanocellulose-Based Composites for Flexible Functional Energy Storage Devices. *Adv. Mater.* 33, 2101368. doi:10.1002/adma.202101368
- Yang, G., An, X., and Yang, S. (2021). The Effect of Ball Milling Time on the Isolation of Lignin in the Cell Wall of Different Biomass. *Front. Bioeng. Biotechnol.* 9, 807625. doi:10.3389/fbioe.2021.807625
- You, H., Chen, A., Sun, K., and Liu, T. (2011). Chondrogenesis of Precartilaginous Stem Cells in KLD-12 Self-Assembling Peptide Nanofiber Scaffold Loading TGF-β3 Gene. *J. Wuhan Univ. Technol.-Mat. Sci. Edit.* 26, 634–640. doi:10.1007/s11595-011-0282-5
- Yu, P., Zheng, L., Wang, P., Chai, S., Zhang, Y., Shi, T., et al. (2020). Development of a Novel Polysaccharide-Based Iron Oxide Nanoparticle to Prevent Iron Accumulation-Related Osteoporosis by Scavenging Reactive Oxygen Species. *Int. J. Biol. Macromolecules* 165, 1634–1645. doi:10.1016/j.ijbiomac.2020.10.016
- Yue, K., Trujillo-de Santiago, G., Alvarez, M. M., Tamayol, A., Annabi, N., and Khademhosseini, A. (2015). Synthesis, Properties, and Biomedical Applications of Gelatin Methacryloyl (GelMA) Hydrogels. *Biomaterials* 73, 254–271. doi:10.1016/j.biomaterials.2015.08.045
- Zhang, F. Y., Zhen, Y. F., Guo, Z. X., Dai, J., Zhu, L. Q., Cao, X., et al. (2020). MiR-132/212 Promotes the Growth of Precartilaginous Stem Cells (PCSCs) by Regulating Ihh/PTHrP Signaling Pathway. *Biosci. Rep.* 40, BSR20191654. doi:10.1042/BSR20191654
- Zhang, Y., Kong, N., Zhang, Y., Yang, W., and Yan, F. (2017). Size-dependent Effects of Gold Nanoparticles on Osteogenic Differentiation of Human Periodontal Ligament Progenitor Cells. *Theranostics* 7, 1214–1224. doi:10.7150/thno.17252
- Zhang, Y., Li, Y., Liao, W., Peng, W., Qin, J., Chen, D., et al. (2021a). Citrate-Stabilized Gold Nanorods-Directed Osteogenic Differentiation of Multiple Cells. *Ijn* 16, 2789–2801. doi:10.2147/ijn.s299515
- Zhang, Y., Wang, P., Mao, H., Zhang, Y., Zheng, L., Yu, P., et al. (2021b). PEGylated Gold Nanoparticles Promote Osteogenic Differentiation in *In Vitro* and *In Vivo* Systems. *Mater. Des.* 197, 109231. doi:10.1016/j.matdes.2020.109231
- Zheng, J., Zhao, H., Dong, E., Kang, J., Liu, C., Sun, C., et al. (2021). Additively-manufactured PEEK/HA Porous Scaffolds with Highly-Controllable Mechanical Properties and Excellent Biocompatibility. *Mater. Sci. Eng. C* 128, 112333. doi:10.1016/j.msec.2021.112333
- Zheng, L., Zhuang, Z., Li, Y., Shi, T., Fu, K., Yan, W., et al. (2021). Bone Targeting Antioxidative Nano-Iron Oxide for Treating Postmenopausal Osteoporosis. *Bioactive Mater.*

**Conflict of Interest:** The authors declare that the research was conducted in the absence of any commercial or financial relationships that could be construed as a potential conflict of interest.

**Publisher's Note:** All claims expressed in this article are solely those of the authors and do not necessarily represent those of their affiliated organizations, or those of the publisher, the editors, and the reviewers. Any product that may be evaluated in this article, or claim that may be made by its manufacturer, is not guaranteed or endorsed by the publisher.

Copyright © 2022 Liao, Lu, Wang, Yan, Li, Zhang, Wang, Jiang and Gu. This is an open-access article distributed under the terms of the Creative Commons Attribution License (CC BY). The use, distribution or reproduction in other forums is permitted, provided the original author(s) and the copyright owner(s) are credited and that the original publication in this journal is cited, in accordance with accepted academic practice. No use, distribution or reproduction is permitted which does not comply with these terms.



# Three-Dimensional Cartilage Regeneration Using Engineered Cartilage Gel With a 3D-Printed Polycaprolactone Framework

## OPEN ACCESS

### Edited by:

Lan Li,  
Nanjing Drum Tower Hospital, China

### Reviewed by:

Bingyang Dai,  
The Chinese University of Hong Kong,  
China

Yongcong Fang,  
Tsinghua University, China

### \*Correspondence:

Runjie Shi  
runjieshi@hotmail.com  
Guangdong Zhou  
guangdongzhou@126.com  
Shengli Li  
shengli@163.com

<sup>†</sup>These authors have contributed  
equally to this work and share first  
authorship

### Specialty section:

This article was submitted to  
Biomaterials,  
a section of the journal  
Frontiers in Bioengineering and  
Biotechnology

**Received:** 08 February 2022

**Accepted:** 18 April 2022

**Published:** 24 May 2022

### Citation:

Wu G, Lu L, Ci Z, Wang Y, Shi R,  
Zhou G and Li S (2022) Three-  
Dimensional Cartilage Regeneration  
Using Engineered Cartilage Gel With a  
3D-Printed  
Polycaprolactone Framework.  
Front. Bioeng. Biotechnol. 10:871508.  
doi: 10.3389/fbioe.2022.871508

Gaoyang Wu<sup>1†</sup>, Lixing Lu<sup>2†</sup>, Zheng Ci<sup>3,4†</sup>, Yahui Wang<sup>4</sup>, Runjie Shi<sup>2,5\*</sup>, Guangdong Zhou<sup>1,3,4\*</sup>  
and Shengli Li<sup>1\*</sup>

<sup>1</sup>Department of Plastic and Reconstructive Surgery, Shanghai Ninth People's Hospital, Shanghai Jiao Tong University School of Medicine, Shanghai, China, <sup>2</sup>Department of Otorhinolaryngology Head and Neck Surgery, Shanghai Ninth People's Hospital, Shanghai Jiao Tong University School of Medicine, Shanghai, China, <sup>3</sup>National Tissue Engineering Center of China, Shanghai, China, <sup>4</sup>Research Institute of Plastic Surgery, Weifang Medical University, Weifang, China, <sup>5</sup>Shanghai Key Laboratory of Translational Medicine on Ear and Nose Diseases, Ear Institute Shanghai Jiao Tong University School of Medicine, Shanghai, China

The feasibility of the three-dimensional (3D) cartilage regeneration technology based on the “steel (framework)-reinforced concrete (engineered cartilage gel, ECG)” concept has been verified in large animals using a decalcified bone matrix (DBM) as the framework. However, the instability of the source, large sample variation, and lack of control over the 3D shape of DBM have greatly hindered clinical translation of this technology. To optimize cartilage regeneration using the ECG–framework model, the current study explores the feasibility of replacing the DBM framework with a 3D-printed polycaprolactone (PCL) framework. The PCL framework showed good biocompatibility with ECG and achieved a high ECG loading efficiency, similar to that of the DBM framework. Furthermore, PCL-ECG constructs caused a milder inflammatory response *in vivo* than that induced by DBM-ECG constructs, which was further supported by an *in vitro* macrophage activation experiment. Notably, the PCL-ECG constructs successfully regenerated mature cartilage and essentially maintained their original shape throughout 8 weeks of subcutaneous implantation. Quantitative analysis revealed that the GAG and total collagen contents of the regenerated cartilage in the PCL-ECG group were significantly higher than those in the DBM-ECG group. The results indicated that the 3D-printed PCL framework—a clinically approved biomaterial with multiple advantages including customizable shape design, mechanical strength control, and standardized production—can serve as an excellent framework for supporting the 3D cartilage regeneration of ECG. This provides a feasible novel strategy for the clinical translation of ECG-based 3D cartilage regeneration.

**Keywords:** 3D cartilage regeneration, engineered cartilage gel, Polycaprolactone, inflammatory response, tissue engineering

# 1 INTRODUCTION

The repair of craniofacial cartilage defect has always been a great clinical challenge (Raub et al., 2013; Xue et al., 2018), and recent development of tissue engineering technology has provided a promising strategy for repair and reconstruction of various cartilage defects (Makris et al., 2015; Kwon et al., 2019; Wei et al., 2021). By obtaining a small piece of autologous cartilage for chondrocyte isolation, followed by *in vitro* amplification, large-volume autologous cartilage regeneration can be achieved (Armiento et al., 2018; Wang et al., 2020; Liao et al., 2021). However, up to now, how to construct three-dimensional (3D) cartilage with specific shape and mechanical strength for the repair of craniofacial cartilage defects remains a huge challenge (Xia et al., 2018; Chae et al., 2021).

Various animal and clinical experiments have demonstrated that scaffold-free cartilage sheet technology can stably regenerate high-quality cartilage tissue *in vivo*. The injectable engineered cartilage gel (ECG) technology that derived from these examples has shown excellent performance for cartilage regeneration (unpublished data). To expand the scope of ECG technology application to the repair of craniofacial cartilage defects requiring a specific shape and strength (such as ear and nose reconstruction), our previous study proposed a novel 3D cartilage regeneration model based on the design concept of steel (framework)-reinforced concrete (ECG) and successfully regenerated homogeneous mature 3D cartilage in large animals using a decalcified bone matrix (DBM) as the framework (Ci et al., 2021). However, the main source of DBM is cadaveric donation, and the large diversity of donors, as well as of body sites from each donor, inevitably results in wide variation among DBM samples (Zhang et al., 2019). Moreover, the control of DBM morphology relies on manual cutting (Haghwerdi et al., 2021), which makes it difficult for it to be processed into particular shapes for the reconstruction of cartilage defects with complex 3D shapes (such as ear and nose) and thus greatly limits the clinical translation of regenerated cartilage based on DBM frameworks.

To further optimize the steel-reinforced concrete cartilage regeneration model, this study investigates the replacement of DBM with a 3D-printed polycaprolactone (PCL) framework to support 3D cartilage regeneration of the ECG. PCL is an FDA-approved biodegradable polyester material (Zou et al., 2015) with excellent biocompatibility (Arif et al., 2019; Yang et al., 2020; Lim et al., 2021) that can be prepared with a variety of 3D structures using customized design and 3D-printing technology (Li et al., 2020; Saracino et al., 2021). However, PCL has not yet been shown to be a suitable framework for the steel-reinforced concrete cartilage regeneration model. Therefore, to determine whether it is feasible to regenerate mature 3D cartilage using PCL-ECG constructs, the following key questions must be answered: first, does the PCL framework show good integration with ECG to achieve appropriate loading efficiency? Second, does the PCL framework trigger an inflammatory response that could interfere with cartilage regeneration? Third, do the PCL-ECG constructs successfully regenerate mature cartilage and retain their original shape in an immunocompetent large animal?

To answer the aforementioned questions, the current study explores the feasibility of 3D cartilage regeneration by combining a 3D-printed PCL framework with ECG, based on the previously established cartilage regeneration model. The characterization, biocompatibility, and inflammatory response of the PCL framework as well as the cartilage regeneration performance of the PCL-ECG constructs were systematically evaluated *in vitro* and in autologous large animals. The current study provides a feasible novel strategy for the clinical translation of ECG-based 3D cartilage regeneration for the repair of craniofacial cartilage defects.

# 2 MATERIALS AND METHODS

## 2.1 Framework Preparation

DBM frameworks (Daqing Bio Co. Ltd., Chongqing, China) were cut into 7-mm-long, 5-mm-wide, and 2.5-mm-thick cuboid constructs. The PCL framework was fabricated using a 3D-printer. The properties of the PCL framework were designed using CAD and Mimics 17.0 software, and the frameworks were printed using a 3D layer-by-layer fused deposition modeling (FDM) printer (FoChif Tech HTS, China). In brief, PCL pellets (Mw 80,000, Sigma, United States) were melted (at 120°C) in a printing chamber and then printed with a lay down pattern of 0°/45°/90°/135° (top layer) or 0°/90° (bottom layer) along the z-axis. Thus, a double-layered PCL framework model was produced and then subsequently cut into cuboids with length, width, and height of 7, 5, and 2.5 mm, respectively. All frameworks were sterilized using ethylene oxide before use. The mechanical analysis of PCL and DBM framework was carried out using a mechanical testing machine (Instron-5542, Canton, MA, United States). All samples ( $n = 5$  per group) were processed into a cuboid shape, and a constant compressive strain rate of 0.5 mm/min was applied until 80% of the maximum deformation. The stress and strain curves were obtained from the first 40%. The Young's modulus was calculated from the stress and strain curves. The endotoxin content in the leach solutions of the frameworks were analyzed using a chromogenic endpoint Tachypleus amebocyte lysate (TAL) assay kit (Xiamen Houshiji, China), following the kit instructions as previously described (Wei et al., 2015).

## 2.2 Animals

A total of three 6-month-old goats (Shanghai Jiagan Biological Technology Co., Shanghai, China) were used in this study. All protocols of animal study were approved by the Animal Care and Experiment Committee of Shanghai Jiao Tong University School of Medicine.

## 2.3 Cell Culture

### 2.3.1 Isolation and Culture of Goat Chondrocytes

After anesthetizing with 5% sodium pentobarbital (0.5 ml/kg), a slice of auricular cartilage (5 cm × 5 cm) was harvested from one ear of a goat and then dissected into 1-mm<sup>3</sup> pieces, which were washed in phosphate-buffered saline (PBS) containing 1% penicillin-streptomycin (Gibco, Grand Island, NY, United States). The pieces were then treated with 0.15%

**TABLE 1 |** Primers used in this study.

Gene	Primer
Mouse <i>TNF-α</i>	Forward: CCA CTC TGA CCC CTT TAC TC Reverse: GCC ATA ATC CCC TTT CTA AGT
Mouse <i>IL-6</i>	Forward: CGG AGA GGA GAC TTC ACA GAG Reverse: ATT TCC ACG ATT TCC CAG AG
Mouse <i>Cox-2</i>	Forward: TGG ATT CTA TGG TGA AAA CTG TA Reverse: TTG AAG TGG GTC AGG ATG TA
Mouse <i>β-actin</i>	Forward: CCT CTA TGC CAA CAC AGT Reverse: AGC CAC CAA TCC ACA CAG

collagenase II (Gibco) in Dulbecco's modified Eagle medium (DMEM; Gibco) for 12 h at 37°C. Then, the isolated cells were collected and cultured in Dulbecco's modified Eagle medium (Gibco BRL, Grand Island, New York, United States) containing 10% fetal bovine serum (Gibco BRL) and 1% antibiotic-antimycotic (Gibco BRL) T32U. Cells were passaged at >80% confluence. Chondrocytes in passage two or three were harvested to conduct the following experiments.

### 2.3.2 RAW 264.7 Cells

Cells were cultured in Dulbecco's modified Eagle medium (DMEM, Gibco BRL, Grand Island, NY, United States) containing 10% fetal bovine serum (Gibco BRL) and 1% antibiotic-antimycotic (Gibco BRL) and incubated in a humidified atmosphere of 95% air and 5% CO<sub>2</sub> at 37°C. Cells were passaged at >80% confluence. Samples for fluorescent staining were seeded on 14-mm microscope cover glasses in a 24-well plate. To determine the inflammatory response of the frameworks, upon reaching 60–80% confluence, each group of RAW 263.7 cells was cultured in leach solution (supernatant from frameworks soaked in DMEM containing 10% fetal bovine serum for 72 h) and then cultured for 24, 48, and 72 h. In the positive control groups, 10 μg/ml lipopolysaccharide (LPS) was added to the culture medium, and a standard DMEM medium was used for the negative control.

## 2.4 Preparation of Engineered Cartilage Gel-Framework Constructs

Cartilage sheets were prepared as previously reported (Li et al., 2017). Furthermore, two- or three-passage goat chondrocytes were harvested, suspended, and then seeded in six-well cell culture plates at a density of  $1.5 \times 10^7$  cells/well. The chondrocytes were then cultured in a chondrogenic medium, containing 100 ng/ml IGF-I (R&D Systems Inc. Minneapolis, MN, United States), 10 ng/ml TGF-β1 (R&D Systems Inc. Minneapolis, MN, United States), 40 ng/ml dexamethasone (Sigma-Aldrich, St. Louis, MO, United States), 1% insulin-transferrin-selenium-linoleic acid (ITS, ScienCell, CA, United States), and 1% antibiotic-antimycotic (Gibco BRL) in DMEM for 5 days. The cartilage sheets were then minced into a gelatinous mass and collected in a syringe before being seeded in their respective frameworks to form constructs. The constructs were incubated for 2 h and then transferred into a 6-well plate

containing the culture medium. After 3 days, the constructs were subcutaneously implanted in autologous goats. The cellular viability of the cartilage sheets and minced cartilage sheet (ECG) was evaluated using the Live/Dead Cell Viability Assay (Invitrogen, Carlsbad, CA, United States), following the manufacturer's instructions, and examined by confocal microscopy (Nikon, Japan).

## 2.5 Biocompatibility of the Frameworks

### 2.5.1 Scanning Electron Microscopy

The surface morphology and pore size distribution of the PCL and DBM frameworks were observed by SEM (Philips XL-30, Amsterdam, The Netherlands) at an accelerating voltage of 15 kV. The two types of ECG-framework constructs cultured for 24 and 72 h *in vitro* were washed with PBS and fixed overnight in 0.05% glutaraldehyde at 4°C. After dehydration in a graded ethanol series and critical point drying, the surface morphology and extracellular matrix (ECM) production of the constructs were observed by SEM.

### 2.5.2 Engineered Cartilage Gel-Loading Rate

The ECG loading rate was determined from the ratio of the initial DNA content of the constructs and that 24 h after combination with ECG. The DNA content of the samples ( $n = 5$  per group) was quantified using a Quant-iT PicoGreen dsDNA assay (Invitrogen, Carlsbad, CA, United States) as previously described (Chen et al., 2021).

### 2.5.3 Live/Dead Cell Viability Assay

After 24, 48, and 72 h of culture in DBM and PCL leach solutions, the cellular viability of the cartilage sheets was evaluated using the Live/Dead Cell Viability Assay (Invitrogen, Carlsbad, CA, United States), following the manufacturer's instructions, and examined by confocal microscopy (Nikon, Japan). Quantification of the ratio of dead cells to live cells was carried out using ImageJ and IHC Profiler Software ( $n = 5$  per group).

## 2.6 Subcutaneous Implantation in Goats

After *in vitro* culture for 3 days, both constructs (PCL-ECG and DBM-ECG,  $n = 15$  constructs per group in each goat) were subcutaneously implanted in autologous goats. As control groups, frameworks without ECG (DBM and PCL framework,  $n = 15$  frameworks per group in each goat) and ECG without a framework were also implanted and injected into the goats, respectively. During surgery, each goat was anesthetized and endotracheally intubated. The constructs and frameworks were implanted in subcutaneous pockets made in the abdominal area. ECG without framework was injected using a syringe. The animals were allowed to recover from anesthesia after closure of the incisions. Samples were harvested at 1, 4, and 8 weeks postimplantation for gross, histological, immunohistochemical, and quantitative evaluation.

## 2.7 Inflammatory Response Evaluations

After 1 and 4 weeks of implantation, samples from all groups ( $n = 5$  samples per group in each goat) were harvested for analysis of the inflammatory response. After gross observation, samples were



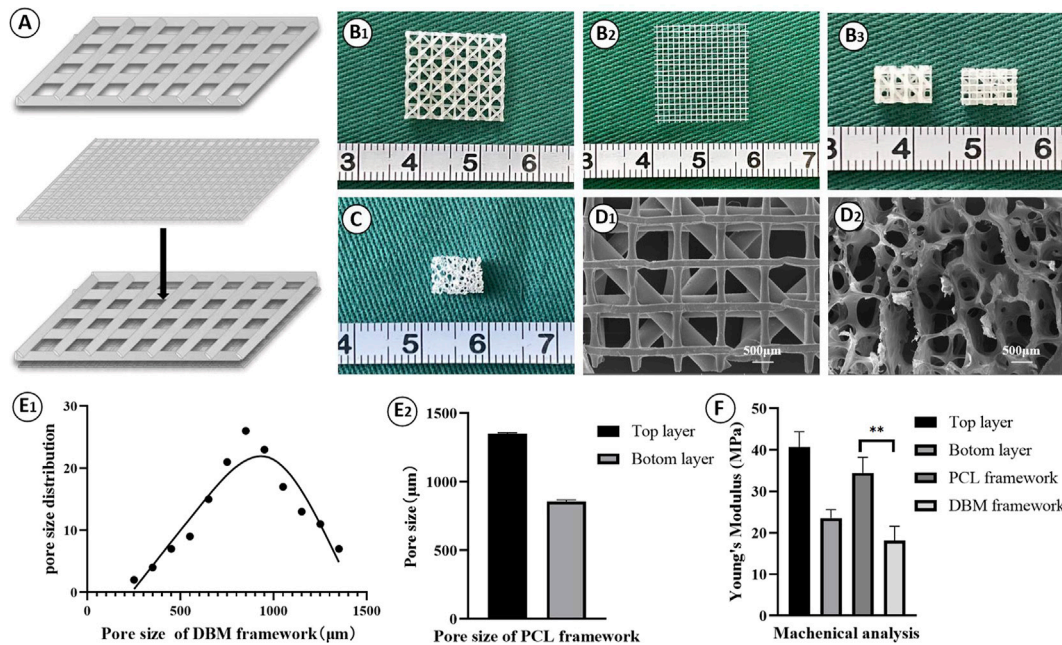


**FIGURE 1 |** Fabrication and characterization of PCL framework: **(A)** The design of the 3D-printed PCL framework; Gross view of the top layer **(B1)**, the bottom layer **(B2)**, and the front and the back views **(B3)** for the 3D-printed PCL frameworks; **(C)** Gross view of the DBM framework; SEM images of PCL framework **(D1)** and DBM framework **(D2)**; Pore size of DBM framework **(E1)** and PCL framework **(E2)**; **(F)** Young's modulus of the frameworks. Statistical significance: \*\* $p < 0.01$ .

fixed in 4% paraformaldehyde for 48 h, then embedded in paraffin, and sectioned into 5-mm-thick slices. Slices were stained with hematoxylin and eosin (HE). For immunohistochemical analysis, CD68 was detected using mouse anti-CD68 monoclonal antibody (ab955, 1:200, Abcam), followed by goat anti-mouse IgG H&L (HRP) (ab205719, 1:2000, Abcam). Apoptotic cells were detected by terminal deoxynucleotidyl transferase biotin-dUTP nick end labeling (TUNEL) using a TUNEL kit (Roche, Indianapolis, IN, United States), following the manufacturer's instructions. The quantification of CD68 and TUNEL position area (%) was performed using ImageJ and IHC Profiler software ( $n = 5$  per group).

## 2.8 Cell Morphology

For fluorescent staining, the cells were permeabilized with 0.1% Triton X-100 (Sigma-Aldrich) for 5 min at room temperature, washed with PBS, and then stained with DAPI and FITC-phalloidin. FITC and phalloidin (Sigma-Aldrich) were diluted in PBS in a 1:200 ratio and incubated on the samples away from light for 30 min. After incubation, the samples were washed with PBS three times. Cell nuclei were stained with DAPI for 8 min, after which the samples were washed with PBS three times. Imaging of RAW 264.7 cells was performed using a fluorescence confocal microscope (Nikon, Japan).

## 2.9 Enzyme Linked Immunosorbent Assay

Cell culture supernatant (1 ml) was collected after 24, 48, and 72 h of incubation and used for enzyme-linked immunosorbent assay

(ELISA). Mouse IL-6 ELISA Kit, Mouse TNF- $\alpha$  ELISA Kit, and Mouse Cox-2 ELISA Kit (all ELISA kits; Invitrogen, Thermo Fisher Scientific, Waltham, MA, United States) were used according to the manufacturer's instructions.

## 2.10 Quantitative Polymerase Chain Reaction

Gene expression of inflammatory cytokines was investigated using the real-time polymerase chain reaction (RT-PCR). The expression levels of *IL-6*, *TNF- $\alpha$* , and *Cox-2* genes were analyzed. Each group of RAW 264.7 cells was collected, and the total RNA was extracted using the TRIzol reagent (Invitrogen), after which the total RNA was reverse transcribed using Moloney murine leukemia virus reverse transcriptase (Invitrogen). qPCR was performed using a Fast Synergy Brands Green Master Kit and a Light Cycler 480 system (Roche), following the manufacturer's instructions. The forward and reverse primer sequences are listed in **Table 1**. The results were analyzed using the comparative threshold cycle method and normalized to the endogenous reference gene  *$\beta$ -actin*.

## 2.11 Histological and Immunohistochemical Evaluations of Regenerative Tissues

After 8 weeks of culturing *in vivo*, samples of the PCL-ECG, DBM-ECG, and ECG groups ( $n = 5$  samples per group in each goat) were carefully extracted from the goats. After gross observation and measurement, part of each sample (the rest of

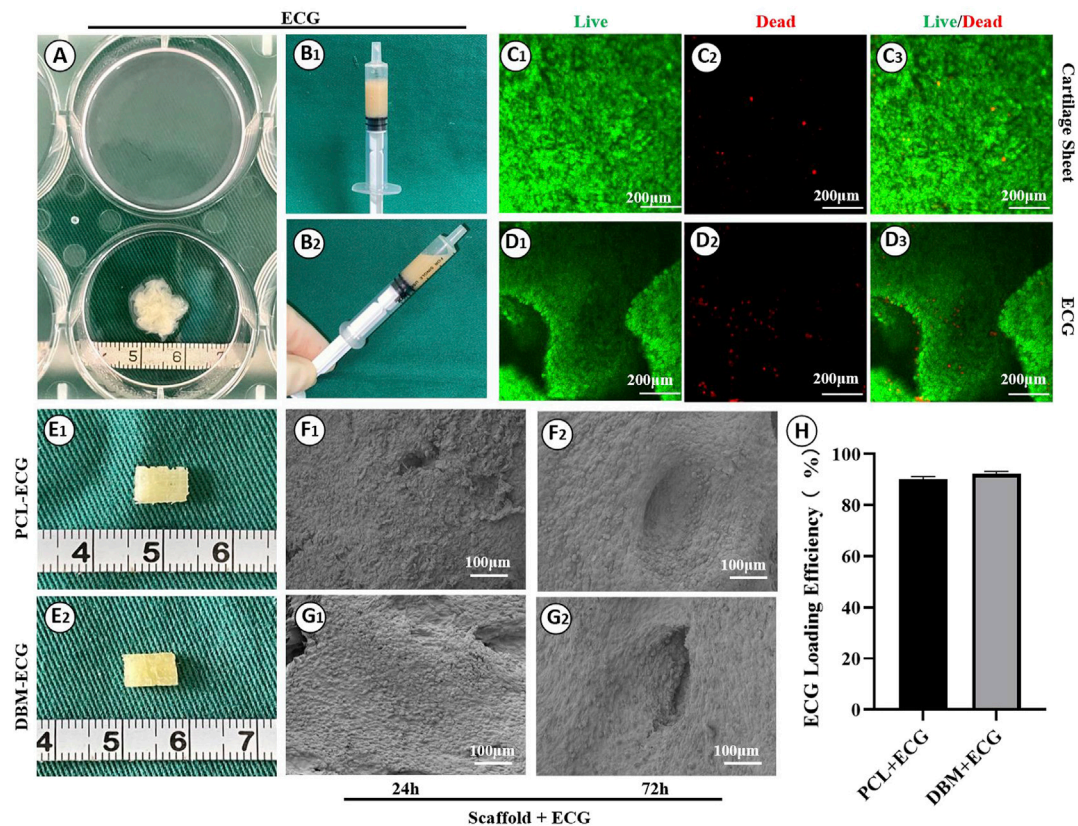


**FIGURE 2 |** Preparation of engineered cartilage gel and its biocompatibility with the frameworks: Gross images of cartilage sheet (A) and ECG (B1, B2); Live/dead staining of cartilage sheet (C1–C3) and ECG (D1–D3); Gross images of the PCL-ECG (E1) and DBM-ECG (E2) constructs; SEM images of PCL-ECG (F1, F2) and DBM-ECG (G1, G2) constructs after culture in vitro for 24 h and 72 h; (H) ECG loading efficiency. Statistical significance: ns, no statistical significance.

the sample was used for subsequent biochemical analysis) was fixed in 4% paraformaldehyde, embedded in paraffin, sectioned to give 5-mm thicknesses, and then mounted on glass slides for histological and immunohistochemical analyses. The slices were stained with H&E and safranin-O to evaluate the histological structure of the engineered cartilage (EC), and for the immunohistochemical analysis, expression of type II collagen (COL II) was evaluated to determine ECM deposition of the ECGs using rabbit anti-collagen II polyclonal antibody (ab34712, 1:100, Abcam) with goat anti-rabbit IgG H&L (HRP) (ab205718, 1:2000, Abcam) as a secondary antibody. Quantification of the regenerated cartilage area (%) was performed using ImageJ and IHC Profiler software ( $n = 5$  per group).

## 2.12 Quantitative Analysis

Quantitative analysis was performed as previously described (Jia et al., 2020). In brief, an electronic balance was used to measure the weight of all samples ( $n = 5$  per group). The volume of each sample was measured using the water displacement method ( $n = 5$  per group). The total glycosaminoglycan (GAG) content and the total collagen content of the samples ( $n = 5$  per group) was quantified using the alcian blue method and hydroxyproline assay, respectively.

## 2.13 Statistical Analysis

Statistical analyses were performed using SPSS 23 (IBM, United States). Student's t-test was performed to compare the mechanical properties and ECG loading efficiency of the frameworks. One-way ANOVA was performed to compare the results of the cytotoxicity evaluation of the frameworks and immunohistochemistry results. Two-way ANOVA was performed to test the interaction between two independent variables (time and material type for the quantitative analysis results, and time and leach solution type for the quantitative RT-PCR and ELISA results). Tukey's honestly significant difference (HSD) *post hoc* tests were performed after ANOVA. Data are presented as the mean  $\pm$  standard deviation (SD). The value of  $*p < 0.05$  was considered statistically significant.

## 3 RESULTS

### 3.1 Fabrication, Characterization, and Biocompatibility of the Frameworks

Fabrication and characterization of the PCL framework was the first step of PCL-ECG construct preparation. As shown in Figure 1, a double-layered PCL framework structure was 3D-

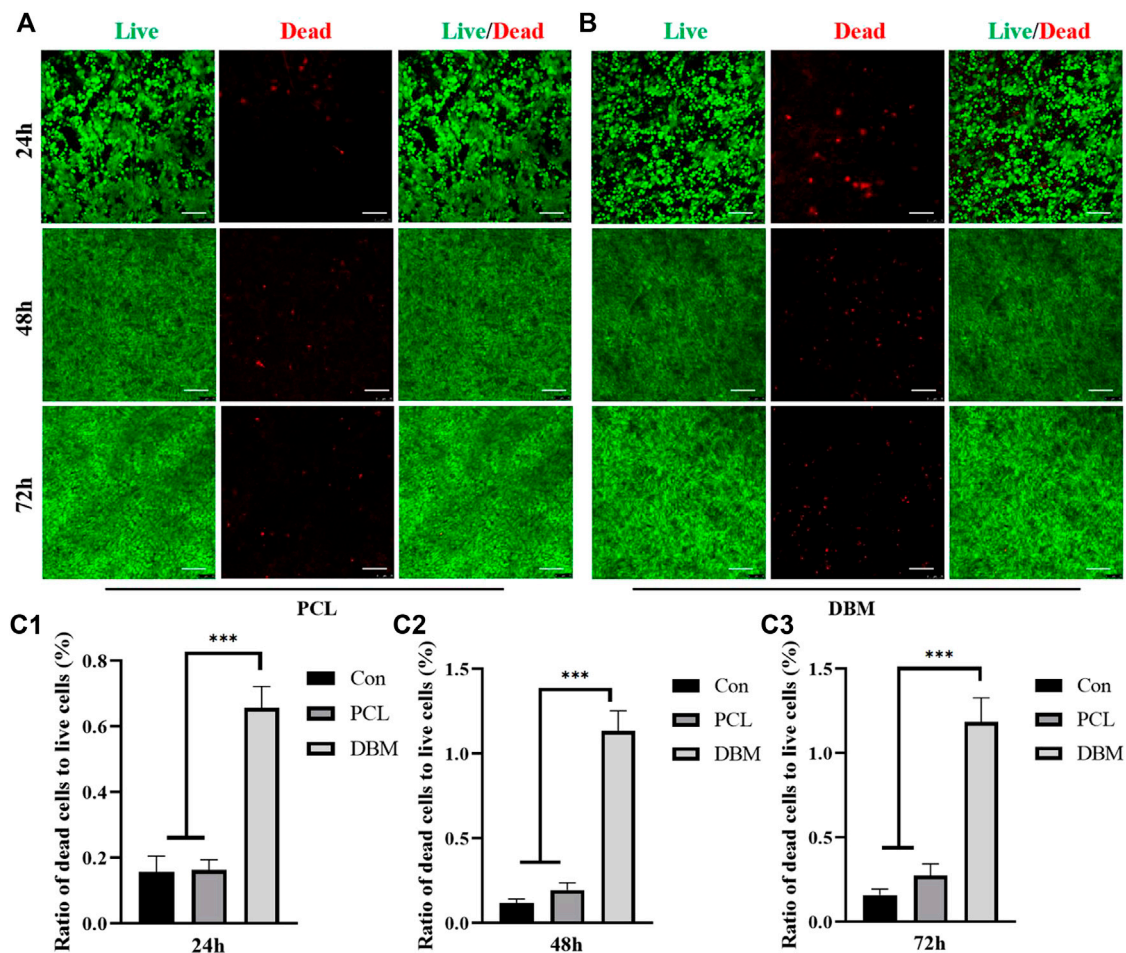


**FIGURE 3 |** Cytotoxicity evaluation of the frameworks to ECG. **(A)** Live/dead staining of ECG in PCL leach solution for 24, 48, and 72 h; **(B)** Live/dead staining of ECG in DBM leach solution for 24, 48, and 72 h; Semi-quantitative analysis for the ratio of dead cells to live cells at 24h **(C1)**, 48h **(C2)**, and 72h **(C3)**. Statistical significance: \*\*\* $p < 0.001$ . Scale bar: 100µm.

printed and assembled. The top layer with large pores was suitable for ECG loading, while the bottom layer with small pores was designed to prevent ECG loss (Figures 1A,B). Both SEM and pore size analysis revealed that the PCL framework had a uniform pore structure, while the DBM framework presented a clearly heterogeneous structure with varied pore sizes (Figures 1D,E), indicating the relative homogeneity and controllability of the PCL framework in terms of ECG distribution, mechanical properties, degradation rate, and shape maintenance. The mechanical analysis revealed that the mechanical strength of the PCL framework was significantly higher than that of the DBM framework (Figure 1F). The PCL framework had a mechanical strength close to that of native ear cartilage (Zhou et al., 2018), which may help it to maintain the original shape of the regenerated cartilage.

The biocompatibility was then evaluated by loading ECG into the frameworks. Similar to our previous reports, cartilage sheets

cultured *in vitro* for 5 days presented soft fragile membranes that could be easily collected, minced into gel form (Figures 2A,B) while maintaining good cellular viability (Figures 2C,D), and then loaded into the frameworks (Figure 2E). SEM showed that ECG adhered well to the frameworks and completely covered the frameworks after 3 days of *in vitro* culture owing to the abundant ECM production (Figures 2F,G). The quantification analysis revealed that the ECG loading efficiencies in the two frameworks were both higher than 90% with no statistical difference (Figure 2H), indicating good cytocompatibility for both frameworks. Cytotoxicity evaluation showed that cartilage sheets survived well in the leach solutions of both frameworks with visible cell proliferation over time (Figures 3A,B). Notably, few dead cells were observed in the group treated with PCL leach solution (no significant difference with the DMEM control group, Supplementary Figure S1), while some dead cells were found in the group treated with DBM leach solution (Figure 3C). This



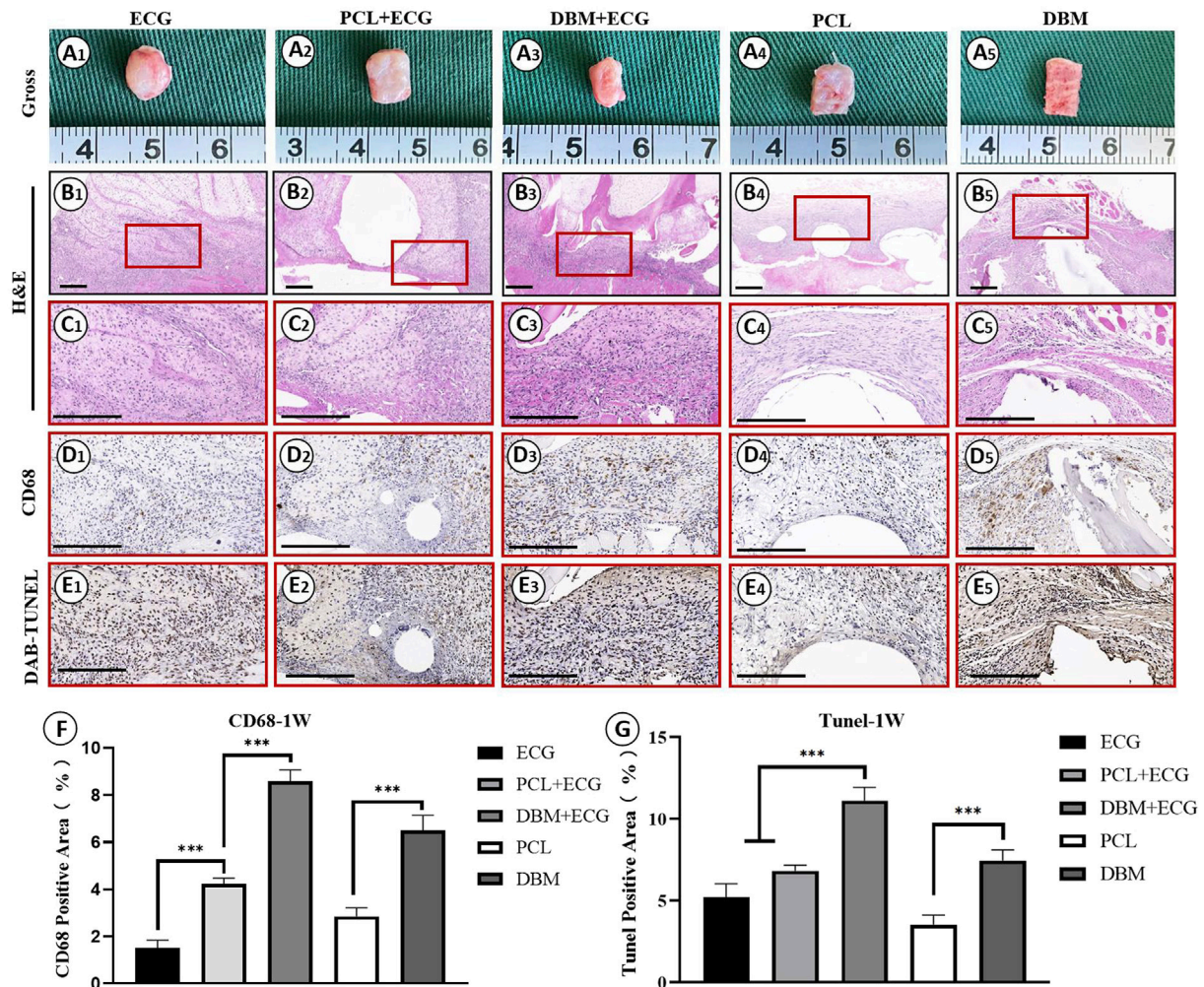


**FIGURE 4 |** Inflammatory response evaluations of ECG, frameworks, and framework-ECG constructions after 1 week of subcutaneous implantation: Gross observation (A1–A5); H&E staining with different magnification (B1–B5, C1–C5); CD68 immunohistochemical staining (D1–D5); DAB-TUNEL immunohistochemical staining (E1–E5); Semi-quantitative analysis of the CD68 (F) and DAB-TUNEL (G) positive area (%). Statistical significance: \* $p < 0.05$ , \*\* $p < 0.01$ , \*\*\* $p < 0.001$ . Scale bar: 200  $\mu$ m.

indicates the higher cytotoxicity of the DBM framework compared with the PCL framework, which might be related to higher endotoxin residue in the DBM framework (Supplementary Figure S2).

### 3.2 *In Vivo* Inflammatory Response Triggered by Polycaprolactone and Decalcified Bone Matrix Frameworks

*In vivo* inflammatory responses were evaluated to predict the feasibility of cartilage regeneration using the PCL-ECG constructs. The observations after 1 week show that all samples were easily extracted from the implantation sites without obvious adhesion to peripheral tissues (Figure 4A), suggesting relatively low inflammatory responses in all groups. H&E and CD68 immunohistochemical staining showed that the

inflammatory responses for both the PCL-ECG and DBM-ECG groups were much stronger than that for the ECG group, indicating that both the PCL and DBM frameworks showed some immunogenicity. This was further supported by the inflammatory responses triggered by the implantation of frameworks without ECG (Figures 4B–D). TUNEL immunohistochemical staining also confirmed that more apoptotic cells caused by inflammatory response were found for the groups containing frameworks than for the ECG group (Figure 4E). It was worth noting that the PCL framework triggered a milder inflammatory response with less cell apoptosis than the DBM framework (Figures 4D,E), which was further confirmed by a semiquantitative analysis (Figures 4F,G), indicating that the PCL framework had lower immunogenicity than the DBM framework. As anticipated, the intensity of the inflammatory responses at 4 weeks was lower than



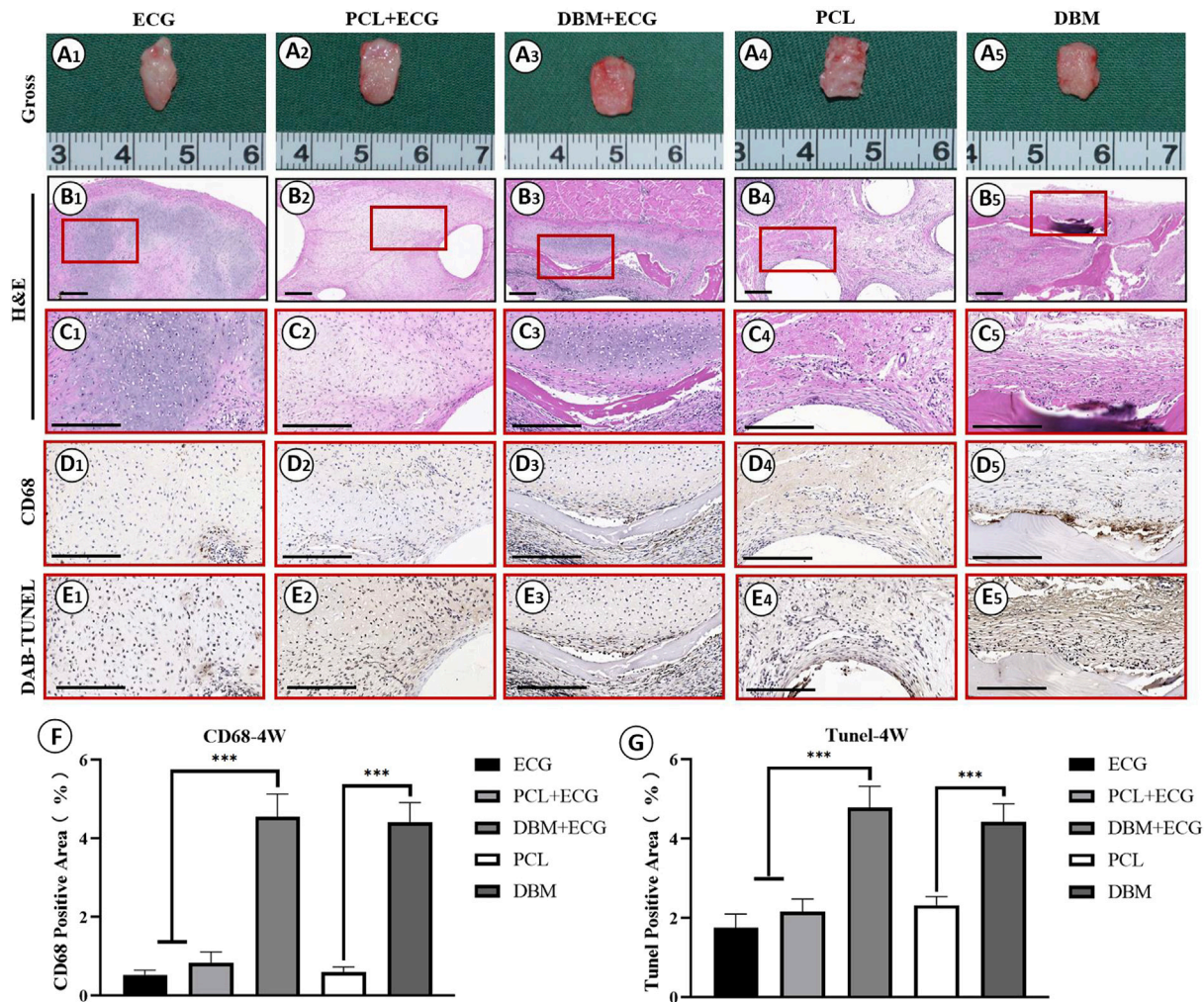


**FIGURE 5 |** Inflammatory response evaluations of ECG, frameworks, and framework-ECG constructions after 4 week of subcutaneous implantation: Gross observation (A1–A5); H&E staining with different magnification (B1–B5, C1–C5); CD68 immunohistochemical staining (D1–D5); DAB-TUNEL immunohistochemical staining (E1–E5); Semi-quantitative analysis of the CD68 (F) and DAB-TUNEL (G) positive area (%). Statistical significance:  $*p < 0.05$ ,  $**p < 0.01$ ,  $***p < 0.001$ . Scale bar: 200  $\mu\text{m}$ .

those for the samples after 1 week, with less cell apoptosis in all groups (Figures 5A–E). Semiquantitative analysis further revealed that both the ECG and PCL-ECG groups presented minimal inflammatory infiltration and cell apoptosis (with no significant difference), while the DBM framework still exhibited higher levels of inflammatory response and cell apoptosis (Figures 5F,G). This indicates that the PCL framework is more suitable for supporting cartilage regeneration of ECG than the DBM framework in terms of immunogenicity.

### 3.3 *In Vitro* Macrophage M1 Polarization Triggered by Polycaprolactone and Decalcified Bone Matrix Frameworks

An *in vitro* macrophage M1 polarization experiment was conducted to further evaluate the framework immunogenicity.

As shown in Figure 6, RAW 264.7 cells cultured in DMEM presented relatively uniform morphology with small round cortical actin rings (Figure 6A), while the cells treated with LPS exhibited typical M1 polarization morphology with large dendritic cortical actin rings (Figure 6B). Cells cultured in the leach solution of the PCL framework showed minor morphology changes essentially maintaining small round cortical actin rings (Figure 6C), while cells cultured in the leach solution of the DBM framework presented a discernible morphology change, exhibiting relatively large and irregular cortical actin rings (Figure 6D). The results of qPCR and ELISA were consistent with the cell morphology changes, further confirming that the expressions of M1 polarization related cytokines (IL-6, COX-2, and TNF- $\alpha$ ) in the PCL group were significantly lower than those for the DBM group in terms of both gene and protein levels (Figure 7). These results indicate that the leach solution of the

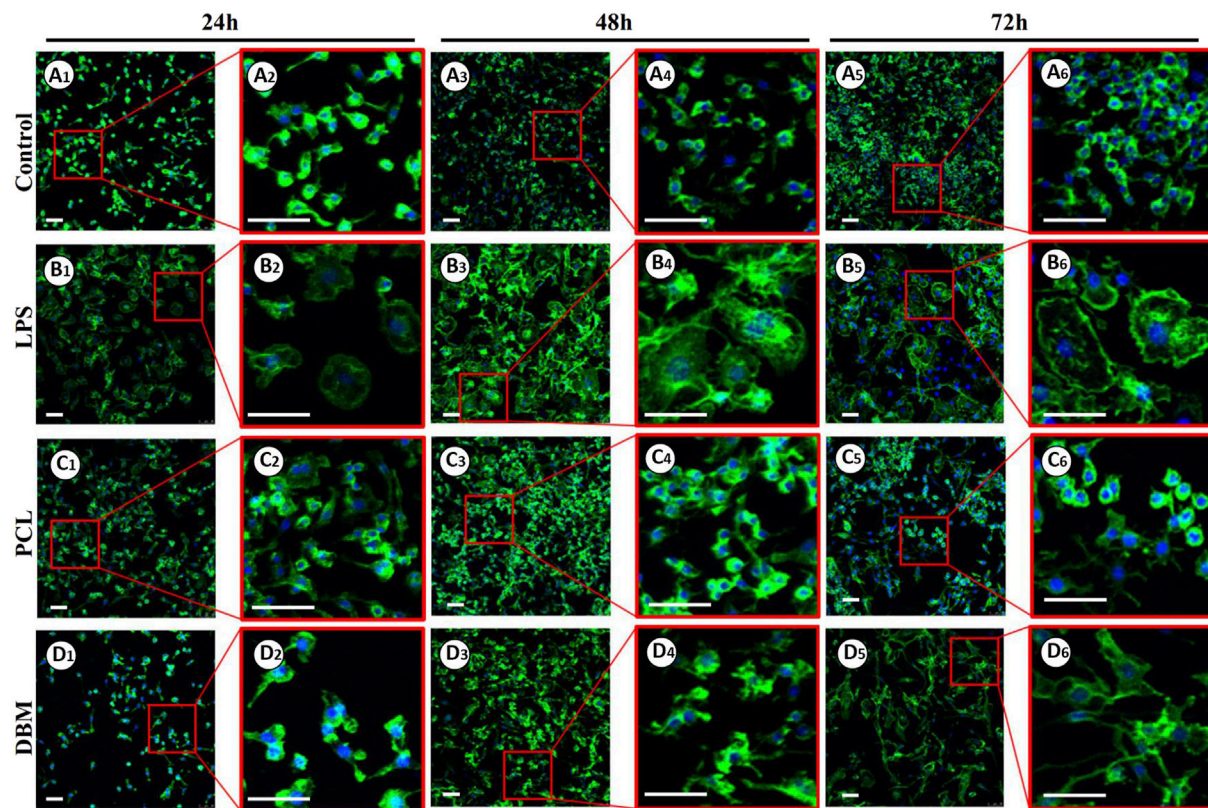


**FIGURE 6 |** Phalloidine immunofluorescence staining of RAW 264.7 cells treated by leach solutions of PCL and DBM frameworks: Negative control cultured in DMEM (A1–A6); Positive control activated by LPS (B1–B6); RAW 264.7 cells treated by PCL leach solution (C1–C6); RAW 264.7 cells treated by DBM leach solution (D1–D6). Scale bar: 100  $\mu$ m.

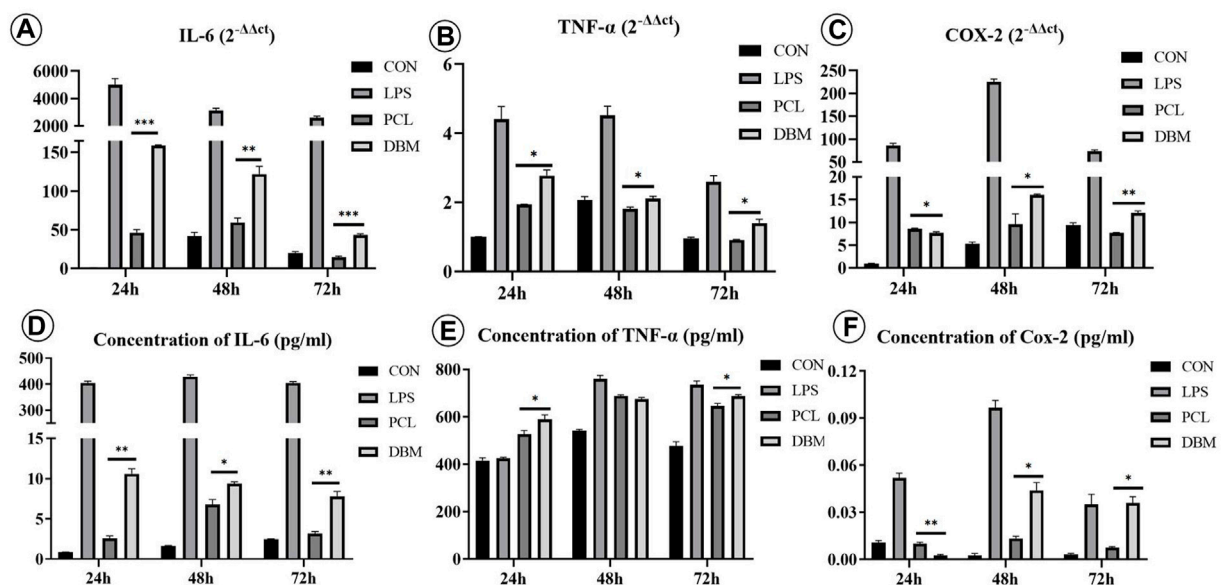


**FIGURE 7 |** Gene expression and cytokine secretion related to M1 polarization of RAW 264.7 cells treated by leach solutions of PCL and DBM frameworks: (A–C) qPCR analysis of M1 polarization-related genes IL-6 (A), TNF- $\alpha$  (B), and COX-2 (C); (D–F) ELISA quantification of M1 polarization-related cytokines IL-6 (D), TNF- $\alpha$  (E), and COX-2 (F). Statistical significance: \* $p < 0.05$ , \*\* $p < 0.01$ , \*\*\* $p < 0.001$ .



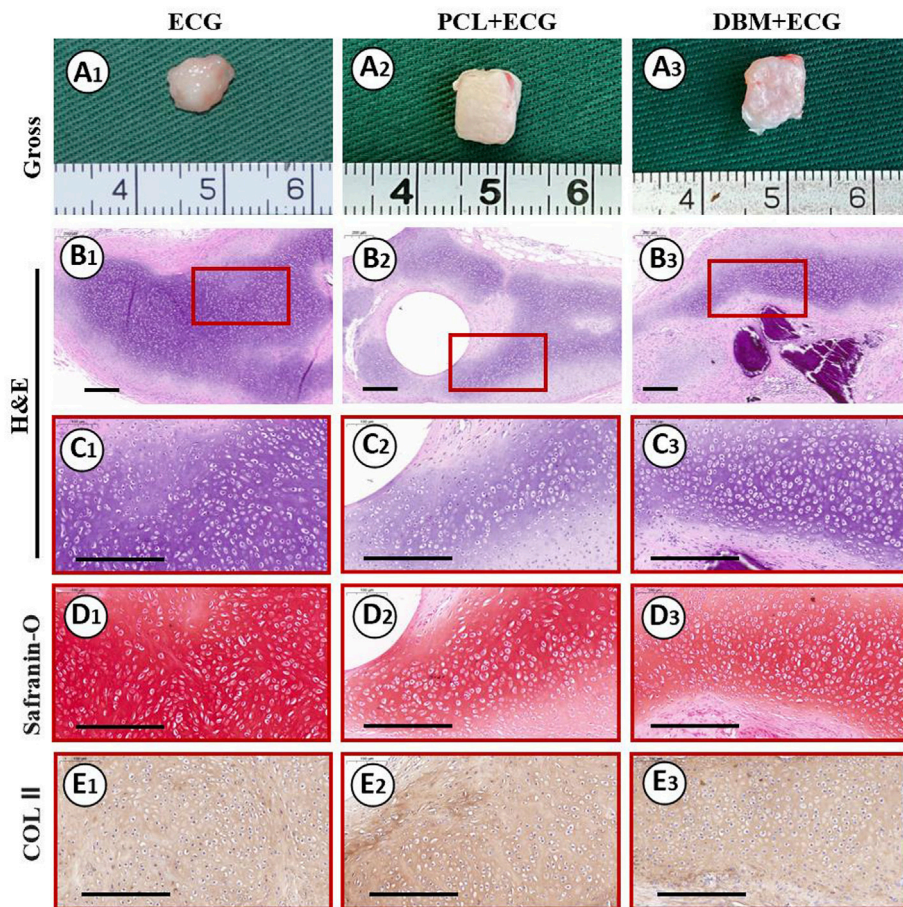


**FIGURE 8 |** Gross view and histological examinations of the regenerated cartilage in ECG, PCL-ECG, and DBM-ECG groups after 8 weeks of subcutaneous implantation: Gross observation (**A1–A3**); H&E staining with different magnification (**B1–B3**, **C1–C3**); Safranin-O staining (**D1–D3**); COL II immunohistochemical staining (**E1–E3**). Scale bar: 200  $\mu$ m.

PCL framework triggered milder M1 polarization of macrophages than the leach solution of the DBM framework, suggesting that the PCL framework showed lower immunogenicity than the DBM framework.

### 3.4 *In Vivo* Cartilage Regeneration of the Framework–Engineered Cartilage Gel Constructs

The *in vivo* cartilage regeneration performance was analyzed to evaluate the clinical translational potential of the PCL-ECG strategy. Gross observation showed that the regenerated cartilage in all groups gradually matured as evidenced by a reddish appearance at 1 week to an ivory appearance at 8 weeks (**Figures 4A, 5A, 8A**). The samples in the PCL-ECG group essentially maintained their original shape and size, showing relatively regular cuboids, while the samples in the DBM-ECG group showed slight deformation with an irregular cuboid shape (**Figure 8A**). As anticipated, the samples in the ECG

group showed an irregular shape due to lack of a supporting framework (**Figure 8A**). Histological analysis revealed that the samples in all groups formed mature cartilage-like tissue with typical lacuna structures and abundant cartilage-specific ECM deposition evidenced by strong positive staining of safranin-O and collagen II (**Figures 8B–E**). The quantitative analysis showed that the GAG and total collagen content of the regenerated cartilage in all groups showed a gradually increasing trend, indicating the gradual maturation of neo-cartilage, which was further supported by the gradually increasing wet weights and volumes observed for both the PCL-ECG and DBM-ECG groups. Notably, the wet weight and volume of the ECG group decreased over time, which might be related to stress induced absorption due to lack of a supporting framework (**Supplementary Figure S3**). In addition, it is worth noting that all of the quantitative data for the PCL-ECG group were higher than those for the DBM-ECG group (**Figure 9**), indicating relatively higher cartilage yield in the PCL-ECG group. These results suggest excellent clinical

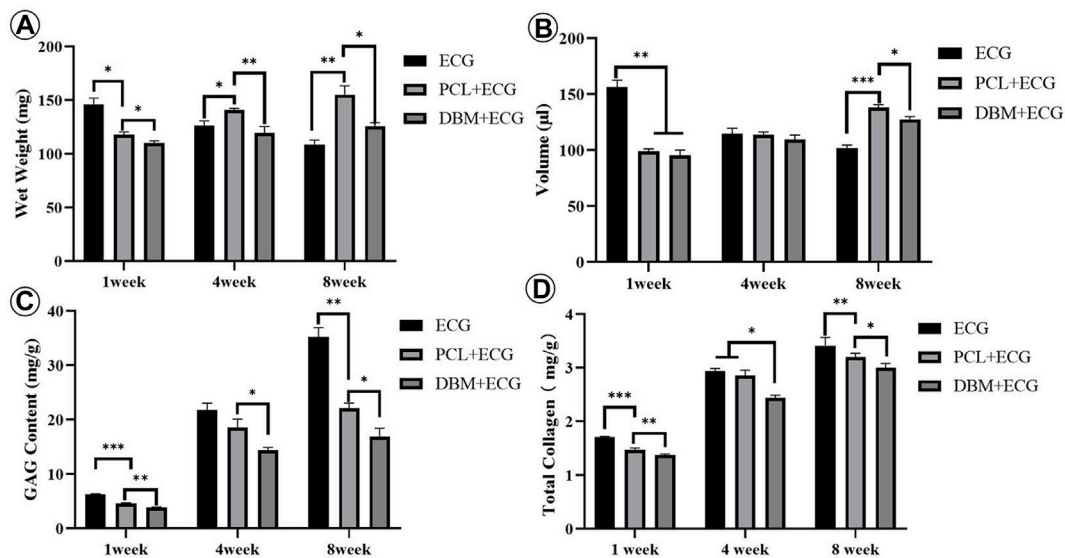


**FIGURE 9 |** Quantitative evaluations of the regenerated cartilage in ECG, PCL-ECG, and DBM-ECG groups after 1, 4, and 8 weeks of subcutaneous implantation: (A) wet weight, (B) volume, (C) total glycosaminoglycan (GAG) content, and (D) total collagen content. Statistical significance: \* $p < 0.05$ , \*\* $p < 0.01$ , \*\*\* $p < 0.001$ .

translation potential for the PCL-ECG cartilage regeneration strategy.

## 4 DISCUSSION

Although the feasibility of the steel-reinforced concrete cartilage regeneration model with ECG inoculated into DBM frameworks was confirmed by our previous study (Ci et al., 2021), the disadvantages of DBM hindered the further clinical translation of this technology. The current study shows that a 3D-printed PCL framework exhibits better biocompatibility and immunogenicity than the DBM framework. More importantly, after 8 weeks of subcutaneous implantation in large animals, the PCL-ECG constructs successfully regenerated mature cartilage and essentially maintained their original shape, which indicated that the PCL framework could serve as a promising framework to replace DBM in supporting 3D cartilage regeneration of ECG. As an FDA-approved 3D-printable biomaterial, PCL can be prepared in a variety of 3D shapes with controlled mechanical strength by computer-assisted design and thus has excellent potential for clinical translation.

The suitability of the 3D-printed PCL frameworks for ECG loading was the primary concern of this study. To provide a solid mechanical support while ensuring high loading efficiency, a double-layered PCL framework structure was designed. The top layer—the supporting and loading layer—was printed with thick strands and large pores to provide sufficient mechanical strength and ECG loading space, while the bottom layer was printed as a dense grid with thin strands and small pores to prevent ECG loss. The validity of this framework design was fully

confirmed by the findings that the PCL framework exhibited high mechanical strength and could integrate well with ECG with high loading efficiency. Notably, although there are still no unified criteria for the mechanical strength of the frameworks, the strong and controllable mechanical properties mean that the framework provided sufficient mechanical support for the early implantation of the constructs, particularly for the repair of cartilage defects in the subcutaneous environment, and to make necessary adjustments according to the specific situation of different patients. Furthermore, the PCL framework could be filled with ECG, which effectively reduced the exposure of the PCL framework. A cell viability assay confirmed that the PCL leach solution had no negative effects on the survival and proliferation of the cartilage sheets. However, in the control group, the DBM leach solution showed clear cytotoxicity and caused a small amount of apoptosis in the cartilage sheets, which is attributed to endotoxin residues in the DBM framework. These results suggest that the 3D-printed PCL framework could serve as an ideal supporting material for ECG loading in terms of mechanical strength, loading efficiency, and biocompatibility.

Inflammatory responses in large animals are important factors that affects cartilage regeneration and its clinical translation (Padmanabhan and Kyriakides, 2015; Koh et al., 2020). Therefore, the immunogenicity of the PCL framework was evaluated. The results show that the PCL framework caused a milder inflammatory response with less macrophage infiltration and chondrocyte apoptosis than the DBM framework. *In vitro* results further confirmed that the M1 polarization of macrophages activated by the PCL framework was significantly weaker than that caused by the DBM framework. PCL is an FDA-approved polyester biomaterial (Yadav et al., 2022) that has good biocompatibility and a relatively slow degradation rate with



neutral and nontoxic degradation products (Panigrahy and Rath, 2018; Backes et al., 2021; Bazgir et al., 2021), which may explain the low immunogenicity shown in this study. Although DBM is a natural biomaterial, during the production process, certain harmful bioactive components such as endotoxin and xenogenic protein are unavoidably retained to preserve the bioactivity of DBM (Shi et al., 2018; Amirazad et al., 2022) (**Supplementary Figure S2**), which might be why DBM triggered a more severe inflammatory response. These results suggest that the 3D-printed PCL framework is a better support for ECG loading than the DBM framework in terms of immunogenicity.

The ability of the PCL-ECG constructs to regenerate high-quality cartilage is the final criterion for evaluating the clinical potential of the strategy. The results show that the PCL-ECG constructs successfully regenerated mature cartilage with typical lacuna and cartilage-specific ECM deposition. Furthermore, the regenerated cartilage in the PCL-ECG group exhibited better shape maintenance with a higher cartilage-specific matrix content than that of the DBM-ECG group. The better shape maintenance exhibited by the PCL-ECG constructs is attributed to the appropriate mechanical strength (Olubamiji et al., 2016) and homogeneous structure throughout the PCL framework. In contrast, the DBM framework had relatively low mechanical strength and a heterogeneous structure, which led to poorer shape maintenance. In addition, the biocompatibility and low immunogenicity of the PCL framework ensured satisfactory cartilage regeneration in the PCL-ECG group, while the observed cytotoxicity and immunogenicity of the DBM framework led to relatively poorer cartilage regeneration in the DBM-ECG group. Notably, the ECG group with no framework triggered the mildest inflammatory reaction and achieved the optimal cartilage regeneration. Nevertheless, the uncontrolled shape and visible absorption, likely caused by the lack of mechanical support, would greatly limit its clinical application in cartilage defects with specialized shape. These results indicate that the 3D-printed PCL framework provided a stable support for ECG cartilage regeneration with satisfactory shape maintenance and cartilage quality.

## 5 CONCLUSION

A novel strategy for 3D cartilage regeneration based on a 3D-printed PCL framework and ECG was demonstrated. The PCL framework exhibited controllable 3D shape, homogeneous structure, appropriate mechanical strength, high loading efficiency, good biocompatibility, and low immunogenicity and successfully supported mature cartilage regeneration of ECG with satisfactory shape maintenance and cartilage quality. Although further investigations are required—for example, to optimize of the 3D-printing parameters for the PCL framework, determine the feasibility of regenerating cartilage with complex 3D shapes, and repair cartilage defects with complex 3D shapes in a large animal model—the current study demonstrates a novel strategy for ECG-based 3D cartilage regeneration for the repair of craniofacial cartilage defects.

## DATA AVAILABILITY STATEMENT

The original contributions presented in the study are included in the article/**Supplementary Material**, further inquiries can be directed to the corresponding authors.

## ETHICS STATEMENT

The animal study was reviewed and approved by the Animal Care and Experiment Committee of Shanghai Jiao Tong University School of Medicine.

## AUTHOR CONTRIBUTIONS

Conceptualization: GZ and SL; methodology: RS; software: LL; validation: GW and ZC; data curation: YW; writing—original draft preparation: GW; writing—review and editing: GZ; supervision: SL; and funding acquisition: GZ. All authors contributed to the article and approved the submitted version.

## FUNDING

This research was funded by the National Key Research and Development Program of China (2017YFC1103900, 2018YFC1105800), National Natural Science Foundation of China (81871502, 81701843, and 81671837), Shanghai Excellent Technical Leader (18XD1421500), Program of Shanghai Academic/Technology Research Leader (19XD1431100), Shanghai Collaborative Innovation Program on Regenerative Medicine and Stem Cell Research (2019CXJQ01), and Clinical Research Plan of SHDC (No. SHDC2020CR 2045B).

## ACKNOWLEDGMENTS

We thank Lijuan Zong, Sisi Shen, Junhong Lu, Zhengya Tang, Wanyao Xia, and Juanjuan Wu of the Shanghai Key Laboratory of Tissue Engineering and the National Tissue Engineering Center of China for their technical support and other assistance. We also thank Sarah Dodds from Liwen Bianji (Edanz) ([www.liwenbianji.cn](http://www.liwenbianji.cn)) for editing the English text of a draft of this manuscript.

## SUPPLEMENTARY MATERIAL

The Supplementary Material for this article can be found online at: <https://www.frontiersin.org/articles/10.3389/fbioe.2022.871508/full#supplementary-material>

## REFERENCES

- Amirazad, H., Dadashpour, M., and Zarghami, N. (2022). Application of Decellularized Bone Matrix as a Bioscaffold in Bone Tissue Engineering. *J. Biol. Eng.* 16 (1), 1. doi:10.1186/s13036-021-00282-5
- Arif, U., Haider, S., Haider, A., Khan, N., Alghyamah, A. A., Jamila, N., et al. (2019). Biocompatible Polymers and Their Potential Biomedical Applications: A Review. *Curr. Pharm. Des.* 25 (34), 3608–3619. doi:10.2174/1381612825999191011105148
- Armiento, A. R., Stoddart, M. J., Alini, M., and Eglin, D. (2018). Biomaterials for Articular Cartilage Tissue Engineering: Learning from Biology. *Acta Biomater.* 65, 1–20. doi:10.1016/j.actbio.2017.11.021
- Backes, E. H., Harb, S. V., Beatrice, C. A. G., Shimomura, K. M. B., Passador, F. R., Costa, L. C., et al. (2021). Polycaprolactone Usage in Additive Manufacturing Strategies for Tissue Engineering Applications: A Review. *J. Biomed. Mater. Res. B Appl. Biomater.* doi:10.1002/jbm.b.34997
- Bazgir, M., Zhang, W., Zhang, X., Elies, J., Saeinasab, M., Coates, P., et al. (2021). Degradation and Characterisation of Electrospun Polycaprolactone (PCL) and Poly(lactic-Co-Glycolic Acid) (PLGA) Scaffolds for Vascular Tissue Engineering. *Mater. (Basel)* 14 (17). doi:10.3390/ma14174773
- Chae, S., Lee, S. S., Choi, Y. J., Hong, D. H., Gao, G., Wang, J. H., et al. (2021). 3D Cell-Printing of Biocompatible and Functional Meniscus Constructs Using Meniscus-Derived Bioink. *Biomaterials* 267, 120466. doi:10.1016/j.biomaterials.2020.120466
- Chen, X. Q., Tu, L., Zou, J. S., Zhu, S. Q., Zhao, Y. J., and Qin, Y. H. (2021). The Involvement of Neutrophil Extracellular Traps in Disease Activity Associated with IgA Vasculitis. *Front. Immunol.* 12, 668974. doi:10.3389/fimmu.2021.668974
- Ci, Z., Zhang, Y., Wang, Y., Wu, G., Hou, M., Zhang, P., et al. (2021). 3D Cartilage Regeneration with Certain Shape and Mechanical Strength Based on Engineered Cartilage Gel and Decalcified Bone Matrix. *Front. Cell Dev. Biol.* 9, 638115. doi:10.3389/fcell.2021.638115
- Haghwirdi, F., Khozaei Ravari, M., Taghiyar, L., Shamekhi, M. A., Jahangir, S., Haririan, I., et al. (2021). Application of Bone and Cartilage Extracellular Matrices in Articular Cartilage Regeneration. *Biomed. Mater* 16 (4). doi:10.1088/1748-605X/ac094b
- Jia, L., Zhang, Y., Yao, L., Zhang, P., Ci, Z., Zhang, W., et al. (2020). Regeneration of Human-Ear-Shaped Cartilage with Acellular Cartilage Matrix-Based Biomimetic Scaffolds. *Appl. Mater. Today*, 20. doi:10.1016/j.apmt.2020.100639
- Koh, R. H., Jin, Y., Kim, J., and Hwang, N. S. (2020). Inflammation-Modulating Hydrogels for Osteoarthritis Cartilage Tissue Engineering. *Cells* 9 (2). doi:10.3390/cells9020419
- Kwon, H., Brown, W. E., Lee, C. A., Wang, D., Paschos, N., Hu, J. C., et al. (2019). Surgical and Tissue Engineering Strategies for Articular Cartilage and Meniscus Repair. *Nat. Rev. Rheumatol.* 15 (9), 550–570. doi:10.1038/s41584-019-0255-1
- Li, D., Zhu, L., Liu, Y., Yin, Z., Liu, Y., Liu, F., et al. (2017). Stable Subcutaneous Cartilage Regeneration of Bone Marrow Stromal Cells Directed by Chondrocyte Sheet. *Acta Biomater.* 54, 321–332. doi:10.1016/j.actbio.2017.03.031
- Li, H., Yin, Y., Xiang, Y., Liu, H., and Guo, R. (2020). A Novel 3D Printing PCL/GelMA Scaffold Containing USPIO for MRI-Guided Bile Duct Repair. *Biomed. Mater* 15 (4), 045004. doi:10.1088/1748-605X/ab797a
- Liau, L. L., Hassan, M., Tang, Y. L., Ng, M. H., and Law, J. X. (2021). Feasibility of Human Platelet Lysate as an Alternative to Foetal Bovine Serum for *In Vitro* Expansion of Chondrocytes. *Int. J. Mol. Sci.* 22 (3). doi:10.3390/ijms22031269
- Lim, W. L., Chowdhury, S. R., Ng, M. H., and Law, J. X. (2021). Physicochemical Properties and Biocompatibility of Electrospun Polycaprolactone/Gelatin Nanofibers. *Int. J. Environ. Res. Public Health* 18 (9). doi:10.3390/ijerph18094764
- Makris, E. A., Gomoll, A. H., Malizos, K. N., Hu, J. C., and Athanasiou, K. A. (2015). Repair and Tissue Engineering Techniques for Articular Cartilage. *Nat. Rev. Rheumatol.* 11 (1), 21–34. doi:10.1038/nrrheum.2014.157
- Olubamiji, A. D., Izadifar, Z., Si, J. L., Cooper, D. M., Eames, B. F., and Chen, D. X. (2016). Modulating Mechanical Behaviour of 3D-Printed Cartilage-Mimetic PCL Scaffolds: Influence of Molecular Weight and Pore Geometry. *Biofabrication* 8 (2), 025020. doi:10.1088/1758-5090/8/2/025020
- Padmanabhan, J., and Kyriakides, T. R. (2015). Nanomaterials, Inflammation, and Tissue Engineering. *Wiley Interdiscip. Rev. Nanomed Nanobiotechnol* 7 (3), 355–370. doi:10.1002/wnan.1320
- Panigrahy, N., and Rath, S. N. (2018). Degradation of Poly( $\epsilon$ -Caprolactone) and Bio-Interactions with Mouse Bone Marrow Mesenchymal Stem Cells. *Colloids Surf. B Biointerfaces* 163, 107–118. doi:10.1016/j.colsurfb.2017.12.039
- Raub, C. B., Hsu, S. C., Chan, E. F., Shirazi, R., Chen, A. C., Chnari, E., et al. (2013). Microstructural Remodeling of Articular Cartilage Following Defect Repair by Osteochondral Autograft Transfer. *Osteoarthritis Cartil.* 21 (6), 860–868. doi:10.1016/j.joca.2013.03.014
- Saracino, E., Cirillo, V., Marrese, M., Guarino, V., Benfenati, V., Zamboni, R., et al. (2021). Structural and Functional Properties of Astrocytes on PCL Based Electrospun Fibres. *Mater. Sci. Eng. C Mater. Biol. Appl.* 118, 111363. doi:10.1016/j.msec.2020.111363
- Shi, M., Wang, C., Wang, Y., Tang, C., Miron, R. J., and Zhang, Y. (2018). Deproteinized Bovine Bone Matrix Induces Osteoblast Differentiation via Macrophage Polarization. *J. Biomed. Mater. Res. A* 106 (5), 1236–1246. doi:10.1002/jbm.a.36321
- Wang, Y., Xu, Y., Zhou, G., Liu, Y., and Cao, Y. (2020). Biological Evaluation of Acellular Cartilaginous and Dermal Matrixes as Tissue Engineering Scaffolds for Cartilage Regeneration. *Front. Cell Dev. Biol.* 8, 624337. doi:10.3389/fcell.2020.624337
- Wei, L., Huang, C., Yang, H., Li, M., Yang, J., Qiao, X., et al. (2015). A Potent Anti-inflammatory Peptide from the Salivary Glands of Horsefly. *Parasit. Vectors* 8, 556. doi:10.1186/s13071-015-1149-y
- Wei, W., Ma, Y., Yao, X., Zhou, W., Wang, X., Li, C., et al. (2021). Advanced Hydrogels for the Repair of Cartilage Defects and Regeneration. *Bioact. Mater* 6 (4), 998–1011. doi:10.1016/j.bioactmat.2020.09.030
- Xia, H., Zhao, D., Zhu, H., Hua, Y., Xiao, K., Xu, Y., et al. (2018). Lyophilized Scaffolds Fabricated from 3D-Printed Photocurable Natural Hydrogel for Cartilage Regeneration. *ACS Appl. Mater. Interfaces* 10 (37), 31704–31715. doi:10.1021/acsami.8b10926
- Xue, J., He, A., Zhu, Y., Liu, Y., Li, D., and Yin, Z. (2018). Repair of Articular Cartilage Defects with Acellular Cartilage Sheets in a Swine Model. *Biomed. Mater* 13 (2), 025016. doi:10.1088/1748-605X/aa99a4
- Yadav, A., Ghosh, S., Samanta, A., Pal, J., and Srivastava, R. K. (2022). Emulsion Templated Scaffolds of Poly( $\epsilon$ -Caprolactone) - a Review. *Chem. Commun. (Camb)*. doi:10.1039/d1cc04941k
- Yang, L., Li, X., Wang, D., Mu, S., Lv, W., Hao, Y., et al. (2020). Improved Mechanical Properties by Modifying Fibrin Scaffold with PCL and its Biocompatibility Evaluation. *J. Biomater. Sci. Polym. Ed.* 31 (5), 658–678. doi:10.1080/09205063.2019.1710370
- Zhang, H., Yang, L., Yang, X. G., Wang, F., Feng, J. T., Hua, K. C., et al. (2019). Demineralized Bone Matrix Carriers and Their Clinical Applications: An Overview. *Orthop. Surg.* 11 (5), 725–737. doi:10.1111/os.12509
- Zhou, G., Jiang, H., Yin, Z., Liu, Y., Zhang, Q., Zhang, C., et al. (2018). Vitro Regeneration of Patient-specific Ear-Shaped Cartilage and its First Clinical Application for Auricular Reconstruction. *EBioMedicine* 28, 287–302. doi:10.1016/j.ebiom.2018.01.011
- Zou, T., Dembele, F., Beugnet, A., Sengmanivong, L., Trepout, S., Marco, S., et al. (2015). Nanobody-functionalized PEG-B-PCL Polymersomes and Their Targeting Study. *J. Biotechnol.* 214, 147–155. doi:10.1016/j.jbiotec.2015.09.034

**Conflict of Interest:** The authors declare that the research was conducted in the absence of any commercial or financial relationships that could be construed as a potential conflict of interest.

**Publisher's Note:** All claims expressed in this article are solely those of the authors and do not necessarily represent those of their affiliated organizations, or those of the publisher, the editors, and the reviewers. Any product that may be evaluated in this article, or claim that may be made by its manufacturer, is not guaranteed or endorsed by the publisher.

Copyright © 2022 Wu, Lu, Ci, Wang, Shi, Zhou and Li. This is an open-access article distributed under the terms of the Creative Commons Attribution License (CC BY). The use, distribution or reproduction in other forums is permitted, provided the original author(s) and the copyright owner(s) are credited and that the original publication in this journal is cited, in accordance with accepted academic practice. No use, distribution or reproduction is permitted which does not comply with these terms.



# Customized Design 3D Printed PLGA/ Calcium Sulfate Scaffold Enhances Mechanical and Biological Properties for Bone Regeneration

Tao Liu<sup>1†</sup>, Zhan Li<sup>2†</sup>, Li Zhao<sup>3†</sup>, Zehua Chen<sup>4†</sup>, Zefeng Lin<sup>5</sup>, Binglin Li<sup>3,5</sup>, Zhibin Feng<sup>1</sup>, Panshi Jin<sup>1</sup>, Jinwei Zhang<sup>1</sup>, Zugui Wu<sup>4</sup>, Huai Wu<sup>6</sup>, Xuemeng Xu<sup>6\*</sup>, Xiangling Ye<sup>4\*</sup> and Ying Zhang<sup>1,3\*</sup>

<sup>1</sup>General Hospital of Southern Theatre Command of PLA, The First School of Clinical Medicine, Southern Medical University, Guangzhou, China, <sup>2</sup>General Hospital of Southern Theatre Command of PLA, Guangzhou University of Chinese Medicine, Guangzhou, China, <sup>3</sup>Department of Trauma Orthopedics, Hospital of Orthopedics, General Hospital of Southern Theatre Command of PLA, Guangzhou, China, <sup>4</sup>The Fifth Clinical College of Guangzhou University of Chinese Medicine, Guangzhou, China, <sup>5</sup>Guangdong Key Lab of Orthopedic Technology and Implant Materials, General Hospital of Southern Theatre Command of PLA, Guangzhou, China, <sup>6</sup>Department of Orthopedics, Guangdong Second Traditional Chinese Medicine Hospital, Guangzhou, China

## OPEN ACCESS

### Edited by:

Changchun Zhou,  
Sichuan University, China

### Reviewed by:

Qin Zou,  
Sichuan University, China  
Kai Zheng,  
Nanjing Medical University, China

### \*Correspondence:

Xuemeng Xu  
xuxuemeng@163.com  
Xiangling Ye  
yxl20160228@163.com  
Ying Zhang  
ying\_zhang121@163.com

<sup>†</sup>These authors have contributed  
equally to this work

### Specialty section:

This article was submitted to  
Biomaterials,  
a section of the journal  
Frontiers in Bioengineering and  
Biotechnology

Received: 13 February 2022

Accepted: 11 May 2022

Published: 23 June 2022

### Citation:

Liu T, Li Z, Zhao L, Chen Z, Lin Z, Li B,  
Feng Z, Jin P, Zhang J, Wu Z, Wu H,  
Xu X, Ye X and Zhang Y (2022)  
Customized Design 3D Printed PLGA/  
Calcium Sulfate Scaffold Enhances  
Mechanical and Biological Properties  
for Bone Regeneration.  
Front. Bioeng. Biotechnol. 10:874931.  
doi: 10.3389/fbioe.2022.874931

Poly(lactic glycolic acid) copolymer (PLGA) has been widely used in tissue engineering due to its good biocompatibility and degradation properties. However, the mismatched mechanical and unsatisfactory biological properties of PLGA limit further application in bone tissue engineering. Calcium sulfate ( $\text{CaSO}_4$ ) is one of the most promising bone repair materials due to its non-immunogenicity, well biocompatibility, and excellent bone conductivity. In this study, aiming at the shortcomings of activity-lack and low mechanical of PLGA in bone tissue engineering, customized-designed 3D porous PLGA/ $\text{CaSO}_4$  scaffolds were prepared by 3D printing. We first studied the physical properties of PLGA/ $\text{CaSO}_4$  scaffolds and the results showed that  $\text{CaSO}_4$  improved the mechanical properties of PLGA scaffolds. *In vitro* experiments showed that PLGA/ $\text{CaSO}_4$  scaffold exhibited good biocompatibility. Moreover, the addition of  $\text{CaSO}_4$  could significantly improve the migration and osteogenic differentiation of MC3T3-E1 cells in the PLGA/ $\text{CaSO}_4$  scaffolds, and the PLGA/ $\text{CaSO}_4$  scaffolds made with 20 wt.%  $\text{CaSO}_4$  exhibited the best osteogenesis properties. Therefore, calcium sulfate was added to PLGA could lead to customized 3D printed scaffolds for enhanced mechanical properties and biological properties. The customized 3D-printed PLGA/ $\text{CaSO}_4$  scaffold shows great potential for precisely repairing irregular load-bearing bone defects.

**Keywords:** bone defect, 3D printing scaffold, polylactic glycolic acid copolymer, calcium sulfate, mechanical properties, biological properties

## 1 INTRODUCTION

Although bone is a tissue with superior self-healing potential, massive irregular bone defects created by trauma, tumor resection, or infection remain a challenge in the clinic (Kuss et al., 2017; Ye et al., 2018; Nulty et al., 2021; Yang et al., 2021; Ye et al., 2021). Autologous bone is considered an ideal material for the treatment of large bone defects due to its retention of osteoblasts and bioactive

molecules, including growth factors with osteogenic induction properties (Cheng et al., 2018; Pforringer et al., 2018). However, there are some problems with autologous bone, such as limited donor bone and the risk of bleeding and infection during collection (Ishikawa et al., 2017; Lee et al., 2020). Allografts can also be used to treat bone defects to compensate for the limitations of autografts, but carry the risk of immune rejection (Lai et al., 2019). Thus, we needed to construct new materials as substitutes for autografts and allografts.

The success of load-bearing materials is largely dependent on physical and chemical properties that are known to drive cellular response and it is of great importance to construct a scaffold with an ability to promote cells proliferation, adhesion, migration, and differentiation for bone regeneration (Kim et al., 2017; Li H. et al., 2020). With the rapid development of bone tissue engineering, the interconnected porous scaffolds prepared by 3D printing technology to simulate the extracellular matrix of living bone are showing obvious advantages (Cui et al., 2018). More importantly, the 3D printing technology could fabricate custom-fit scaffolds based on a computed tomography scan of the defect site to repair irregular bone defects with complex geometry (Lai et al., 2019; Wu et al., 2021; Zhu et al., 2022). Besides, the customized design of 3D scaffolds can not only achieve the perfect match between the material and the bone defect but also regulate the structure of the material and the arrangement of cells in the microstructure, which is more conducive to promoting the growth and differentiation of cells and supporting the bone tissue regeneration process (Han et al., 2022).

In recent years, a variety of materials including polymers (Oryan and Sahviah, 2017; Cui et al., 2019; Ranganathan et al., 2019; Lavanya et al., 2020; Hu et al., 2021; Yu et al., 2021), nanomaterials (Xia et al., 2018; Lu et al., 2019; Singh et al., 2019), metal materials (Lai et al., 2019; Tan et al., 2021), ceramic (Gao et al., 2017; Ma H. et al., 2018; Adithya et al., 2020), and other biological materials (Zimmermann and Ritchie, 2015; Daly et al., 2017; Bose and Sarkar, 2020; Cao et al., 2022; Pang et al., 2022) have been widely used in 3D printing technology to fabricate scaffolds for bone defect repair.

Among a variety of materials for bone tissue engineering, polylactic glycolic acid copolymer (PLGA) has been approved by US Food and Drug Administration (FDA) for human use due to its good biocompatibility and biodegradability (Jia et al., 2016). However, although PLGA is widely used in various tissue engineering applications, it still has the problems of mismatched mechanical and unsatisfactory biological properties owing to the low stiffness between PLGA-based implants and natural bones and the hydrophobic surface of PLGA-based scaffolds (Zou et al., 2020; Jin et al., 2021; Oizumi et al., 2021; Wei et al., 2021; Zhao et al., 2021). Many researchers address these problems by introducing inorganic material in the modification of PLGA-based scaffolds. To overcome the disadvantages of poor mechanical properties and osteogenic properties of PLGA, Zhu TT designed PLGA/nHA scaffolds to repair large bone defects and achieved good results (Zhu et al., 2022). Lai Y X constructed bone repair scaffolds by adding TCP to improve the mechanical properties of PLGA (Lai et al., 2019). In addition, PCL and bioglass are also used to

improve the performance of PLGA (Cheng et al., 2018; Qian et al., 2019).

Calcium sulfate ( $\text{CaSO}_4$ ) is a commercial bone graft replacement material with a long history of application in a variety of medical applications, such as bone defect filling and tissue regeneration guidance. Calcium sulfate as a bone graft material has the advantages of the minimal inflammatory response, complete degradation, osteoconductive, and  $\text{Ca}^{2+}$  released during dissolution may promote osteogenic differentiation (Arun Kumar et al., 2016). As a synthetic bone graft material,  $\text{CaSO}_4$  could induce a biological reaction similar to that generated during bone remodeling, creating a calcium-rich environment in the implanted area (Zhou et al., 2014; Aquino-Martínez et al., 2017). Moreover, as an inorganic material,  $\text{CaSO}_4$  could enhance the mechanical strength and hydrophilicity of the polymeric scaffolds (Ye et al., 2018).

Herein we aim to develop 3D-printed customized scaffolds with proper mechanical and bioactivity properties for repairing irregular bone defects. In this study, we incorporated  $\text{CaSO}_4$  powder into PLGA and then fabricated 3D porous PLGA/ $\text{CaSO}_4$  scaffolds using fused deposition modeling (FDM) system (**Scheme 1**). The prepared PLGA, PLGA/10% $\text{CaSO}_4$ , PLGA/20% $\text{CaSO}_4$ , and PLGA/30% $\text{CaSO}_4$  scaffolds all had a Customized 3D porous structure. We found that the addition of  $\text{CaSO}_4$  improved the mechanical properties of PLGA scaffolds, and with the increase of the  $\text{CaSO}_4$  ratio, the scaffolds could stand more pressure. Moreover, *in vitro* experiments showed that all scaffolds had good biocompatibility, and the PLGA/ $\text{CaSO}_4$  scaffolds improved the migration of MC3T3-E1 cells compared with PLGA scaffolds. Furthermore, PLGA/ $\text{CaSO}_4$  scaffolds significantly improved the osteogenic differentiation of MC3T3-E1 cells, and PLGA/20% $\text{CaSO}_4$  scaffolds exhibited the best osteogenic properties. The customized-designed 3D porous PLGA/ $\text{CaSO}_4$  with satisfactory mechanical and proper biological are expected to solve the problems of PLGA scaffolds and be further used for irregular bone defects.

## 2 MATERIALS AND METHODS

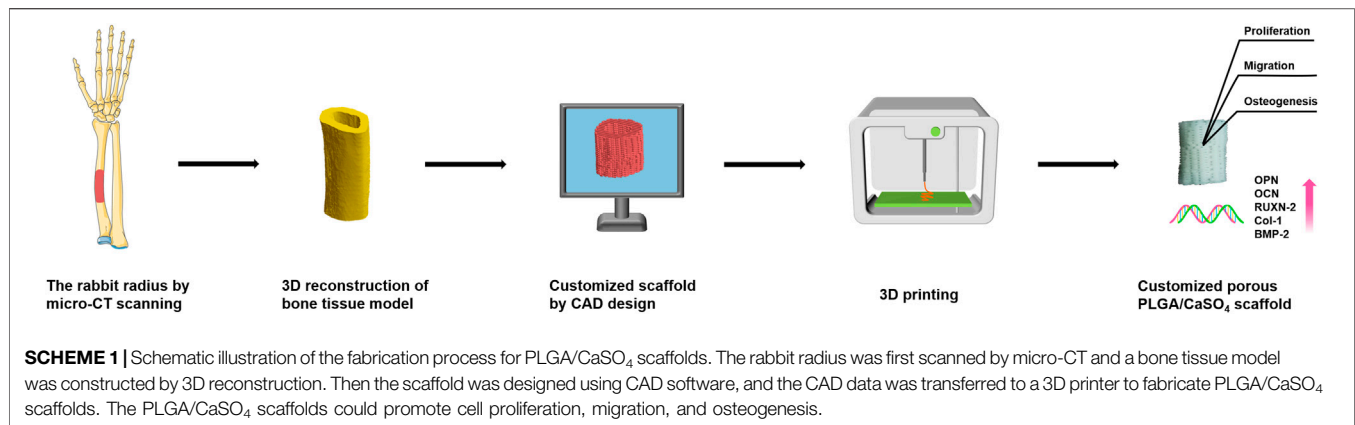
### 2.1 Materials

Polylactic glycolic acid copolymer (PLGA, MW = 15,000 g/mol) was purchased from Dai Gang Biology Co., Ltd. (Jinan, China). Anhydrous calcium sulfate ( $\text{CaSO}_4$ , MW = 136.14 g/mol) was obtained from Macklin Biochemical Co., Ltd. (Shanghai, China).

### 2.2 Customized Design of Bone Defect Models

We scanned the rabbit radius bone by microcomputed tomography (micro-CT). Then the CT scan data of bone was imported into computer-aided design (CAD) software to establish a customized bone defect model, and generate the model file. The CAD data was utilized to design the scaffolds with the desired shape and 3D porous structure and then transferred to a 3D printer.





## 2.3 Fabrication of Customized 3D Polylactic Glycolic Acid Copolymer/CaSO<sub>4</sub> Scaffold

The PLGA/CaSO<sub>4</sub> scaffolds in different proportions were fabricated by a biological 3D printer (Livprint® N series, Medprin, Guangzhou, China) layer by layer (**Supplementary Figure S1**). Firstly, PLGA and CaSO<sub>4</sub> (CaSO<sub>4</sub> accounts for 0, 10, 20, and 30 wt% of the quality of PLGA) powder were added into the beaker and then stirred evenly at 200°C (Du et al., 2018; Nulty et al., 2021). The mixture was then injected into the 3D printer and the scaffold was printed by following the constructed bone model. The nozzle temperature was 180°C, and the temperature of supporting substrates during FDM printing was 120°C.

## 2.4 Characterization of the Scaffolds

### 2.4.1 Scanning Electron Microscopy Analysis

The surface morphology and pore size of the calcium sulfate powder and the scaffolds were observed using an Scanning Electron Microscopy (SEM) (Sigma 300, ZEISS, Germany). After being frozen in a refrigerator, freeze-dried in a lyophilizer, and coated with gold, the scaffolds were analyzed by SEM.

### 2.4.2 Contact Angle

The hydrophilicity of each scaffold was measured using a contact angle measurement system (ASUMI GIKEN Limited, Tokyo, Japan). A droplet of deionized water was deposited on the scaffold. Then, the image of the static liquid deposition was obtained within a few seconds and the contact angles were measured. Three samples were assessed for each group to ensure reproducibility and the average value.

### 2.4.3 Fourier Transform Infrared Spectroscopy Analysis

The Fourier transform infrared spectroscopy [(FTIR), Nicolet iS10, Thermo Fisher Scientific, United States] was used to evaluate the changes in the chemical structures of the scaffolds.

### 2.4.4 X-ray Diffraction Analysis

X-ray diffraction (XRD) patterns were obtained using an Ultima IV X-ray diffractometer (Rigaku, Japan) in the range of 10°–80°.

## 2.4.5 Mechanical Properties

The mechanical properties of the scaffold were evaluated by a universal machine (RGT-3, Shenzhen Reger Instrument Co., Ltd., China) with a constant speed of 1 mm/min. Three repeated measurements were made for each scaffold (Ye et al., 2018; Ma et al., 2020).

## 2.4.6 Swelling Behavior

The swelling ratio of different scaffolds was weighed and placed in centrifuge tubes with 5 ml of simulated body fluid (SBF), and then placed on a shaker (37°C, 150 rpm/min). After 24 h, the scaffolds were taken out, removed the surface water by filter paper, and weighed. The swelling ratio was determined by using Eq. 1:

$$\text{Swell ratio (\%)} = (W_w - W_d) / W_d \times 100\% \quad (1)$$

where  $W_w$  and  $W_d$  are the wet and dry weights, respectively.

## 2.4.7 Biodegradation

The initial weight of each scaffold was recorded and placed in a centrifuge tube containing 5 ml of SBF. The tubes were placed in a shaker stirring at a speed of 150 rpm at 37°C. Scaffolds were removed from the tubes every 3 days and weighted, and then replaced with the SBF solution (Li et al., 2021). The percentage of degradation was calculated using Eq. 2:

$$\text{Degradation (\%)} = W_i / W_t \times 100\% \quad (2)$$

Where  $W_i$  is the initial weight of the samples and  $W_t$  is the weight at each time interval.

## 2.5 Biocompatibility *In Vitro*

### 2.5.1 Cell Culture

Human umbilical vein endothelial cells (HUVECs) were purchased from Cyagen Biotechnology (United States), and cultured with Dulbecco's Modified Eagle's Medium (DMEM high glucose, Gibco, United States) containing 10% fetal bovine serum (FBS, Biological Industries, United States) and 1% penicillin-streptomycin (Gibco, United States) at 37°C in a humidified and 5% CO<sub>2</sub> incubator.

### 2.5.2 Cell Proliferation

Cell Counting Kit-8 (CCK-8) assay was used to evaluate the cell viability for proliferation in the scaffold. HUVEC cells were seeded in a 24-well plate at a density of  $1 \times 10^4$  cells per well and incubated with different scaffolds for 1, 2, and 3 days, respectively (Kim DS et al., 2021). The scaffolds were removed from the plate and the media solution was replaced with 300  $\mu$ L CCK-8 solution (Biosharp, China) in each well and incubated for 2 h. 100  $\mu$ L of the supernatant was removed to a 96-well plate and the OD value was measured with a microplate (Multiskan GO, Thermo Fisher Scientific, United States).

### 2.5.3 Live/Dead Cell Staining

Live/dead staining was used to evaluate the cytocompatibility of the scaffolds. The HUVECs were co-cultured with different scaffolds for 1, 2, and 3 days. After being washed with PBS, Calcein-AM/palladium staining solution (Bestbio, China) was added to each well for 30 min at room temperature. A fluorescence microscope (DMI4000, Leica, Germany) was employed to record the fluorescent images of HUVEC cells.

### 2.5.4 Hemolysis Tests

Healthy human blood containing EDTA was collected and diluted with PBS in a ratio of 4:5. Then the different scaffolds were immersed in 1.8 ml of PBS in each group and incubated at 37°C for 30 min, and 2 ml of ddH<sub>2</sub>O and PBS were set as positive and negative controls, respectively. Next, 0.2 ml of the diluted whole blood was added to each scaffold sample, and the scaffolds were incubated at 37°C for 1 h. Then, the samples were centrifuged at room temperature (3,000 rpm, 5 min). The supernatant was removed from the samples and the absorbance at 545 nm was measured with a microplate reader (Ye et al., 2018). The hemolysis rate (HR) was calculated using Eq. 3:

$$HR(\%) = (OD_s - OD_n) / (OD_p - OD_n) \times 100\% \quad (3)$$

where  $OD_s$ ,  $OD_p$ , and  $OD_n$  are the OD values of the scaffold, positive control, and negative control groups, respectively.

## 2.6 Cell Migration and Adhesion

### 2.6.1 Cell Culture

Mouse embryo osteoblast precursor cells (MC3T3-E1) were purchased from Cyagen Biotechnology (United States), and cultured with Minimum essential medium alpha (MEM- $\alpha$ , Gibco, United States) containing 1% penicillin-streptomycin and 10% fetal bovine serum at 37°C in a humidified and 5% CO<sub>2</sub> incubator.

### 2.6.2 Wound Healing Assay

For the cell migration assay, MC3T3-E1 cells were seeded in 12-well plates at a density of  $5 \times 10^4$  cells per well. After the cells were cultured to confluence, a straight scratch was made with a 200  $\mu$ L pipette tip, and then the scaffolds were directly co-culture with MC3T3-E1 cells for 12 h and stained with Calcein-AM/PI kit for 30 min at room temperature. After removing the free dyes, the distance of the scratch was visualized with a fluorescence

microscope and the wound healing rate was calculated using Eq. 4:

$$\text{Cell migration rate}(\%) = (A_{0h} - A_{24h}) / A_{0h} \times 100 \quad (4)$$

where  $A_{0h}$  and  $A_{24h}$  are the initial distance and the gap after 24 h of coculture, respectively.

### 2.6.3 Transwell Migration Assay

The migration of MC3T3-E1 cells was also tested using a transwell assay. Briefly, 80  $\mu$ L of Matrigel (Corning, United States) was added to the upper chambers of a 24-well transwell plate (Corning; pore size = 8  $\mu$ m) and gelatinized for 2 h at 37°C. The scaffolds were completely immersed in MEM- $\alpha$  culture medium, which contained 10% FBS, and 1% penicillin-streptomycin at a concentration of 10 mg/ml. The samples were maintained in a shaker at 37°C with a speed of 120 rpm to obtain the extract solutions. 600  $\mu$ L extracted liquid from each scaffold containing 20% FBS was added to the lower chamber. Then, MC3T3-E1 were seeded in the upper chambers at a density of  $1 \times 10^5$  cells per well. After incubation at 37°C for 24 h, the Matrigel was erased with a swab, and MC3T3-E1 migrated to the opposite side of the membrane were fixed with 4% paraformaldehyde for 30 min and stained with 0.5% crystal violet (Macklin, China) for 1 h. Three random fields from each plate were recorded using an optical microscope. The stained MC3T3-E1 were lysed in 95% ethanol for 1 h to measure the OD value at 590 nm using a microplate reader.

### 2.6.4 Cytoskeleton Analysis

Cytoskeleton staining was used to evaluate cell morphology on the scaffold surface. Briefly, MC3T3-E1 cells were incubated with different scaffolds at a density of  $1 \times 10^4$  per well in a 24-well plate. After incubation for 3 days, cells were fixed with 4% paraformaldehyde for 2 h and then permeabilized with 0.1% Triton X-100 (Sigma-Aldrich, United States) for 5 min at room temperature. After washed with PBS, the cells were stained with Actin Cytoskeleton/Focal Adhesion Staining Kit (FAK 100, Sigma-Aldrich, United States) for 1 h and DAPI (Solarbio, China) for 5 min at room temperature. The reaction was stopped by removing the DAPI solution and washing it with PBS, the cells were visualized with confocal laser scanning microscopy (CLSM) (TCS SP-2, Leica, Germany).

## 2.7 Osteogenic Activity In Vitro

### 2.7.1 Alkaline Phosphatase Staining

The Alkaline Phosphatase (ALP) activity assay was performed to analyze the effect of scaffolds on the early osteogenic differentiation of cells. For ALP staining, MC3T3-E1 cells were seeded in a 6-well plate at a density of  $1 \times 10^4$  cells per well and incubated with different scaffolds for 7 and 14 days, respectively. The ALP activity assay was then performed with the BCIP/NBT alkaline phosphatase color development kit (Beyotime, China) according to the manufacturer's instructions. After removing the ALP stain working solution and washing with PBS. Stained MC3T3-E1 cells were visualized with an inverted research microscope (DMI4000, Leica, Germany).

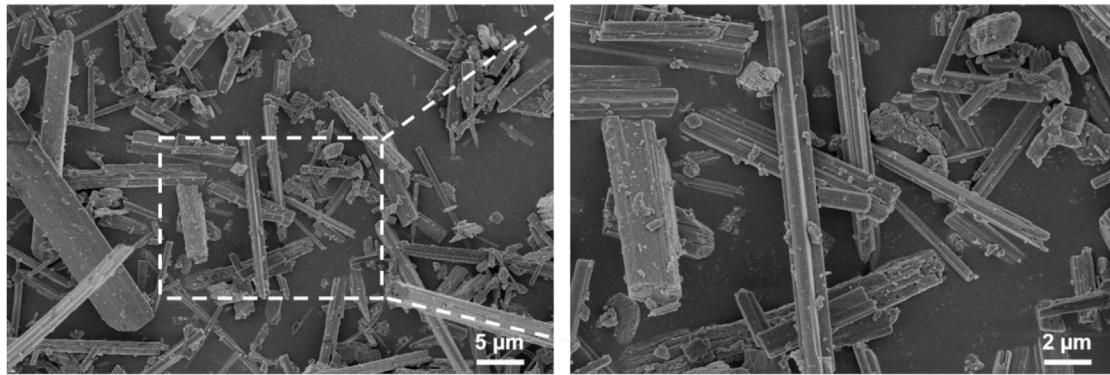


**FIGURE 1** | SEM morphology of  $\text{CaSO}_4$  particles.

### 2.7.2 Alkaline Phosphatase Activity

The ALP activity was also employed to evaluate the effect of scaffolds on the osteogenic differentiation of cells. MC3T3-E1 cells were seeded in a 6-well plate at a density of  $1 \times 10^4$  cells per well and incubated with different scaffolds for 7 and 14 days, respectively. After the incubation, cells were washed with PBS and lysed using 0.2% Triton X-100 for 12 h at 4°C. ALP activity was determined using an ALP detection kit (P0321, Beyotime Biotechnology, China). The total protein content in the samples was determined by the BCA protein assay kit (Thermo Fisher Scientific, United States) with the same protocol above. The relative ALP activity was finally normalized to the corresponding total protein content.

### 2.7.3 Alizarin Red Staining

For the Alizarin red assay, MC3T3-E1 cells were fixed with 4% paraformaldehyde for 30 min at room temperature after culturing with scaffolds for 7 and 14 days. Then the cells were stained with 400  $\mu\text{l}$  Alizarin red S solution (ARS, Sigma, United States) for 3 h. The plates were then observed with a microscope.

### 2.7.4 Gene Expression

MC3T3-E1 cells were seeded in a 6-well plate at a density of  $1 \times 10^4$  cells per well and incubated with different scaffolds for 7 and 14 days, respectively. The osteogenesis-related genes include osteoprotein (OPN), osteocalcin (OCN), runt-related transcription factor 2 (RUNX2), type I collagen (COL-1), and bone morphogenetic protein-2 (BMP-2) were analyzed by real-time quantitative polymerase chain reaction (RT-qPCR). Total RNA was obtained from the MC3T3-E1 cells with a total RNA extraction kit (Accurate Biology, China) and reversed transcribed into complementary DNA with the PrimeScript TM reagent kit (Takara, Japan). The gene expression levels were quantified using an ABI Prism 7000 machine (Thermo Fisher Scientific, United States) with TB Green Premix Ex Taq II (Takara, Japan). Primers were presented in **Supplementary Table S1**.

## 2.8 Statistical Analysis

Analysis was performed using SPSS 19.0 software (IBM, United States). A two-tailed Student's t-test was used in the comparison between the two groups. One-way analysis of variance (ANOVA) followed by Tukey's multiple comparisons was carried out in the comparison among more than two groups ( $*p < 0.05$ ,  $**p < 0.01$ , and  $***p < 0.005$ ). All the data are expressed with mean  $\pm$  standard deviation.

## 3 RESULTS

### 3.1 Preparation and Characterization of the Scaffolds

The shape, size, and morphology of the  $\text{CaSO}_4$  particles are closely related to the formation of 3D printed scaffolds. The morphology of  $\text{CaSO}_4$  particles was evaluated using SEM. As shown in **Figure 1**, the particle size of  $\text{CaSO}_4$  was about 2.0–20.0  $\mu\text{m}$ , and the particles were evenly dispersed without agglomeration.  $\text{CaSO}_4$  particles are a new type of fiber with high mechanical strength compared with polymers due to the near-perfect crystal structures (Fm et al., 2021), so they could be used as a potential reinforcement material for PLGA.

We successfully constructed customized-designed PLGA, PLGA/10% $\text{CaSO}_4$ , PLGA/20% $\text{CaSO}_4$ , and PLGA/30% $\text{CaSO}_4$  scaffolds by a 3D printer in the FDM system, respectively (**Figure 2A**). SEM was employed to observe the microstructure and surface morphology of the scaffolds. As shown in **Figure 2B**, all the scaffolds had a three-dimensional network structure and there was no statistical difference between the pore size of different scaffolds (**Figure 2E**). The scaffolds had a regular structure with interconnected pores of about 400  $\mu\text{m}$ . The interconnected macropores facilitate the diffusion of oxygen and nutrients, providing sufficient space for the proliferation, adhesion, migration, and differentiation of cells (Zhao et al., 2018; Yan et al., 2019; Gu et al., 2021; Kim H. D. et al., 2021). High-resolution SEM showed that the surface of the pure PLGA scaffold was smooth. However, with the incorporation of calcium sulfate, the roughness of the surface was improved

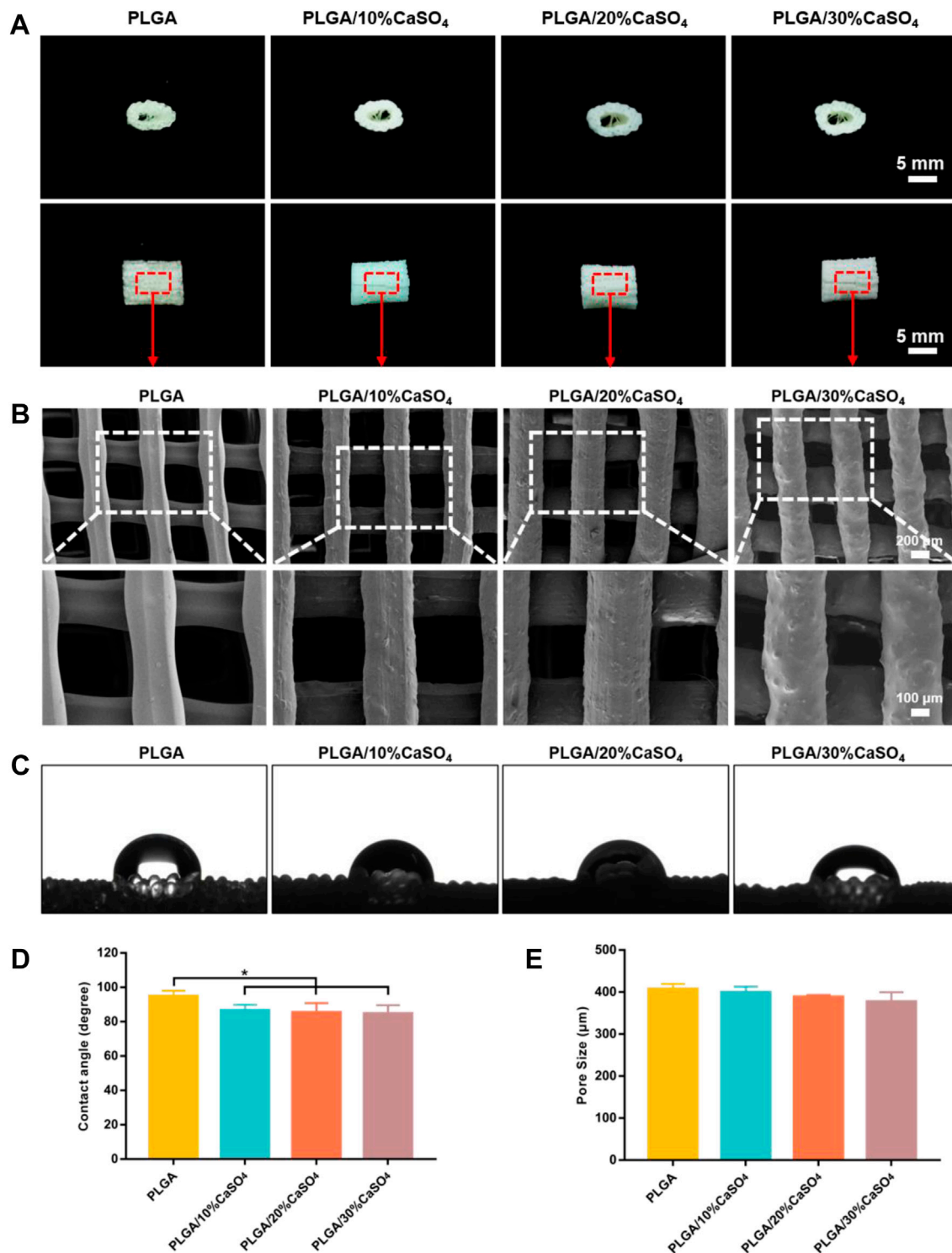
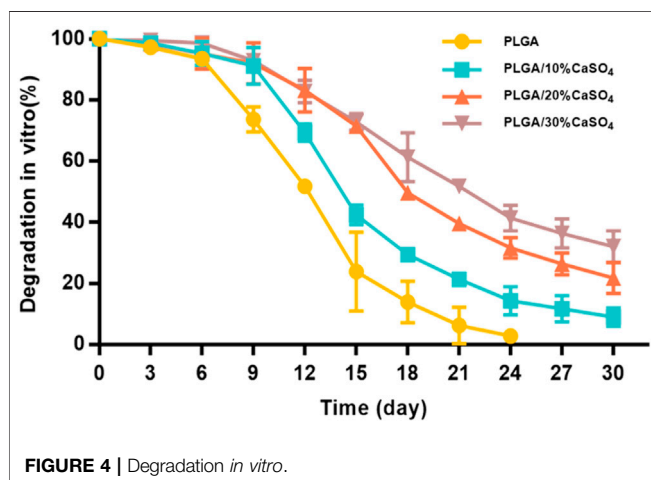
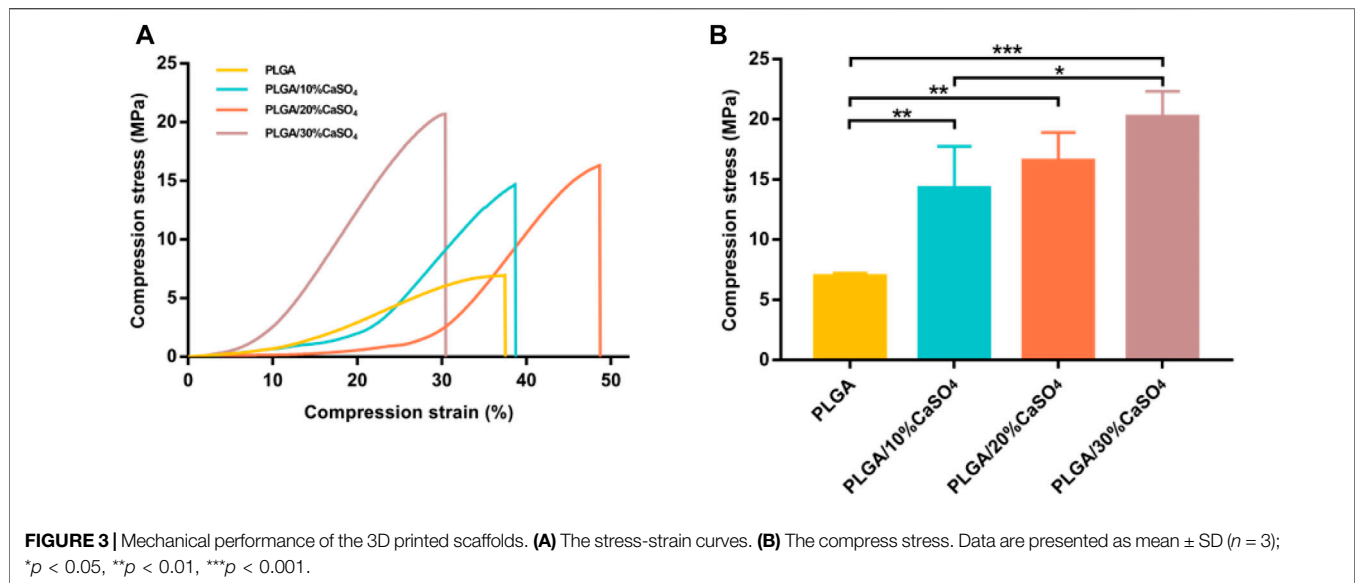


**FIGURE 2 |** Characterization of the scaffolds. **(A)** Representative pictures of 3D printed PLGA, PLGA/10%CaSO<sub>4</sub>, PLGA/20%CaSO<sub>4</sub>, and PLGA/30%CaSO<sub>4</sub> scaffolds. Scale bar = 5 mm. **(B)** SEM images of the side of the different scaffolds. Scale bar = 200 and 100  $\mu$ m, respectively. **(C)** Water contact angle images of different scaffolds. **(D)** Contact angle (degree) of PLGA, PLGA/10%CaSO<sub>4</sub>, PLGA/20%CaSO<sub>4</sub>, and PLGA/30%CaSO<sub>4</sub> scaffolds, respectively. **(E)** The pore size of each scaffold. Data are presented as mean  $\pm$  SD ( $n = 3$ ); \* $p < 0.05$ , \*\* $p < 0.01$ , \*\*\* $p < 0.001$ .





(Sivashanmugam et al., 2017), which facilitated cell adhesion and migration (Kim D.-S. et al., 2021).

The water contact angle test was performed to evaluate the surface hydrophilicity of the scaffolds. **Figure 2C** showed the contact angle images of each scaffold. Due to the intrinsic hydrophobicity of PLGA (Zhu et al., 2022), the water contact angle of the PLGA scaffold was  $94.88 \pm 3.20^\circ$ , while the contact angle of PLGA/10%CaSO<sub>4</sub>, PLGA/20%CaSO<sub>4</sub>, and PLGA/30%CaSO<sub>4</sub> were  $86.57 \pm 3.30^\circ$ ,  $85.33 \pm 5.47^\circ$ , and  $84.75 \pm 4.91^\circ$ , respectively (**Figure 2D**). The incorporation of CaSO<sub>4</sub> decreased the contact angle of the scaffolds. Thus, CaSO<sub>4</sub> improved the hydrophilicity of the composite scaffold. Considering that the hydrophilicity of the materials played an important role in protein absorption and cell proliferation (Liu et al., 2018), the improvement in the hydrophilicity of the PLGA/CaSO<sub>4</sub> scaffold may determine the subsequent cellular behavior.

Excellent mechanical properties are essential for scaffolds. Hence, we performed compress tests on different groups of

scaffolds. As shown in **Figure 3A**, PLGA scaffolds had minimum compress stress. **Figure 3B** showed the compressive strength of the scaffolds. The compressive strength of the PLGA scaffold was 6.95 MPa. After adding different CaSO<sub>4</sub> content, the compression stress of the scaffolds had improved, which were 14.27, 16.54, and 20.21 MPa, respectively. The scaffolds made with 30% CaSO<sub>4</sub> exhibited maximum compressive stress. When CaSO<sub>4</sub> is combined with H<sub>2</sub>O, a hydration reaction can occur to form needle-like calcium sulfate dihydrate whiskers. These whiskers bridge and stack with each other to solidify into deposits of a certain shape and strength, which has better mechanical properties (Chiang et al., 2021). Therefore, CaSO<sub>4</sub> could enhance the mechanical properties when combined with polymer materials, enable the material to withstand greater deformation, and give it better mechanical properties (Zhao et al., 2008). The result indicated that the addition of CaSO<sub>4</sub> could greatly enhance the mechanical properties of the PLGA scaffold to bear loads.

The changes in the chemical structure of the composite before and after the addition of CaSO<sub>4</sub> could be observed in the FTIR spectra. As shown in **Supplementary Figure S2**, PLGA spectrum showed an intense peak of characteristic carbonyl (C=O) at  $1,850 \text{ cm}^{-1}$ . In the same spectrum could also be observed a characteristic peak of the C-C(=O)-O at  $1,150 \text{ cm}^{-1}$  (Fernandes et al., 2017; Chen et al., 2021). After adding CaSO<sub>4</sub>, the PLGA/CaSO<sub>4</sub> peaks became less intense and narrow, showing a decrease in the PLGA ratio. The XRD patterns (**Supplementary Figure S3**) of the PLGA/CaSO<sub>4</sub> scaffolds showed characteristic crystalline peaks at 15, 25, 30, 31, and  $48^\circ$  corresponding to (200), (020), (002), (102), and (302) planes of CaSO<sub>4</sub> (Sindhura et al., 2014; Zhu et al., 2022). These characteristic peaks of the CaSO<sub>4</sub> in the scaffolds intensified with the increasing proportion of the CaSO<sub>4</sub>, thereby indicating the successful doping of the CaSO<sub>4</sub> into the PLGA/CaSO<sub>4</sub> scaffold. The swelling ratio represents the ability of the material to absorb water. As shown in **Supplementary Figure S4**, the swelling ratio

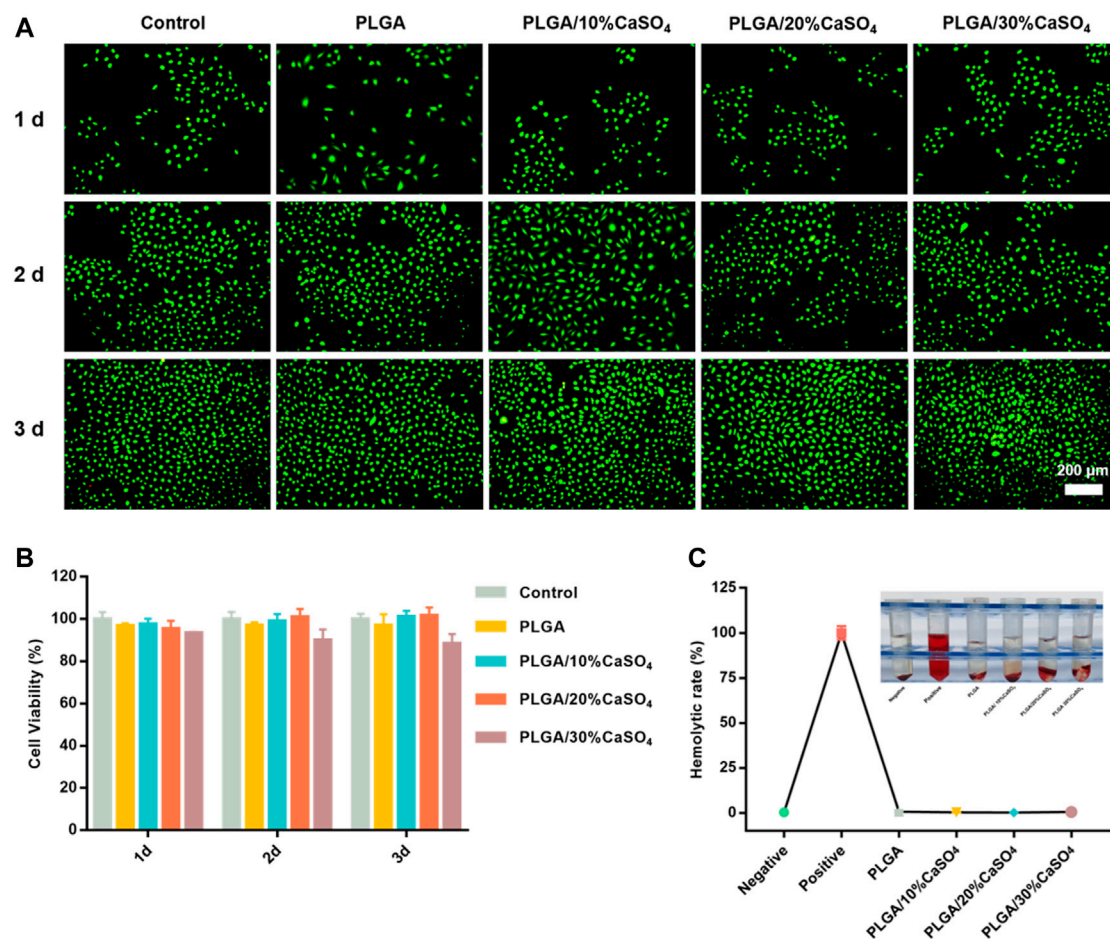


**FIGURE 5 |** *In vitro* biocompatibility. **(A)** Representative fluorescence images for HUVEC cells cultured with different scaffolds. Live cells were stained by calcein-AM (green color). Scale bar = 200  $\mu$ m. **(B)** CCK-8 assay for HUVECs cultured with the PLGA, PLGA/10%CaSO<sub>4</sub>, PLGA/20%CaSO<sub>4</sub>, and PLGA/30%CaSO<sub>4</sub> scaffolds, respectively. **(C)** *In vitro* hemolysis of different scaffolds and Hemolytic rate (%). Data are presented as mean  $\pm$  SD ( $n = 3$ ); \* $p < 0.05$ , \*\* $p < 0.01$ , \*\*\* $p < 0.001$ .

of the different scaffolds was similar and had no statistical difference ( $p > 0.05$ ), indicating that the addition of CaSO<sub>4</sub> could not change the swelling of the scaffolds.

### 3.2 The *In Vitro* Degradation

The biodegradability of materials is highly beneficial for clinical applications since it could be able to prevent damage caused by secondary surgical removal (Li et al., 2021). An ideal biomimetic scaffold composed of biodegradable materials should provide proper mechanical support while degrading to non-toxic products being excreted from the body ultimately. The weight loss of scaffolds in SBF was evaluated to study the *in vitro* degradation (Figure 4). We found that all scaffolds degrade slowly in the first 6 days, which meant that the scaffold could provide effective support and protection for bone in the initial stage of bone defect repair (Qian et al., 2014; Tan et al., 2021; Xue et al., 2021). Subsequently, the degradation rate of the scaffolds accelerated in all groups. PLGA degraded fastest and could be completely degraded within 24 days, which was inconsistent with the rate of bone repair. This indicated that PLGA could not be used as

a scaffold alone to repair bone defects (Qian et al., 2014; Jia et al., 2016; Lai et al., 2019; Dos Santos et al., 2020; Kim H. D. et al., 2021). The degradation rate of PLGA/CaSO<sub>4</sub> scaffolds was decreased than that of PLGA. PLGA was completely degraded in 4 weeks and the degradation products were polylactic acid and glycolic acid. CaSO<sub>4</sub> was difficult to dissolve in water and it can combine with H<sub>2</sub>O to form calcium sulfate whiskers (Chiang et al., 2021). The whiskers were interconnected and stacked together to make their structure even tighter, which made CaSO<sub>4</sub> have a relatively slow degradation rate and can be completely degraded within 6 weeks. What's more, CaSO<sub>4</sub> mixed with PLGA can form a dense solid, which can slow down the degradation rate (Amirthalingam et al., 2021). The addition of CaSO<sub>4</sub> slowed down the degradation rate of PLGA (Arun Kumar et al., 2016). This indicated that CaSO<sub>4</sub> improved the degradation performance of PLGA scaffolds. The bone-bonding ability and *in vivo* bone bioactivity of bone repair materials could be evaluated by examining the ability of apatite to form on its surface in SBF (Kokubo and Takadama, 2006). Chan et al. (2004) observed that calcium sulfate could form apatite on the surface both in SBF and *in vivo*. The findings indicated that

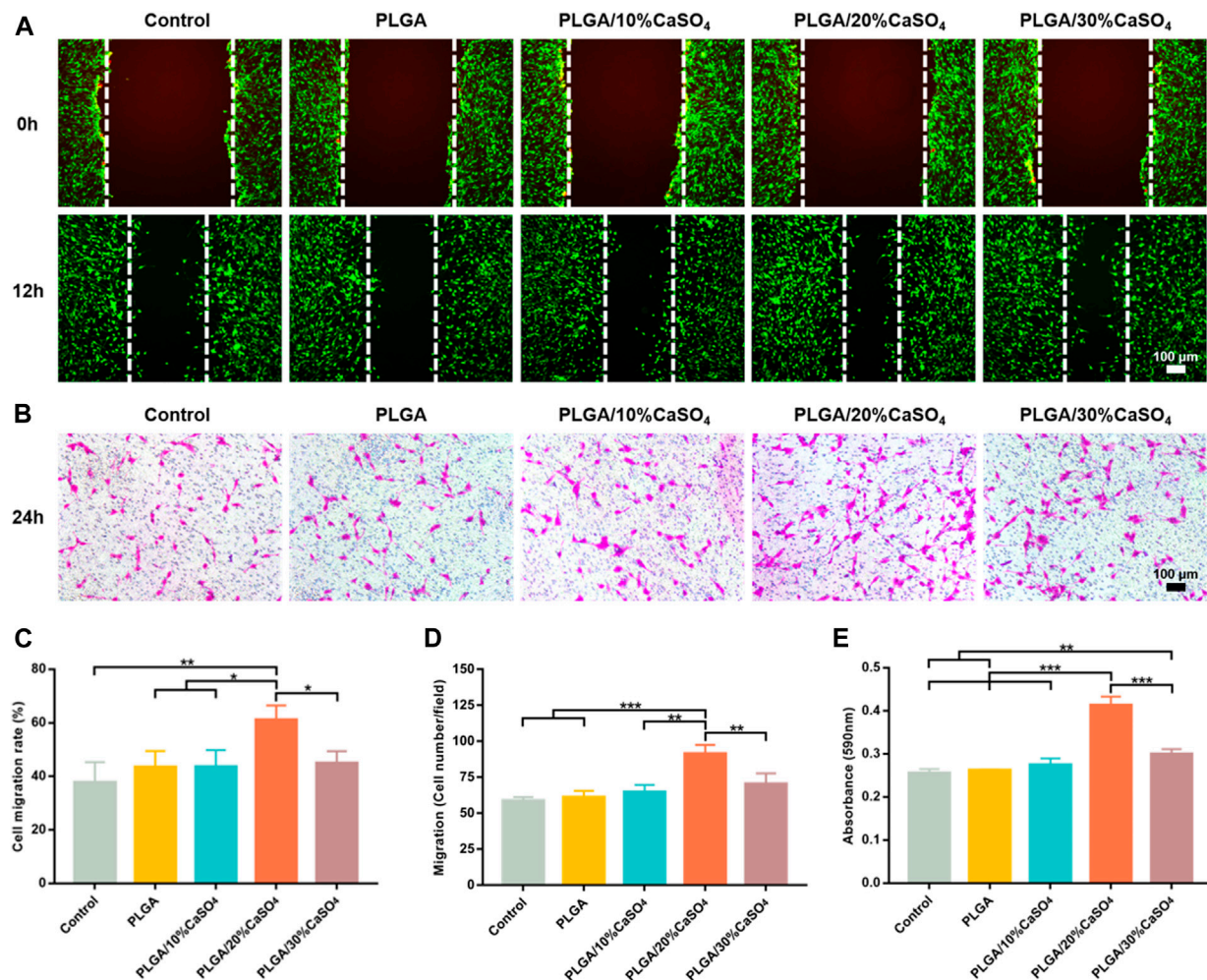


**FIGURE 6 |** *In vitro* cell migration. **(A)** *In vitro* wound healing assay of MC3T3-E1 cell. Scale bar = 100  $\mu$ m. **(B)** Transwell assay of MC3T3-E1 cells. Scale bar = 100  $\mu$ m. **(C)** Cell migration rate (%) of cells. **(D)** Cell migration number of MC3T3-E1 cells per field. **(E)** Absorbance at 590 nm. Data are presented as mean  $\pm$  SD ( $n = 3$ ); \* $p < 0.05$ , \*\* $p < 0.01$ , \*\*\* $p < 0.001$ .

calcium sulfate precipitation as carbonate-containing hydroxyapatite and its surface apatite formation in SBF could enhance the acellular and bone bioactivity. Hence, the addition of CaSO<sub>4</sub> would promote the formation of apatite on the scaffolds and enhance the acellular bioactivity.

### 3.3. *In Vitro* Biocompatibility

Biocompatibility is an important indicator for the clinical use of biomaterials in orthopedics. Therefore, biocompatibility assessment is an important part of biomedical materials and a primary requirement for the development of biomaterials. First, HUVECs proliferation in different scaffolds was evaluated by CCK-8 assay. As shown in **Figure 5B**, the scaffolds had good cell viability after incubating with HUVEC cells for 1, 2, and 3 days. However, PLGA/30%CaSO<sub>4</sub> scaffolds had the lowest cell viability rate. This might be because Ca<sup>2+</sup> was the second messenger in cells, and excessive Ca<sup>2+</sup> affects cell signaling, thereby inhibiting cell proliferation and migration (Teparat-Burana et al., 2015). We

further evaluated the biocompatibility by live/dead staining assay (**Figure 5A**). HUVEC cells indicated by green fluorescence were still alive after incubating with different scaffolds for 1, 2, and 3 days. The number of cells in control, PLGA, PLGA/10%CaSO<sub>4</sub>, PLGA/20%CaSO<sub>4</sub>, and PLGA/30%CaSO<sub>4</sub> groups increased with the culturing time, suggesting that the scaffolds had non-toxicity to HUVEC cells. Hemolysis rate is another indicator to evaluate the biocompatibility of materials (Li et al., 2021). Hemolysis experiment results showed that the supernatant in the positive control group turned red because the relatively low osmotic pressure caused a large number of erythrocytes to rupture (**Figure 5C**) (Li et al., 2021). While the supernatant in the negative control group and the scaffold groups was still clear, demonstrating that almost no red blood cells were broken. In addition, the hemolysis ratio of the different scaffolds was less than 5%, which met the requirements for the hemolysis rate of medical materials (Tang et al., 2020). These observations suggested that PLGA, PLGA/10%CaSO<sub>4</sub>, PLGA/20%CaSO<sub>4</sub>, and PLGA/30%CaSO<sub>4</sub> scaffolds had good biocompatibility.



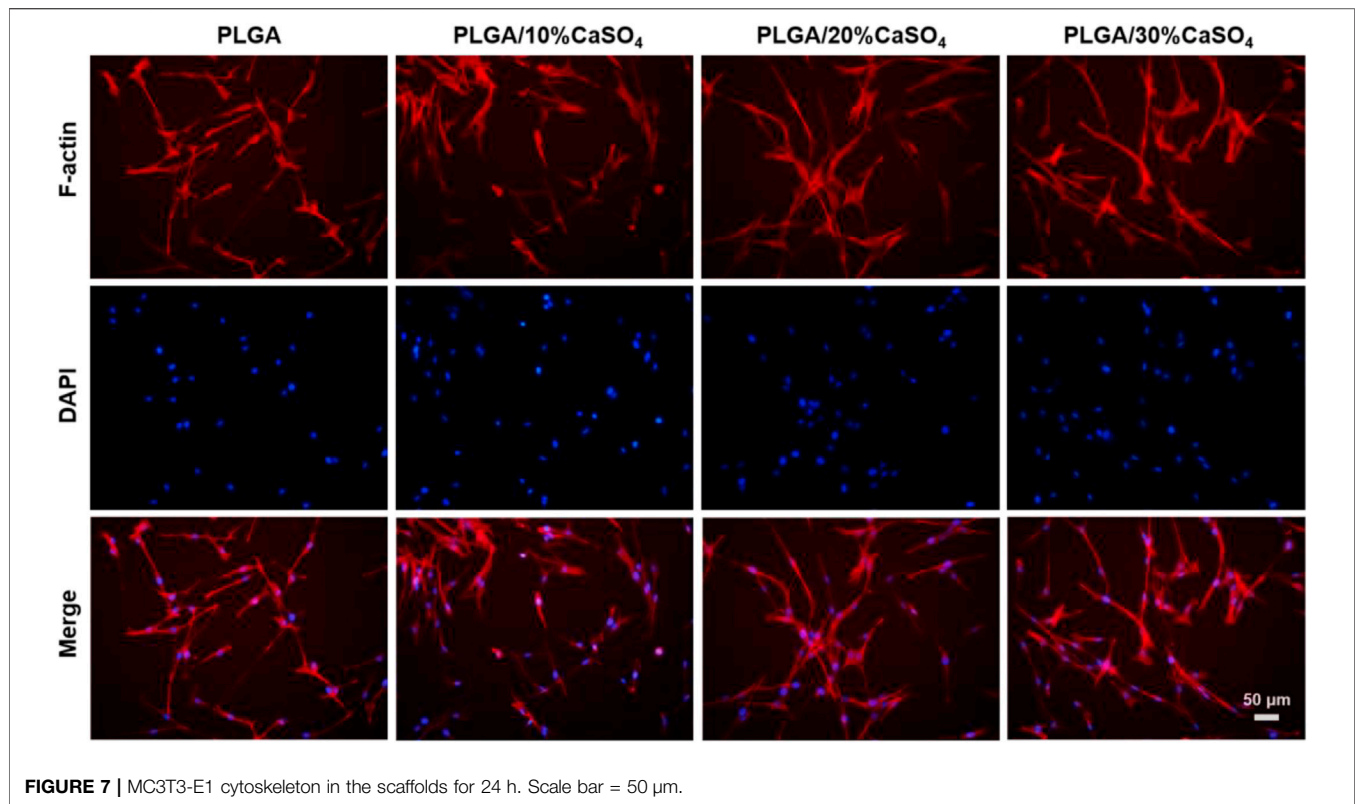


**FIGURE 7 |** MC3T3-E1 cytoskeleton in the scaffolds for 24 h. Scale bar = 50 μm.

### 3.4 In Vitro Cell Migration and Adhesion

The repair of bone defects depends on the proliferation and migration of cells, so the ideal bone repair material should be able to promote the migration of osteoblasts. Wound healing assay and transwell assay were used to simulate the effect of scaffolds on osteoblast migration. As shown in **Figure 6A**, compared with control, PLGA, PLGA/10%CaSO<sub>4</sub>, and PLGA/30%CaSO<sub>4</sub> groups, PLGA/20%CaSO<sub>4</sub> could significantly promote MC3T3-E1 cells migration. **Figure 6C** showed that the PLGA/20%CaSO<sub>4</sub> group had the highest cell migration rate (61.16%). The transwell assay (**Figure 6B**) also showed that PLGA/20%CaSO<sub>4</sub> group had the highest number of cell migrations per field (**Figure 6D**). What's more, compared with other groups, PLGA/20%CaSO<sub>4</sub> group had a higher OD value (**Figure 6E**). Calcium sulfate as a bone graft material had osteoconductive properties, completely degradable. CaSO<sub>4</sub> promotes cell migration in a concentration-dependent manner. It recruits cells to migrate to sites with high concentrations of CaSO<sub>4</sub>. But CaSO<sub>4</sub> to promote cell migration requires a suitable concentration range. When calcium levels exceed this range, cell migration is inhibited (Arun Kumar et al., 2016; Aquino-Martínez et al., 2017). What's more, excessive calcium ions will affect cell proliferation, and cell migration will also be affected when the number of cell proliferation is reduced (Teparat-Burana et al., 2015), which was consistent with the results of *in vitro* biocompatibility. The PLGA/20%CaSO<sub>4</sub> scaffold had the highest cell viability, while the cell viability in PLGA/30%CaSO<sub>4</sub> decreased compared with 20%. Therefore, scaffolds in

the 20% group had a strong ability to promote cell migration, which plays a critical role in bone reconstruction.

We also carried out the cytoskeleton staining to evaluate the cell extension and adhesion on the scaffolds (**Figure 7**), which showed spindle MC3T3-E1 cells presented well-stretch morphology and favorable proliferation status on PLGA/10%CaSO<sub>4</sub>, PLGA/20%CaSO<sub>4</sub>, and PLGA/30%CaSO<sub>4</sub> scaffolds than on PLGA scaffold. Moreover, the number of adhered cells on the surface of the PLGA/10%CaSO<sub>4</sub>, PLGA/20%CaSO<sub>4</sub>, and PLGA/30%CaSO<sub>4</sub> scaffolds were more than that of PLGA scaffolds, and the number and distribution density of actin microfilaments in the cytoskeleton were also more than those on the surface of PLGA scaffolds. Spreading and differentiation of cells were particularly affected by microscopic roughness and hydrophilicity. Hydrophilic biomaterial surfaces could promote cell growth and improve biocompatibility. Besides, CaSO<sub>4</sub> could promote cell proliferation, extension, and adhesion (Phang et al., 2004). Thus, the PLGA/CaSO<sub>4</sub> scaffold constructed by adding CaSO<sub>4</sub> with PLGA had good properties to promote cell expansion and adhesion due to the improvement of surface hydrophilicity.

### 3.5 Evaluation of Osteogenic Differentiation In Vitro

Osteogenic differentiation property is the key to evaluating the success of a biomaterial (Huan and Chang, 2007; Ma L. et al., 2018; Wang et al., 2018; Freeman et al., 2019). We detected the osteogenic differentiation of the different scaffolds based on ALP staining, ALP activity assay, alizarin red staining, and osteogenesis-related



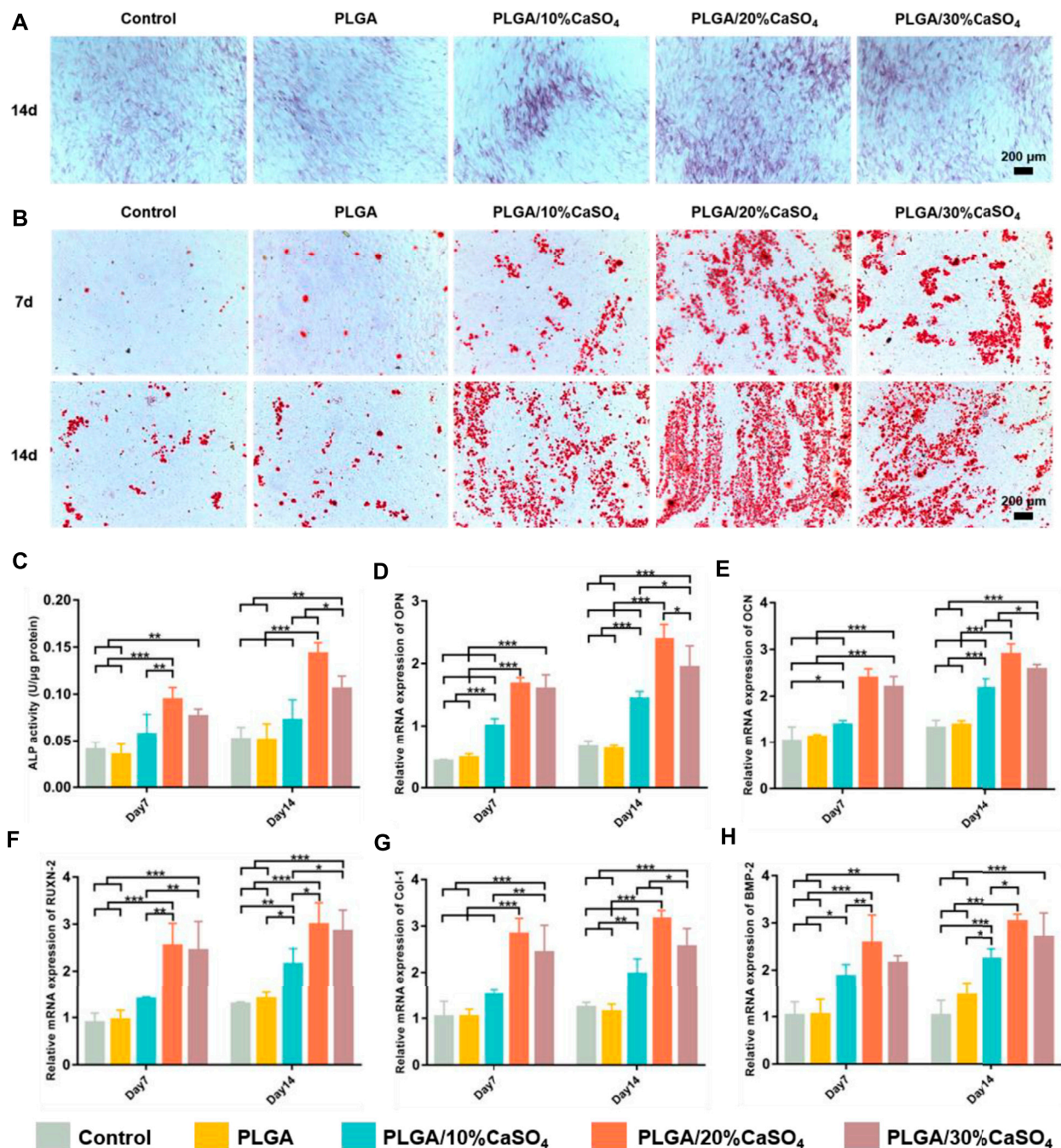


**FIGURE 8 |** *In vitro* osteogenesis capability of the scaffolds. **(A)** ALP staining. Scale bar = 200  $\mu$ m. **(B)** Staining area of Alizarin red. Scale bar = 200  $\mu$ m. **(C)** The ALP activity of the MC3T3-E1 cells co-cultured with the scaffolds on days 7 and 14. ALP level was significantly high in the PLGA/20%CaSO<sub>4</sub> scaffolds compared to the other scaffolds. **(D–H)** Relative mRNA expression of the osteogenic genes (OPN, OCN, RUNX-2, Collagen I, and BMP-2). Data are presented as mean  $\pm$  SD ( $n = 3$ ); \* $p < 0.05$ , \*\* $p < 0.01$ , \*\*\* $p < 0.001$ .

genes expression. As an important early osteogenic enzyme during osteogenesis, the activity of ALP was represented as a typical marker of osteogenic differentiation (Yin et al., 2019; Li M. et al., 2020; Zhai et al., 2021). ALP staining result was shown in **Figure 8A**. It was found that the PLGA/20%CaSO<sub>4</sub> exhibited deeper dyeing than other groups on day 14. This indicated that more ALP was produced in the

PLGA/20%CaSO<sub>4</sub> group. The ALP activity of the MC3T3-E1 cells in the PLGA/20%CaSO<sub>4</sub> and PLGA/30%CaSO<sub>4</sub> groups was significantly higher than in other groups on day 7 (**Figure 8C**). And the ALP activity in the PLGA/20%CaSO<sub>4</sub> group was significantly higher than in other groups on day 14. Therefore, compared with other groups, PLGA/20%CaSO<sub>4</sub> group can effectively promote the

production of ALP, which was consistent with the above results of ALP staining. **Figure 8B** showed the results of Alizarin staining on days 7 and 14. Compared with the control group and PLGA group, PLGA/10%CaSO<sub>4</sub>, PLGA/20%CaSO<sub>4</sub>, and PLGA/30%CaSO<sub>4</sub> group scaffolds could promote the production of calcium nodules. Cells cultured with PLGA/20%CaSO<sub>4</sub> scaffold had the largest red staining area and the most calcium nodules compared with the other groups.

Moreover, we examined the expression levels of several critical osteogenic genes including OPN, OCN, RUNX-2, Collagen I, and BMP-2. As shown in **Figures 8D–H**, the expression levels of BMP-2, Col-1, RUNX-2, and OCN genes in PLGA/20%CaSO<sub>4</sub> and PLGA/30%CaSO<sub>4</sub> groups were higher than in other groups on day 7, and the expression level of OPN in the PLGA/20%CaSO<sub>4</sub> group was the highest at day 7. And the expression levels of all these genes in the PLGA/20%CaSO<sub>4</sub> group were higher than in other groups on day 14. These results suggested that CaSO<sub>4</sub> could promote osteogenic differentiation *in vitro*, which could make up for the lack of osteogenic induction activity of PLGA (Du et al., 2018; Kim D.-S. et al., 2021). And PLGA/20%CaSO<sub>4</sub> scaffold had the best osteogenic performance among all the scaffolds we constructed.

Calcium sulfate is the most commonly used bone repair material in clinical, which can cause changes in local calcium ions concentration after implantation, thereby regulating the process of bone tissue regeneration. As an intracellular second messenger and an important signaling molecule, Ca<sup>2+</sup> controls many key processes in cells, including proliferation, migration, and differentiation (Teparat-Burana et al., 2015). Ca<sup>2+</sup> is released during CaSO<sub>4</sub> degradation Ca<sup>2+</sup> can bind to calmodulin (CaM) to Ca<sup>2+</sup>-CaM form complexes and promote osteoblast differentiation and matrix mineralization through corresponding signaling pathways (Cao et al., 2022). The favorable osteogenic property of CaSO<sub>4</sub> could improve the insufficient osteoinductive activity of polymer materials (Du et al., 2018; Kim H. D. et al., 2021). As mentioned above, we think that the incorporation of CaSO<sub>4</sub> in the PLGA scaffolds provides Ca<sup>2+</sup> ions that might enhance the osteogenic differentiation of cells. In addition, the prepared PLGA/CaSO<sub>4</sub> scaffolds improved the hydrophilicity of the scaffold surface, which was more conducive to cell proliferation and adhesion on the scaffold, and further promoted osteogenic differentiation.

## 4 CONCLUSION

We fabricated PLGA/CaSO<sub>4</sub> scaffolds of different proportions by 3D printing and then evaluated their properties. Physical performance tests showed that adding CaSO<sub>4</sub> into the PLGA scaffold improved the mechanical properties of the scaffold and made the surface of the scaffold rougher. *In vitro* cytotoxicity experiments showed that PLGA, PLGA/10%CaSO<sub>4</sub>, PLGA/20%CaSO<sub>4</sub>, and PLGA/30%CaSO<sub>4</sub> groups had good biocompatibility. In addition, the PLGA/20%CaSO<sub>4</sub> scaffold also promoted the migration of MC3T3-E1 cells. *In vitro* osteogenic experiments showed that PLGA/10%CaSO<sub>4</sub>, PLGA/20%CaSO<sub>4</sub>, and PLGA/30%CaSO<sub>4</sub> scaffolds had osteogenic properties. Among them, PLGA/20%CaSO<sub>4</sub> scaffolds significantly promoted the new bone formation *in vitro*. The whisker formed by the combination of CaSO<sub>4</sub> and H<sub>2</sub>O can make its structure even tighter. The mechanical and degradation

properties of PLGA were improved when combined with CaSO<sub>4</sub> thanks to its tight structure. The rough surface of CaSO<sub>4</sub> was conducive to cell migration and extension, so PLGA/CaSO<sub>4</sub> scaffolds could promote cell migration compared with PLGA scaffolds. And CaSO<sub>4</sub> could also make up for the lack of osteogenic induction activity of PLGA due to its good osteogenesis properties. Therefore, CaSO<sub>4</sub> could significantly improve the performance of the PLGA scaffold. Among them, PLGA/20%CaSO<sub>4</sub> showed the best overall performance. In summary, PLGA/20%CaSO<sub>4</sub> scaffolds were promising for bone tissue engineering applications.

## DATA AVAILABILITY STATEMENT

The original contributions presented in the study are included in the article/**Supplementary Material**, further inquiries can be directed to the corresponding authors.

## AUTHOR CONTRIBUTIONS

TL: Conceptualization, Methodology, Data curation, Visualization, and Writing-original draft preparation. ZhL: Conceptualization, Software, Investigation, and Methodology. LZ: Conceptualization, Methodology, Data curation. ZC: Supervision, Project administration, and Data curation. ZeL: Conceptualization, Investigation, Methodology, and Data curation. BL: Supervision, Project administration, and Data curation. ZF: Conceptualization, Investigation, Methodology, and Data curation. PJ: Supervision, Project administration, and Data curation. JZ: Supervision, Project administration, and Data curation. ZW: Supervision, Project administration, and Data curation. HW: Project administration and Investigation. XX: Supervision, Funding acquisition, Writing—review and editing. XY: Supervision, Funding acquisition, Writing—review and editing. YZ: Supervision, Funding acquisition, Writing—review and editing.

## FUNDING

This work was supported by the Research Program of PLA (No. 20WQ030 and 2021NZC026); Natural Science Foundation of Guangdong Province of China (No. 2021A1515011545); Science and Technology Innovation Strategy Special Fund of Guangdong Province (No. 2021B1111610007); the National Natural Science Foundation of China (No. 81972080); the Research Foundation of Medical Science and Technology of Guangdong Province (No. 2020112693915296); the Science and Technology Planning Project of Guangdong Province (No. 2017B030314139).

## SUPPLEMENTARY MATERIAL

The Supplementary Material for this article can be found online at: <https://www.frontiersin.org/articles/10.3389/fbioe.2022.874931/full#supplementary-material>

## REFERENCES

- Adithya, S. P., Sidharthan, D. S., Abhinandan, R., Balagangadharan, K., and Selvamurugan, N. (2020). Nanosheets-incorporated Bio-Composites Containing Natural and Synthetic Polymers/ceramics for Bone Tissue Engineering. *Int. J. Biol. Macromol.* 164, 1960–1972. doi:10.1016/j.ijbiomac.2020.08.053
- Amirthalingam, S., Lee, S. S., Rajendran, A. K., Kim, I., Hwang, N. S., and Rangasamy, J. (2021). Addition of Lactoferrin and Substance P in a chitin/PLGA-CaSO<sub>4</sub> Hydrogel for Regeneration of Calvarial Bone Defects. *Mater. Sci. Eng. C* 126, 112172. doi:10.1016/j.msec.2021.112172
- Aquino-Martínez, R., Angelo, A. P., and Pujol, F. V. (2017). Calcium-containing Scaffolds Induce Bone Regeneration by Regulating Mesenchymal Stem Cell Differentiation and Migration. *Stem Cell Res. Ther.* 8 (1), 265. doi:10.1186/s13287-017-0713-0
- Arun Kumar, R., Sivashanmugam, A., Deepthi, S., Bumgardner, J. D., Nair, S. V., and Jayakumar, R. (2016). Nano-fibrin Stabilized CaSO<sub>4</sub> Crystals Incorporated Injectable Chitin Composite Hydrogel for Enhanced Angiogenesis & Osteogenesis. *Carbohydr. Polym.* 140, 144–153. doi:10.1016/j.carbpol.2015.11.074
- Bose, S., and Sarkar, N. (2020). Natural Medicinal Compounds in Bone Tissue Engineering. *Trends Biotechnol.* 38 (4), 404–417. doi:10.1016/j.tibtech.2019.11.005
- Cao, R., Xu, Y., Xu, Y., Brand, D. D., Zhou, G., Xiao, K., et al. (2022). Development of Tri-Layered Biomimetic Atelocollagen Scaffolds with Interfaces for Osteochondral Tissue Engineering. *Adv. Healthc. Mater.* 8, e2101643. doi:10.1002/adhm.202101643
- Chan, H., Mijares, D., and Ricci, J. L. (2004). “In Vitro dissolution of Calcium Sulfate: Evidence of Bioactivity,” in Transactions-7th World Biomaterials Congress, Sydney, Australia, 17–21 May, 2004.
- Chen, I.-C., Su, C.-Y., Lai, C.-C., Tsou, Y.-S., Zheng, Y., and Fang, H.-W. (2021). Preparation and Characterization of Moldable Demineralized Bone Matrix/Calcium Sulfate Composite Bone Graft Materials. *Jfb* 12 (4), 56. doi:10.3390/jfb12040056
- Cheng, T., Qu, H., Zhang, G., and Zhang, X. (2018). Osteogenic and Antibacterial Properties of Vancomycin-Laden Mesoporous Bioglass/PLGA Composite Scaffolds for Bone Regeneration in Infected Bone Defects. *Artif. Cells, Nanomedicine, Biotechnol.* 46 (8), 1–13. doi:10.1080/21691401.2017.1396997
- Chiang, C.-C., Hsieh, M.-K., Wang, C.-Y., Tuan, W.-H., and Lai, P.-L. (2021). Cytotoxicity and Cell Response of Preosteoblast in Calcium Sulfate-Augmented PMMA Bone Cement. *Biomed. Mat.* 16 (5), 055014. doi:10.1088/1748-605X/ac1ab5
- Cui, Y., Zhu, T., Li, A., Liu, B., Cui, Z., Qiao, Y., et al. (2018). Porous Particle-Reinforced Bioactive Gelatin Scaffold for Large Segmental Bone Defect Repairing. *ACS Appl. Mat. Interfaces* 10 (8), 6956–6964. doi:10.1021/acsami.7b19010
- Cui, Z.-K., Kim, S., Baljon, J. J., Wu, B. M., Aghaloo, T., and Lee, M. (2019). Microporous Methacrylated Glycol Chitosan-Montmorillonite Nanocomposite Hydrogel for Bone Tissue Engineering. *Nat. Commun.* 10 (1), 3523. doi:10.1038/s41467-019-11511-3
- Daly, A. C., Freeman, F. E., Gonzalez-Fernandez, T., Critchley, S. E., Nulty, J., and Kelly, D. J. (2017). 3D Bioprinting for Cartilage and Osteochondral Tissue Engineering. *Adv. Healthc. Mat.* 6 (22), 1700298. doi:10.1002/adhm.201700298
- Dos Santos, V. I., Merlini, C., Aragones, Á., Cesca, K., and Fredel, M. C. (2020). In Vitro evaluation of Bilayer Membranes of PLGA/hydroxyapatite/ $\beta$ -tricalcium Phosphate for Guided Bone Regeneration. *Mater. Sci. Eng. C* 112, 110849. doi:10.1016/j.msec.2020.110849
- Du, X., Yu, B., Pei, P., Ding, H., Yu, B., and Zhu, Y. (2018). 3D Printing of pearl/CaSO<sub>4</sub> composite Scaffolds for Bone Regeneration. *J. Mat. Chem. B* 6 (3), 499–509. doi:10.1039/c7tb02667f
- Fernandes, K. R., Magri, A. M. P., Kido, H. W., Parisi, J. R., Assis, L., Fernandes, K. P. S., et al. (2017). Biosilicate/PLGA Osteogenic Effects Modulated by Laser Therapy: In Vitro and In Vivo Studies. *J. Photochem. Photobiol. B* 173, 258–265. doi:10.1016/j.jphotobiol.2017.06.002
- Fm, A., Chang, C., and Yw, C. (2021). Mechanical Behavior of Calcium Sulfate Whisker-Reinforced Paraffin/gypsum Composites. *Constr. Build. Mater.* 305, 124795. doi:10.1016/j.conbuildmat.2021.124795
- Freeman, S., Ramos, R., AlexisChando, P., Zhou, L., Reeser, K., Jin, S., et al. (2019). A Bioink Blend for Rotary 3D Bioprinting Tissue Engineered Small-Diameter Vascular Constructs. *Acta Biomater.* 95, 152–164. doi:10.1016/j.actbio.2019.06.052
- Gao, C., Feng, P., Peng, S., and Shuai, C. (2017). Carbon Nanotube, Graphene and Boron Nitride Nanotube Reinforced Bioactive Ceramics for Bone Repair. *Acta Biomater.* 61, 1–20. doi:10.1016/j.actbio.2017.05.020
- Gu, J., Zhang, Q., Geng, M., Wang, W., Yang, J., Khan, A. u. R., et al. (2021). Construction of Nanofibrous Scaffolds with Interconnected Perfusible Microchannel Networks for Engineering of Vascularized Bone Tissue. *Bioact. Mater.* 6 (10), 3254–3268. doi:10.1016/j.bioactmat.2021.02.033
- Han, P., Gomez, G. A., Duda, G. N., Ivanovski, S., and Poh, P. S. P. (2022). Scaffold Geometry Modulation of Mechanotransduction and its Influence on Epigenetics. *Acta Biomater.* 15 (22), S174200021–S174200616. doi:10.1016/j.actbio.2022.01.020
- Hu, J., Wang, Z., Miszuk, J. M., Zhu, M., Lansakara, T. I., Tivanski, A. V., et al. (2021). Vanillin-bioglass Cross-Linked 3D Porous Chitosan Scaffolds with Strong Osteopromotive and Antibacterial Abilities for Bone Tissue Engineering. *Carbohydr. Polym.* 271, 118440. doi:10.1016/j.carbpol.2021.118440
- Huan, Z., and Chang, J. (2007). Self-setting Properties and In Vitro Bioactivity of Calcium Sulfate Hemihydrate-Tricalcium Silicate Composite Bone Cements. *Acta Biomater.* 3 (6), 952–960. doi:10.1016/j.actbio.2007.05.003
- Ishikawa, K., Kawachi, G., Tsuru, K., and Yoshimoto, A. (2017). Fabrication of Calcite Blocks from Gypsum Blocks by Compositional Transformation Based on Dissolution-Precipitation Reactions in Sodium Carbonate Solution. *Mater. Sci. Eng. C* 72, 389–393. doi:10.1016/j.msec.2016.11.093
- Jia, P., Chen, H., Kang, H., Qi, J., Zhao, P., Jiang, M., et al. (2016). Deferoxamine Released from Poly(lactic-Co-Glycolic Acid) Promotes Healing of Osteoporotic Bone Defect via Enhanced Angiogenesis and Osteogenesis. *J. Biomed. Mat. Res.* 104 (10), 2515–2527. doi:10.1002/jbm.a.35793
- Jin, S., Xia, X., Huang, J., Yuan, C., Zuo, Y., Li, Y., et al. (2021). Recent Advances in PLGA-Based Biomaterials for Bone Tissue Regeneration. *Acta Biomater.* 127, 56–79. doi:10.1016/j.actbio.2021.03.067
- Kim, D.-S., Lee, J.-K., Kim, J. H., Lee, J., Kim, D. S., An, S., et al. (2021). Advanced PLGA Hybrid Scaffold with a Bioactive PDRN/BMP2 Nanocomplex for Angiogenesis and Bone Regeneration Using Human Fetal MSCs. *Sci. Adv.* 7 (50), eabj1083. doi:10.1126/sciadv.abj1083
- Kim, H. D., Amirthalingam, S., Kim, S. L., Lee, S. S., Rangasamy, J., and Hwang, N. S. (2017). Biomimetic Materials and Fabrication Approaches for Bone Tissue Engineering. *Adv. Healthc. Mat.* 6 (23), 1700612. doi:10.1002/adhm.201700612
- Kim, H. D., Hong, X., An, Y. H., Park, M. J., Kim, D. G., Greene, A. K., et al. (2021). A Biphasic Osteovascular Biomimetic Scaffold for Rapid and Self-Sustained Endochondral Ossification. *Adv. Healthc. Mater.* 10 (13), 2100070. doi:10.1002/adhm.202100070
- Kokubo, T., and Takadama, H. (2006). How Useful Is SBF in Predicting In Vivo Bone Bioactivity? *Biomaterials* 27 (15), 2907–2915. doi:10.1016/j.biomaterials.2006.01.017
- Kuss, M. A., Harms, R., Wu, S., Wang, Y., Untrauer, J. B., Carlson, M. A., et al. (2017). Short-term Hypoxic Preconditioning Promotes Prevascularization in 3D Bioprinted Bone Constructs with Stromal Vascular Fraction Derived Cells. *RSC Adv.* 7 (47), 29312–29320. doi:10.1039/c7ra04372d
- Lai, Y., Li, Y., Cao, H., Long, J., Wang, X., Li, L., et al. (2019). Osteogenic Magnesium Incorporated into PLGA/TCP Porous Scaffold by 3D Printing for Repairing Challenging Bone Defect. *Biomaterials* 197, 207–219. doi:10.1016/j.biomaterials.2019.01.013
- Lavanya, K., Chandran, S. V., Balagangadharan, K., and Selvamurugan, N. (2020). Temperature- and pH-Responsive Chitosan-Based Injectable Hydrogels for Bone Tissue Engineering. *Mater. Sci. Eng. C* 111, 110862. doi:10.1016/j.msec.2020.110862
- Lee, C. S., Hwang, H. S., Kim, S., Fan, J., Aghaloo, T., and Lee, M. (2020). Inspired by Nature: Facile Design of Nanoclay-Organic Hydrogel Bone Sealant with Multifunctional Properties for Robust Bone Regeneration. *Adv. Funct. Mat.* 30 (43), 2003717. doi:10.1002/adfm.202003717



- Li, H., Wang, H., Pan, J., Li, J., Zhang, K., Duan, W., et al. (2020). Nanoscaled Bionic Periosteum Orchestrating the Osteogenic Microenvironment for Sequential Bone Regeneration. *ACS Appl. Mat. Interfaces* 12 (33), 36823–36836. doi:10.1021/acsami.0c06906
- Li, M., Zhang, Z., Liang, Y., He, J., and Guo, B. (2020). Multifunctional Tissue-Adhesive Cryogel Wound Dressing for Rapid Nonpressing Surface Hemorrhage and Wound Repair. *ACS Appl. Mat. Interfaces* 12 (32), 35856–35872. doi:10.1021/acsami.0c08285
- Li Z., Z., Li, B., Li, X., Lin, Z., Chen, L., Chen, H., et al. (2021). Ultrafast *In-Situ* Forming Halloysite Nanotube-Doped Chitosan/oxidized Dextran Hydrogels for Hemostasis and Wound Repair. *Carbohydr. Polym.* 267, 118155. doi:10.1016/j.carbpol.2021.118155
- Liu, P., Sun, L., Liu, P., Yu, W., Zhang, Q., Zhang, W., et al. (2018). Surface Modification of Porous PLGA Scaffolds with Plasma for Preventing Dimensional Shrinkage and Promoting Scaffold-Cell/tissue Interactions. *J. Mat. Chem. B* 6 (46), 7605–7613. doi:10.1039/c8tb02374c
- Lu, H.-T., Lu, T.-W., Chen, C.-H., and Mi, F.-L. (2019). Development of Genipin-Crosslinked and Fucoidan-Adsorbed Nano-Hydroxyapatite/hydroxypropyl Chitosan Composite Scaffolds for Bone Tissue Engineering. *Int. J. Biol. Macromol.* 128, 973–984. doi:10.1016/j.ijbiomac.2019.02.010
- Ma, H., Feng, C., Chang, J., and Wu, C. (2018). 3D-printed Bioceramic Scaffolds: From Bone Tissue Engineering to Tumor Therapy. *Acta Biomater.* 79, 37–59. doi:10.1016/j.actbio.2018.08.026
- Ma, L., Cheng, S., Ji, X., Zhou, Y., Zhang, Y., Li, Q., et al. (2020). Immobilizing Magnesium Ions on 3D Printed Porous Tantalum Scaffolds with Polydopamine for Improved Vascularization and Osteogenesis. *Mater. Sci. Eng. C* 117, 111303. doi:10.1016/j.msec.2020.111303
- Ma, L., Wang, X., Zhao, N., Zhu, Y., Qiu, Z., Li, Q., et al. (2018). Integrating 3D Printing and Biomimetic Mineralization for Personalized Enhanced Osteogenesis, Angiogenesis, and Osteointegration. *ACS Appl. Mat. Interfaces* 10 (49), 42146–42154. doi:10.1021/acsami.8b17495
- Nulty, J., Freeman, F. E., Browe, D. C., Burdis, R., Ahern, D. P., Pitacco, P., et al. (2021). 3D Bioprinting of Prevascularised Implants for the Repair of Critically-Sized Bone Defects. *Acta Biomater.* 126, 154–169. doi:10.1016/j.actbio.2021.03.003
- Oizumi, I., Hamai, R., Shiwaku, Y., Mori, Y., Anada, T., Baba, K., et al. (2021). Impact of Simultaneous Hydrolysis of OCP and PLGA on Bone Induction of a PLGA-OCP Composite Scaffold in a Rat Femoral Defect. *Acta Biomater.* 124, 358–373. doi:10.1016/j.actbio.2021.01.048
- Oryan, A., and Sahviah, S. (2017). Effectiveness of Chitosan Scaffold in Skin, Bone and Cartilage Healing. *Int. J. Biol. Macromol.* 104 (Pt A), 1003–1011. doi:10.1016/j.ijbiomac.2017.06.124
- Pang, L., Zhao, R., Chen, J., Ding, J., Chen, X., Chai, W., et al. (2022). Osteogenic and Anti-tumor Cu and Mn-Doped Borosilicate Nanoparticles for Synergistic Bone Repair and Chemodynamic Therapy in Bone Tumor Treatment. *Bioact. Mater.* 12, 1–15. doi:10.1016/j.bioactmat.2021.10.030
- Pförringer, D., Harrasser, N., Mühlhofer, H., Kiöckli, M., Stemberger, A., van Griensven, M., et al. (2018). Osteoinduction and -conduction through Absorbable Bone Substitute Materials Based on Calcium Sulfate: *In Vivo* Biological Behavior in a Rabbit Model. *J. Mater. Sci. Mater. Med.* 29 (2), 17. doi:10.1007/s10856-017-6017-1
- Phang, M. Y., Ng, M. H., Tan, K. K., Aminuddin, B. S., Ruszymah, B. H., and Fauziah, O. (2004). Evaluation of Suitable Biodegradable Scaffolds for Engineered Bone Tissue. *Med. J. Malays.* 59 (Suppl. B), 198–199.
- Qian, J., Xu, W., Yong, X., Jin, X., and Zhang, W. (2014). Fabrication and *In Vitro* Biocompatibility of Biomimetic PLGA/nHA Composite Scaffolds for Bone Tissue Engineering. *Mater. Sci. Eng. C* 36, 95–101. doi:10.1016/j.msec.2013.11.047
- Qian, Y., Zhou, X., Zhang, F., Diekwisch, T. G. H., Luan, X., and Yang, J. (2019). Triple PLGA/PCL Scaffold Modification Including Silver Impregnation, Collagen Coating, and Electrospinning Significantly Improve Biocompatibility, Antimicrobial, and Osteogenic Properties for Orofacial Tissue Regeneration. *ACS Appl. Mat. Interfaces* 11 (41), 37381–37396. doi:10.1021/acsami.9b07053
- Ranganathan, S., Balagangadharan, K., and Selvamurugan, N. (2019). Chitosan and Gelatin-Based Electrospun Fibers for Bone Tissue Engineering. *Int. J. Biol. Macromol.* 133, 354–364. doi:10.1016/j.ijbiomac.2019.04.115
- Sindhura Reddy, N., Sowmya, S., Bumgardner, J. D., Chennazhi, K. P., Biswas, R., and Jayakumar, R. (2014). Tetracycline Nanoparticles Loaded Calcium Sulfate Composite Beads for Periodontal Management. *Biochimica Biophysica Acta (BBA) - General Subj.* 1840 (6), 2080–2090. doi:10.1016/j.bbagen.2014.02.007
- Singh, B. N., Veeresh, V., Mallick, S. P., Jain, Y., Sinha, S., Rastogi, A., et al. (2019). Design and Evaluation of Chitosan/chondroitin Sulfate/nano-Bioglass Based Composite Scaffold for Bone Tissue Engineering. *Int. J. Biol. Macromol.* 133, 817–830. doi:10.1016/j.ijbiomac.2019.04.107
- Sivashanmugam, A., Charoenlarp, P., Deepthi, S., Rajendran, A., Nair, S. V., Iseki, S., et al. (2017). Injectable Shear-Thinning CaSO<sub>4</sub>/FGF-18-Incorporated Chitin-PLGA Hydrogel Enhances Bone Regeneration in Mice Cranial Bone Defect Model. *ACS Appl. Mat. Interfaces* 9 (49), 42639–42652. doi:10.1021/acsami.7b15845
- Tan, S., Wang, Y., Du, Y., Xiao, Y., and Zhang, S. (2021). Injectable Bone Cement with Magnesium-Containing Microspheres Enhances Osteogenesis via Anti-inflammatory Immunoregulation. *Bioact. Mater.* 6 (10), 3411–3423. doi:10.1016/j.bioactmat.2021.03.006
- Tang, Q., Lim, T., Wei, X.-J., Wang, Q.-Y., Xu, J.-C., Shen, L.-Y., et al. (2020). A Free-Standing Multilayer Film as a Novel Delivery Carrier of Platelet Lysates for Potential Wound-Dressing Applications. *Biomaterials* 255, 120138. doi:10.1016/j.biomaterials.2020.120138
- Teparat-Burana, T., Onsiri, N., and Jantararat, J. (2015). Cytotoxicity and Migration of Fibroblasts on Two Types of Calcium Sulfate Dihydrate. *J. Invest. Clin. Dent.* 8 (1), e12177. doi:10.1111/jicd.12177
- Wang, L., Zhu, L.-x., Wang, Z., Lou, A.-j., Yang, Y.-x., Guo, Y., et al. (2018). Development of a Centrally Vascularized Tissue Engineering Bone Graft with the Unique Core-Shell Composite Structure for Large Femoral Bone Defect Treatment. *Biomaterials* 175, 44–60. doi:10.1016/j.biomaterials.2018.05.017
- Wei, J., Yan, Y., Gao, J., Li, Y., Wang, R., Wang, J., et al. (2021). 3D-printed Hydroxyapatite Microspheres Reinforced PLGA Scaffolds for Bone Regeneration. *Mater. Sci. Eng. C* 23, 112618. doi:10.1016/j.msec.2021.112618
- Wu, N., Liu, J., Ma, W., Dong, X., Wang, F., Yang, D., et al. (2021). Degradable Calcium Deficient Hydroxyapatite/poly(lactic-Glycolic Acid Copolymer) Bilayer Scaffold through Integral Molding 3D Printing for Bone Defect Repair. *Biofabrication* 13 (2), 025005. doi:10.1088/1758-5090/abcb48
- Xia, Y., Sun, J., Zhao, L., Zhang, F., Liang, X.-J., Guo, Y., et al. (2018). Magnetic Field and Nano-Scaffolds with Stem Cells to Enhance Bone Regeneration. *Biomaterials* 183, 151–170. doi:10.1016/j.biomaterials.2018.08.040
- Xue, Y., Zhu, Z., Zhang, X., Chen, J., Yang, X., Gao, X., et al. (2021). Accelerated Bone Regeneration by MOF Modified Multifunctional Membranes through Enhancement of Osteogenic and Angiogenic Performance. *Adv. Healthc. Mat.* 10 (6), 2001369. doi:10.1002/adhm.202001369
- Yan, Y., Chen, H., Zhang, H., Guo, C., Yang, K., Chen, K., et al. (2019). Vascularized 3D Printed Scaffolds for Promoting Bone Regeneration. *Biomaterials* 190–191, 97–110. doi:10.1016/j.biomaterials.2018.10.033
- Yang, G., Liu, H., Cui, Y., Li, J., Zhou, X., Wang, N., et al. (2021). Bioinspired Membrane Provides Periosteum-Mimetic Microenvironment for Accelerating Vascularized Bone Regeneration. *Biomaterials* 268, 120561. doi:10.1016/j.biomaterials.2020.120561
- Ye Li, Li., Xu, J., Mi, J., He, X., Pan, Q., Zheng, L., et al. (2021). Biodegradable Magnesium Combined with Distraction Osteogenesis Synergistically Stimulates Bone Tissue Regeneration via CGRP-FAK-VEGF Signaling axis. *Biomaterials* 275, 120984. doi:10.1016/j.biomaterials.2021.120984
- Ye, X., Li, L., Lin, Z., Yang, W., Duan, M., Chen, L., et al. (2018). Integrating 3D-Printed PHBV/Calcium Sulfate Hemihydrate Scaffold and Chitosan Hydrogel for Enhanced Osteogenic Property. *Carbohydr. Polym.* 202, 106–114. doi:10.1016/j.carbpol.2018.08.117
- Yin, S., Zhang, W., Zhang, Z., and Jiang, X. (2019). Recent Advances in Scaffold Design and Material for Vascularized Tissue-Engineered Bone Regeneration. *Adv. Healthc. Mat.* 8 (10), 1801433. doi:10.1002/adhm.201801433
- Yu, Y., Yu, X., Tian, D., Yu, A., and Wan, Y. (2021). Thermo-responsive Chitosan/silk Fibroin/amino-Functionalized Mesoporous Silica Hydrogels with Strong and Elastic Characteristics for Bone Tissue Engineering. *Int. J. Biol. Macromol.* 182, 1746–1758. doi:10.1016/j.ijbiomac.2021.05.166
- Zhai, Y., Schilling, K., Wang, T., ElKhatib, M., Vinogradov, S., Brown, E. B., et al. (2021). Spatiotemporal Blood Vessel Specification at the Osteogenesis and Angiogenesis Interface of Biomimetic Nanofiber-Enabled Bone Tissue Engineering. *Biomaterials* 276, 121041. doi:10.1016/j.biomaterials.2021.121041



- Zhao, D., Zhu, T., Li, J., Cui, L., Zhang, Z., Zhuang, X., et al. (2021). Poly(lactic-co-glycolic Acid)-Based Composite Bone-Substitute Materials. *Bioact. Mater.* 6 (2), 346–360. doi:10.1016/j.bioactmat.2020.08.016
- Zhao, F., Lei, B., Li, X., Mo, Y., Wang, R., Chen, D., et al. (2018). Promoting *In Vivo* Early Angiogenesis with Sub-micrometer Strontium-Contained Bioactive Microspheres through Modulating Macrophage Phenotypes. *Biomaterials* 178, 36–47. doi:10.1016/j.biomaterials.2018.06.004
- Zhao, W., Chang, J., and Zhai, W. (2008). Self-setting Properties and *In Vitro* Bioactivity of  $\text{Ca}_3\text{SiO}_5/\text{CaSO}_4 \cdot 1/2\text{H}_2\text{O}$  Composite Cement. *J. Biomed. Mat. Res.* 85A (2), 336–344. doi:10.1002/jbm.a.31523
- Zhou, Z., Buchanan, F., Mitchell, C., and Dunne, N. (2014). Printability of Calcium Phosphate: Calcium Sulfate Powders for the Application of Tissue Engineered Bone Scaffolds Using the 3D Printing Technique. *Mater. Sci. Eng. C* 38, 1–10. doi:10.1016/j.msec.2014.01.027
- Zhu, T., Jiang, M., Zhang, M., Cui, L., Yang, X., Wang, X., et al. (2022). Biofunctionalized Composite Scaffold to Potentiate Osteoconduction, Angiogenesis, and Favorable Metabolic Microenvironment for Osteonecrosis Therapy. *Bioact. Mater.* 9, 446–460. doi:10.1016/j.bioactmat.2021.08.005
- Zimmermann, E. A., and Ritchie, R. O. (2015). Bone as a Structural Material. *Adv. Healthc. Mat.* 4 (9), 1287–1304. doi:10.1002/adhm.201500070
- Zou, F., Jiang, J., Lv, F., Xia, X., and Ma, X. (2020). Preparation of Antibacterial and Osteoconductive 3D-Printed PLGA/Cu(I)/ZIF-8 Nanocomposite Scaffolds for Infected Bone Repair. *J. Nanobiotechnol* 18 (1), 39. doi:10.1186/s12951-020-00594-6

**Conflict of Interest:** The authors declare that the research was conducted in the absence of any commercial or financial relationships that could be construed as a potential conflict of interest.

**Publisher's Note:** All claims expressed in this article are solely those of the authors and do not necessarily represent those of their affiliated organizations, or those of the publisher, the editors and the reviewers. Any product that may be evaluated in this article, or claim that may be made by its manufacturer, is not guaranteed or endorsed by the publisher.

Copyright © 2022 Liu, Li, Zhao, Chen, Lin, Li, Feng, Jin, Zhang, Wu, Wu, Xu, Ye and Zhang. This is an open-access article distributed under the terms of the Creative Commons Attribution License (CC BY). The use, distribution or reproduction in other forums is permitted, provided the original author(s) and the copyright owner(s) are credited and that the original publication in this journal is cited, in accordance with accepted academic practice. No use, distribution or reproduction is permitted which does not comply with these terms.



# Surface Roughness and Biocompatibility of Polycaprolactone Bone Scaffolds: An Energy-Density-Guided Parameter Optimization for Selective Laser Sintering

Jian Han<sup>1,2</sup>, Zehua Li<sup>1,2</sup>, Yuxuan Sun<sup>2</sup>, Fajun Cheng<sup>1,3</sup>, Lei Zhu<sup>1</sup>, Yaoyao Zhang<sup>1,2</sup>, Zirui Zhang<sup>4</sup>, Jinzhe Wu<sup>5\*</sup> and Junfeng Wang<sup>1,2,3,6\*</sup>

## OPEN ACCESS

### Edited by:

Lei Zhang,  
Wenzhou Medical University, China

### Reviewed by:

Henrique de Amorim Almeida,  
Polytechnic Institute of Leiria, Portugal  
Saeed Saber-Samandari,  
Amirkabir University of  
Technology, Iran

### \*Correspondence:

Jinzhe Wu  
jzw2014@mail.ustc.edu.cn  
Junfeng Wang  
junfeng@hmf.ac.cn

### Specialty section:

This article was submitted to  
Biomaterials,  
a section of the journal  
Frontiers in Bioengineering and  
Biotechnology

**Received:** 02 March 2022

**Accepted:** 23 May 2022

**Published:** 11 July 2022

### Citation:

Han J, Li Z, Sun Y, Cheng F, Zhu L,  
Zhang Y, Zhang Z, Wu J and Wang J  
(2022) Surface Roughness and  
Biocompatibility of Polycaprolactone  
Bone Scaffolds: An Energy-Density-  
Guided Parameter Optimization for  
Selective Laser Sintering.  
Front. Bioeng. Biotechnol. 10:888267.  
doi: 10.3389/fbioe.2022.888267

<sup>1</sup>High Magnetic Field Laboratory, CAS Key Laboratory of High Magnetic Field and Ion Beam Physical Biology, Hefei Institutes of Physical Science, Chinese Academy of Sciences, Hefei, China, <sup>2</sup>University of Science and Technology of China, Hefei, China, <sup>3</sup>School of Basic Medical Sciences, Anhui Medical University, Hefei, China, <sup>4</sup>School of Electronic Engineering and Intelligent Manufacturing, Anqing Normal University, Anqing, China, <sup>5</sup>School of Electronic Engineering, Naval University of Engineering, Wuhan, China, <sup>6</sup>Institutes of Physical Science and Information Technology, Anhui University, Hefei, China

Three-dimensional porous polycaprolactone (PCL) bone scaffolds prepared by selective laser sintering (SLS) have demonstrated great potential in the repair of non-load-bearing bone defects. The microgeometry and surface roughness of PCL scaffolds during the SLS process may change the biocompatibility and bioactivity of the scaffolds. However, in addition to the widely concerned mechanical properties and structural accuracy of scaffolds, there is still a lack of systematic research on how SLS process parameters affect the surface roughness of PCL scaffolds and the relationship between roughness and biocompatibility of scaffolds. In this study, we use the energy density model (EDM) combined with the thermodynamic properties of PCL powder to calculate the energy density range ( $Ed_1$ – $Ed_3$ ) suitable for PCL sintering. Five PCL scaffolds with different laser powers and scanning speeds were prepared; their dimensional accuracy, mechanical strength, and surface properties were comprehensively evaluated, and the bioactivities were compared through the attachment and proliferation of MC3T3-E1 cells on the scaffolds. It was found that the high energy density ( $Ed_3$ ) reduced the shape fidelity related to pore size and porosity, and the dense and smooth surface of the scaffolds showed poor cytocompatibility, while the low energy density ( $Ed_1$ ) resulted in weak mechanical properties, but the rough surface caused by incomplete sintered PCL particles facilitated the cell adhesion and proliferation. Therefore, the surface roughness and related biocompatibility of PCL bone scaffolds should be considered in energy-density-guided SLS parameter optimization.

**Keywords:** selective laser sintering, surface roughness, biocompatibility, energy density model, polycaprolactone

# 1 INTRODUCTION

Polycaprolactone (PCL) has attracted extensive attention owing to its good biodegradability and biocompatibility and has been approved by the U.S. Food and Drug Administration (FDA) as an implantable biomedical material for tissue engineering (TE) (Yeong et al., 2010; Munir and Callanan, 2018; Farazin et al., 2021; Navaei et al., 2021). Due to its relatively poor mechanical properties, PCL matrix bone scaffolds were usually utilized to repair the non-load-bearing regions, such as cartilage (Hajiali et al., 2018). The biocompatibility and repair ability of bone scaffolds are closely related to their surface properties. Many researchers are focusing on the chemical and biological activities of the scaffold through surface coating; the physical properties of the scaffold surface, including the surface microgeometry and roughness, can also significantly alter the biocompatibility and repair ability of the scaffold (Bachle and Kohal, 2004; Kim et al., 2004; Czelusniak and Amorim, 2020). For example, Jeon et al. (2014) have manufactured PCL scaffolds and then modified the scaffold surface *via* oxygen plasma treatment. Their results indicated that appropriate roughness induces favorable cell responses. Borsari et al. (2005) utilized two innovative vacuum plasma sprayed (VPS) coating techniques, with coated hydroxyapatite (HA) on Ti<sub>6</sub>Al<sub>4</sub>V scaffolds. The results have shown that the surface morphology and the HA coating strongly affected cell behavior. Mustafa et al. (2001) varied the surface roughness of the titanium implant material and examined the effect of cellular attachment, proliferation, and differentiation. There are a lot of reports which said that the selective laser sintering (SLS) technique can fabricate PCL scaffolds with a rough surface.

As a three-dimensional (3D) printing technology, SLS uses CO<sub>2</sub> laser to sinter polymer thin layers or their composite powders to form solid 3D objects. It is self-supporting, has high precision, is customizable, and is particularly suitable for making porous scaffolds (Du et al., 2017). Different from the traditional method of surface reprocessing on the prefabricated scaffold, SLS can effectively control the surface microgeometry while 3D printing the scaffold. By adjusting the process parameters, including laser power, scanning speed, layer thickness, incubation space, and powder bed temperature, SLS provides users with good control over the surface roughness of the scaffold (Beal et al., 2009; Duan and Wang, 2011; Sachdeva et al., 2013). PCL is a semicrystalline synthetic polymer with a low melting point, making it easy to process (Du et al., 2022). The SLS parameter optimization of PCL scaffolds had been extensively and vigorously performed. Williams et al. (2005) varied the laser power from 1 to 7 W in steps of 1 W at a constant scan speed (3,810 mm/s) and powder bed temperature (40°C) to determine the suitable laser power. Partee et al. (2006) reported that the optimal SLS processing parameters of PCL powder can be optimized by systematic factorial experimental design so that the dimensional accuracy can reach within 3–8% of the design specification, and the density is about 94% of the full density. Doyle et al. (2015) studied the influence of the laser power and scanning spacing on the dimensional accuracy of PCL scaffolds. In the recent SLS process parameter optimization by Tortorici

et al. (2021), not only the dimensional accuracy of PCL scaffolds but also the mechanical stability is considered. These studies provide good guidance for SLS preparation of PCL scaffolds, and their optimization parameters have been directly used in many cases (Sudarmadji et al., 2011; Bobbert et al., 2017). However, since the effects of these sintering variables are often interdependent, the optimization of the SLS process parameters of PCL scaffolds is still a challenge.

Therefore, in addition to the widely concerned mechanical properties and structural accuracy of scaffolds, the effects of the SLS process parameters on the surface properties of PCL scaffolds should be systematically studied. After all, the microgeometry and roughness of the scaffolds have a direct and significant impact on their bioactivity. Compared with the post-treatment surface modification method, it is expected that the regional SLS processing method under the optimized parameters achieves the one-step integration of bulk mechanical properties and surface properties, which will not only greatly save manufacturing time but also improve the stability of scaffold performance.

In this study, we took the energy density model (EDM) as the theoretical basis for optimizing the SLS process parameters, which was originally proposed by Nelson (1993), and it has been used in the SLS parameters by many researchers (Gibson and Shi, 1997; Ho et al., 1999; Beal et al., 2009). The basic properties of PCL powder, including morphology and thermal behavior, were evaluated. Three SLS energy densities (Ed<sub>1</sub>, Ed<sub>2</sub>, and Ed<sub>3</sub>) were determined according to the energy density theory (Figure 1). Five PCL scaffolds with different laser powers and scanning speeds were prepared, and then their dimensional accuracy, mechanical strength, and surface properties were characterized. Finally, the bioactivities of PCL scaffolds prepared under different SLS parameters were compared through the attachment and proliferation of MC3T3-E1 cells on the scaffolds.

## 2 MATERIALS AND METHODS

### 2.1 Characterization of Polycaprolactone Powder

Polycaprolactone powder (CAPA® 6500 PCL) was purchased from Solvay (Belgium).

#### 2.1.1 Powder Morphology

The surface morphology of the PCL powder was characterized by using a scanning electron microscope (SEM, FEI, Quanta FEG 250, United States).

#### 2.1.2 Particle Size Distribution

The average particle size of the PCL powder was determined by using a Mastersizer (Malvern, Mastersizer 2000, United Kingdom).

#### 2.1.3 Thermodynamic Properties

The thermodynamic properties of the PCL powder are determined by using differential scanning calorimetry (DSC, TA, Q2000, United States) and thermogravimetric analysis (TGA, TA, Q5000, United States) with a heating rate of 10°C/min.

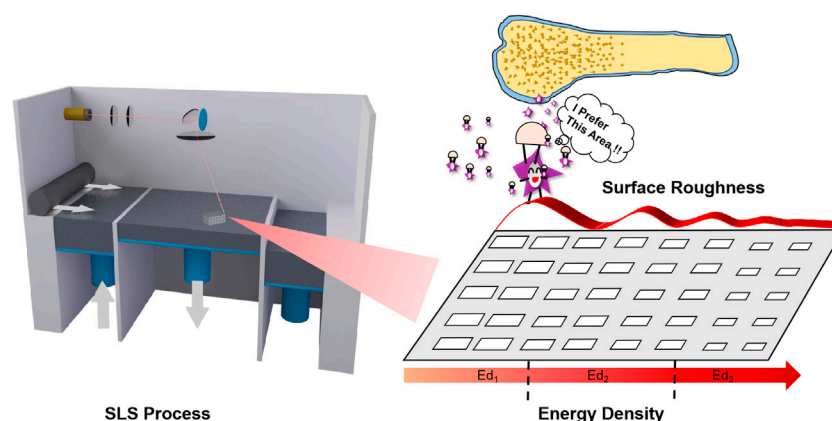


**FIGURE 1** | The Schematic diagram of this work.

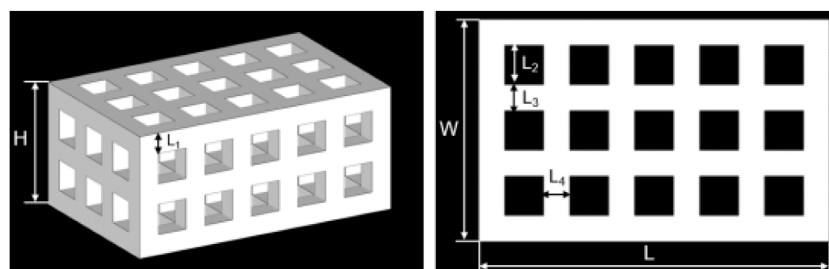


**FIGURE 2** | The 3D model of the porous scaffold for SLS.

**TABLE 1** | Parameters of the 3D porous scaffold model.

Parameters of the 3D porous scaffold model							
H (mm)	W (mm)	L (mm)	L <sub>1</sub> (mm)	L <sub>2</sub> (mm)	L <sub>3</sub> (mm)	L <sub>4</sub> (mm)	Porosity (%)
12.0	17.0	27.0	2.0	3.0	2.0	2.0	45.75

## 2.2 Design, Fabrication, and Characterizations of Porous Scaffolds

### 2.2.1 Model Design

A tetragonal porous scaffold with a three-dimensional (3D) orthogonal periodic porous square architecture was designed by Magics 21.0 (Materialise, Belgium), as shown in **Figure 2**. The dimensions and porosity of the model are listed in **Table 1**. The design was converted to STL file format.

### 2.2.2 Selective Laser Sintering Process of Scaffolds

An HK P320 SLS machine (Huazhong university of science and technology, China) with a controlled CO<sub>2</sub> laser was used for scaffold manufacturing. After the scanning process, the scaffolds were held at the temperature for 2 h and then removed from the powder bed. Afterward, a high-power blower was used to blow away the unsintered powders on the surface and in the pores of

the SLS-fabricated scaffolds from different angles as much as possible. Finally, all the scaffolds were rinsed with ddH<sub>2</sub>O several times until there were no obvious powders and debris. Then, the scaffolds were dried naturally for further use.

### 2.2.3 Pore Size and Porosity

Micro-CT scanning (Skyscan, Bruker, Germany) was performed on five samples from each group. Meanwhile, the dimension and porosity were calculated from the 3D reconstructed images using CTAn1.13 software (Bruker, Germany).

### 2.2.4 Water Absorption

The scaffolds were weighed after soaking in water for 30 min to get the wet weight. The water absorption of the scaffold was obtained by subtracting the dry weight from the wet weight and dividing it by the dry weight in the air, according to the following formula (Lei et al., 2012)



$$P = (W_{\text{wet}} - W_{\text{dry}}) / W_{\text{dry}} \times 100\% \quad (2-1)$$

$W_{\text{wet}}$ : wet weight of the scaffold;  $W_{\text{dry}}$ : dry weight of the scaffold.

### 2.2.5 Compressive Property

Compression tests of the scaffolds were performed using an RGM3000 electromechanical test frame (REGER, China) with 1 mm/min displacement rate. A total of five samples were tested for each type of scaffold. Their compression modulus was obtained from the initial region of the stress-strain curve.

### 2.2.6 Scanning Electron Microscopy

The morphology of the scaffold's surface and fracture surface were observed by scanning electron microscopy (SEM, FEI, Quanta FEG 250, United States).

### 2.2.7 Surface Roughness

The surface roughnesses (SRs) from the top surface of circular specimens with different processing parameters were measured by using an Optical digital microscope (DSX510, Olympus, Japan).  $S_a$  and  $S_q$  are described as indicators.  $S_a$  is the arithmetic mean deviation, which is defined as the arithmetic average or centerline average from the centerline.  $S_q$  (root mean square value) represents the positive square root of the arithmetic mean of the value of the squares of the values in the set (Sachdeva et al., 2013).

## 2.3 In Vitro Biological Evaluation

### 2.3.1 Protein Adsorption

The scaffolds with different SLS parameters were immersed overnight in a green fluorescent protein (GFP) solution that was expressed by *E. coli*. The scaffolds were taken out and carefully cleaned with phosphate buffer solution (PBS) three times to remove the unabsorbed GFP. Then, the scaffolds were observed under a fluorescence microscope (Leica OMI4000B, Germany) with the laser and camera parameters conditions consistent when taking fluorescent photos of the different groups.

### 2.3.2 Cell Culture

MC3T3-E1 (mouse embryo osteoblast precursor cells, Chinese Academy of Medical Sciences, China) cells were cultured in Dulbecco's modified Eagle's medium (DMEM) containing 10% fetal bovine serum (FBS, Biochrom AG), 1% penicillin/streptomycin (P/S, Biochrom AG), and 1% L-glutamine (GlutaMAX, Invitrogen) and incubated at 37°C in a humidified atmosphere with 5% CO<sub>2</sub>. Cells were trypsinized (Gibco, United States) at approximately 80% confluency, and in passage 3 or 4, cells were used for seeding.

### 2.3.3 Cell Seeding on the Scaffold

Five kinds PCL discs with the same diameter (5 mm) and height (1 mm) but different SLS parameters were used for *in vitro* experiments. At first, all the scaffolds were sterilized for 30 min by UV light and severally moved into the 24-well plate and marked. Each well was added 2 ml  $1 \times 10^3$  cells/ml cell suspension. Three repetitions were set for every group (Ed<sub>1</sub>, Ed<sub>21</sub>, Ed<sub>22</sub>, Ed<sub>23</sub>, and Ed<sub>3</sub>). The plate was gently shaken so that the cells were evenly

distributed over the PCL discs' surface. After 24 h culture, the scaffolds with cells adhered were taken out and gently cleaned with PBS three times. Then, the scaffolds were placed into a new 24-well plate, and 2 ml fresh medium was added to continue the culture.

### 2.3.4 Fluorescence Staining

The time points selected to evaluate the live/dead test of cells on the scaffolds were 1, 3, and 5 days after seeding. At each time point, the surfaces of the five kinds of scaffolds (Ed<sub>1</sub>, Ed<sub>21</sub>, Ed<sub>22</sub>, Ed<sub>23</sub>, and Ed<sub>3</sub>) with cells were carefully cleaned three times with sterile PBS. The cells were incubated in a solution containing 2.5 μM calcein acetoxymethylester (Calcein/AM, 40747ES76, Yeason, China) and 4.5 μM propidium iodide (PI, 40747ES76, Yeason, China) diluted in PBS for 30 min at room temperature, and then the excess dye was rinsed by PBS. After that, taking out the sample and laying it on the rectangular cover glass sheet, the cell surface was placed on the bottom. Live (green) and dead (red) cells were identified by using a laser confocal machine (FV3000, Olympus, Tokyo, Japan).

### 2.3.5 Cell Proliferation

The diluted suspensions (2 ml), containing different cell densities, were added into the wells of 24-well plates and cultured for 24 h. Specifically, the number of cells in each well was 0, 500, 1,000, 2,000, 5,000, 10,000, 20,000, and 40,000. Discarding the medium and cleaning three times with PBS, 450 μl medium and 50 μl CCK8 kit (BestBio, Shanghai, China) solution were added into the wells and then incubated at 37°C for another 2 h. Then, the culture medium was mixed thoroughly, and the supernatant with a volume of 100 μl was taken to a 96-well plate to measure the absorbance at 450 nm with a microplate reader (BL340, Biotech, United States). With the number of cells as the abscissa and the absorbance value as the ordinate, the standard curve was drawn and the relationship between the number of cells and the absorbance value was obtained by linear regression fitting. CCK8 test of the cells on the scaffolds was repeated every 24 h for 5 days. The number of cells on the scaffold with five different SLS parameters at each selected time point (days 1, 2, 3, 4, and 5 after cell seeding) was calculated according to the obtained equation.

### 2.3.6 Statistical Analysis

The results of the experiments were statistically analyzed using the Origin software (version 2020, OriginLab, United States). All the data were presented as the mean ± SD. Statistical analyses among the multiple group data were carried out using a one-way analysis of variance (ANOVA) test to determine the significant differences. Tukey's post-hoc test was used to determine the difference between any two groups with \* $p < 0.05$  considered statistically significant.

## 3 RESULTS

### 3.1 Selective Laser Sintering Theoretical Energy Density Model and Parameter Optimization of Polycaprolactone Powder

The SEM image (Figure 3A) exhibited the uniformly nonspherical microscopic morphology of PCL powder. As

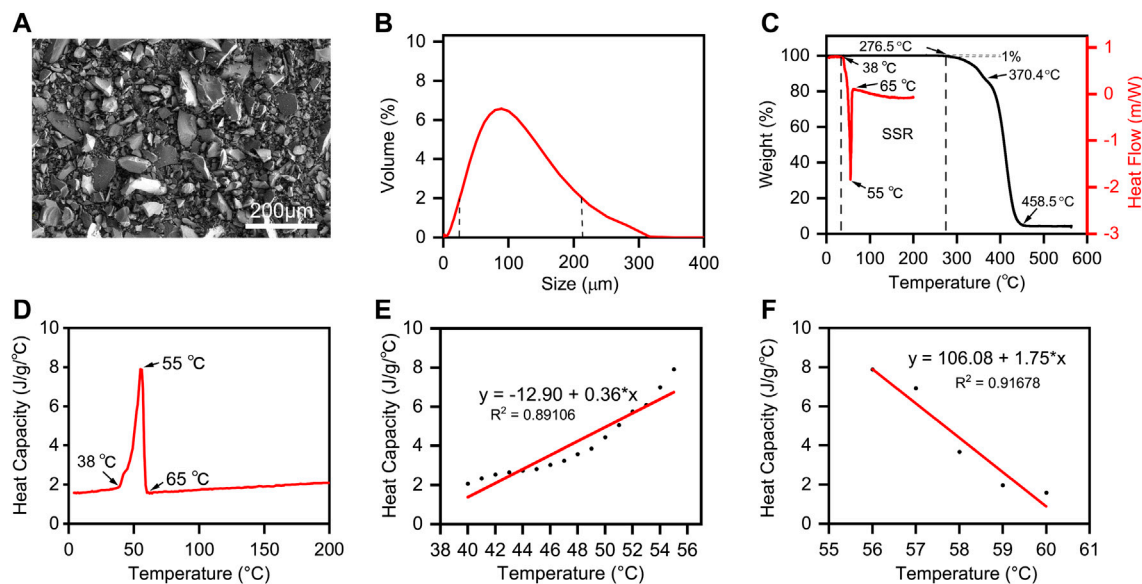


**FIGURE 3 |** The Properties of PCL powder. **(A)** SEM image and **(B)** size distribution of PCL powders; **(C)** DSC and TGA analysis of PCL powder. The endo- and exothermal heat flow of PCL powders was characterized by heating and cooling from 0°C to 200°C at the rate of 10°C/min. The weight ratio of PCL decomposition started from 0°C to 600°C at the rate of 10°C/min. The stable sintering region (SSR) is indicated from the onset of melting to the onset (1%) of decomposition. **(D)** Plot of the temperature-dependent specific heat capacity of PCL powders from 0°C to 200°C. **(E)** Linear fitting of heat capacity with temperature from melting initiation to the melting point. **(F)** Linear fitting of heat capacity with temperature from the melting point to the recrystallization temperature.

shown in **Figure 3B**, the curve shows good symmetry. The PCL particle size distribution increased from 28 to 200  $\mu\text{m}$  when the value of volume percent is greater than 2%, and the average particle size is about 90  $\mu\text{m}$ . The size range of the PCL powder meets the requirements of SLS printing because the excessive size of the powder will affect the powder spreading process, and the too small size of the powder will cause the agglomeration of the powder (Shi et al., 2016). Hence, the minimum layer thickness was chosen as 0.15 mm.

According to the theoretical EDM, the offset melting temperature ( $T_{\text{mf}}$ ) and onset decomposing temperature ( $T_{\text{ds}}$ ) are the key points. We defined the temperature range from  $T_{\text{mf}}$  to  $T_{\text{ds}}$  as “Sintering stable range (SSR)” (Berretta et al., 2016). Differential scanning calorimetry (DSC) and thermogravimetric analysis (TGA) are applied to identify the SSR of PCL, and their curves and SSR region are shown in **Figure 3C**. We can conclude that the SSR of PCL is 38.0°C–276.5°C, and the sintering temperature should be within. Additionally, the heat capacity of PCL with different temperature ranges is shown in **Figure 3D**, while the linear fitting of heat capacity with temperature is shown in **Figures 3E,F**.  $C_{\text{pp}}$  means the heat capacity of PCL in the powder form, and  $C_{\text{pm}}$  means the heat capacity of PCL in the liquid phase. To calculate the energy per volume required for melting  $E_{\text{mv}}$  and the energy per volume required for decomposing  $E_{\text{dv}}$  listed in **Eqs 3-1, 3-2**, the linear data fittings, applied for  $C_{\text{pp}}$  and  $C_{\text{pm}}$  curves, the corresponding linear equations, and the other important material properties of PCL powders are listed in **Table 2**.

Based on the material properties of PCL powders, we used a theoretical method to investigate the influences of sintering parameters based on the thermal properties of PCL powders which were obtained from the above experiments. To sinter PCL powders effectively and prevent their decomposition, we should calculate  $E_{\text{mv}}$  and  $E_{\text{dv}}$  (Yuan et al., 2017). They are defined as

$$E_{\text{mv}} = \rho^*(T)\phi \int_{T_b}^{T_m} C_p^*(T)dT, \quad (T_b < T < T_{\text{mf}}) \quad (3-1)$$

where  $T_b$  is the preheating temperature of laser sintering,  $T_{\text{mf}}$  is the onset and offset of melting, the PCL powder density  $\rho^*(T)$  is a function of temperature, and the modified specific heat  $C_p^*$  is a function of temperature.  $\phi$  is the packing factor of polymer powders.

$$E_{\text{dv}} = \rho^*(T) \int_{T_{\text{mf}}}^{T_{\text{ds}}} C_p^*(T)dT, \quad (T_b < T < T_{\text{mf}}) \quad (3-2)$$

where  $T_{\text{ds}}$  is the onset of decomposing, which is indicated by the 1% weight loss in the decomposition plot.

The energy density ( $E_d$ ) is a comprehensive numerical parameter to express the critical parameters of the SLS process including laser power ( $P$ ), scanning speed ( $V$ ), the layer thickness of each layer ( $H$ ), and the hatch space ( $D$ )

$$E_d = P/VHD \quad (3-3)$$

These energy calculations should satisfy a relationship expressed as

$$E_{\text{mv}} < \alpha E_d < E_{\text{dv}} \quad (3-4)$$

**TABLE 2 |** Material properties of PCL powders.

Material properties	Value
Specific heat ( $C_p^*$ , J/g°C)	$C = 0.0227e^{0.1059T}$ , (30–65°C) $C = 0.0034 T + 1.400$ , (65°C–277°C)
Melting temperature ( $T_m$ , °C)	52.96
Onset melting temperature ( $T_{ms}$ , °C)	38.0
Offset melting temperature ( $T_{mf}$ , °C)	65.22
Onset decomposing temperature ( $T_{ds}$ , °C)	276.5
Modified density ( $\rho^*$ , g/cm <sup>3</sup> )	$1.1-7.81 \times 10^{-4}T + 0.519 \times 10^{-6}T^2$
Packing fraction ( $\phi$ )	0.4
Light absorptivity ( $\alpha$ , %) at 10.6 $\mu$ m	0.9 Franco et al. (2010)

**TABLE 3 |** Evaluations of  $E_{mv}$ ,  $E_{dv}$ , and  $E_d$  of PCL powders.

Energy parameter	Value
Volume energy for melting ( $E_{mv}$ , J/mm <sup>3</sup> )	0.090
Volume energy before decomposition ( $E_{dv}$ , J/mm <sup>3</sup> )	0.184
Energy input range of laser ( $E_d$ , J/mm <sup>3</sup> )	0.100–0.204

**TABLE 4 |** Main SLS process parameters of PCL scaffolds in this study.

Energy density Ed (J/mm <sup>3</sup> )	SLS process parameters			
	P (W)	V (mm/s)	D (mm)	H (mm)
Ed <sub>1</sub> (0.089)	2	1,500	0.1	0.15
Ed <sub>21</sub> (0.178)	2	750	0.1	0.15
Ed <sub>22</sub> (0.178)	4	1,500	0.1	0.15
Ed <sub>23</sub> (0.178)	6	2,250	0.1	0.15
Ed <sub>3</sub> (0.267)	6	1,500	0.1	0.15

where  $\alpha$  is the effective heat absorptivity of polymer powders during the SLS process.

As can be seen, the material properties of PCL powders are listed in **Table 2**. In addition, to ensure the minimum of the thermal gradient, the powder bed temperature must be maintained as close as possible to the onset melting point; otherwise, the powder bed would get caked. Usually, the powder bed temperature is maintained between 3 and 15°C below the onset melting point. Hence, we set the powder bed temperature as 35°C. According to the energy calculation formulas described above, the evaluations of  $E_{mv}$ ,  $E_{dv}$ , and  $E_{vol}$  for PCL powders are listed in **Table 3**.

According to the energy input theoretical range of laser  $E_d$  (0.100–0.204 J/mm<sup>3</sup>), we chose three different densities Ed<sub>1</sub>, Ed<sub>2</sub>, and Ed<sub>3</sub> by varying the laser power to 2, 4, and 6 W with the same scanning speed of 1,500 mm/s. Furthermore, to compare the actual effect of laser power and scanning speed on the properties of scaffolds, the laser power and scanning speed were varied simultaneously to keep the energy density constant, marked as Ed<sub>21</sub>, Ed<sub>22</sub>, and Ed<sub>23</sub>. The main process parameters are shown in **Table 4**.

### 3.2 Characterizations of Polycaprolactone Scaffolds With Different Selective Laser Sintering Parameters

As shown in **Figure 4A**, five kinds PCL scaffolds (Ed<sub>1</sub>, Ed<sub>21</sub>, Ed<sub>22</sub>, Ed<sub>23</sub>, and Ed<sub>3</sub>) with different SLS parameters were successfully

produced. Subsequently, the 3D reconstruction images of the scaffolds by micro-CT are shown in **Supplementary Figure S1**. It is easily noticed that their pore sizes were different. Therefore, the area of pores was measured from the horizontal direction (**Figure 4B**) and vertical direction (**Supplementary Figure S2**). Increasing the energy density by increasing the laser power from 2 W (Ed<sub>1</sub>) to 4 W (Ed<sub>22</sub>) and 6 W (Ed<sub>3</sub>) at a fixed scanning speed (1,500 mm/s) resulted in a decrease in the pore area. Due to the “bonus-z” effect (Ho and Gibson, 2000), the difference between vertical pores was more inapparent than that of horizontal pores. Specifically, in the horizontal direction, the measured pore area was 11.05 mm<sup>2</sup> when the energy density was the lowest in this study at 0.089 J/mm<sup>3</sup> (Ed<sub>1</sub>). The energy density increases to 0.178 J/mm<sup>3</sup> (Ed<sub>22</sub>), and the pore area decreases to 9.88 mm<sup>2</sup>. Further increasing the energy density to 0.267 J/mm<sup>3</sup> (Ed<sub>3</sub>), the originally designed 9 mm<sup>2</sup> pore was only 3.24 mm<sup>2</sup> with the lowest shape fidelity. When the laser power and scanning speed were increased in the same proportion under the same energy density (Ed<sub>2</sub>), the pore size was decreased from 10.26 mm<sup>2</sup> (Ed<sub>21</sub>) to 9.17 mm<sup>2</sup> (Ed<sub>23</sub>).

The porosity of scaffolds (**Figure 4C**) was consistent with the results of pore size. It can be observed that the porosity decreased from 63.80% to 23.60% when increasing the energy density from 0.089 (Ed<sub>1</sub>) to 0.267 (Ed<sub>3</sub>) J/mm<sup>3</sup>. The porosity was decreased from 55.78% (Ed<sub>21</sub>) to 45.31% (Ed<sub>23</sub>) as the laser power and scanning speed were increased in the same energy density (Ed<sub>2</sub>) as well.

Meanwhile, **Figure 4D** illustrates that the mass increased from 1.371 g (Ed<sub>1</sub>) to 3.638 g (Ed<sub>3</sub>) with the increase in energy density and the masses of scaffolds with the same energy density were 2.036 g (Ed<sub>21</sub>), 2.497 g (Ed<sub>22</sub>), and 2.530 g (Ed<sub>23</sub>).

The mechanical strength is also an important parameter for bone tissue scaffolds. Therefore, the compression strength and the stress–strain curves are assessed in **Figures 4E,F**. First, we found that all the stress–strain curves show the same tendency. Then, our results indicate that the improved mechanical properties can be achieved by the energy density increased from 0.089 to 0.267 J/mm<sup>3</sup>, and the mechanical performance of the scaffolds improved from 0.260 to 3.320 MPa. Moreover, when the energy density is the same (Ed<sub>2</sub>), the compression strength increased from 1.429 (Ed<sub>21</sub>) to 1.779 (Ed<sub>22</sub>) and 1.844 (Ed<sub>23</sub>) MPa with the increase of laser power and scanning speed.

As shown in **Figure 4G**, according to the study of Kim and Kim (2015) and our inference, the water absorption of the Ed<sub>1</sub> group (21.94%) was much higher than that of other groups, which

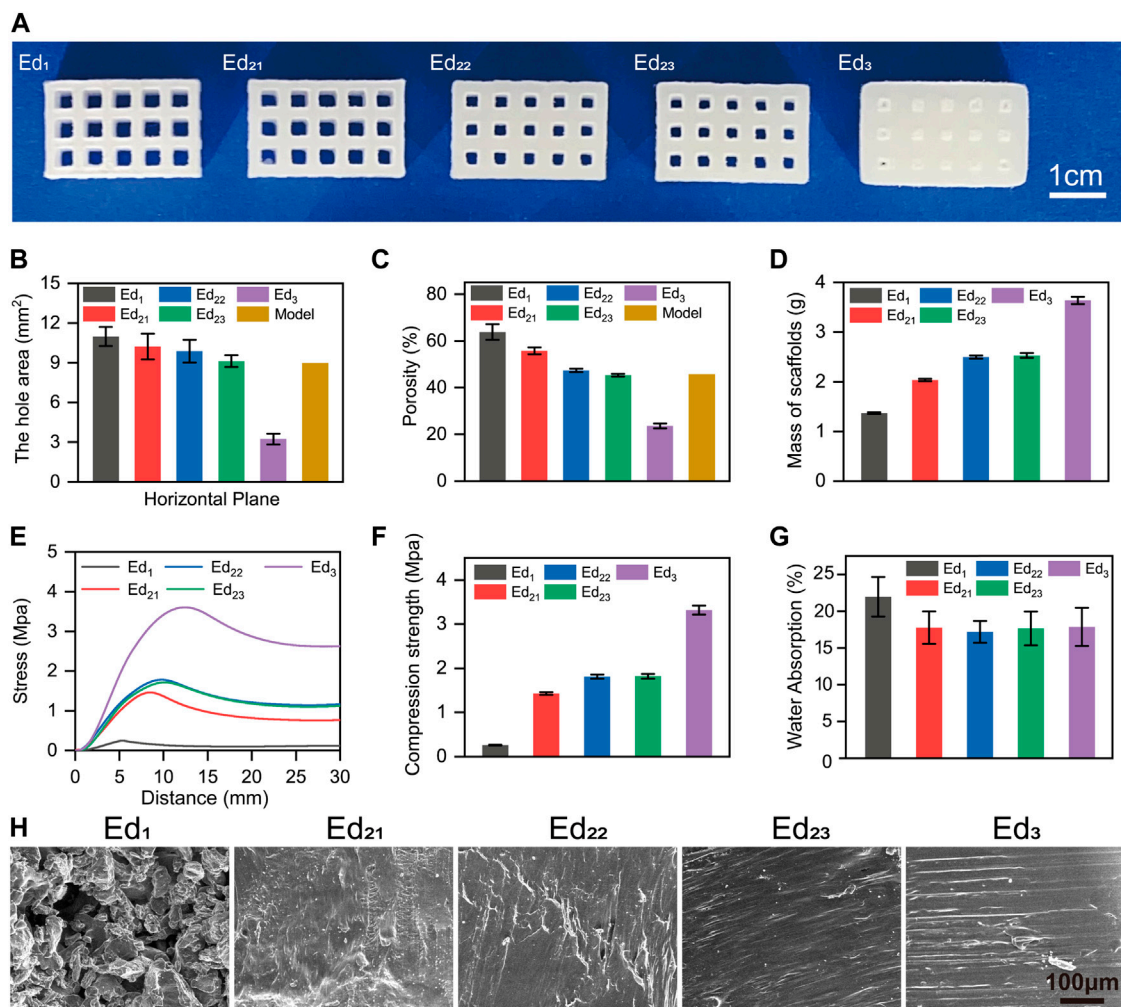


**FIGURE 4 |** Characterizations of five kinds PCL scaffolds with different SLS parameters. **(A)** Photo of SLS-fabricated PCL scaffolds, **(B)** horizontal pore area, **(C)** porosity, **(D)** mass, **(E)** stress–strain curves, **(F)** maximum compressive strength, **(G)** water absorption, and **(H)** cross-section SEM images of scaffolds.

was related to the existence of a large number of unsintered PCL particles and undesigned micropores on the scaffolds.

The SEM images of the cross-section of the different scaffolds (**Figure 4H**) can explain the mechanical properties described above. As can be seen, the micropores disappeared and the cross-sectional microstructure became dense gradually with the increase in energy density. Meanwhile, the same tendency was also observed from Ed<sub>21</sub> to Ed<sub>23</sub>.

The SEM images of the different scaffolds' surfaces are shown in **Figure 5A**. There were a lot of semisintered particles which remained on the surface of the Ed<sub>1</sub> scaffold, which was caused by a low energy density. These incomplete sintered PCL particles and undesigned pores resulted in a very rough surface of the Ed<sub>1</sub> group. When the energy density was increased to Ed<sub>2</sub>, PCL particles were further fused so that the surface morphology became smoother, but some peaks were still found protruding from the surface. Moreover, compared with the three different scaffolds in the same energy density (Ed<sub>2</sub>), with the increase in

laser power and scanning speed, smaller unsintered PCL particles and fewer undesigned micropores were observed on the scaffolds' surfaces. As the energy density was further increased to Ed<sub>3</sub>, the peaks and the microstructure pores disappeared so that the surface became very compact and smooth.

As shown in **Figures 3D, 5B**, topographical images were used to evaluate the SR. Meanwhile, the quantitative results of SR, **Figures 5C,D** (Sa) and (Sq), indicated that the Ed<sub>1</sub> scaffolds showed highly roughened surfaces with average roughnesses of 56.42 µm (Sa) and 44.02 µm (Sq), and Ed<sub>3</sub> scaffolds had the smoothest surface with average roughnesses of 31.02 µm (Sa) and 23.60 µm (Sq). These results indicated that the SR was decreased with increasing energy density. Similarly, the SR values of Ed<sub>21</sub>, Ed<sub>22</sub>, and Ed<sub>23</sub> were measured: the average values of Sa were 32.84, 28.32, and 28.05 µm, respectively; the values of Sq were 41.95, 35.97, and 36.62 µm, respectively. Interestingly, the SR of the specimens with the



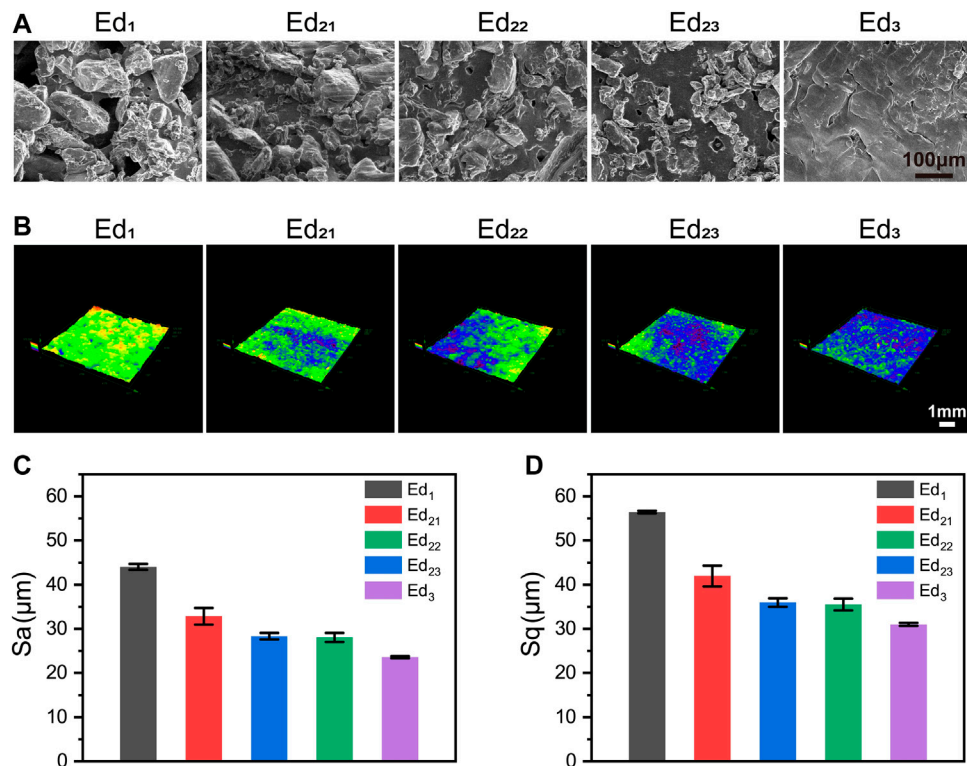


**FIGURE 5 |** Characterizations of SR with different SLS parameters. **(A)** Surface SEM images of scaffolds; **(B)** 3D morphology; **(C)** Sa and **(D)** Sq statistical of the samples' surface.

same energy density was decreased with increasing laser power and scanning speed.

### 3.3 In Vitro Biocompatibility of Polycaprolactone Scaffolds With Different Selective Laser Sintering Parameters

Generally, the composition of this adsorbed protein layer is a key mediator of cell behavior (Ngandu Mpoyi et al., 2016) and is very important for the biocompatibility of scaffolds. Therefore, **Figure 6A** shows the protein adsorption ability of the SLS-derived scaffolds when incubated with GFP for 24 h. Specifically, with the increase in energy density, fewer fluorescent areas appeared on the scaffolds when fluorescence images were taken under the same shooting parameters, inferring that less GFP was attached to the surface. Compared with the Ed<sub>2</sub> and Ed<sub>3</sub> groups, proteins seem to be more readily adsorbed to the surface of the Ed<sub>1</sub> scaffold. Therefore, a lower energy density or lower laser power and scanning speed at the same energy density are favorable for protein adsorption on the scaffold surface. More protein on the surface will facilitate the cells to adhere on the scaffold, according to Kim et al. (2019).

The viability of MC3T3-E1 cells was assayed using live/dead staining after 1, 3, and 5 days of cell culture, where live cells were stained with calcein acetoxymethylester (Calcein-AM, green) and

dead cells were stained with propidium iodide (PI, red) under a fluorescence microscope (**Figure 6B**). It is easily seen that all the scaffolds possessed the capability for cell proliferation, and the number and optical density of live cells on the scaffold surface increased with culture time prolonging. Very few dead cells were observed for all the culture time points, indicating that even after processing with SLS with a wide range of process parameters, PCL remains cytocompatible (Tortorici et al., 2021). After 1 day of culturing, the cells were evenly distributed on the scaffold and the number of live cells on all the scaffolds was similar. These phenomena demonstrated that the uniformly initial conditions of the cells on the scaffolds were suitable for further comparison of the biological differences on different scaffold surfaces.

Confocal laser scanning microscopy images displayed that the surfaces of all scaffolds were uneven with the cells spatially distributed. The cells could be observed at different levels within a range in the direction of observation, while the range of the Ed<sub>1</sub> group is the largest. Moreover, the number of cells on scaffolds with the same energy density (Ed<sub>21</sub>, Ed<sub>22</sub>, and Ed<sub>23</sub>) showed a trend that increased with the laser power and scanning speed. Evidently, a large proportion of live cells adhered to the Ed<sub>1</sub> and Ed<sub>2</sub> scaffold's surface where cells attached tightly with the well-flattened and well-spread morphology and grew in colonies without contact inhibition so that cells formed a confluent layer at day 5. However, cells adhering to the Ed<sub>3</sub> group were sparsely distributed and presented a morphology

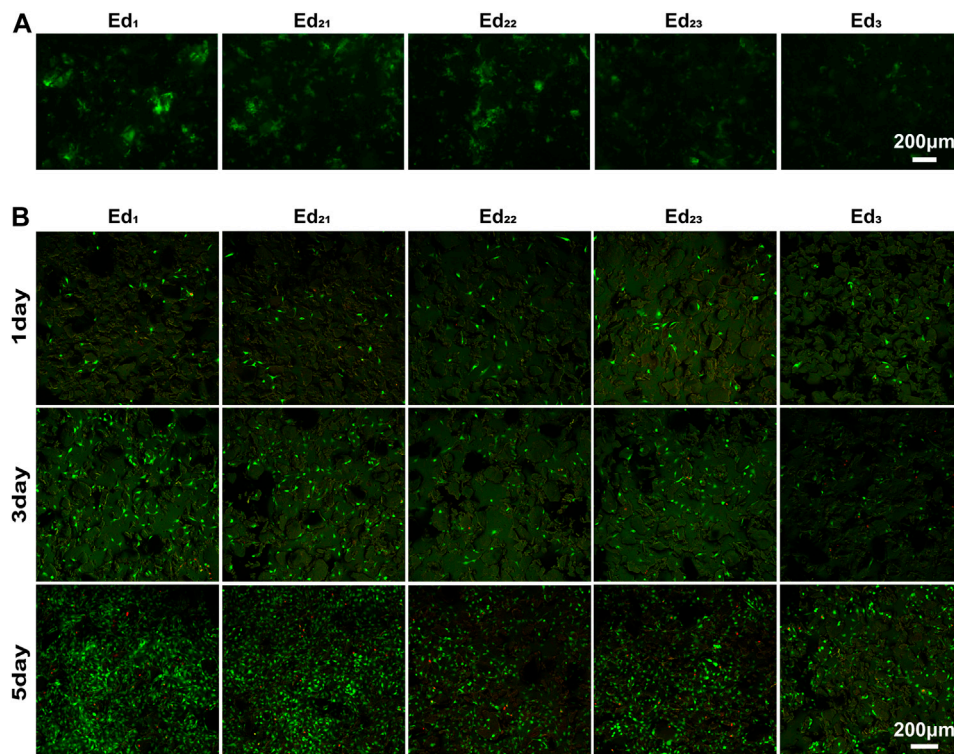


**FIGURE 6 |** Qualitative analysis of *in vitro* biological properties of scaffolds. **(A)** Fluorescence images of GFP adsorption on the surface of scaffolds after 24 h. **(B)** Confocal laser images of MC3T3-E1 cells growing on the surface of scaffolds for 1, 3, and 5 days after live/death staining.

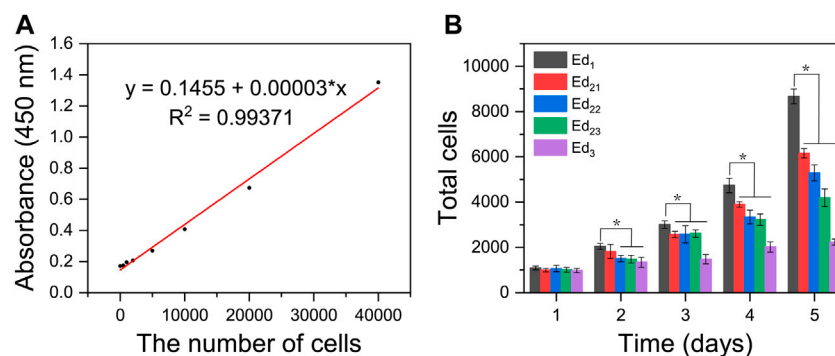


**FIGURE 7 |** Quantitative analysis of *in vitro* biological characteristics of scaffolds. **(A)** Absorbance value at 450 nm of different amounts of MC3T3-E1 cells. **(B)** Proliferation activity of the adhered MC3T3-E1 cells on different scaffolds after 1, 2, 3, 4, and 5 days of incubation, detected by the CCK8 assay. ( $n = 7$ , error bar represents the mean  $\pm$  SD, \* indicates a significant difference compared with Ed<sub>1</sub>,  $p < 0.05$ ).

with more round and less filopodia. Summarily, the distribution range, number, and viability of cells increased significantly with declining energy density.

A linear function was formed between the amounts of cells and the absorbance value at 450 nm based on **Figure 7A**. Through quantitative analysis, the same number of cells ( $1 \times 10^3$ ) were initially inoculated on all the five types of scaffolds, and with the extension of time, the cells showed a tendency of continuous

growth, manifesting that all the SLS-fabricated scaffolds supported MC3T3-E1 cell proliferation with low toxicity and high safety. However, it was easily seen that MC3T3-E1 cells showed different proliferation on the printed scaffolds with different parameters. The results were consistent with that of AM/PI staining. As shown in **Figure 7B**, the proliferation rates and maximum cell number on the Ed<sub>1</sub> group were significantly higher than those of Ed<sub>2</sub> and Ed<sub>3</sub> groups when the culture time

was increased to 5 days ( $p < 0.05$ ) and also exhibited a negative correlation between energy density and cellular proliferation. In addition, the number of cells on the scaffolds with the same energy density ( $Ed_2$ ) also showed a significant difference that decreased as the laser power and scanning speed increased at day 5 ( $Ed_{21}$ ,  $Ed_{22}$ , and  $Ed_{23}$ ;  $p < 0.05$ ).

## 4 DISCUSSION

In this study, the theoretical EDM was used for the first time to systematically optimize the SLS process parameters of PCL scaffolds. Five PCL scaffolds with different SLS processing parameters were manufactured successfully, which means that the calculated energy density range was pretty suitable based on PCL powder properties and EDM. According to our attempts not demonstrated in this study, PCL porous scaffolds were hard to form when the energy density was not in this range. In addition, as the energy density gradually increased, the performance of PCL scaffolds showed obvious differences in porosity, mechanical properties, surface properties, and cytocompatibility. Moreover, under the same energy density, the change of laser power and scanning speed in the same proportion was basically the same as the change in energy density. However, the effects of varying laser power and scanning speed respectively need to be further compared.

Most importantly, although none of the scaffolds prepared from a wide range of SLS process parameters displayed cytotoxicity, the cytocompatibility of scaffolds showed a negative correlation with the significantly varied energy density. All the *in vitro* experimental results indicate that the cell adhesion and proliferation effect of the  $Ed_1$  scaffold was superior to that of other groups, which was evidently related to the improved roughness of the scaffold's surface that was caused by the decrease of energy density. The lower energy density prevents the PCL particles on the surface of the scaffold from melting completely, which leads to a lot of unsintered PCL particles adhered to the surface. Meanwhile, these unsintered PCL particles also resulted in poor packing of the particles in the powder bed so that the tendency of the layers to curl with the roller increases, which restricts the next layer from proper sintering, resulting in the rough surface. Previous studies have demonstrated that roughness might be responsible for improving cell responses such as proliferation (Van Bael et al., 2013). Similarly, it can be analyzed from our results that rough surfaces not only provide a wider growth space to accommodate more cells but also allow the scaffold to absorb more water and expose more protein adsorption sites (Figures 5D, 6A), thus affecting cell attachment and proliferation. The same phenomenon can be observed when the energy density was the same and the laser power and scanning speed were changed in the same proportion.

The increase in energy density will reduce the shape accuracy of the scaffold in terms of pore size and porosity. There might be two reasons: one is that the higher energy density leads to a higher heat-affected area, resulting in a larger shrinkage of consolidated PCL powder, and the other is that the higher energy density with a higher temperature gradient transfers heat from the center to the edge of the molten pool more effectively, generating a wider molten pool (Czelusniak and

Amorim, 2020). Hulbert et al. (1971) claimed that a minimum pore size of 100  $\mu\text{m}$  is necessary for the porous implant materials so that it is conducive to the growth of neovascular substances to transport nutrients needed for cell growth and the exchange of metabolites. Therefore, considering the overall biocompatibility of scaffolds, the scaffolds with low porosity prepared by using the  $Ed_3$  parameters are unsuitable for implantation. The *in vivo* biological properties of scaffolds with different porosities made by varying SLS parameters need to be further studied.

However, as observed in the SEM images (Figure 5A), the increase in energy density results in a coherent structure with good adhesion and low porosity, which improved compression strength in a step-like pattern from 0.26 to 3.32 MPa. The synergistic effect of incomplete sintering of PCL particles and large porosity leads to poor compression strength of the  $Ed_1$  scaffold. During the long process of bone tissue repair, the 3D structure of the scaffold without the necessary mechanical capacity may collapse so that it cannot occupy the expected space for cells' growth.

This finding will bring some new enlightenment to the field of bone tissue scaffold manufacturing as well. First of all, it must be recognized that the change of the SLS process parameters for preparing PCL scaffolds will not only affect the porosity, mechanical properties, and surface properties of the scaffolds but also affect the biological properties. The excellent biological properties of bone tissue scaffolds are the original and desirable results of using SLS technology to fabricate the PCL scaffolds. Therefore, when the SLS process parameters of biomedical polymer materials such as PCL are optimized, the biological properties should become a key factor to determine whether the technical parameters are appropriate or even should be given top priority in the repair of non-load-bearing bone defects. In addition, it should be considered that different SLS technological parameters can be used in different regions to prepare tissue engineering scaffolds in the future. Specifically, a higher energy density should be applied when the main part of the inner scaffold is sintered, while a lower energy density should be used for printing scaffolds in areas where the surface is in direct contact with the cells or tissues, increasing the surface roughness and enabling the scaffolds to have good mechanical properties and biocompatibility. Evidently, compared with other surface modification methods, such as grit blasting, porous metallic coatings, and plasma spray coatings (Le Guéhennec et al., 2007; Park et al., 2016; Orinaková et al., 2020), continuous processing of the SLS not only greatly saves time but also ensures the stability and repeatability of the scaffold performance.

## 5 CONCLUSION

EDM can be used for narrowing the energy density range of PCL sintering and guiding the direction of SLS process parameter optimization. Within our study, changing the SLS process parameters affects not only the porosity and mechanical properties but also SR so that it affects the biological properties of the scaffolds. Increasing the energy density or the laser power and scanning speed at the same energy density will smooth the surface of the scaffold so that the biological

performance of the scaffolds will be decreased. Biological properties should be an important factor to optimize the SLS process parameters of the PCL scaffolds for non-load-bearing bone repairing. In the future, SLS regional processing, like PCL, will be a necessity when making bone scaffolds with gradient performance so that further advantages of SLS will be presented.

## DATA AVAILABILITY STATEMENT

The raw data supporting the conclusion of this article will be made available by the authors, without undue reservation.

## AUTHOR CONTRIBUTIONS

JuW and JiW conceived the ideas and directed the work. JH integrally designed and carried out the study. FC and YZ

participated in the cell culture. YS and ZL performed the scaffold mechanics performance testing. ZZ and LZ were involved in the result discussion.

## FUNDING

This work was supported by the grants from the Hefei Institutes of Physical Science Director's Fund (Grant No. YZJJZX202014 to JuW) and USTC Innovation and Entrepreneurship Fund for Graduate Students (Grant No. WK5290000002 to JH). A portion of this work was supported by the High Magnetic Field Laboratory of Anhui Province.

## SUPPLEMENTARY MATERIAL

The Supplementary Material for this article can be found online at: <https://www.frontiersin.org/articles/10.3389/fbioe.2022.888267/full#supplementary-material>

## REFERENCES

- Bachle, M., and Kohal, R. J. (2004). A Systematic Review of the Influence of Different Titanium Surfaces on Proliferation, Differentiation and Protein Synthesis of Osteoblast-like MG63 Cells. *Clin. Oral Implants Res.* 15, 683–692. doi:10.1111/j.1600-0501.2004.01054.x
- Beal, V. E., Paggi, R. A., Salmoria, G. V., and Lago, A. (2009). Statistical Evaluation of Laser Energy Density Effect on Mechanical Properties of Polyamide Parts Manufactured by Selective Laser Sintering. *J. Appl. Polym. Sci.* 113, 2910–2919. doi:10.1002/app.30329
- Berretta, S., Evans, K. E., and Ghita, O. R. (2016). Predicting Processing Parameters in High Temperature Laser Sintering (HT-LS) from Powder Properties. *Mater. Des.* 105, 301–314. doi:10.1016/j.matdes.2016.04.097
- Bobbert, F. S. L., Lietaert, K., Eftekhari, A. A., Pouran, B., Ahmadi, S. M., Weinans, H., et al. (2017). Additively Manufactured Metallic Porous Biomaterials Based on Minimal Surfaces: A Unique Combination of Topological, Mechanical, and Mass Transport Properties. *Acta Biomater.* 53, 572–584. doi:10.1016/j.actbio.2017.02.024
- Borsari, V., Giavaresi, G., Fini, M., Torricelli, P., Salito, A., Chiesa, R., et al. (2005). Physical Characterization of Different-Roughness Titanium Surfaces, with and without Hydroxyapatite Coating, and Their Effect on Human Osteoblast-like Cells. *J. Biomed. Mat. Res.* 75, 359–368. doi:10.1002/jbm.b.30313
- Czelusniak, T., and Amorim, F. L. (2020). Influence of Energy Density on Selective Laser Sintering of Carbon Fiber-Reinforced PA12. *Int. J. Adv. Manuf. Technol.* 111, 2361–2376. doi:10.1007/s00170-020-06261-2
- Doyle, H., Lohfeld, S., and McHugh, P. (2015). Evaluating the Effect of Increasing Ceramic Content on the Mechanical Properties, Material Microstructure and Degradation of Selective Laser Sintered Polycaprolactone/ $\beta$ -Tricalcium Phosphate Materials. *Med. Eng. Phys.* 37, 767–776. doi:10.1016/j.medengphys.2015.05.009
- Du, Y., Liu, H., Yang, Q., Wang, S., Wang, J., Ma, J., et al. (2017). Selective Laser Sintering Scaffold with Hierarchical Architecture and Gradient Composition for Osteochondral Repair in Rabbits. *Biomaterials* 137, 37–48. doi:10.1016/j.biomaterials.2017.05.021
- Du, X., Dehghani, M., Alsaadi, N., Nejad, M. G., Saber-Samandari, S., Toghraie, D., et al. (2022). A Femoral Shape Porous Scaffold Bio-Nanocomposite Fabricated Using 3D Printing and Freeze-Drying Technique for Orthopedic Application. *Mater. Chem. Phys.* 275, 125302. doi:10.1016/j.matchemphys.2021.125302
- Duan, B., and Wang, M. (2011). Selective Laser Sintering and its Application in Biomedical Engineering. *MRS Bull.* 36, 998–1005. doi:10.1557/mrs.2011.270
- Farazin, A., Aghadavoudi, F., Motifard, M., Saber-Samandari, S., and Khandan, A. (2021). Nanostructure, Molecular Dynamics Simulation and Mechanical Performance of PCL Membranes Reinforced with Antibacterial Nanoparticles. *J. Appl. Comput. Mech.* 7, 1907–1915.
- Franco, A., Lanzetta, M., and Romoli, L. (2010). Experimental Analysis of Selective Laser Sintering of Polyamide Powders: An Energy Perspective. *J. Clean. Prod.* 18, 1722–1730. doi:10.1016/j.jclepro.2010.07.018
- Gibson, I., and Shi, D. (1997). Material Properties and Fabrication Parameters in Selective Laser Sintering Process. *Rapid Prototyp. J.* 3, 129–136. doi:10.1108/13552549710191836
- Hajiali, F., Tajbakhsh, S., and Shojaei, A. (2018). Fabrication and Properties of Polycaprolactone Composites Containing Calcium Phosphate-Based Ceramics and Bioactive Glasses in Bone Tissue Engineering: A Review. *Polym. Rev.* 58, 164–207. doi:10.1080/15583724.2017.1332640
- Ho, H., and Gibson, I. (2000). "Effects of Energy Density on Bonus Z, Surface Roughness and Warp Age of Selective Laser Sintered Polycarbonate," *The 8th International Conference on Rapid Prototyping* (Hong Kong: The University of Hong Kong), 99–103.
- Ho, H. C. H., Gibson, I., and Cheung, W. L. (1999). Effects of Energy Density on Morphology and Properties of Selective Laser Sintered Polycarbonate. *J. Mater. Process. Technol.* 89–90, 204–210. doi:10.1016/s0924-0136(99)00007-2
- Hulbert, S. F., Klawitter, J. J., and Leonard, R. B. (1971). *Compatibility of Bioceramics with the Physiological Environment*. Berlin, Germany: Springer US.
- Jeon, H., Lee, H., and Kim, G. (2014). A Surface-Modified Poly( $\epsilon$ -Caprolactone) Scaffold Comprising Variable Nanosized Surface-Roughness Using a Plasma Treatment. *Tissue Eng. Part C. Methods* 20, 951–963. doi:10.1089/ten.tec.2013.0701
- Kim, Y., and Kim, G. (2015). Highly Roughened Polycaprolactone Surfaces Using Oxygen Plasma-Etching and *In Vitro* Mineralization for Bone Tissue Regeneration: Fabrication, Characterization, and Cellular Activities. *Colloids Surfaces B Biointerfaces* 125, 181–189. doi:10.1016/j.colsurfb.2014.11.033
- Kim, H.-K., Jang, J.-W., and Lee, C.-H. (2004). Surface Modification of Implant Materials and its Effect on Attachment and Proliferation of Bone Cells. *J. Mater. Sci. Mater. Med.* 15, 825–830. doi:10.1023/b:jmsm.0000032824.62866.a1
- Kim, Y., Lim, J. Y., Yang, G. H., Seo, J.-H., Ryu, H.-S., and Kim, G. (2019). 3D-printed PCL/bioglass (BGS-7) Composite Scaffolds with High Toughness and Cell-Responses for Bone Tissue Regeneration. *J. Industrial Eng. Chem.* 79, 163–171. doi:10.1016/j.jiec.2019.06.027
- Le Guéhennec, L., Soueidan, A., Layrolle, P., and Amouriq, Y. (2007). Surface Treatments of Titanium Dental Implants for Rapid Osseointegration. *Dent. Mater.* 23, 844–854. doi:10.1016/j.dental.2006.06.025
- Lei, B., Shin, K.-H., Noh, D.-Y., Koh, Y.-H., Choi, W.-Y., and Kim, H.-E. (2012). Bioactive Glass Microspheres as Reinforcement for Improving the Mechanical



- Properties and Biological Performance of Poly( $\epsilon$ -Caprolactone) Polymer for Bone Tissue Regeneration. *J. Biomed. Mat. Res.* 100, 967–975. doi:10.1002/jbm.b.32659
- Munir, N., and Callanan, A. (2018). Novel Phase Separated Polycaprolactone/collagen Scaffolds for Cartilage Tissue Engineering. *Biomed. Mat.* 13, 051001. doi:10.1088/1748-605x/aac91f
- Mustafa, K., Wroblewski, J., Lopez, B. S., Wennerberg, A., Hultenby, K., and Arvidson, K. (2001). Determining Optimal Surface Roughness of TiO<sub>2</sub>blasted Titanium Implant Material for Attachment, Proliferation and Differentiation of Cells Derived from Human Mandibular Alveolar Bone. *Clin. Oral Implants Res.* 12, 515–525. doi:10.1034/j.1600-0501.2001.120513.x
- Navaei, T., Milan, P. B., Samadikuchaksaraei, A., Davari, H. R., Hardy, J. G., and Mozafari, M. (2021). Design and Fabrication of Polycaprolactone/gelatin Composite Scaffolds for Diaphragmatic Muscle Reconstruction. *J. Tissue Eng. Regen. Med.* 15, 78–87. doi:10.1002/term.3151
- Nelson, J. C. (1993). *Selective Laser Sintering: A Definition of the Process and an Empirical Sintering Model*. US: University of Texas at Austin.
- Ngandu Mpoyi, E., Cantini, M., Reynolds, P. M., Gadegaard, N., Dalby, M. J., and Salmerón-Sánchez, M. (2016). Protein Adsorption as a Key Mediator in the Nanotopographical Control of Cell Behavior. *ACS Nano* 10, 6638–6647. doi:10.1021/acsnano.6b01649
- Orinaková, R., Gorejová, R., Orságová Králová, Z., and Orinak, A. (2020). Surface Modifications of Biodegradable Metallic Foams for Medical Applications. *Coatings* 10, 819. doi:10.3390/coatings10090819
- Park, Y. O., Myung, S. W., Kook, M. S., Jung, S. C., Kim, B. H., and Kim, B. (2016). Cell Proliferation on Macro/Nano Surface Structure and Collagen Immobilization of 3D Polycaprolactone Scaffolds. *J. Nanosci. Nanotechnol.* 16, 1415–1419. doi:10.1166/jnn.2016.11920
- Partee, B., Hollister, S. J., and Das, S. (2006). Selective Laser Sintering Process Optimization for Layered Manufacturing of CAPA 6501 Polycaprolactone Bone Tissue Engineering Scaffolds. *J. Manuf. Sci. Eng. Trans. ASME.* 128, 531–540. doi:10.1115/1.2162589
- Sachdeva, A., Singh, S., and Sharma, V. S. (2013). Investigating Surface Roughness of Parts Produced by SLS Process. *Int. J. Adv. Manuf. Technol.* 64, 1505–1516. doi:10.1007/s00170-012-4118-z
- Shi, Y., Li, Z., Sun, H., Huang, S., and Zeng, F. (2016). Effect of the Properties of the Polymer Materials on the Quality of Selective Laser Sintering Parts. *Proc. Institution Mech. Eng. Part L J. Mater. Des. Appl.* 218, 247–252. doi:10.1177/146442070421800308
- Sudarmadji, N., Tan, J. Y., Leong, K. F., Chua, C. K., and Loh, Y. T. (2011). Investigation of the Mechanical Properties and Porosity Relationships in Selective Laser-Sintered Polyhedral for Functionally Graded Scaffolds. *Acta Biomater.* 7, 530–537. doi:10.1016/j.actbio.2010.09.024
- Tortorici, M., Gayer, C., Torchio, A., Cho, S., Schleifenbaum, J. H., and Petersen, A. (2021). Inner Strut Morphology Is the Key Parameter in Producing Highly Porous and Mechanically Stable Poly( $\epsilon$ -Caprolactone) Scaffolds via Selective Laser Sintering. *Mater. Sci. Eng. C* 123, 111986. doi:10.1016/j.msec.2021.111986
- Van Bael, S., Desmet, T., Chai, Y. C., Pyka, G., Dubruel, P., Kruth, J.-P., et al. (2013). *In Vitro* cell-biological Performance and Structural Characterization of Selective Laser Sintered and Plasma Surface Functionalized Polycaprolactone Scaffolds for Bone Regeneration. *Mater. Sci. Eng. C* 33, 3404–3412. doi:10.1016/j.msec.2013.04.024
- Williams, J. M., Adewunmi, A., Schek, R. M., Flanagan, C. L., Krebsbach, P. H., Feinberg, S. E., et al. (2005). Bone Tissue Engineering Using Polycaprolactone Scaffolds Fabricated via Selective Laser Sintering. *Biomaterials* 26, 4817–4827. doi:10.1016/j.biomaterials.2004.11.057
- Yeong, W. Y., Sudarmadji, N., Yu, H. Y., Chua, C. K., Leong, K. F., Venkatraman, S. S., et al. (2010). Porous Polycaprolactone Scaffold for Cardiac Tissue Engineering Fabricated by Selective Laser Sintering. *Acta Biomater.* 6, 2028–2034. doi:10.1016/j.actbio.2009.12.033
- Yuan, S., Shen, F., Bai, J., Chua, C. K., Wei, J., and Zhou, K. (2017). 3D Soft Auxetic Lattice Structures Fabricated by Selective Laser Sintering: TPU Powder Evaluation and Process Optimization. *Mater. Des.* 120, 317–327. doi:10.1016/j.matdes.2017.01.098

**Conflict of Interest:** The authors declare that the research was conducted in the absence of any commercial or financial relationships that could be construed as a potential conflict of interest.

**Publisher's Note:** All claims expressed in this article are solely those of the authors and do not necessarily represent those of their affiliated organizations or those of the publisher, the editors, and the reviewers. Any product that may be evaluated in this article or claim that may be made by its manufacturer is not guaranteed or endorsed by the publisher.

Copyright © 2022 Han, Li, Sun, Cheng, Zhu, Zhang, Zhang, Wu and Wang. This is an open-access article distributed under the terms of the Creative Commons Attribution License (CC BY). The use, distribution or reproduction in other forums is permitted, provided the original author(s) and the copyright owner(s) are credited and that the original publication in this journal is cited, in accordance with accepted academic practice. No use, distribution or reproduction is permitted which does not comply with these terms.

# Advantages of publishing in Frontiers



## OPEN ACCESS

Articles are free to read  
for greatest visibility  
and readership



## FAST PUBLICATION

Around 90 days  
from submission  
to decision



## HIGH QUALITY PEER-REVIEW

Rigorous, collaborative,  
and constructive  
peer-review



## TRANSPARENT PEER-REVIEW

Editors and reviewers  
acknowledged by name  
on published articles

## Frontiers

Avenue du Tribunal-Fédéral 34  
1005 Lausanne | Switzerland

Visit us: [www.frontiersin.org](http://www.frontiersin.org)

Contact us: [frontiersin.org/about/contact](http://frontiersin.org/about/contact)



## REPRODUCIBILITY OF RESEARCH

Support open data  
and methods to enhance  
research reproducibility



## DIGITAL PUBLISHING

Articles designed  
for optimal readership  
across devices



## FOLLOW US

@frontiersin



## IMPACT METRICS

Advanced article metrics  
track visibility across  
digital media



## EXTENSIVE PROMOTION

Marketing  
and promotion  
of impactful research



## LOOP RESEARCH NETWORK

Our network  
increases your  
article's readership